Small Molecules and Porous Silica Nanoparticle Encapsulated Gd(III) and Mn(II) Complexes as MRI Contrast Agents

A Dissertation Submitted in Partial Fulfilment of the Requirement for the Degree of Doctor of Philosophy at IIT Guwahati

by

Riya Mallik

Roll No. 186122030

Department of Chemistry
Indian Institute of Technology Guwahati
Guwahati–781039, Assam
India

November 2023

To my loving PARENTS

भारतीय प्रौद्योगिकी संस्थान गुवाहाटी
Indian Institute of Technology Guwahati

"Determination is the power that sees us through all our frustrations and obstacles; it helps us in building our willpower which is the very basis of success"

—Dr. A. P. J. Abdul Kalam

भारतीय प्रौद्योगिकी संस्थान गुवाहाटी
Indian Institute of Technology Guwahati

Indian Institute of Technology Guwahati

Department of Chemistry

Declaration

I do hereby declare that research work embodied in this thesis entitled "***Small Molecules and Porous Silica Nanoparticle Encapsulated Gd(III) and Mn(II) Complexes as MRI Contrast Agents***" has been carried out by me under the supervision of Prof. Chandan Mukherjee, Department of Chemistry, Indian Institute of Technology Guwahati, Assam–781039, India. The research works have been carried out in the period of August, 2018 to October, 2023.

In keeping with the general practice of reporting scientific observations, due acknowledgements have been made wherever the work described is based on the finding of other investigators.

Riya Mallik

IIT Guwahati — Riya Mallik

November, 2023 — Roll No. 186122030

भारतीय प्रौद्योगिकी संस्थान गुवाहाटी
Indian Institute of Technology Guwahati

Prof. Chandan Mukherjee
Professor
Department of Chemistry
Indian Institute of Technology Guwahati
Guwahati, 781039, Assam, India

Phone no. +91-361-258-2327(O)
Fax no. +91-361-258-2349
Email: cmukherjee@iitg.ac.in

CERTIFICATE

This is to certify that the research work presented in this thesis entitled "***Small Molecules and Porous Silica Nanoparticle Encapsulated Gd(III) and Mn(II) Complexes as MRI Contrast Agents***" is an authentic record of the results obtained from the research work carried out by **Miss. Riya Mallik** (**Roll No. 186122030**) under my supervision in Department of Chemistry, Indian Institute of Technology Guwahati, India. This work is original and has not been submitted elsewhere for a degree or award.

Chandan Mukherjee

Place: IIT Guwahati
Date: 08/05/2024

Prof. Chandan Mukherjee
(Thesis Supervisor)

भारतीय प्रौद्योगिकी संस्थान गुवाहाटी
Indian Institute of Technology Guwahati

Acknowledgment

My deepest gratitude and appreciation to all the people who have helped, in one way or the other, during my journey to complete this thesis work. I am extremely privileged to have their help, support, and inspiration all along. It required a lot of effort from each individual involved with me during this path and I would like to thank them all.

- First and foremost, I would like to express my sincere gratitude to my supervisor **Prof. Chandan Mukherjee** for his guidance and inspiration during the course of my research work. I am indebted to him for introducing me to this research area of coordination chemistry. I have been enlightened by his wide knowledge and logical way of thinking. This thesis would not have been possible without his assistance. His encouragement has given me so much confidence. I especially thank him for spending numerous hours on my project, along with getting this thesis through its final stages.
- I am highly indebted to "**Indian Institute of Technology Guwahati**" for giving me the opportunity to pursue my research work and providing the doctoral fellowship.
- I would like to thank my doctoral committee members **Prof. Subhendu Sekhar Bag** (IIT Guwahati), **Prof. Bhubaneswar Mandal** (IIT Guwahati), and **Dr. Shyam Prosad Biswas** (IIT Guwahati) for their valuable suggestions during progress my research work.
- I would like to express my sincere thanks to **Dr. Hari Mohan Saini** (Maharshi Dayanand University) for generously sharing his time and ideas for biological studies. I am highly grateful to him for giving me the opportunity to work in his laboratory and for providing me with a chance to learn animal handling along with further *in vivo* studies.
- I am obliged to **Prof. S Senthil Kumaran** (All India Institute of Medical Sciences, New Delhi) for allowing me to utilize the lab and instrumental facilities to obtain *in vivo* MRI.
- I am highly thankful to the whole team of radiology and imaging department from **GNRC Hospital**, and **Primus Diagnosis**, Guwahati for helping me during MRI imaging at the clinical imager.
- I am beholden to **Dr. Amrit Sarmah** (Institute of Organic Chemistry and Biochemistry, Czech Republic) for theoretical measurement.
- I am indebted to **Muktashree Saha** for her constant help and participation throughout the research work.

- I would like to acknowledge **SAIF** (IIT Bombay), **CIF** (IIT Guwahati), and the **Department of Chemistry** (IIT Guwahati) for availing the instrument facilities.
- I am thankful to **Dr. Babulal Das**, **Mr. Imdadul Islam**, **Mr. Aniruddha Gogoi**, **Mr. Diganta Kumar Hira**, **Dr. Kulakamal Senapati**, and **Mr. Kh Kesho Singh** for their help in the instrumental laboratory.
- I take this opportunity to thank all my extraordinary former and present lab mates for their kind cooperation and friendship. I am grateful to my seniors, **Dr. Mahmuda Khannam** and **Dr. Prasenjit Sarkar** for helping me a lot to pursue the research work. I am very happy to cherish my time with my juniors; **Anurupa Naskar**, **Sumana Nath**, **Rohit Kumar**, **Priya Gurung**, **Deepak**, and **Mitali Machiwal**. I am deeply thankful to **Geetanjali Deka**, **Chinmay Jana**, **Aditi Das**, **Ritwik Adhikari**, **Ismile Sk**., and **Rahul Halder** for sharing this wonderful bond. Their advice, well wishes, encouragement, and constant support meant a lot to me during this exhausting journey.
- I would like to reveal my deepest gratitude to my teachers; **Mr. Sk. Farukh**, **Mr. Nazim Mallick**, **Mr. Kamal Koska Roy**, **Mrs. Shampa Koley**, **Dr. Ranajit Dey**, **Dr. Harideb Sil**, and **Prof. Alak Kumar Ghosh** for their encouragement, advices and trust throughout my entire educational career. They have supported and guided me to the fullest extent.
- I am thankful to my friends and cousins; **Tanushree**, **Tania**, **Debashree**, **Soma**, **Chandan**, **Meenakshi**, **Rituporna**, **Mrinmoy**, **Shivani**, **Subrata**, **Jayanta**, **Sumanta**, **Vandna** di **Bhargabi** di, **Mampi** didi, **Santu** dada, **Kanu** da, and **Amitava** da, for providing a comfortable and entertaining atmosphere. I am especially grateful to **Sandip** da for his constant help, motivation, and mental support throughout the journey.
- I am obligated to all my family members who have helped by all possible means. I especially thank **Tapan** Kaku and **Ashima** Kakima for their understanding and well wishes.
- Finally, yet most importantly, I am utterly grateful to my **Maa** (**Mrs. Namita Mallik**) and **Bapi** (**Mr. Narayan Chandra Mallik**) for their unconditional love, blessing, support, and unbreakable trust throughout my entire life. It is an eternal truth that any kind of words of gratitude will fall short of their patience, dedication, and sacrifices. Thank you both for always believing in me and giving me the strength to chase my dreams.
- Last but not the least, I would like to thank and pay respect to **Almighty God** for blessing me and always being on my side.

Riya Mallik

Thesis Title:

"*Small Molecules and Porous Silica Nanoparticle Encapsulated Gd(III) and Mn(II) Complexes as MRI Contrast Agents*"

Date of Submission of Thesis:

30-11-2023

List of Patents and Publications:

1. **Indian Patent** filed on 28 August, 2021, under Application No. 202131039091 entitled "STABLE AQUATED Mn(II) COMPLEX AND ITS ENCAPSULATED POROUS SILICA NANOPARTICLE AS T_1-T_2 MRI CONTRAST AGENT" (Chandan Mukherjee and **Riya Mallik**).

2. **Riya Mallik**, Muktashree Saha and Chandan Mukherjee*, "Porous Silica Nanospheres with a Confined Mono(aquated) Mn(II)-Complex: A Potential T_1−T_2 Dual Contrast Agent for Magnetic Resonance Imaging", ***ACS Appl. Bio Mater.*, 2021, 4, 8356−8367**.

3. **Riya Mallik**,‡ Mahmuda Khannam,‡ Muktashree Saha, Sivani Marandi, Sachin Kumar and Chandan Mukherjee*, "Electrostatic Confinement of Aquated Monocationic Gd(III) Complex-Molecules within the Inner Core of Porous Silica Nanoparticles Endows a Highly Efficient T_1 Contrast Agent for Magnetic Resonance Imaging", ***Dalton Trans.*, 2022, 51, 14138**.

4. **Riya Mallik**, Muktashree Saha, Vandna Singh, Hari Mohan, S. Senthil Kumaran and Chandan Mukherjee*, "Mn(II) Complex Impregnated Porous Silica Nanoparticles as Zn(II)- Responsive "Smart" MRI Contrast Agent for Pancreas Imaging", ***J. Mater. Chem. B*, 2023, 11, 8251-8261**.

5. **Riya Mallik**, Muktashree Saha, Vandna Singh, Hari Mohan, S. Senthil Kumaran, Amrit Sharmah and Chandan Mukherjee*, "A Bis(Aquated) Mn(II)-Based MRI Contrast Agent with a Rigid Hydroquinazoline Unit: Synthesis, Characterization and *in vivo* MR Imaging Study" ***ACS Appl. Bio Mater.*, 2024, 7, 1831–1841**.

6. **Riya Mallik**, Muktashree Saha, Basab Ghosh, Nisha Chauhan, Hari Mohan, S. Senthil Kumaran and Chandan Mukherjee*, "Folate Receptor Targeting Mn(II) Complex Encapsulated Porous Silica Nanoparticle as an MRI Contrast Agent for Early-State Detection of Cancer", ***Small,*** **Manuscript Accepted**.

7. Divya Rajendran, **Riya Mallik**, Chandan Mukherjee, Senthil Kumaran, Sellamuthu Anbu, Elangovan Natarajan and Jebasingh Bhagavathsingh*, "Synthesis, Characterisation, and Relaxometry Validations of Gd(III)-DO3NN Type Complex Using Tri-Followed by Mono-Conjugation Approach", ***ChemBioChem,*** **Manuscript submitted**.

List of Symposium/Conferences:

- **Recent Trends in Chemical Science** (RTCS-2021), Oral presentation, Indian Chemical Society, 21st–24th December 2021 at Kolkata, India, [Excellence Award (Oral)].
- **Frontiers in Chemical Sciences** (FICS-2022), Poster Presentation, 2nd–4th December 2022, Department of Chemistry, at IIT Guwahati, Assam, India, [Best Poster Award].
- **Research and Industrial Conclave** (RIC-2023), Oral presentation, 14th–16th May 2023, at IIT Guwahati, Assam, India.
- **Modern Trends in Inorganic Chemistry** (MTIC XX), Poster presentation, 14th -17th December, 2023, Division of Chemical Sciences, Indian Institute of Science (IISc), Bangalore, India, [Best Poster Award].
- **6th Symposium on Advanced Biological Inorganic Chemistry** (SABIC-2024), Poster presentation, 07th -11th January, Tata Institute of Fundamental Research (TIFR) and Indian Association for the Cultivation of Science (IACS), Kolkata, India.

Doctoral Committee:

Prof. Subhendu Shekar Bag (Chairman)

Prof. Bhubaneswar Mandal (Member)

Dr. Shyam Prosad Biswas (Member)

Prof. Chandan Mukherjee (Supervisor)

Abstract

भारतीय प्रौद्योगिकी संस्थान गुवाहाटी
Indian Institute of Technology Guwahati

Chapter I

General Introduction and Motivation

MRI is a powerful and non-invasive imaging modality that gives useful three-dimensional images of soft tissues. It measures ^{1}H-NMR signals of *in vivo* water molecules. Depending on the variation of longitudinal ($R_1 = 1/T_1$) and transverse ($R_2 = 1/T_2$) relaxation rates of the water molecules in different tissues, spatial images are constructed. However, this technique is quite less sensitive, and often a contrast agent (CA) is administered prior to the imaging to have conspicuous images in a relatively shorter time span. Contrast agents (CAs) are paramagnetic (Gd^{III}, Mn^{II}, and Fe^{III}-based) substances that shorten the longitudinal (T_1) and transverse (T_2) relaxation times of the water protons in the vicinity of their locations. The effectiveness of a contrast agent is generally compared in terms of relaxivity {$(1/T_{1,2})_{obs} = (1/T_{1,2})_d + r_{1,2}$[M], [M] in mM} and this value is affected by the number of coordinated water molecules (q) and overall correlation rotation time (τ_R) of the paramagnetic unit. A brighter image can be produced by diminishing the T_1 relaxation time, while, the shortening of the T_2 relaxation time engenders a darker image. Image darkening effect, imparted by the T_2-weighted CAs (*e.g.*, SPIONs), often mislead the diagnosis. Hence, designing novel T_1-weighted or T_1-T_2 dual-mode CAs has remained a priority.

The recent reports stipulated the link of free Gd(III) ions with nephrogenic systemic fibrosis (NSF) in patients with renal failure, and long-term accumulation affecting the central nervous system as well, restricting its use to some extent. Nonetheless, more biogenic Mn(II) ions with five unpaired electrons in the high-spin state have emerged as a promising alternative to the Gd(III)-based contrast agents (GCBAs). Meanwhile, lacking crystal field stabilization energy (CFSE), Mn(II)-chelates are quite unstable. Retention of high concentrations of free Mn(II)-ions inside the body sporadically leads to 'Manganism'. Hence an efficient and rigid ligand framework is required for complexation that can minimize metal leaching during MRI scans. Consequently, the development of low molecular weight, slowly rotating paramagnetic units with a high spin value (S), and adequate inner sphere water-coordination sites (q) have been the primary interest.

Increasing the hydration state obviously increases relaxivity, but it ends up lowering the thermodynamic and kinetic stability, both of which are extremely crucial factors. Hence, reducing the tumbling rate is a better pathway to increase the relaxation rates. In this context, porous silica

nanoparticles with large surface area and tunable pore volume can be exploited judicially to make target-specific, less toxic, and stable contrast agents. On this note, designing rigid Gd(III)-/Mn(II)-chelates and nanocontrasts that can effectively satisfy the requirements for high relaxivity and minimize the metal leaching issue, altogether, has drawn attention. Despite rigorous studies, there is a wide chance for further optimization of various factors like hydration number, water exchange rate, rigidity, dissociation kinetics, retention time, *etc*., while designing novel complexes and nanoparticle-based contrast agents to achieve efficient contrast enhancement in MRI.

Chapter II

Rigid Hydroquinazoline Appended Bis-Aquated Mn(II)-Complex as a Potential T_1-Contrast Agent for MRI

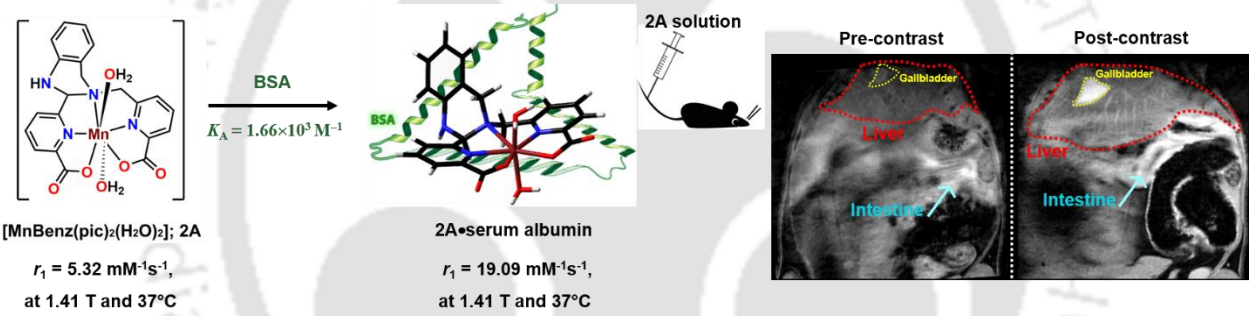

Figure 1. Schematic representation of the interaction between **2A** and serum albumin protein, and the corresponding 10 min post-contrast signal enhancement in the liver, gallbladder, and intestine.

Considering the hydration, lipophilicity, stability, and rigidity factors for designing a novel acyclic Mn(II)-complex, a new pentadentate ligand **Li_2[BenzPic$_2$]** comprised of two picolinate moieties and a rigid hydroquinazoline unit has been synthesized. The DFT-optimized structure and concentration-dependent ^{1}H NMR chemical shifts of the corresponding Mn(II)-complex (**2A**) suggested a hepta-coordinated geometry with two hydration numbers (q = 2). The complex exhibited logK_{cond} = 11.62, at pH ~ 7.4, which is 0.6 log$K$ units higher than that for the mono-aqated MnEDTA complex. Simultaneously, **2A** showed impressive relaxometric properties with r_1 = 6.77 mM^{-1}s^{-1} at 25 °C and 5.32 mM^{-1}s^{-1} at 37 °C; r_2 = 23.94 mM^{-1}s^{-1} at 25 °C and 19.20 mM^{-1}s^{-1} at 37 °C, 1.41 T and pH ~ 7.4; higher than several bis-aquated Mn(II)-based complexes

reported earlier. The relaxivity value further escalated to 19.09 $mM^{-1}s^{-1}$ in the presence of 0.67 mM BSA at 37 °C, indicating a ~360 % amplification in the longitudinal relaxivity. A substantial interaction between the protein and **2A** was anticipated and it was investigated by the Proton Relaxation Enhancement (PRE) experiment. Assuming one independent binding site of the protein moiety for the complex, *i.e.*, $n = 1$, the relaxivity of the bound complex (r_1^b) was found to be 27.62 $mM^{-1}s^{-1}$ and albumin association constant $K_A = 1.66\times10^3\ M^{-1}$.

The complex was impervious to physiological anions (bicarbonates, biphosphates, and citrates) and protons, as a negligible change in relaxivity value was observed when challenged with high equivalents of these ions. The kinetic inertness of complex **2A** [pseudo-first-order rate constant for the transmetallation reaction challenged by 10 equiv. Zn(II) ion, $k = 1.04 \times 10^{-2}\ s^{-1}$; at pH 6.5] was about 8.5 times higher than that of $[Mn(EDTA)(OH_2)]^{2-}$ ($k = 8.86 \times 10^{-2}\ s^{-1}$) and almost same as that of $[Gd(DTPA)(OH_2)]^{2-}$ ($k = 1.16 \times 10^{-2}\ s^{-1}$). Moreover, the complex showed 5 times higher kinetic stability ($k = 2.13 \times 10^{-3}\ s^{-1}$) at the physiological conditions, when kinetic studies were done by following the time profile of R_2 value of **2A** solution, challenged by 10 fold excess of Zn(II) ions in serum albumin (0.67 mM), in 0.15 M NaCl, pH 6.5, and 25 °C. Hence, a higher kinetic inertness has been achieved for complex **2A** through the rigidified ligand framework despite having two inner-sphere water molecules.

The contrast ability and serum binding contrast enhancement property of the synthesized complex were verified by recording phantom images of complex **2A** in water and in the presence of BSA, at 25 °C and 7 T. A 43 % signal enhancement was achieved by aqueous 0.5 mM complex **2A** solution, which subsequently increased by another 57% with the addition of 0.67 mM BSA.

The synthesized complex was found to be biocompatible and hence employed for *in vivo* imaging. Correspondingly, a healthy C57BL/6 mice was imaged at 7 T, before and after 0.08 mmol/kg intravenous administration of complex **2A** solution. An intense contrast enhancement in the gallbladder (~160 %) and kidneys (~110 %) was noticed after 10 minutes of the contrast agent application. Moreover, as reflected by serum protein association experiments for complex **2A**, the highly vascularized liver region corresponding to the long retention of the contrast material in the blood vessels was realized.

Chapter III

Non-Covalent Confinement of Gd(III)-/Mn(II)-Complex in Porous Silica Nanosphere Rendering Nanocontrast for MRI

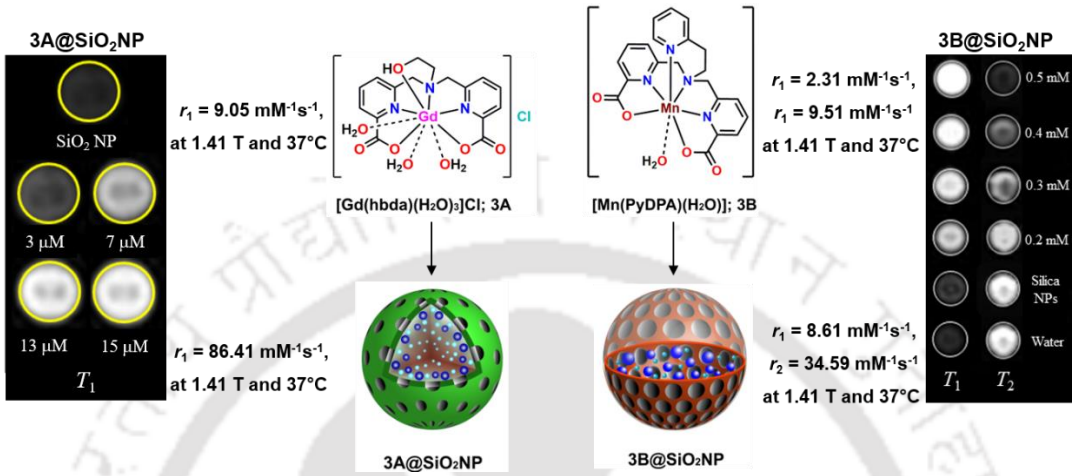

Figure 2. Schematic representation of the incorporation of **3A** and **3B** complexes within the PSNs, and the subsequent increase in relaxivity and signal intensity values values.

Small molecules that are thoroughly investigated as contrast agents for MRI over the decade are mostly Gd(III) or Mn(II) based aquated complexes having moderate relaxivity value. They mostly suffered from low kinetic stability and toxic free metal ions leached out over time, leading to fatal diseases. As discussed in the introduction section, increasing the relaxivity value by reducing the tumbling rate within an applied magnetic field range of 0.5 to 1.5 T is a better alternative. Thus, the grafting of stable small complexes onto a nanosystem or confining the complexes within a nanosphere should serve the purpose, thereby protecting the paramagnetic core from scavenger ions. To pursue this objective, two novel thermodynamically stable complexes – mono-positive, tris(aquated) Gd(III)-complex {Complex **3A**, $[Gd(OH_2)_3(hbda)]^{1+}$} and neutral mono-aquated Mn(II)-complex {Complex **3B**, $[Mn(PyDPA)(OH_2)]^0$} has been non-covalently incorporated within porous silica nanoparticles (PSNs).

Electrostatic confinement of complex 3A: A Tris(aquated) Gd(III)-complex (**3A**) with high thermodynamic stability (pGd 18.5), was reproduced and was non-covalently incorporated within the porous silica nanosphere by reverse micelle mechanism forming **3A**@SiO_2NP. The morphology, presence of complex, and porous nature of the isolated nanoparticles were

investigated explicitly. The electrostatic entrapment and the geometrical confinement within the nanosphere decreased the motion of complex **3A** and resulted in ~ 9-fold enhancement in r_1 value compared to the untrapped complex molecules (the value increased to 86.41 $mM^{-1}s^{-1}$/ Gd(III) at 1.41 T, pH ~ 7.4, 37 °C). The efficiency of the **3A**@SiO_2 as a T_1-based MRI contrast agent was examined by recording phantom images. Concentration-dependent enhancement of relaxivity was visualized; efficient signal brightening was evidenced at a very small [Gd (III)] concentration of 15 μM. The biocompatibility of **3A**@SiO_2NP was further tested on HeLa, macrophages, RBC, and human plasma to ascertain its bio-applicability. Moreover, cellular uptake of the synthesized nanoparticles was visualized by FETEM images of treated HeLa cells, and also by fluorescence microscopy images of cells treated with Tb(III) congener of **3A**@SiO_2NP.

Non-covalent confinement of complex 3B: Ligand H_2PyDPA and its corresponding neutral, mono-aqauted Mn(II) complex (complex **3B)** was synthesized and characterized. Complex evidenced commendable thermodynamic stability with logK_{MnL} = 14.80(7) and pMn = 8.97. To increase relaxivity and impart stability, complex molecules were further incorporated inside porous silica nanoparticles by reverse microemulsion procedure. 14±2 nm sized spherical nanoparticles (**3B**@SiO_2NP) were obtained and were thoroughly characterized. The porous silica layer allowed to and fro- movement of water molecules across towards the core of the nanoparticle, but selectively prohibited the entrance of physiological ions (bicarbonates, biphosphates, citrates, Zn(II) and protons) that may affect the relaxivity of the paramagnetic complexes trapped inside. The synthesized **3B**@SiO_2 nanoparticles exhibited r_1 = 8.5 $mM^{-1}s^{-1}$ and r_2 = 33.2 $mM^{-1}s^{-1}$, at pH ~ 7.4, 1.41 T, and 25 °C, which was three-fold higher than the bare complex molecules. A significant increase in r_1 (24.76 $mM^{-1}s^{-1}$) and r_2 (63.96 $mM^{-1}s^{-1}$) in the presence of 0.67 mM BSA. Synthesized nanoparticles were found to be biocompatible when tested on the HeLa cell line (82% of cells were viable when treated with 200 mM suspension of **3B**@SiO_2NP). Cellular uptake was also visualized by recording FETEM images of **3B**@SiO_2NP-treated HeLa cells. Finally, phantom MR-imaging of **3B**@SiO_2NP established its use as a T_1-T_2 dual-mode MRI contrast agent.

Henceforth, the strategy demonstrated for confining acyclic ligand-based aquated Gd(III)- and Mn(II)-complex molecules within the biocompatible PSNs successfully enhanced the relaxivity and mitigated the leaching of free metal ions. Moreover, it helped to penetrate the cell membrane, thus widening the scope for judicious designing of cell-targeting contrast agents

Chapter IV

A Zn(II)-Responsive Mn(II)-Complex Confined Porous Silica Nanoparticles as "Smart" MRI CA for Pancreas Imaging

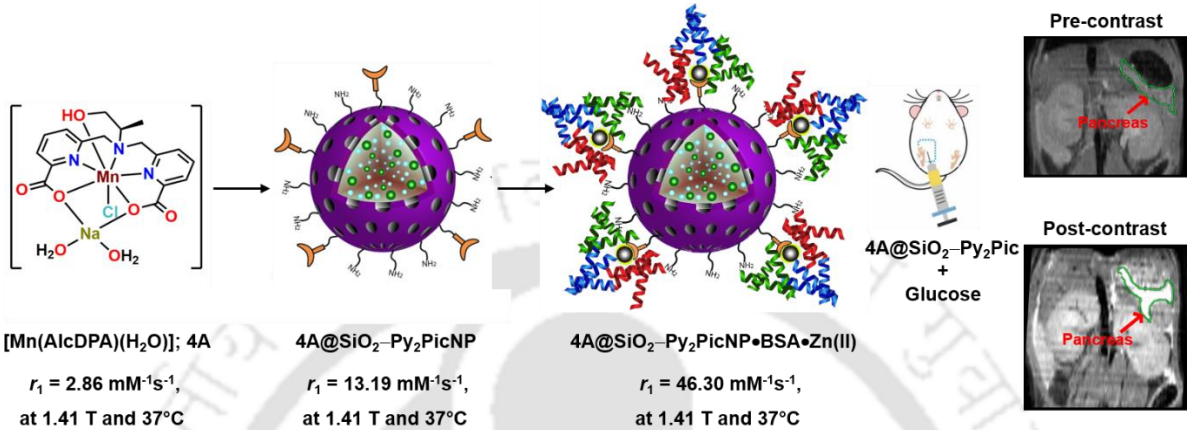

Figure 3. Illustration representing relaxivity along with signal intensity enhancement achieved by the confinement of complex **4A** and further association with serum albumin protein and Zn(II) ions.

Gd(III)-based commercially used MRI contrast agents are primarily nonspecific, and imparted signal enhancement solely due to the distribution of the contrast agent across the body. Hence, developing non-gadolinium-based organ-specific and bio-responsive contrast agents due to changes in pH, enzyme activity, temperature, and ion efflux has drawn prime attention for better diagnosis of a lesion and non-invasive pathology. The blood glucose level is a key factor controlling the normal functionality of the acinar and β-cells in the pancreas. The higher glucose level in the blood triggers the release of insulin, simultaneously increasing the concentration of Zn(II) ions in the extracellular space from 40 μM to 500 μM. Hence, Zn(II) ion concentration-dependent contrast enhancement as a whole or as "hot spots" would enlighten the pathological condition of the pancreas and/or the β-cells.

In this context, ligand H_2AlcDPA and corresponding neutral, mono-aquated Mn(II) complex (**4A**) was synthesized and the thermodynamic stability was elucidated to be logK_{MnL} = 15.06, with pMn = 9.18. Complex **4A** molecules were further impregnated within porous silica nanoparticles with amine functionalization on the surface, naming **4A**@SiO_2–NH_2, each of size ~ 14 nm. Afterward, the Zn(II)-selective HPy_2Pic ligand was linked with the amine units through

amide bonds to engender the surface-modified **4A**@SiO_2–Py_2PicNPs. A 4.6-fold enhancement in the longitudinal relaxivity (r_1) value from 2.86 $mM^{-1}s^{-1}$ (complex **4A**) to 13.19 $mM^{-1}s^{-1}$ (**4A**@SiO_2–Py_2Pic) was realized at 1.41 T, 37 °C, and pH ~ 7.4. Moreover, a 53 % increment in the relaxivity value to r_1 = 20.38 $mM^{-1}s^{-1}$ was accounted for in the presence of 0.6 mM BSA at the same experimental conditions, suggesting a considerable interaction between the nanoparticle and the negatively charged serum albumin protein to engender a slowly rotating binary system.

Unlike the **4A**@SiO_2–NH_2 nanoparticles, a discernible and gradual augmentation in r_1 relaxivity was noticed on the successive elevation in the concentration of Zn(II) ions in HEPES buffer in the case of **4A**@SiO_2–Py_2PicNPs, at pH 7.4, and the r_1 value reached to = 46.30 $mM^{-1}s^{-1}$ in the presence of 40 equivalent amounts of the zinc ion. Hence, the presence of the surface-bound Py_2Pic unit reinforced the ternary interaction of the nanoparticle with BSA in the presence of Zn(II) ions. Subsequent fluorescence quenching experiments consolidated the static nature of the interaction between the serum albumin protein and **4A**@SiO_2–Py_2PicNP in the presence of Zn(II) ions.

Moreover, **4A**@SiO_2–Py_2PicNP showed no alteration in the relaxivity (13.19 $mM^{-1}s^{-1}$) in the pH range 4-8 and in the presence of 50-folds of Mg(II), Ca(II), Zn(II) and Cu(II) ions or 200-fold excess of physiological anions, manifesting its stability and selectivity towards Zn(II) ions only in the presence of serum albumin. The *in vitro* contrast ability of **4A**@SiO_2–Py_2PicNP in the presence of BSA and Zn(II) ions was visualized by recording phantom images at 1.5 T and 25 °C.

Additionally, the biocompatibility of **4A**@SiO_2–Py_2PicNPs was examined on PC3 and HeLa cells and 80 % cell viability was realized at 150 μM concentration for both types of cells. Hereafter, post-contrast *in vivo* MR imaging was recorded on a batch of C57BL/6 mice at 7 T. The contrast enhancement became almost twice (ΔCNR ~ 100 %) in the pancreas compared to the pre-injected MR image in the presence of **4A**@SiO_2–Py_2PicNP after 1 hour of the bolus injection (NPs injected only). However, in the presence of glucose, a substantial contrast enhancement (ΔCNR ~ 138 %) was realized reinforcing the ternary interaction of the contrast agent with the secreted Zn(II) ions in the presence of HSA [**4A**@SiO_2–Py_2PicNPs•HSA•Zn(II)]. In a nutshell, we have reported a non-gadolinium-based Mn(II)-complex entrapped silica nanoparticles that can behave as a "smart" MRI contrast agent in the presence of Zn(II) ions.

Chapter V

Folate decorated Mn(II)-Complex Confined Porous Silica Nanoparticles as MRI Contrast Agent to Detect Cancer Cells

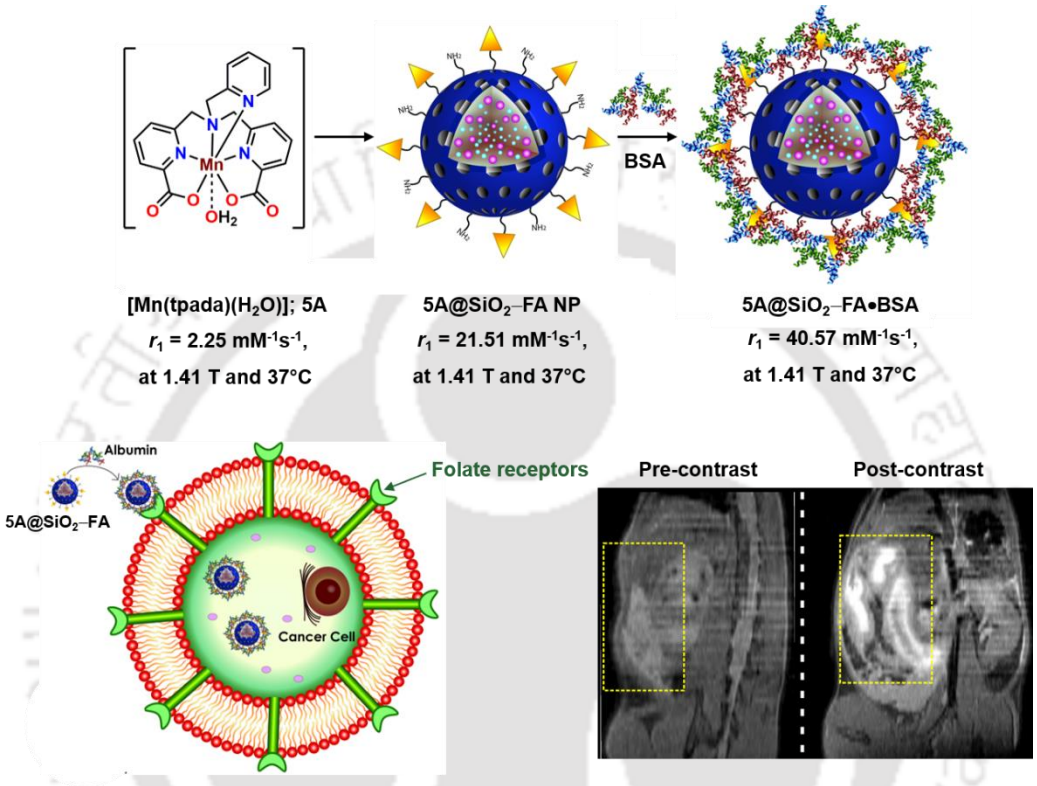

Figure 4. Schematic representation of relaxivity enhancement on the incorporation of complex **5A** inside folate functionalized PSNs and further association with serum albumin protein. Folate-mediated internalization of **5A**@SiO_2–FA NPs and corresponding *in vivo* cancer-cell detection is illustrated accordingly.

MRI being non-invasive, has become a prime molecular imaging modality to assess the initial development, location, and size of the tumour site. Commercial GCBAs are mostly extracellular and their usage has been restricted due to their link to renal toxicity. Consequently, there has been a profound urge to develop alternative non-gadolinium-based contrast agents for targeted tumour diagnosis. Manganese oxide-based nanocontrasts have exhibited improved sensitivity and hence are widely investigated for molecular imaging of cancer cells. Despite substantial improvements, relaxivity values for these systems are obtained to be lower than the Gd(III)-based agents.

Additionally, poor bioavailability and internal toxicity are some important drawbacks that severely impact their overall performance as potential *in vivo* contrast agents. Henceforth, there has been a large scope to develop a suitable Mn(II)-based nanoprobe that would render high relaxivity for efficient tracking of tumour cells at the initial stage.

In this circumstance, H_2tpada-based Mn(II)-complex, **5A**, was synthesized that exhibited high thermodynamic stability ($\log K_{MnL}$ = 14.67 and pMn = 8.80). **5A** molecules were thereafter incorporated inside amine functionalized porous silica nanoparticles forming **5**@SiO_2–NH_2NP of size 19.3 nm. Folic acid was further conjugated to the silica surface through amide linkage forming **5A**@SiO_2–FA NPs and characterized correspondingly. The finalized nanomaterial showed a longitudinal relaxivity value of 21.51 $mM^{-1}s^{-1}$, at pH ~ 7.4, 1.41 T, and 37 °C which improved to 40.97 $mM^{-1}s^{-1}$ in the presence of 4.5% (w/v) BSA (to replicate the plasma model). Huge plausible electrostatic and van der Waals interaction between nanoparticles and protein had been detected following changes in the overall ζ potential of the composite material from 16.4 mV (in the absence of BSA) to -11.7 mV (in the presence of BSA) and TGA plots of dried samples. Moreover, **5A**@SiO_2–FA showed negligible change in relaxivity when challenged with 200 equivalent excess physiological anions (biphosphate, bicarbonate, citrate, *etc*.) and 40 equivalent excess of Zn^{II} ions, reflecting high kinetic inertness of the developed material.

Metal concentration-dependent phantom signal intensity enhancement (at 1.5 T and 25 °C) and biocompatibility studies guaranteed the formation of a potential MRI contrast agent. Furthermore, cell uptake studies of FITC-labelled **5A**@SiO_2–FA nanoparticles, conducted on the HeLa and HEK293 cell line, demonstrated the rapid internalization of the nanoparticles within an hour. Hence, the inclusion of folate groups in the nanosystem utilized the folate receptor-mediated pathway to enter the intracellular scape. This effect was further authenticated by injecting the **5A**@SiO_2–FA suspensions in cancer-infected C57BL/6 mice. MR images, recorded after 30 minutes of administration of the **5A**@SiO_2–FA NP suspension, demonstrated a ~100% contrast enhancement in the region where the cancer cells were accumulated, normalized to that of the control mice (healthy mice, injected with the same dosage of **5A**@SiO_2–FA NPs). A slight drop in signal intensity was observed by 1 h and the significant contrast was evident till 4 h of contrast administration, validating a longer retention time for the synthesized folate-modified nanosystem.

भारतीय प्रौद्योगिकी संस्थान गुवाहाटी
Indian Institute of Technology Guwahati

Contents

Chapter III

Non-Covalent Confinement of Gd(III)-/Mn(II)-Complex in Porous Silica Nanosphere Rendering Nanoparticulate CA for MRI

Chapter IV

A Zn(II)-Responsive Mn(II)-Complex Confined Porous Silica Nanoparticles as "Smart" MRI CA for Pancreas Imaging

Chapter V

Folate decorated Mn(II)-Complex Confined Porous Silica Nanoparticles as MRI Contrast Agent to Detect Cancer Cells

Abbreviation

Symbols:

m/z : mass per charge

λ : wavelength (nm)

ε : extinction coefficient ($M^{-1}cm^{-1}$)

δ : isomer shift

B : magnetic field

k_{ex} : water exchange rate

T_1 : longitudinal relaxation time

R_1 : longitudinal relaxation rate

r_1 : longitudinal relaxivity

T_2 : transverse relaxation time

R_2 : transverse relaxation rate

r_2 : transverse relaxivity

× : multiplication

E : total energy

q = number of coordinated-water molecules attached to metal ion

τM = residence time of water molecule

τR = rotational tumbling time

τ_C = correlation time defining dipole-dipole relaxation

J : coupling constant (cm–1) /or Hz

S : electron spin

s : singlet

d = doublet

t = triplet

q = quartet

TR : repetition time

TE : echo time

μ_{eff} : magnetic moment (μ_B)

ν : frequency

K_A : association constant

k : pseudo-first-order dissociation rate constant

k_{obs} : observed rate constant

ζ : zeta potential

° : degree

@ : incorporated

n_{cplx} : number average of confined complex molecules/nanoparticle

rt : room temperature (30 °C)

Units:

Å : Angstrom

cm : centimeter

nm : nanometer

mm: millimeter

h : hour

s : second

ms : millisecond

Hz : hertz

T : tesla

g : gram

K : kelvin

M : molar

N : normal

Min : minute

mL : milliliter

mM : millimolar

μM : micromolar

mg : milligram

μg : microgram

°C : degree centigrade

Å : Angstrom

μ_B : bohr magnetron

mV : millivolt

ppm : parts per million

Solvents and Reagents:

CH_2Cl_2 : dichloromethane

$CHCl_3$: chloroform

Et_2O : diethyl ether

Et_3N : triethylamine

MeOH : methanol

EtOH : ethanol

CH_3CN : acetonitrile

DMF : dimethylformamide

DMSO : dimethyl sulfoxide

THF : tetrahydrofuran

KBr : potassium bromide

KCl: potassium chloride

K_2CO_3 : potassium carbonate

$MnCl_2 \bullet 4H_2O$: manganese chloride tetrahydrate

$GdCl_3 \bullet xH_2O$: gadolinium chloride hydrate

$TbCl_3 \bullet 6H_2O$: terbium chloride hexahydrate

DMEM : Dulbecco's Modified Eagle Medium

NH_4OH : Ammonium hydroxide

TFA : trifluoroacetic acid

NaOH : sodium hydroxide

NaCl : sodium chloride

LiOH : lithium hydroxide

HCl : hydrochloric acid

H_2SO_4 : sulphuric acid

HNO_3 : nitric acid

HPF_6 : hexafluorophosphoric acid

HEPES : 2-[4-(2-hydroxyethyl)-1-piperazinyl]ethanesulfonic acid)

MES : (2-(N-morpholino)ethanesulfonic acid)

TEOS : tetraethyl orthosilicate

APTES : (3-Aminopropyl)triethoxysilane

FA : folic acid

FITC : Fluorescein isothiocyanate

BSA : bovine serum albumin

MTT : (3-[4,5-dimethylthiazol-2-yl]-2,5 diphenyl tetrazolium bromide)

Techniques:

NMR : nuclear magnetic resonance

IR : infrared

UV-Vis : ultraviolet-visible

ICP-AES : inductively coupled plasma atomic emission spectroscopy

ICP-MS : inductively coupled plasma emission spectroscopy

MS : mass spectroscopy

HPLC : High-performance liquid chromatography

FETEM : field emission transmission electron microscopy

EDX : Energy Dispersive X-ray

TGA : Thermogravimetric analysis

DLS : Dynamic light scattering

EPR : electron paramagnetic resonance

ESI : electrospray ionization

EA : elemental analysis

Latin expressions:

et al.: and co-workers

e.g.: for example

vs.: versus

viz.: namely

i.e.: that is

tert-: tertiary

via.: through

vide supra : see above

vide infra : see below

ab initio : from the beginning

Chapter I

General Introduction and Motivation

1.1 Magnetic Resonance Imaging

MRI is one of the most effective imaging modalities to obtain useful three-dimensional images.[1] This technique utilizes ^{1}H-NMR signals of water molecules to generate high-resolution anatomical images of soft tissues. Water content varies in different regions inside our body. MRI machines harness *in vivo* water protons to generate differential ^{1}H-NMR signals.[2] Other imaging techniques, *e.g.*, X-rays, Computed Tomography scans (CT-scan), Positron Emission Tomography (PET), and Ultrasound, use harmful ionizing radiation to penetrate inside the body. Being non-invasive, MRI is advantageous and widely used for early physiopathological detection of endogenous abnormalities.[3]

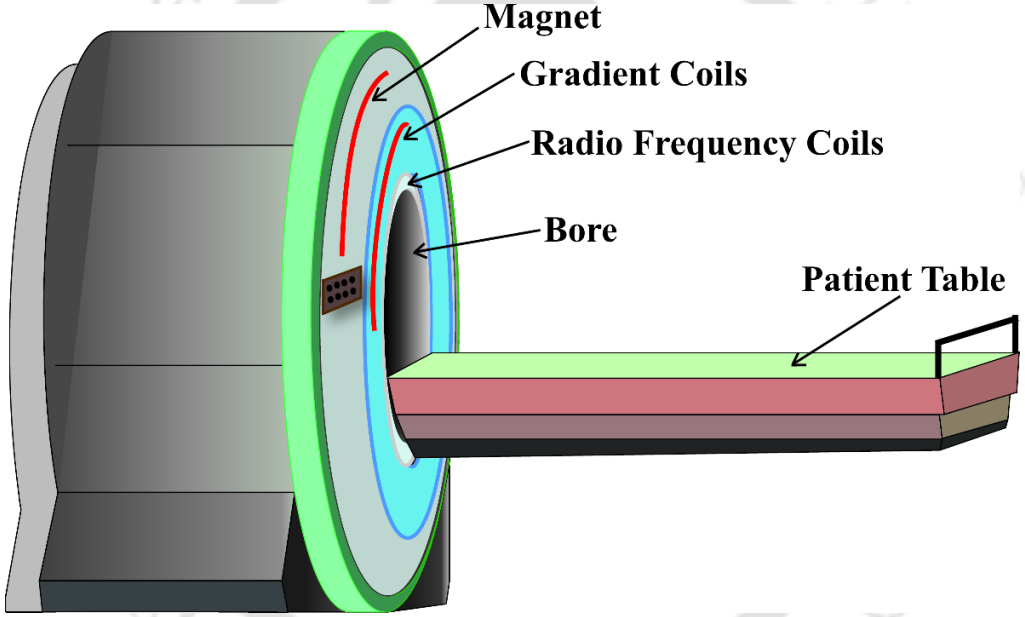

Figure 1.1. MRI scanner cutaway: basic components of a representative scanner.

A schematic diagram of a clinical MRI scanner is presented in **Figure 1.1**. It comprises of following components: a superconducting magnet that generates a homogenous magnetic field; gradient coils; radio frequency coils and the patient table in the perpendicular direction. The MRI machine applies a radio-frequency pulse to generate a free-induction decay signal, which on Fourier transformation by a signal-receiving computer, forms the image depending on the NMR signals. Depending on the water proton distribution in different local environments, NMR signal intensity varies resulting in detailed spatial-resolution imaging.[4]

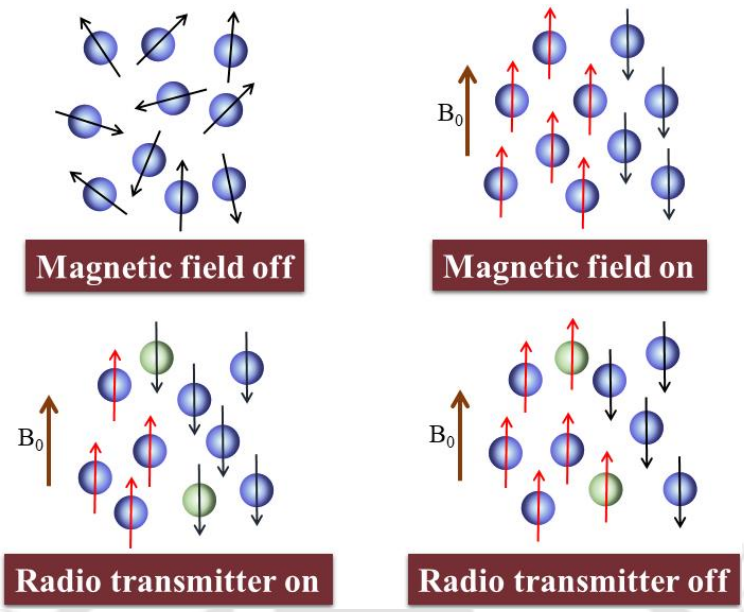

Figure 1.2. Alignment of water proton nuclei with respect to the applied magnetic field, during the course of MRI experiment.

Elaborately, the patient's body (sample) with an overall 70% water content (water concentration varying in different tissues), is strongly influenced by the application of a static magnetic field.[6] Primarily, unaligned water proton nuclei behave as small spinning magnets in the presence of the external magnetic field, orienting themselves either along (low energy state) or against (high energy state) the direction of the field. Henceforth, charged nuclei precess (Larmor precession) in a larger population in the low energy state, consequently creating a population difference that is largely dependent on temperature and magnetic field strength attained during measurement.[7] When a radio frequency pulse resonating with the Larmor frequency of the protons is applied, some of the proton nuclei in the low energy state gain energy and go to the high energy state changing their orientation, precessing in phase with the external magnetic field afterward.[8] This phenomenon results in a decrease in net magnetization along the longitudinal direction of the applied magnetic field, *i.e.*, the z-direction. There is a simultaneous gain in net magnetization in the xy-plane, also known as transverse magnetization. Turning off the radio frequency pulse resulted in a gradual shift of the whole system to the initial equilibrium state, termed as relaxation process.[9] This causes a gain in longitudinal magnetization and a parallel loss of transverse magnetization (**Figure 1.3**). The process of relaxation is classified in accordance with the way of going back to the equilibrium state, as mentioned below.

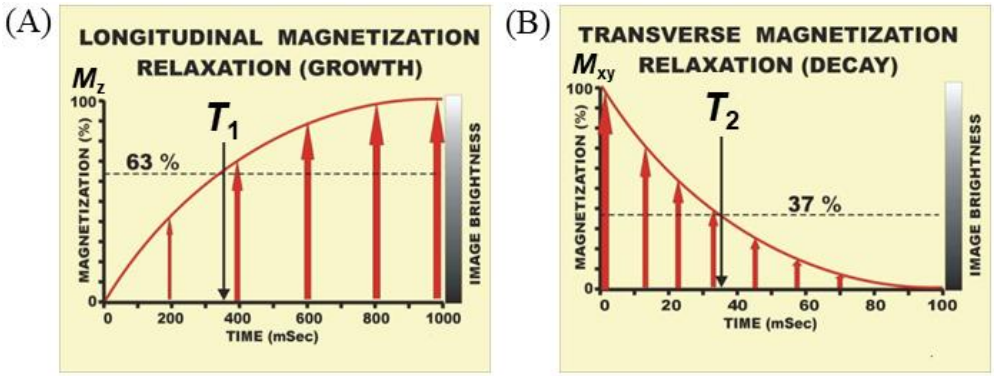

Figure 1.3. Changes in net magnetization while returning to the equilibrium energy state after the radio frequency pulse. (A) Gain in magnetization along the z-axis. (B) Decay in magnetization along the xy-plane.

Longitudinal relaxation (T_1 relaxation)

The process of exponential increase in net magnetization along the z-axis (M_z), finally reaching the maximum value (M_0) is termed as longitudinal relaxation (**Figure 1.3A**). Here, the excess energy is dissipated to the surrounding lattice, and thus, also known as spin-lattice relaxation. T_1 is the time taken to reach 63% of the initial magnetization along the longitudinal axis, referred to as longitudinal relaxation time. This relaxation process follows the following equation.

$$M_z = M_0(1-e^{t/T_1})$$

Transverse relaxation (T_2 relaxation)

Here, net magnetization in the xy-plane gradually diminishes because of the loss of spin coherence (**Figure 1.3B**). This is also called spin-spin relaxation. T_2 is the time in which magnetization decreases to 37% of its original value, according to the following equation.

$$M_{xy} = M_0 e^{t/T_2}$$

Differential signals arise due to the biochemical changes in the local environments of soft tissues under consideration, and depending on the variation of longitudinal ($R_1 = 1/T_1$) and transverse ($R_2 = 1/T_2$) relaxation rates of the water molecules, and thereby images are constructed depicting abnormalities.[10] In T_1-weighted imaging, tissues with short T_1 appear brighter since most

of the longitudinal magnetization is regained. In T_2-weighted imaging, tissues with short T_2 appear darker as the complete signal is lost faster. T_1 and T_2 are highly sensitive to the environment.

1.2 MRI Contrast Agents

In the MR imaging technique, intrinsic sensitivity is improved by employing certain paramagnetic, superparamagnetic, or ferromagnetic substances, known as contrast agents (CAs).[1d] *In vivo* administration of these external chemical agents, prior to the imaging, leads to diverse endogenous distribution across the body and immediately influences the relaxation rates of water protons in the local surroundings.[11] Henceforth, a difference in signal intensity between normal and diseased tissues is achieved, creating useful contrast in the recorded images that helps in the early identification of abnormalities in a relatively shorter time span (**Figure 1.4**).[2c]

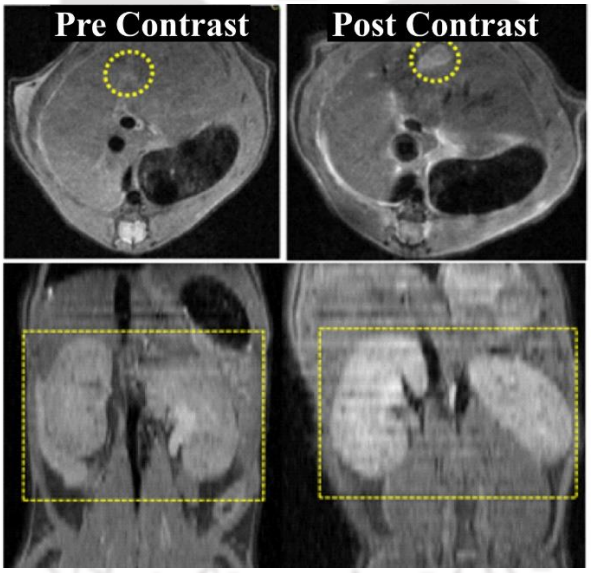

Figure 1.4. MRI scans performed before and after the administration of the contrast agent.

The usage of these contrast agents has been popularised nowadays, and at present, approximately 40 % of clinical MRI measurements are carried out in the presence of contrast agents.[12] CAs are capable of efficiently accelerating both the longitudinal and transverse relaxation rates ($R_i = 1/T_i$, i = 1 or 2; **Figure 1.5**). Meanwhile, they are broadly classified into two groups depending on their dominant effect.[13]

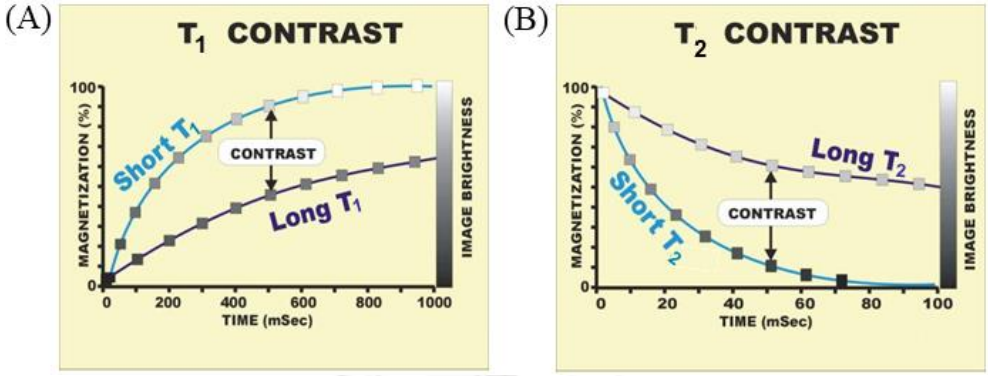

Figure 1.5. Effect of contrast agent on the relaxation process of water protons.

T_1-Contrast Agents

These compounds are mostly based on paramagnetic metal ions, *viz.*, high spin Gd(III), Mn(II), and Fe(III) ions.[14] They have a large number of unpaired electrons and thus offer a strong magnetic moment producing a fluctuating magnetic field. This, consequently, fastens the longitudinal relaxation process of water protons in the vicinity thereby lowering the T_1 relaxation time and simultaneously improving the signal intensity. Since they impart a brightening effect in the region of accumulation, are also known as positive contrast agents.[4b]

T_2-Contrast Agents

Superparamagnetic and ferromagnetic substances, especially iron oxide nanoparticles, behave as small moving magnets and impose large anisotropic magnetic susceptibility.[15] They effectively dephase the transverse magnetization reducing the transverse relaxation time T_2. This consequently resulted in dropping signal intensity, and hence these compounds are termed as negative contrast agents.

1.3 Relaxivity and Solomon-Bloembergen-Morgan Theory

The contrast ability of the administered external chemical agent, CA, is quantized in terms of relaxivity value. It is defined as the change in the relaxation rates of water protons, per mM concentration of the paramagnetic ions.[16] The efficiency of a CA is thus been determined by its high relaxivity value. In an aqueous medium, the paramagnetic ions move in Brownian motion,

generating a moving magnetic field that catalytically increases the water proton relaxation rates (both longitudinal and transverse rates), engendering a paramagnetic relaxation enhancement (PRE) effect.[3c] In an aqueous solution containing the paramagnetic ions, the observed relaxation rate, $(1/T_i)_{obs}$, is an additive resultant of the diamagnetic and paramagnetic relaxation rates, as illustrated in equation **(1)**.

$$(1/T_i)_{obs} = (1/T_i)_d + (1/T_i)_p \qquad i = 1, 2 \qquad \textbf{(1)}$$

Where, $(1/T_i)_{obs}$ = observed relaxation rate of water protons in an aqueous solution containing paramagnetic ions; $(1/T_i)_d$ = relaxation rate of the proton nuclei in the absence of any paramagnetic contrast species; and $(1/T_i)_p$ = paramagnetic contribution to the relaxation rate due to the presence of paramagnetic ions.

Thus, from this paramagnetic relaxation enhancement effect we observe the direct dependence of the relaxation rate of solvent protons on the millimolar concentration of the paramagnetic ions, [M]. This linear dependence is represented in equation **(2)**. Relaxivity (r_i) is the slope of the linear regression of relaxation rate *versus* paramagnetic agent concentration and is expressed in the unit of $mM^{-1}s^{-1}$.

$$(1/T_i)_{obs} = (1/T_i)_d + r_i[M] \qquad i = 1, 2 \qquad \textbf{(2)}$$

The PRE effect involves chemical interaction between the paramagnetic ion and aqueous protons, thereby altering the relaxation process. The extent of influence on the relaxation rate is pivoted on the distance and time of interaction. It depends on the interaction with water molecules that are directly coordinated to the paramagnetic metal center (inner coordinated water molecules) as well as the water molecules in the outer coordination sphere, which affects the system through hydrogen bonding, residency time, diffusion constant, *etc*. (**Figure 1.6**).[17] Thus, the overall relaxivity value of the contrast agent is the summation of the relaxation rate contribution from both the immediately bound water molecules, $(1/T_i)^{IS}$, and the bulk $(1/T_i)^{OS}$.

$$(1/T_i)_p = (1/T_i)^{IS} + (1/T_i)^{OS} \qquad i = 1, 2 \qquad \textbf{(3)}$$

The inner-sphere relaxation rate is largely affected by the exchange of water molecules within the coordination sphere of the paramagnetic metal ion and the bulk; the relation is depicted in equation **(4)**.

$$(1/T_1)^{IS} = P_M q/(T_{1M} + \tau_M) \quad \textbf{(4)}$$

Here, P_M represents the mole fraction of paramagnetic metal ion; q is the number of directly coordinated water molecules, pet metal ion; T_{1M} stands for relaxation time of the bound water molecule; and τ_M is the mean water residence time.

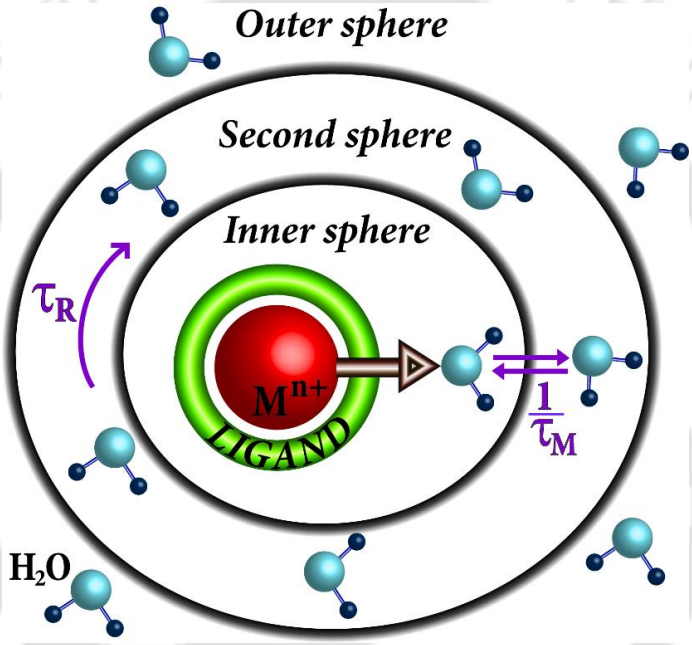

Figure 1.6. Schematic representation of selected factors that govern relaxivity of proton nuclei in the presence of paramagnetic contrast agent.

The inner-sphere relaxation process is governed by dipole-dipole through-space interactions along with scaler (through direct contact) interactions, described by a set of analytical equations, known as Solomon-Bloembergen-Morgan (SBM) equations [equation **(5)** and **(6)**].[18] According to this theory, the relaxation time of the bound water molecule, T_{1M} is explained as given below.

$$\frac{1}{T_{1m}} = \frac{2}{15}\frac{\gamma^2 g^2 \mu_B^2 S(S+1)}{r_{MH}^6}\left[\left(\frac{3\tau_{C1}}{1+\omega_H^2\tau_{C1}^2}\right) + \left(\frac{7\tau_{C2}}{1+\omega_S^2\tau_{C2}^2}\right)\right] \quad \textbf{(5)}$$

$$\frac{1}{\tau_C} = \frac{1}{\tau_m} + \frac{1}{\tau_{1e}} + \frac{1}{\tau_r} \quad \textbf{(6)}$$

Here, γ = proton gyromagnetic ratio, g = electronic g-factor, S = total electron spin of the metal ion, μ_B = Bohr magneton, r = distance of proton from the metal ion, ω_S and ω_H are electronic and proton Larmor precession frequencies, respectively, τ_C = correlation time defining dipole-dipole relaxation, T_{1e} = longitudinal electron spin relaxation time, τ_M = residence time of water molecule, and τ_R = rotational tumbling time of the whole molecule.

Equation **(4)-(6)** signified that an increase in q along with a faster water exchange rate (short τ_M value, about 10 ns) would directly elevate the inner-sphere relaxation rate. The SBM theory emphasizes the effect of elongating the rotational correlation time (τ_R) to elevate the relaxivity value without compromising with stability of the contrast moiety. By optimizing all these governing parameters, remarkable relaxivity values could be achieved. This theory is applicable in designing contrast agents for most cases of the MRI scans, except for very low magnetic fields.

1.4 Paramagnetic Contrast Agents

Gd(III) ion with 7 unpaired *f*-electrons provides a high magnetic moment (7.9 BM) and an entirely symmetric electronic ground state ($^8S_{7/2}$) that is ambient for long electronic relaxation time (10^{-8}-10^{-9} s).[1a,19] These features enable the suitability of Gd(III) ion-based compounds to fasten the relaxation rate of solvent protons, and thus, these are effective as T_1-weighted contrast agents. However, aquated free Gd(III) ion is non-biogenic and highly toxic.[20] Leaching and long-term endogenous retention have been reported to affect the central nervous system and develop nephrogenic systemic fibrosis (NSF) in patients with kidney diseases.[21] Efficient chelation with a proper ligand framework is used to mitigate the health hazards of free metal ions. Gd(III) ions having hard Lewis acid character, prefer N- and O- donors containing organic ligand framework to form stable chelates.[22] Clinically used Gadolinium Based Contrast Agents (GBCAs) are Gd(III) based complexes with linear or macrocyclic ligand backbones (**Figure 1.7**) with relaxivity values in the range of 3-5 $mM^{-1}s^{-1}$, at 1.41 T and 37 °C.[4b,23]

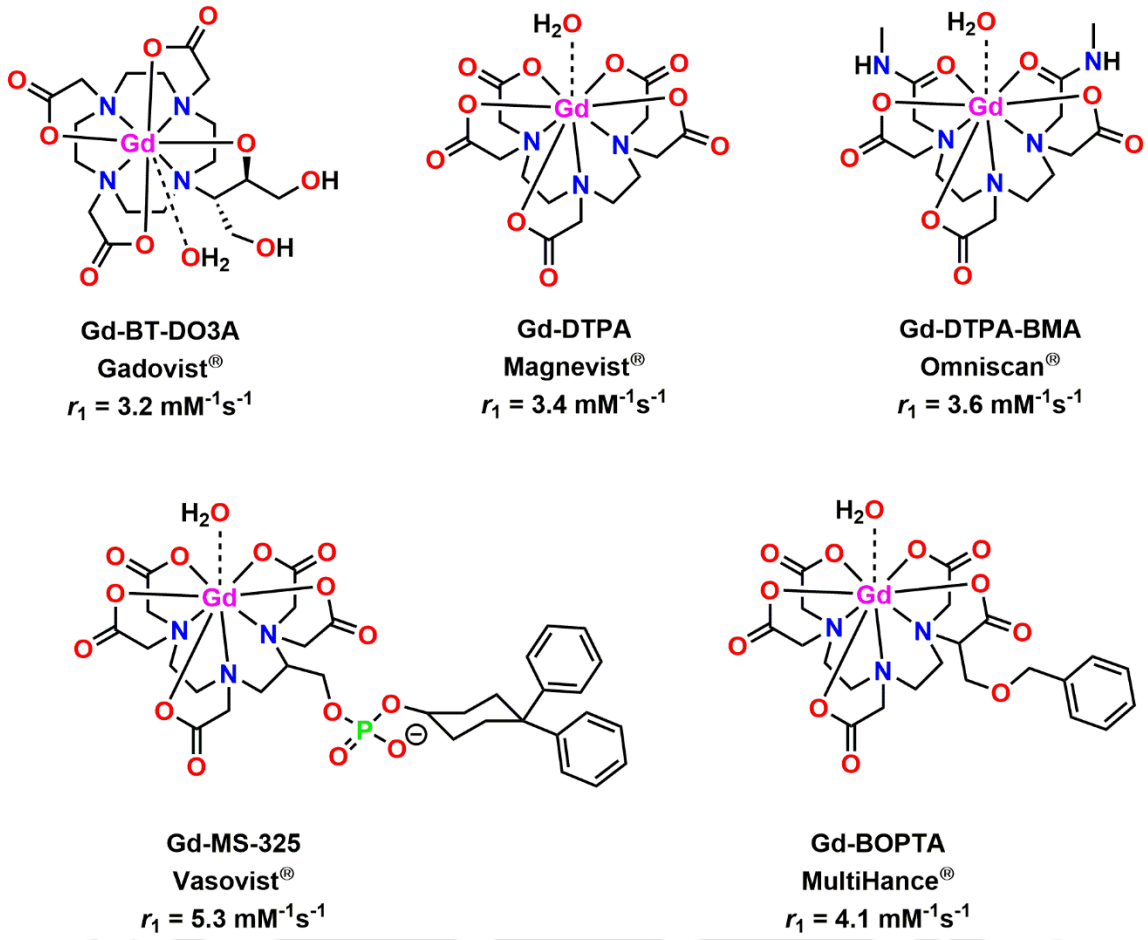

Figure 1.7. Some commercially administered contrast agents and their relaxivity values, obtained in water, at 37 °C and 1.41 T.

Physiologically important endogenous Ca(II) and Zn(II) ions have a similar ionic radius to that for Gd(III) and pose a threat for transmetallation to the GBCAs, thereby releasing toxic Gd(III) ions which causes nephrogenic systemic fibrosis (NSF).[4b] It also disturbs the Ca(II)-driven signaling process. Studies have shown accumulation of gadolinium in kidneys, brain, skin, and heart after prolonged usage, resulting in adverse health impairment and even death (**Figure 1.8**).[24] In fact, U.S. Food and Drug Administration (FDA) and Europan Medicines Agency (EMA) have recently restricted the usage of clinically approved, kinetically labile Gd(III)-based MRI CAs made of acyclic linear ligands.[25] Macrocyclic ligand-based complexes with challenging synthetic procedures, have major concerns about low thermodynamic stability and offer limited scope for ligand improvisation.[1c]

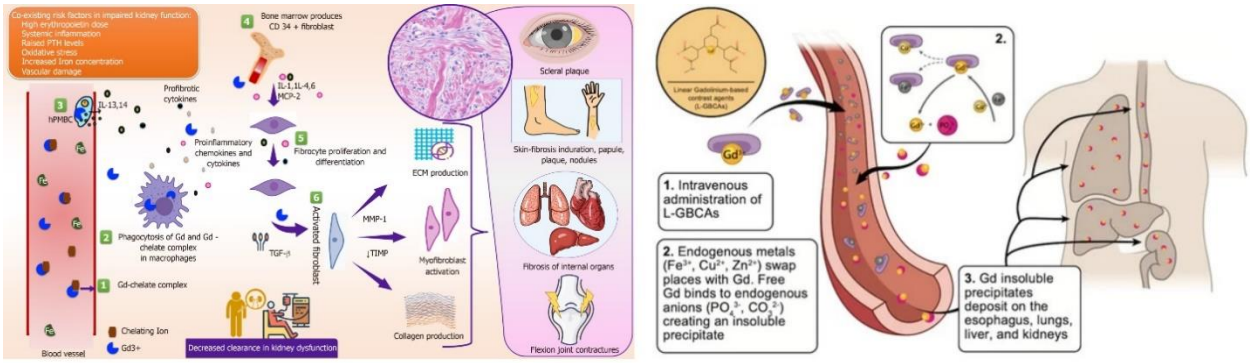

Figure 1.8. NSF pathophysiology: transmetalation and deposition of GCBAs affecting different organs.[24a,b]

Mn(II) and Fe(III) ions in the high-spin state contained five unpaired electrons (μ_{eff} = 5.9 BM) and shorter M^{n+}-water proton bond distance (2.5-2.8 Å).[26] Hence, these have been considered as plausible substitutes for Gd(III) ions. Nonetheless, both of the ions belong to the 3*d* transition series and did not provide additional stability through *d*-orbitals splitting (CFSE = crystal field stabilization energy). These metal ions are biogenic and essential nutritional elements.[27] Although, higher retention of Mn(II) ions leads to Parkinson-type disease called "Manganism".[28] Therefore, efficient complexation and fortification are urgently required for designing new generation CAs. Mn(II)-based chelates predominate over the Fe(III)-analogs as the latter are often devoid of inner sphere water molecules and form oxo-bridged clusters, offering very low relaxivity values.[29]

In Mn(II)-based complexes, stable systems could be achieved by designing an appropriate organic framework that offers strong metal ions-ligand interactions.[30] In this regard, the development of low molecular weight, slowly rotating seven-coordinate Mn(II)-based chelates with a high spin value (*S*) and adequate inner sphere water-coordination sites (*q*) have been the primary interest.[31] Moderate crystal field stabilization and less positive charge for the Mn(II) system compared to the lanthanide Gd(III) analog can be compensated by chelation with an efficiently rigid ligand framework with appropriate geometry. It imparts vital stability and inertness, balancing other physicochemical parameters (like water exchange rate, relaxation properties, *etc*.) establishing the field of Mn(II)-based MRI contrast agents. To date, only one Mn(II)-complex was clinically approved, named Mn-DPDP or Teslascan®; however, discontinued recently. Unlike Gd(III)-complexes that are mostly responsible for extracellular contrast, Mn(II)-

ion-based system, being endogenous to the living body, can easily penetrate the cell membrane.[32] Proper improvisations in ligand designing can furnish bio-responsive contrast agents that can selectively target the local diseased environment. Correspondingly, a series of linear or macrocyclic ligand skeletons have been thoroughly studied for Mn(II) complexation, as an alternative to GCBAs (**Scheme 1.1**).[24c,33]

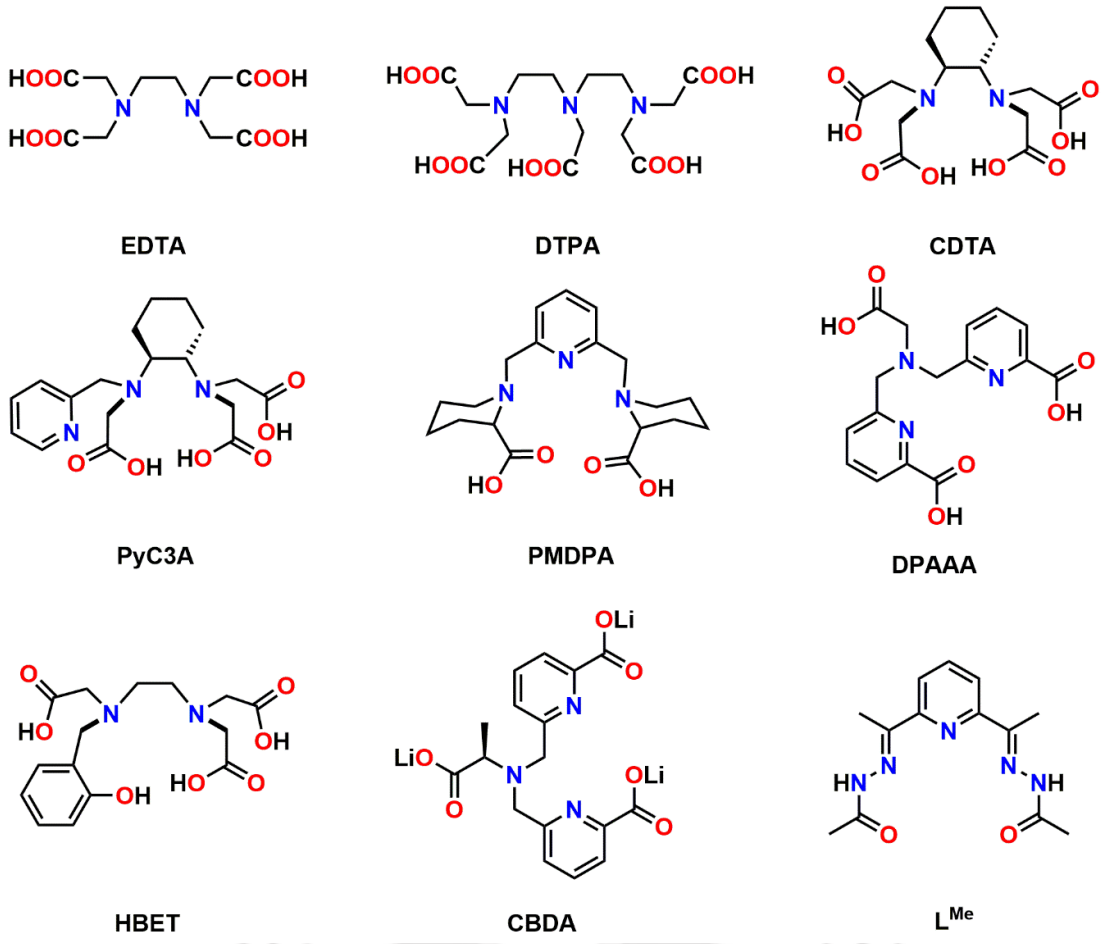

Scheme 1.1. Acyclic ligand frameworks used for Mn(II) chelation.

Most polyaminocarboxylate ligands are incapable of providing sufficient kinetic inertness and lead to rapid leaching of free Mn(II) ions on *in vivo* administration.[26a] The pyridine unit being a σ-donor and π-acceptor ligand, has been recognized as the important ligating unit to impart stability in Mn(II) complexes with acyclic coordinating ligands.[30a,34] As a result, the inclusion of pyridine in the ligand motif increased the rigidity of the chelating backbone and contributed to improving thermodynamic and kinetic stability. Penta- and hexadentate ligand frameworks

including picolyl, picolinate, and acetate units are thus designed and explored to form thermodynamically stable chelates. The paramagnetic metal chelates with ambient lipophilic character are achieved by the association of pyridyl or benzyl units, which facilitated further attachment to biomacromolecules (*e.g.*, albumin proteins) to modulate the rotational correlation time and enhance proton relaxivity.[35]

Despite vast comprehensive studies, an ideal balance of different contradicting factors (hydration number, water exchange rate, rigidity, dissociation kinetics, *etc*.,) in complex designing has still not been achieved. In addition, low retention time in the blood vessel post *in vivo* administration and rapid clearance of the contrasting probe is a major limitation of the recently explored contrast agents. This paves a scope for further modulations in novel ligands and corresponding complex systems.

1.5 Nanoparticle-based Contrast Agents

From the interpretation of SBM theory, we summarize the method of modulating the relaxation rate by optimizing hydration number (q), rotational correlation time (τ_R), and the water exchange rate (τ_M).[36] Increasing the hydration state obviously increases relaxivity, but comes with the limitations of lowering thermodynamic and kinetic stability, both of which are extremely crucial factors, especially for the Mn(II) chelates.[26a] Hence, reducing the tumbling rate (τ_R) is a better pathway to increase the relaxation rates. It is done by the covalent or non-covalent association of complexes or metal salts with biological macromolecules or nanostructures. Literature shows the successful surface grafting or confinement of metal silicates, oxides, or even chloride salts inside mesoporous silica nanoparticles (**Figure 1.9**).[37] Nanoparticulate MRI contrast agents are non-classical, which are more sensitive, efficient, and therefore a flourishing topic. They offer large surface area and pore volume that can be exploited judicially to make target-specific, less toxic, and stable contrast agents.[38] They have been extensively studied to effectively increase the relaxivity value per metal ion. Biological factors (changes in pH, enzymes, or micronutrient concentration) can trigger physicochemical alterations in the nano-contrasting systems causing differences in relaxivity, and hence, are more sensitive MRI contrast agents.[39] The porous silica matrix is biocompatible, allows rapid access of water molecules to the nanocore, and provides a

longer retention time inside the body, imparting efficient contrast for long-term MR imaging analyses, *e.g.*, oncological imaging.[40]

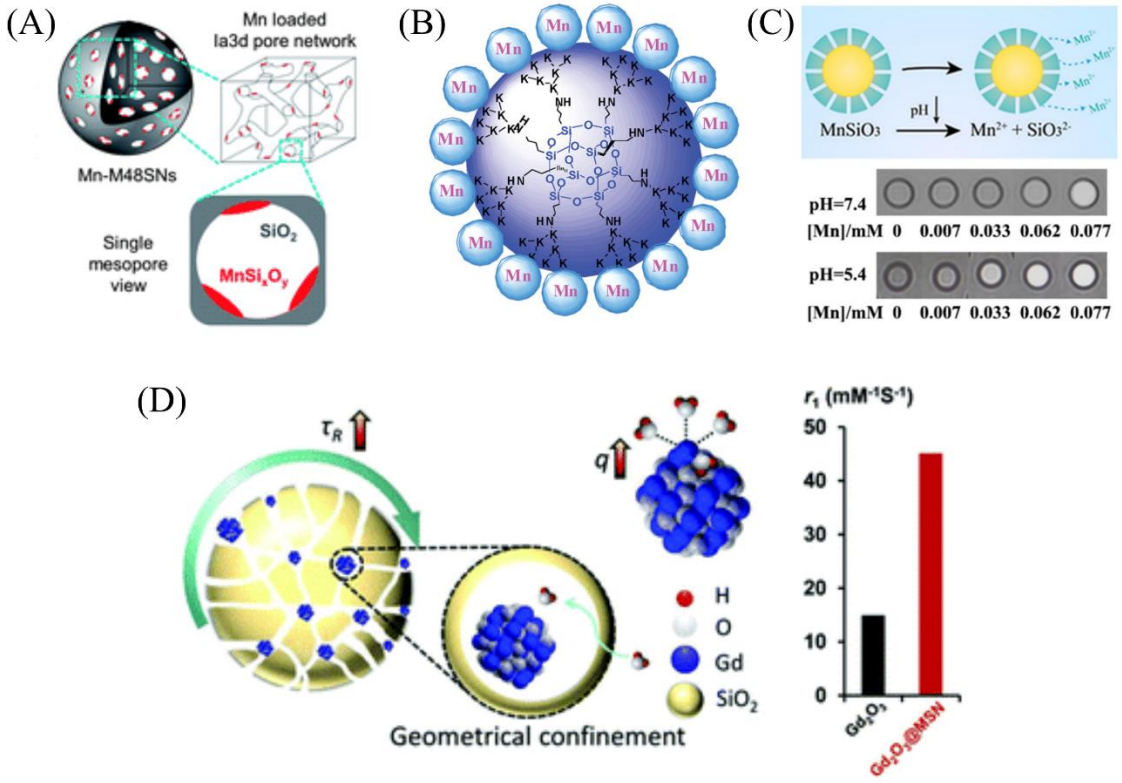

Figure 1.9. Some examples of paramagnetic nano-contrasts.[36c,39]

Non-covalent nanoconfinement of the thermodynamically stable metal complexes inside porous silica nanoparticles (PSNs) is expected to lower the overall tumbling rate and increase water accessibility simultaneously.[41] This strategy can also help in imparting useful kinetic inertness to the metal chelate against scavenger ions, hence improving the comprehensive stability. The localization of multiple paramagnetic molecules within a nanosphere is anticipated to promote r_2 relaxivity concurrently, by imparting a superior extent of spin − spin interactions. As a result, a T_1 or a $T_1 - T_2$ dual contrast agent can be designed. Furthermore, the fabrication of appropriate functional groups (folate, fibrin, protein, or ion-sensing organic fragments) onto the nanoparticle surface can evolve "smart" contrasting probes that are more specific to biochemical changes in the local environments.[42] Proper improvements and adaptations may help in designing paramagnetic

complex incorporated porous silica nanoprobes that are specific to pathological needs, in the clinical field.

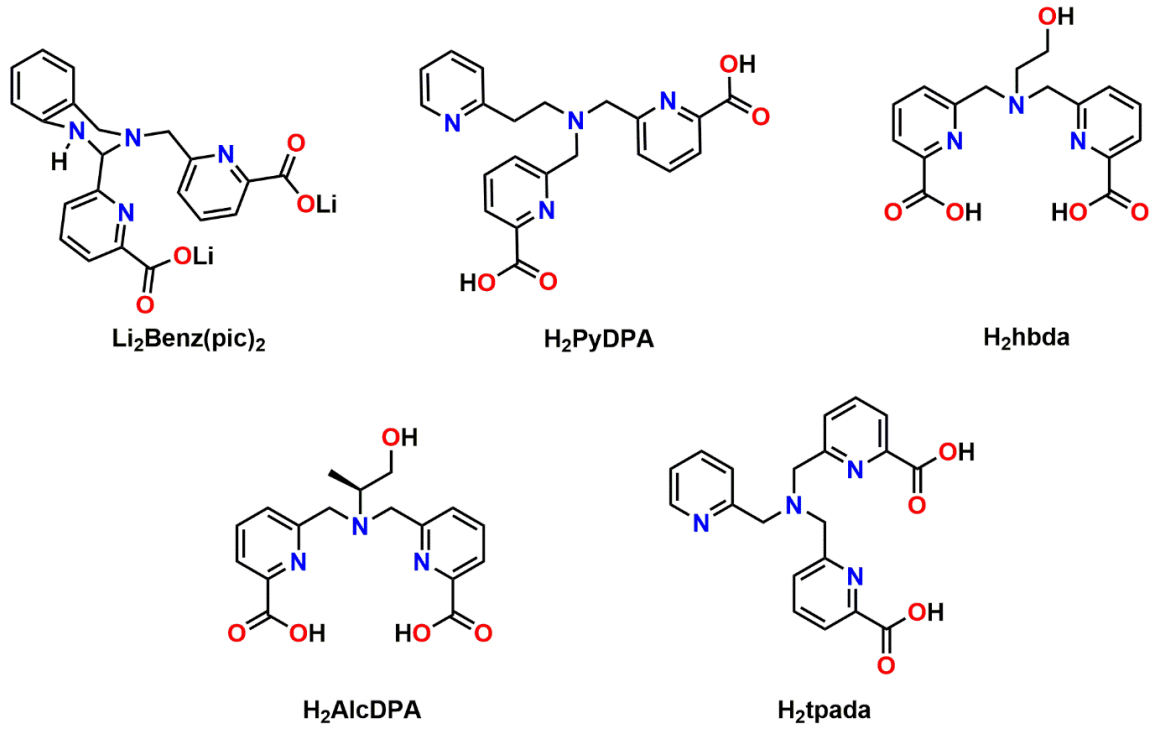

Scheme 1.2. Ligand frameworks synthesized and discussed in the thesis.

In this thesis, syntheses of the mentioned series of novel ligand frameworks have been discussed (**Scheme 1.2**). Aiming to introduce rigidity to the ligand skeleton, hydroquinazoline, polyaminopicolate, pyridyl, or alcohol fragments are included. Furthermore, the addition of chiral attributes is anticipated to increase stability. The corresponding Gd(III) or Mn(II) chelates have been extensively studied as potential MRI contrast agents with the following properties: (i) high relaxivity, (ii) presence of inner-sphere water molecule (*q*), (iii) kinetic inertness, (iv) high thermodynamic stability, and (v) optimum water exchange rates, tumbling rate and water residence time. Incorporation strategies of the paramagnetic chelates inside the porous silica nanoparticles and their physicochemical studies have been reported onwards. *In-vitro* or *in-vivo* MRI applicability of novel contrast systems has been correspondingly established.

1.6 References

1. (a) R. B. Lauffer, *Chem. Rev.*, 1987, **87**, 901; (b) P. Caravan, J. Ellison, T. McMurry and R. Lauffer, *Chem. Rev*., 1999, **99**, 2293; (c) P. Caravan, *Chem. Soc. Rev*., 2006, **35**, 512; (d) E. J. Werner, A. Datta, C. J. Jocher and K. N. Raymond, *Angew. Chem. Int. Ed*., 2008, **47**, 8568; (e) G. M. Lanza, S. D. Caruthers, P. M. Winter, M. S. Hughes, A. H. Schmieder, G. Hu and S. A. Wickline, *Eur. J. Nucl. Med. Mol. Imaging*, 2010, **37**, S114eS126.

2. (a) A. Datta and K. N. Raymond, *Acc. Chem. Res*., 2009, **42**, 938; (b) R. Salzer, *Biomedical Imaging*: *Principles and applications*, a John Wiley and Sons, Inc., 2012; (c) E. Terreno, D. D. Castelli, A. Viale and S. Aime, *Chem. Rev.*, 2010, **110**, 3019 − 3042; (d) The Chemistry of Contrast Agent in Medical Magnetic Resonance Imaging, A. E. Merbach, L. Helm and E. Tóth, 2nd ed.; *Wiley*, 2013; pp 1 − 23.

3. (a) R. Weissleder, ProQuest (Firm), Molecular Imaging Principles and Practice; People's Medical Pub. House: Shelton, CT, 2009; (b) J. Wahsner, E. M. Gale, A. Rodríguez-Rodríguez and P. Caravan, *Chem. Rev.*, 2019, **119**, 957–1057; (c) H. Li and T. J. Meade, *J. Am. Chem. Soc.*, 2019, **141**, 17025−17041.

4. (a) P. Caravan, C. T. Farrar, L. Frullano, and Ritika Uppal, *Contrast Media Mol Imaging*, 2009, **4**, 89–100; (b) L. M. de Leõn-Rodríguez, A. F. Martins, M. C. Pinho, N. M. Rofsky and A. D. Sherry, *J. Magn. Reson. Imaging*, 2015, **42**, 545–565.

5. P. Caravan and RB. Lauffer, RR. Edelman, JR. Hesselink, MB. Zlatkin and JV. Crues, editors. *Clinical Magnetic Resonance Imaging.*, 3rd ed. Vol. 1. Saunders; Philadelphia: 2005. p. 357-375.

6. M. Rohrer, H. Bauer, J. Mintorovitch, M. Requardt and HJ. Weinmann, *Invest. Radiol*., 2005, **40**, 715–724.

7. R. R. Edelman, J. R. Hesselink, M. B. Zlatkin and J. V. Crues, *III Clinical Magnetic Resonance Imaging;* Elsevier Health: St. Louis, 2006, **3**.

8. (a) A. Viale, F. Reineri, D. Santelia, E. Cerutti, S. Ellena, R. Gobetto and S. Q. J. Aime, *Nucl. Med. Mol. Imaging*, 2009, **53**, 604; (b) N. Bloembergen and L. O. Morgan, *J. Chem. Phys.*, 1961, **34**, 842.

9. *The Chemistry of Contrast Agents in Medical Magnetic Resonance Imaging*, ed. A. E. Merbach, and E´. Tóth, John Wiley & Sons, Chichester (England), 2001; (b) S. Avedano, L. Tei, A. Lombardi, G. B. Giovenzana, S. Aime, D. Longo and M. Botta, *Chem. Commun.*, 2007, 4726.

10. (a) G. M. Nicolle, E´. Tóth, K. P. Eisenwiener, H. R. Mäcke and A. E. Merbach, *J. Biol. Inorg. Chem.*, 2002, **7**, 757; (b) D. A. Fulton, M. O'Halloran, D. Parker, K. Senanayake, M. Botta and S. Aime, *Chem. Commun.*, 2005, 474–476.

11. (a) E. L. Que and C. J. Chang, *Chem. Soc. Rev.*, 2010, **39**, 51 − 60.; (b) E. Boros, S. Karimi, N. Kenton, L. Helm and P. Caravan, *Inorg. Chem.*, 2014, **53**, 6985 − 6994. (c) A. Gupta, P. Caravan, W. S. Price, C. Platas-Iglesias and E. M. Gale, *Inorg. Chem.*, 2020, **59**, 6648 − 6678.

12. H. Su, C. Wu, J. Zhu, T. Miao, D. Wang, C. Xia, X. Zhao, Q. Gong, B. Song and H. Ai, *Dalton Trans.*, 2012, **41**, 14480-14483.

13. L. Frullano, and P. Caravan, *Curr Org Synth.*, 2011, **8**, 535–565.

14. (a) A. Bianchi, L. Calabi, F. Corana, S. Fontana, P. Losi, A. Maiocchi, L. Paleari and B. Valtancoli, *Coord. Chem. Rev.*, 2000, **204**, 309 − 393.; (b) M. Rohrer, H. Bauer, J. Mintorovitch, M. Requardt and H. J. Weinmann, *Invest. Radiol.*, 2005, **40**, 715–724; (c) P.

Boehm-Sturm, A. Haeckel, R. Hauptmann, S. Mueller, C. K. Kuhl and E. A. Schellenberger, *Radiology*, 2018, **286**, 537-546.

15. (a) S. Laurent, D. Forge, M. Port, A. Roch, C. Robic, L. Vander Elst and R. N. Muller, *Chem. Rev.*, 2008, **108**, 2064; (b) S. Caspani, R. Magalhães, J. Pedro Araújo and C. Tavares Sousa, *Materials*, 2020, **13**, 2586.

16. (a) R. Sethi, J. S. Ananta, C. Karmonik, M. Zhong, S. H. Fung, X. Liu, K. Li, M. Ferrari, L. J. Wilson and P. Decuzzi, *Contrast Media Mol. Imaging*, 2012, **7**, 501–508; (b) S. Aime, S. Baroni, D. Delli Castelli, E. Brücher, I. Fábián, S. C. Serra, A. Fringuello Mingo, R. Napolitano, L. Lattuada, F. Tedoldi and Z. Baranyai, *Inorg. Chem.*, 2018, **57**, 5567 − 5574.

17. (a) J. Z. Bojorquez, S. Bricq, C. Acquitter, F. Brunotte, P. M. Walker and A. Lalande, *Magn. Reson. Imaging*, 2017, **35**, 69 − 80; (b) A. Borel, L. Helm and A. E. Merbach, *Chem. - Eur. J.*, 2001, **7**, 600 − 610.

18. (a) I. Solomon and N. Bloembergen, *J. Chem. Phys*., 1956, **25**, 261; (b) J. Kowalewski, L. Nordenskiöld, N. Benetis and P.-Olof Westlund, *Prog Nucl Magn Reson Spectrosc*., 1985, **17**, 141-185.

19. (a) M. Bottrill, L. Kwok and N. J. Long, *Chem. Soc. Rev*., 2006, **35**, 557; (b) P. Hermann, J. Kotek, V. Kubíček and I Lukeš, *Dalton Trans.*, 2008, 3027–3047.

20. I. A. Dekkers, R. Roos and A. J. van der Molen, *Eur. Radiol.*, 2018, **28**, 1579 − 1584.

21. (a) T. Grobner, *Nephrol., Dial., Transplant.*, 2006, **21**, 1104−1108; (b) P. Marckmann, L. Skov, K. Rossen, A. Dupont, M. B. Damholt, J. G. Heaf and H. S. Thomsen, *J. Am. Soc. Nephrol.*, 2006, **17**, 2359 − 2362.

22. A. D. Sherry, P. Caravan and R. E. Lenkinski, *J. Magn. Reson. Imaging*, 2009, **30**, 1240.

23. S. Laurent, L. V. Elst and R. N. Muller, *Contrast Med. Mol. Imaging*, 2006, **1**, 128–137.

24. (a) V. Bhargava, K. Singh, P. Meena, R. Sanyal, Nephrogenic systemic fibrosis: A frivolous entity. *World J Nephrol*, 2021, **10**, 29-36; (b) S. Gallo-Bernal, N. Patino-Jaramillo, C. A. Calixto, S. A. Higuera, J. F. Forero, J. Lara Fernandes, C. Góngora, M. S. Gee, B. Ghoshhajra and H. M. Medina, *Diagnostics*, 2022, **12**, 1816; (c) S. Anbu, S. H. L. Hoffmann, F. Carniato, L. Kenning, T. W. Price, T. J. Prior, M. Botta, A. F. Martins and G. J. Stasiuk, *Angew. Chem. Int. Ed.*, 2021, **60**, 10736–10744.

25. (a) PRAC Confirms Restrictions on the Use of Linear Gadolinium Agents; EMA/424715/2017; *European Medicines Agency*, July 7, 2017; (b) FDA Drug Safety Communication: FDA Warns That Gadolinium-based Contrast Agents (GBCAs) are Retained in the Body; Requires New Class Warnings; U.S. Food and Drug Administration, December 19, 2017.

26. (a) B. Drahoš, I. Lukeš, and É. Tóth, *Eur. J. Inorg. Chem.*, 2012, 1975–1986; (b) E. M. Gale, I. P. Atanasova, F. Blasi, I. Ay and P. Caravan, *J. Am. Chem. Soc.*, 2015, **137**, 15548 − 15557; (c) E. M Snyder, D. Asik, S. M Abozeid, A. Burgio, G. Bateman, S. G. Turowski, J. A. Spernyak, and J. R. Morrow, *Angew. Chem. Int. Ed*., 2020, **59**, 2414–2419.

27. (a) R. Uzal-Varela, D. Lalli, I. Brandariz, A. Rodríguez-Rodríguez, C. Platas-Iglesias, M. Botta and D. Esteban-Gómez, *Dalton Trans.*, 2021, **50**, 16290-16303; (b) A. R. Reddi, L. T. Jensen and V. C. Culotta, *Chem. Rev*., 2009, **109**, 4722.

28. (a) D. Pan, S. D. Caruthers, A. Senpan, A. H. Schmieder, S. A. Wickline and G. M. Lanza, *Wiley Interdiscip Rev Nanomed Nanobiotechnol*., 2011, **3**, 162-173; (b) S. Rivera-Mancía, C. Rios and S. Montes, *BioMetals*, 2011, **24**, 811–825.

29. (a) M. Jeon, M. V. Halbert, Z. R. Stephen and M. Zhang, *Adv.Mater*., 2021, **33**, 1906539; (b) R. Uzal-Varela, F. Lucio-Martínez, A. Nucera, M. Botta, D. Esteban-Gómez, L. Valencia, A. Rodríguez-Rodríguez and C. Platas-Iglesias, *Inorg. Chem. Front*., 2023, **10**, 1633–1649; (c) O. Udochukwu Akakuru, M. Zubair Iqbal, M. Saeed, C. Liu, T. Paunesku, G. Woloschak, N. S. Hosmane and A. Wu, *Bioconjugate Chem*., 2019, **30**, 2264−2286.

30. (a) B. Drahoš, J. Kotek, P. Hermann, I. Lukeš and É. Tóth, *Inorg. Chem*., 2010, **49**, 3224–3238; (b) E. Molnár, N. Camus, V. Patinec, G A. Rolla, M. Botta, G. Tircsó, F. K. Kálmán, T. Fodor, R. Tripier and C. Platas-Iglesias, *Inorg. Chem*., 2014, **53**, 5136 − 5149.

31. C. Vanasschen, E. Molnár, G. Tircsó, F. K. Kálmán, É. Tóth, M. Brandt, H. H. Coenen, and B. Neumaier, *Inorg. Chem*., 2017, **56**, 7746 − 7760.

32. K. Chen, P. Li, C. Zhu, Z. Xia, Q. Xia, L. Zhong, B. Xiao, T. Cheng, C. Wu, C. Shen, X. Zhang and J. Zhu, *J. Med. Chem*., 2021, **64**, 9182−9192.

33. (a) H. Su, C. Wu, J. Zhu, T. Miao, D. Wang, C. Xia, X. Zhao, Q. Gong, B. Song, H. Ai, *Dalton Trans*., 2012, **41**, 14480-14483 ; (b) A. Forgács, R. Pujales-Paradela, M. Regueiro-Figueroa, L. Valencia, D. Esteban-Gómez, M. Botta and C. Platas-Iglesias, *Dalton Trans*., 2017, **46**, 1546–1558; (c) M. Khannam, T. Weyhermüller, U. Goswami and C. Mukherjee, *Dalton Trans*., 2017, **46**, 10426 − 10432. (d) R. Uzal-Varela, D. Lalli, I. Brandariz, A. Rodríguez-Rodríguez, C. Platas-Iglesias, M. Botta and D. Esteban-Gómez, *Dalton Trans*., 2021, **50**, 16290–16303.

34. Z. Garda, E. Molnár, F. K. Kálmán, R. Botár, V. Nagy, Z. Baranyai, E. Brücher, Z. Kovács, I. Tóth and G. Tircsó, *Front. Chem*., 2018, **6**, 232.

35. (a) M. K. Islam, S. Kim, H.-K. Kim, S. Park, G.-H. Lee, H. J. Kang, J.-C. Jung, J.-S. Park, T.-J. Kim and Y. Chang, *J. Med. Chem.*, 2017, **60**, 2993-3001; (b) F. K. Kálmán, V. Nagy,

B. Váradi, Z. Garda, E. Molnár, G. Trencsényi, J. Kiss, S. Même, W. Même, É. Tóth and G. Tircsó, *J. Med. Chem*., 2020, **63**, 6057-6065.

36. (a) K. M. L. Taylor, J. S. Kim, W. J. Rieter, H. An, W. Lin, W. Lin, *J. Am. Chem. Soc*., 2008, **130**, 2154 − 2155; (b) J. S. Ananta, B. Godin, R. Sethi, L. Moriggi, X. Liu, R. E. Serda, R. Krishnamurthy, R. Muthupillai, R. D. Bolskar, L. Helm, M. Ferrari, L. J. Wilson, P. Decuzzi, *Nat. Nanotechnol*., 2010, **5**, 815 − 821. ; (c) K. Ni, Z. Zhao, Z. Zhang, Z. Zhou, L. Yang, L. Wang, H. Ai and J. Gao, *Nanoscale*, 2016, **8**, 3768–3774.

37. (a) J. L. Vivero-Escoto, R. C. Huxford-Phillips and W. Lin, *Chem. Soc. Rev*., 2012, **41**, 2673–2685; (b) F. Carniato, L. Tei and M. Botta, *Eur. J. Inorg. Chem*., 2018, 4936–4954; (c) L. García-Hevia, M. Bañobre-López and J. Gallo, *Chem. Eur. J*., 2019, **25**, 431 – 441; (d) G. Jamalipour Soufi, A. Hekmatnia, S. Iravani and R. S. Varma, *ACS Appl. Nano Mater*., 2022, **5**, 10151 − 10166.

38. (a) P. S. Low, W. A. Henne and D. D. Doorneweerd, *Acc. Chem. Res*., 2008, **41**, 1, 120–129; (b) R. Guillet-Nicolas, J.-Luc Bridot, Y. Seo, M.-A. Fortin and F. Kleitz, *Adv. Funct. Mater*., 2011, **21**, 4653–4662; (c) Z. Zhang, F.-L. Zhou, G.-L. Davies and G. R. Williams, *VIEW*, 2022, **3**, 20200134; (d) K. Zhang, C. Qi and K. Cai, *Adv. Mater*., 2023, **35**, 2205409.

39. (a) D. Pan, A. H. Schmieder, S. A. Wickline and G. M. Lanza, *Tetrahedron*, 2011, **67** 8431e8444 ; (b) M. Tan, Z. Ye, E.-Kee Jeong, X. Wu, D. L. Parker and Z.-Rong Lu, *Bioconjugate Chem*., 2011, **22**, 931–937; (c) R. Guillet-Nicolas, M. Laprise-Pelletier, M. M. Nair, P. Chevallier, J. Lagueux, Y. Gossuin, S. Laurent, F. Kleitz and M. André Fortin, *Nanoscale*, 2013, **5**, 11499-11511; (d) X. Li, W. Zhao, X. Liu, K. Chen, S. Zhu, P. Shi, Y. Chen and J. Shi, *Acta Biomater*., 2016, **30**, 378–387; (e) H. Hu, F. Arena, E. Gianolio, C. Boffa, E. Di Gregorio, R. Stefania, L. Orio, S. Baroni and S. Aime, Nanoscale, 2016, **8**, 7094–7104; (f) B. Geun Cha and J. Kim, *WIREs Nanomed Nanobiotechnol*., 2019,**11**, e1515.

40. Y. Liu, M. Solomon and S. Achilefu, *Med. Res. Rev*., 2013, **33**, 3 − 32.

41. (a) L. Moriggi, C. Cannizzo, E. Dumas, C. R. Mayer, A. Ulyanov and L. Helm, *J. Am. Chem. Soc*., 2009, **131**, 10828–10829; (b) R. Zairov, G. Khakimullina, S. Podyachev, I. Nizameev, G. Safiullin, R. Amirov, A. Vomiero and A. Mustafina, *Sci. Rep*., 2017, **7**, 14010; (c) X. Qian, X. Han, L. Yu, T. Xu and Y. Chen, *Adv. Funct. Mater*., 2020, **30**, 1907066; (d) M. M. Karimdjy, G. Tallec, P. H. Fries, D. Imbert and M. Mazzanti, *Chem. Commun*., 2015, **51**, 6836–6838.

42. (a) Z. Zhou, R. Bai, Z. Wang, H. Bryant, L. Lang, H. Merkle, J. Munasinghe, L. Tang, W. Tang, R. Tian, G. Yu, Y. Ma, G. Niu, J. Gao, and X. Chen, *Bioconjugate Chem*., 2019, **30**, 1821−1829; (b) A. M. Denim, A. G. Pershina, A. S., Minin, O. Y. Brikunova, A. M., Murzakaev, N. A. Perekucha, A. V. Romashchenko, O. B. Shevelev, M. A. Uimin, I. V. Byzov, D. Malkeyeva, E. Kiseleva, L. V. Efimova, S. V. Vtorushin, L. M. Ogorodova, and V. P. Krasnov, *ACS Appl. Mater. Interfaces*, 2021, **13**, 36800-36815; (c) R. Antwi-Baah, Y. Wang, X. Chen and K. Yu, *Adv. Mater. Interfaces*, 2022, **9**, 2101710; (d) R. R. Zairov, B.S. Akhmadeev, S.V. Fedorenko and A.R. Mustafina, *Chem. Eng. J*, 2023, **459**, 141640.

भारतीय प्रौद्योगिकी संस्थान गुवाहाटी
Indian Institute of Technology Guwahati

भारतीय प्रौद्योगिकी संस्थान गुवाहाटी
Indian Institute of Technology Guwahati

Chapter II

Rigid Hydroquinazoline Appended Bis-Aquated Mn(II)-Complex as a Potential T_1-Contrast Agent for MRI

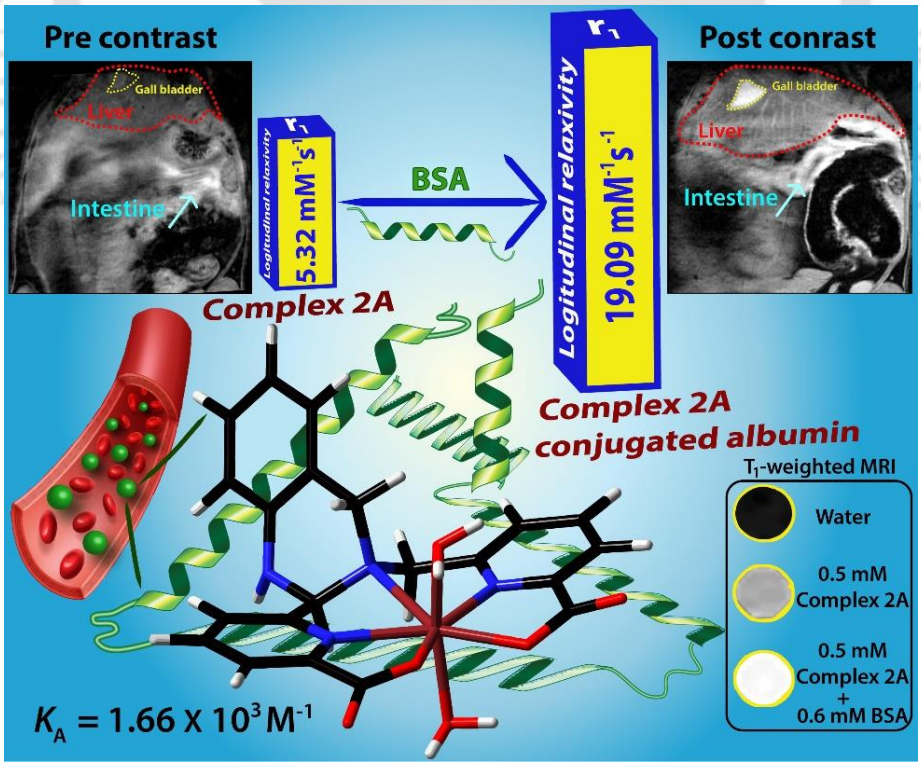

∗ Results have been reported in *ACS Appl. Bio Mater*., 2024, **7**, 1831–1841.

2.1 Introduction

Recently, adverse health effects have caused rising concerns from different regulatory agencies like the FDA, EMA, etc., regarding the usage of gadolinium-based contrast agents (GCBAs).[1] It created a pressing urgency to shift the focus toward manganese-based contrast agents as a safer alternative.[2] Mn(II) ions with five unpaired electrons are more biogenic as well as have favorable electronic properties and short metal–water proton effective distance to enhance the relaxation rates of water protons.[3] However, it lacks crystal field stabilization energy (CFSE), hence efficient ligand framework is required to thermodynamically and kinetically stabilize the corresponding complex. There is only one commercially used Mn(II)-based CA, $[Mn(DPDP)]^{4-}$, exhibiting a relaxivity value of 1.6 $mM^{-1}s^{-1}$ at 37 °C and 1.5 T.[4]

According to the SBM theory, the relaxivity value is directly proportional to the number of coordinated water molecules in the primary sphere (q) and inversely proportional to the overall rotation correlation time (τ_R).[5] Therefore, there is an urge to develop novel thermodynamically stable and kinetically inert slowly tumbling Mn(II)-based complex with multiple inner-sphere water molecules. Rigidification and preorganization of the ligand backbone are very important aspects to impart a useful stabilizing effect on the coordinated complex.[6] Picoly and picolinate units are particularly included in the ligand framework to maintain a balance between rigidity, thermodynamic, kinetic, and hydration properties governing the relaxivity of the corresponding complex.[7] Comba, Tóth, and colleagues stated the importance of introducing strain to the ligand motif to improve the kinetic inertness of the corresponding Mn(II)-complex.[8]

For the Mn(II) system, by restricting the ligand coordination to five, two inner-coordinated water molecules could be accommodated and that would be rapidly exchanged with bulk water. Previous investigations described this as a direct strategy to effectively accelerate the water proton relaxation rate irrespective of the applied magnetic field strength.[9] Some bis-aquated Mn(II)-complexes are presented in **Figure 2.1** along with the relaxivity values.[3c,6a,10] However, this tactic of elevating relaxivity adversely affects the thermodynamic stability of the complex, resulting in the spontaneous release of free Mn^{2+} ions. Conditional stability constant values ($\log \boldsymbol{K}^{\mathbf{c}}_{\mathbf{MnL}}$) of some Mn(II)-complex with one or two coordinated water molecules are listed in **Table 2.1**.[2a,6a,10a] This data reflected the inversely proportional relationship between hydration number and thermodynamic stability.

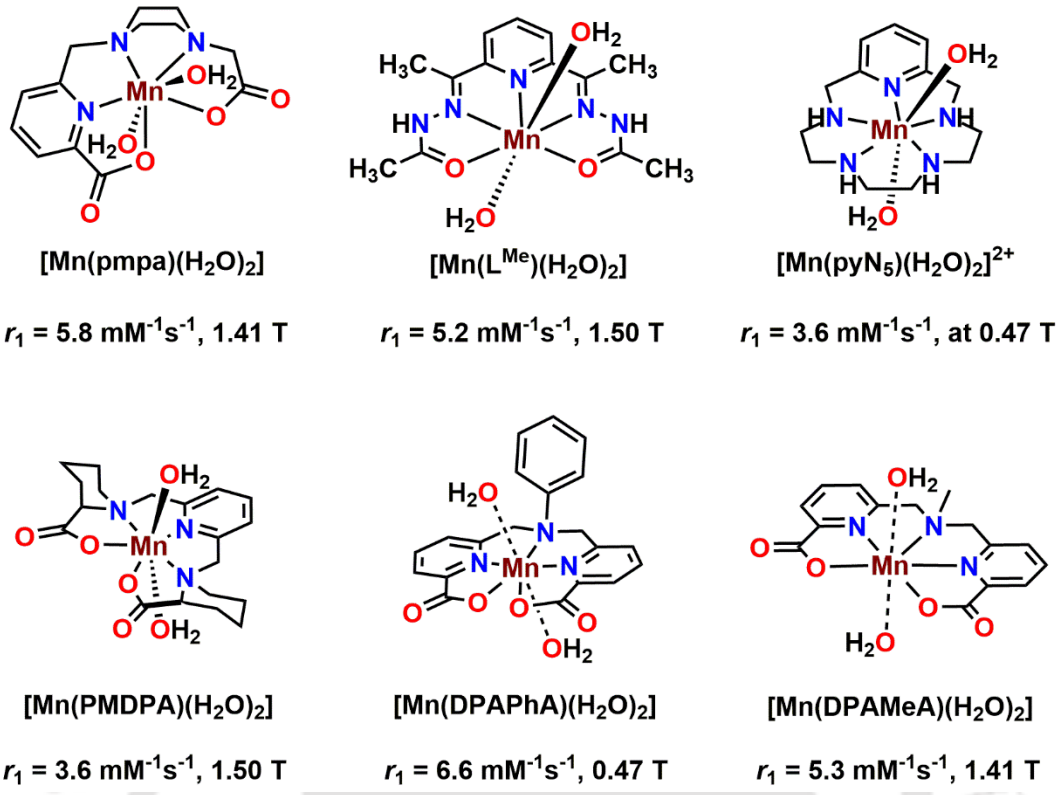

Figure 2.1. Some bis-aquated Mn(II)-based complexes along with respective relaxivity values, measured at 25 °C.

Table 2.1. Conditional stability constants of some Mn(II)-based complexes.[2a,6a,10a]

Mn(II) system	*q* value	$\log K^{c}_{MnL}$, pH ~ 7.4
EDTA	1	11.02
CDTA	1	12.64
15-pyN_5	2	7.72
15-pyN_3O_2	2	5.20
PMDPA	2	6.82

For Mn(II)-complexes, reducing the rotational correlation time (τ_R) is another indisputable strategy adopted to significantly improve relaxivity. This could be done by covalent or non-covalent binding of the paramagnetic complex unit with biological macromolecules *e.g.*, peptides, proteins, lipids, *etc*.[11] Serum albumin being one of the most abundant components of blood plasma and extracellular space, is largely targeted by the contrast agents.[12] The incorporation of phenyl and pyridine appendants in the ligand framework increases the overall aromatic character, enhancing the interaction strength with the hydrophobic pockets of the albumin protein moiety (**Figure 2.2**). Such interaction results in a concurrent increase in relaxivity and circulation time of the contrasting metal complex (**Table 2.2**). [12b,13]

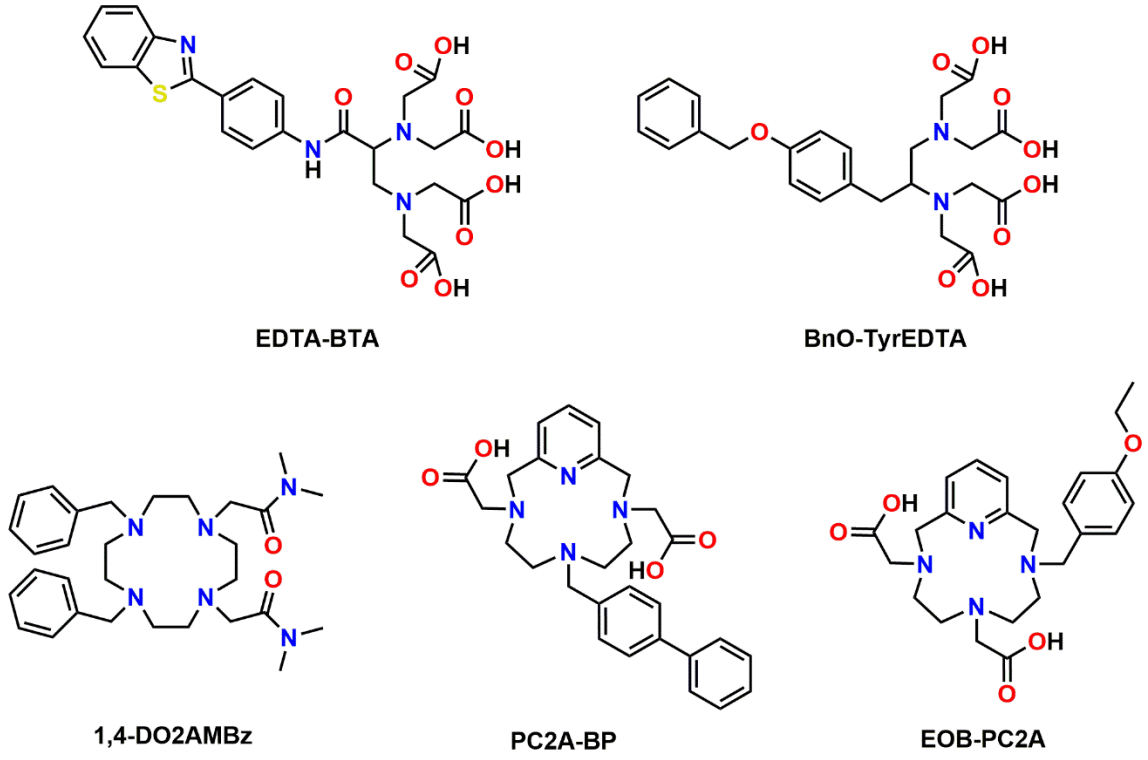

Figure 2.2. Ligand framework with phenyl and pyridine units, used for Mn(II)-complexation.

Most of the commercially used hydrophilic contrast agents undergo renal clearance and rarely impact any contrast in abdominal organs.[14] Unlike extracellular GCBAs, the enhanced lipophilic character of these improvised Mn(II)-based complexes also helps in cell permeability, thereby improving their organ-specific properties. The inclusion of the phenyl group in the ligand backbone has specifically proved to increase the hepatic uptake of the contrast agents and hence, could be used as potential liver-specific contrast agents.[6b,13a,b]

Table 2.2. Comparison of relaxivity, serum affinity constants, and octanol-water partition coefficients (lipophilicity) of few Mn(II)-based systems.[12b,13]

	log *P*	r_1 ($mM^{-1}s^{-1}$)		r_2 ($mM^{-1}s^{-1}$)		r_1^b ($mM^{-1}s^{-1}$)	K_A (M^{-1})
		Water	Serum albumin	Water	Serum albumin		
Mn-PC2A-BP[a]	-0.45	3.80	23.50	—	—	35.7	2.51×10^3
Mn-1,4-DO2AMBz[b]	—	3.5	17.50	—	—	27.4	1.90×10^3
Mn-EOB-PC2A[c]	—	2.83	5.85	5.27	14.31	—	—
Mn[EDTA-BTA][d]	-1.84	3.5	15.1	4.9	34.5	—	95
Mn-BnO-TyrEDTA[e]	0.18	4.34	15.81	6.21	20.70	—	—
Mn[EDTA][e]	-2.27	2.83	3.46	3.90	4.57	—	—

[b]Experimental condition: 0.7 mM BSA, at pH ~ 7.4 (HEPES), 0.49 T, and 37 °C. [b]Experimental condition: 0.67 mM HSA, at pH ~ 7.4, 0.49 T, and 25 °C. [c]Experimental condition: 0.67 mM HSA, at pH ~ 7.4 and 1.5 T. [d]Experimental condition: 0.67 mM HSA, at pH ~ 7.4, 1.5 T, and 24 °C. [e]Experimental condition: 0.67 mM BSA, at pH ~ 7.4, 0.47 T, and 32 °C.

To balance the contradictory key factors of hydration number and stability, herein we have reported the novel pentadentate ligand with rigid hydroquinazoline and two picolinate appendants and its corresponding Mn(II)-complex adopting a planar geometry with two coordinated water molecules in the axial position. The inclusion of the hydroquinazoline unit in the ligand framework has triple advantages: 1) this unit reduces the flexibility of the corresponding bis(aquated) Mn(II) complex, imposing high thermodynamic and kinetic stability, 2) the phenyl ring present in the hydroquinazoline unit fortifies the interaction of the chelate with albumin protein; as a result, enhances relaxivity and the circulatory lifetime of the chelate, and 3) the additional lipophilicity of the unit accompanied by the picolinate moieties have exerted an amphiphilic nature. The obtained complex, therefore, could be uptaken by hepatocytes to some extent along with regular renal pathway facilitating the imaging options of both systems.

2.2 Syntheses and Characterization of Ligand $Li_2[Benz(pic)_2]$

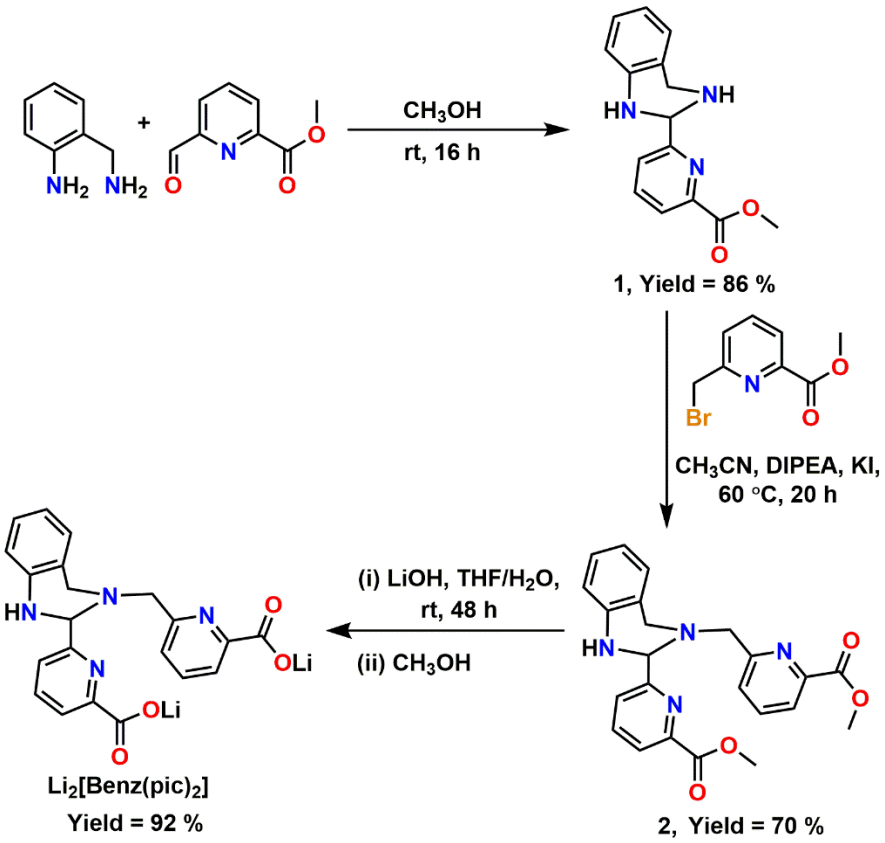

Scheme 2.1. Schematic representation for the synthesis of ligand **$Li_2[Benz(pic)_2]$**.

The pentadentate ligand $Li_2[Benz(pic)_2]$ was prepared as presented in **Scheme 2.1**. Equivalent amounts of 2-aminobenzylamine and methyl 6-formyl-2-pyridinecarboxylate were reacted in a methanolic medium to obtain compound **1** with 86% yield. The isolated compound was then reacted with one equivalent of methyl 6-(bromomethyl)picolinate in CH_3CN, in the presence of N, N-diisopropylethylamine (DIPEA), and KI, to yield compound **2** at a 70% yield. Upon base hydrolysis by LiOH in the THF/H_2O solvent mixture in a ratio of 3:1, the expected ligand $Li_2[Benz(pic)_2]$ was acquired as a white solid in 92% yield. The isolated ligand was further characterized by FTIR, ESI-MS, ^1H-NMR, and ^{13}C-NMR, spectroscopic techniques.

The infrared spectra of the synthesized ligand are depicted in **Figure 2.3A**. A broad band with a hump at 3482 cm^{-1} and centered at 3359 cm^{-1} appeared corresponding to the ν_{O-H} (water) and ν_{N-H} (secondary amine) stretching, respectively.[15a] Minor peaks in the region 3100-2859 cm^{-1} were observed due to aromatic and non-aromatic ν_{C-H} stretching. The $\nu_{C=O}$ asymmetric stretching

due to the two carboxylate groups appeared at 1615 cm^{-1}, which is lower than the $\nu_{C=O}$ stretching of the free acid group (~1710 cm^{-1}), implying the presence of the carboxylate group as the corresponding Li-carboxylate salt.[15b] The sharp peaks at 1584 cm^{-1} and 1574 cm^{-1} correlated with the characteristic aromatic $\nu_{C=N}$ stretching (pyridine group) and ν_{N-H} bending (secondary amine) respectively.[15c] The $\nu_{C=O}$ symmetric stretching was observed at 1427 cm^{-1} and ν_{C-O} stretching appeared at 1264 cm^{-1}.

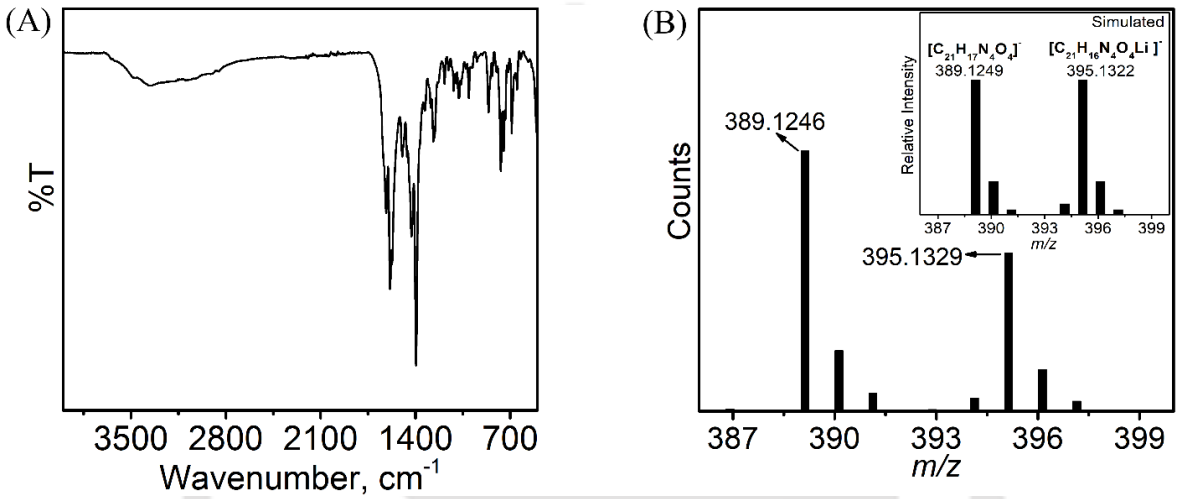

Figure 2.3. (A) FTIR and (B) ESI-MS (–ve) spectra of ligand Li_2[Benz(pic)$_2$]. The simulated spectrum is given as an inset.

The electrospray ionization mass spectrum (ESI-MS) of ligand Li_2[Benz(pic)$_2$] in aqueous medium was recorded in the negative mode showing a 100% molecular ion peak at *m/z* = 389.12 (**Figure 2.3B**). The isotope distribution pattern of the observed mass corresponded to the composition of the ligand $[C_{21}H_{17}N_4O_4]^-$. Another minor peak appeared at *m/z* = 395.13 corresponding to the composition of ligand $[C_{21}H_{16}N_4O_4Li]^-$.

The ^{1}H NMR spectrum of ligand Li_2[Benz(pic)$_2$] in D_2O solvent (**Figure 2.4**) showed signals in the region δ = 7.82-6.82 ppm, corresponding to 10 aromatic protons present in two pyridine and one benzene units. A sharp singlet peak at δ = 5.31 ppm appeared for the substituted –CH proton, adjacent to the picolinate unit. Non-aromatic signals in the range δ = 4.02-3.75 ppm were due to 4 protons of two methylene units adjacent to the tertiary amine. The ^{13}C NMR spectrum of the ligand in D_2O solvent represented 21 characteristic signals for 21 different kinds of carbon atoms present in the ligand.

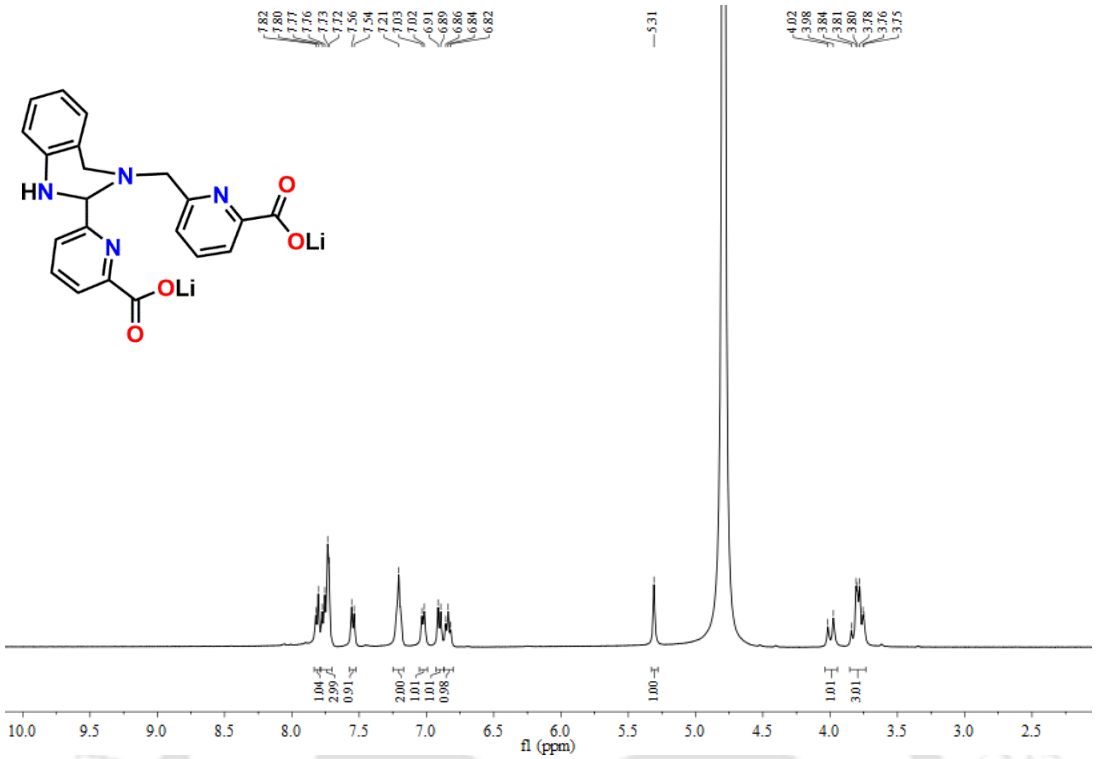

Figure 2.4. ^{1}H NMR spectrum of ligand $Li_2[Benz(pic)_2]$ in D_2O solvent.

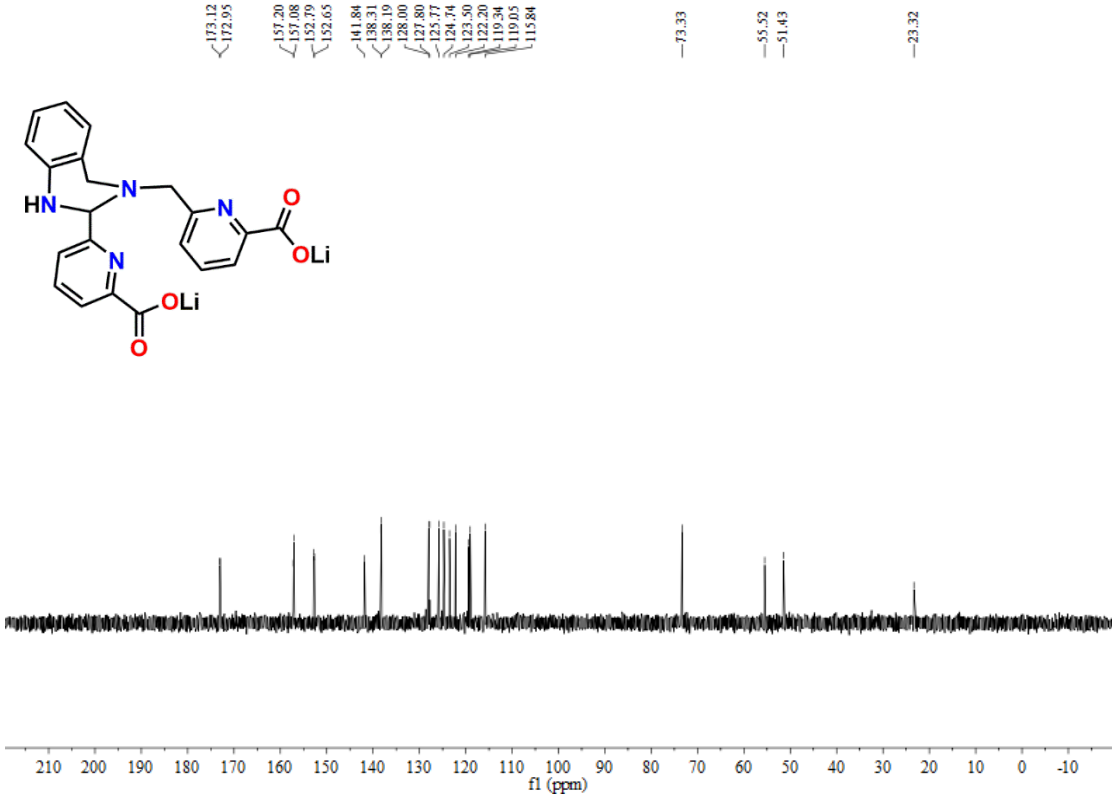

Figure 2.5. ^{13}C NMR spectrum of ligand $Li_2[Benz(pic)_2]$ in D_2O solvent.

2.3 Syntheses and Characterization of Bis-aquated Mn(II)-Complex of Ligand $Li_2[Benz(pic)_2]$, 2A

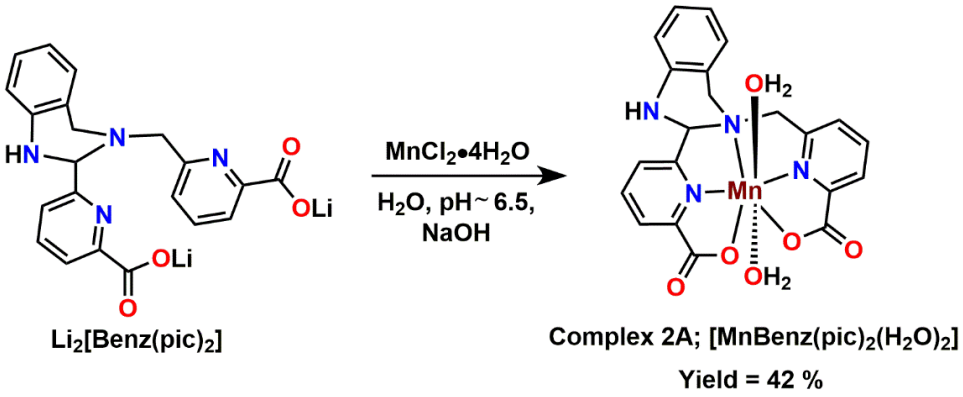

Scheme 2.2. Schematic representation for the synthesis of complex **2A**, $[C_{21}H_{20}N_4O_6Mn]$.

Mn(II)-complex, **2A**, was prepared by reacting stoichiometric amount of the ligand $Li_2[Benz(pic)_2]$ and $MnCl_2•4H_2O$ in an aqueous medium at pH ~ 6.5, attained by dilute NaOH solution. After 24 h, the reaction mixture was evaporated and the methanolic solution of the resultant solid was kept under a diethyl ether diffusion environment for 5 days. The complex was obtained as white solid, and thoroughly washed with diethyl ether. However, repeated trials to obtain single crystals suitable for X-ray diffraction analyses from aqueous or any other solvent medium were unsuccessful.

The synthesized complex was characterized by FTIR and ESI-MS spectra analyses. The infrared spectrum showed a broad band with two blunt peaks at 3473 cm^{-1} and 3388 cm^{-1} due to the ν_{O-H} (water) and ν_{N-H} (secondary amine) stretching, respectively (**Figure 2.6A**). The $\nu_{C=O}$ asymmetric stretching peak appeared at 1622 cm^{-1}, showing a slight shift from the corresponding band position of the ligand (1615 cm^{-1}). The positive mode ESI-MS spectrum of the aqueous complex **2A** solution showed a 100% molecular ion peak at *m/z* = 444.0519, which corresponded to the composition $[C_{21}H_{16}N_4O_4Mn + H]^+$ for the Mn-complex (**Figure 2.6B**). This is also reflected in the isotropic pattern analysis. The purity of the complex (>95%) was ascertained by the presence of a single dominant peak in reverse phase HPLC-UV measurement (**Figure 2.7**).

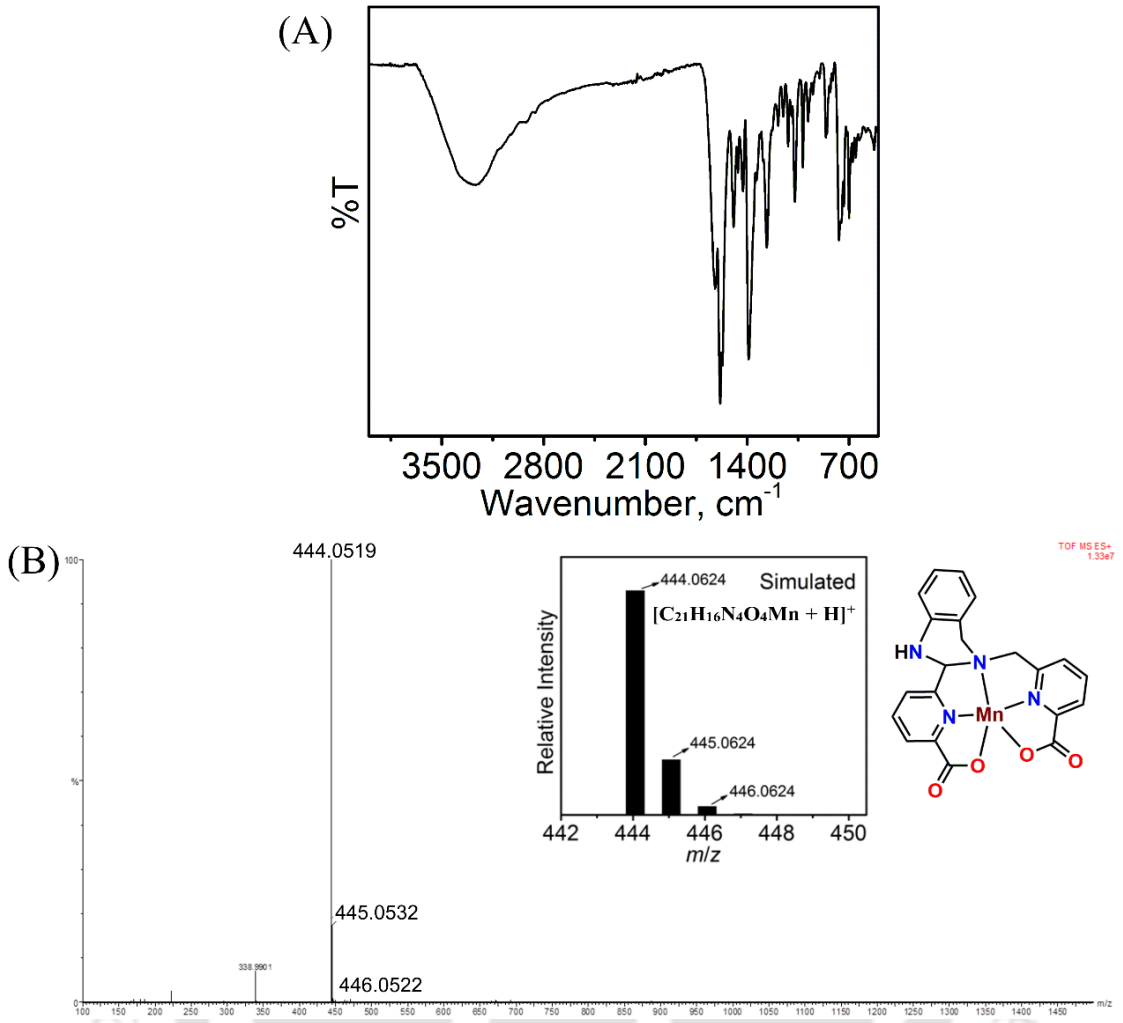

Figure 2.6. (A) FTIR and (B) ESI-MS (+ve) spectra of complex **2A**. The simulated spectrum is given as an inset.

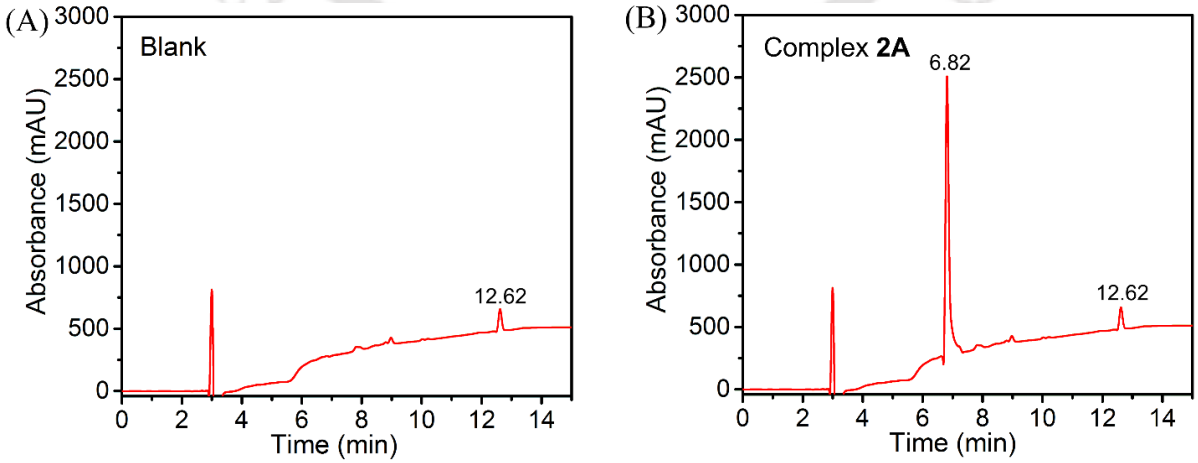

Figure 2.7. HPLC-UV analysis of (A) Blank and (B) complex **2A** (t_R = 6.82), detected at 214 nm.

To analyze the physicochemical and relaxometric properties of the Mn(II)-complex, determination of hydration number is crucial. Literature depicted the existence of Mn^{2+} ion as either a six– or seven–coordinated complex.[3c,6a,11a] The synthesized pentadentate ligand $Li_2[Benz(pic)_2]$ could generate either a six–coordinated complex with one inner-sphere water molecule or a seven–coordinated complex with two inner-sphere water molecules. Considering the inability to grow X-ray-suitable single crystals of complex **2A**, we employed DFT-level optimization to determine the optimal structure of the same. The computational simulations were performed using the Gaussian 16[16a] program and visualized with the GaussView V.5.09[16b] packages. The calculations were done at the ωB97XD[16c]/cc-pVDZ[16d] level. Using long-range corrected RS-functionals was advantageous since the range separation parameter (ω) provided a better description of the charge transfer prospect in the calculations.[16e] Moreover, the use of all-electron basis sets (cc-PVDZ), including the transition metal atoms for the system, maintained consistency throughout the calculations. Global minima in the energy landscape were determined by performing subsequent frequency calculations on the optimized structures.

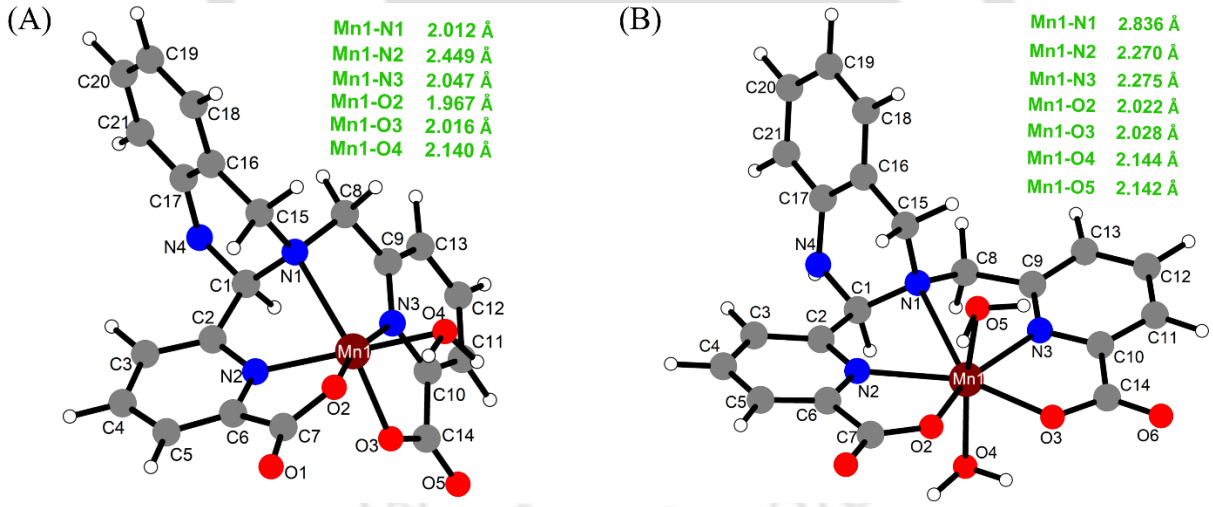

Figure 2.8. The DFT-optimized structures of complex **2A** with some selected bond distances; (A) mono-aquated form, and (B) bis-aquated form.

Our calculations involved varying considering complex frameworks with mono-aqua or bis-aqua coordination and we screened DFT-optimized structures to identify the most probable configuration, represented in **Figure 2.8**. The relevant computed binding energy was found to be -29.32 Kcal/mol and -43.16 Kcal/mol for the optimized mono–and bis–aquated complex

structures, stability exhibiting the highest thermodynamic of the latter one. The theoretical simulation data verified the fact that ligand coordination around the Mn(II) is most likely to be in a planer disposition. So, the coordination of water molecules along the axial positions *i.e.*, above and below the ligand mean plane, was favorable. The addition of a second water molecule had a significant impact on the complex's geometry, enhancing its inherent stability through the aquation process. When a single water molecule was attached at an axial position, the complex exhibited noticeable distortion, as seen in the optimized structure (**Figure 2.8A**). However, the addition of a second water molecule to the Mn center relieved torsional strain, resulting in a planar orientation around the metal center in the overall structure (**Figure 2.8B**).

The theoretical simulated structural data favored the existence of **2A** as a seven-coordinated Mn(II)-complex. Three nitrogen and two oxygen atoms of the ligand chelated along the pentagonal equatorial plane and two water molecules occupied the axial positions. The obtained bond lengths were in accordance with similar Mn(II)-based complexes reported previously.[17]

Furthermore, the existence of two inner-coordinated water molecules for complex **2A** (q = 2) was further supported by the concentration-dependent paramagnetic chemical shift studies, obeying equation (**1**).[2e,2f]

$$\Delta\omega_p = \Delta\omega_{obs} - \Delta\omega_{ref} = \frac{q[\mathbf{Mn}]}{[\mathbf{H_2O}]} \frac{g_L S(S+1) B_0}{3k_B T} \left(\frac{A_0}{\hbar}\right) \quad \textbf{(1)}$$

Where, ω_p, ω_{obs}, and ω_{ref} represented the paramagnetic chemical shift, observed chemical shift, and chemical shift of proton in the absence of paramagnetic ions, respectively. B_0 is the applied magnetic field, $\left(\frac{A_0}{\hbar}\right)$ represented the hyperfine coupling constant, and other symbols have their usual meanings. According to this equation, the hydration number can be determined from the slope of the linear plot of $\Delta\omega_p$ *versus* paramagnetic concentration, at a fixed temperature.

The ^{1}H NMR analysis of complex **2A** solutions in H_2O/D_2O medium (1:2), evidenced an increase in paramagnetic chemical shift with increasing [Mn(II)] concentration, at 55 °C and 9.4 T (**Figure 2.9**). A similar experiment was done for the mono-aquated Mn(EDTA) and Mn(AlcDPA) complex. The slope for **2A** was found to be ~ 2-fold higher than that for the previously reported Mn(EDTA) complex, suggesting the presence of two metal-coordinated water molecules in complex **2A**.

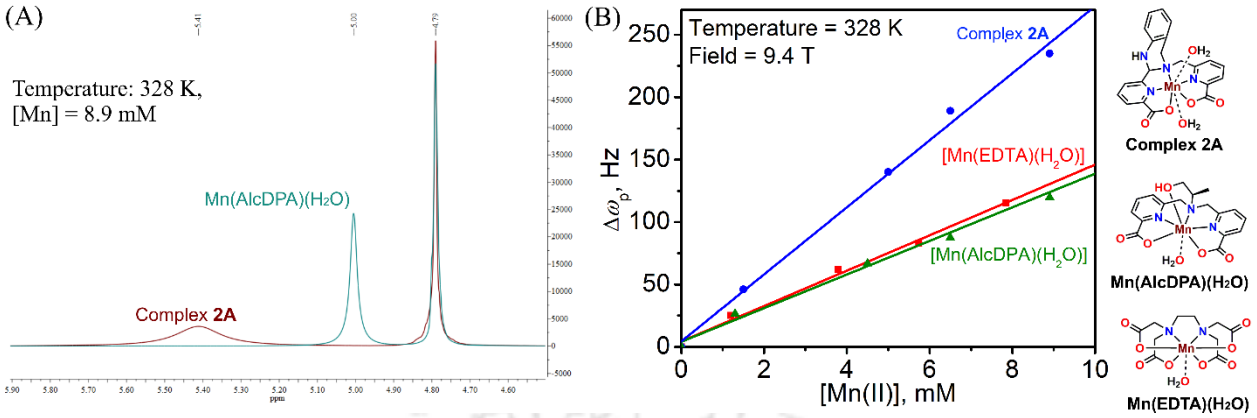

Figure 2.9. ^{1}H NMR resonance shift for complex **2A**, [Mn(EDTA)(H_2O)], and [Mn(AlcDPA)(H_2O)] as a function of [Mn(II)] concentration. Measurements were done at 9.4 T and 55 °C.

Table 2.3. Optimized coordinates of the mono-aquated form of complex **2A**.

N	19.2263	-12.5599	0.6699
C	18.6819	-12.9906	-0.6452
C	18.3006	-14.4548	-0.5024
C	17.1435	-15.0493	-0.9821
C	16.903	-16.3862	-0.6492
C	17.7689	-17.0462	0.2183
C	18.891	-16.3638	0.6766
N	19.1843	-15.1339	0.235
C	19.7353	-16.8049	1.8672
O	19.6268	-17.925	2.3207
C	20.0259	-11.3387	0.5417
C	21.2838	-11.661	-0.2303
N	21.6862	-12.9368	-0.1289
C	22.7691	-13.3586	-0.7979
C	23.5246	-12.4984	-1.5867
C	23.1256	-11.1698	-1.6879
C	21.9807	-10.7454	-1.0099
O	20.433	-15.8109	2.3386
O	22.2402	-15.4561	0.1301
Mn	20.839	-14.3579	1.0757
O	22.2522	-13.9581	2.6317
C	23.0834	-14.8454	-0.6288
O	24.0611	-15.2993	-1.1995
C	18.1322	-12.4496	1.6461
C	17.0016	-11.5789	1.1536
C	16.7954	-11.4574	-0.2292
N	17.604	-12.1608	-1.1324
C	16.172	-10.8773	2.0296
C	15.1505	-10.0593	1.5578
C	14.9627	-9.9302	0.1805
C	15.7756	-10.6234	-0.7075

H	19.505	-12.9358	-1.3713
H	16.4418	-14.4635	-1.5746
H	16.008	-16.8873	-1.0218
H	17.5824	-18.0529	0.5914
H	19.4778	-10.5084	0.0603
H	20.2953	-11.0104	1.5578
H	24.3946	-12.9041	-2.1023
H	23.69	-10.4656	-2.3015
H	21.6289	-9.7156	-1.087
H	21.9811	-14.7834	3.0803
H	17.7771	-13.4706	1.861
H	18.5494	-12.0587	2.585
H	17.796	-11.6674	-1.9939
H	16.342	-10.9708	3.1053
H	14.5107	-9.5195	2.2566
H	14.1712	-9.2864	-0.2071
H	15.621	-10.5309	-1.7851
H	23.1217	-14.1799	2.2695

Table 2.4. Optimized coordinates of the bis-aquated form of complex **2A**.

N	19.1678	-12.7646	-0.2864
C	18.0884	-13.3842	-1.0268
C	17.7572	-14.7188	-0.3761
C	16.4524	-15.1874	-0.2786
C	16.228	-16.4507	0.2656
C	17.3176	-17.1965	0.6911
C	18.5899	-16.6445	0.5696
N	18.8147	-15.4287	0.0473
C	19.8133	-17.4006	1.0634
O	19.6753	-18.5317	1.496
C	19.8436	-11.7235	-1.0327
C	21.3165	-11.6893	-0.7129
N	21.9056	-12.8592	-0.4203
C	23.2373	-12.8618	-0.2306
C	24.024	-11.7177	-0.3167
C	23.4063	-10.5052	-0.5907
C	22.0291	-10.4944	-0.79
O	20.9025	-16.7151	0.977
O	23.0195	-15.1547	0.2495
Mn	21.0136	-14.8733	0.1491
O	21.3431	-15.7117	-1.7962
O	21.0456	-14.4129	2.2406
C	23.8761	-14.2069	0.0892
O	25.0913	-14.2749	0.1677
C	18.7039	-12.3268	1.0314
C	17.4683	-11.4603	0.9314
C	16.6402	-11.5828	-0.1974
N	16.9136	-12.542	-1.1859
C	17.1476	-10.5146	1.9073
C	16.0326	-9.6924	1.7817
C	15.2265	-9.8066	0.6476

C	15.5245	-10.7446	-0.3325
H	18.4702	-13.6191	-2.0325
H	15.6388	-14.5533	-0.6265
H	15.2126	-16.8403	0.3559
H	17.2337	-18.1911	1.1274
H	19.7492	-11.9464	-2.1082
H	19.3993	-10.7219	-0.8806
H	25.096	-11.8258	-0.1561
H	23.983	-9.5805	-0.648
H	21.4984	-9.5667	-1.0101
H	20.9824	-16.6083	-1.7606
H	22.2858	-15.8447	-1.584
H	21.0816	-15.3765	2.4069
H	18.5188	-13.2215	1.6466
H	19.5241	-11.7846	1.5235
H	16.7444	-12.2188	-2.1299
H	17.7995	-10.4184	2.7797
H	15.7979	-8.961	2.556
H	14.353	-9.1633	0.528
H	14.8857	-10.8449	-1.2133
H	21.9492	-14.1263	2.4321

2.4 Thermodynamic Stability of Complex 2A

Ligand frameworks are cautiously designed to stabilize the Mn(II) ion, thereby reducing the leaching of free metal ions during *in-vivo* administration for MRI scans. The conditional stability constant (logK_{cond}) of the ligated complex has been a very important parameter to compare the respective thermodynamic aspects at physiological conditions.[2a,18]

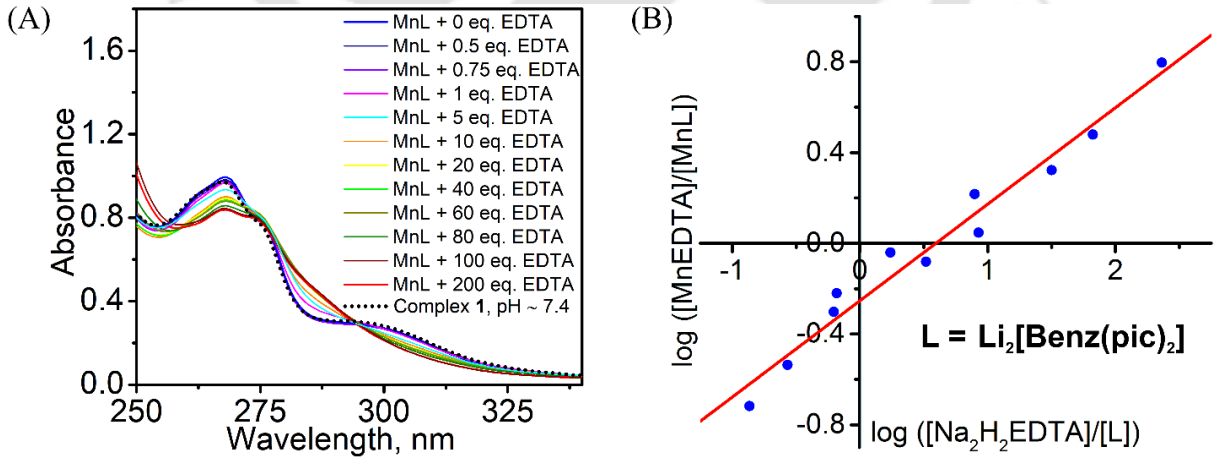

Figure 2.10. (A) UV-Vis spectral changes during the spectrophotometric competition batch titration of ligand $Li_2[Benz(pic)_2]$ = L against H_2Na_2EDTA, at pH 7.4 and 25 °C. (B) Competitive batch titration plot of ligand $Li_2[Benz(pic)_2]$ against EDTA.

The spectrophotometric batch titrations against competing hexadentate H_2Na_2EDTA ligand were performed in determining the conditional stability constant ($\log K_{cond}$) of the corresponding Mn(II) complex of $Li_2[Benz(pic)_2]$ ligand in terms of value, equation **(2)**.[18a]

$$[MnL] + [Na_2H_2EDTA] \rightleftharpoons [MnEDTA] + [L];$$

$$K_{cond} = \frac{[MnEDTA][L]}{[MnL][Na_2H_2EDTA]};$$

$$\log([MnEDTA]/[MnL]) = \log K_{cond} + \log([Na_2H_2EDTA]/[L]) \quad \textbf{(2)}$$

The equilibrium constant for the competition reaction was determined at specific experimental conditions: [M] = 10 μM, [L] = 10 μM, I = 0.15 M NaCl, at pH ~ 7.4 (HEPES buffer) and 25 °C. The increasing volume of standardized H_4EDTA stock solution ranging from 0.5 to 200 equivalents relative to the ligand [$Li_2Benz(pic)_2$ = L] concentration was added to a [Mn(II)-L] solution. The resulting solutions were allowed to equilibrate for 48 hours at 25 °C. The overall UV-Vis absorbance spectra were observed and a particular range of wavelengths was selected where gradual spectral changes were considered (**Figure 2.10A**). The absorbance value of each set was recorded with respect to the value of ligand $Li_2[Benz(pic)_2]$ (represented as L) at that particular wavelength. Na_2H_2EDTA solution of exact concentration and pH was used as background for each scan. Utilizing the respective absorbance values, further calculations gave the concentrations of $MnBenz(pic)_2$ complex, MnEDTA complex, free ligand $Li_2[Benz(pic)_2]$, and free Na_2H_2EDTA for each set were calculated from the variation in absorbance in each set of samples. The X-intercept of [Mn-EDTA]/[Mn-L] *versus* [EDTA]/[L] plot represented the relative affinity of $Li_2[Benz(pic)_2]$ ligand for Mn(II) (**Figure 2.10B**), which was found to be 0.6 log*K* units higher than that for EDTA ($\log K_{cond}$ = 11.62, for $Li_2[Benz(pic)_2]$, 11.02, for Na_2H_2EDTA).[2b] Noteworthy, the hexadentate $[EDTA]^{4-}$ ligand results in a seven-coordinate mono(aquated) Mn(II)-EDTA complex, while the bis(aquated) complex **2A** with the pentadentate $Li_2[Benz(pic)_2]$ ligand provided seven-coordinate complex with superior stability. Conditional stability constants of some bis-aquated Mn(II)-complexes, *viz*, $[Mn(15\text{-}pyN_5)(H_2O)_2]^{2+}$, $[Mn(15\text{-}pyN_3O_2)(H_2O)_2]$, $[Mn(PMDPA)(H_2O)_2]$, *etc*, are in the range 5.2-7.8 (**Table 2.1**).[6a,7a] Thus, the ligand rigidity imparted by the hydroquinazoline backbone imposed significantly higher thermodynamic stability in the complex with the pentadentate ligand (complex **2A**).

2.5 Relaxometric Studies of Complex 2A

At a constant temperature and magnetic field, the proficiency of 1 mM concentration of the paramagnetic metal ions to enhance the relaxation rates of the water protons is defined as relaxivity, r_i (i = 1, longitudinal relaxivity; 2, transverse relaxivity).[19] It is a decisive parameter to examine the potential of the complex as an MRI contrast agent. T_1 and T_2 values of complex **2A** solutions were recorded using BRUKER minispec mq60 NMR analyzer following the inversion recovery method, at pH ~ 7.4, 1.41 T, 25 °C, and 37 °C. Relaxivity values (r_i, i =1/2) were obtained from the slope of linear plots of relaxation rates ($1/T_i$) versus Mn(II) concentration (**Figure 2.11**). The exact metal concentration in the sample stock was determined by the ICP-AES technique (Model- ARCOS, Simultaneous ICP Spectrometer, SPECTRO Analytical Instruments GmbH, Germany) after digesting the solution with HNO_3. pH was maintained using 0.01 M HEPES buffer.

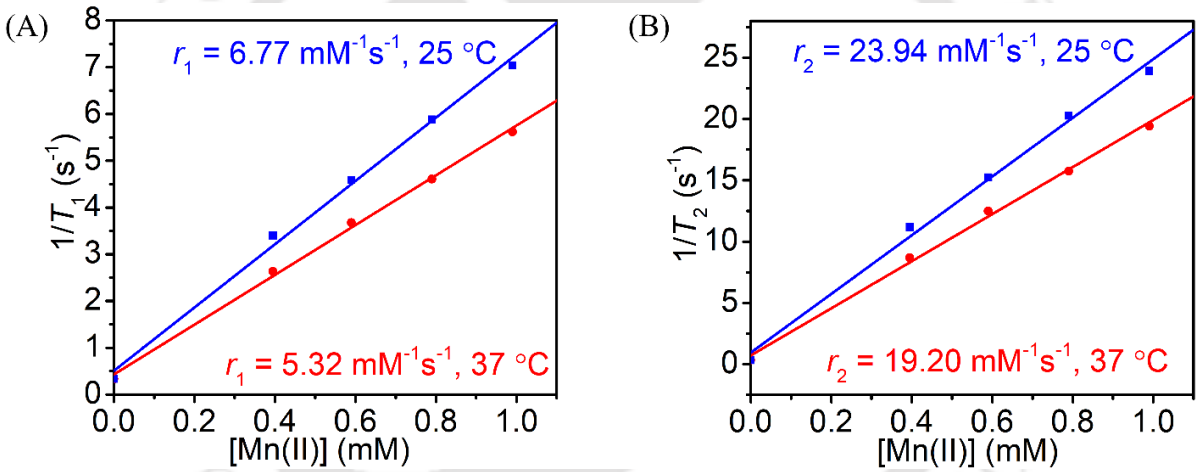

Figure 2.11. (A) $1/T_1$ and (B) $1/T_2$ *versus* [Mn(II)] plot for complex **2A**, measurements were performed at 1.41 T and pH ~ 7.4.

2A showed impressive relaxometric properties with r_1 = 6.77 mM^{-1}s^{-1} at 25 °C and 5.32 mM^{-1}s^{-1} at 37 °C; r_2 = 23.94 mM^{-1}s^{-1} at 25 °C and 19.20 mM^{-1}s^{-1} at 37 °C, 1.41 T and pH ~ 7.4. Besides other commercially available contrast agents, the observed longitudinal relaxivity values were a little higher than the previously reported acyclic bis(aquated) Mn(II) complexes as presented in **Figure 2.12**.[3c, ,6a,10b,c] The presence of rigid hydroquinazoline unit, restricting the overall rotation of the chelate, along with the two coordinated water molecules accounted for the elevated relaxivity values for complex **2A**. The r_2/r_1 ratio was found to be 3.6 at 37 °C, and thus the synthesized complex could efficiently influence both the R_1 and R_2 values of water protons.

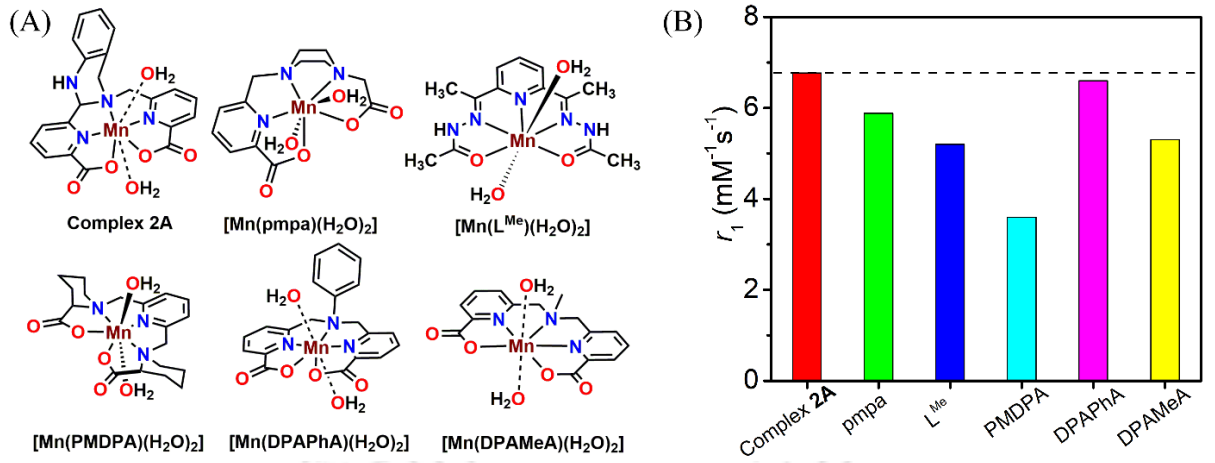

Figure 2.12. r_1 values of different bis-aquated Mn(II)-chelates compared to complex **2A**, measurements were done at pH 7.4, 1.41 T, 25 °C.

Bicarbonate(HPO_4^{2-}), bicarbonate (HCO_3^-), and citrate ($C_6H_5O_7^{3-}$) are some common anions that are prevalently present in the bloodstream as well as in the extracellular space in different organs.[20] They could potentially replace the inner sphere water molecule if the complex is not sufficiently stable.[21] Anion tolerance study of complex **2A** was therefore examined by measuring T_1 of **2A** solution, after incubation with 200 equivalents of respective anion, at 37 °C (**Figure 2.13A**).

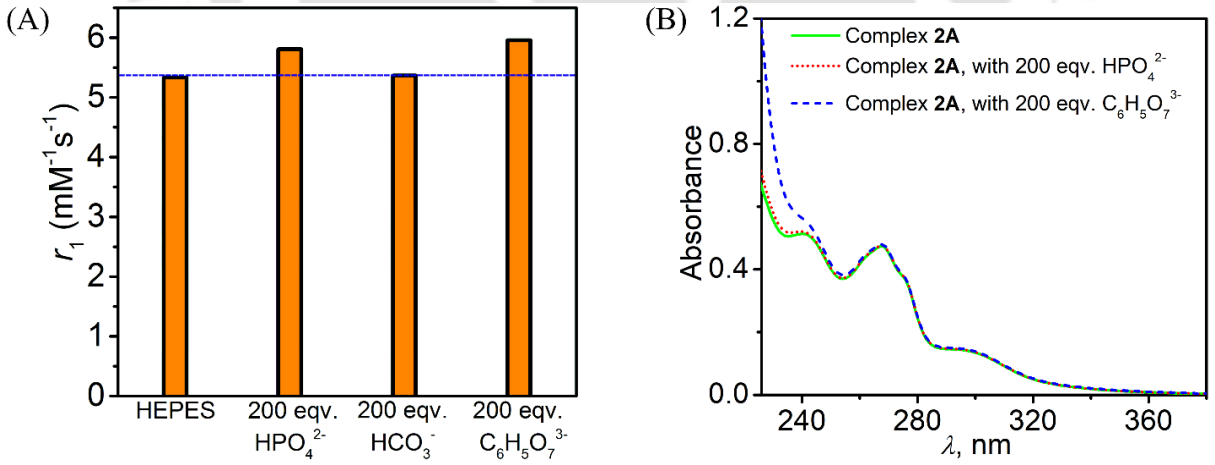

Figure 2.13. (A) r_1 values for complex **2A** solution (0.5 mM), at 1.41 T, pH ~ 7.4, and 37 °C, and (B) UV-Vis spectra for complex **2A** solution (0.05 mM) in the absence and presence of 200 equivalents excess of different challenging anions at pH ~ 7.4 and 25 °C. Data was recorded after 1 h incubation.

No appreciable alteration in the relaxivity value confirmed that the coordination sphere of the complex had not been affected by these anions. This result corroborated well with the fact that no considerable change in UV-Vis spectra of **2A** was observed after the addition of previously mentioned anions (**Figure 2.13B**). A slight increase in the relaxation value in the presence of HPO_4^{2-} and $C_6H_5O_7^{3-}$ alluded to a supramolecular aggregation in the presence of the anions, which increased the rotational correlation time.[7a,22]

Unlike in blood serum (pH ~ 7.4), pH varies in different organs and vessels inside the living body. Mn(II)-complexes can undergo dechelation at low pH *via* ligand protonation.[23] Furthermore, the substitution of inner-sphere water molecules or deprotonation of water molecules to hydroxide anion at a higher pH can significantly affect the contrast ability and the stability of the Mn(II)-based contrast agents.

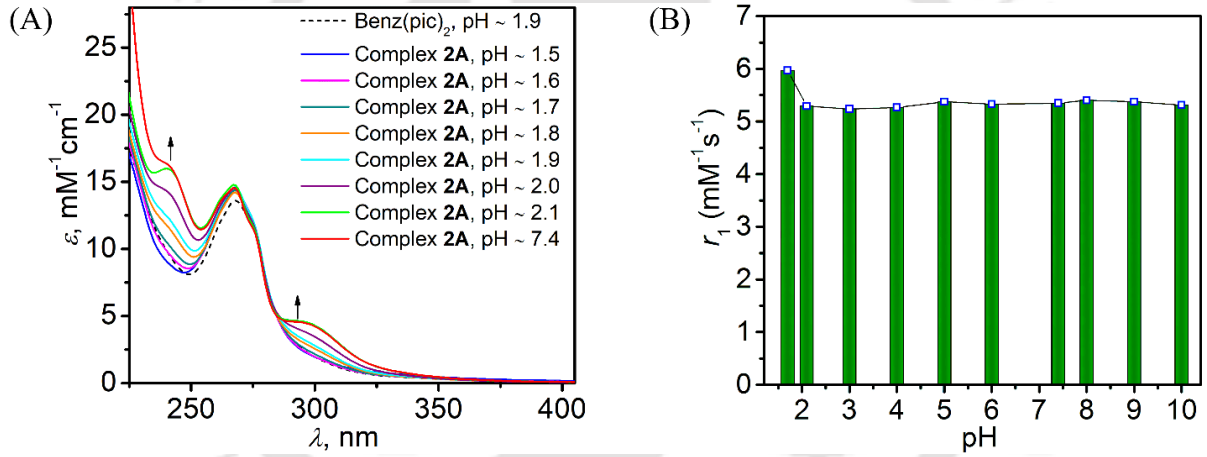

Figure 2.14. (A) UV-Vis spectra for complex **2A** at various pH and 25 °C, (B) r_1 values for complex **2A** solution (0.5 mM) at different pH ranging from 1.7 to 10.0, at 1.41 T, pH ~ 7.4, and 37 °C.

Thus, the stability of complex **2A** was examined in a broad pH range from pH 2.0 to 10. The UV-Vis spectra were recorded at a different pH (**Figure 2.14A**). The spectral envelope obtained at pH 2.1 and pH 7.4 was the same, confirming the complex's stability at pH 2.1. To reconsolidate the stability, the r_1 relaxation of the **2A** solution was measured in the pH range of 2.1 to 10.0 at 1.41 T, 37 °C (**Figure 2.14B**). Gratifyingly, no alteration in the relaxivity buttressed the stability of the complex in the pH range.

2.6 Kinetic Inertness of Complex 2A

Kinetic inertness is an indispensable parameter to assess the applicability of paramagnetic chelates for *in-vivo* imaging. Mn(II)-complexes of acyclic ligands often succumb to transmetallation in the presence of Zn(II) ions *in vivo*.[10a,b,13a,24] Thus, release free Mn(II) ions. The Mn(II) ion is a nutritional element and can be either physiologically absorbed or excreted from the body.[25] Thus, discard the possibility of long-term accumulation and the subsequent toxicity, which is the neurological disorder called manganism.[26] However, an accumulation of free Mn(II) ions over 3.38 mmol/kg would engender such toxicity.[27] Complex **2A** exhibited a high r_1 relaxivity (*vide infra*); hence, a lower dose of 0.1 mmol/kg can be administered for MR imaging.

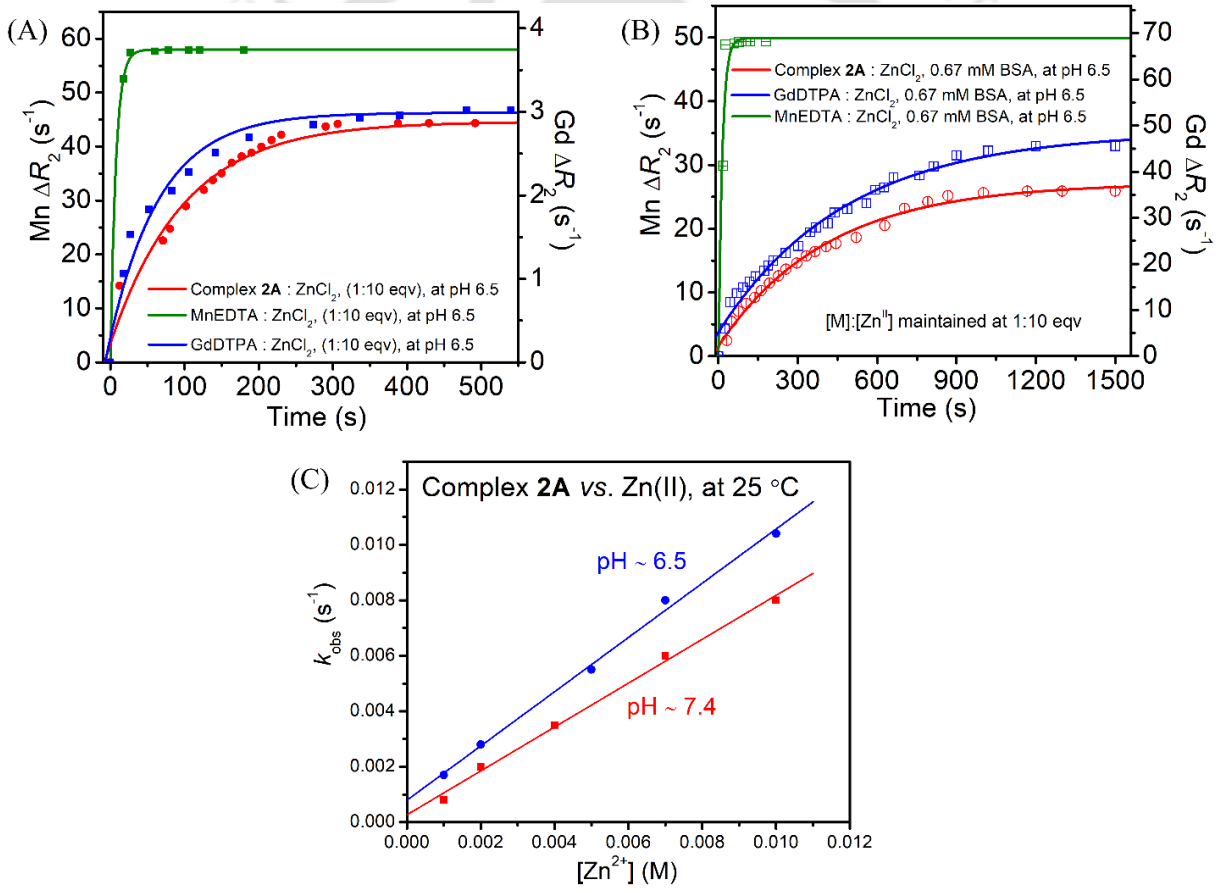

Figure 2.15. Transmetallation kinetic studies of complex **2A** (1 mM) when challenged by Zn(II) ions (10 mM), (A) in aqueous medium, and (B) in BSA solution (0.67 mM). R_2 value recorded as a function of time, at 1.41 T, pH ~ 6.5 (MES buffer), and 25 °C. (C) Plot of k_{obs} versus [Zn(II)] for the displacement reaction between complex **2A** and Zn(II) at 25 °C.

The kinetic inertness of complex **2A** has been investigated in the presence of a 10-fold excess of Zn(II) ions. Gradual changes in the transverse relaxation rate (R_2) of the sample containing **2A** solution (1mM), challenged with 10 equivalents of $ZnCl_2$, was monitored over time. Measurements were done in either an aqueous medium or in BSA medium (0.67 mM), at pH ~ 6.5 and 7.4 (MES and HEPES buffer), I = 0.15 M NaCl, 1.41 T and 25 °C, using BRUKER minispec mq60 NMR analyzer. The same experiment was repeated employing the standard $[Mn(EDTA)(OH_2)]^{2-}$ and the clinically approved commercially available $[Gd(DTPA)(OH_2)]^{2-}$ (Magnevist®) contrast agents for comparison. ΔR_2 value *versus* time was plotted for each sample and data points were fitted to the pseudo-first-order equation to evaluate the rate constant values (**Figure 2.15**).

It was observed that the kinetic inertness of complex **2A** (pseudo-first-order, $k = 1.04 \times 10^{-2}$ s^{-1}, at pH ~ 6.5) was about 8.5 times higher than that of $[Mn(EDTA)(OH_2)]^{2-}$ ($k = 8.86 \times 10^{-2}$ s^{-1}) and almost same as that of $[Gd(DTPA)(OH_2)]^{2-}$ ($k = 1.16 \times 10^{-2}$ s^{-1}). Moreover, the synthesized complex showed 5 times higher kinetic stability ($k = 2.13 \times 10^{-3}$ s^{-1}) at the physiological conditions, when kinetic studies were done by following the time profile of the R_2 value of **2A** solution, challenged by a 10-fold excess of Zn(II) ions in serum albumin (0.67 mM), in 0.15 M NaCl, pH 6.5, and 25 °C (**Figure 2.15B**). Hence, despite having two inner-sphere water molecules and the pentadentate coordinating ligand, a higher kinetic inertness in the Mn(II) ions-based complex **2A** could be harnessed by imparting the ligand-based rigidity. In summary, the incorporation of the hydroquinazoline unit in the ligand backbone successfully boosted the kinetic stability of the corresponding chelate.

2.7 Serum Albumin Interaction of Complex 2A

Serum albumin, the most prominent protein in blood plasma, is known to bind with various lipophilic ligand systems.[12] Interaction between small molecules of paramagnetic contrast agents with the bulky protein moiety significantly reduces the rotational correlation time (τ_R) and consequently, enhances the relaxivity value.[11b,28] The complex **2A** with a hydroquinazoline and two pyridine units, has considerable lipophilic character. The octanol-water partition coefficient (log *P*) value for the complex was calculated to be – 0.45, proving its amphiphilic nature. Thus, an

efficient binding interaction between the complex and the hydrophobic albumin protein was expected.

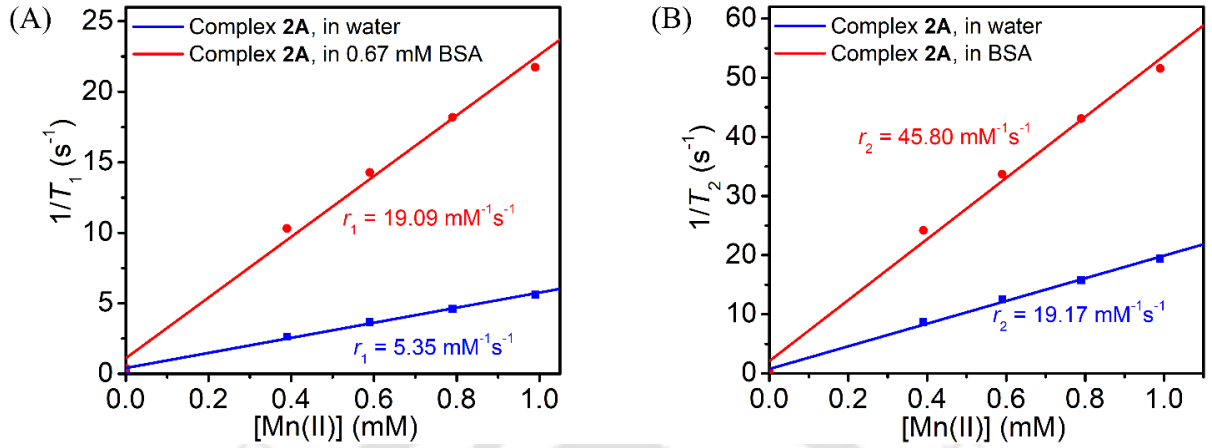

Figure 2.16. (A) $1/T_1$ and (B) $1/T_2$ *vs* [Mn(II)] plot for complex **2A** in water (HEPES solution, 0.01 M) or 0.67 mM BSA, at pH ~ 7.4, 37 °C, and 1.41 T.

r_1 values for **2A** solutions were measured after 30 minutes of incubation of samples in the presence of 0.67 mM bovine serum albumin (BSA) at physiological conditions (pH ~ 7.4, 37 °C, BSA concentration maintained at 0.67 mM; measured at 1.41 T). Complex **2A** showed ~360 % amplification in the longitudinal relaxivity in the presence of the physiological concentration of serum protein, reaching up to r_1 = 19.09 mM^{-1}s^{-1} in the presence of BSA *versus* r_1 = 5.32 mM^{-1}s^{-1} in water, at pH ~ 7.4, 1.41 T, and 37 °C (**Table 2.5, Figure 2.16**). Thus, it demonstrated a substantial interaction between the protein and **2A**. Notably, the longitudinal relaxivity values obtained are considerably higher than previously reported mono-aquated Mn-EDTA (3.5 mM^{-1}s^{-1}), Mn-EDTA-BTA (15.1 mM^{-1}s^{-1}), Mn-BnO-TyrEDTA (15.8 mM^{-1}s^{-1}), Mn-EOB-PC2A (5.85 mM^{-1}s^{-1}), Mn-1,4-DO2AMBz (17.5 mM^{-1}s^{-1}), *etc*., systems mentioned in **Table 2.2**.[12b,13] Parallelly, ~252 % augmentation in r_2 value (45.80 mM^{-1}s^{-1} in 0.67 mM BSA *versus* 19.17 mM^{-1}s^{-1} in water, at pH ~ 7.4, 1.41 T, and 37 °C) has also been noticed (**Figure 2.16B**), which reflected the possibility of the T_1-T_2 dual-mode imaging character of complex **2A** *in vivo*.

***Proton Relaxation Enhancement study*:** A deeper insight into the non-covalent interaction between complex **2A** and the albumin protein was done by following the observed relaxation rate (R_1^{obs}) values of the complex aqueous solutions with a constant Mn(II) ions concentration in the presence of an increasing amount of protein at 37 °C. The binding constant of the corresponding

interaction was determined following the established Proton relaxation enhancement (PRE) titration.[29] In the experiment, R_1 value of 30 minutes incubated samples containing a fixed concentration of **2A** (0.35 mM) and increasing concentration of BSA (0-1.8 mM) were recorded at pH ~ 7.4, 37 °C, and 1.41 T (**Figure 2.17A**).

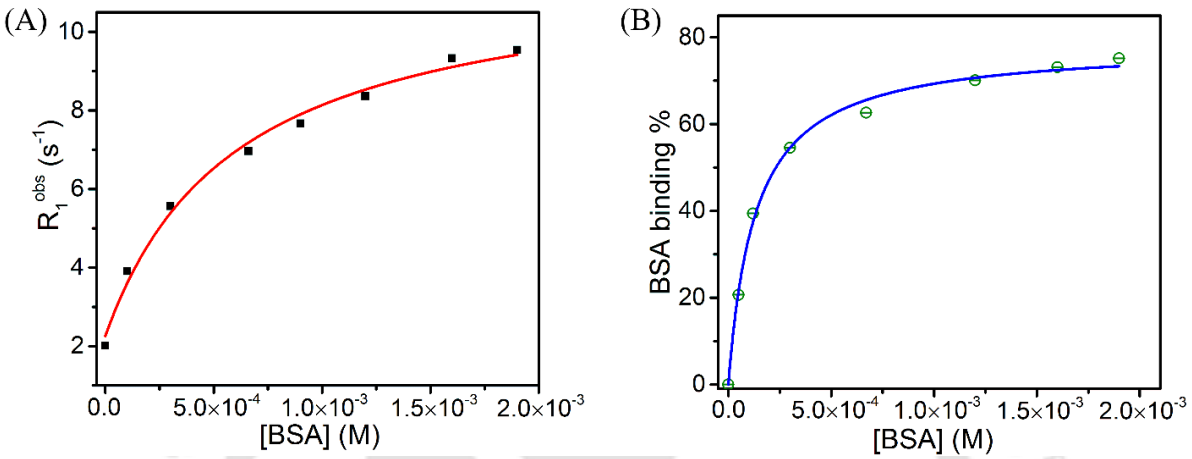

Figure 2.17. (A) Proton longitudinal relaxation rates of **2A** solution (0.35 mM) were observed after the addition of increasing concentration of BSA, at 1.41 T, pH ~ 7.4, and 37 °C. The red line represents 1:1 binding isotherm fitting. (B) Ultrafiltration and ICP-MS-based complex **2A**-BSA binding percentage fit assuming one site-specific binding.

Table 2.5. Relaxivity, serum affinity constants, and octanol-water partition coefficients of complex **2A**.

	log *P*	r_1 ($mM^{-1}s^{-1}$)		r_2 ($mM^{-1}s^{-1}$)		r_1^b ($mM^{-1}s^{-1}$)	K_A (M^{-1})
		Water	Serum albumin	Water	Serum albumin		
Complex **2A**	-0.45	5.32	19.09	19.20	45.80	27.62	1.66×10^3

The R_1^{obs} of the prepared samples gradually amplified with the increment in albumin concentration. This finding was due to the albumin-bound-complex fragment fraction increase, as determined by the ultrafiltration method (**Figure 2.17B**), described afterward. Experimental data

were fitted to a 1:1 binding isotherm following the Proton Relaxation Enhancement (PRE), equation **(3)**.

$$R_1^{obs} = 10^3\left[(r_1^f \cdot c_1) + \left\{\frac{1}{2}(r_1^b - r_1^f) \times \left(n \cdot c_{BSA} + c_1 + \frac{1}{K_A} - \sqrt{\left(n \cdot c_{BSA} + c_1 + \frac{1}{K_A}\right)^2 - (4n \cdot c_{BSA} \cdot c_1)}\right)\right\}\right] \quad \textbf{(3)}$$

Where,

R_1^{obs} = Observed proton relaxation rate,

r_1^f = relaxivity of Complex **2A** in free-state,

r_1^b = relaxivity of Complex **2A** in bound-state,

n = number binding site on the protein,

c_1 = concentration of Complex **2A** and

c_{BSA} = concentration of BSA.

Assuming one independent binding site of the protein moiety for the complex, *i.e.*, $n = 1$, the relaxivity of the bound complex (r_1^b) was found to be 27.62 $mM^{-1}s^{-1}$ and albumin association constant $K_A = 1.66\times10^3\ M^{-1}$. The obtained values were comparable to reported Mn(II)-based ligand systems containing the hydrophobic benzyl unit (**Table 2.2**).[12b,13]

***Ultrafiltration binding*:** The percentage binding between complex **2A** and BSA was determined by the ultrafiltration method. Samples were prepared by adding an increasing concentration of BSA to a 0.35 mM **2A** solution at pH ~ 7.4, and vortexed at 37 °C for 30 minutes. After that, 500 µL aliquots from each sample were placed over ultra-centrifugal filters with 10 kDa membranes and centrifuged at 3500g for ten minutes. Mn(II) concentration in the filtrate was estimated by the ICP-MS technique. Data estimated were plotted against protein concentration and fitted to equation **(4)**,[30] specific to one-site protein binding. Results reciprocated to 65% binding of complex molecules to the albumin protein at physiological conditions (**Figure 2.17B**).

$$B = \frac{B_{max}\cdot[L]}{[L]+K_D} \quad \textbf{(4)}$$

Where, B = fraction of bound complex **2A** to total complex **2A**, and B_{max} = maximum binding coefficient, $[L]$ is the concentration of BSA, and K_D is the dissociation constant.

Stability of complex 2A in the serum

Serum albumin also possesses some chelating properties, hence could replace the ligand resulting in the release and subsequent binding of free Mn(II) ion to the protein.[31] Mn(II)•albumin showed a very high relaxivity value, but a high concentration of manganese in the blood causes toxicity and further adverse health issues. Therefore, the stability of complex **2A** in serum or plasma needs to be established before validating its interaction with the protein moiety.

The serum stability for complex **2A** was evaluated by monitoring the change in longitudinal relaxation rate (R_1 value) of its aqueous solution (0.28 mM) with time, in the presence of 0.67 mM BSA, at pH ~ 7.4, 37 °C and 1.41 T (**Figure 2.18A**). The R_1 values for **2A** solution or $MnCl_2$ solution ($[Mn^{II}]$ = 0.80 mM) were also monitored in human plasma for 24 hours and plotted against time.

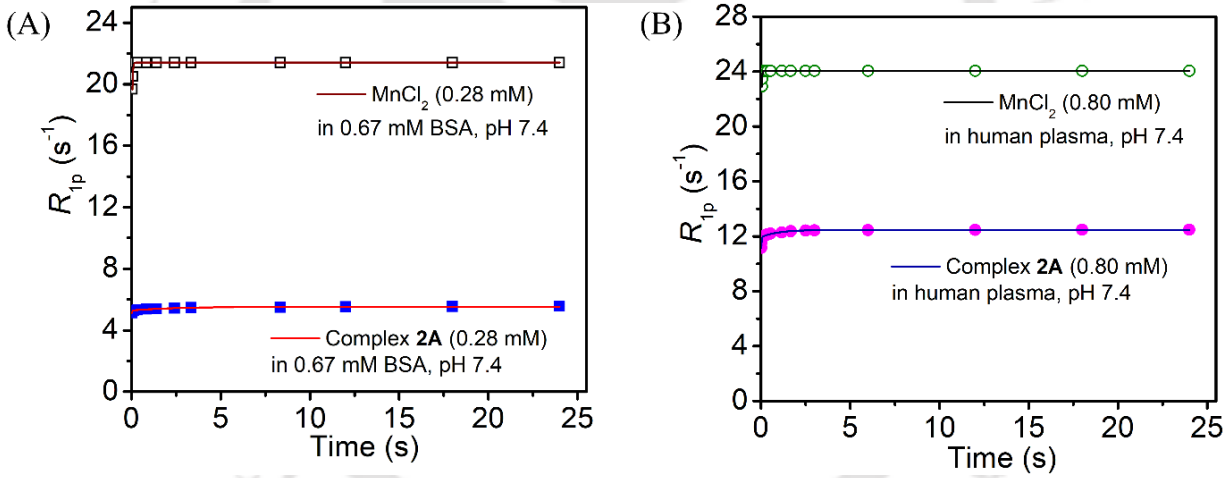

Figure 2.18. Stability of complex **2A** examined in (A) 0.67 mM BSA and (B) human plasma. Measurements were done at 37 °C and 1.41 T.

The relaxivity value (r_1) for **2A** in the BSA medium increased to 18.6 $mM^{-1}s^{-1}$ within 90 s due to the binding of the complex with the albumin protein (*vide supra*). To note, under the same measurement condition, the relaxivity value of 70.74 $mM^{-1}s^{-1}$ was observed by employing an aqueous $MnCl_2$ solution as the complex substitute. A minor change in the relaxivity value from 18.6 $mM^{-1}s^{-1}$ to 19.93 $mM^{-1}s^{-1}$ was noticed within 24 h in the presence of **2A,** thus eliminating the serum albumin protein-induced complete dechelation possibility of the complex. The stability

of the complex was also been investigated in human plasma by replicating the *in vivo* analysis condition, *i.e.*, maintaining the complex concentration at 0.8 mM as administered in mice blood (*vide infra*). The r_1 relaxivity value in this case escalated to 13.95 $mM^{-1}s^{-1}$ in 60 s, and the maximum value attained was ~ 15.6 $mM^{-1}s^{-1}$ in 24 hours (**Figure 2.18B**). A complete dechelation would provide r_1 = 30.11 $mM^{-1}s^{-1}$ as determined using free Mn(II) ions of the same concentration, thus, reflecting the existence of **2A** in the chelated form during *in-vivo* studies.

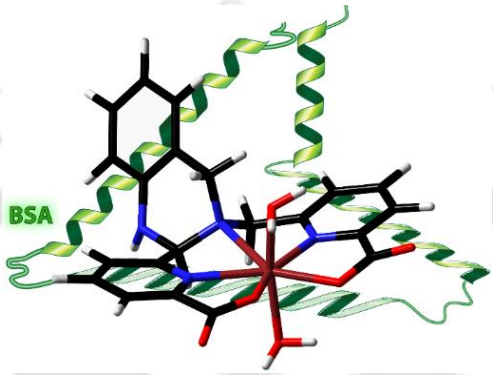

Figure 2.19. Proposed schematic representation of serum albumin–**2A** interaction.

Henceforth, we proved the importance of the inclusion of the phenyl ring containing hydraquinazoline uint as it effectively interacted with the serum albumin protein, reducing the rotation correlation time (τ_M) of the complex. The enhanced rigidity and lipophilic character of the ligand backbone coherently contributed to boosting the relaxivity and elongating the retention time of **2A** in the physiological medium (serum) containing different albumin and globulin proteins.

2.8 Phantom MR imaging of Complex 2A, at 7 T

To evaluate the protein-dependent boost in the relaxivity in terms of magnetic resonance image brightness, T_1-weighted phantom images of aqueous 0.5 mM complex **2A** solution in the absence and the presence of 0.67 mM BSA at pH ~ 7.4 and 25 °C were recorded *in vitro* using 7 T Biospec 70/20, M/s Bruker Biospin GmBH, Germany. Parameters adopted are mentioned: Bruker:RAREVTR sequence, TR (repetition time) = 700.0 ms, TE (echo time) = 8.5 ms, slice thickness = 2.5 mm, field of view (FOV) = 6.00 cm, and matrix = 256×192 (**Figure 2.20**). The signal intensity was enhanced by 43 % in the presence of the complex, confirming the signal brightening property (T_1-contrast agent). Perceptibly, a substantial boost in the image contrast

(57 %) on adding 0.67 mM BSA to the complex **2A** solution complied with the protein-binding-dependent r_1 amplification.

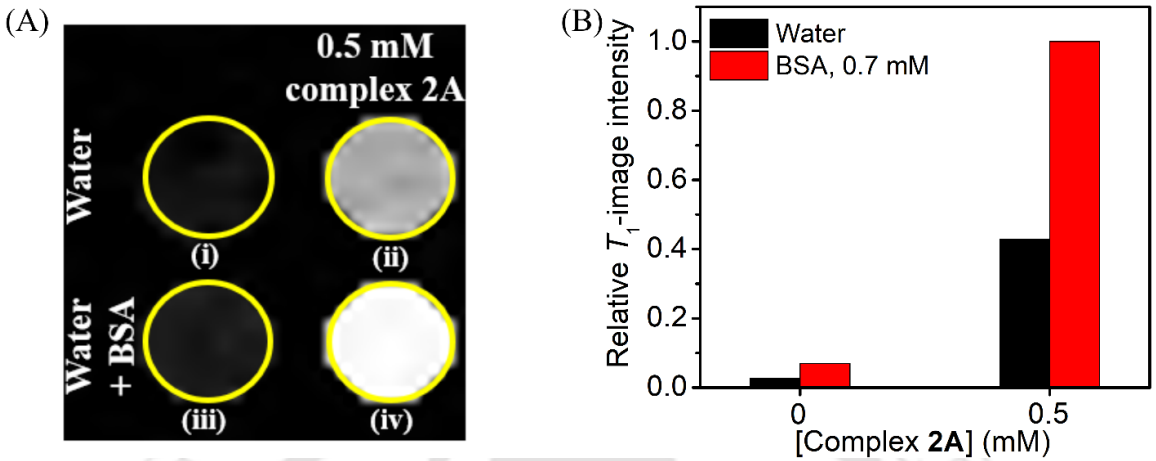

Figure 2.20. (A) T_1-weighted phantom MR images of (i) water, (ii) 0.5 mM complex **2A**, (iii) 0.67 mM BSA, (iv) 0.5 mM complex **2A** in the presence of 0.67 mM BSA, at 7 T, pH ~ 7.4, and 25 °C. (B) Respective relative MR-image intensity plot using *ImageJ* software.

2.9 Cytotoxicity assay of Complex 2A

Prior to *in vivo* examination of **2A** as an MR-contrast agent, the biocompatibility of the complex was investigated by performing MTT [3-(4,5-dimethyl-thiazol-2-yl)-2,5 diphenyltetrazolium bromide]–assay on Cervical cancer (HeLa) cell line. Cells were maintained in Dulbecco's modified Eagle's medium (DMEM) buffer, supplemented with 10% (v/v) fetal bovine serum (FBS), 1% penicillin, and streptomycin at 37 °C in humidified air containing 5% CO_2. Cells were grown in a 96-well plate at a density of 5×103 cells/well for overnight. Succeeding, cell-line was treated with increasing concentration of **2A** (0-1 mM) for 48 h, and 0.5 mg/ml of MTT in DMEM was added to each well and incubated for 1.5 h, afterwards. DMSO (150 µl) was added to each well and absorbance was recorded at 570 nm. Untreated cells were considered as control with 100% viability, and respective cell viability was calculated.

The percentage of viable cells was quantified and presented in **Figure 2.21**. A subtle decline in the viability was noticed up to 200 μM concentration of the complex. Upon increasing the concentration, the cell viability decreased gradually and reached 74% at the concentration of 1 mM. Thus, the cell viability experiments conferred the low cytotoxicity of the complex.

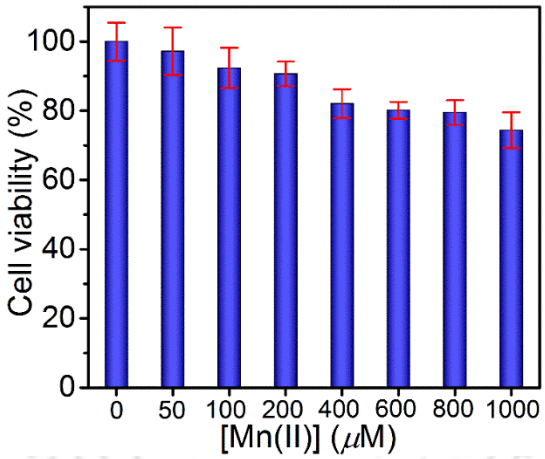

Figure 2.21. Percentage of cell viability analysis after 48 h treatment of complex **2A** on HeLa cells.

2.10 in-vivo MRI of Complex 2A, at 7 T

Eventually, the contrast ability of complex **2A**, *in vivo*, was tested by imaging healthy 8-week-old C57BL/6 mice (n = 3) on a small-bore animal MR scanner (Biospec 70/20, M/s Bruker Biospin GmBH, Germany) at 7 T, before and after 0.08 mmol/kg intravenous administration (*via* tail vein) of the synthesized contrast agent. The mice were anesthetized with 1-3% isoflurane/oxygen mixture maintaining the body temperature to 37 °C and sequentially imaged prior to- and post-contrast injection up to 90 minutes using T_1-weighted 3D fast low-angle low-shot (FLASH) and two-dimensional rapid acquisition with refocused echo (RARE) imaging protocols. Imaging protocols adopted: T_1-FLASH, TR/TE = 316.0 ms/4.5 ms, Flip angle = 30 °, matrix = 256×256, slice thickness = 0.7 mm, 22 slices; T_1-RARE: TR/TE = 3647.4 ms/8.0 ms, Flip angle = 90 °, field of view (FOV) = 50×50 mm, matrix = 256×256, slice thickness = 0.5 mm, 86 slices. Coronal and axial T_1-weighted MR images at different time points are presented in **Figures 2.22** and **2.23**.

Images were analyzed by quantizing the signal intensity (SI) in the region of interest (ROI) of respective organs using *ImageJ* software, after subtracting over the noise intensity. Normalized signal-to-noise ratio (nSNR) was calculated by dividing the SI at each time point by the prior contrast image SI. Contrast to noise ratio (CNR) was estimated by normalizing the signal intensity of ROIs with that of the back muscles in the same slide. Pre-injection SNRs and CNRs were considered as baseline and percentage change in the respective CNR (% ΔCNR) upon contrast

injection was plotted. The ROIs analyzed were considered and statistical significances were examined using unpaired two-tailed t-tests to validate the significance of the experiment; results with *P*-values < 0.05 were considered useful.

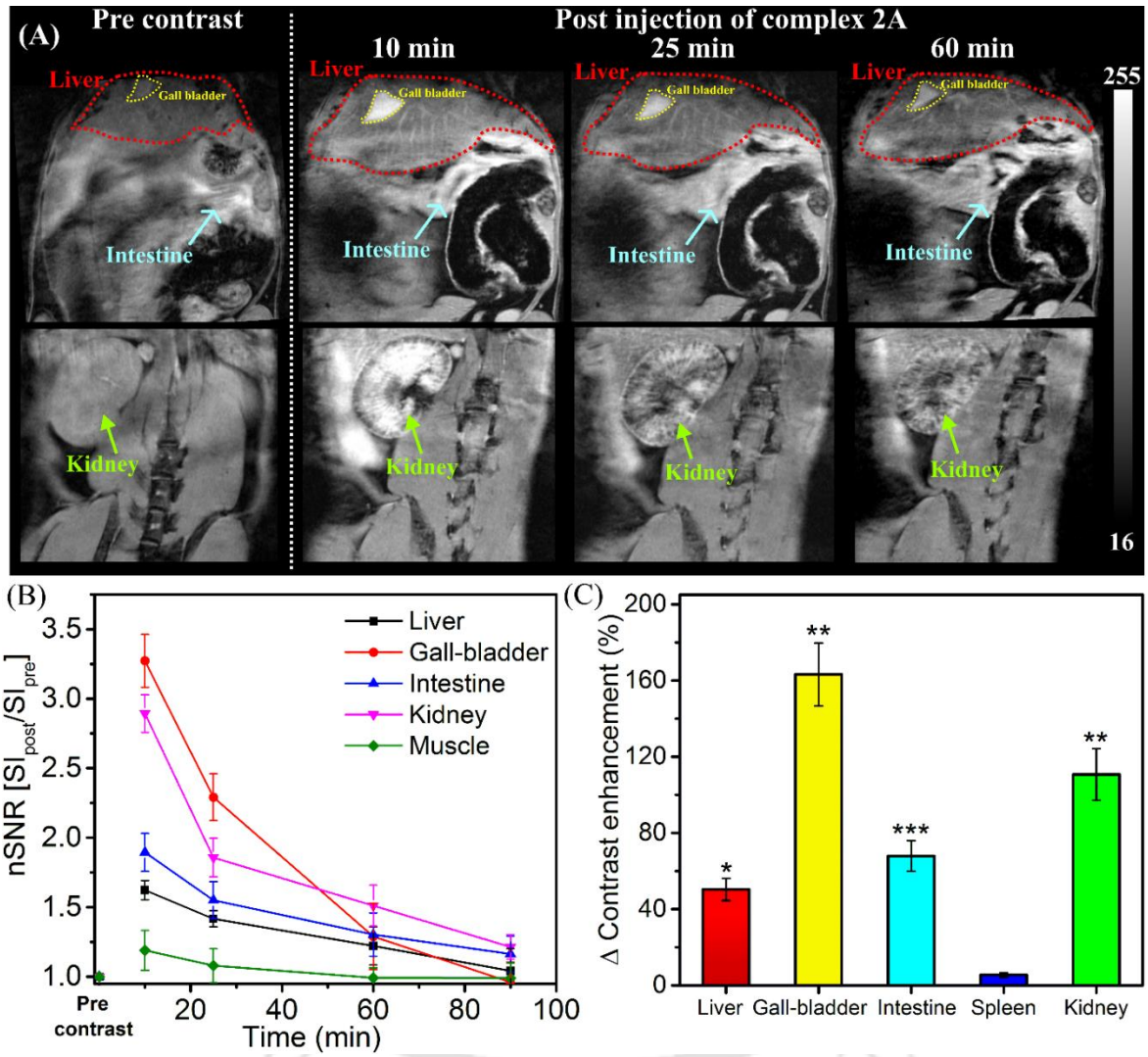

Figure 2.22. (A) T_1-weighted coronal (FLASH sequence) images of C57BL/6 mice showing contrast changes in liver (red dotted line), gallbladder (yellow dotted line), intestine (cyan arrow) and kidneys (green arrow) at different time points, pre- and post-administration of complex **2A** (0.08 mmol/kg w.r.t. [Mn^{II}]), at 7 T animal MR scanner. (B) Normalized signal-to-noise ratio (nSNR) (relative to pre-injection) plot for different ROIs as a function of time subsequent to complex **2A** administration. (C) Quantitative image analysis by measuring signal intensity changes in each organ post 10 minutes of contrast injection, normalized to muscle. Bars represent the standard error of the mean (n = 3 animals per group); $*P < 0.05$, $**P < 0.02$, $***P < 0.001$).

An intense contrast enhancement in the gallbladder (160 %; **Figure 2.22C**) and kidneys (110 %; **Figure 2.22C**) was noticed after 10 minutes of the contrast agent application. Moreover, as reflected by serum protein association experiments for complex **2A**, the highly vascularized liver region corresponding to the long retention of the contrast material in the blood vessels was realized (**Figure 2.23**, Liver part). Thus, **2A** could also be examined as a blood pool contrast agent. Neutral complex **2A** molecules with amphiphilic nature (log *P* = -0.45) are believed to be partially assimilated by hepatocytes with low retention time and excreted *via* the biliary system.[13b] Consequently, the high signal intensity in the gall bladder and intestine was apprehended within 10 minutes of the contrast agent administration.

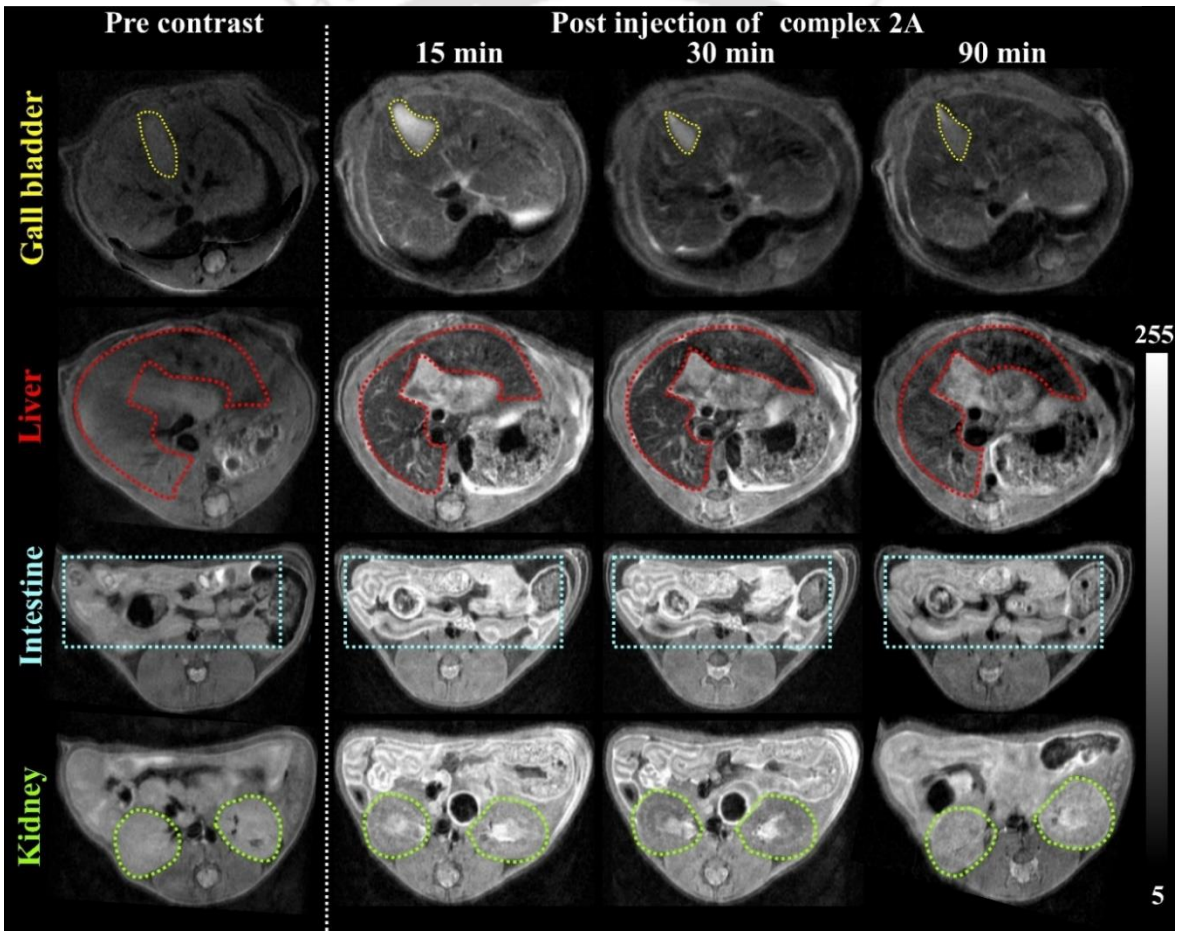

Figure 2.23. T_1-weighted axial (RARE sequence) images of C57BL/6 mice showing contrast changes in gallbladder (yellow dotted line), liver (red dotted line), intestine (cyan dotted line) and kidneys (green dotted line) at different time points, pre- and post-administration of complex **2A** (0.08 mmol/kg w.r.t. [Mn^{II}]), at 7 T animal MR scanner.

The time-dependent signal intensity changes under the region of interest (ROIs) of different organs, as depicted in **Figure 2.22**, were analyzed by *ImageJ* software. Pre-contrast signal values were considered as the baseline, and the normalized signal-to-noise ratio (nSNR) for different organs was calculated and plotted as a function of time in **Figure 2.22B**. While, the brightness engendered by the contrast agent in the gallbladder region gradually fades out within an hour, a considerable residual contrast was noticed in the kidneys compared to the pre-contrast images (**Figure 2.22B** and **2.23**). This indicated a longer retention of **2A** in the tubules of the cortex. It is to be noted that no acute toxicity in the mice was observed post-injection while monitored for 15 days.

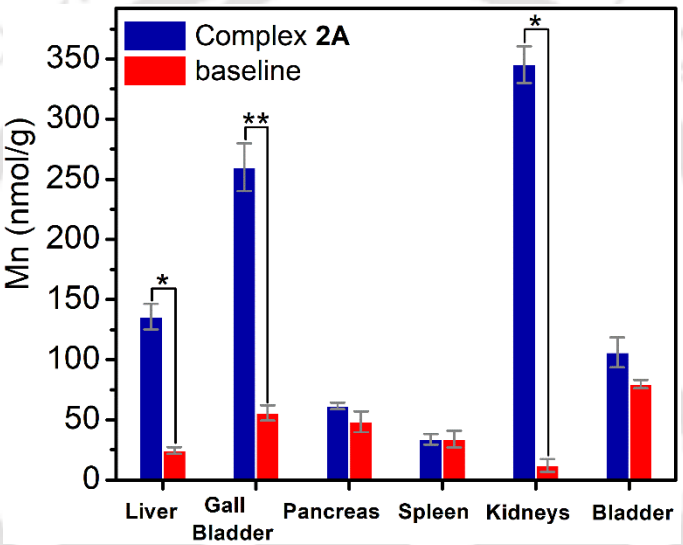

Figure 2.24. Manganese content in mice organ tissues, obtained by ICP-MS studies, 10 min after intravenous administration of complex **2A**. n = 3/group; $*P < 0.05$, ** < 0.01.

Nonetheless, *in vivo* bio-distribution of complex **2A** was determined by estimating the Mn content in the various organ tissues (liver, gall bladder, pancreas, spleen, kidneys, and bladder) after 10 minutes of its administration. Mice (n =3/group) were sacrificed after 10 minutes post similar administration of **2A** along with another group receiving saline (0.9%) only. Selected organs were dissected and digested upon treatment with 2 mL of freshly prepared aqua regia (1:3 mixture of HNO_3 and HCl) and lysed for 24 h. The tissue samples were dried by heating at 120 °C, sonicated thoroughly after the addition of 0.5 N HCl and centrifuged (4000g, 5 min) to collect a clear supernatant solution. This crude was diluted with 4% HNO_3 acid solution and subsequent Mn content in each sample as estimated by the ICP-MS technique.

The highest manganese content was obtained in the kidneys (**Figure 2.24**) followed by gallbladder and liver. These findings corroborate well with the organ-based contrast enhancement and consolidated the hepatic and renal uptake of the contrast agent as realized from the MR contrast images.

Concerning the kinetic parameters of complex **2A**, data we estimated the content of additional Mn in the liver and kidneys from the biodistribution, which are ~ 0.11 µmol/g and ~ 0.34 µmol/g respectively. Zinc content in these organs was reported to be ~ 0.24–0.27 µmol/g.[32] Therefore, the respective Mn:Zn ratio in the liver was 1:2.5. *In-vitro* kinetic inertness studies of **2A** (when challenged with 2.5 fold excess Zn(II) ions at pH ~ 7.4 and 25 °C, **Figure 2.15C**) showed dissociation rate constant = 2.2×10^{-3} s^{-1}, implying a $t_{1/2}$ value of 5.25 min. Complex **2A** showed 5 times higher kinetic stability in the presence of albumin protein (**Figure 2.15A** and **2.15B**). The liver is reported to be the producer of albumin protein.[33] Hence some amount of interaction between complex molecules and albumin could be possible in the liver region, lowering the dissociation rate. In the kidneys, Mn:Zn ratio was 1:0.8, corresponding to complex **2A** dissociation rate constant = 8.9×10^{-4} s^{-1}, $t_{1/2}$ = 12.98 min; at similar conditions. However, we could not neglect the possibility of partial leaching of free Mn(II) at the time of *in-vivo* MR imaging.

2.11 Conclusion

- In this chapter, the pentadentate ligand Li_2[Benz(Pic)$_2$] comprising of two picolinate moieties and a rigid hydroquinazoline unit along with the corresponding bis(aquated) Mn(II) complex (complex **2A**) were successfully synthesis and characterized.

- The probable structure of the complex was optimized by DFT-based theoretical studies. It revealed a pentagonal bipyramidal co-ordinational geometry with ligand atoms chelating from the equatorial plane and two water molecules occupying the axial positions.

- The thermodynamic stability of **2A** was found to be logK_{cond} = 11.62, higher than that of mono-aquated Mn(II)-EDTA, and some of the reported bis-aquated complexes.

- The complex exhibited r_1 = 5.32 $mM^{-1}s^{-1}$ that amplified to 19.09 $mM^{-1}s^{-1}$ at 1.41 T, 37 °C, and pH 7.4 in the presence of 0.67 mM BSA protein.

- The complex showed moderate kinetic inertness when challenged with 10-fold Zn(II) ions, with a $t_{1/2}$ = 5.42 min at the physiological concentration of serum albumin. However, complex **2A** was found to be sufficiently kinetically stable in human plasma.

- The presence of a hydroquinazoline unit in the ligand backbone engendered a lipophilic character (log P = -0.45) in the complex, which facilitated the interaction of **2A** with serum albumin protein with an association constant, $K_A = 1.66\times10^3\ M^{-1}$.

- *In-vitro* phantom MRI and cytotoxicity results of complex **2A** ratified its administration for further *in-vivo* investigations.

- On an intravenous dose of 0.08 mM/kg in a healthy C57BL/6 mouse, an excellent vascularization of the mouse liver along with brightening of the gallbladder, the kidney, and the liver, was realized.

2.12 References

1. (a) R. Agarwal, S. M. Brunelli, K. Williams, M. D. Mitchell, H. I. Feldman and C. A. Umscheid, *Nephrol. Dial.Transplant.*, 2009, **24** (3), 856–863; (b) E. D. Gregorio, G. Ferruato, C. Furlan, S. Lanzardo, R. Nuzzi, E. Gianolio and S. Aime, *Invest. Radiol.*, 2018, **53**, 167–172; (c) L. Yang, I. Krefting, A. Gorovets, L. Marzella, J. Kaiser, R. Boucher and D. Rieves, *Radiology*, 2012, **265**, 248–253; (d) I. A. Dekkers, R. Roos and A. J. Van Der Molen, *Eur. Radiol.*, 2018, **28**, 1579–1584; (e) PRAC Confirms Restrictions on the Use of Linear Gadolinium Agents; EMA/424715/2017; *European Medicines Agency*, July 7, 2017; (f) FDA Drug Safety Communication: FDA Warns That Gadolinium-based Contrast Agents (GBCAs) are Retained in the Body; Requires New Class Warnings; U.S. Food and Drug Administration, December 19, 2017.

2. (a) B. Drahoš, I. Lukeš, and É. Tóth, *Eur. J. Inorg. Chem.*, 2012, 1975–1986; (b) E. M. Gale, I. P. Atanasova, F. Blasi, I. Ay and P. Caravan, *J. Am. Chem. Soc.*, 2015, **137**, 15548−15557; (c) J. Wahsner, E. M. Gale, A. Rodríguez-Rodríguez and P. Caravan, *Chem. Rev.*, 2019, **119**, 957–1057; (d) S. W. McRae, M. Cleary, D. DeRoche, F. M. Martinez, Y. Xia, P. Caravan, E. M. Gale, J. A. Ronald and T. J. Scholl, *J. Med. Chem.*, 2023, **66** (10), 6567–6576; (e) E. M. Gale, J. Zhu and P. Caravan, *J. Am. Chem. Soc.*, 2013, **135**, 18600 −18608; (f) E. M. Snyder, D. Asik, S. M. Abozeid, A. Burgio, G. Bateman, S. G. Turowski, J. A. Spernyak and J. R. Morrow, *Angew. Chem. Int. Ed.*, 2020, **59**, 2414–2419.

3. (a) Q. Zhang, J. D. Gorden, R. J. Beyers and C. R. Goldsmith, *Inorg. Chem.*, 2011, **50** (19), 9365-9373; (b) E. Molnár, N. Camus, V. Patinec, G. A. Rolla, M. Botta, G. Tircsó, F. K. Kálmán, T. Fodor, R. Tripier and C. Platas-Iglesias, *Inorg. Chem.*, 2014, **53** (10), 5136-5149; (c) B. Phukan, C. Mukherjee, U. Goswami, A. Sarmah, S. Mukherjee, S. K. Sahoo, S. C. Moi, A New Bis(aquated) High Relaxivity Mn(II) Complex as an Alternative to Gd(III)-Based MRI Contrast Agent. *Inorg. Chem.*, 2018, **57,** 2631−2638.

4. M. Rohrer, H. Bauer, J. Mintorovitch, M. Requardt, H.-J. Weinmann, *Invest. Radiol.*, 2005, **40**, 715−724.

5. (a) I. Solomon and N. Bloembergen, *J. Chem. Phys*., 1956, **25**, 261; (b) J. Kowalewski, L. Nordenskiöld, N. Benetis and P.-Olof Westlund, *Prog Nucl Magn Reson Spectrosc*., 1985, **17**, 141-185.

6. (a) H. Su, C. Wu, J. Zhu, T. Miao, D. Wang, C. Xia, X. Zhao, Q. Gong, B. Song and H. Ai, *Dalton Trans*., 2012, **41**, 14480-14483; (b) K. Pota, Z. Garda, F. K. Kálmán, J. L. Barriada, D. Esteban-Gómez, C. Platas-Iglesias, I. Tóth, E. Brücher and G. Tircsó, *New J. Chem.*, 2018, **42**, 8001-8011; (c) Z. Garda, E. Molnár, N. Hamon, J. L. Barriada, D. Esteban-Gómez, B. Váradi, V. Nagy, K. Pota, F. K. Kálmán, I. Tóth, N. Lihi, C. Platas-Iglesias, É. Tóth, R. Tripier and G. Tircsó, *Inorg. Chem.*, 2021, **60**, 1133-1148.

7. (a) B. Drahoš, J. Kotek, P. Hermann, I. Lukeš and É. Tóth, *Inorg. Chem*., 2010, **49**, 3224–3238; (b) Z. Garda, E. Molnár, F. K. Kálmán, R. Botár, V. Nagy, Z. Baranyai, E. Brücher, Z. Kovács, I. Tóth and G. Tircsó, *Front. Chem*., 2018, **6**, 232.

8. (a) D. Ndiaye, P. Cieslik, H. Wadepohl, A. Pallier, S. Même, P. Comba and É. Tóth, *J. Am. Chem. Soc*., 2022, **144** (48), 22212-22220; (b) P. Cieslik, P. Comba, B. Dittmar, D. Ndiaye, É. Tóth, G. Velmurugan and H. Wadepohl, *Angew. Chem. Int. Ed.*, 2022, **61**, e202115580.

9. P. Caravan, C. T. Farrar, L. Frullano and R. Uppal, *Contrast Media Mol. Imaging*, 2009, **4** (2), 89–100.

10. (a) B. Drahoš, J. Kotek, P. Hermann, I. Lukeš, E. Tóth, *Inorg. Chem.*, 2010, **49**, 3224; (b) A. Forgács, R. Pujales-Paradela, M. Regueiro-Figueroa, L. Valencia, D. Esteban-Gómez, M. Botta and C. Platas-Iglesias, *Dalton Trans*., 2017, **46**, 1546-1558; (b) S. Anbu, S. H. L. Hoffmann, F. Carniato, L. Kenning, T. W. Price, T. J. Prior, M. Botta, A. F. Martins and G. J. Stasiuk, *Angew. Chem. Int. Ed.*, 2021, **60**, 10736–10744.

11. (a) A. Forgács, M. Regueiro-Figueroa, J. L. Barriada, D. Esteban-Gómez, A. de Blas, T. Rodríguez-Blas, M. Botta and C. Platas-Iglesias, *Inorg. Chem.*, 2015, **54**, 9576-9587; (b) G. Rolla, V. De-Biasio, G. B. Giovenzana, M. Botta and L. Tei, Dalton Trans., 2018, **47**, 10660–10670.
12. (a) E. Boros and P. Caravan, *J. Med. Chem*., 2013, **56**, 1782−1786; (b) F. K. Kálmán, V. Nagy, B. Váradi, Z. Garda, E. Molnár, G. Trencsényi, J. Kiss, S. Même, W. Même, É. Tóth and G. Tircsó, *J. Med. Chem*., 2020, **63** (11), 6057-6065.
13. (a) M. K. Islam, S. Kim, H.-K. Kim, S. Park, G.-H. Lee, H. J. Kang, J.-C. Jung, J.-S. Park, T.-J. Kim and Y. Chang, *J. Med. Chem.*, 2017, **60** (7), 2993-3001; (b) K. Chen, P. Li, C. Zhu, Z. Xia, Q. Xia, L. Zhong, B. Xiao, T. Cheng, C. Wu, C. Shen, X. Zhang and J. Zhu, *J. Med. Chem.*, 2021, **64**, 9182−9192; (c) R. C. Hall, J. Qin, V. Laney, N. Ayat and Z.-R. Lu, *ACS Appl. Bio Mater*., 2022, **5** (2), 451–458.
14. S. Aime and P. Caravan, *J. Magn. Reson. Imaging*, 2009, **30**, 1259-1267.
15. (*a*) J. Wang, G. R. Gao, Z. H. Zhang, X. D. Zhang, X. Z. Liu, Y. M. Kong and Y. Li, *Russ. J. Coord. Chem*., 2007, **33**, 258; (*b*) B. C. Smith, *Infrared Spectral Interpretation:A Systematic Approach*, CRC press, 1998; (c) J. Coates, Interpretation of Infrared Spectra: A Practical Approach, John Wiley & Sons Ltd, Chichester, 2000.
16. (a) M. J. Frisch, *et al*. Gaussian 09, Revision A.01, Gaussian, Inc., Wallingford CT, 2009; (b) Gaussview Rev. 5.09, Linux version, Gaussian Inc., Pittsburgh; (c) J.-D. Chai and M. Head-Gordon, Long-range corrected hybrid density functionals with damped atom–atom dispersion corrections. *Phys. Chem. Chem. Phys*., 2008, **10**, 6615-6620; (d) T. H. Dunning, Gaussian basis sets for use in correlated molecular calculations. I. The atoms boron through neon and hydrogen. *J. Chem. Phys*., 1989, **90**, 1007–1023; (e) C. H. Moorea, P. Jena and J. T. Jr. McLeskey, Tuning range-separated DFT functionals for modeling the peak absorption of MEH-PPV polymer in various solvents. *Comp. and Theo. Chem*., 2019, **1162**, 112506.

17. (a) Q. Zhang, J. D. Gorden, R. J. Beyers and C. R. Goldsmith, *Inorg. Chem*., 2011, **50**, 9365; (b) E. Molńar, N. Camus, V. Patinec, G. A. Rolla, M. Botta, G. Tircsó, F. K. Kálmán, T. Fodor, R. Tripier and C. Platas-Iglesias, *Inorg. Chem*., 2014, **53**, 5136; (c) B. Drahoš, J. kotek, I. Císařová, P. Hermann, L. Helm, I. Lukeš and É. Tóth, *Inorg. Chem*., 2011, **50**, 12785.

18. (a) P. Caravan, C. Comuzzi, W. Crooks, T. J. McMurry, G. R. Choppin and S. R. Woulfe, *Inorg. Chem*., 2001, **40**, 2170-2176; (b) V. C. Pierre, M. Botta, S. Aime and K. N. Raymond, *Inorg. Chem*., 2006, **45**, 8355-8364; (c) M. Duraiyarasu, S. S. Kumaran and R. Mayilmurugan, *ACS Biomater. Sci. Eng.* 2023, **9**, 3570−3580.

19. (a) R. Sethi, J. S. Ananta, C. Karmonik, M. Zhong, S. H. Fung, X. Liu, K. Li, M. Ferrari, L. J. Wilson and P. Decuzzi, *Contrast Media Mol. Imaging*, 2012, **7**, 501–508; (b) S. Aime, S. Baroni, D. Delli Castelli, E. Brücher, I. Fábián, S. C. Serra, A. Fringuello Mingo, R. Napolitano, L. Lattuada, F. Tedoldi and Z. Baranyai, *Inorg. Chem.*, 2018, **57**, 5567−5574.

20. (a) R. S. Dickins, S. Aime, A. S. Batsanov, A. Beeby, M. Botta, J. Bruce, J. A. K. Howard, C. S. Love, D. Parker, R. D. Peacock and H. Puschmann, *J. Am. Chem. Soc*., 2002, **124**, 12697; (b) J. I. Bruce, R. S. Dickins, L. J. Govenlock, T. Gunnlaugsson, S. Lopinski, M. P. Lowe, D. Parker, R. D. Peacock, J. J. B. Perry, S. Aime and M. Botta, *J. Am. Chem. Soc*., 2000, **122**, 9674.

21. S. Aime, M. Botta, J. I. Bruce, V. Mainero, D. Parker and E. Terreno, *Chem. Commun.*, **2001**, 115.

22. S. Develay, R. Tripier, M. L. Baccon, V. Patinec, G. Serratrice and H. Handel, *Dalton Trans.*, 2005, **18**, 3016-3-3024.

23. Z. Garda, A. Forgács, Q. N. Do, F. K. Kálmán, S. Timári, Z. Baranyai, L. Tei, I. Tóth, Z. Kovács and G. Tircsó, *J. Inorg. Biochem*., 2016, **163**, 206.

24. F. K. Kálmán and G. Tircsó, *Inorg. Chem.*, 2012, **51**, 10065−10067;

25. (a) R. Uzal-Varela, D. Lalli, I. Brandariz, A. Rodríguez-Rodríguez, C. Platas-Iglesias, M. Botta and D. Esteban-Gómez, *Dalton Trans.*, 2021, **50**, 16290-16303; (b) A. R. Reddi, L. T. Jensen and V. C. Culotta, *Chem. Rev*., 2009, **109**, 4722-4732.

26. D. Pan, S. D. Caruthers, A. Senpan, A. H. Schmieder, S. A. Wickline and G. M. Lanza, *Wiley Interdiscip Rev Nanomed Nanobiotechnol*., 2011, **3** (2), 162-173.

27. (a) D. S. Poole, N. Doorenweerd, J. J. Plomp, A. Mahfouz, M. J. T. Reinders and L. van der Weerd, *Neuroimage*, 2017, **147**, 1−9; (b) N. N. Nystrom, H. Liu, F. M. Martinez, X.-A. Zhang, T. J. Scholl and J. A. Ronald, *J. Med. Chem.*, 2022, **65**, 9846−9857.

28. A. Forgács, L. Tei, Z. Baranyai, D. Esteban-Gómez, C. Platas-Iglesias and M. Botta, *Dalton Trans.*, 2017, **46**, 8494-8504.

29. A. F. Martins, J.-F. Morfin, C. F. G. C. Geraldes and É. Tóth, *J Biol Inorg Chem*, 2014, **19**, 281–295.

30. G. E. Sokolow, M. R. Crawley, D. R. Morphet, D. Asik, J. A. Spernyak, A. J. R. McGray, T. R. Cook and J. R. Morrow, *Inorg. Chem.*, 2022, **61**, 2603-2611.

31. L. Leone, A. Anemone, A. Carella, E. Botto, D. L. Longo and L. Tei, *ChemMedChem*, 2022, **17**, e202200508.

32. (a) P. M-M , U. Merle, R. Weiskirchen and J. S. Becker, *Int. J. Mass Spectrom*, 2013, **354–355**, 281–287; (b) M. Lenartowicz, M. Kowal, D. Buda-Lewandowska and J. Styrna, *J. Inherit. Metab. Dis.* 2002, **25**, 647-659.

33. A. J. Malina, C. Lesseur, S. A. Busgang, P. Curtin, R. O. Wright and A. P. Sanders, *Environ. Int*. 2019, **132**, 105012.

भारतीय प्रौद्योगिकी संस्थान गुवाहाटी
Indian Institute of Technology Guwahati

Chapter III

Non-Covalent Confinement of Gd(III)-/Mn(II)-Complex in Porous Silica Nanosphere Rendering Nanoparticulate CA for MRI

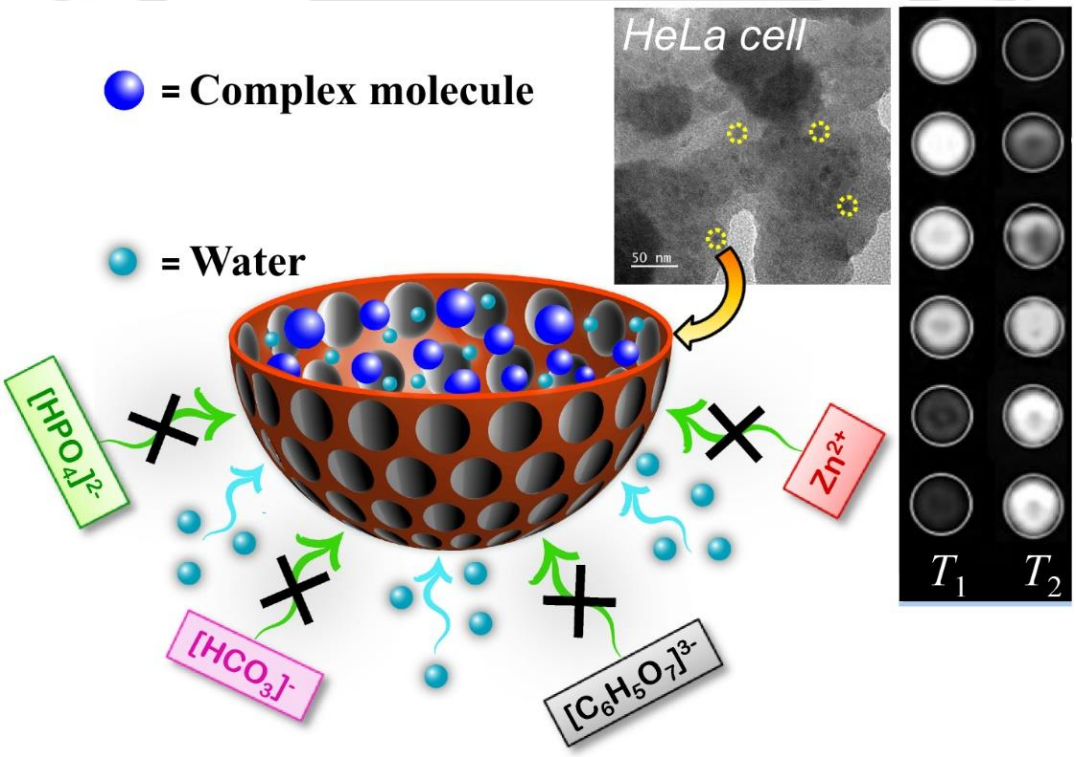

∗ Results have been reported in *ACS Appl. Bio Mater*., 2021, **4**, 8356−8367 and *Dalton Trans*., 2022, **51**, 14138-14149.

3.1 Introduction

The Solomon-Bloembergen-Morgan (SBM) theory summarizes the straightforward effect of hydration number (q), water residence time (τ_M), and rotational correlation time (τ_R) on the relaxation rate of water protons present in the vicinity of paramagnetic substances.[1] To augment the relaxation rate by increasing the number of inner-sphere water molecules in six-coordinate Mn(II)- or nine-coordinate Gd(III)-complexes, the denticity of coordinating ligands needs to be reduced and consequently diminishes stability, thereby resulting in the leaching of free metal ions.[2] Therefore, reducing the rotational correlation time of a contrast agent is a better strategy to improve the relaxivity value within an applied magnetic field range of 0.5-3 T.[3] This can be achieved by covalent or non-covalent attachment of the paramagnetic complex molecules into bulky nanostructures or biological macromolecules.[4] A vivid illustration of this effect can be verified when Gd(III) complex of the thiol derivative of DTTA was immobilized onto Au nanoparticles exerting relaxivity value of 60 $mM^{-1}s^{-1}$ at 0.70 T.[5] Richard *et al.* showed that non-covalent immobilization of a mono(aquated) Gd(III) complex of an amphiphilic ligand, made of a lipid chain and diethylenetriamine pentaacetate (DTPA) chelate, onto multiwalled carbon nanotubes increases r_1 relaxivity values to 50.3 $mM^{-1}s^{-1}$ compared to 4.7 $mM^{-1}s^{-1}$ of $[Gd(OH_2)(DTPA)]^{2-}$ at 0.47 T.[6] Similarly, Mn(II)-based nanosystems also have been developed by immobilizing Mn(II)-complexes onto solid silica nano-sphere and solid nanodiamond and entrapping Mn(II)-complexes within lipidic nanovesicles or nanobeads.[7]

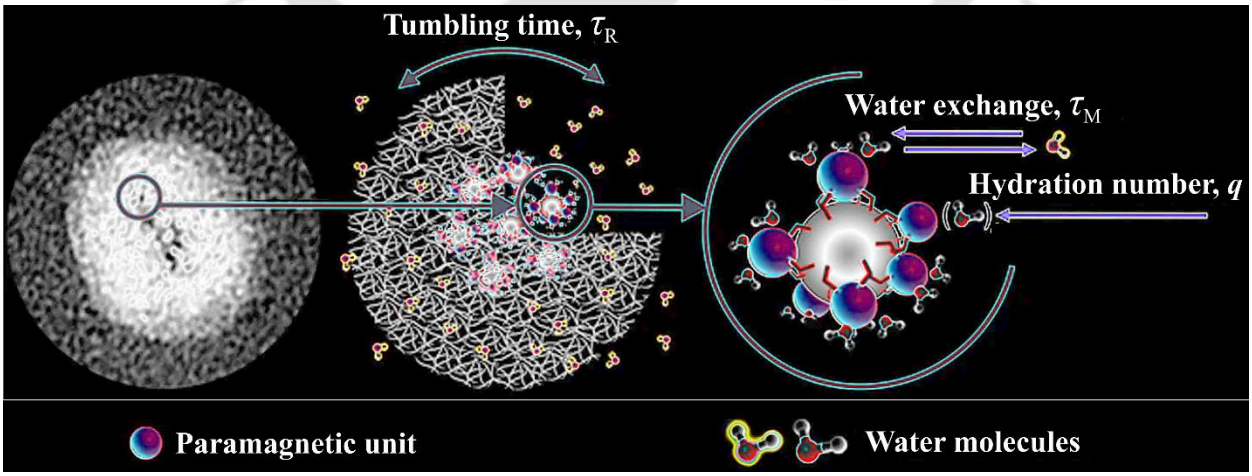

Figure 3.1. Schematic representation of a metal ion confined porous nanostructure influencing tumbling time and water exchange rate.

Among various nanosized materials that have been extensively studied in the last decade, porous silica nanoparticles are safe, convenient, and tunable templates to accommodate paramagnetic units.[8] Being more sensitive and efficient, they are a flourishing topic. They offer large surface area and pore volume that can be exploited judicially to make target-specific, less toxic, and stable contrast agents. Literature shows the successful immobilization of metal complexes onto the surface of the solid or porous nanosized silica particles, as well as, the confinement of metal silicates, oxides, or even chloride salts inside mesoporous silica nanoparticles.[9] For example, Lin and co-workers have developed mesoporous hybrid silica nanoparticles with covalent attachment of bis(aquated) Gd(III)-Si-diethylenetriaminetetraacetate (DTTA) complex within the inner core of the nanoparticles. The synthesized hybrid nanosystem showed a high longitudinal relaxivity value of 28.8 $mM^{-1}s^{-1}$ at 3 T, and 10.2 $mM^{-1}s^{-1}$ at 9.4 T.[3b] The entrapment of trianionic tris(aquated) Gd(III) complex of 2,2'-(2-hydroxy-5-sulfonatobenzylazanediyl)bis(methylene)bis(8-hydroxy-quinoline-5-sulfonic acid (H_3dhqN-SO_3H) ligand, $[Gd(OH_2)_3(dhqN\text{-}SO_3)]^{3-}$, into mesoporous silica nanoparticles is reported to exhibit a high r_1 relaxivity, 78 $mM^{-1}s^{-1}$ at 1.2 T.[10] In another case, Gd(III) or Mn(II) ions were inserted inside three-dimensional cubic mesoporous silica nanoparticles to display r_1 relaxivity of 18.5 $mM^{-1}s^{-1}$ or 8.4 $mM^{-1}s^{-1}$ at 1.5 T and 37 °C.[11]

Table 3.1. Relaxivity of some Gd-based nanocontrast agents.

Gd-based Contrast agents	*q*	r_1 ($mM^{-1}s^{-1}$), at pH 7.4
[Gd(TCAS)]- SN-III[12a]	—	46.49, at 37 °C, 1.41 T 50.91, at 25 °C, in presence of BSA
MSN-Gd[3b]	2	28.8, at 3 T
PSS-Na[Gd·2][5b]	2.65	12.41, at 25 °C, 0.47 T
Si25NPs[10]	3	77, at 37 °C, 1.2 T
GdDOTA⊂NPs[12b]	1	72.3, at 37 °C, 1.41 T
FSb-EuGd[12c]	—	38.8 at 25 °C, 9.4 T
Gd_2O_3@MSN[1d]	—	45.08 at 0.5 T
Gd@SiO_2–PEG500[12d]	—	18.5, at 40 °C, 1.41 T

Table 3.2. Relaxivity of some Mn-based nanocontrast agents.

Mn-based Contrast agents	r_1 ($mM^{-1}s^{-1}$), at pH 7.4, 37 °C	r_2 ($mM^{-1}s^{-1}$), at pH 7.4, 37 °C
MnL-SiNPs[13a] (Mn(II)-Surface Conjugated silica nanoparticles)	7.3, at 1.47 T	—
Mn-DMSSs[7a] (Manganese-Loaded Dual-Mesoporous Silica Spheres)	10.1, at 3.0 T	169.7, at 3.0 T
Mn–M48SNs[11b] (Manganese-impregnated mesoporous silica Nanoparticles)	8.4, at 1.41 T	16.8, at 1.41 T
PEOMSNs[13b] (PEO–SiO_2-encapsulated MnO nanoparticles)	1.17, at 7.0 T	30.73, at 7.0 T
Mn_xO_y[13c] (Manganese Oxide Nanostructures)	1.53, at 1.41 T	—
Mn-DTPA-MSNSs[7c] (Mn^{2+} chelated complex onto microporous silica nanospheres)	7.18, at 1.0 T	—
Mn_3O_4@PEG-RGD NPs[13d]	0.35, at 0.5 T	—

Moreover, small-sized Gd(III)/Mn(II)-complex molecules have lower retention time when administered inside the body and are rapidly expelled by the renal pathway (within a few minutes) along with a fractional hepatic uptake.[4a,14] This is disadvantageous for MRI scans that require a longer time, e.g., oncological imaging. Nanoparticulate-contrast agents with hydrodynamic diameter >100 nm preferably avoid fast clearance and thus offer long retention time *in vivo*.[15]

Hence, the attempts to develop contrast agents with a high r_1 relaxivity value and a sufficient vascular retention time, covalent and non-covalent confinement/immobilization of aquated Gd(III)-complexes within/onto nanosized silica particles have been under continuous investigation. Although, a significant improvement to the quest of Gd(III)-based contrast agents with a high r_1 relaxivity value has been attained, the expected high relaxivity value in the order of 100 $mM^{-1}s^{-1}$ has rarely been achieved.[16] For Mn(II)-based systems, similar entrapment of free metal ions has been done instead.[7] The main reason for this is presumably the fact that the

attainment of kinetic inertness of the surface-bound, aquated, small-molecule Mn(II) complexes has always remained an intriguing task; indeed.

To sum up, 1) high relaxivity values can be obtained by encapsulating thermodynamically stable aquated Gd(III)/Mn(II) complexes inside the core of porous silica nanoparticles. 2) Alongside, the silica outer sphere would restrict the entrance of scavenger ions, preventing dechelation of the complex inside. Thus, high kinetic inertness can be achieved by this process. 3) A low probability of the paramagnetic metal ions being leached out through the small pores would diminish toxicity as well.

In this endeavor, we have reported the syntheses and characterization of two picolyl- and picolinate-based ligands and corresponding Gd(III)- and Mn(II)-complexes. Pyridine rings with π-acceptor properties, imparted high thermodynamic stability to the corresponding complexes. Further, we investigate the encapsulation of the mono-positive tris-aquated Gd(III)- and neutral mono-aquated Mn(II)-complex inside the porous silica nanoparticle employing a reverse microemulsion process. Depending on the hydration number and charge of the overall complex, the paramagnetic chelates are placed either in the internal space or near the inner surface of the silica outer sphere showing varied fold increase in relaxivity value. The number average of complex molecules confined within the NPs was determined by the equation **(1)**.[17]

$$N_1 = \frac{cVN_A}{\eta/m_{NP}} = \frac{cVN_A(\frac{1}{6}\pi\rho_{NP}d^3)}{\eta} \quad \textbf{(1)}$$

Where, c = concentration in mother suspension, V = volume of mother suspension, N_A = Avogadro's number, η = yield from synthesis, m_{NP} = mass of nanoparticle, ρ_{NP} = density of nanoparticle (considered same as that of pure silica, 1.95 g cm^{-3}), d = diameter of the nanoparticle.

The biocompatibility and cell permeability of the synthesized nanoparticles were examined afterward. Phantom MR images of the nanoparticle suspensions on a clinical MRI machine proved the potential applicability of the synthesized nanomaterials

3.2 Synthesis of Tris-aquated Gd(III)-Complex of Ligand H_2hbda, 3A

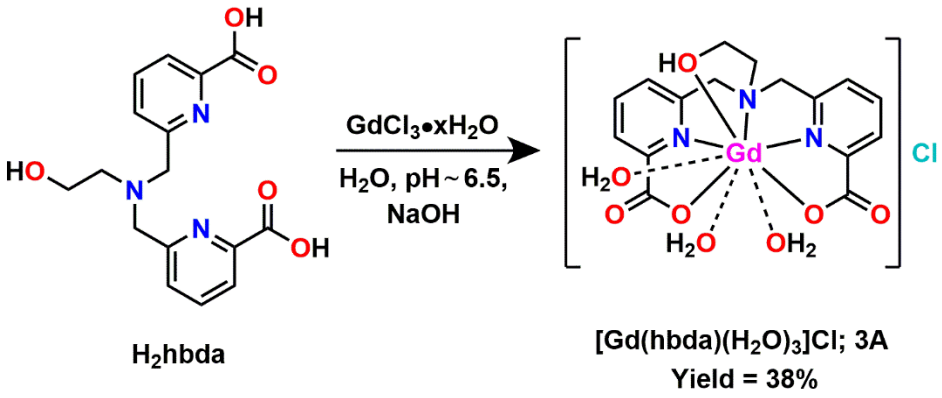

H_2hbda

[Gd(hbda)(H_2O)$_3$]Cl; 3A
Yield = 38%

Scheme 3.1. Schematic representation for the synthesis of complex **3A**, $[C_{16}H_{21}N_3O_8Gd]Cl$.

Ligand H_2hbda and the corresponding tris-aquated mono-positive Gd(III)-complex, **3A** were reproduced following the procedure reported by M. Khannam in 'Synthesis, characterization and investigation on water-soluble, aquated Gd(III) and Mn(II) complexes as MRI contrast agents' (TH-2022_136122016), [Doctoral thesis, IIT Guwahati]. The hydration number of the complex was verified by performing a photoluminescence study on the corresponding Tb(III)-congener.

The complex **3A** showed high thermodynamic stability, as determined by competition titration against increasing concentration of reported ligand H_5DTPA, at pH ~ 7.4. pGd value was reported to be 18.5, *i.e.*, 0.58 unit lower than mono-aquated $[GdDTPA]^{2-}$.[18a] The value was commendable for a tris(aquated) Gd(III) complex and found to be better when compared with some of earlier reported tris(aquated) Gd(III) based complexes *e.g.*, [Gd(dpaa)] (pGd = 12.3), [Gd(tpaa)] (pGd = 11.2), and close to $[Gd(OH_2)_3(dhqN\text{-}SO_3)]^{3-}$ (pGd = 18.9).[10,18] The high thermodynamic stability correlates with the incorporation of the picolinate and alcoholic groups in the ligand backbone.

The pH-dependent stability of the complex ascertained by relaxometry indicated that at pH ~ 10.0, the *q* (hydration number) of **3A** value diminished to 2 reflecting the replacement of one coordinating water molecule with hydroxyl species. However, UV-Vis spectra of the complex at the higher pH (~9.5) suggested no adverse effect on the complex structure.

3.3 Synthesis and Characterization of Complex 3A Confined Porous Silica Nanoparticle, 3A@SiO_2NP

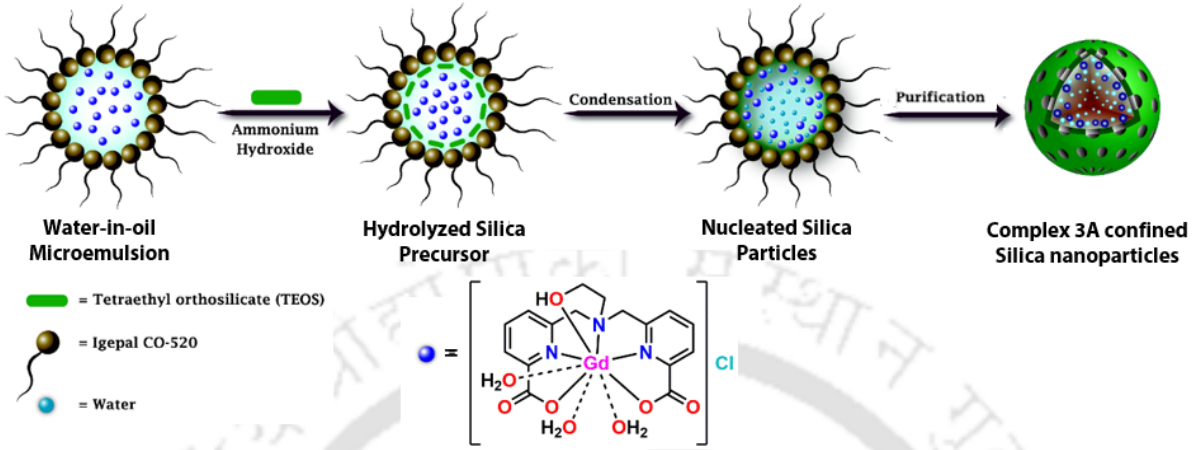

Scheme 3.2. Schematic illustration depicting the synthesis of **3A**@SiO_2NP.

The thermodynamically stable complex **3A** molecules were incorporated within the porous silica nanosphere following the reverse micelle mechanism. A homogenous solution of Igepal-CO-520 (1.3 mL) in cyclohexane (10 mL) was prepared by stirring for 10 min. A doping solution comprising **3A** solution (160 μL, 4.2 mM) in water (320 μL) at pH ~ 7.4 was cautiously added to the surfactant mixture to create a reverse microemulsion (water-in-oil). It was followed by NH_4OH (120 µL, 25% by w/v) and stirred for another 30 minutes. Finally, tetraethyl orthosilicate (TEOS, 100 μL) was added, and the resultant mixture was kept at room temperature for 24 h with gentle stirring. The expected porous nanoparticles with impregnated complex **3A,** *i.e.*, **3A**@SiO_2NP were obtained by adding acetone (30 mL) to the mixture, which was repeatedly washed with ethanol and water by centrifugation at 10,000 rpm for 15 minutes. The residue obtained was dispersed in 400 μL water (pH maintained at 7.4) to obtain 500 μL of 0.088 mM suspension, concentration given in terms of Gd(III), (0.088 mM, 8% complex molecules incorporated inside nanoparticles). The mother suspension (500 µL) was lyophilized for 24 h and 14 mg of dry silica were obtained. For each nanoparticle sized 23.4 nm, the number average of complex **3A** in each nanoparticle, n_{cplx}, came out to be ~ 20 (equation **1**). The morphology, presence of complex, and the porous nature of the isolated nanoparticles were investigated by field-emission transmission electron microscope (FETEM) imaging, elemental mapping, energy dispersive X-ray spectroscopy (EDS), Fourier transform infrared (FTIR), and N_2 adsorption-desorption isotherm analyses.

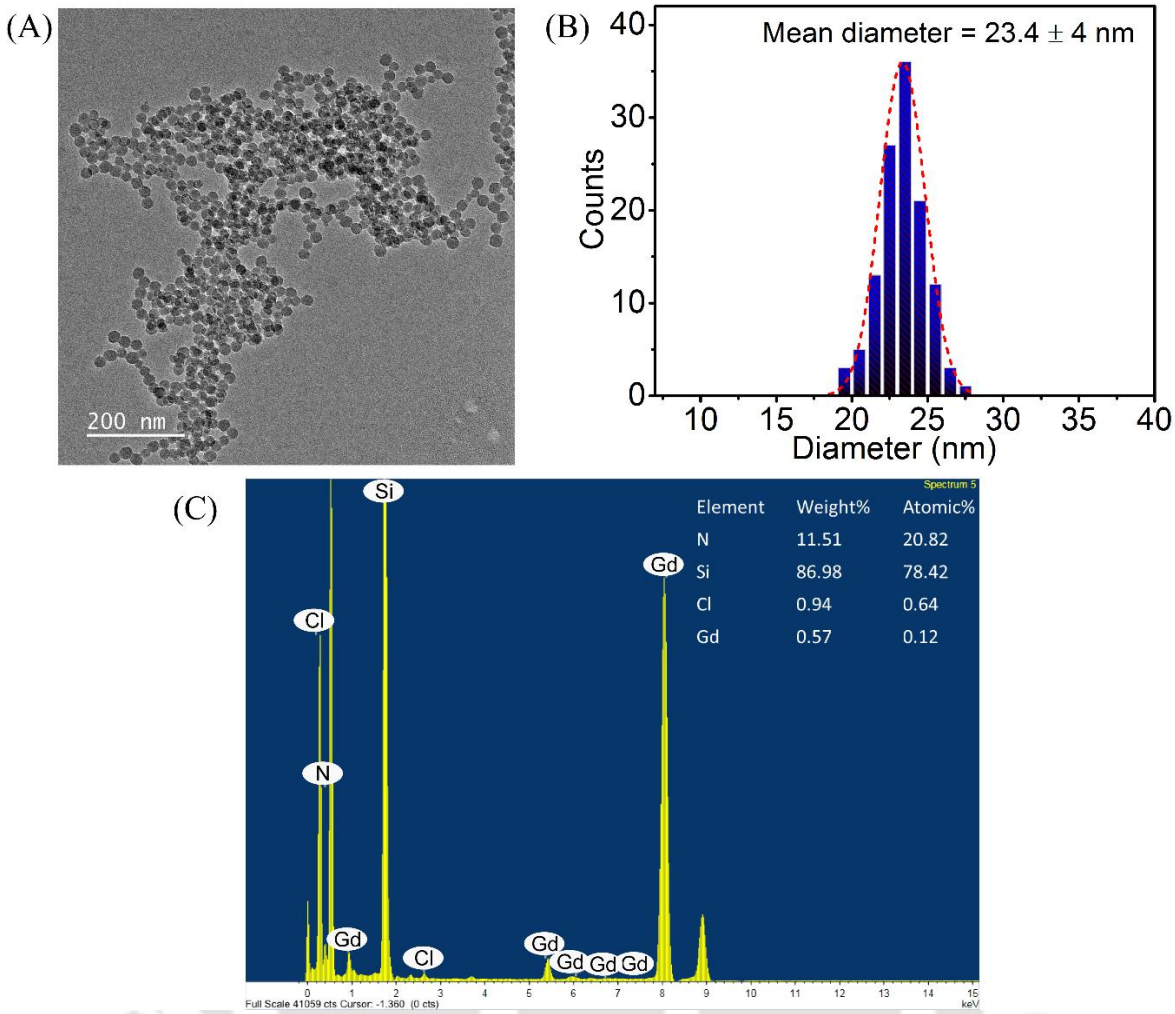

Figure 3.2. (A) Representative TEM image, (B) Corresponding particle size distribution diagram considering a minimum of 100 particles, and (C) Energy dispersive X-ray (EDS) analysis of **3A**@SiO_2NP showing the existence of Gd, Si, N, and Cl elements in the isolated nanoparticles.

The FETEM images of **3A**@SiO_2NPs nanoparticles, validated the formation of mono-dispersed and spherical nanoparticles of size 23.4 ± 4 nm (**Figure 3.2**). Corresponding EDS analyses (**Figure 3.2C**) of a selected area recognized the coexistence of Gd, N, Si, and Cl atoms in the synthesized nanoparticles and therefore, stipulated the presence of complex **3A** molecules within the nanoparticles. Furthermore, on comparing the FTIR spectrum of **3A**@SiO_2NP with the same for the bare complex, the stretching band at 1626 cm^{-1} due to the coordinated carboxylate $\nu_{C=O}$ group existed in both of the spectra consolidating the incorporation of the complex within the porous nanoparticle (**Figure 3.3**). To note, nanoparticles were thoroughly washed with water and

suspended in an aqueous medium. Negligible metal leaching, even after 15 days, discarded any possibility of entrapment of complex molecules (water soluble) outside the nanosphere.

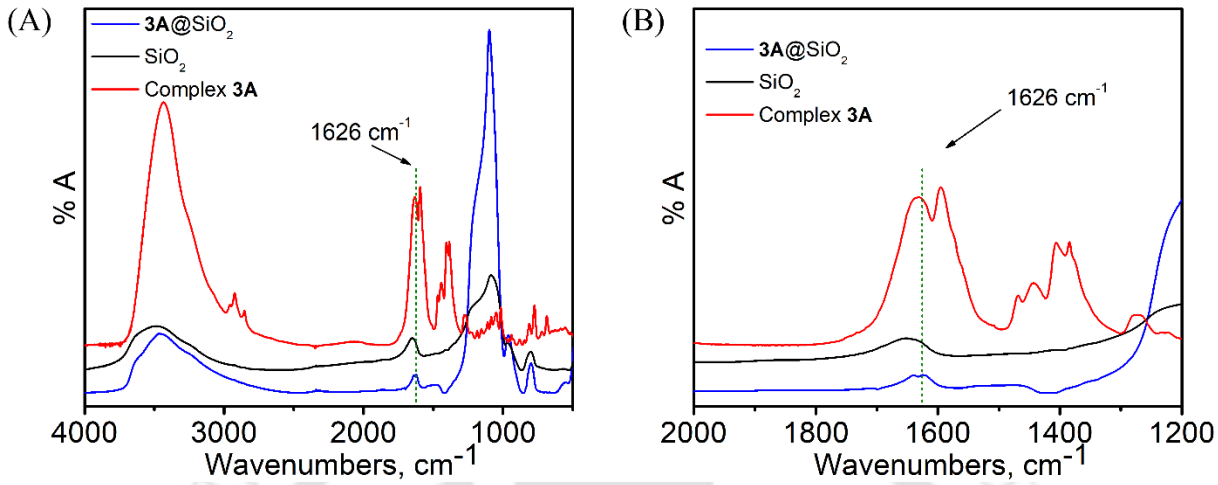

Figure 3.3. FTIR spectrum of complex **3A**, **3A**@SiO_2NP, and SiO_2 NPs.

The hollow and porous nature of the isolated **3A**-incorporated NPs was elucidated by recording the N_2 adsorption-desorption isotherm on a Quantachrome, Model: Autosorb-IQ MP surface area and pore size analyzer, at 77 K. Before the experiment, dry samples (obtained by lyophilizing the suspension for 24 h) were degassed at 100 °C for 4 h.

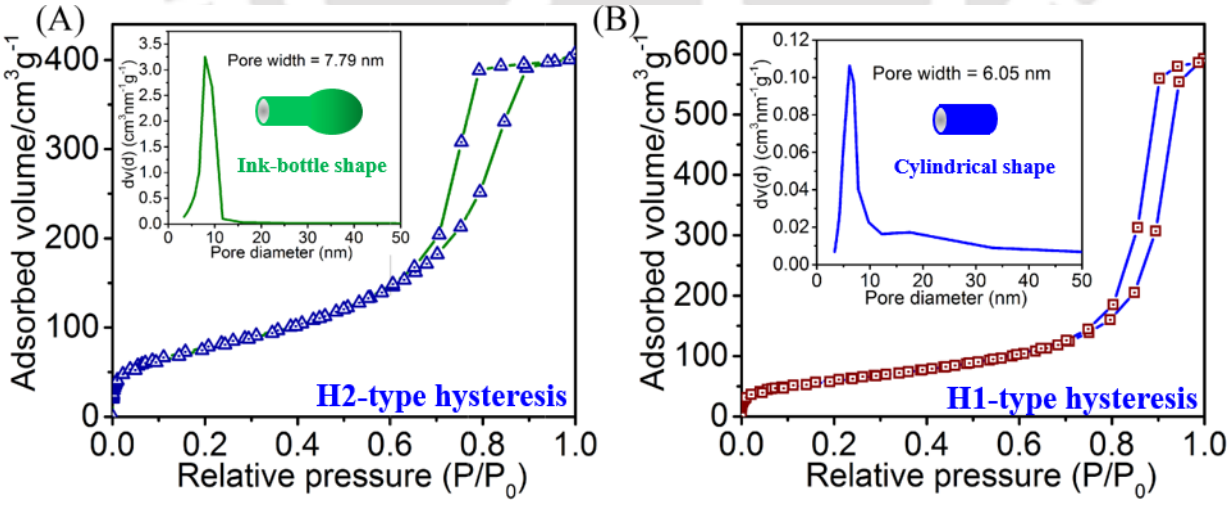

Figure 3.4. Nitrogen adsorption-desorption isotherm and pore size distribution (inset) of (A) pristine SiO_2NP, and (B) complex **3A**@SiO_2NPs.

A type-IV isotherm was realized with a hysteresis loop (**Figure 3.4**, **Table 3.3**), which confirmed the formation of the mesoporous nanoparticles.[19a] Barrett-Joiner-Halenda (BJH) pore diameter was 6.05 nm, slightly smaller than the bare porous silica nanoparticles having pores of 7.79 nm width. Noteworthy, bare porous silica nanoparticles (SiO_2NP) were synthesized following the same procedure for **3A**@SiO_2NPs, replacing the doping solution with 0.01 M HEPES buffer (pH ~ 7.4). A change in the hysteresis pattern from H2-type to H1-type upon confinement of complex **3A** within the nanospheres inferred the adsorption of the complex in the inner core of the pore rendering a cylindrical pore shape from an ink-bottle form.

Table 3.3. Textural properties of blank SiO_2NP and **3A**@SiO_2NP.

	BET surface area (m^2/g)	**Pore volume (cc/g)**	**Particle size (nm)**	**Hydrodynamic diameter, d_h**	**Zeta potential, mV**
SiO_2NP	281.70	1.65	22.02±2	310.4, PdI = 0.31	-23.9±3.7
3A@SiO_2NP	269.61	1.19	23.40±2	295.6, PdI = 0.36	-19.0±3.5

Additionally, the nanopores of the silica sphere must allow the free movement of water molecules to maintain sufficient water accessibility to the entrapped paramagnetic chelate. It is a crucial parameter to attain a high relaxivity value. Hence, the water exchangeability across the nanopores of the silica sphere was tested by comparing the infrared spectra of **3A**@SiO_2NP (recovered from aqueous suspension, then lyophilized for 24 h) to that of lyophilized **3A**@SiO_2NP_D_2O (dried **3A**@SiO_2NP suspended in D_2O for 12 h, then lyophilized for 24 h). A broadband appeared for **3A**@SiO_2NP_D_2O, centered at 2505 cm^{-1} due to the ν(O–D) and ν(H–O–D) asymmetric stretches along with the decrease in intensity of the region 3150-3470 cm^{-1} proved the entrance of D_2O molecules inside the nanoparticles (**Figure 3.5**). Therefore, the entrance of water molecules into and out of the silica sphere of **3A**@SiO_2NPs was consolidated.

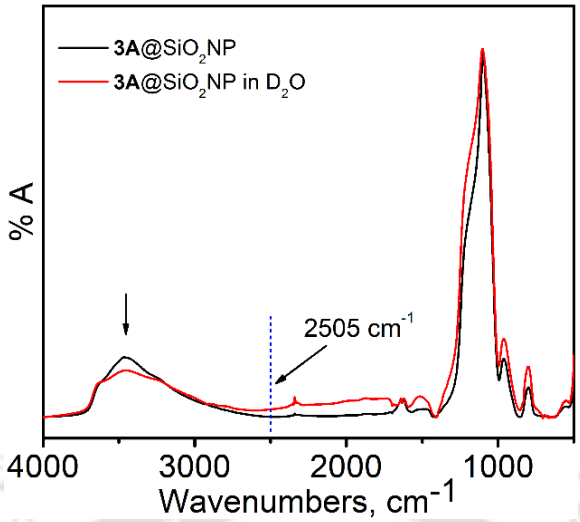

Figure 3.5. FTIR spectrum of **3A**@SiO_2NP and **3A**@SiO_2NP_D_2O. Normalized with respect to 1100 cm^{-1} band.

3.4 Relaxometric studies of 3A@SiO_2NP in Water and Serum

The longitudinal relaxivity value (r_1), which is defined as the change in the T_1 relaxation time with respect to its medium in the presence of 1 mM paramagnetic ions, is determined from the slope of the linear plot of relaxation rates ($1/T_1$) versus Gd concentration. The longitudinal relaxation time of four different samples containing **3A**@SiO_2 (with increasing Gd(III) concentration) was measured at 1.41 T using a BRUKER minispec mq60NMR analyzer and consecutively plotted. The exact concentration of Gd in the samples was determined by the ICP-MS technique (Model-Element XR, Thermo Fisher Scientific). Nanoparticle suspensions were treated with dilute HNO_3 solution (45%) at 90 °C, for 12 hours and the supernatant solution was tested by ICP-MS for quantification of Gd(III) content.

r_1 of complex **3A** was found to be 9.05 $mM^{-1}s^{-1}$ at pH ~7.4, 1.41 T, and 37 °C. A about 9.5-fold increase in the relaxivity value was observed on the incorporation of the complex molecules as **3A**@SiO_2NP exhibited r_1 = 86.41 $mM^{-1}s^{-1}$ at the same experimental condition (**Figure 3.6**).

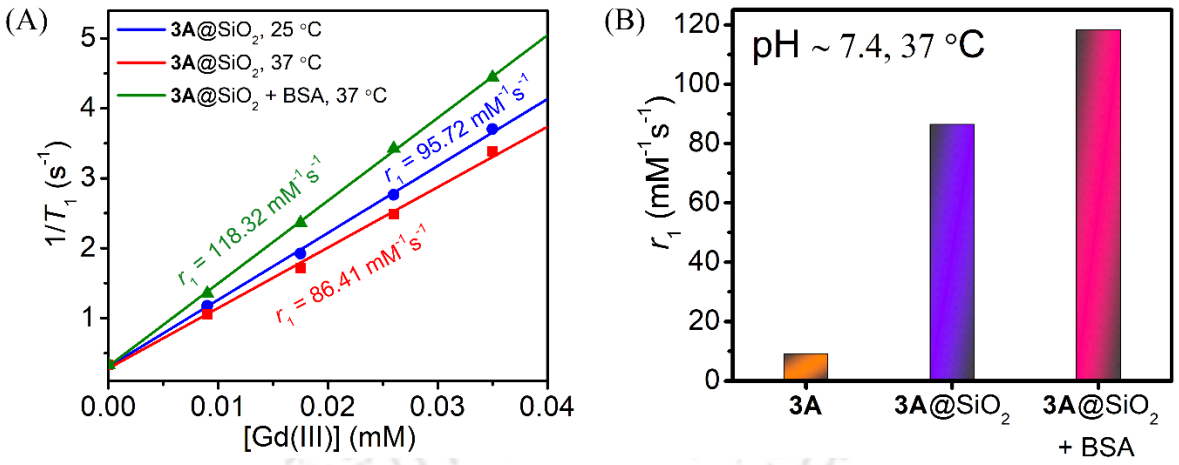

Figure 3.6. ($1/T_1$) *versus* **[**Gd(III)] for **3A**@SiO_2NPs, recorded at 25 °C, 37 °C, and in the presence of 4.5% (w/v) BSA. (B) r_1 values compared with bare complex **3A**. Measurements were done at pH ~ 7.4, and 1.41 T.

To investigate the role of entrapment of the complex molecules in elevating relaxivity value, surface zeta potential (ζ) of pristine silica nanoparticle and complex incorporated nanoparticle suspensions (at pH 7.4 and 25 °C) were measured using Malvern ZETASIZER Nano-ZS90 (equilibrium time set to 2 min; 5 measurements taken on each sample set, only quality criteria values were accepted). The pristine porous nanoparticle of size 22.0 ± 2 nm in the absence of complex **3A** exhibited zeta (ζ) potential -23.9 mV (**Table 3.3**). The value in **3A**@SiO_2NPs at the same pH was -19.0 mV. Thus, the shift in the value to the more positive direction was a clear indication that mono-positively charged complex **3A** interacted with the negatively charged layer of the silica nanoparticles (**Figure 3.7**). This static entrapment and the geometrical confinement within the nanosphere decreased the motion of **3A** and enhanced the longitudinal relaxivity, r_1.

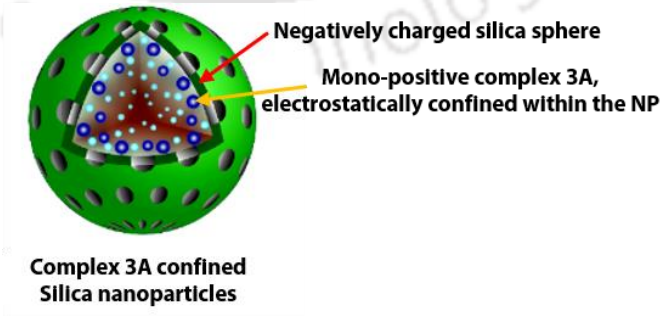

Figure 3.7. Schematic representation of **3A**@SiO_2NP, showing the presence of complex **3A**(blue) close inside the silica layer (green sphere) and water (cyan) molecules.

A further amplification in r_1 relaxivity value of **3A**@SiO_2NP to 118.32 $mM^{-1}s^{-1}$ (**Figure 3.6A**, green line) in the presence of serum albumin protein was observed (samples incubated for 3 h at 37 °C). This implied the formation of a slower tumbling system due to the interaction between the nanoparticles and the protein. To investigate the possible interactions, the ζ potential values of **3A**@SiO_2NP in the absence and the presence of serum albumin protein (4.5%, w/v) in the pH range of 3.0 to 8.6 were recorded. The hydrodynamic diameter of the nanoparticles employing dynamic light scattering (DLS) techniques has also been determined simultaneously in the presence of the protein in the pH range of 3.4 to 8.6. The findings are presented in **Figure 3.8**. The significant changes in ζ potential values of the nanoparticles in the presence of the serum albumin protein were realized in the pH range- 3.0 to 4.0 and 5.0 to 8.6. While, the ζ potential values increased towards positive values at the lower pH range (below pH 5.5), an increase in the potential toward negative values was noticed at the higher pH than 5.5. The isoelectric point for BSA lies at pH 4.7. Below that pH, the overall charge of the protein is positive, and at the higher pH, it is negatively charged. Therefore, the pH-dependent changes in the ζ potential values (positive-negative interaction at lower pH, and negative-negative interaction at higher pH) warranted interactions of serum albumin protein with the nanoparticles whose ζ potential values ranged from -13.6 to -20.2 in the pH 3.0-8.6. The interactions could be a combination of supramolecular, van der Waals, and electrostatic interactions.

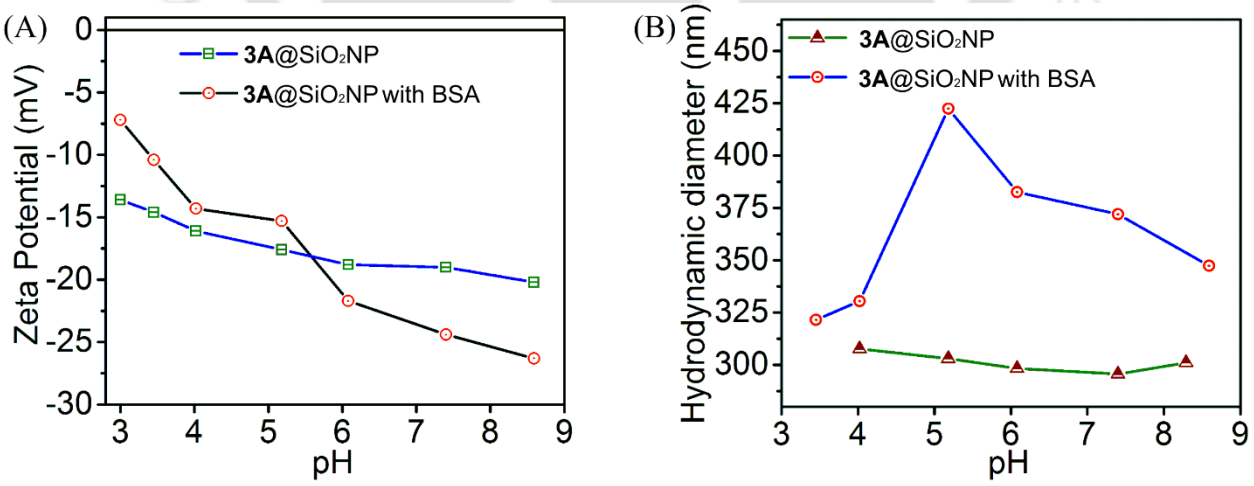

Figure 3.8. (A) Zeta potentials of **3A**@SiO_2NP recorded in the absence and presence of 4.5% (w/v) BSA at different pH. (B) Hydrodynamic diameter of **3A**@SiO_2NP in the absence and presence of 4.5 % (w/v) BSA at different pH.

The hydrodynamic diameter of **3A**@SiO_2NP in the presence of the protein increased with the increased pH and reached the maxima at pH 5.2. Above the pH, the diameter of the nanoparticles diminished, however, it remained higher than that found in the pH range of 3.4 to 4.0. The findings suggested that the maximum interaction between the protein and the nanoparticles occurred when it was neural in charge, followed by the negatively charged protein. These results also discerned the presence of a substantial amount of supramolecular and van der Waals interactions between the nanoparticles and the protein. Concerned experimental results along with relaxivity values of **3A**@SiO_2NP at physiological pH are summarized in **Table 3.4**.

Table 3.4. DLS hydrodynamic diameters, FETEM particle size, and longitudinal relaxivity values of bare silica nanoparticles, **3A**@SiO_2NP in the absence and presence of BSA, at pH ~ 7.4.

Material	Hydrodynamic diameter (nm)	ζ (mV)	Particle Size (nm)	r_1 ($mM^{-1}s^{-1}$) at 37 °C, pH ~ 7.4, 1.41 T
SiO_2 NP	284.1, PdI = 0.26	-23.9	22.0	—
3A@SiO_2NP	295.6, PdI = 0.37	-19.0	23.4	86.41
3A@SiO_2NP + 4.5 % BSA (w/v)	372.0, PdI = 0.47	-24.6	24.4	118.32

To further ascertain the existence of the interactions, thermogravimetric analysis (TGA) of **3A**@SiO_2NP in the absence and the presence of the protein was recorded at pH 3.0, 5.0, and 7.4 using lyophilized nanoparticles (**Figure 3.9A**). The percentage of weight loss for each protein-added sample was compared with that of **3A**@SiO_2NP itself. The weight loss sequence, pH 5 (26.0 %) > pH 7.4 (23.0 %) > pH 3.0 (21.4 %), suggested a higher protein loading at pH 7.4 compared to pH 3.0. This protein adsorption trend was in accordance with similar reports in literature[19b] and herein, established that supramolecular and van der Waals interactions predominated over the electrostatic interaction. Hence, at pH 7.4, the association of the protein, which was due to van der Waals and supramolecular interactions, rendered a slow-tumbling system and presumably also lowered the mobility of outer-sphere water molecules as suggested previously.[1c] These cumulative

effects consequently elevated r_1 relaxivity value to 118.32 $mM^{-1}s^{-1}$ compared to r_1 = 86.41 $mM^{-1}s^{-1}$ found for **3A**@SiO_2NP. With an increase in the concentration of BSA, the relaxivity value further increased and attained the maximum value of 128 $mM^{-1}s^{-1}$ at a 1.6 mM concentration of BSA (**Figure 3.9B**).

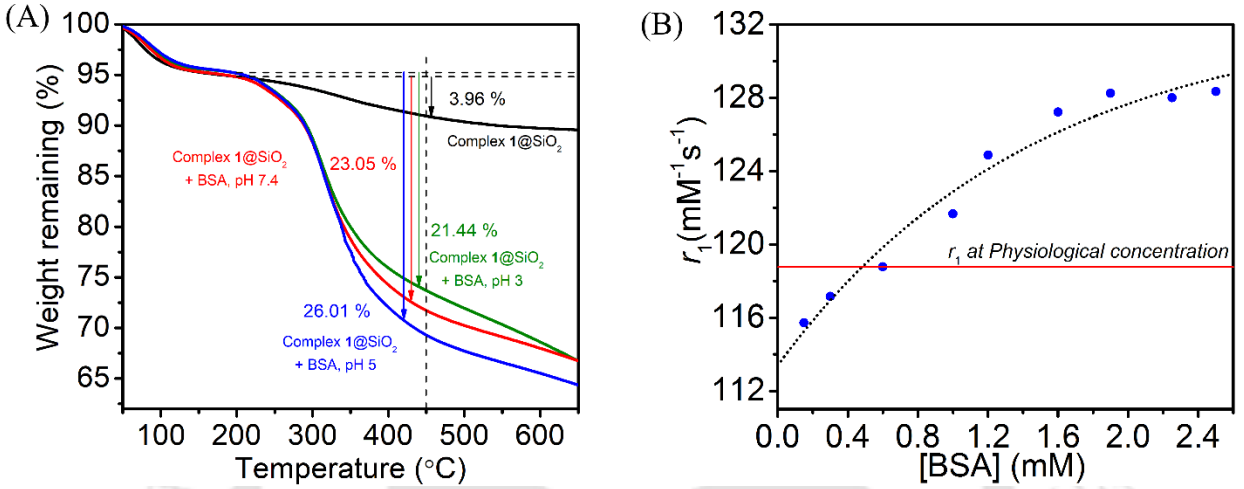

Figure 3.9. (A) TGA analysis spectra for **3A**@SiO_2NP (black line), in the presence of 4.5% (w/v) BSA at pH 3 (green line), pH 5 (blue line), and pH 7.4 (red line). (B) r_1 values for **3A**@SiO_2 measured in the presence of an increasing concentration of BSA, at 37 °C, pH 7.4, and 1.41 T.

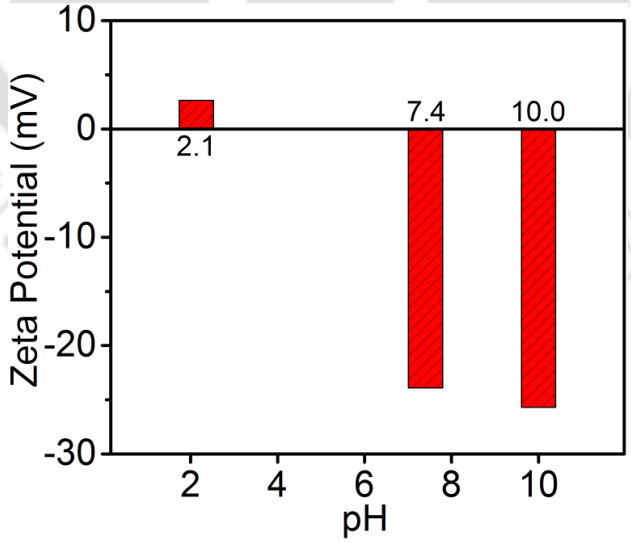

Figure 3.10. Zeta potentials of hollow porous pristine silica nanoparticles (in the absence of complex **3A**) measured in the pH range of 2 to 10.

3.5 Stability of 3A@SiO$_2$NP at Different pH

According to earlier reported data, complex **3A** showed pH-dependent change in relaxivity as r_1 was found to be 9.82 $mM^{-1}s^{-1}$ at 1.41 T, pH 7.4, 25 °C increased to 13.08 $mM^{-1}s^{-1}$ upon lowering the pH to 2.13. Contrarily, the relaxivity value diminished to 6.70 $mM^{-1}s^{-1}$ at pH 10.0. The increase in relaxivity upon decreasing pH was explained due to the aggregation of complex molecules leading to a slowly rotating system, which increases overall correlation time and thus the longitudinal relaxivity.[20] Thus, complex **3A** remained intact even at pH 2. These diminishing effect at higher pH was attributed to the alteration in hydration number with pH as *q* was found to be ~ 2 at pH 10.

Here, the r_1 relaxivity of **3A**@SiO$_2$NPs (0.05 mM) was determined at 1.41 T, 25 °C within the pH range 2-10 to elucidate the effect of pH on complex **3A**-molecules after the impregnation within the nanoparticles (**Figure 3.11** and **Table 3.5**). pH of each solution was attained with the addition of an appropriate amount of dilute HCl or NaOH solution.

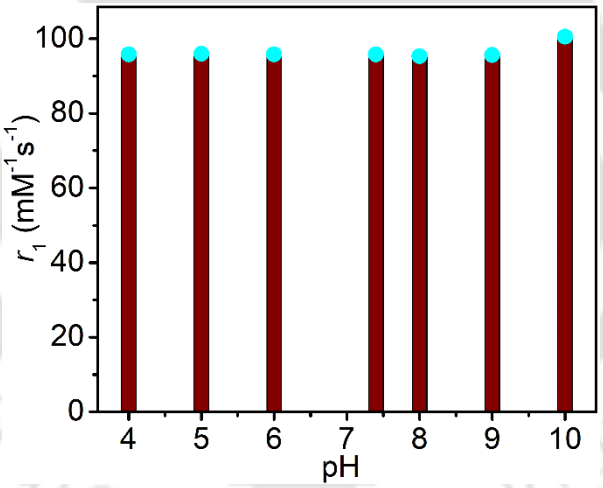

Figure 3.11. r_1 values for **3A**@SiO$_2$NP recorded in the pH range 2.1-10.0. Experiments were performed at 25 °C, and 1.41 T.

While a constant value of 95.3 ± 0.5 $mM^{-1}s^{-1}$ was observed between pH 4.0 to 9.0, a subtle elevation in the relaxivity value (100.53 $mM^{-1}s^{-1}$) was noticed at pH 10.0. Contrarily, a discernible pH effect was apprehended at pH = 2.13, and a ~ 37 % drop in the relaxivity value to 59.54 $mM^{-1}s^{-1}$ was realized. To rationalize the observation, ζ potentials of hollow porous pristine silica nanospheres were considered in the pH range of 2.13 to 10.0 (**Figure 3.10**). With the decrease in

pH from 7.4 to 2.13, the ζ potential simultaneously increased to +2.65 mV from -23.9 mV. This change in ζ potential to the positive value at pH 2.13 caused a repulsive interaction between the cationic complex **3A** and the nanoparticles-layers. As a result, some of the layer-confined-complex-molecules, having a calculated volume of 631 $Å^3$/molecule (**Figure 3.12**), transuded from the porous nanospheres to the solution. To quantify this leaching effect at lower pH, a 100 μM **3A**@SiO_2NP suspension was kept for 20 h, at pH 2.13. The percolated-out gadolinium ions concentration in the supernatant solution was measured to be 38.3 μM which was almost 39 % of the total concentration of the confined molecules. Owing to the fact that **3A** was stable at pH 2.04) and exhibited r_1 = 13.08 $mM^{-1}s^{-1}$ at 1.41 T, 25 °C (*vide supra*), the coexistence of both unconfined and confined complex molecules prevailed in the pH 2.13 solution, consequently diminishing the overall relaxivity value. At pH 10.0, the reduction in ζ potential to -25.7 mV strengthened the interactions between the silica nanosphere and the entrapped cationic complex **3A**. The interactions possibly reduced the molecular motion further to engender a subtle increase in the relaxivity value from 95.24 $mM^{-1}s^{-1}$ to 100.53 $mM^{-1}s^{-1}$.

Table 3.5. Hydrodynamic diameter and longitudinal relaxivity of **3A**@SiO_2NP determined in the pH range 4-8.

3A@SiO_2NP at different pH	**Hydrodynamic diameter (nm)**	**PdI**	**r_1 ($mM^{-1}s^{-1}$) at 25 °C, 1.41 T**
4.02	307.6	0.32	95.81
5.18	303.0	0.31	95.97
6.08	298.3	0.27	95.61
7.40	295.6	0.36	95.32
8.29	301.1	0.30	95.44

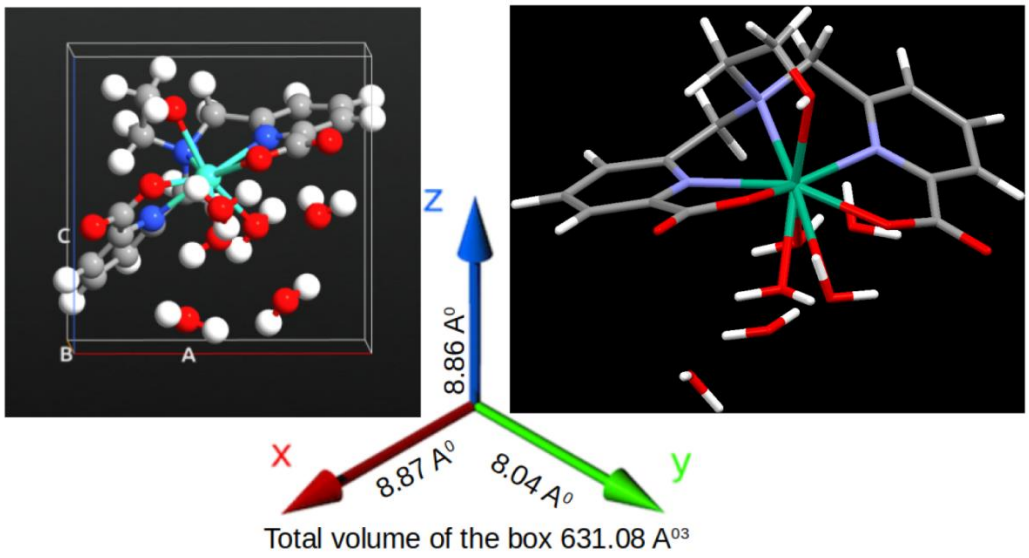

Figure 3.12. Optimized structure of tris(aquated) complex **3A**. Optimized at B97D3 level containing a pure functional, B97. Red = oxygen, blue = nitrogen, grey = carbon, green = gadolinium, and white = hydrogen. According to the calculations the molecule could be fitted within a cavity having an estimated volume of 631.08 $Å^3$ (*i.e.*, 8.87A°×8.04A°×8.86A°).

Table 3.6. Optimized coordinates of the complex **3A** at B97D3 level of theory containing a pure functional, B97, with the Grimme's D3BJ dispersion (B97D3) (in xyz format). The DFT calculations are performed using the Gaussian16 package.[21]

C	-4.04E+00	7.00E-01	-3.39E+00
C	-3.17E+00	2.50E-01	-2.45E+00
N	-2.22E+00	1.04E+00	-2.01E+00
C	-2.17E+00	2.29E+00	-2.23E+00
C	-2.96E+00	2.86E+00	-3.17E+00
C	-3.93E+00	2.04E+00	-3.80E+00
C	-3.19E+00	-1.15E+00	-1.81E+00
O	-2.29E+00	-1.41E+00	-9.28E-01
O	-4.05E+00	-2.01E+00	-2.12E+00
C	-1.17E+00	3.02E+00	-1.32E+00
N	-1.18E+00	2.19E+00	-9.70E-02
C	-3.43E-01	2.73E+00	9.93E-01
C	1.09E+00	2.24E+00	8.44E-01
N	1.19E+00	1.05E+00	3.88E-01
C	2.27E+00	3.23E-01	5.45E-01
C	3.45E+00	8.89E-01	9.30E-01

C	3.46E+00	2.26E+00	1.24E+00
C	2.23E+00	2.96E+00	1.22E+00
C	2.06E+00	-1.17E+00	2.78E-01
O	2.99E+00	-2.01E+00	4.39E-01
O	9.03E-01	-1.54E+00	-1.07E-01
C	-2.50E+00	2.03E+00	4.16E-01
Gd	-5.70E-01	9.50E-02	-7.42E-01
O	8.75E-01	9.96E-01	-2.24E+00
O	2.77E+00	2.59E+00	-2.03E+00
O	-2.74E-01	-1.36E+00	-2.46E+00
C	-2.36E+00	1.04E+00	1.61E+00
O	-1.60E+00	-5.20E-02	1.31E+00
H	-4.79E+00	5.70E-02	-3.80E+00
H	-2.87E+00	3.90E+00	-3.42E+00
H	-4.56E+00	2.44E+00	-4.56E+00
H	-1.94E-01	3.07E+00	-1.75E+00
H	-1.50E+00	4.02E+00	-1.11E+00
H	-6.78E-01	2.32E+00	1.93E+00
H	-4.28E-01	3.80E+00	1.01E+00
H	4.34E+00	3.06E-01	9.97E-01
H	4.37E+00	2.76E+00	1.49E+00
H	2.18E+00	3.99E+00	1.50E+00
H	-3.12E+00	1.60E+00	-3.48E-01
H	-2.94E+00	2.95E+00	7.33E-01
H	3.81E-01	1.38E+00	-2.97E+00
H	1.40E+00	1.68E+00	-1.82E+00
H	3.51E+00	2.14E+00	-1.62E+00
H	2.58E+00	3.40E+00	-1.55E+00
H	-7.20E-02	-2.23E+00	-2.11E+00
H	-1.08E+00	-1.40E+00	-2.99E+00
H	-1.87E+00	1.54E+00	2.42E+00
H	-3.34E+00	7.29E-01	1.91E+00
O	-1.26E+00	-1.85E+00	-4.89E+00
H	-1.83E+00	-2.60E+00	-4.68E+00
H	-4.03E-01	-2.17E+00	-5.18E+00
O	-2.78E-01	-3.16E+00	-1.52E+00
H	5.56E-01	-3.17E+00	-1.04E+00
H	-9.90E-01	-2.94E+00	-9.14E-01
O	1.77E+00	1.43E+00	-4.50E+00
H	1.29E+00	1.91E+00	-5.17E+00
H	2.43E+00	2.00E+00	-4.10E+00
H	-2.16E+00	-8.35E-01	1.32E+00

3.6 Stability of 3A@SiO$_2$NP in the Presence of Interfering Ions

The physiologically available ions (HCO_3^{1-}, HPO_4^{2-}, Zn(II), Cu(II), *etc.*), which are present in a non-negligible concentration in blood plasma, may remove the ligated water molecules thereby reducing the relaxivity value or induce transmetallation, releasing highly toxic free Gd(III) ions in the body subsequently.[22] Thus, the effect of these cations and anions on **3A**@SiO$_2$NP must be assessed.

Bicarbonate and biphosphate solutions were added to **3A**@SiO$_2$NP suspension [0.05 mM w.r.t. Gd(III)] in 200-fold excess, at pH 7.4 and 25 °C. The change in the r_1 relaxivity value of the resultant suspension was then determined at 1.41 T, after 12 h of incubation. Gratifyingly, no change in r_1 = 95.24 $mM^{-1}s^{-1}$ was realized (**Figure 3.13A**). To note, bare complex **3A** showed affinity towards the mentioned anions, and relaxivity values were significantly diminished when exposed to 100 equivalents of bicarbonates (43%) or biphosphates (50%). Thus, upon confinement, the negatively charged silica nanosphere effectively protected the entrapped positively charged **3A** molecule from any deleterious interactions by the external anions.

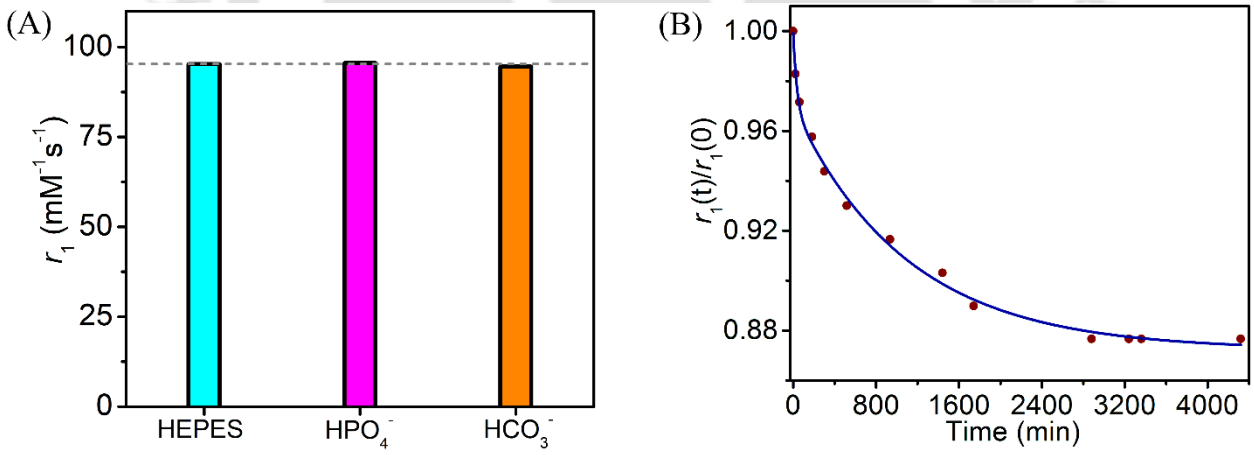

Figure 3.13. (A) r_1 values for **3A**@SiO$_2$NP measured in the presence of 200 equivalent excess of different physiological anions, at pH ~ 7.4, 1.41 T, and 25 °C. (B) Time profile of percentage changes in relative relaxivity, r_1 (t)/r_1 (0), of **3A**@SiO$_2$NP, [Gd(III)] = 0.01 mM; when challenged with an equivalent amount of Zn(II) ions. pH was maintained at ~ 7.0 using phosphate buffer and the experiment was done at 37 °C.

To elucidate the effect of Zn^{2+} ions (an essential micronutrient *in vivo*) on bare and entrapped complex **3A** molecules, transmetallation studies were done following the changes in the initial r_1 relaxivity values with time, in the presence of an equivalent amount of Zn(II) ions in phosphate buffer at pH 7.0, 37 °C.[23] Usually, the index of kinetic inertness is given as the time required for the reach 80 % of the initial r_1 relaxivity value. The reduction would be because of the transmetallation, releasing free Gd(III) and thereafter insoluble $Gd(PO_4)$ precipitate formation. Gd(III) in ionic form is highly toxic and could be directly related to nephrogenic systemic fibrosis (NSF). Hence, high kinetic stability is an inevitable parameter for developing novel Gd(III)-based contrast agents.

For bare **3A** molecules, the 20 % decrease in the r_1 value was reached by 43 min. The same index for clinically approved mono(aquated) GdDTPA(BMA) [Omniscan®], GdDTPA [Magnevist®], and GdDOTA [Dotarem®]values are 70 min, 250 min, and > 5000 min, respectively.[24] Herein, the lower value abided low denticity of the H_2hbda ligand.

Nonetheless, upon encapsulation within the porous nanoparticles, there was only a 3 % decrease in the initial relaxivity value at 50 min. The total reduction in the initial value was restricted to only 12 % in ≥ 4320 min (**Figure 3.13B**). Thus, the encapsulation paved the kinetic inertness in complex **3A**. A similar effect in terms of increase in kinetic inertness has also been observed by Mazzanti and colleagues, where 80 % of the initial relaxivity value was reached in 1000 min by entrapping trianionic $[Gd(OH_2)_3(dhqN\text{-}SO_3)]^{3-}$ complex.[10] Thus, a significant improvement in the depletion time of the initial relaxivity value has been achieved by implanting monocationic complex **3A** closer to the inner negatively charged surface of the nanoparticles. The attenuation in the initial r_1 value of **3A**@SiO_2NP originated merely because of agglomeration. In the phosphate buffer, the hydrodynamic diameter (d_h) of the **3A** incorporated nanoparticle was 644 nm (PDI = 0.395). In the presence of Zn(II) ions (incubated for 24 h), the value inflated to 1352 nm (PDI = 0.196). The agglomeration reduced the exposure of entrapped-complex **3A**-molecules to outer-nanosphere water molecules and consequently diminished the values. Nonetheless, the agglomeration did not exert a substantial change in the relaxivity value.

3.7 Phantom MR Imaging of 3A@SiO$_2$NP, at 1.5 T

To judge the capability of the synthesized **3A**@SiO$_2$NP as a potential T_1-weighted contrast agent, *in vitro* phantom images of suspensions with varied Gd(III) concentrations were recorded at pH 7.4 on BRIVO MR355 1.5 T MRI scanner at TR = 560 ms, TE = 15ms, slice thickness = 5.0 mm and field of view (FOV) = 512×512 mm^2. By considering the same area for all the images, relative image intensity was plotted as a bar diagram. The MR images and the corresponding intensity plot (**Figure 3.14**) demonstrated enhancement in brightness with increasing concentration of **3A**@SiO$_2$NPs [Gd(III) ions] and thus, consolidated **3A**@SiO$_2$NP as a T_1-weighted contrast agent.

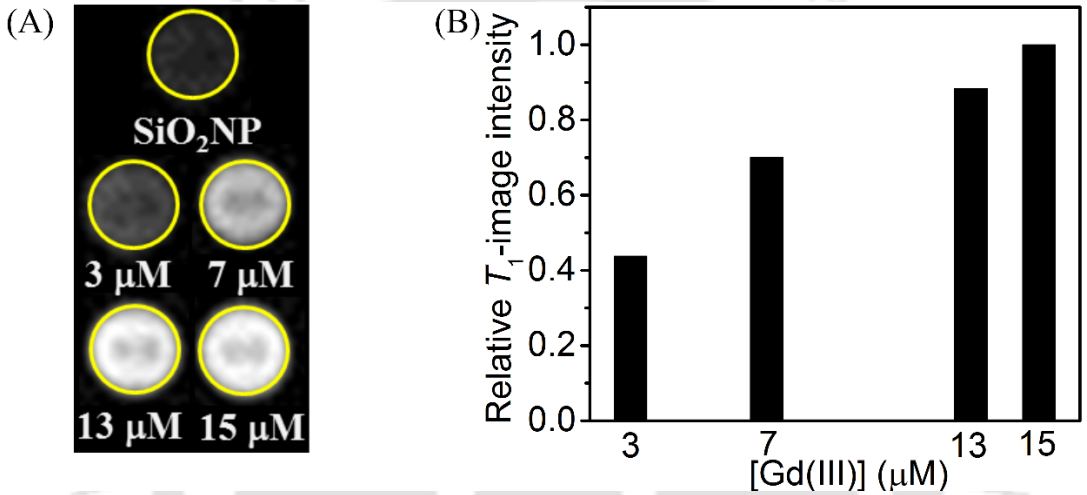

Figure 3.14. (A) T_1-weighted phantom MR images of micro-centrifuge tubes containing suspensions of different concentrations of **3A**@SiO$_2$NP, recorded at 25 °C, and 1.5 T; (B) Relative image intensity plot using *ImageJ* software considering the same area for each phantom.

3.8 Cytotoxicity Assay and Cell-Uptake of 3A@SiO$_2$NP

Theranostic applications of nanoparticulate contrast agents that exhibited cellular uptake, followed by cell tracking, therapy, drug delivery, etc., have become important in modern medical sciences.[25] In this context, the biocompatibility of the synthesized complex **3A** confined porous silica nanoparticles was assessed on HeLa cells and macrophages by performing the MTT (3-[4,5-dimethylthiazol-2-yl]-2,5 diphenyl tetrazolium bromide) assay.[8b,13a] In this experiment, cell lines were maintained in Dulbecco's modified Eagle's medium (DMEM) supplemented with 10% (v/v) fetal bovine serum (FBS) and 1%

penicillin & streptomycin at 37 °C in humidified air containing 5% CO_2. Cells were seeded in a 96-well plate at a density of 5×10^3 cells/well and allowed to attach for 24 h, maintaining the same conditions mentioned above. Afterward, respective cells were incubated with an increasing concentration of **3A**@SiO_2NPs. For HeLa, treatment was continued for 48 h, whereas for macrophages, cells were incubated with nanoparticles for 4 h. 0.5 mg/ml of MTT in DMEM was added to each well. Subsequently, 150 µL DMSO was added to each well. Absorbance was measured at 570 nm using Cary 60 UV-Vis spectrophotometer, and after that, cell viability was calculated, considering 100% viability for untreated cells.

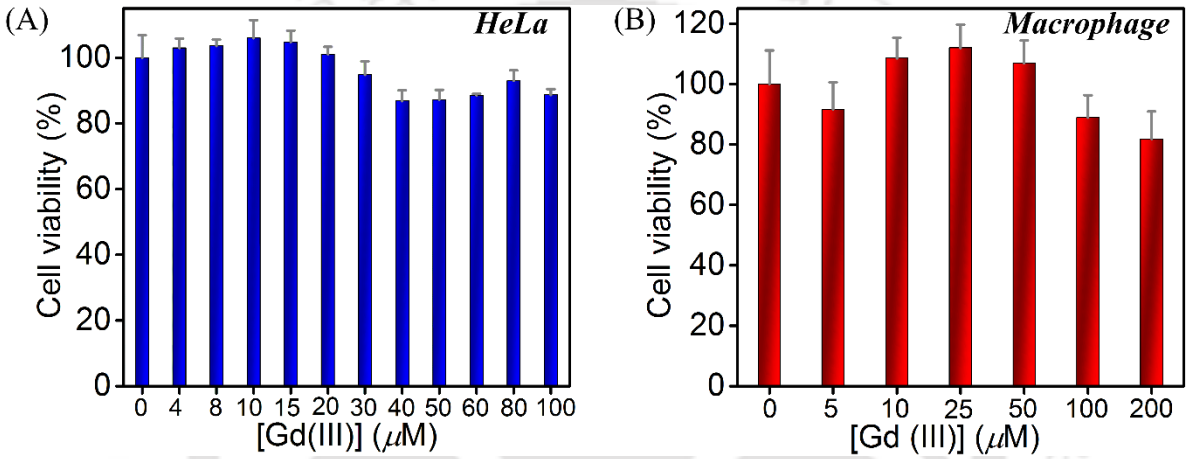

Figure 3.15. *In vitro* cytotoxicity analysis of **3A**@SiO_2NPs done by MTT assay on (A) HeLa cell line and (B) Macrophages. Measurements were done in triplicate.

88 % cell viability in HeLa cells (**Figure 3.15A**) was realized after 48 h exposure to **3A**@SiO_2NPs at 100 μM Gd(III) concentration (*i.e.*, [silica nanoparticles] = 32 mg/mL). In the case of macrophages, 82 % viability (**Figure 3.15B**) was noticed in 4 h incubation of 200 μM of the nanoparticles. Thus, the biocompatibility of the synthesized nanoparticles was apprehended.

Furthermore, RBC pellets were collected by centrifugation of 4 mL EDTA-stabilized human blood at 1600 rpm for 5 minutes. Blood plasma was removed and the remaining RBC was washed with PBS twice. Finally, the collected RBC pellet was re-suspended in PBS (10 mL). Hemocompatibility was assessed by incubating freshly isolated red blood cells (RBC) and plasma with varied concentrations of **3A**@SiO_2NPs.[26] Results are presented in **Figure 3.16**. **3A**@SiO_2NPs exhibited mild toxicity toward human RBC

and caused about 18 % haemolysis on treatment with 50 μM complex incorporated nanoparticles. Furthermore, no toxicity of the nanoparticles was recorded in the plasma.

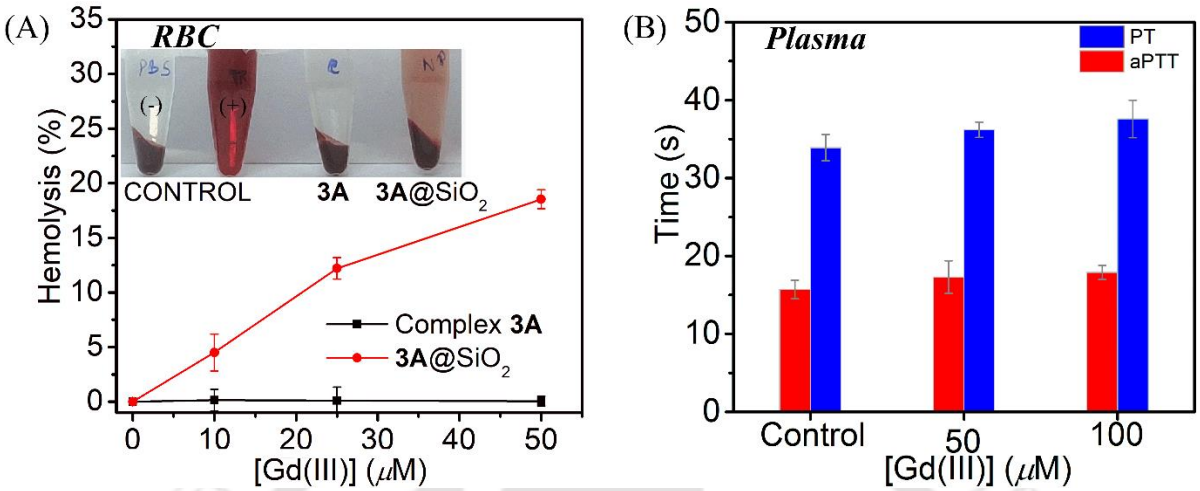

Figure 3.16. Hemolysis percentage after treatment of RBC with complex **3A** and **3A**@SiO_2NPs. Inset: photographs of RBC pellets after treatment with negative control, positive control, complex **3A** (50 μM) [denoted as C], and **3A**@SiO_2NPs (50 μM) [denoted as NP]. (D) Coagulation properties of **3A**@SiO_2NPs were tested by PT and aPTT measurements. Measurements were done in triplicate.

Parallelly, the cell permeability of **3A**@SiO_2NPs was tested on HeLa cells. To visualize the cell uptake, post 12 h and 48 h incubation with 25 μM amount of **3A**@SiO_2NP, Hela cells were subsequently washed with PBS (phosphate-buffered saline) to remove any unbound nanoparticles. Cells were then trypsinized and fixed using 4 % formaldehyde for 15 min and washed twice with PBS. The corresponding FETEM images, particle size analysis, and EDS elemental analyses, presented in **Figure 3.17**, suggested the incorporation of **3A**@SiO_2NPs within the cells in the measurement time frame.

The cellular uptake was quantified by ICP-MS of the solution prepared by digesting the treated cells (48 h) in conc. HNO_3. Gd content was estimated to be about 55 % of the initially treated amount.

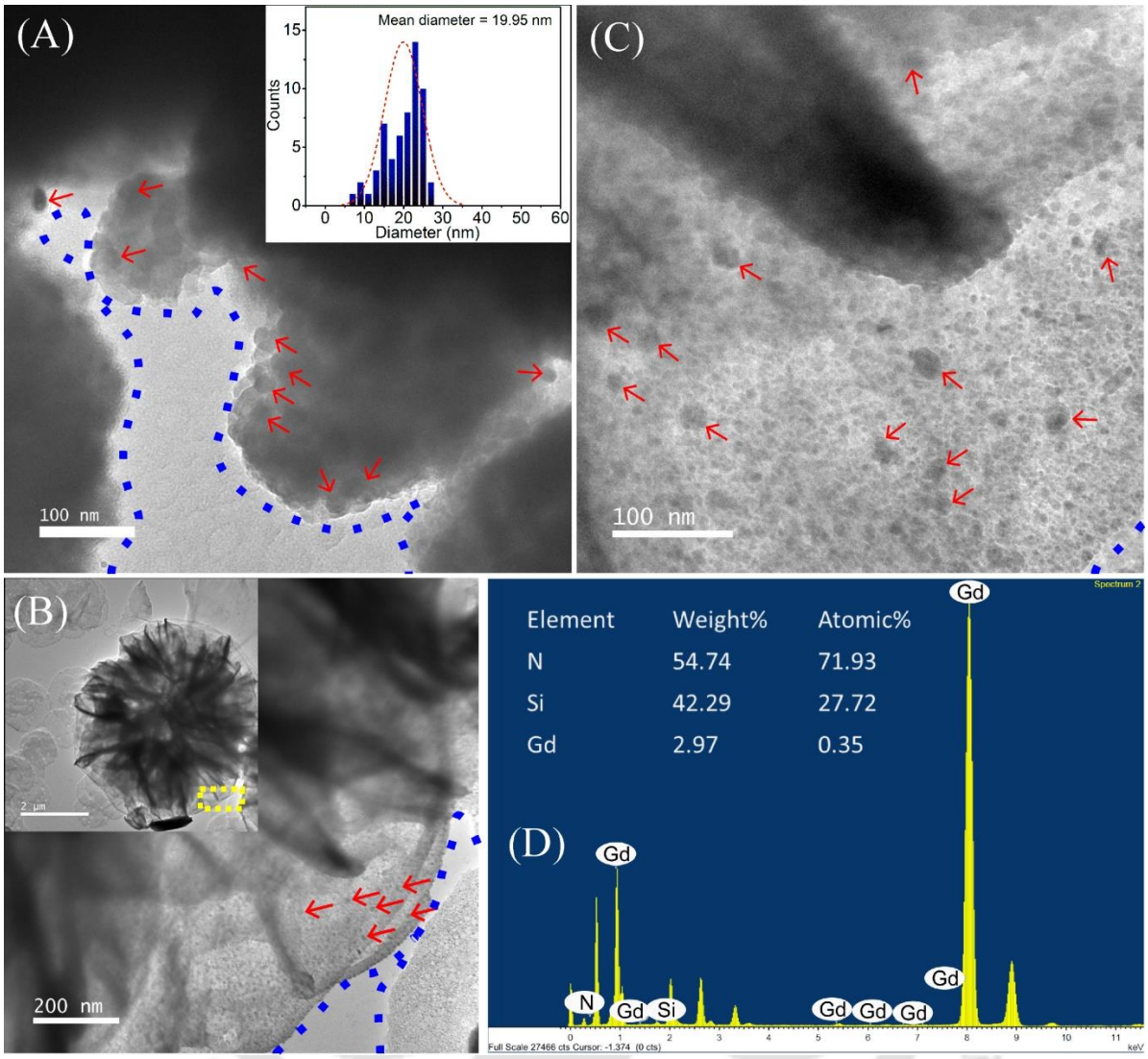

Figure 3.17. TEM images of HeLa cell (A) after 12 hours of incubation (corresponding nanoparticle size in the inset), (B) and (C) after 48 hours of incubation with **3A**@SiO_2NP, showing uptake of nanoparticles. (B) Inset: Full view of the cell that was zoomed in. Red arrows are used to locate the presence of **3A**@SiO_2NP inside the cell. The yellow marked area in (C) inset is magnified to visualize the internalization of nanoparticles. (D) EDS analysis inside the cell, indicating the presence of Gd, Si, and N. Cell membrane is indicated by a blue-dotted line for the zoomed-in images.

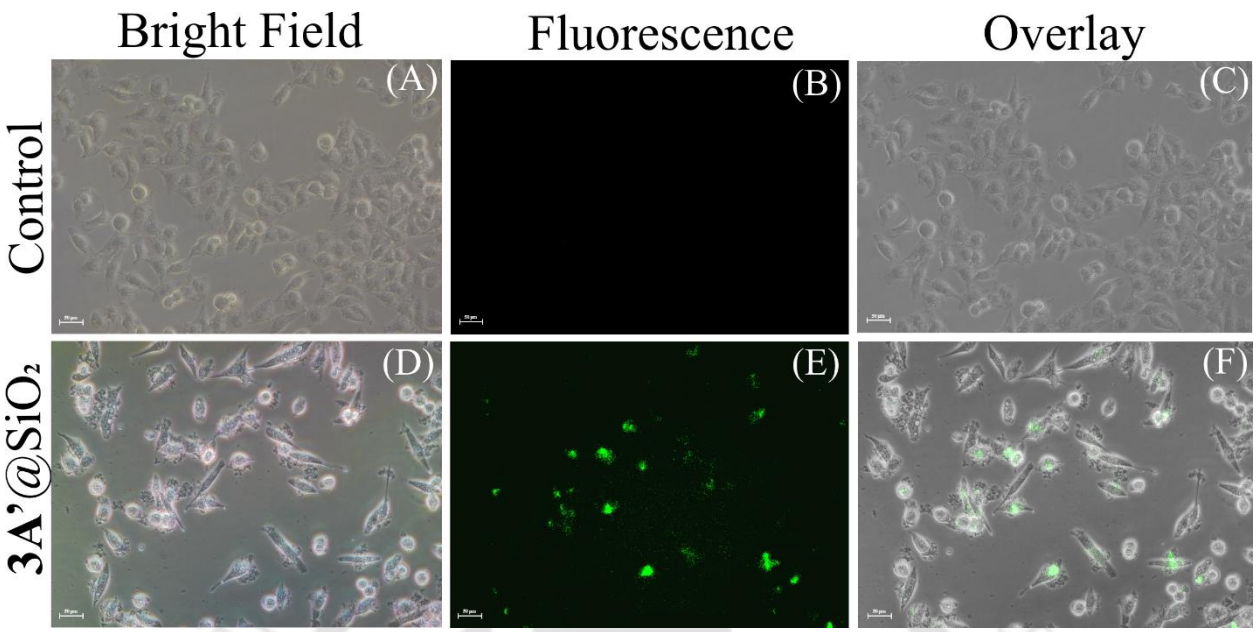

Figure 3.18. Fluorescence microscopy images of HeLa cells (A)-(C): untreated; (D)-(F): treated with **3A′**@SiO_2 *i.e.*, Tb(III)-congener confined porous silica nanoparticles.

To further support the cell uptake phenomenon, cells were treated and incubated with fluorescent active Tb(III) congener of complex **3A**, *i.e.*, **3A′**@SiO_2NPs (Gd^{III} concentration ~ 100 μM) and were subsequently fixed with 4% formaldehyde solution for 15 mins, thoroughly washed with PBS. Cells were imaged using Fluorescence inverted microscope *Nikon* ECLIPSE T*i*-U. The fluorescence images of cells showed green fluorescence due to intracellular incorporation of **3A′**-based nanoparticles (**Figure 3.18**). Therefore, the study directly concurred with incorporating and possibly using the synthesized nanosystem for cell labeling. Functionalization of the presented system for selective cell internalization and its therapeutic application thereafter could be done afterward.

3.9 Synthesis and Characterization of Ligand H_2PyDPA

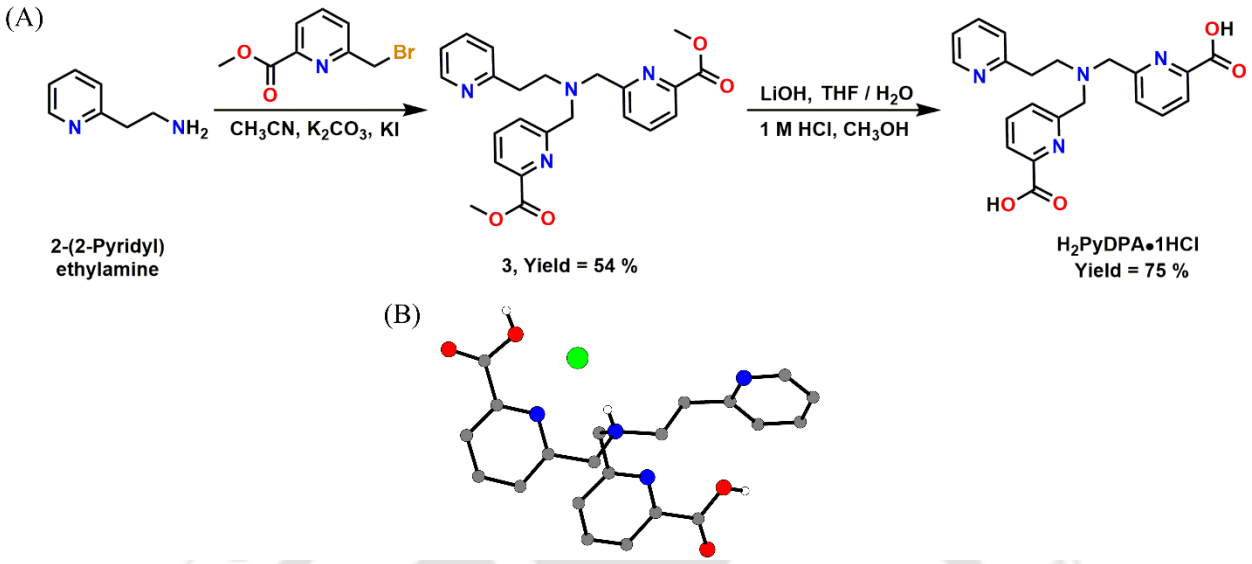

Scheme 3.3. (A) Schematic representation for the synthesis of ligand **H_2PyDPA**. (B) Molecular structures of the protonated ligand. C = grey; N = blue; O = red and Cl = green.

The synthetic route for the preparation of ligand H_2PyDPA is shown in **Scheme 3.3**. Compound **3** was isolated in 54 % yield by reacting 1:2.2 equivalent amounts of 2-(2-Pyridyl)ethylamine and 6-(bromomethyl)picolinate in CH_3CN in the presence of K_2CO_3 and KI. Ligand H_2PyDPA was obtained as monohydrochloride salt (H_2PyDPA•1HCl) in 75 % yield by the hydrolysis of compound **3** with an aqueous LiOH solution in THF/H_2O solvent mixture followed by acidification of the solution with 1 M HCl. Slow evaporation of a methanolic solution of crude, colourless crystals was obtained (H_2PyDPA•HCl•5.5H_2O). X-ray single-crystal diffraction measurement revealed the existence of tertiary nitrogen in protonated form. The ligand was further characterized by FTIR, ESI-MS, ^{1}H-NMR, and ^{13}C-NMR spectroscopy.

In the infrared spectra of ligand H_2PyDPA (**Figure 3.19A**), bands at 3529 cm^{-1} and 3371 cm^{-1} were due to ν_{O-H} asymmetric stretching of water and carboxylic acid group, respectively. Broad band in the range 2804–2542 cm^{-1} appeared due to the ν_{N-H} of the protonated tert-amine group. Characteristic $\nu_{C=O}$ asymmetric stretching (carboxylic acid groups) were observed as sharp bands at 1722 cm^{-1} and 1710 cm^{-1}. The peak at 1590 cm^{-1} correlated with the characteristic aromatic $\nu_{C=N}$ stretching (pyridine group). The electrospray ionization mass spectrum (ESI-MS)

of ligand H_2PyDPA in aqueous medium was recorded in the positive mode showing a 100% molecular ion peak at *m/z* = 393.1565 (**Figure 3.19B**). The isotope distribution pattern of the observed mass corresponded to the composition of the ligand $[C_{21}H_{20}N_4O_4 + H]^+$ (*m/z* = 393.1557).

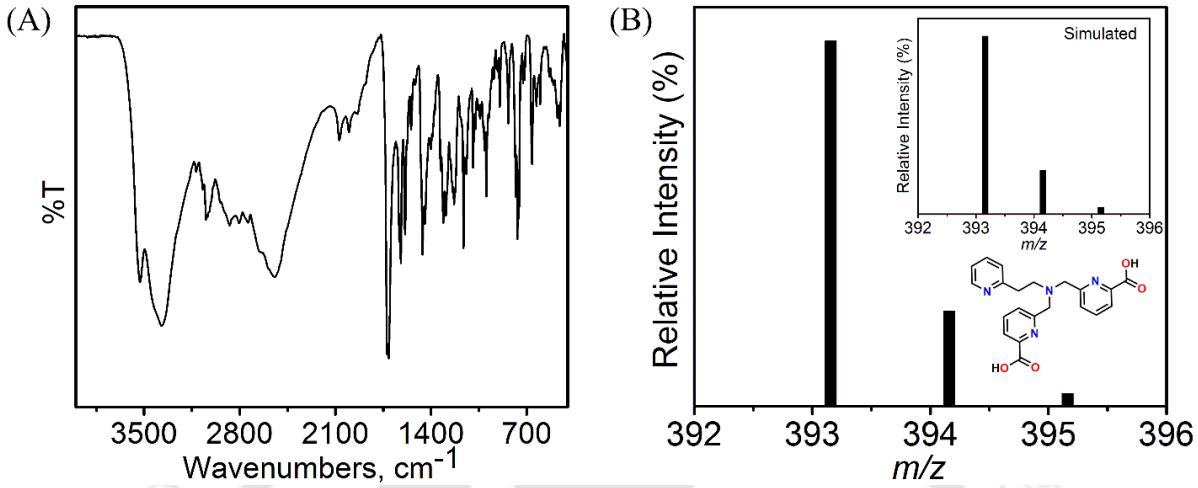

Figure 3.19. (A) FTIR and (B) ESI-MS (+ve) spectra of ligand H_2PyDPA. The simulated spectrum is given as an inset.

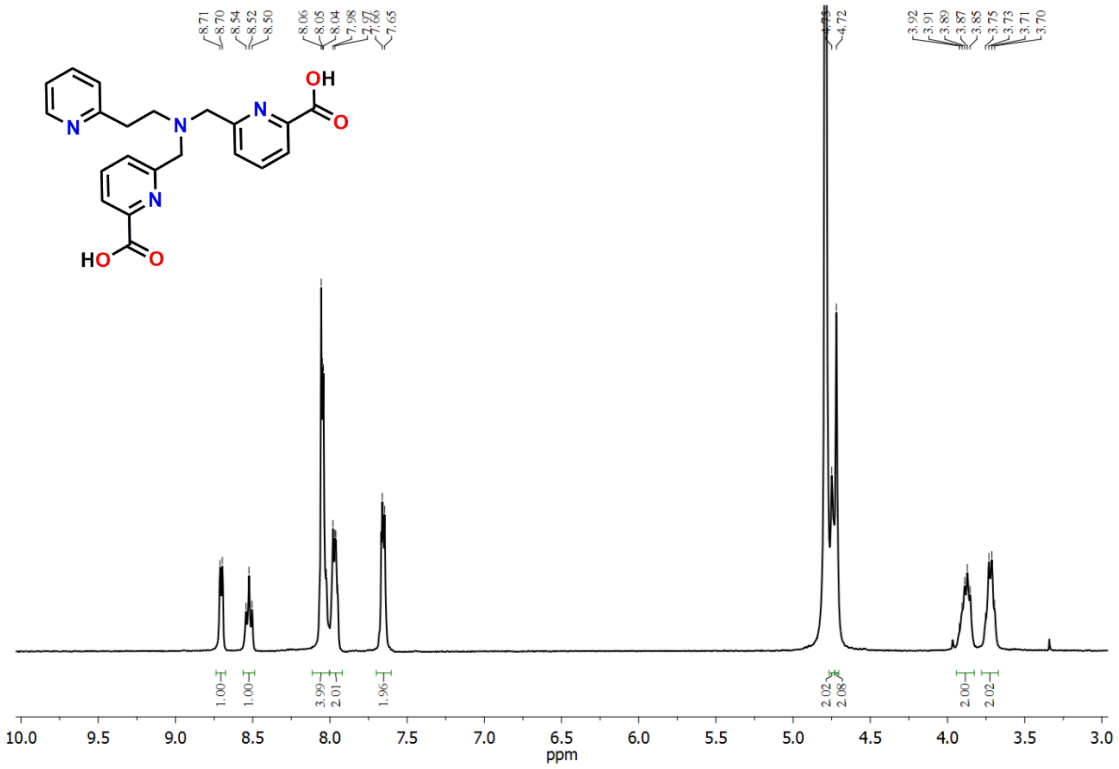

Figure 3.20. ^{1}H-NMR spectrum of ligand H_2PyDPA in D_2O solvent.

The ^{1}H-NMR spectra of ligand H_2PyDPA, recorded in the D_2O medium, showed signals in the 8.71-7.65 ppm corresponding to 10 aromatic protons of three pyridine rings. Two singlet peaks at 4.75 and 4.72 ppm appeared due to the methylene protons of the picolinate groups. The 4 protons of substituted ethyl group adjacent to the pyridine group arise at 3.92-3.70 ppm. The ^{13}C-NMR spectrum of the ligand (**Figure 3.21**) exhibited 11 peaks in the aromatic region and 3 peaks in the non-aromatic region.

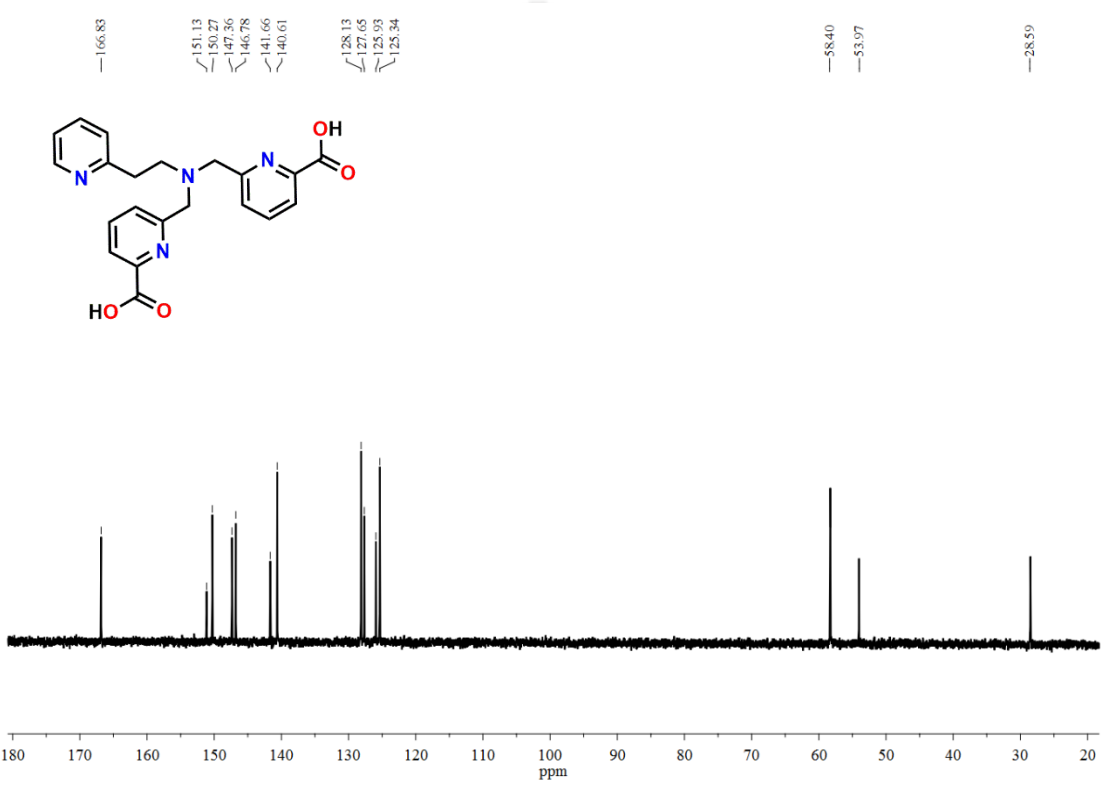

Figure 3.21. ^{13}C-NMR of ligand H_2PyDPA measured in D_2O solvent.

3.10 Synthesis and Characterization of Mono-aquated Mn(II)-Complex of Ligand H_2PyDPA, 3B

Equivalent amounts of the ligand H_2PyDPA and $MnCl_2 \bullet 4H_2O$ were reacted in water at pH ~ 6.5, attained using a dilute NaOH solution. Subsequently, the reaction mixture was kept for slow evaporation, providing needle-shaped pale-yellow X-ray suitable single crystals of complex **3B** in 45 % yield. The reaction pathway is shown in **Scheme 3.4**.

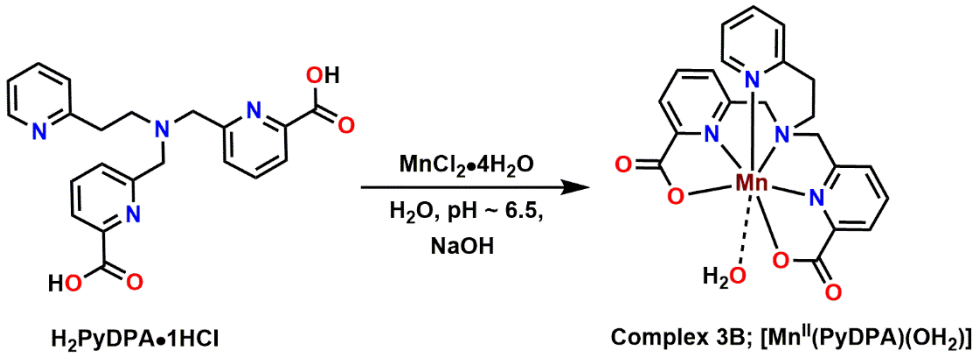

Scheme 3.4. Schematic representation for the synthesis of complex **3B**, $[C_{21}H_{20}N_4O_5Mn]$.

The FTIR and ESI-MS spectra of complex **3B** are presented in **Figure 3.22**. A broad peak, centered at 3392 cm-1 corresponded to the ν_{O-H} asymmetric stretching of water molecules. A shift in the $\nu_{C=O}$ asymmetric stretching from 1722 cm^{-1} (for H_2PyDPA) to 1625 cm^{-1} in **3B** indicated the formation of the complex. The (+ve) mode ESI-MS spectrum of the aqueous **3B** solution showed a 100% molecular ion peak at *m/z* = 446.09, which corresponded to the composition $[\{(C_{21}H_{20}MnN_4O_5)-(H_2O)\}+H]^+$ for the concerned Mn-complex (**3B**). The exact composition of the complex was determined by CHNS analysis, reciprocating to $C_{21}H_{20}MnN_4O_5\bullet5H_2O$ (Analytically calculated for $C_{21}H_{20}MnN_4O_5\bullet5H_2O$: C, 45.56; H, 5.47; N, 10.13. Found: C, 45.58; H, 5.23; N, 10.15.). Thus, five water of crystallization existed in the unit cell of **3B**.

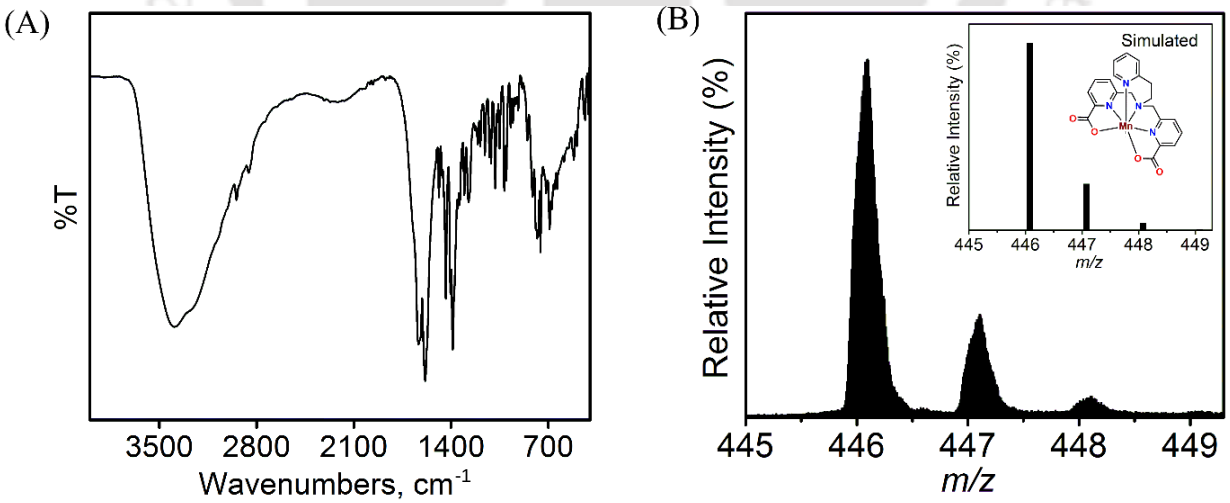

Figure 3.22. (A) FTIR and (B) ESI-MS (+ve) spectra of complex **3B**. The simulated mass spectrum is given as an inset.

X-ray single-crystal diffraction measurement of complex **3B** crystals revealed that the central Mn atom was seven-coordinate with pentagonal bipyramidal geometry (**Figure 3.23B**). The coordination of two picolinate units and the aliphatic N2 atom constructed the basal N_3O_2 plane. Pyridine N3 occupied one of the apical positions, and the other position was empty and eventually occupied by a solvent water molecule. Selected bond distances and bond angles are tabulated in **Table 3.8**. The observed bond distance and bond angles are in agreement with other Mn(II)-complexes with similar coordinating geometry, as reported earlier.[27] The presence of a water molecule in the primary coordination sphere of the Mn(II) ion indicated that the complex could be a potential T_1-weighted contrast agent.

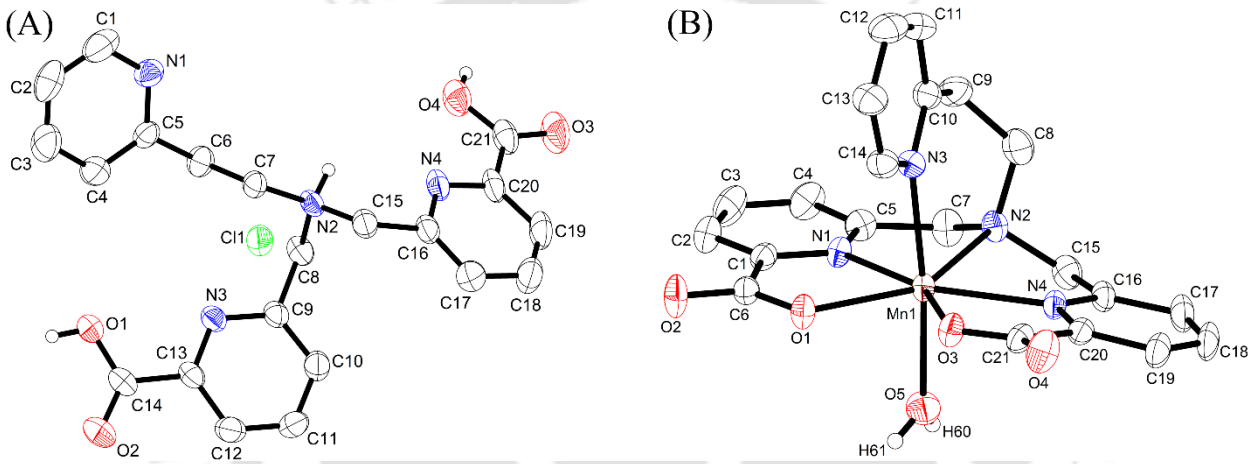

Figure 3.23. ORTEP representations of (A) ligand H_2PyDPA•HCl, and (B) complex **3B**, drawn at 40% probability level. All the hydrogen atoms, except for the ammonium proton in the ligand and solvent protons in the complex were omitted for clarity.

Table 3.7. Selected bond distances (Å) and bond angles (°) for ligand H_2PyDPA•HCl.

O1–C14	1.312(5)	O2–C14–O1	123.8(3)
O2–C14	1.210(4)	O3–C21–O4	122.4(4)
O3–C21	1.217(4)	C7–N2–C8	115.5(2)
O4–C21	1.322(5)	C15–N2–C7	110.9(2)
N2–C7	1.501(4)	C15–N2–C8	112.2(3)
N2–C8	1.509(4)		
N2–C15	1.488(4)		

Table 3.8. Selected bond distances (Å) and bond angles (°) for complex **3B**.

Mn1–O1	2.235(2)	O1–Mn1–O3	81.10(9)
Mn1–O3	2.266(3)	O1–Mn1–N1	71.56(10)
Mn1–O5	2.213(4)	O3–Mn1–N4	70.83(10)
Mn1–N1	2.280(3)	O5–Mn1–N3	174.00(14)
Mn1–N2	2.509(3)	N1–Mn1–N2	69.47(10)
Mn1–N3	2.318(3)	N4–Mn1–N2	68.57(10)
Mn1–N4	2.292(3)		

Table 3.9. Crystallographic and structural refinement parameters for ligand H_2PyDPA•HCl.

Empirical formula	$C_{21}H_{21}ClN_4O_4$
CCDC Number	2096635
Formula weight	428.87
Crystal habit, colour	Needle-shaped/ colourless
Crystal size, mm^3	0.32×0.30×0.28
Temperature, T	293(2)
Wavelength, λ(Å)	0.71073
Crystal system	Triclinic
Space group	'P -1'
Unit cell dimension	a = 7.1977(4) Å, b = 13.2326(9) Å, c = 13.4013(10) Å, α = 99.432(6)°, β= 98.036(5)°, γ = 92.551(5)°
Volume, V ($Å^3$)	1243.80(15)
Z	2
Calculated density, mg•mm^{-3}	1.145
Absorption coefficient, μ (mm^{-1})	0.183
F(000)	448
θ range for data collection	2.3760° to 25.8870°
Limiting indices	$-8\leq h \leq 8$, $-15\leq k\leq 15$, $-11\leq l\leq 15$
Reflection collected / unique	9542/2974 [$R_{(int)}$ = 0.0249]
Completeness to θ	99.7% (θ = 25°)
Max. and min. transmission	1.00000/0.66355
Refinement method	'SHELXL-2013 (Sheldrick, 2013)'
Data / restrains / parameters	4365/0/277
Goodness-of-fit on F^2	1.068
Final R indices [I>2sigma(I)]	R_1 = 0.0687, wR_2 = 0.2139
R indices (all data)	R_1 = 0.0903, wR_2 = 0.2352
Largest diff. peak and hole	0.484/-0.222

Table 3.10. Crystallographic and Structural refinement parameters for complex **3B**.

Empirical formula	$C_{21}H_{20}MnN_4O_5$
CCDC Number	2096636
Formula weight	463.35
Crystal habit, colour	Needle-shaped/ colourless
Crystal size, mm^3	0.35×0.32×0.30
Temperature, T	293(2)
Wavelength, λ(Å)	0.71073
Crystal system	orthorhombic
Space group	'P b c n'
Unit cell dimension	a = 18.4469(8) Å, b = 18.0189(10) Å, c = 15.4102(5) Å, α = 90.00°, β= 90.00°, γ = 90.00°
Volume, V ($Å^3$)	5122.2(4)
Z	8
Calculated density, $mg•mm^{-3}$	1.202
Absorption coefficient, μ (mm^{-1})	0.549
F(000)	1912
θ range for data collection	2.8270° to 24.8610°
Limiting indices	$-14 \le h \le 21$, $-10 \le k \le 21$, $-18 \le l \le 10$
Reflection collected / unique	11927/2990 [$R_{(int)}$ = 0.0476]
Completeness to θ	99.8% (θ = 25°)
Max. and min. transmission	1.00000/0.55685
Refinement method	'SHELXL-2013 (Sheldrick, 2013)'
Data / restrains / parameters	4514/0/288
Goodness-of-fit on F^2	1.070
Final R indices [I>2sigma(I)]	R_1 = 0.0561, wR_2 = 0.1533
R indices (all data)	R_1 = 0.0845, wR_2 = 0.1676
Largest diff. peak and hole	0.410/-0.343

3.11 Thermodynamic Stability of Complex 3B

The protonation constants of the ligand H_2PyDPA and the stability constant of the corresponding complex **3B** were determined by direct pH-potentiometric titrations in the pH range of 2.3-12.0. Experiments were performed at a constant ionic strength using 0.15 M NaCl and 25 °C. For ligand protonation constants, pH-potentiometric titration was done with 0.001 M ligand solution against standardized 0.1 M NaOH solution as titrant. The thermodynamic stability of the complex was obtained by direct pH-potentiometric titration using 1:1 ligand-to-metal (Mn^{II}/Cu^{II}/Zn^{II}) molar ratio.

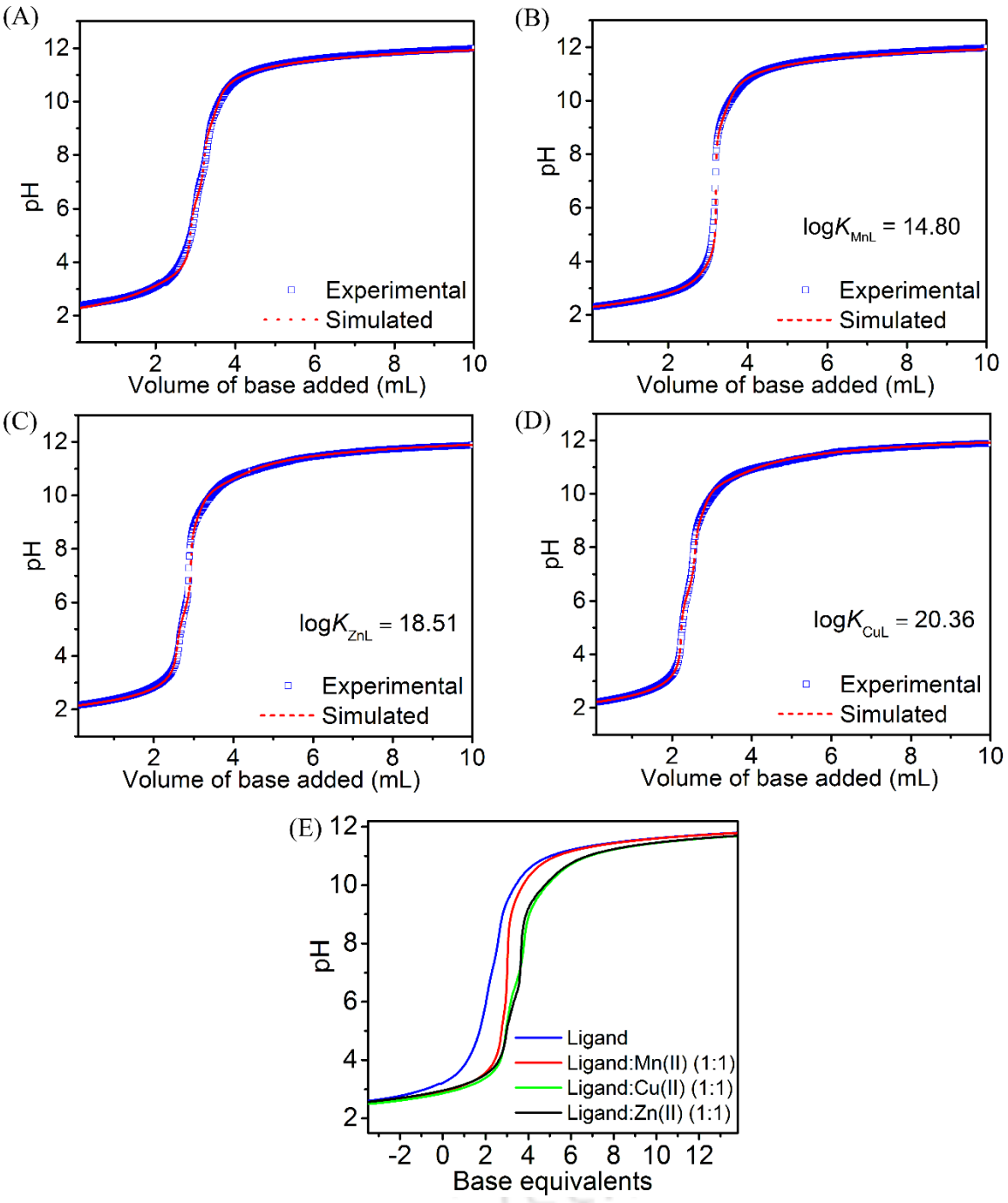

Figure 3.24. Experimental and simulated curves representing pH-potentiometric titration of (A) ligand H_2PyDPA solution, (B) ligand H_2PyDPA:Mn(II) (1:1) solution, (C) ligand H_2PyDPA:Zn(II) (1:1) solution, and (D) ligand H_2PyDPA:Cu(II) (1:1) solution against standard NaOH solution in 0.15 M NaCl and 25 °C. (E) Potentiometric titration curves of the ligand H_2PyDPA solution with 1 equivalent of $MnCl_2 \bullet 4H_2O$ salt (red solid line), $CuCl_2 \bullet 2H_2O$ salt (green solid line), and $ZnCl_2$ salt (black solid line) in H_2O in 0.15 M NaCl, and 25 °C.

Equilibrium constants were calculated from the data obtained by simulating each titration curve using *Hyperquad2008*. For the Mn-complex of the synthesized ligand, the stability constant was found to be $\log K_{MnL}$ = 14.80(7). The value was comparatively higher than the previously reported mono(aquated), seven-coordinate Mn(II) complexes of PyC3A, DPAAA, *trans*-CDTA, and EDTA ligands (**Table 3.11**).[2c,27b,28] The presence of three pyridine moieties in the ligand H_2PyDPA thus imparted high thermodynamic stability in complex **3B** due to Mn(II)(t_{2g})-to-pyridine π*-interactions. Under physiological conditions, the thermodynamic stability of any metal complex is represented by its pM value.[2c] pM value is defined as $-\log[M]_{free}$ considering [M] = [L] = 10^{-5} M at pH ~ 7.4.[29] The complex $[Mn^{II}(PyDPA)(OH_2)]^0$ exhibited a pMn value of 8.97 that further consolidated the high thermodynamic stability. However, this value was indeed lower than the corresponding Cu(II) and Zn(II) complexes, obeying the Irving-Williams series.[30]

Table 3.11 Ligand protonation constants and corresponding stability constants for Mn(II) complexes.

		PyC3A[a]	DPAAA[b]	TPAA[c]	PhDTA[d]	*t*CDTA[d]	EDTA[d]	CBDA[e]	PyDPA[f]
H^+	$\log K_1^H$	10.16	7.26	6.78	6.66	9.36	9.17	8.10	9.21(12)
	$\log K_2^H$	6.39	3.90	4.11	4.85	5.95	5.99	2.97	6.45(7)
	$\log K_3^H$	3.13	3.29	3.3	3.53	3.62	2.73	2.35	3.50(9)
	$\log K_4^H$	—	1.77	2.5	3.32	2.57	2.01	—	—
	$\log K_5^H$	—	—	—	—	1.49	1.38	—	—
	$\sum \log K_i^H$	19.68	16.22	16.69	18.36	22.99	21.28	13.42	19.16
Mn^{2+}	$\log K_{MnL}$	14.14	13.19	—	11.79	14.32	12.46	—	14.80(7)
	$\log K_{MnHL}$	2.43	2.90	—	2.84	2.90	2.95	—	3.82(4)
	$\log K_{MnH2L}$	—	—	—	1.91	1.89	—	—	2.55(9)
	$\log K_{MnL(OH)}$	—	—	—	—	—	—	—	5.41(6)
	$\log K_{MnL(OH)2}$	—	—	—	—	—	—	—	–8.06(2)
	pMn	8.17	8.98	—	8.38	8.68	7.83	—	8.97
Zn^{2+}	$\log K_{ZnL}$	—	—	—	13.03	16.75	15.92	—	18.51(2)
	$\log K_{ZnHL}$	—	—	—	3.556	2.57	3.23	—	9.28(3)
	$\log K_{ZnH2L}$	—	—	—	1.90	—	1.50	—	5.59(10)
Cu^{2+}	$\log K_{CuL}$	—	—	—	15.21	19.78	19.02	—	20.36(3)
	$\log K_{CuHL}$	—	—	—	3.23	2.91	3.15	—	9.25(5)
	$\log K_{CuH2L}$	—	—	—	1.50	1.10	2.04	—	6.32(8)

[a][2c] (I= 0.15 M NaCl, 25 °C). [b][27b] (I= 0.15 M NaCl, 25 °C). [c][18c] (I = 0.1 M KCl, 25 °C). [d][28] (I= 0.15 M NaCl, 25 °C). [e][27a] (I= 0.15 M NaCl, 25 °C). [f]This work (I= 0.15 M NaCl, 25 °C).

Prior to the encapsulation of complex **3B** molecules into the silica nanosphere, the stability of the complex in the presence of NH_4OH was tested by recording the UV-Vis spectrum at pH ~ 9.5 (attained by the addition of ammonia solution). No appreciable change in the UV-Vis spectrum at the experimental conditions refuted the possibility of decomposition of the complex during the encapsulation. (**Figure 3.25**).

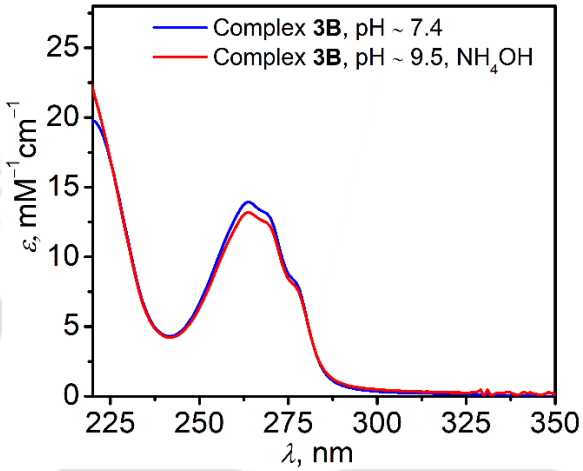

Figure 3.25. UV-Vis spectroscopy of complex **3B** at pH ~ 7.4 and pH ~ 9.5 (attained by addition of NH_4OH).

3.12 Synthesis and Characterization of Complex 3B Confined Porous Silica Nanoparticles, 3B@SiO₂NP

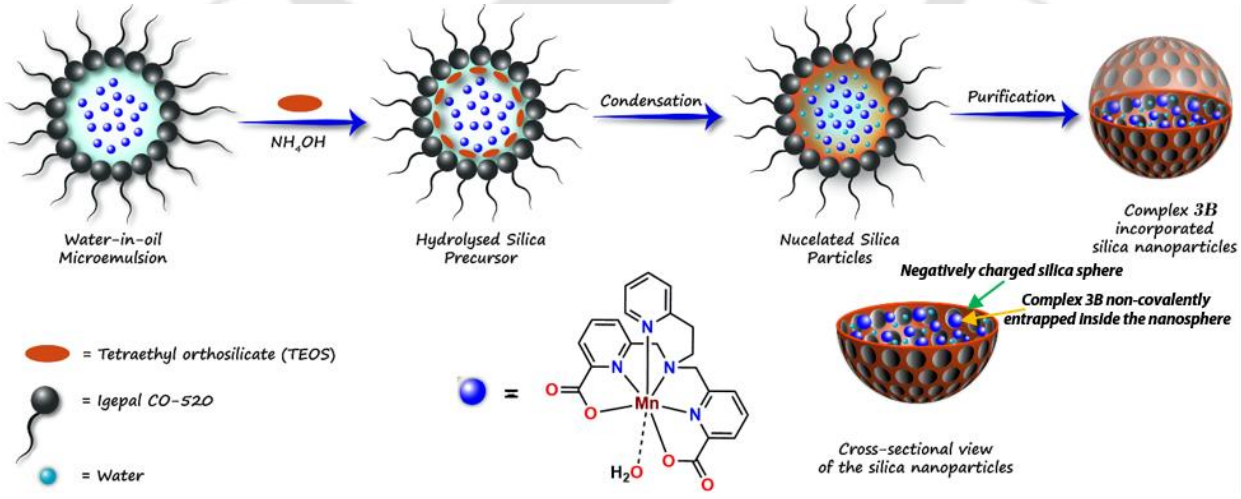

Scheme 3.5. Schematic illustration depicting the synthesis of **3B**@SiO_2NP.

Similar to the synthesis of **3A**@SiO_2NP (**Section 3.3**), a reverse microemulsion method was used to confine molecules of complex **3B** within a porous silica nanosphere (**Scheme 3.5**). Here, an aqueous **3B** solution (160 μL, 13.40 mM) in water (320 μL) at pH ~ 7.4 was used as the doping solution. Finally, complex **3B** entrapped porous silica nanospheres (**3B**@SiO_2NPs) were collected as a residue by centrifugation. It was dispersed in 400 μL water (pH maintained at 7.4), and 500 μL of this mother suspension was lyophilized for 24 h to afford 13 mg of dry silica. Mn(II) concentration of this stock solution was found to be 1.24 mM and each nanoparticle sized 14 nm, n_{cplx} = 80 [determined following equation **(1)**]. The morphology, existence of complex inside the NP, and the porous nature of the isolated nanoparticles were explored by FETEM imaging, elemental mapping, energy dispersive X-ray spectroscopy (EDS), Fourier transform infrared (FTIR), X-band EPR and N_2 adsorption-desorption isotherm analyses, as analyzed subsequently.

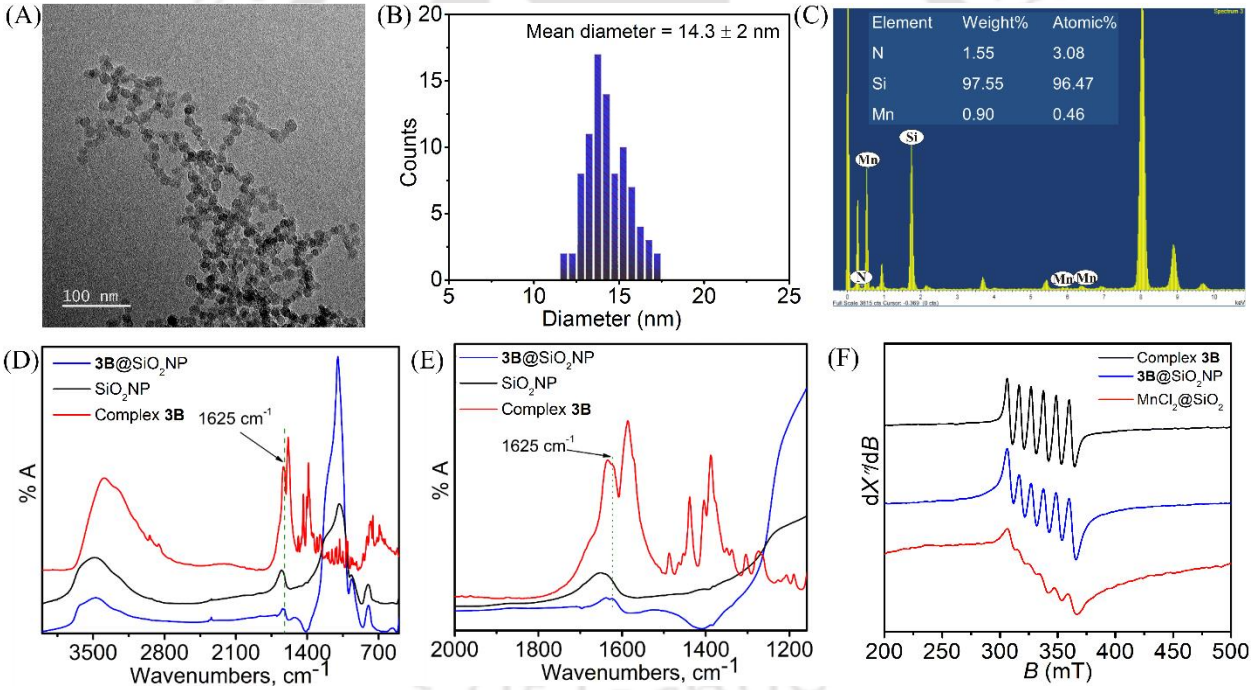

Figure 3.26. Characterization of **3B**@SiO_2NPs. (A) Representative TEM image, (B) Corresponding particle size distribution diagram considering a minimum of 100 particles, and (C) Energy dispersive X-ray (EDS) analysis of **3B**@SiO_2NP showing the existence of Mn, Si, and N elements in the isolated nanoparticles. (D) and (E) FTIR spectrum of complex **3B**, **3B**@SiO_2NP, and pristine SiO_2 NPs. (F) X-band EPR spectra of aqueous solution of complex **3B**, complex **3B**@SiO_2, and $MnCl_2$@SiO_2 measured at room temperature, power = 0.995 mW, modulation frequency = 100 kHz, and modulation amplitude = 10 G.

The formation of monodispersed and spherical nanoparticles of **3B**@SiO_2NP with a uniform size of 14.3 ± 2 nm was recognized by transmission electron microscopy (FETEM) images of dried nanoparticles (**Figure 3.26**). The elemental analysis using the energy-dispersive X-ray spectroscopy (EDS) technique consolidated the co-existence of Mn, Si, and N elements (**Figure 3.26C**) and indicated the presence of complex molecules within the nanosphere. The presence of an infrared band at 1625 cm^{-1} [ν(C=O)] (**Figure 3.26D**) and a six-line X-band EPR spectrum (**Figure 3.26F**), which is typical for Mn(II) ions-based systems, also indicated the incorporation.

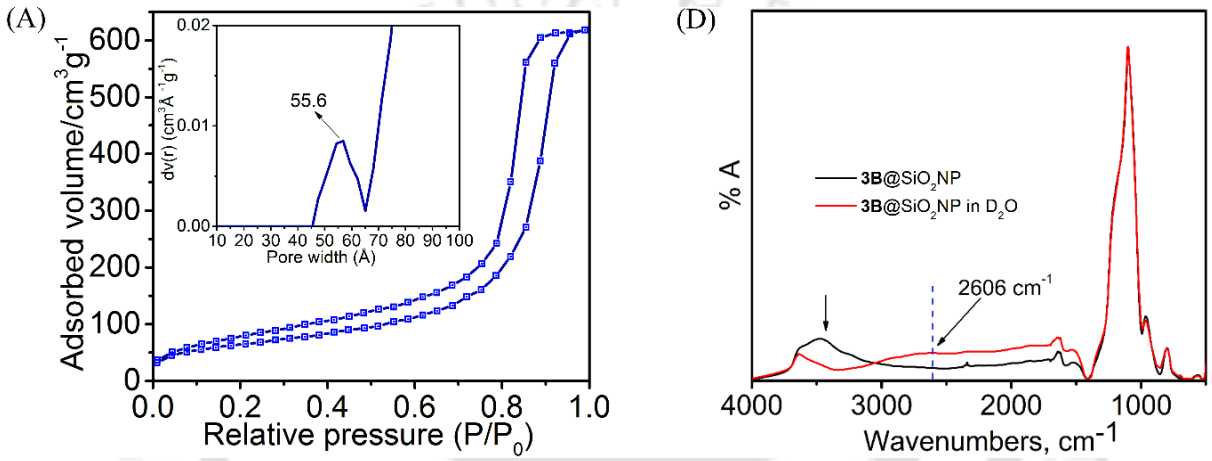

Figure 3.27. (A) Nitrogen adsorption-desorption isotherm and pore size distribution (inset) of **3B**@SiO_2NPs. (B) FTIR spectrum of **3B**@SiO_2NP and **3B**@SiO_2NP_D_2O. Normalized with respect to 1100 cm^{-1} band.

The hollow and porous nature of the silica nanosphere was verified by nitrogen gas (N_2) adsorption-desorption isotherm recorded on lyophilized **3B**@SiO_2. Type-IV isotherm was observed with a hysteresis loop (**Figure 3.27A**) as expected for silica nanospheres with mesopores.[19a] Nanospheres were of 211.03 m^2/g surface area. By the Barrett-Joyner-Helenda (BJH) method, pore diameter was calculated. The pore size distribution plot indicated the presence of two peaks, one at 5.56 nm, which presumably attributed to internal pores of **3B**@SiO_2 and the other at 9.04 nm was anticipated due to inter-particle voids.[31] The presence of such large pores on the silica spheres is envisaged to allow the free movement of small water molecules across the outer layer. Sufficient water molecules reached the core of the nanoparticles and interacted with entrapped complex **3B** molecules. To investigate water exchangeability by **3B**@SiO_2NPs through the pores, the lyophilized nanoparticles were suspended in D_2O for 48 hours and then lyophilized

for 24 hours to isolate dry **3B**@SiO_2NP with feasibly incorporated D_2O (**3B**@SiO_2NP_D_2O). FTIR spectra of **3B**@SiO_2NPs and **3B**@SiO_2NPs_D_2O were being recorded. The decrease in the band intensity in the region 3100-3450 cm^{-1} and the appearance of a broad band, due to ν_{O-D} and ν_{H-O-D} asymmetric stretches, centered around 2606 cm^{-1} indicated the presence of D_2O inside the nanoparticles *via* the exchange of H_2O (**Figure 3.28B**). Hence, the water-exchange capability of the synthesized **3B** incorporated porous silica nanoparticles was consolidated.

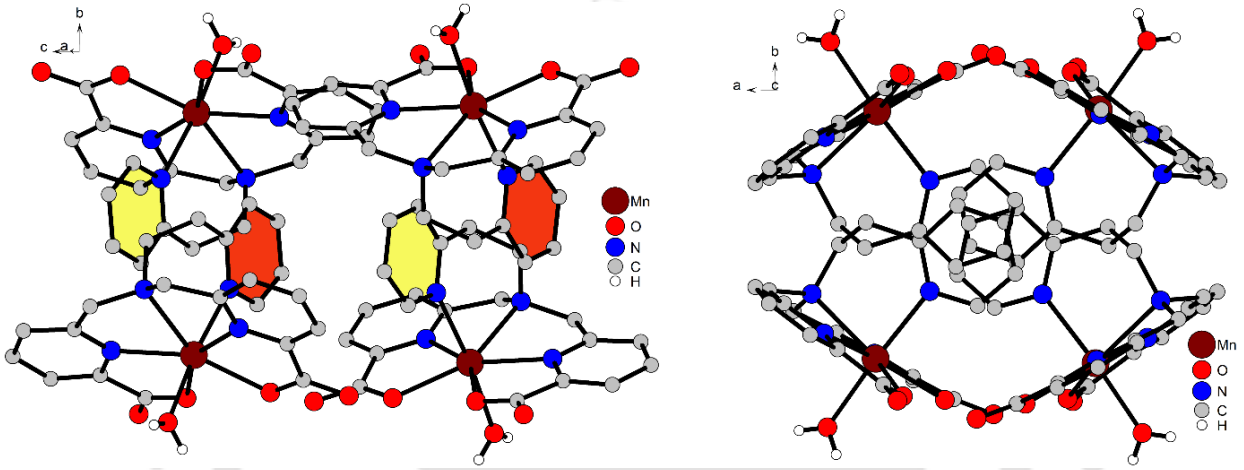

Figure 3.28. Molecular structure of four molecules of complex **3B**, showing stacking π-π interactions amongst pyridine units of different molecules. Red- and yellow-color rings represent two adjacent, interacting pyridine units of two closely located molecules.

Noteworthy, synthesized nanoparticles were thoroughly washed with water and suspended in an aqueous medium. Negligible metal leaching, even after 15 days, discarded any possibility of entrapment of complex molecules (water soluble) outside the nanosphere. X-ray single crystal structure analyses of complex **3B** indicated the presence of π-to-π interactions within the complex molecules through pyridine units, as shown in **Figure 3.28**. Thus, a big cluster of molecules might result within the sphere, which would be less prone to come out from the sphere rendering a stable **3B**@SiO_2 nanosystem.

3.13 Relaxometric Studies of 3B and 3B@SiO$_2$NP in Water and Serum

Concentration-dependent T_1 and T_2 relaxation times of complex **3B** solutions and **3B**@SiO$_2$NP suspensions in HEPES buffer were recorded at 1.41 T, pH ~ 7.4, 25 °C, and 37 °C, using the Inversion Recovery (IR) and Curr-Purcell-Meiboom-Gill (CPMG) methods. A linear increase in $1/T_i$ as a function of increasing Mn(II) ions concentration, determined by ICP-MS analyses of each solution, was noticed. Relaxivity values were obtained from the slope of respective plots, presented in **Figure 3.29**. For complex **3B**, linear fitting of the plots elucidated r_1 = 2.88 mM^{-1}s^{-1} and r_2 = 11.02 mM^{-1}s^{-1}, at 25 °C and r_1 = 2.31 mM^{-1}s^{-1} and r_2 = 9.51 mM^{-1}s^{-1} at 37 °C. The r_1 relaxivity value of complex **3B** was higher than Mn(II)-based commercially available contrast agent Teslascan® (1.6 mM^{-1}s^{-1})[32] and in agreement with other acyclic mono-aquated Mn(II)-based complexes.[2c,27]

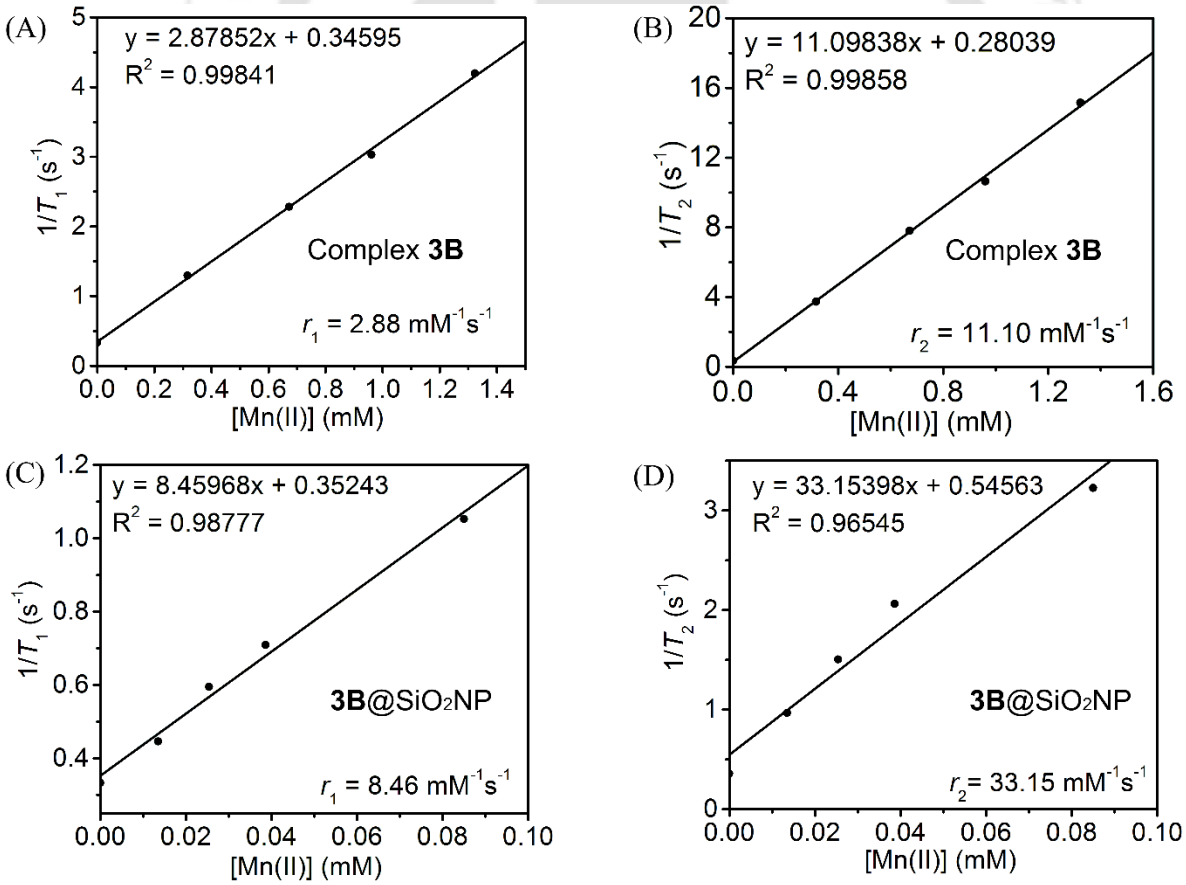

Figure 3.29. (A) ($1/T_1$), and (B) ($1/T_2$) versus [Mn(II)] plot for complex **3B**. Likewise, (C) ($1/T_1$), and (D) ($1/T_2$) versus [Mn(II)] plot for **3B**@SiO$_2$NPs. Measurements were done at pH ~ 7.4, 1.41 T, and 25 °C.

Upon the entrapment of the complex within a nanosphere, *i.e.*, of **3B**@SiO_2NP, the respective r_1 and r_2 values increased to 8.46 $mM^{-1}s^{-1}$ and 33.15 $mM^{-1}s^{-1}$ with r_2/r_1 = 3.92. Notably, the ratio was found to be r_2/r_1 = 5.62 $mM^{-1}s^{-1}$/2.12 $mM^{-1}s^{-1}$ =2.65 using $MnCl_2$ instead of complex during the synthesis of NPs. Interestingly, an approximately 3-fold increase in the respective relaxivity values of **3B** was attained by confining the complex molecules within a porous nanosphere. The relaxivity values of **3B**@SiO_2NPs were greater than those of reported manganese oxide-impregnated silica nanoparticles and were better or almost equal to the silica-surface-attached mono(aquated) Mn(II) complexes as tabulated in **Table 3.2**. Noteworthy, the relaxivity values increased slightly (8.61 $mM^{-1}s^{-1}$ and 34.59 $mM^{-1}s^{-1}$) with the increase in the temperature of the medium to physiological temperature (37 °C). The observation demonstrated stronger interactions between the molecules, and as a result, the effect of temperature on the rotation correlation time was insignificant.[33]

It is worth noting that the r_1 relaxivity value of **3B**@SiO_2 was much greater than that found in clinically approved superparamagnetic iron oxide (SPIO)-based contrast agent Feridex® (4.7 $mM^{-1}s^{-1}$) and very much similar to another SPIO-based contrast agent Resovist® (8.7 $mM^{-1}s^{-1}$).[32] However, the advantage of this present nanovesicles, *i.e.*, complex **3B** entrapped nanosphere system, is the r_2/r_1 = 4.02, which is much higher in the case of Feridex® (r_2/r_1 = 8.72) and Resovist® (r_2/r_1 = 7.01). Thus, unlike the clinically approved superparamagnetic contrast agents, which are mainly T_2 contrast agents, **3B**@SiO_2NPs can be utilized as either a T_1- or T_1-T_2 dual-mode contrast agent.

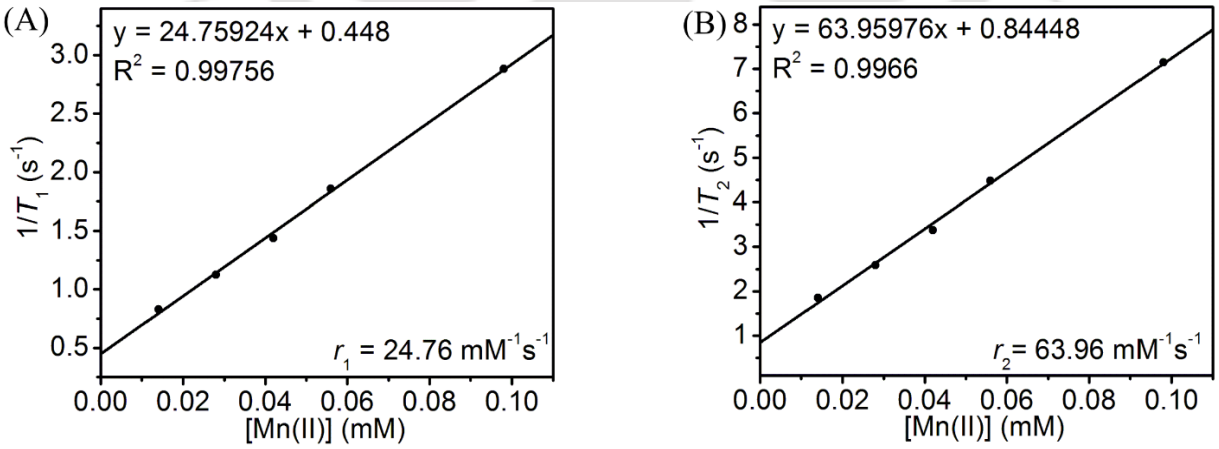

Figure 3.30. (A) ($1/T_1$), and (B) ($1/T_2$) versus [Mn(II)] plot for **3B**@SiO_2NPs in the presence of 4.5% (w/v) BSA; at pH ~ 7.4, 1.41 T and 37 °C.

Possible interactions of **3B**@SiO_2NP with serum albumin were realized by estimating the relaxivity values of nanoparticle suspensions in 4.5 % (w/v) bovine serum albumin (BSA), at pH ~ 7.4, 37 °C, 1.41 T. A significant boost in r_1 (24.76 $mM^{-1}s^{-1}$) and r_2 (63.96 $mM^{-1}s^{-1}$) values inferred significant interactions between the protein and the Mn(II)-complex-encapsulated nanoparticles which reduced the mobility and rendered a higher relaxivity.

Table 3.12. DLS hydrodynamic properties and longitudinal relaxivity values of **3B**@SiO_2NP in the absence and presence of BSA, at pH ~ 7.4.

Material	**Hydrodynamic diameter (nm)**	**ζ (mV)**	**r_1 ($mM^{-1}s^{-1}$) at 37 °C, pH ~ 7.4, 1.41 T**
3B@SiO_2NP	307.4, PdI = 0.27	-18.3	8.61
3B@SiO_2NP + 4.5 % BSA (w/v)	796.1, PdI = 0.49	-27.5	24.76

Hydrodynamic properties of suspended **3B**@SiO_2 nanoparticles were measured at 25 °C by Dynamic Light Scattering (DLS) using Malvern ZETASIZER Nano-ZS90, at pH ~ 7.4 (**Table 3.12**). The zeta (ζ) potential -18.3 mV of **3B**@SiO_2 at pH ~ 7.4 evinced the negatively charged surface of the nanosphere. The albumin protein under the experimental conditions (pH ~ 7.4) remains in its anionic form. Therefore, coulombic interactions between the protein and complex entrapped nanoparticles would not be feasible. It has previously been established that negatively surface-charged protein corona, generated by functionalizing mesoporous silica nanoparticles with hyaluronic acid, interacts with BSA at pH 7.4 *via* van der Waal interaction.[77] Akin to the earlier reports, herein, non-covalent supramolecular interactions and van der Waal interactions between **3B**@SiO_2 and BSA were suggested. Indeed, ζ potential of the synthesized nanoparticles suspended in BSA was -27.5 mV at pH 7.4. Thus, the decrease in the ζ potential in the presence of BSA consolidated the proposed interactions. Furthermore, the measurement of dynamic light scattering (DLS) inferred the increase in the hydrodynamic diameter from 307.4 nm to 796.1 nm supported the association of **3B**@SiO_2NP with BSA.

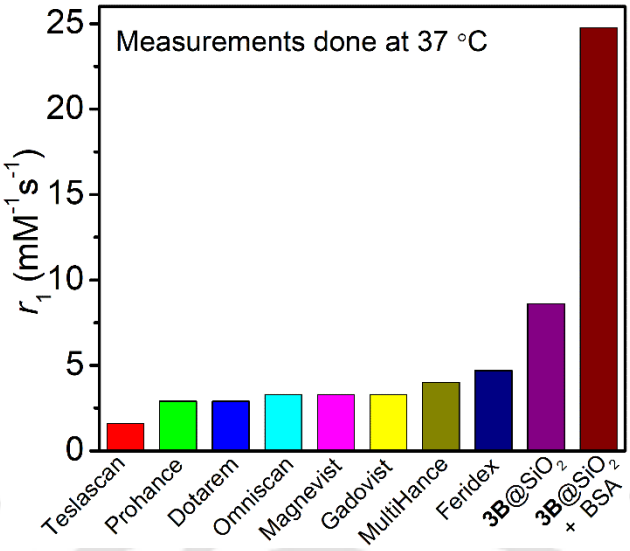

Figure 3.31. Longitudinal relaxivity value for **3B**@SiO_2NP and **3B**@SiO_2NP•BSA compared with the commercially used contrast agents. Measurements were done at 1.4 T.

3.14 Stability of Complex 3B and 3B@SiO$_2$NP at Different pH

To investigate the effect of pH on complex **3B** and **3B**@SiO_2NP, the change in r_1 relaxivity of the entities as a function of pH was determined. A sharp increase in the relaxivity value of complex **3B** was noticed with decreasing the pH of the medium below 4, while, the relaxivity moderately diminished at pH higher than 8 (**Figure 3.32**).

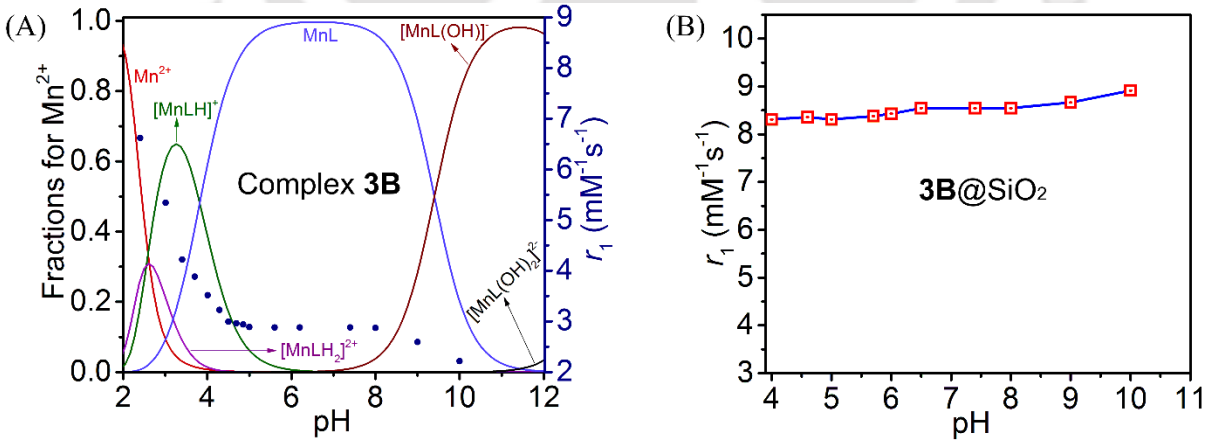

Figure 3.32. (A) Species distribution diagram for Mn/H_2PyDPA: [Mn(II)] = [L] = 1 mM, and pH-dependent relaxometry of the complex **3B**, and (B) r_1 values for **3B**@SiO_2NPs in the pH range from 4.0-10.0 at 1.41 T and 25 °C.

To rationalize the phenomena, the species distribution of the synthesized complex across the pH range of 2-12, determined from the potentiometric titration of **3B**, was examined. The formation of monoprotonated $[Mn^{II}(HPyDPA)(OH_2)_n]^+$ species followed by the decomposition of **3B** finally resulted in free Mn(II) ions in the solution (**Figure 3.32A**). The formed $[Mn(OH_2)_6]^{2+}$ exhibit r_1 = 6.62 $mM^{-1}s^{-1}$. Hence, r_1 increased with decreasing pH of the medium (pH ≤ 3). In $[Mn^{II}(HPyDPA)(OH_2)_n]^+$ species, the *tert*-amine N atom was anticipated to undergo protonation as suggested by the X-ray structure (**Figure 3.23B**) of the isolated ligand and hence, the N atom no longer participated in the metal coordination. The originated vacant site thus facilitated the inner-sphere coordination of another water molecule. Therefore, due to the formation of species with inner-sphere coordination number, q = 2, an elevation in the relaxivity resulted in the pH range 3-4. At pH above 8, the r_1 value slightly diminished due to the appearance of $[Mn^{II}(PyDPA)(OH)]^-$ species by either deprotonation of a proton of the coordinated water molecule or substitution of the water molecule by a hydroxyl anion (HO^-). Contrarily, r_1 = 8.45 $mM^{-1}s^{-1}$ diminished by ~ 2% at pH 4 and elevated by ~ 5% at pH 10 in **3B**@SiO_2NP. Hence, the unfavorable influence of protons on the complex molecules was successfully eliminated by confining **3B** within the porous silica nanosphere.

3.15 Stability of Complex 3B and 3B@SiO_2NP in the Presence of Interfering Ions

To examine the effect of physiologically relevant anions, both complex **3B** and **3B**@SiO_2NPs were treated with the excess amount of biphosphate ($[HPO_4]^{2-}$), bicarbonate ($[HCO_3]^{1-}$), citrate ($[C_6H_5O_7]^{3-}$) and Zn(II). These ions could disintegrate the Mn(II)-complex, thereby replacing the Mn(II)-coordinated inner-sphere water molecule or inducing transmetallation.

In the case of anions, the r_1 relaxivity value will decrease as the longitudinal relaxation time of water protons will be affected by the secondary interactions only. However, the substantial increase in the value refers either to the decomposition of the complex and release of Mn(II) ions (r_1 = 6.62 $mM^{-1}s^{-1}$) or aggregation of complex molecules by the quaternary interactions with the anions. This aggregation renders a slowly rotating molecular system and consequently increases the relaxivity. When treated with zinc ions, the dechelation of the complex may occur releasing free Mn^{2+}. This could result in a steep increase in the relaxivity value of the solution.

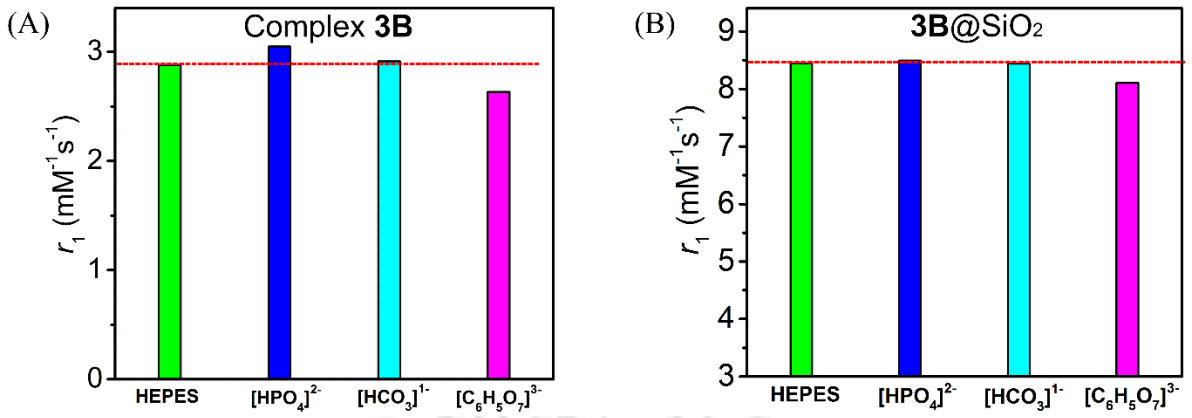

Figure 3.33. Longitudinal relaxivity (r_1) of (A) complex **3B** and (B) **3B**@SiO_2, recorded after incubating samples with 200 equivalents of different physiological anions for 12 h, at pH ~ 7.4, 1.41 T, and 25 °C. During experiments, Mn(II) concentrations were maintained at 0.67 mM and 0.10 mM for **3B** and **3B**@SiO_2NPs, respectively.

Challenging complex **3B** solution by the physiological anions, only a slight change in the r_1 value: Δr_1 = 0.17; ~ 6% increase for biphosphate and Δr_1 = 0.24; ~ 8% decrease for citrate, as illustrated in the above figure. This feature indicated no pronounced interactions between the complex coordination sphere and the anions. Moreover, on confining the complex molecules inside the nanoparticles, the relaxivity value remained almost unaltered (Δr_1 = 0.33; ~ 4% decrease only for citrate) in the presence of the anions. Thus, the synthesized nanospheres were impervious to the anions.

Additionally, to evaluate the kinetic inertness of **3B** and **3B**@SiO_2NP, the samples containing the paramagnetic compound were challenged with $ZnCl_2$ at pH 6.0 and 25 °C. The change in the relaxivity ratio was then monitored as a function of time.

Complex **3B** was found to be kinetically labile and simultaneously attacked by the scavenger zinc ions. A rapid increase in r_2 value upon the addition of 30-fold excess of Zn(II) ions indicated a fast transmetallation of the complex (**Figure 3.34A**). High thermodynamic stability of the Zn(II)-complex, as reported in **Section 3.11**, is reflected in this result.

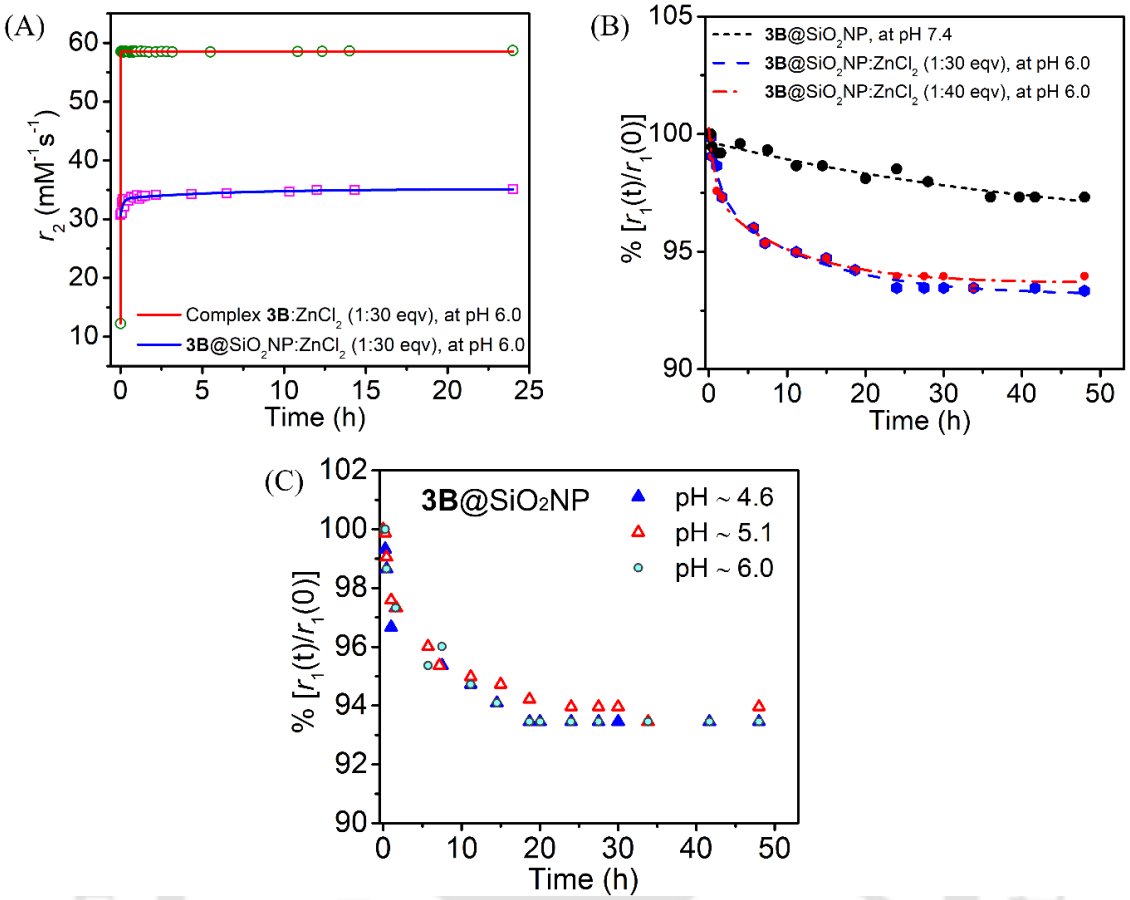

Figure 3.34. (A) Changes in r_2 for complex **3B** and **3B**@SiO$_2$NPs with time, when challenged with 30 equivalent excess of Zn(II) ions at pH ~ 6.0 (MES buffer). Percentage changes in r_1(t)/r_1(0) for **3B**@SiO$_2$NPs with time, (B) when challenged with 30 and 40 equivalent excess of Zn(II) ions at pH ~ 6.0 (MES buffer). (C) when challenged with 40 equivalent excess of Zn(II) ions at pH ~ 4.6, 5.1, and 6.0. The samples containing **3B** solution, [Mn(II)] = 1 mM or **3B**@SiO$_2$NPs suspensions, [Mn(II)] = 0.056 mM were incubated with zinc ions, and measurements done at 1.41 T and 25 °C.

When **3B**@SiO$_2$NPs were incubated with zinc ions, initially a sharp change (~ 3% in 1.5 h) was noticed, irrespective of the concentration of Zn(II) ions, and the rate of the change was almost equal in both cases (**Figure 3.34B**). This result discarded the possibility of substitution of Mn(II) ions from the complex molecules by Zn(II) ions as no Zn(II) ions-dependent decrease in the relaxivity was realized. Gratifyingly, the change in the relaxivity ratio was limited to only ~ 6% in 24 hours and remained unaltered for up to 48 hours. The slight change could be because of the lowering of water accessibility inside the nanoparticles due to the coagulation (*vide infra*).

To elucidate, the effect of Zn(II) ions on the NPs, TEM images of the isolated NPs were recorded after 48 hours of exposure to 40 equivalent amounts of Zn(II) ions at pH 6.0. No disintegration in the nanosphere was noticed (**Figure 3.35A** and **3.35B**). The diameter of the isolated particles remained almost unaltered to be 14.6 ± 3.0 nm. Thus, no adverse effect was exerted by Zn(II) ions on the morphology of **3B**@SiO_2NPs.

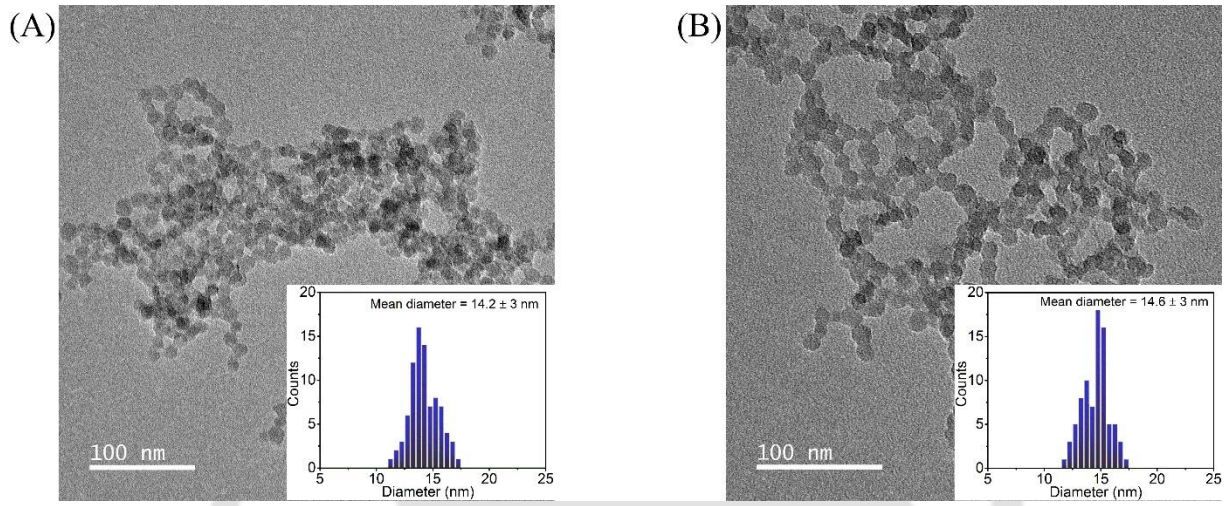

Figure 3.35. Representative TEM images of dried **3B**@SiO_2NPs obtained after 48 hours of suspension at pH 6.0 (A) without and (B) with 40 equivalent Zn^{2+} ions along with corresponding size distribution plots in the inset.

Table 3.13. Hydrodynamic diameters and zeta potentials of suspensions of **3B**@SiO_2NPs when challenged with increasing equivalence excess of Zn^{2+} ions at pH ~ 6.0.

Equivalents of Zn(II)	Zeta Potential (mV)	Hydrodynamic diameter (nm)	PdI
0.0	-18.1	319.7	0.456
10.0	-15.2	543.1	0.400
20.0	-13.3	716.4	0.364
30.0	-11.1	817.7	0.358
40.0	-9.07	833.2	0.350

To examine the possible adsorption of Zn(II) ions on the surface of the nanoparticles, the zeta potential (ζ) and hydrodynamic diameter (d_h) of the pristine **3B**@SiO_2NPs and the Zn(II) added systems were recorded at pH 6.0. The linear decrease of ζ upon progressive addition of Zn(II) ions; -18.1 mV [0.0], -15.2 mV [10], -13.3 mV [20], -11.1 mV [30], and -9.07 mV [40] {parenthesis refers the equivalence of added Zn(II) ions} inferred the adsorption (**Table 3.13**). Furthermore, a square increase in the hydrodynamic diameter with the increasing concentration of Zn(II) ions suggested the coagulation of the nanoparticles facilitated by the decrease in the ζ potential of the resulting nanoparticles. Nonetheless, Zn(II) ions-based competition results demonstrated that **3B**@SiO_2NP was kinetically inert and competent for *in vivo* application.

3.16 Phantom MR Imaging of Complex 3B Solution and 3B@SiO_2NP Suspensions, at 1.5 T

To investigate the contrast ability of complex **3B** and **3B**@SiO_2NP, phantom MR images were recorded using MAGNETOM Avanto 1.5 T clinical MRI scanner on different concentrations of the paramagnetic species in HEPES buffer at pH ~ 7.4, 25 °C. For T_1-weighted images, the following parameters were adopted: TR (repetition time) = 758 ms, TE (echo time) = 10 ms, slice thickness = 2.5 mm and field of view (FOV) = 260×260 mm^2. For T_2-weighted images, TR (repetition time) = 2690 ms, TE (echo time) = 78 ms, slice thickness = 3.0 mm and field of view (FOV) = 320×320 mm^2.

Herein, phantoms are micro-centrifuge tubes filled with solutions or suspensions. The gradual increase in the concentration of complex **3B** resulted in simultaneous brighter T_1-weighted images and darker T_2-weighted images (**Figure 3.36**). The same effects were also noticed for **3B**@SiO_2NP in both imaging modalities (**Figure 3.36**). Moreover, the contrast enhancement, compared to water/silica NPs, in **3B**@SiO_2NP was significantly higher than that in complex **3B**. This result consolidated the formation of a better contrast agent upon the confinement of complex **3B** in silica nanoparticles.

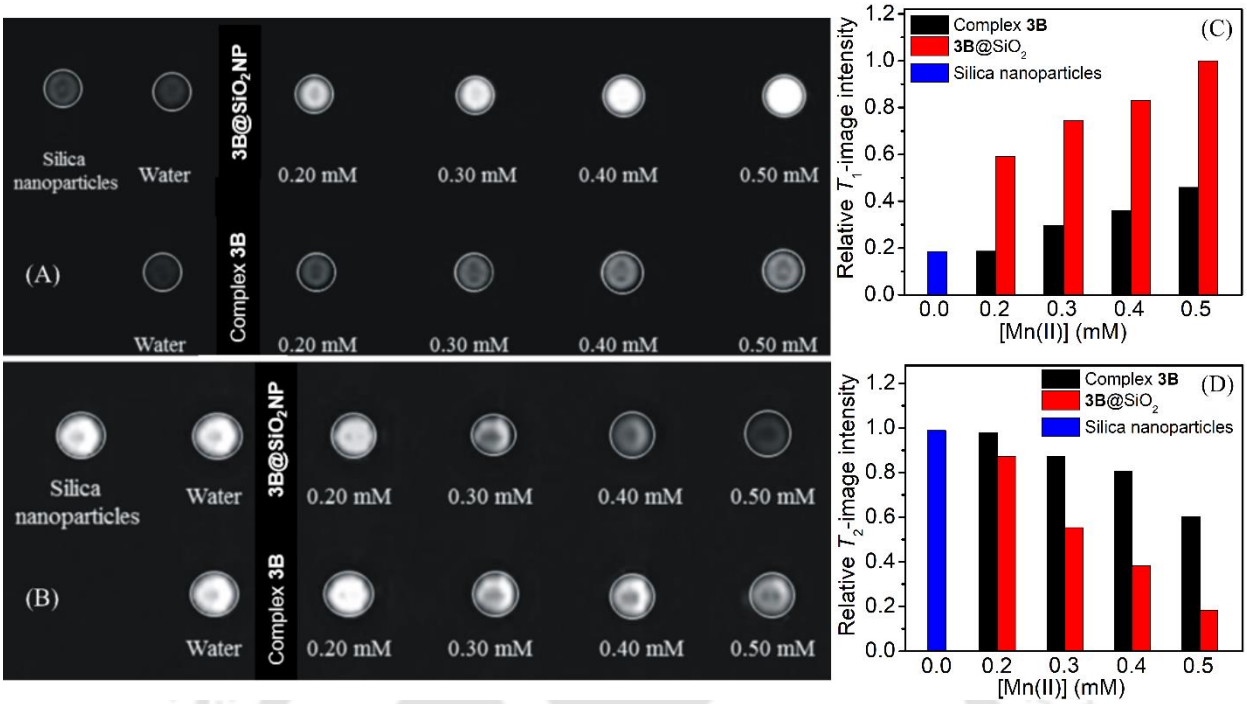

Figure 3.36. (A) T_1-weighted, and (B) T_2-weighted phantom MR images of micro-centrifuge tubes containing different concentrations of complex **3B** and **3B**@SiO_2NP (concentration in terms of Mn(II) ion) at 1.5 T, and 25 °C. (C) and (D) Relative MR-image intensity plots using *ImageJ* software.

3.17 Cytotoxicity Assay and Cell-Uptake of 3B@SiO₂NP

MTT[3-(4,5-dimethyl-thiazol-2-yl)-2,5 diphenyltetrazolium bromide] assays on HeLa (human cervical carcinoma) cell line were performed to determine the cytotoxicity of **3B**@SiO_2NP. In the processes, cells were incubated at 37 °C with different suspensions containing variable amounts of nanoparticles (0 to 100 µM concentrations in Mn(II) ion). After 48 h, 0.5 mg/ml of MTT in DMEM was added to each well and incubated for 1.5 h. Thereafter, 150 µl DMSO was added to each well. Absorbance was measured at 570 nm, and after that, cell viability was calculated, considering 100% viability for untreated cells. **Figure 3.37** illustrates the percentage of cell viability with the increased dosage of **3B**@SiO_2NP relative to untreated cells. While no damage in cells was noticed up to 20 µM in 48 h, a subtle change in the viability was noticed at the elevated concentrations. At 100 µM dosage of **3B**@SiO_2NP, 82% of HeLa cells were viable.

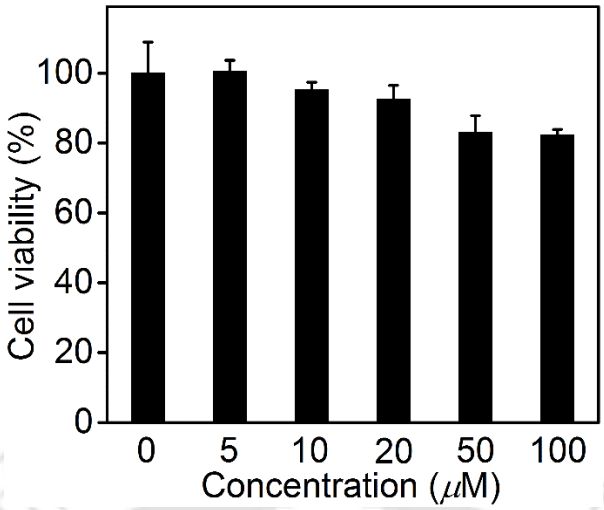

Figure 3.37. % Cell viability for **3B**@SiO_2NP performed on HeLa cell line. Concentration mentioned with respect to Mn(II) ions.

This result interprets that synthesized nanoparticles were biocompatible and could suitably be employed for biological investigation.

Furthermore, the internalization of **3B**@SiO_2NP inside the HeLa cell was visualized by performing respective TEM investigations of the cell line after treatment with the nanoparticles (**Figure 3.38**). Elaborately, cells were seeded in a 30 mm^2 petri plate and thereby treated with 25 μM of the nanoparticles and incubated for 48 h at 37 °C in humidified air containing 5 % CO_2. Subsequently, FETEM images of the cells were analyzed in **Figure 3.38**.

Representative TEM images of the cell confirmed the existence of **3B**@SiO_2NPs (size = 11.7 ± 3 nm) inside the cell. Due to the presence of electron-rich manganese, nanoparticles appeared to be darker than the surroundings inside the cell. Any nanocomposite was not observed outside the cell and it was obvious as cells were washed with PBS to remove any unbound **3B**@SiO_2NP. EDS analysis illustrated the existence of manganese, nitrogen and silicon elements inside the cell (**Figure 3.38B**), further corroborating the presence of **3B**@SiO_2NPs.

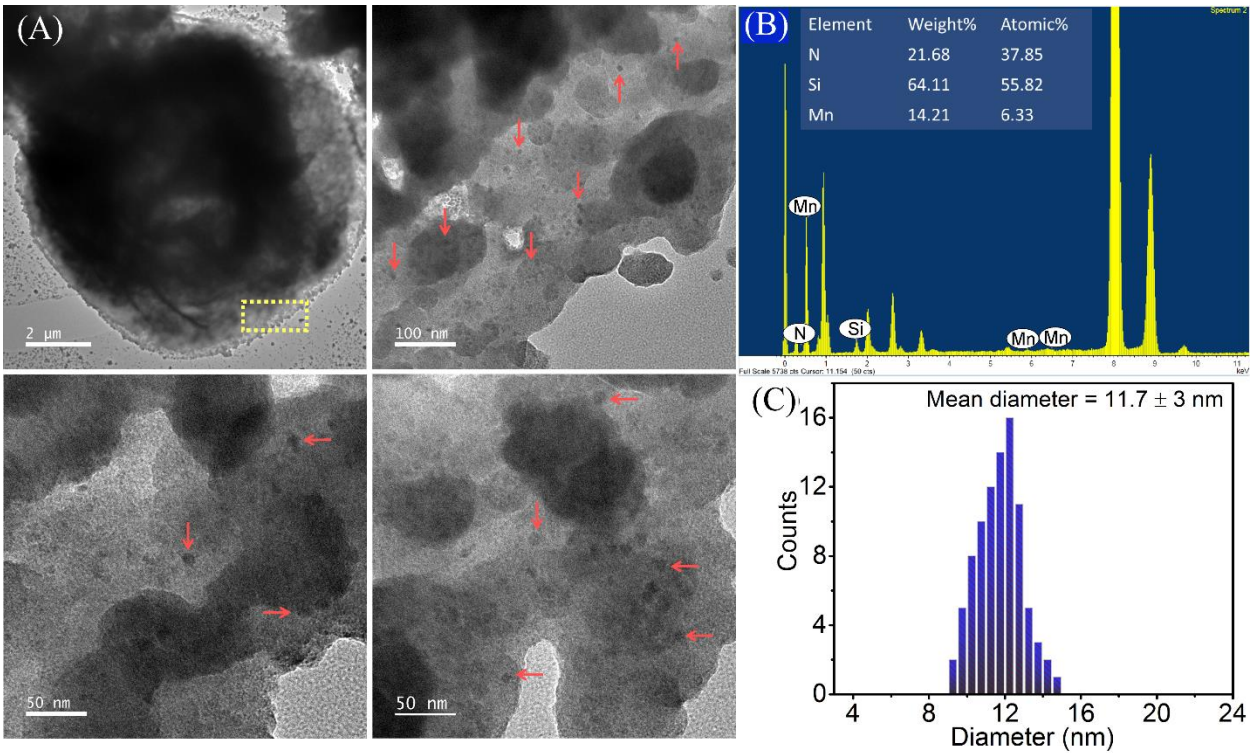

Figure 3.38. (A) TEM images of HeLa cells after internalization of **3B**@SiO_2NPs. Yellow rectangle showing the presence of the NPs inside a cell and magnified to visualize internalization of the nanoparticles. Red arrows indicated the position of **3B**@SiO_2NP inside the cells. (B) TEM-Energy-dispersive X-ray spectroscopy (EDS) analysis illustrating the existence of manganese, nitrogen and silicon elements inside the HeLa cell, and (C) corresponding particle-size distribution plot.

3.18 Conclusion

- In this chapter, we have demonstrated the successful non-covalent encapsulation of aquated and thermodynamically stable Gd(III)- or Mn(II)-complex (**3A** and **3B**) inside porous silica nanospheres by employing the reverse microemulsion technique.

- Depending on the charge of the synthesized paramagnetic unit, molecules were incorporated either close to the inner surface (through electrostatic interactions) or uniformly distributed inside the negatively charged silica nanosphere, affecting the overall water exchangeability.

- Upon entrapment of the complex molecules inside the porous silica nanoparticles, the tumbling rate of the paramagnetic chelate is effectively reduced. This was reflected in the simultaneous increase in the relaxivity value of **3A**@SiO_2NP and **3B**@SiO_2NP.

- For **3A**@SiO_2NP, longitudinal relaxivity was increased by 9.5-fold on confining the tris-aquated Gd(III)-complex (**3A)**, reaching r_1 = 86.41 $mM^{-1}s^{-1}$ at pH 7.4, 37 °C, 1.41 T. A 3-fold elevation in relaxivity was obtained by incorporating mono-aquated Mn(II)-complex (**3B**) exhibiting r_1 = 8.46 $mM^{-1}s^{-1}$ and r_2 = 33.15 $mM^{-1}s^{-1}$ at pH 7.4, 37 °C, 1.41 T. The association of the nanoparticles with serum albumin protein further escalated the relaxivity values.

- The confinement achieved a commendable increase in the kinetic inertness towards the external anions, protons, and Zn(II) metal ions. Thus, the present study paves the way for developing stable Gd(III)- and Mn(II)-complex-based nanocontrast agents, despite employing a kinetically labile complex for incorporation.

- The biocompatibility, HeLa cell internalization study, and the significant contrast ability of the nanoparticles thus conferred them as genuine alternative contrast agents with negligible leaching of toxic-free metal, thereby minimizing the concerning adverse health issues.

3.19 References

1. (a) I. Solomon and N. Bloembergen, *J. Chem. Phys*., 1956, **25**, 261; (b) J. Kowalewski, L. Nordenskiöld, N. Benetis and P.-Olof Westlund, *Prog Nucl Magn Reson Spectrosc*., 1985, **17**, 141-185. (c) J. S. Ananta, B. Godin, R. Sethi, L. Moriggi, X. Liu, R. E. Serda, R. Krishnamurthy, R. Muthupillai, R. D. Bolskar, L. Helm, M. Ferrari, L. J. Wilson, P. Decuzzi, *Nat. Nanotechnol.*, 2010, **5**, 815−821; (d) K. Ni, Z. Zhao, Z. Zhang, Z. Zhou, L. Yang, L. Wang, H. Ai and J. Gao, *Nanoscale*, 2016, **8**, 3768–3774; (e) Also see General Introduction section of this thesis.

2. (a) P. Hermann, J. Kotek, V. Kubíček and I. Lukeš, *Dalton Trans.*, 2008, 3027–3047; (b) B. Drahoš, I. Lukeš, and É. Tóth, *Eur. J. Inorg. Chem.*, 2012, 1975–1986; (c) E. M. Gale, I. P. Atanasova, F. Blasi, I. Ay and P. Caravan, *J. Am. Chem. Soc.*, 2015, **137**, 15548−15557; (d) D. Lalli, I. Hawala, M. Ricci, F. Carniato, L. D. D'Andrea, L. Tei and M. Botta, *Inorg. Chem.*, 2022, **61**, 13199-13209.

3. (a) L. Wang, H. Lin, L. Ma, J. Jin, T. Shen, R. Wei, X. Wang, H. Ai, Z. Chen and J. Gao, *Nanoscale*, 2017, **9**, 4516-4523; (b) K. M. L. Taylor, J. S. Kim, W. J. Rieter, H. An, W. Lin and W. Lin, *J. Am. Chem. Soc.*, 2008, **130**, 2154-2155.

4. (a) J. L. Vivero-Escoto, R. C. Huxford-Phillips and W. Lin, *Chem. Soc. Rev*., 2012, **41**, 2673–2685; (b) F. Carniato, L. Tei and M. Botta, *Eur. J. Inorg. Chem.*, 2018, 4936–4954; (c) L. García-Hevia, M. Bañobre-López and J. Gallo, *Chem. Eur. J*., 2019, **25**, 431 – 441; (d) G. Jamalipour Soufi, A. Hekmatnia, S. Iravani and R. S. Varma, *ACS Appl. Nano Mater.*, 2022, **5**, 10151−10166.

5. (a) L. Moriggi, C. Cannizzo, E. Dumas, C. R. Mayer, A. Ulyanov and L. Helm, *J. Am. Chem. Soc.*, 2009, **131**, 10828-10829. (b) R. Zairov, G. Khakimullina, S. Podyachev, I. Nizameev, G. Safiullin, R. Amirov. A. Vomiero and A. Mustafina, *Sci. Rep*., 2017, **7**, 14010.

6. C. Richard, B.T. Doan, J. C. Beloeil, M. Bessodes, É. Tóth and D. Scherman, *Nano Lett.* 2008, **8**, 232-236.

7. (a) D. Niu, X. Luo, Y. Li, X. Liu, X. Wang and J. Shi, *ACS Appl. Mater. Interfaces*, 2013, **5**, 9942-9948; (b) W. Hou, T. B. Toh, L. N. Abdullah, T. W. Z. Yvonne, K. J. Lee, I. Guenther and E. K. H. Chow, *Nanomed. Nanotechnol.*, 2017, **13**, 783-793; (c) M. Pálmai, A. Pethő, L. N. Nagy, S. Klébert, Z. May, J. Mihály, A. Wacha, K. Jemnitz, Z. Veres, I. Horváth, K. Szigeti, D. Máthé and Z. Varga, *J. Colloid Interf. Sci.*, 2017, **498**, 298-305; (d) V. Dahanayake, C. Pornrungroj, M. Pablico-Lansigan, W. J. Hickling, T. Lyons, D. Lah, Y. Lee, E. Parasido, J. A. Bertke, C. Albanese, O. Rodriguez, E. V. Keuren and S. L. Stoll, *ACS Appl. Mater. Interfaces*, 2019, **11**, 18153-18164; (e) G. Mulas, G. A. Rolla, C. F. G. C. Geraldes, L. W. E. Starmans, M. Botta, E. Terreno and L. Tei, *ACS Appl. Bio Mater.*, 2020, **3**, 2401-2409.

8. (a) Y. Liu, M. Solomon and S. Achilefu, *Med. Res. Rev*., 2013, **33**, 3−32; (b) H. Yan, Y. You, X. Li, L. Liu, F. Guo, Q. Zhang, D. Liu, Y. Tong, S. Ding and J. Wang, *Front. Pharmacol*., 2020, **11**, 898.

9. R. G. Nicolas, J. -L. Bridot, Y. Seo, M.-A. Fortin, and F. Kleitz, *Adv. Funct. Mater.* 2011, **21**, 4653–4662.

10. M. M. Karimdjy, G. Tallec, P. H. Fries, D. Imbert and M. Mazzanti, *Chem. Commun*., 2015, **51**, 6836-6838.

11. (a) R. Guillet-Nicolas, N. Jean, L. Bridot, Y. Seo, M.-A. Fortin and F. Kleitz, *Adv. Funct. Mater.*, 2011, **21**, 4653–4662; (b) R. Guillet-Nicolas, M. Laprise-Pelletier, M. M. Nair, P. Chevallier, J. Lagueux, Y. Gossuin, S. Laurent, F. Kleitz and M.-A. Fortin, *Nanoscale*, 2013, **5**, 11499–11511.

12. (a) S. V. Fedorenko, S. L. Grechkina, A. R. Mustafina, K. V. Kholin, A. S. Stepanov, I. R. Nizameev, I. E. Ismaev, M. K. Kadirov, R. R. Zairov, A. N. Fattakhova, R. R. Amirov and S. E. Soloveva, *Colloids Surf. B: Biointerfaces* 2017, **149**, 243-249; (b) T. Courant, V. G. Roullin, C. Cadiou, M. Callewaert, M. C. Andry, C. Portefaix, C. Hoeffel, M. C. de Goltstein, M. Port, S. Laurent, L.V. Elst, R. Muller, M. Molinari and F. Chuburu, *Angew. Chem. Int. Ed*. 2012, **51**, 9119-9122; (c) S. L. C. Pinho, J. Sereno, A. J. Abrunhosa, M. H. Delville, J. Rocha, L. D. Carlos and C. F. G. C. Geraldes, *Inorg. Chem.* 2019, **58**,

16618−16628; (d) W. I. Lin, C. Y. Lin, Y. S. Lin, S. H. Wu, Y. R. Huang, Y. Hung, C. Chang and C. Y. Mou, *J. Mater. Chem. B*, 2013, **1**, 639–645; (e) Z. Li, J. Guo, M. Zhang, G. Li and L. Hao, *Front. Chem*. 2022, **10**, 837032.

13. (a) D. Lalli, G., Ferrauto, E., Terreno, F., Carniato, and M. Botta, *J. Mater. Chem. B*, 2021, **9**, 8994-9004; (b) B. Y. W. Hsu, M. Wang, Y. Zhang, V. Vijayaragavan, S. Y. Wong, Alex Y. Chang, K. K. Bhakoo, X. Li, and J. Wang, *Nanoscale*, 2014, **6**, 293; (c) M. Bañobre-López, L. García-Hevia, M. F. Cerqueira, F. Rivadulla, and J. Gallo, *Chem. Eur. J.* 2018, **24**,1295 –1303; (d) K. Li, P. Li, Y. Wang, and S. Han, *Front. Oncol*. 2020, **10**, 601538.

14. (a) P. Mathieu, M. Chalet, M. Myriam Clain, L. Teulon, E. Benoist, N. Leygue, C. Picard, S.Boutry, S. Laurent, D. Stanicki, C. Hénoumont, F. Novio, J. Lorenzo, D. Montpeyó, D. Ciuculescu-Pradines and C. Amiens, *New J. Chem.*, 2020, **44**, 18031-18047; (b) J. Wang, H. Wang, I. A. Ramsay, D. J. Erstad, B. C. Fuchs, K. K. Tanabe, P. Caravan and E. M. Gale, *J. Med. Chem.*, 2018, **61**, 8811-8824.

15. R. R. Castillo and M. Vallet-Regí, *Int. J. Mol. Sci.*, 2019, **20**, 929.

16. K. B. Hartman, S. Laus, R. D. Bolskar, R. Muthupillai, L. Helm, E. Toth, A. E. Merbach and L. J. Wilson, Nano Lett. 2008, **8**, 415-419.

17. S. V. Eliseeva, B. Song, C. D. B. Vandevyver, A. -S. Chauvin, J. B. Wacker and J. -C. G. Bünzli, *New J. Chem.*, 2010, **34**, 2915-2921.

18. (a) P. Caravan, J. J. Ellison, T. J. McMurry and R. B. Lauffer, *Chem. Rev.*, 1999, **99**, 2293-2352; (b) A. Nonat, P. Fries, J. Pécaut and M. Mazzanti, *Chem. Eur. J.*, 2007, **13**, 8489-8506; (c) Y. Bretonnière, M. Mazzanti, J. Pécaut, F. A. Dunand and A. E. Merbach, *Inorg. Chem*., 2001, **40**, 6737-6745.

19. (a) N. T. Vo, A. K. Patra and D. Kim, *Phys. Chem. Chem. Phys.*, 2017, **19**, 1937-1944; (b) B. E. Givens, Z. Xu, J. Fiegel and V. H. Grassian, *J. Colloid Interface Sci*. 2017, **493**, 334–341.

20. S. Laus, A. Sour, R. Ruloff, É. Tóth and A. E. Merbach, *Chem.- Eur. J.*, 2005, **11**, 3064.

21. (a) M. J. Frisch, G. W. Trucks, H. B. Schlegel, G. E. Scuseria, M. A. Robb, J. R. Cheeseman, G. Scalmani, V. Barone, B. Mennucci, G. A. Petersson, H. Nakatsuji, M. Caricato, X. Li, H. P. Hratchian, A. F. Izmaylov, J. Bloino, G. Zheng, J. L. Sonnenberg, M. Hada, M. Ehara, K. Toyota, R. Fukuda, J. Hasegawa, M. Ishida, T. Nakajima, Y. Honda, O. Kitao, H. Nakai, T. Vreven, J. A., Jr. Montgomery, J. E. Peralta, F. Ogliaro, M. Bearpark, J. J. Heyd, E. Brothers, K. N. Kudin, V. N. Staroverov, R. Kobayashi, J. Normand, K. Raghavachari, A. Rendell, J. C. Burant, S. S. Iyengar, J. Tomasi, M. Cossi, N. Rega, J. M. Millam, M. Klene, J. E. Knox, J. B. Cross, V. Bakken, C. Adamo, J. Jaramillo, R. Gomperts, R. E. Stratmann, O. Yazyev, A. J. Austin, R. Cammi, C. Pomelli, J. W. Ochterski, R. L. Martin, K. Morokuma, V. G. Zakrzewski, G. A. Voth, P. Salvador, J. J. Dannenberg, S. Dapprich, A. D. Daniels, O. Farkas, J. B. Foresman, J. V. Ortiz, J. Cioslowski and D. J. Fox, Gaussian 09, Revision D.01; Gaussian, Inc.: Wallingford, CT, 2015; (b) A. D. Becke, Density-functional thermochemistry. V. *J. Chem. Phys.* 1997, **107**, 8554-8560; (c) S. Grimme, S. Ehrlich and L. Goerick, *J. Comput. Chem.* 2011, **32**, 1456-1465.

22. (a) E. M. Gale, N. Kenton and P. Caravan, *Chem. Commun*., 2013, **49**, 8060-8062; (b) O. Porcar-Tost, J. A. Olivares, A. Pallier, D. Esteban-Gómez, O. Illa, C. Platas-Iglesias, É. Tóth, and R. M. Ortuño, *Inorg. Chem.*, 2019, **58**, 13170-13183.

23. (a) M. Port, J.M. Idée, C. Medina, C. Robic, M. Sabatou and C. Corot, *Biometals*., 2008, **21**, 469-490; (b) S. Laurent, L. Elst. Vander, C. Henoumont and R. N. Muller, *Contrast Media Mol. Imaging*, 2010, **5**, 305-308.

24. A. Bianchi, L. Calabi, F. Corana, S. Fontana, P. A. Losi, Maiocchi, L. Paleari and B. Valtancoli, *Coord. Chem. Rev.*, 2000, **204**, 309-393.

25. (a) E. Ruoslahti, *Adv. Drug Deliv. Rev*., 2017, **110**, 3-12; (b) N. Rammohan, R. J. Holbrook, M. W. Rotz, K. W. MacRenaris, A. T. Preslar, C. E. Carney, V. Reichova and T. J. Meade, *Bioconjugat Chem.*, 2017, **28**, 153-160; (c) S. Behzadi, V. Serpooshan, W. Tao, M. A. Hamaly, M. Y. Alkawareek, E. C. Dreaden, D. Brown, A.

M. Alkilany, O. C. Farokhzad and M. Mahmoudi, *Chem. Soc. Rev*., 2017, **46**, 4218-4244; (d) A. Verma and F. Stellacci, *Small*, 2010, **6**, 12-21; (e) H. Y. Chiu, W. Deng, H. Engelke, J. Helma, H. Leonhardt and T. Bein, *Sci. Rep.*, 2015, **6**, 25019.

26. A. Yildirim, E. Ozgur and M. Bayindir, *J. Mater. Chem. B.*, 2013, **1**, 1909-1920.

27. (a) M. Khannam, T. Weyhermüller, U. Goswami and C. Mukherjee, *Dalton Trans*., 2017, **46**, 10426–10432; (b) A. Forgács, R. Pujales-Paradela, M. Regueiro-Figueroa, L. Valencia, D. Esteban-Gómez, M. Botta and C. Platas-Iglesias, *Dalton Trans*., 2017, **46**, 1546–1558.

28. K. Pota, Z. Garda, F. K. Kálmán, J. L. Barriada, D. Esteban-Gómez, C. Platas-Iglesias, I. Tóth, E. Brücher and G. Tircsó, *New J. Chem.*, 2018, **42**, 8001-8011.

29. C. Vanasschen, E. Molnár, G. Tircsó, F. K. Kálmán and É. Tóth, *Inorg. Chem.*, 2017, **56**, 7746-7760.

30. D. Ndiaye, M. Sy, A. Pallier, S. Même, I. de Silva, S. Lacerda, A. M. Nonat, L. J. Charbonnière and É Tóth, *Angew. Chem. Int. Ed.*, 2020, **59**, 11958–11963.

31. M. Yu, L. Zhou, J. Zhang, P. Yuan, P. Thorn, W. Gu and C. Yu, *J. Colloid Intef. Sci.*, 2012, **376**, 67-75.

32. M. Rohrer, H. Bauer, J. Mintorovitch, M. Requardt and H. -J. Weinmann, *Invest Radiol*, 2005, **40**, 715-724.

33. V. S. Marangoni, O. Neumann, L. Henderson, C. C. Kaffes, H. Zhang, R. Zhang, S. Bishnoi, C. Ayala-Orozco, V. Zucolotto, J. A. Bankson, P. Nordlander and N. J. Halas, *PNAS*, 2017, **27**, 6960-6965.

Chapter IV

A Zn(II)-Responsive Mn(II)-Complex Confined Porous Silica Nanoparticles as "Smart" MRI CA for Pancreas Imaging

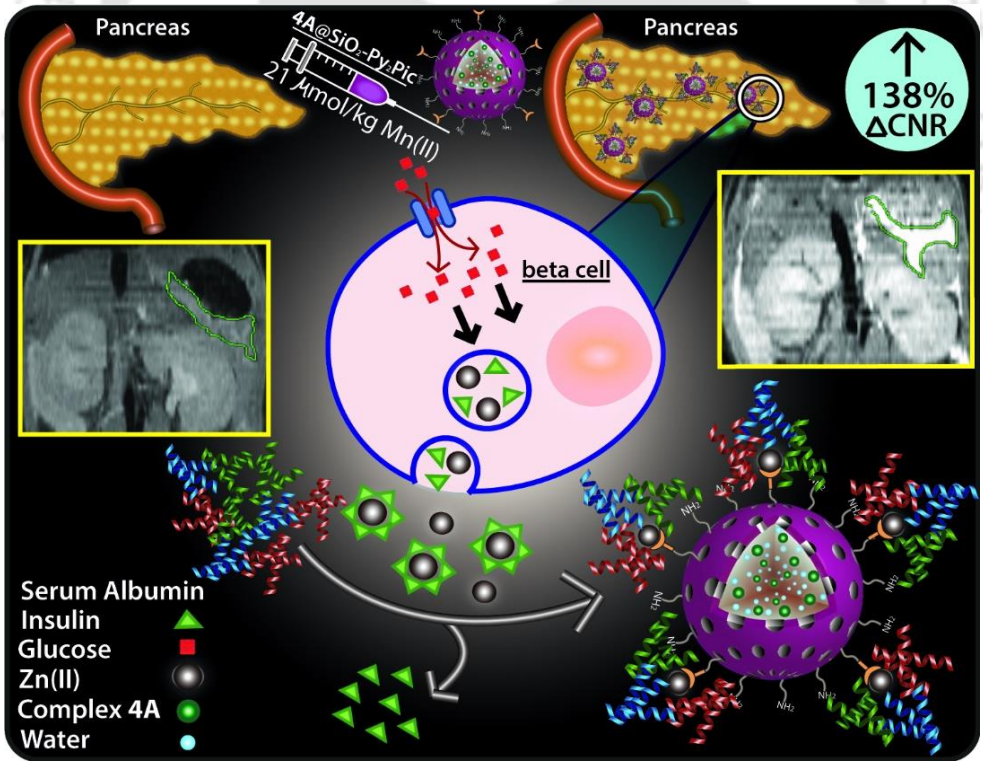

∗ Results have been reported in *J. Mater. Chem. B*, 2023, **11**, 8251-8261.

4.1 Introduction

The majority of the Gd(III)- and Mn(II)-based MRI contrast agents,[1] as discussed in the previous chapters, are found to be primarily extracellular, non-target specific, and exhibit inadequate *in vivo* stability.[2] Because of low relaxivity values, the contrast agents also need to be administered in hefty dosages to obtain conspicuous *in vivo* images. Henceforth, there is a tenacious urge to develop bio-responsive T_1-weighted "smart contrast agents" with high relaxivity values that render useful contrast for recognizing lesions and pathological abnormalities in the vicinity of their localized regions.[3] Because of the intrinsic disadvantages non-gadolinium-based contrast agents have attained special attention. The "smart contrast agents" are designed to amplify positive signals in MR imaging as a response to major physiological changes and metal ion efflux-driven enzymatic activities in selective organs, even while administered in minimal dosage. Thus, the corresponding molecular imaging at the tissue level plays a promising role in non-invasive medical diagnostics.

The blood glucose level is a key factor regulating the normal functionality of the human body.[4] This is directly linked with Type-1 or Type-2 diabetes mellitus, a metabolic disorder caused by the retarded Zn(II)-related metabolism along with dysfunctionalities of pancreatic acinar and β-cells.[5]

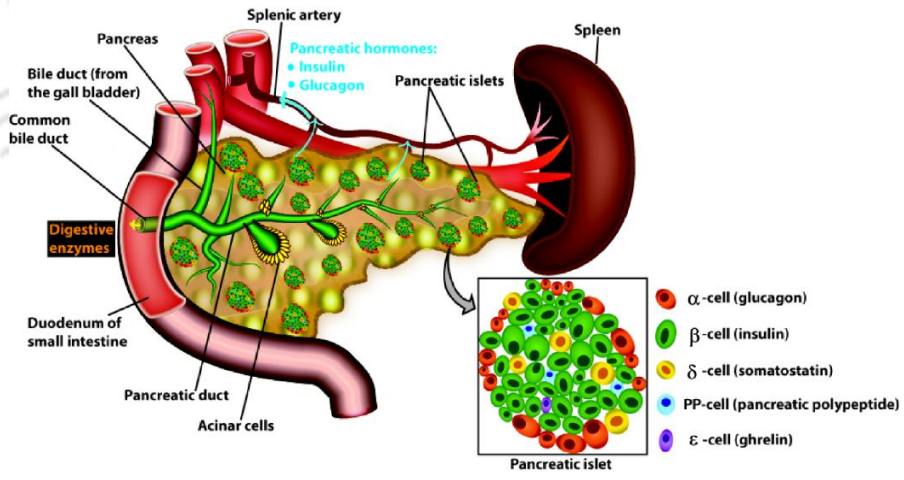

Figure 4.1. The schematic diagram of the pancreas.

Elaborately, the pancreas is a pivotal gland positioned behind the stomach secreting glucagon and insulin hormones into the blood to maintain glucose levels.[6] It is predominantly

comprised of pancreatic β-cells, present in the islets of Langerhans together with α-cells, δ-cells, γ-cells, and ε-cells (**Figure 4.1**). Zinc ions are one of the most important micronutrients, and are involved in many biological processes. It plays a predominant role in the synthesis and storage of insulin in the form of Zn(II)-insulin (2:6) hexamers in the secretory granules.[7] Consequently, healthy β-cells possess relatively high Zn(II) content. High glucose level in the blood plasma triggers insulin secretion along with Zn(II) ions, resulting in the efflux of unbound zinc ion in between the cellular compartments. Quantitatively, this dynamic movement of the metal ion across the cell membrane increased [Zn(II)] concentration in the extracellular space from 40 μM to 500 μM.[8] Hence, designing paramagnetic agents sensitive to dynamic Zn(II) ion concentration (>10-fold increase initiated by glucose stimulation) would result in glucose-driven zinc-dependent contrast enhancement as a whole or as "hot spots", enlightening the pathological condition of the pancreas and/or the β-cells.[9]

Additionally, insulin is active in the monomer form and thus the Zn(II)-insulin hexamer units need to be disintegrated for biological activity.[7b] The serum albumin protein with high Zn(II) affinity, plays a crucial role in this dissociation process thereby regulating insulin availability.[10] Paramagnetic units with a specific anchoring group designated to bind the co-released free Zn(II) ions in the presence of human serum albumin (HSA) protein, generate metal concentration-dependent MR signal contrast in the pancreas by *q* switching or engendering a slowly rotating ternary system. This subset of contrast agents is utilized as Zn(II)--responsive biomarkers to track the glucose-stimulated insulin/zinc secretion (GSIZS) and β-cells functioning in real-time.[11]

Contemporary literature reported some Zn(II)-responsive Gd(III)-based contrast agents which showed utmost 4-fold increase in relaxivity.[11,12] The adverse effects of nephrogenic systemic fibrosis due to Gd(III) retention in various tissues post-administration have prompted the development of alternative Mn(II)-based chelates for similar purposes.[13] However, zinc secretion-dependent Mn(II)-based contrast agents are scarce.[14] In the recent past, Sherry and colleagues have reported a Zn(II) ion-responsive contrast agent by incorporating a BPEN [BPEN = N,N-bis(2-pyridinylmethyl)-1,2-ethanediamine)] tether unit with the acyclic PyC3A (PyC3A = N-picolyl-N,N′,N′-trans-l,2-cyclo-hexylenediaminetriacetate) ligand in $[Mn^{II}PyC3A(OH_2)]^{-}$ complex that provides glucose-stimulated contrast enhancement in pancreas and prostate.[14a] However, it suffers from partial release of free Mn(II) ions due to Zn(II) induced transmetallation. Relaxivity value

up to 17.4 $mM^{-1}s^{-1}$ (0.5 T and 37 °C) was achieved in the presence of Zn(II) and serum albumin protein at physiological conditions.

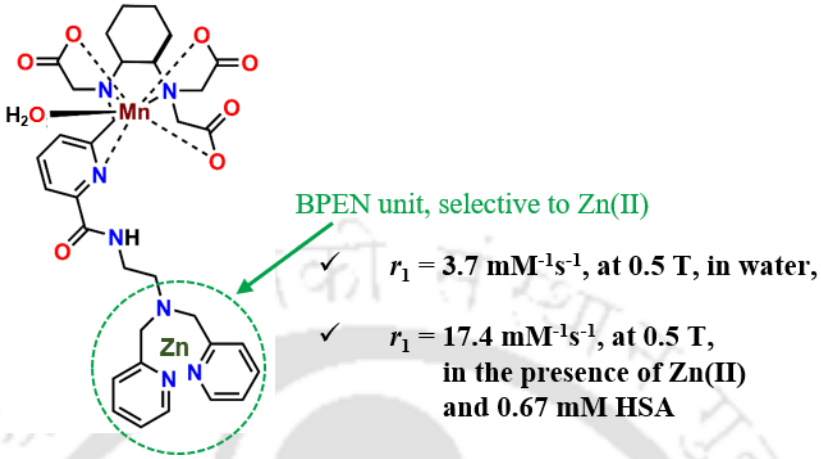

Figure 4.2. Schematic diagram of [Mn^{II}PyC3A(OH_2)]–BPEN system, bound to zinc ion.[14a]

Nevertheless, the Mn(II)-based contrast agents with high thermodynamic stability and kinetic inertness along with high relaxivity values are scanty. While attaining high kinetic inertness in acyclic ligand-based Mn(II) complexes remained a significant challenge, Mn(II) complexes with macrocyclic ligands imparting high thermodynamic stability and large relaxivity values are rare.[15] Furthermore, the core structural modification scope for the macrocyclic ligands is limited. Interestingly, these are the basic requirements for further modifications with an attribute to attach zinc ions and albumin proteins since both of these induce transmetallation issues.[16]

In this context, we envisaged a thermodynamically stable, neutral, and mono-aquated Mn(II)-complex **4A** based on a ligand with a chiral appendant and picolinate units, further confining within a porous silica nanoparticle (PSNs) as a contrasting agent. In the earlier chapter, we have established these PSNs to be biocompatible, and their porous nature will permit free access to water molecules within the nanoparticles. Furthermore, the silica core will protect the entrapped Mn(II)-complex molecules from exposure to other external metal ions, e.g., Zn(II), Cu(II), etc. Hence, the kinetic inertness can be retained. Incorporating Mn(II)-complex molecules within the core of nanoparticles will also restrict the molecular free rotation. Thus, the rotational correlation time (τ_R) is expected to increase, leading to a higher relaxivity value. Here, we report further modification on the surface of the novel silica nanoparticle by covalent attachments of Zn(II) selective Py_2Pic-units, thereby developing bio-responsive nanomaterials that exhibited a

remarkable increase in relaxivity in the presence of albumin protein. Subsequent characterization, *in vitro*, and *in vivo* studies showing efficient MRI contrast enhancement established the role of the synthesized nanoprobe in tracking glucose-stimulated Zn(II) secretion in the pancreas.

4.2 Synthesis and Characterization of Ligand H_2AlcDPA

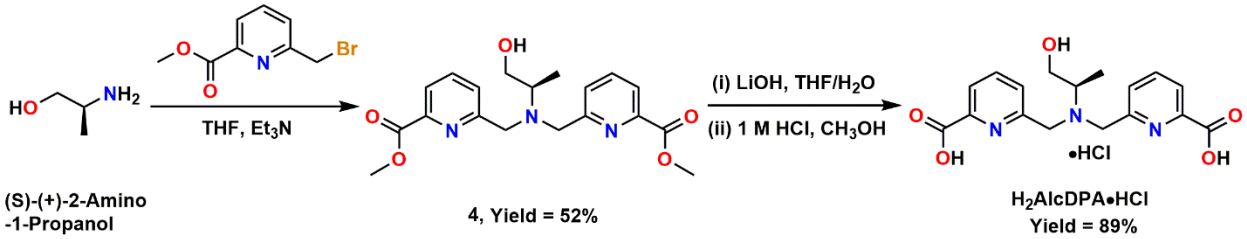

Scheme 4.1. Synthetic pathway for the preparation of ligand **H_2AlcDPA•HCl**.

Ligand H_2AlcDPA•HCl was synthesized in an overall 46 % yield in two steps. (S)-(+)-2-Amino-1-propanol was reacted with 2.1 equivalents of 6-(bromomethyl)picolinate in THF medium, in the presence of Et_3N to obtain compound **4** as a white solid in 52% yield. Subsequently, base hydrolysis of compound **4** with 2.2 equivalent of LiOH in THF/H_2O solution and further acidification with 1(M) HCl yielded the ligand H_2AlcDPA as HCl salt in 89% yield. The crude was washed with methanol to remove excess LiOH. Schematic procedures are presented in **Scheme 4.1**. The ligand obtained was characterized by FTIR, ESI-MS, ^{1}H-NMR, and ^{13}C-NMR spectroscopy.

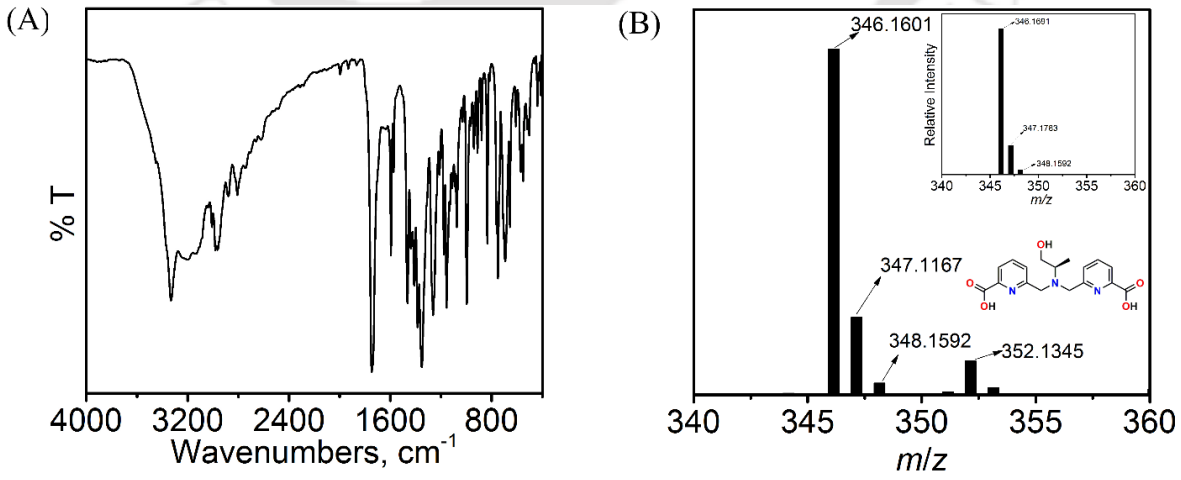

Figure 4.3. (A) FTIR and (B) ESI-MS (+ve) spectra of ligand H_2AlcDPA. The simulated spectrum is given as an inset.

The infrared spectrum (**Figure 4.3A**) revealed peaks at 3331 cm^{-1} (ν_{O-H} stretching, alcohol group); 2877-2808 cm^{-1} band (ν_{N-H} of the protonated tert-amine group); 1746-1735 cm^{-1} ($\nu_{C=O}$ asymmetric stretching, carboxylic acid groups) and 1594 cm^{-1} (aromatic $\nu_{C=N}$ stretching, pyridine group) confirming the formation of H_2AlcDPA ligand as HCl acid salt. The ESI-MS of an aqueous solution of H_2AlcDPA demonstrated a 100% molecular ion peak at m/z = 346.1601 which corresponded to the composition of the ligand as $[C_{17}H_{19}N_3O_5 + H]^+$ (calculated as *m/z* = 346.1691).

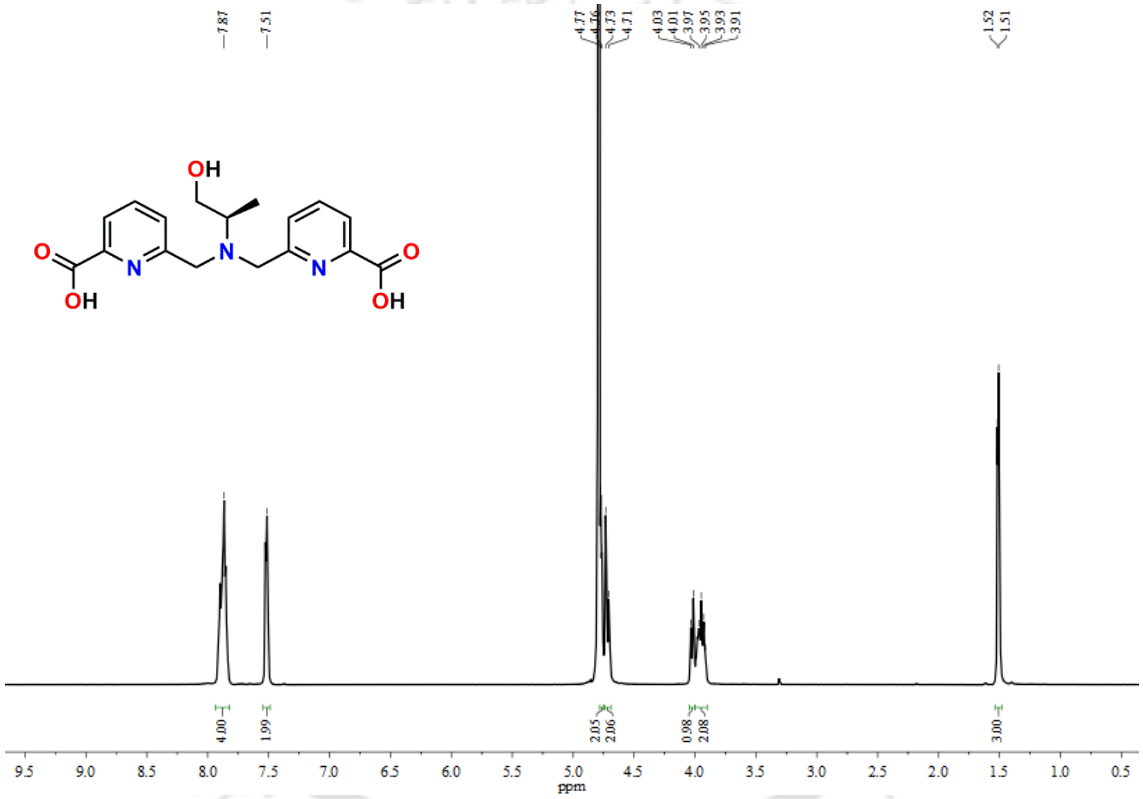

Figure 4.4. ^{1}H-NMR spectrum of ligand H_2AlcDPA in D_2O solvent.

The ^{1}H-NMR spectrum of ligand H_2AlcDPA in D_2O medium exhibited two multiplet signals in the region 7.87-7.51 ppm corresponding to the six aromatic protons of the two pyridine rings present in the ligand. Four protons of the methylene units adjacent to the pyridine ring (picolinate groups) appeared at 4.77-4.71 ppm. The multiplet peaks at 4.03-3.91 correlated to the three protons of the propanol chain along with the methyl protons appearing at 1.52 ppm. The ^{13}C-NMR spectrum of the ligand in the same medium showed the presence of 10 different types of carbon atoms.

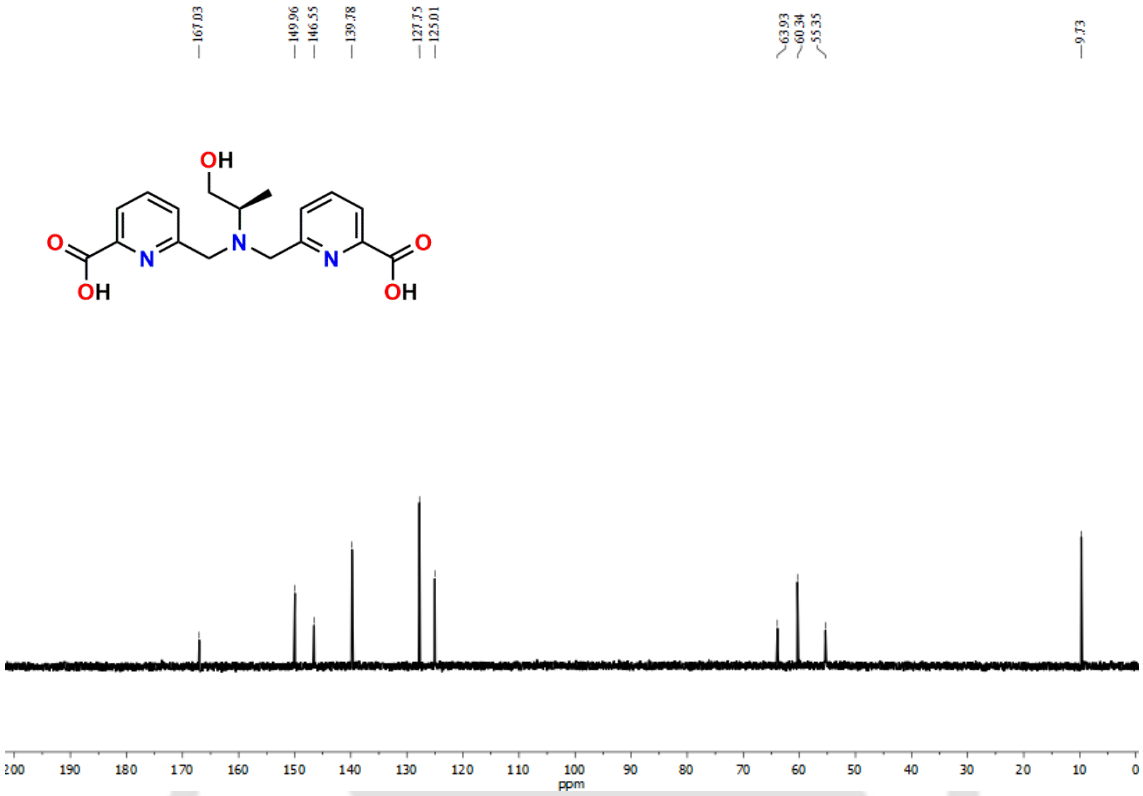

Figure 4.5. ^{13}C-NMR spectrum of ligand H_2AlcDPA in D_2O solvent.

4.3 Synthesis and Characterization of Ligand HPy$_2$Pic

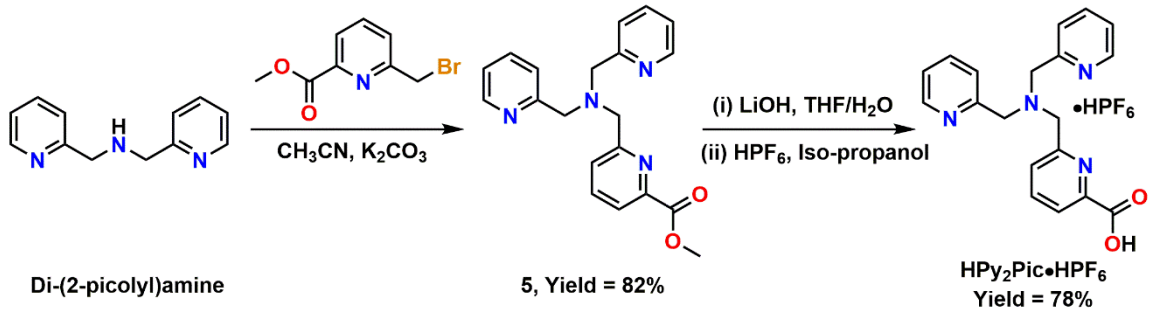

Scheme 4.2. Synthetic pathway for the preparation of ligand **HPy$_2$Pic•HPF$_6$**.

The anchoring ligand, HPy$_2$Pic, was synthesized as represented in **Scheme 4.2** following the procedure mentioned in the literature.[17] In detail, Di-(2-picolyl)amine in acetonitrile was heated with one equivalent of 6-(bromomethyl)picolinate in the presence of K_2CO_3 to give compound **2**. Base hydrolysis of this compound in an aqueous LiOH solution and acidification with HPF_6

afterwards gave $HPy_2Pic{\bullet}HPF_6$ salt in 64% overall yield. Corresponding characterizations (FTIR, ESI-MS, ^{1}H-NMR, and ^{13}C-NMR spectroscopy) proved the formation and purity of the synthesized ligand.

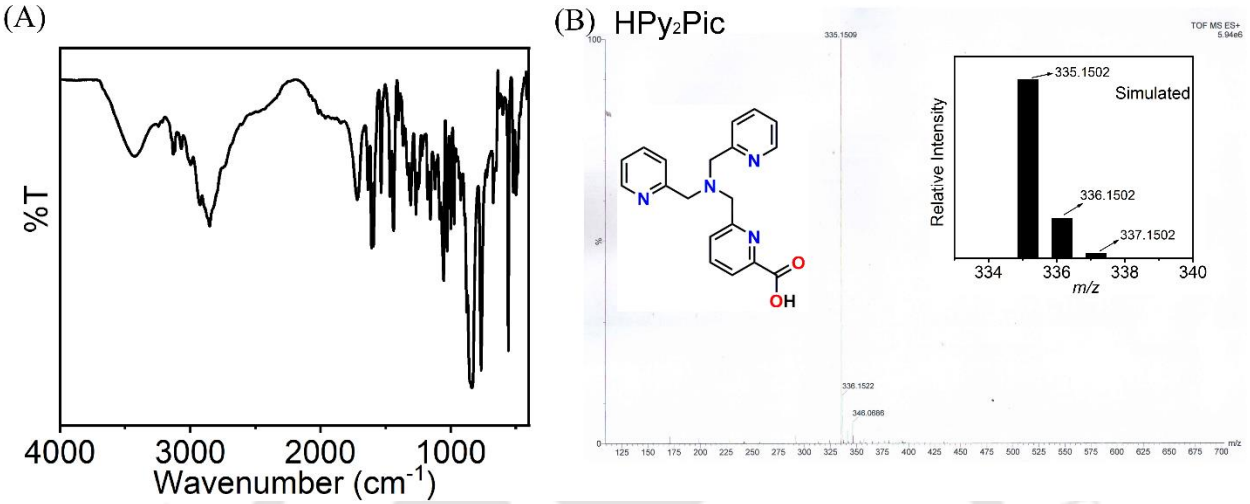

Figure 4.6. (A) FTIR and (B) ESI-MS (+ve) spectra of ligand HPy_2Pic. The simulated spectrum is given as an inset.

In the infrared spectra of the anchoring ligand HPy_2Pic (**Figure 4.6A**), bands at 3430 cm^{-1} arise due to $\nu_{O–H}$ asymmetric stretching of the carboxylic acid group, respectively. Broad band in the 2853–2752 cm^{-1} range corresponded to the $\nu_{N–H}$ stretching of the protonated tert-amine group. Characteristic $\nu_{C=O}$ asymmetric stretching (carboxylic acid group) was observed as a sharp band at 1718 cm^{-1}. The peak at 1594 cm^{-1} appeared due to the $\nu_{C=N}$ stretching (pyridine group). Furthermore, the ESI-MS of the synthesized ligand in aqueous medium was recorded in the positive mode manifesting a 100% molecular ion peak at *m/z* = 335.1509 (**Figure 4.6B**). The isotope distribution pattern of the observed mass correlated to the composition of the ligand $[C_{19}H_{18}N_4O_2 + H]^+$ (*m/z* = 335.1502).

The ^{1}H-NMR spectrum for HPy_2Pic (**Figure 4.7**) was obtained in CD_3OD medium displaying 11 aromatic proton signals in the range 8.89-7.56 ppm, ascribed to the three pyridine rings in the ligand motif. The six methylene protons appeared as sharp singlet peaks at 4.43 and 4.26 ppm. Subsequently, the respective ^{13}C-NMR spectrum signified the presence of 13 different types of carbon atoms (**Figure 4.8**).

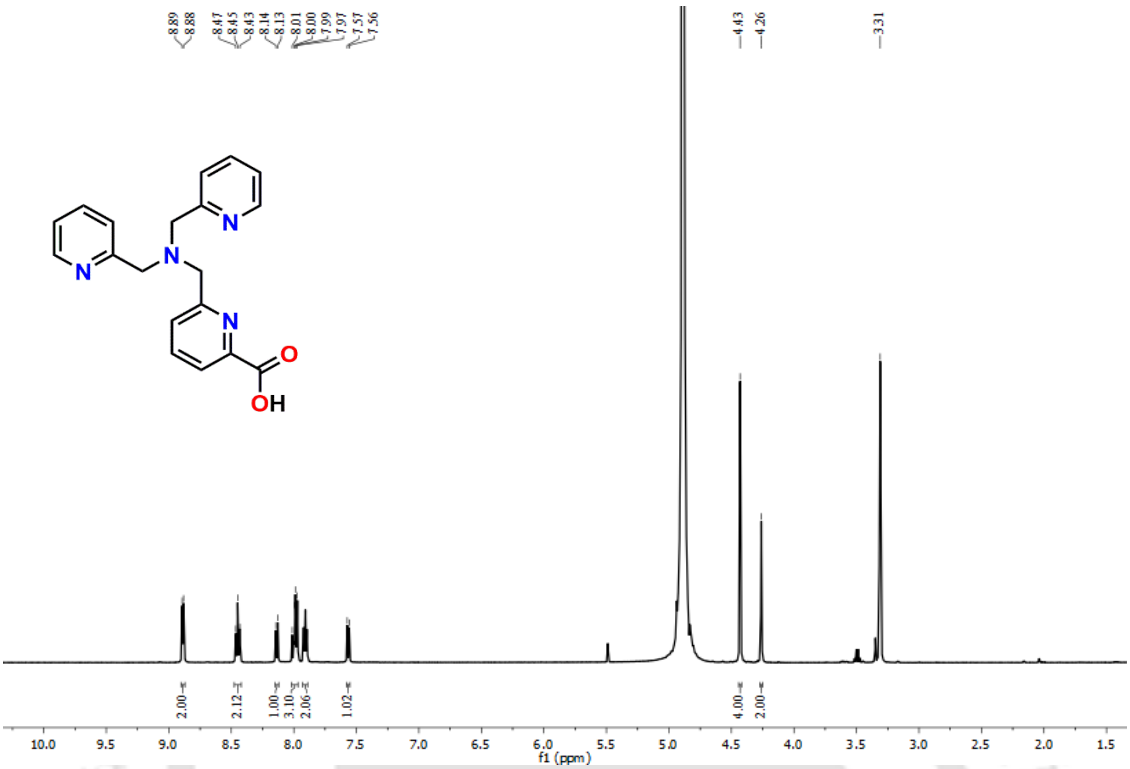

Figure 4.7. ^{1}H-NMR spectrum of ligand HPy_2Pic in CD_3OD solvent.

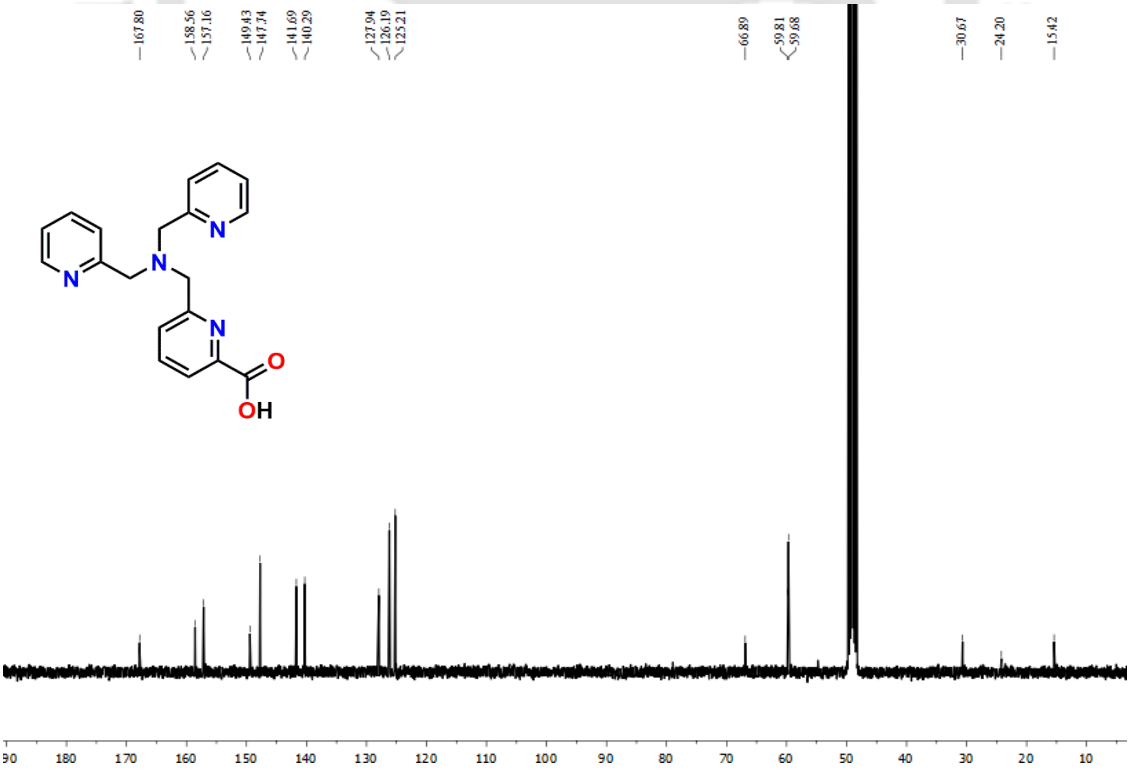

Figure 4.8. ^{13}C-NMR spectrum of ligand HPy_2Pic in CD_3OD solvent.

4.4 Synthesis and Characterization of Mono-aquated Mn(II)-Complex of Ligand H_2AlcDPA, 4A

Complex **4A** was prepared by reacting H_2AlcDPA•HCl with an equivalent amount of $MnCl_2$•$4H_2O$ in the aqueous medium, at pH ~ 6.5 attained with the addition of dilute NaOH solution. Solid crude was obtained after evaporation of the reacting solution, and the corresponding methanolic solution was kept for slow diffusion of the methanolic solution in a diethyl ether environment to obtain needle-shaped colourless crystals of complex **4A** in 64% yield. The synthetic procedure is illustrated in **Scheme 4.3**.

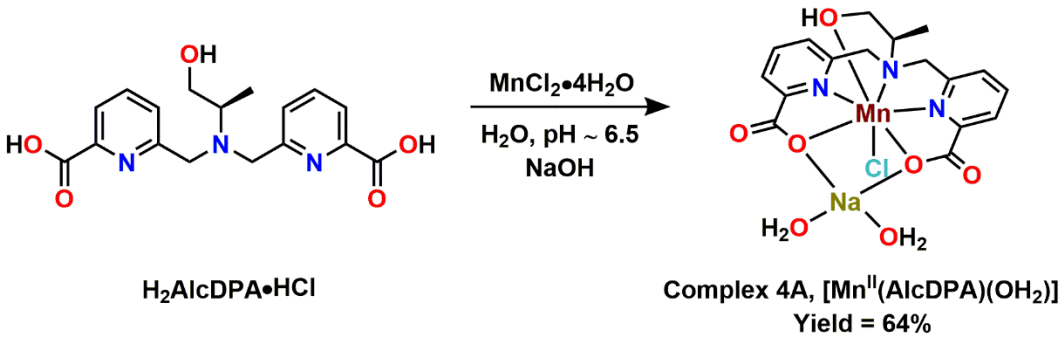

Scheme 4.3. Schematic representation for the synthesis of complex **4A**, $[(C_{17}H_{17}N_3O_5MnCl)Na(H_2O)_2]$.

The infrared spectrum (**Figure 4.9A**) of the complex showed peaks at 3317 cm^{-1} for ν_{O-H} stretching of the alcohol group (shifted from 3331 cm^{-1} in the ligand) along with the shift in the characteristic $\nu_{C=O}$ asymmetric stretching band (carboxylate group) from 1746-1735 cm^{-1} in ligand to 1649 and 1613 cm^{-1} in the **4A** corresponded to the formation of the metal-coordinated chelate. The respective ESI-MS (+)ve mode spectrum of the aqueous solution of complex **4A** provided a 100 % molecular ion peak at m/z = 398.99 (**Figure 4.9B**). The peak corresponded to $[(M–Cl)+H]^+$; where M–Cl = $C_{17}H_{17}N_3O_5Mn$, which is the molecular composition of the complex core. The appearance of the mass peak in the positive mode thus indicated the chloride ion disintegration from the complex core in the water. Therefore, water molecules are expected to interact with the Mn(II) ion at the same position as that occupied by the chloride ion in the molecular structure of the complex.

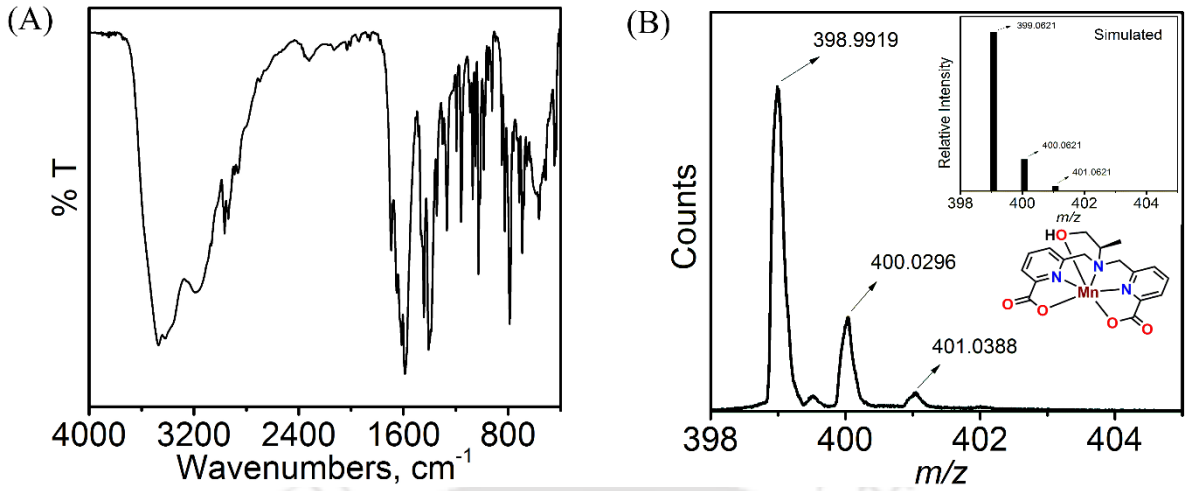

Figure 4.9. FTIR and (B) ESI-MS (+ve) spectra of complex **4A**. The simulated mass spectrum is given as an inset.

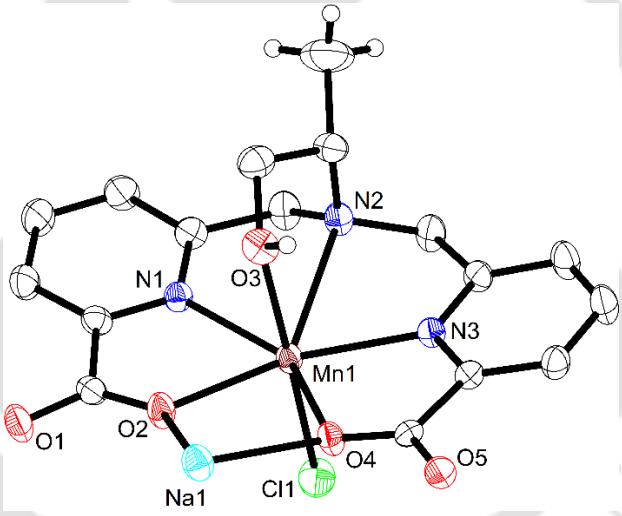

Figure 4.10. ORTEP representations of complex **4A**, drawn at 40% probability level. All the hydrogen atoms in the complex, except for the alcohol and the aliphatic methyl group, were omitted for clarity.

Single crystal X-ray diffraction was measured for complex **4A** at 298 K to evaluate the geometry and the metal ion-ligand coordination motif. The complex crystallized in the monoclinic space group P 21. The ORTEP diagram is presented in **Figure 4.10**. The selected bond distances and bond angles are provided in **Table 4.1**. In the complex, the central Mn atom was seven-coordinate, where the pentagonal basal plane comprised the tert-amine N atom, two N atoms and

two O atoms from the picolinate units. A chloride atom and the alcoholic O atom of the propanol unit occupied the axial positions. The Mn–$N1_{Py}$ = 2.276(2), Mn–$N3_{Py}$ = 2.251(2), Mn–$N2_{amine}$ = 2.540(2), Mn–$O2_{acid}$ = 2.256(2) and Mn–$O4_{acid}$ = 2.261(2) Å bond distances were commensurate well with the previously reported Mn(II) complexes of similar ligands.[18] Thus, in complex **4A**, the Mn atom was in +II oxidation state. The complex core was mono-negative in charge due to the presence of the coordinated chloride ion. A sodium ion was present as the counter-cation.

Table 4.1. Selected bond distances (Å) and bond angles (°) for complex **4A**.

Mn1–O2	2.256(2)	O2–Mn1–O4	77.63(6)
Mn1–O3	2.280(2)	O2–Mn1–N1	70.80(6)
Mn1–O4	2.261(2)	N3–Mn1–O4	72.02(6)
Mn1–N1	2.276(2)	N1–Mn1–N2	69.16(6)
Mn1–N2	2.539(2)	N3–Mn1–N2	68.46(6)
Mn1–N3	2.251(2)	O3–Mn1–Cl1	177.90(5)
Mn1–Cl1	2.485(1)		

Table 4.2. Crystallographic and structural refinement parameters for complex **4A**.

Empirical formula	$C_{34}H_{42}Cl_2Mn_2N_6Na_2O_{14}$
CCDC Number	2260190
Formula weight	985.49
Crystal habit, colour	Needle-shaped/ colourless
Crystal size, mm^3	0.35×0.32×0.30
Temperature, *T*	293(2)
Wavelength, λ(Å)	0.71073
Crystal system	monoclinic
Space group	'P 21'
Unit cell dimension	*a* = 9.1405(3) Å, *b* = 13.8564(5) Å, *c* = 16.7601(6) Å, α = 90.00°, β= 105.4930°, γ = 90.00°
Volume, *V* ($Å^3$)	2045.61(12)
Z	2
Calculated density, mg•mm^{-3}	1.600

Absorption coefficient, μ (mm^{-1})	0.843
F(000)	1012
θ range for data collection	2.93° to 27.28°
Limiting indices	$-10 \leq h \leq 10$, $-16 \leq k \leq 16$, $-19 \leq l \leq 19$
Reflection collected / unique	48385/6849 [$R_{(int)}$ = 0.0257]
Completeness to θ	99.0% (θ = 25°)
Max. and min. transmission	0.7455/0.6402
Refinement method	'SHELXL-2018 (Sheldrick, 2018)'
Data / restrains / parameters	7098/1/578
Goodness-of-fit on F^2	1.062
Final R indices [I>2sigma(I)]	R_1 = 0.0211, wR_2 = 0.0552
R indices (all data)	R_1 = 0.0225, wR_2 = 0.0565
Largest diff. peak and hole	0.202/-0.227

4.5 Thermodynamic Stability of Mn(II)/Zn(II) Complex for Ligand H_2AlcDPA/HPy$_2$Pic

Direct pH-potentiometric titrations were employed to determine the protonation constants of H_2AlcDPA and HPy$_2$Pic ligands along with the stability constants of corresponding metal complexes. Each set of experiments was performed at room temperature and a fixed ionic strength of 0.15 M NaCl, under an argon atmosphere. For ligand protonation constants, titration was done with 0.001 M ligand solution against standardized 0.1 M NaOH solution as titrant. The stability of the complex was obtained by direct pH-potentiometric titration using 1:1 ligand-to-metal molar ratio in the pH range of 2.1-12.0. The protonation constants were calculated by fitting the ligand titration data pairs to the equation $K_i^H = [H_iL]/[H_{i-1}L][H^+]$, i = number of replaceable protons. Likewise, The Mn-L stability constant was calculated by fitting the metal:ligand titrations data pairs to the equation $K_{Mn\text{-}L} = [MnL]/[Mn][L]$.

For H_2AlcDPA-based titrations, the stepwise protonation constant values for the ligand were found to be $\log K_1^H$ = 7.69(3), and $\log K_2^H$ = 3.75(2). The highest pK_a value could be ascribed to the tertiary nitrogen unit and pK_a = 3.75 was due to the carboxylic group of a picolinate moiety.[18a] The thermodynamic stability constant ($\log K_{MnL}$) of the complex was determined as

15.06 (**Figure 4.11**, **Table 4.3**). Noteworthy, the stability constant of complex **4A** was in line with $[Mn^{II}PyC3A(OH_2)]^-$ = 14.14 and [Mn(PC2A-DPA)] = 15.87.[14] A more clear introspection could be done by comparing pMn values (pM = -log[M_{free}], considering $[M]_{total} = [L]_{total} = 10^{-5}$ M, at pH ~ 7.4) of the mentioned complexes. A similar trend was observed as the pMn value for complex **4A** was found to be 9.56, substantially higher than the chelate involved in the reported Zn(II) sensitive CA, (MnPyC3A, pMn = 8.17).[15a] Hence, a thermodynamically stable complex has materialized by the coordination of $[AlcDPA]^{2-}$ ligand, being the predominant species in the pH range 3-10. The inclusion of the chiral propyl chain along with the picolinate units (imparting stability through Mn(II) centre to pyridine π*-interactions) envisaged rigidity in the acyclic Mn(II) complex structure.[19]

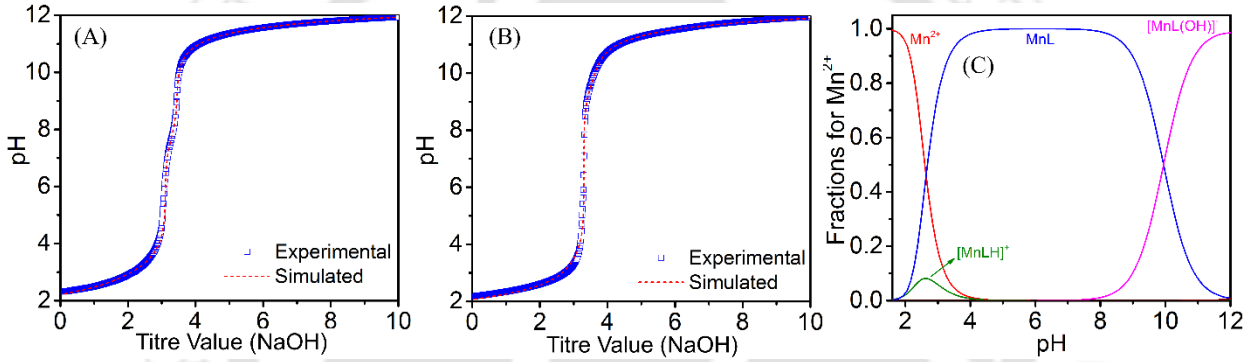

Figure 4.11. Experimental and simulated curves representing pH-potentiometric titration of (A) ligand H_2AlcDPA solution, and (B) ligand H_2AlcDPA:Mn(II) (1:1) solution against standard NaOH solution in 0.15 M NaCl and 25 °C. (C) Corresponding species distribution diagram for Mn/H_2PyDPA: [Mn(II)] = [L] = 1 mM.

Similarly, for HPy_2Pic-based titrations, the stepwise protonation constant values for the ligand were found to be $\log K_1^H$ = 9.52(7), $\log K_2^H$ = 8.31(8), $\log K_3^H$ = 6.34(8) and $\log K_4^H$ = 4.95(8). The affinity of HPy_2Pic towards Zn(II) ions was investigated by determining the $\log K_{ZnL}$ value (= 19.76), and consequently, the pZn value (= 10.82), obtained after simulating the 1:1 HPy_2Pic/Zn(II) potentiometric titration curve (**Figure 4.12**, **Table 4.3**). Calculated log K_{ZnL} and pM values are far higher than that for DPA or BPEN unit (log K_{ZnL} = 7.63), a well-established ligand for chelating Zn(II) ions, and TPA (three-pyridine containing ligand, log K_{ZnL} = 11.00).[20] These parameters suggested the formation of a highly stable Zn(II) complex involving the HPy_2Pic

ligand, as it offered a carboxylic donor centre along with three binding pyridine sites toward the metal ion. Herein, we anticipated strong ligand-Zn(II) interactions for this mentioned unit, even after engaging the carboxylic branch for amide linkage.

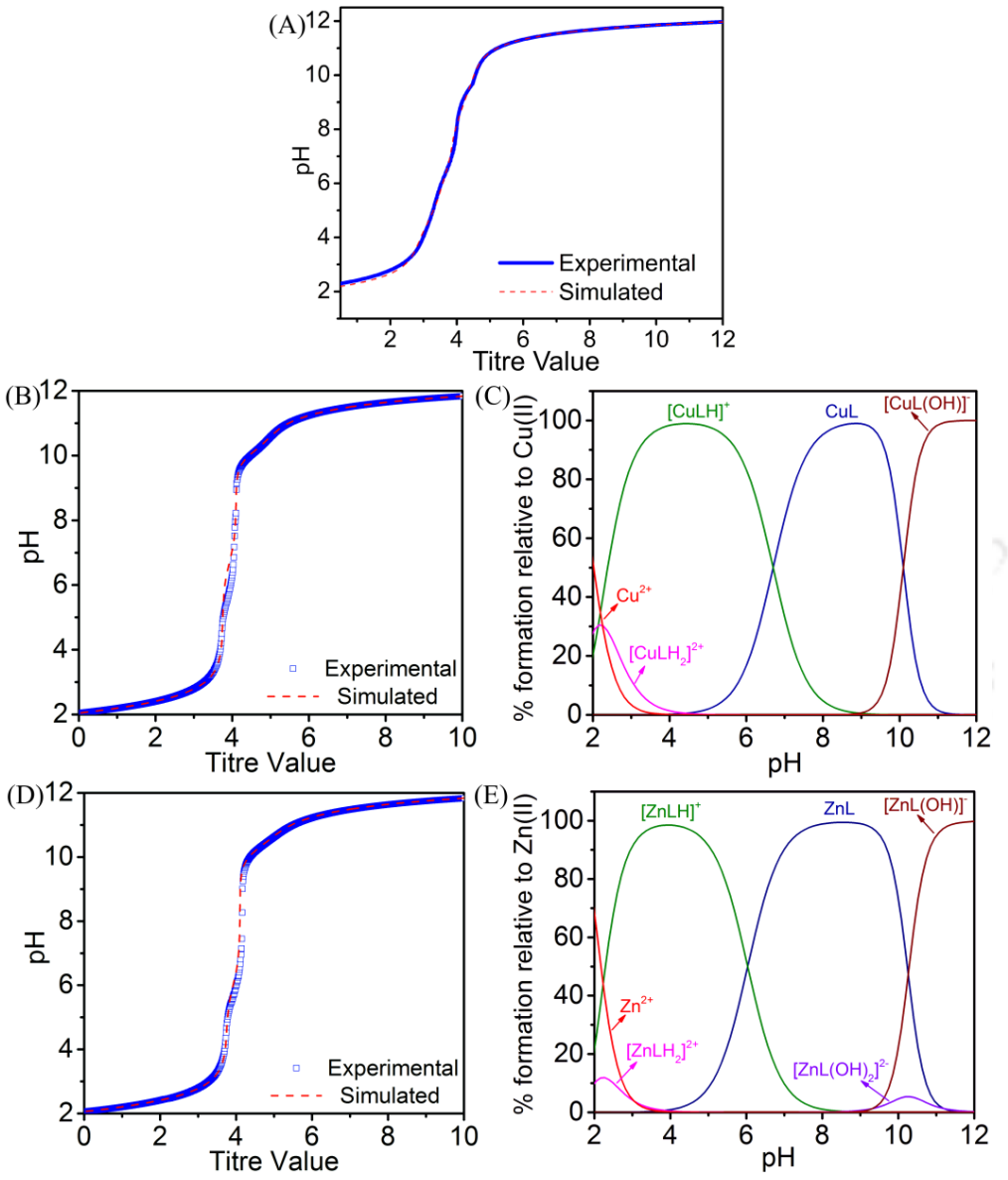

Figure 4.12. Experimental and simulated curves representing pH-potentiometric titration of (A) ligand HPy_2Pic solution, (B) ligand HPy_2Pic:Cu(II) (1:1) solution and (D) ligand HPy_2Pic:Zn(II) (1:1) solution against standard NaOH solution in 0.15 M NaCl and 25 °C. (C) and (E) represented corresponding species distribution plots for HPy_2Pic:Cu(II) and HPy_2Pic:Zn(II) systems, respectively.

Table 4.3. Ligand protonation constants and corresponding stability constants for Mn(II), Zn(II) and Cu(II) complexes.

		PyC3A[a]	PC2A-DPA[b]	AlcDPA[c]	Py_2Pic[c]
H^+	$\log K_1^H$	10.16	10.65	7.69(3)	9.52(7)
	$\log K_2^H$	6.39	6.55	3.75(2)	8.31(8)
	$\log K_3^H$	3.13	5.84	—	6.34(8)
	$\log K_4^H$	—	4.39	—	4.95(8)
	$\sum \log K_i^H$	19.68	16.49	11.45	29.12
Mn^{2+}	$\log K_{MnL}$	14.14	15.87	15.06(8)	—
	$\log K_{MnHL}$	2.43	4.14	3.53(10)	—
	pMn	8.17	8.79	9.56	—
Cu^{2+}	$\log K_{CuL}$	—	19.05	—	19.31(1)
	$\log K_{CuHL}$	—	3.63	—	6.70(1)
	$\log K_{CuH2L}$	—	—	—	2.14(3)
	pCu	—	—	—	10.59
Zn^{2+}	$\log K_{ZnL}$	—	—	—	19.76(1)
	$\log K_{ZnHL}$	—	—	—	6.03(8)
	$\log K_{ZnH2L}$	—	—	—	1.66(7)
	pZn			—	10.82

[a][14a] (I= 0.15 M NaCl, 25 °C). [b][14b] (I= 0.15 M NaCl, 25 °C). [c]This work (I= 0.15 M NaCl, 25 °C).

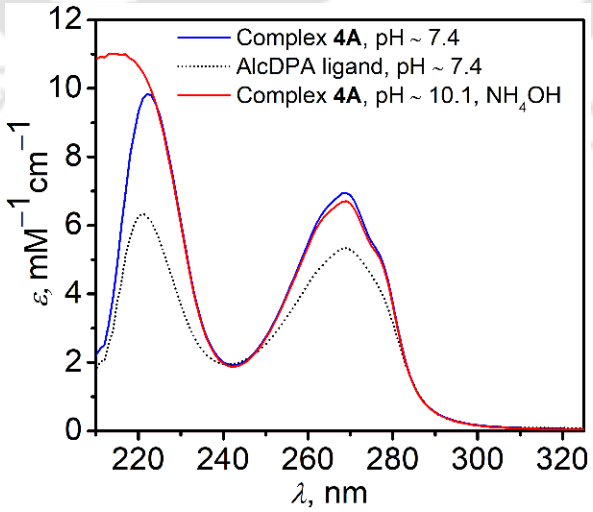

Figure 4.13. UV-Vis spectra of **4A** at pH ~ 7.4 or pH ~ 10.1 (attained by NH_4OH) and 25 °C.

The pH-dependent species distribution diagram for Mn(II)-AlcDPA complex (**4A**) consolidated the stability of the complex molecules at the pH range higher than 8 (**Figure 4.11C**). The UV-Vis spectrum of **4A** at pH ~ 9.5 (attained by NH_4OH solution, **Figure 4.13**) exhibited no appreciable change and thus, discarded the possibility of decomposition of the complex at the mentioned conditions.

4.6 Synthesis and Characterization of Complex 4A Confined PSNs and Surface Modification with HPy_2Pic

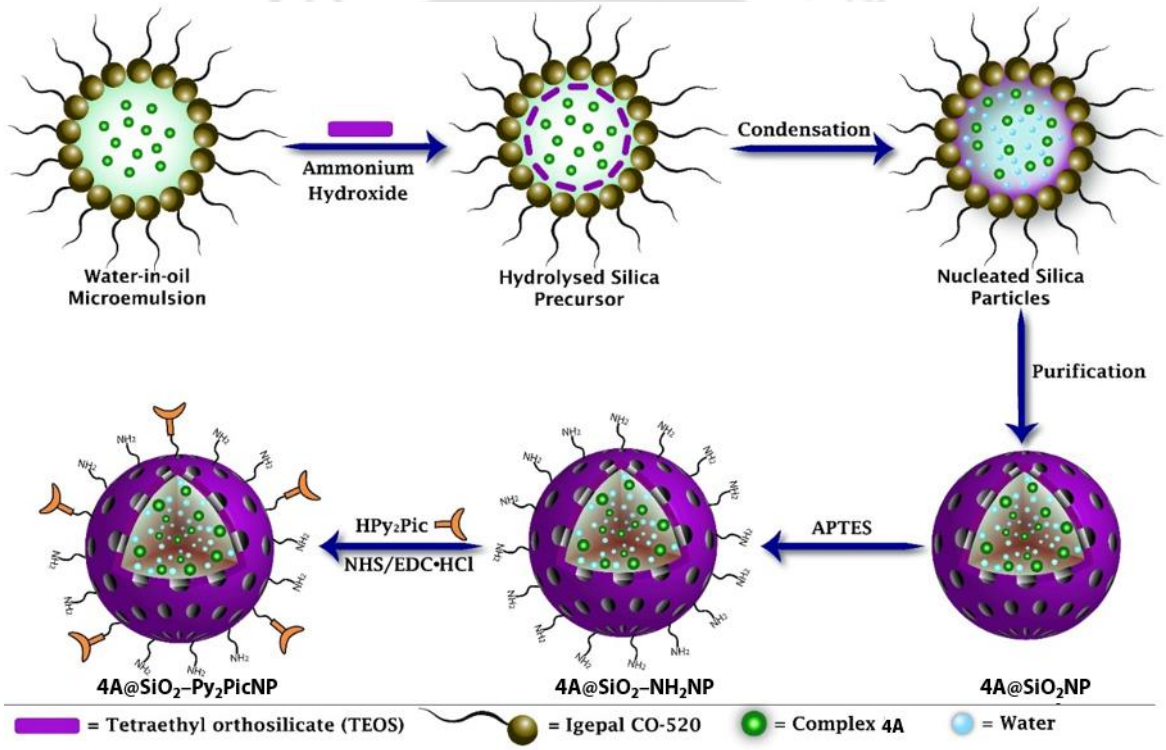

Scheme 4.4. Representative illustration for the preparation of **4A**@SiO_2–NH_2NP and Complex **4A**@SiO_2–Py_2PicNP.

The previously established reverse microemulsion method was followed to engender **4A** incorporated porous silica nanoparticles, **4A**@SiO_2NP (**Scheme 4.6**). A pH ~ 7.4 buffered doping solution of complex **4A** (480 µL, 2.50 mM) was employed and (3-Aminopropyl)triethoxysilane (APTES) was added post-addition of TEOS (tetraethyl orthosilicate) for further amine-functionalization of the silica-surfaced hydroxide units. Surfactant removal finally produced

complex **4A** confined amine surface-functionalized porous silica nanoparticle, **4A**@SiO_2–NH_2NP. Afterwards, HPy_2Pic ligand was conjugated to the amine unit by amide bond formation, promoted by 1-(3-Dimethylaminopropyl)-3-Ethyl Carbodiimide (EDC) and N-Hydroxysuccinimide (NHS) activators, to engender the surface modified **4A**@SiO_2–Py_2PicNP. Isolated finalized nanoparticles were dispersed in 1 mL HEPES buffer (pH ~ 7.4) to form **4A**@SiO_2–Py_2PicNP stock solution. For the non-functionalized nanoparticle system, an average of 34 complex 4A molecules were found to be incorporated within each nanosphere (calculation method identical to that of **Chapter III**).

The formation and morphology of the synthesized nanomaterials were elucidated by FETEM imaging, EDX, FTIR, EPR, TGA and N_2 adsorption-desorption isotherm analyses.

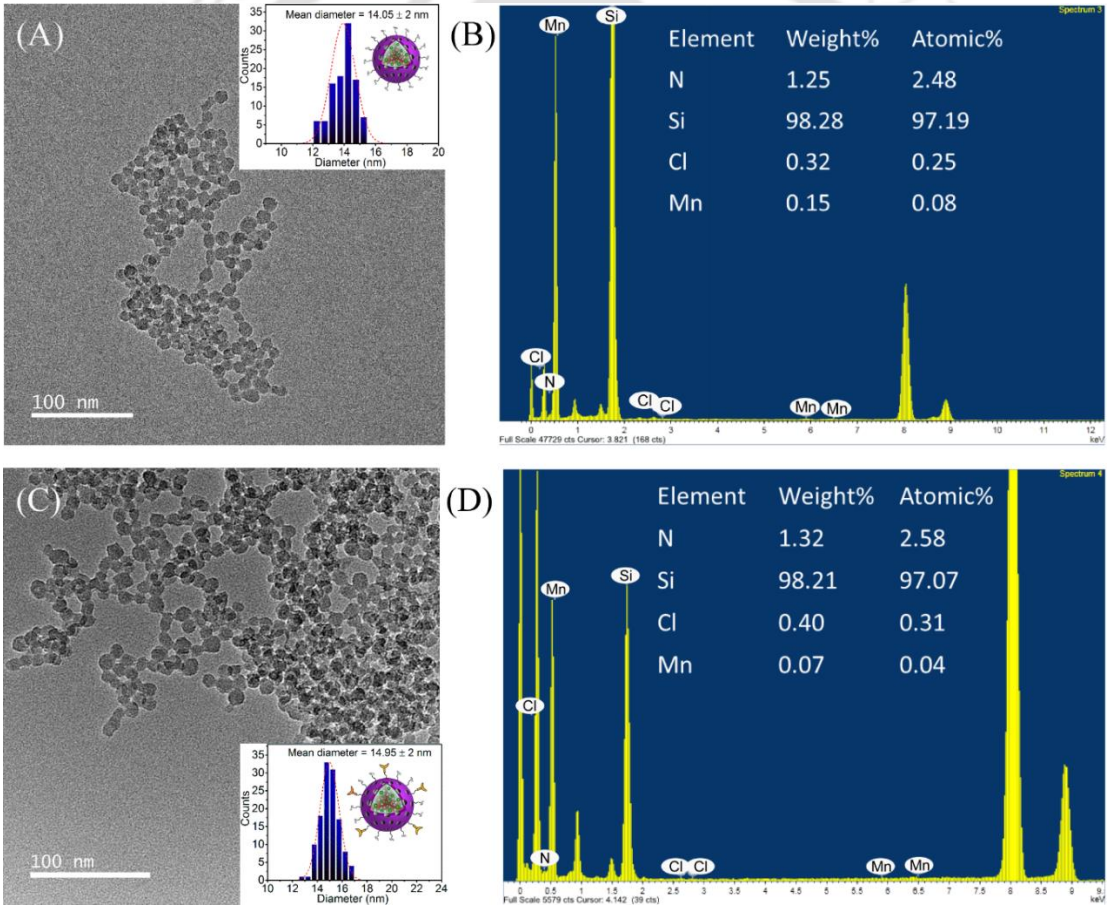

Figure 4.14. (A) FETEM images and (B) corresponding Energy dispersive X-ray (EDS) analysis of **4A**@SiO_2–NH_2NP; (C) and (D) representing similar characterization for **4A**@SiO_2–Py_2PicNP, inset- corresponding particle size distribution.

Spherical-shaped and monodispersed nanoparticles of **4A**@SiO_2–NH_2 and **4A**@SiO_2–Py_2Pic with respective average particle sizes of 14.05 nm and 14.95 nm were recognized by FETEM images (**Figure 4.14**, **Table 4.4**,). Energy-dispersive X-ray spectroscopy (EDS) analysis on the synthesized nanomaterials demonstrated the presence of Mn, N, Cl, and Si atoms. Hence, the study confirmed the confinements of complex **4A**-molecules within the nanospheres.

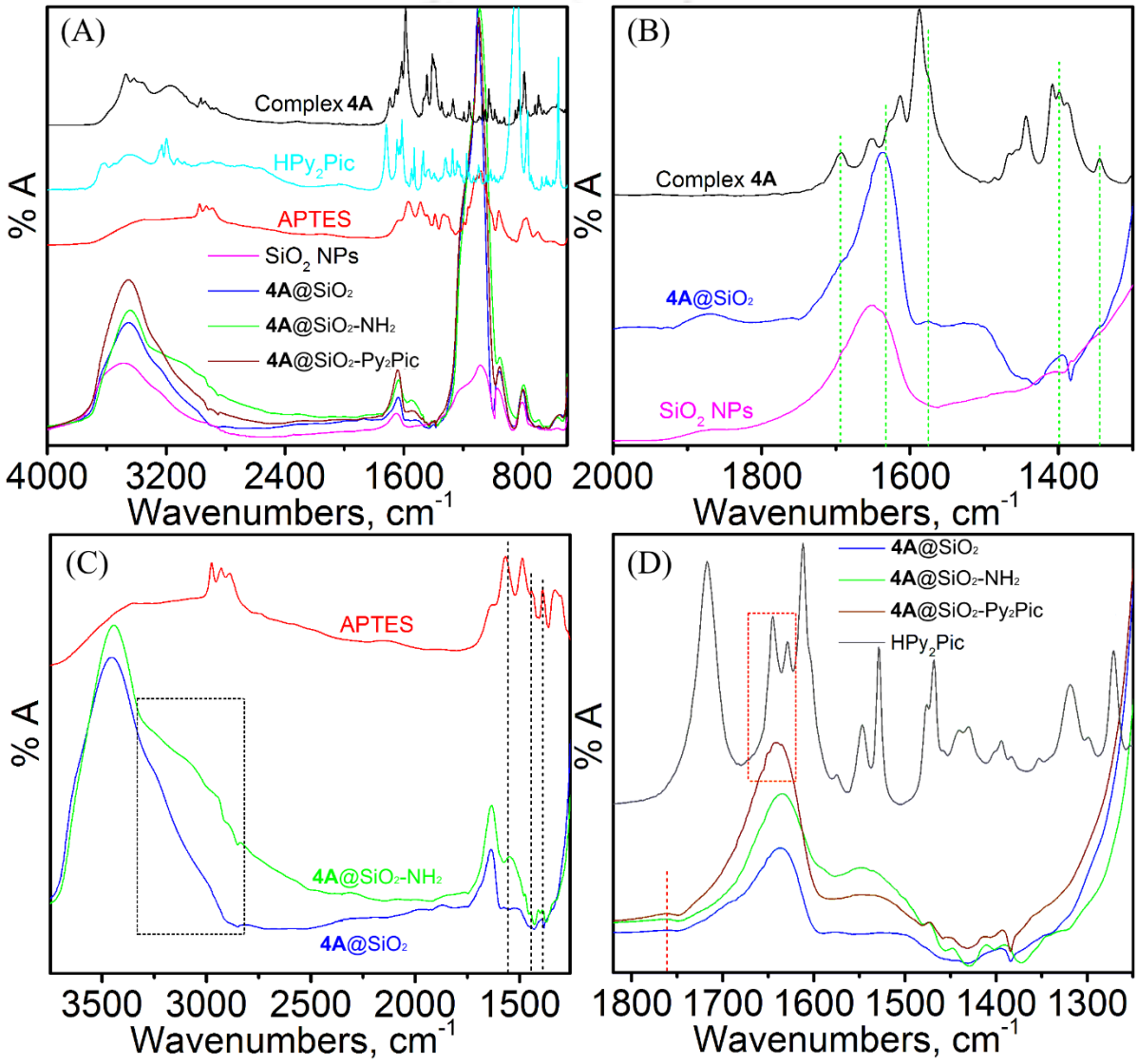

Figure 4.15. (A) FTIR spectra of **4A**@SiO_2NP, **4A**@SiO_2–NH_2NP, and **4A**@SiO_2–Py_2PicNP compared to the spectra for pristine SiO_2 NPs, Complex **4A**, HPy_2Pic and APTES. (B)-(D) Zoomed in regions.

To further support the incubation, infrared (IR) spectra of the lyophilized **4A**@SiO_2 (prepared by omitting the addition of APTES), Complex **4A**, and pristine silica NPs were compared. In the **4A**@SiO_2 IR spectrum, low-intensity bands at 1694, 1578, 1444, and 1400 cm^{-1} appeared, which were also present in the IR spectrum of complex **4A** (**Figure 4.15A** and **4.15B**). Thus, these spectral studies inferred the inclusion of the synthesized complex molecules within the nanoparticle. The presence of the additional broadband at 3321 cm^{-1} due to ν_{N-H} stretching and the moderate peak at 1559 cm^{-1} because of ν_{N-H} bending confirmed the formation of **4A**@SiO_2–NH_2NP (**Figure 4.15C**). The appearance of additional peaks in the 1665-1619 cm^{-1} region ascertained the conjugation of the Py_2Pic moiety with the amine group, resulting in the amide linkage (**Figure 4.15D**).

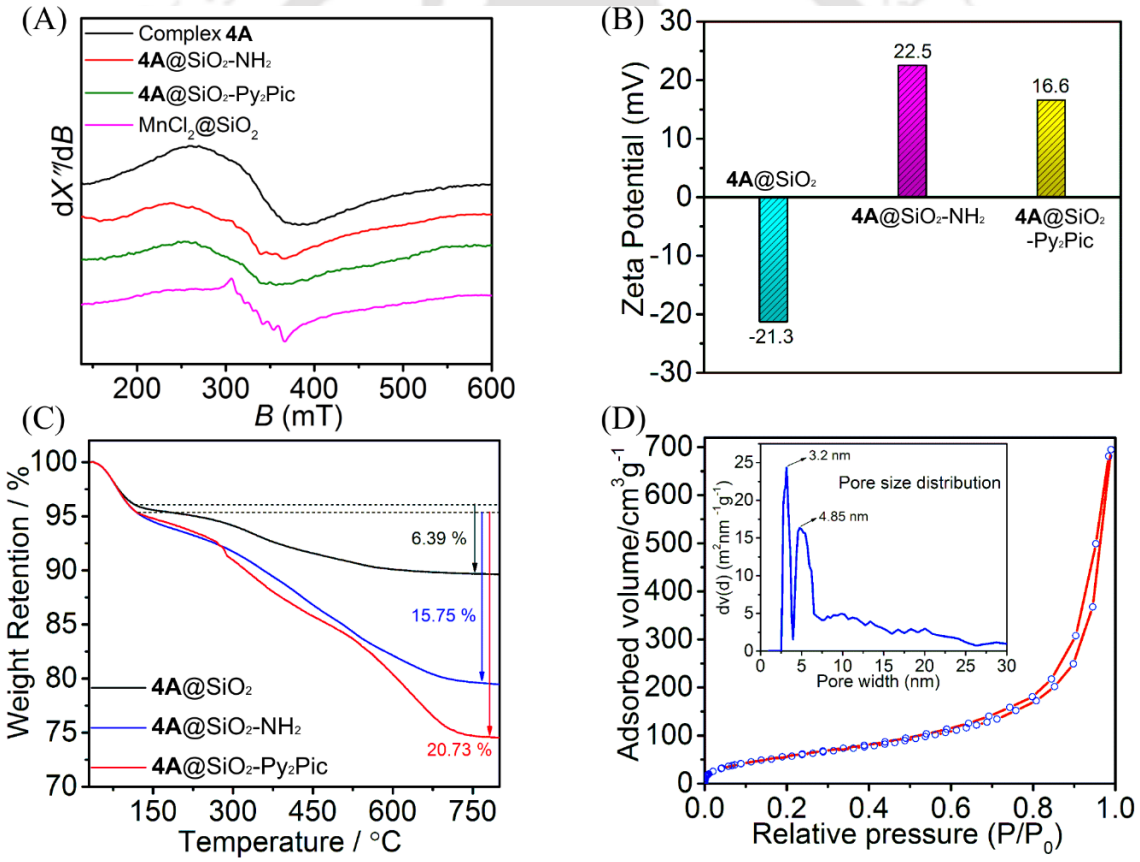

Figure 4.16. (A) X-band EPR spectra of complex **4A**, **4A**@SiO_2–NH_2, **4A**@SiO_2–Py_2Pic and $MnCl_2$@SiO_2 measured in the solid state, at room temperature, power = 0.995 mW, modulation frequency = 100 kHz, and modulation amplitude = 100 G. (B) Zeta potentials (at pH ~ 7.4) and (C) TGA analysis spectra of **4A**@SiO_2NP, **4A**@SiO_2–NH_2NP, and **4A**@SiO_2–Py_2PicNP. (D) N_2 adsorption-desorption isotherm and pore size distribution (inset) of **4A**@SiO_2–Py_2PicNP.

To buttress the confinement, X-band EPR spectra of the dried **4A**@SiO_2–NH_2 and **4A**@SiO_2–Py_2Pic nanomaterials were compared with that of complex **4A**. All the spectra exhibited a similar broad signal, verifying the existence of incorporated complex **4A**-molecules within the nanomaterials (**Figure 4.16A**). Noteworthy, the X-band EPR spectral envelope differed significantly compared to that of bare $MnCl_2$ solution-doped SiO_2 nanoparticles prepared by the identical method (**Figure 4.16A**, pink line). Moreover, the surface modification was further examined by determining the change in the zeta (ζ) potential profile of each nanomaterial in a buffered solution at pH ~ 7.4 (**Figure 4.16B**, **Table 4.4**). **4A**@SiO_2NPs exhibited a strongly negative ζ potential value (–21.3 mV) due to the presence of -OH functional groups at the surface of the NP. Upon the functionalization with the highly basic amino group, an inversion of ζ potential value to 22.5 mV was noticed. The value diminished moderately to 16.6 mV upon Py_2Pic conjugation with some of the amino groups.

Thermogravimetric analyses (TGA) of all three different types of nanomaterials were performed to realize the organic loading percentage (**Figure 4.16C**) on the outer surface. A steep increase in weight loss from 6.39 % in **4A**@SiO_2NP to 15.75 % in **4A**@SiO_2–NH_2 has been observed above 120 °C. This feature implied the inclusion of APTES units on the silica surface. The percentage of weight loss further increased by 5 units in the case of **4A**@SiO_2–Py_2PicNP, suggesting the successful inclusion of Py_2Pic units.

The N_2 adsorption-desorption isotherm was recorded at 77 K to evaluate the porous nature of the silica nanosphere in **4A**@SiO_2–Py_2PicNP. A type-IV isotherm was realized, typical for porous silica nanoparticles (**Figure 4.16D**).[21] The overall surface area of the nanoparticle was 219.48 m^2/g. Pore size distribution, derived by the Barrett-Joyner-Helenda (BJH) method, showed the presence of two different sizes of pores; 3.2 nm and 4.85 nm. The larger pores might be because of inter-particle voids.[3b] Nonetheless, to evaluate the free access of water molecules across the pores, **4A**@SiO_2–Py_2PicNP was suspended in H_2O for 48 hours in the presence of 0.6 mM BSA and 40 equivalent amounts of Zn(II) ions and then lyophilized for 24 hours to isolate dry **4A**@SiO_2@Py_2–PicNP•BSA•Zn ternary system (*vide infra*). A portion of the isolated system was again immersed in D_2O for 48 hours. Followed by lyophilization for 24 hours, the dried nanoparticles were isolated. The IR spectra comparison of the isolated particles from H_2O and D_2O

media revealed the appearance of additional $\nu_{(O-D)}$ asymmetric stretch in 2400-2500 cm^{-1} region in the presence of D_2O, indicating the existence of the molecules inside the nanoparticle (**Figure 4.17**). Therefore, IR spectra analyses confirmed the accessibility of outside water molecules across the nanopores.

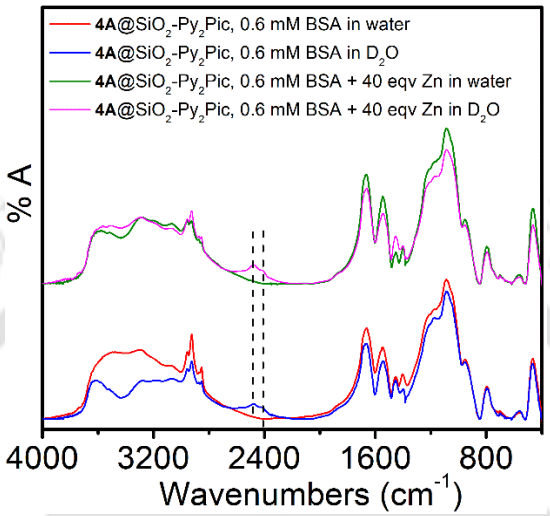

Figure 4.17. FTIR spectra of lyophilized **4A**@SiO_2–Py_2PicNP, recovered after suspending in 0.6 mM BSA solution in water (red line), in 0.6 mM BSA solution in D_2O (blue line), in 0.6 mM BSA and 40 eqv. Zn(II) solution in water (green line), and in 0.6 mM BSA and 40 eqv. Zn(II) solution in D_2O (pink line).

Table 4.4. Characterization of **4A**@SiO_2, **4A**@SiO_2–NH_2, **4A**@SiO_2–Py_2Pic nanomaterials: corresponding FETEM particle size, zeta potential values (at pH 7.4) and percentage organic weight loss, measured at 37 °C, pH ~ 7.4, 1.41 T.

Material	Particle Size (nm)	ζ potential (mV)	TGA, weight loss %
4A@SiO_2	13.22	-21.3	6.39
4A@SiO_2–NH_2	14.05	22.5	15.75
4A@SiO_2–Py_2Pic	14.95	16.6	20.73

4.7 Relaxometry and Physicochemical Studies of 4A Incorporated Nanomaterials

The contrast efficiency of the synthesized complex **4A**, and the subsequent complex confined nanoparticles, **4A**@SiO_2–NH_2 and **4A**@SiO_2–Py_2Pic, was determined by evaluating the relaxivity values, r_1, which is defined as the increment in longitudinal water proton relaxation rates instigated by addition of 1 mM concentration of the paramagnetic contrast species. T_1 and T_2 values of complex **4A** solutions, and **4A**@SiO_2, **4A**@SiO_2–NH_2 and **4A**@SiO_2–Py_2Pic suspensions were determined using BRUKER minispec mq60 NMR analyzer at pH ~ 7.4, 1.41 T, 37 °C. The exact Mn concentration in each sample was determined using ICP-MS and ICP-AES techniques. Plots of relaxation rates ($1/T_1$ and $1/T_2$) *versus* [Mn(II)] gave straight lines, slope representing the respective relaxivity values (r_1).

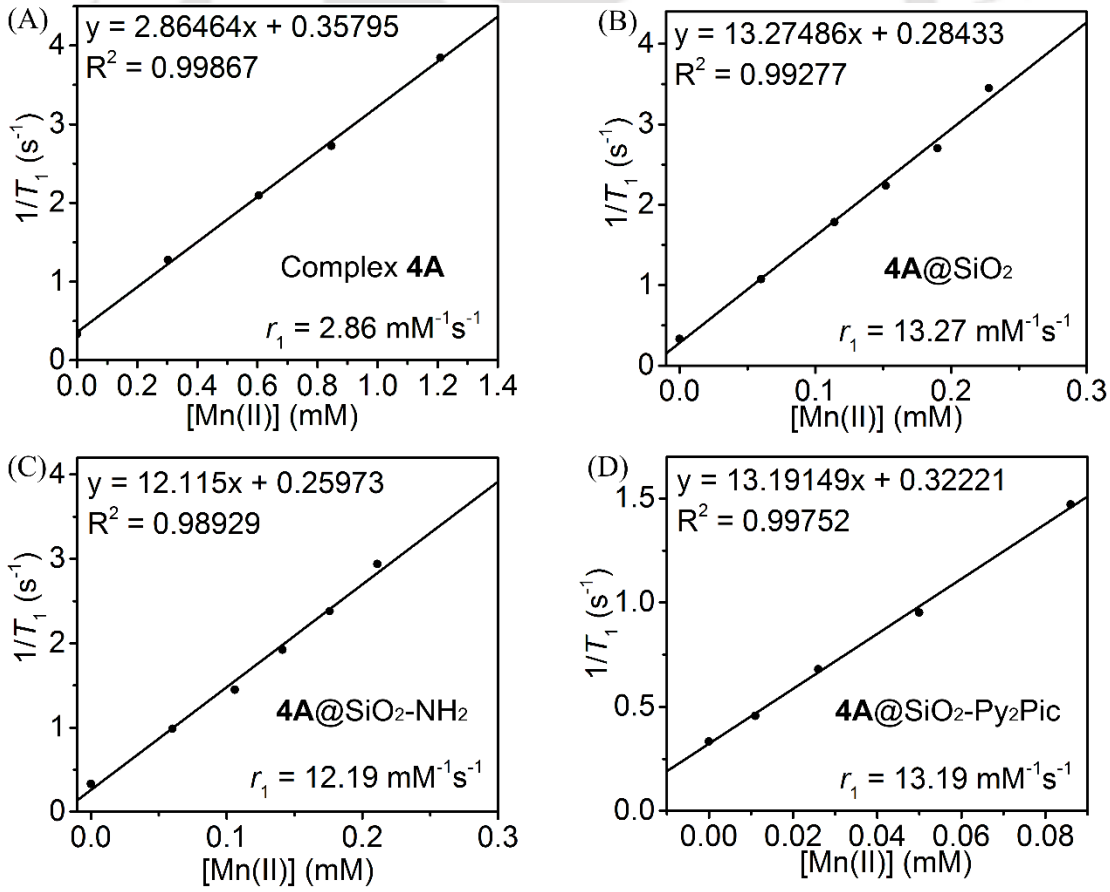

Figure 4.18. $1/T_1$ *vs* [Mn(II)] plot for (A) complex **4A**, (B) **4A**@SiO_2, (C) **4A**@SiO_2–NH_2NP, and (D) **4A**@SiO_2–Py_2PicNP. Experiments were done at 1.41 T, 37 °C, and pH ~ 7.4.

The longitudinal relaxivity (r_1) value of complex **4A** was determined as 2.86 $mM^{-1}s^{-1}$ at 1.41 T, 37 °C, and pH ~ 7.4 (HEPES, 0.01 M). The value increased to 13.27 $mM^{-1}s^{-1}$ in **4A**@SiO_2NP. This result implied that the rotational correlation time (τ_R) of the impregnated Complex **4A** molecules (about 34 molecules confined per nanosphere) has been increased upon the confinement. To note, a similar observation has already been perceived in the previous chapter. Notwithstanding, the surface functionalization of **4A**@SiO_2NP either with APTES or APTES-Py_2Pic imparted no appreciable changes in the relaxivity value (**Figure 4.18**), indicating that the increase in the weight of the nanoparticles employing the outer sphere surface functionalization did not exert any profound effect to τ_R of the incubated complex **4A** molecules.

Relaxivity of synthesized nanomaterials, in the presence of serum albumin and Zn(II) ions

r_1 values for **4A**@SiO_2–NH_2 and **4A**@SiO_2–Py_2Pic suspensions were measured in the presence of bovine serum albumin (BSA) at physiological conditions (pH ~ 7.4, 37 °C, BSA concentration maintained at 4.5 % w/v; measured at 1.41 T), in absence and presence of external ions (Zn^{II}, Cu^{II}, Mg^{II}, and Ca^{II}). Samples were incubated for 3 hours before the experiment.

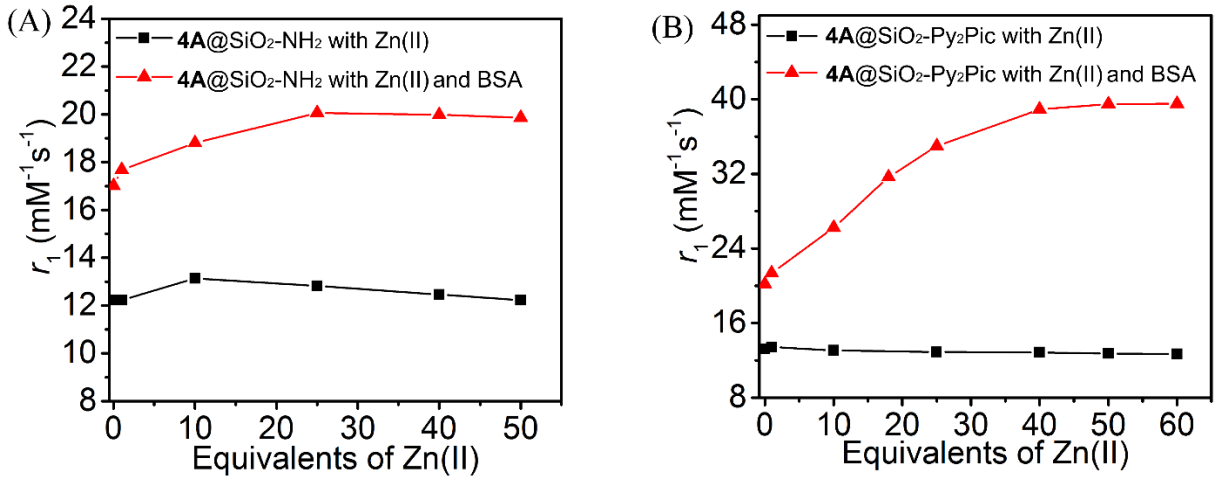

Figure 4.19. Relaxometric titrations for (A) **4A**@SiO_2–NH_2 and (B) **4A**@SiO_2–Py_2Pic suspensions, [Mn(II)] = 0.1 mM; as a function of Zn(II) ions, w.r.t. [Mn(II)] with or without BSA (constant concentration of 0.6 mM), at pH ~ 7.4, 1.41 T, and 37 °C.

Gratifyingly, for **4A**@SiO_2–Py_2PicNP suspensions, a 53 % increment in the relaxivity value to r_1 = 20.38 $mM^{-1}s^{-1}$ was accounted for in the presence of 0.6 mM BSA at 1.41 T, 37 °C, pH ~ 7.4, suggesting a considerable interaction between the nanoparticle and the negatively charged serum albumin protein to engender a slowly rotating binary system (**Figure 4.19B** and **4.20**, **Table 4.5**). The change in the ζ potential value from 16.6 mV to –11.4 mV ensured the substantial electrostatic and non-covalent interactions of the negatively charged serum albumin protein with the nanoparticle forming a corona (**Figure 4.21**, **Table 4.6**). The thermogravimetric weight loss analyses of **4A**@SiO_2–Py_2PicNP (**Figure 4.22A**) in the absence and the presence of BSA exhibited about 19 % more weight loss for the nanoparticle isolated after the interactions with BSA and justified the corona formation. Akin to **4A**@SiO_2–Py_2PicNP, an upliftment of r_1 relaxivity to 17.02 $mM^{-1}s^{-1}$ from 12.19 $mM^{-1}s^{-1}$, *i.e.*, about 40 %, in **4A**@SiO_2–NH_2NP (**Figure 4.19, Table 4.5**) has also been recognized in the presence of 0.6 mM BSA at 1.41 T, 37 °C, pH ~ 7.4. The TGA showed about 18 % more weight loss for the BSA-interacted **4A**@SiO_2–NH_2NP than the pristine nanoparticle (**Figure 4.22B**). Therefore, almost the same loading of BSA onto both nanoparticles was accounted for. The higher relaxivity value for **4A**@SiO_2–Py_2PicNP in the presence of BSA thus recommended a superior interaction between the BSA and the nanoparticle, which materialized due to the existence of Py_2Pic units.

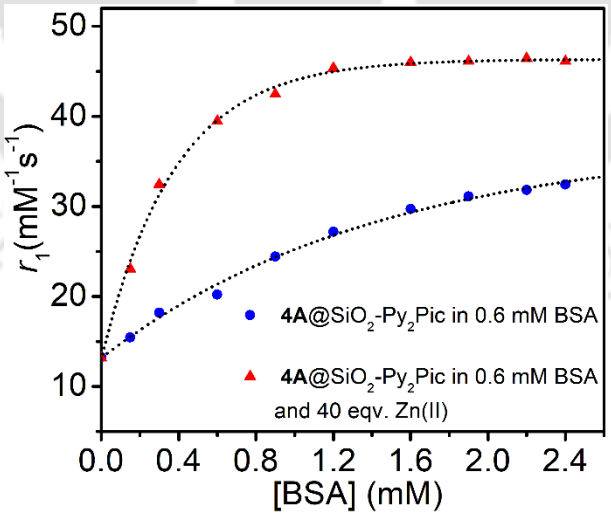

Figure 4.20. Relaxometric titrations of **4A**@SiO_2–Py_2PicNP (0.06 mM Mn(II) concentration) as a function of increasing concentration of BSA, in the absence and presence of 40 equiv. excess of Zn(II) ions. Measurements were done at pH ~ 7.4, 1.41 T, and 37 °C.

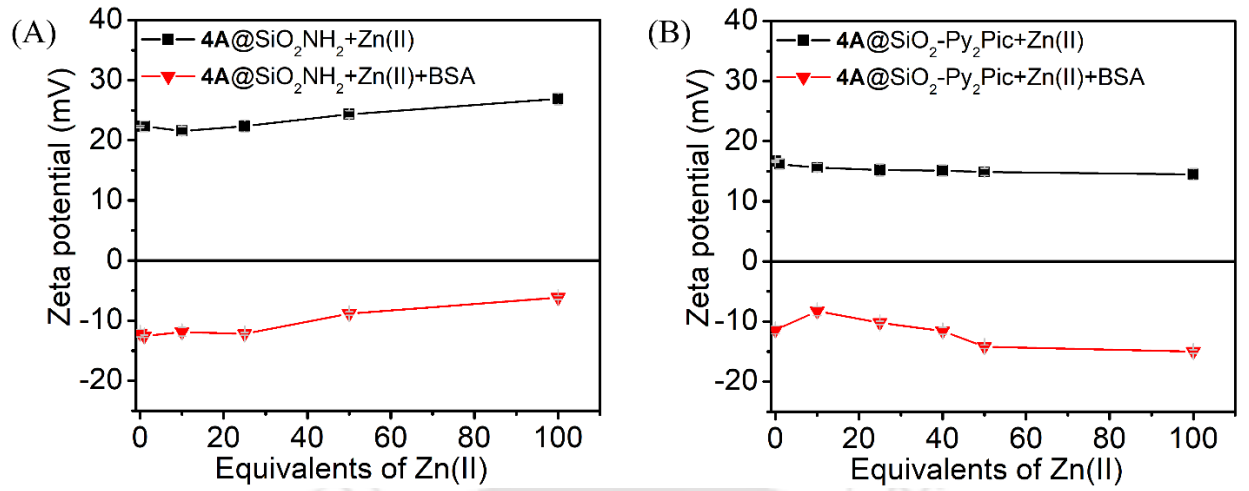

Figure 4.21. Zeta potential changes of (A) **4A**@SiO_2–NH_2NP and (B) **4A**@SiO_2–Py_2PicNP with increasing equivalents of Zn(II), in the absence and presence of 0.6 mM BSA, at pH ~ 7.4.

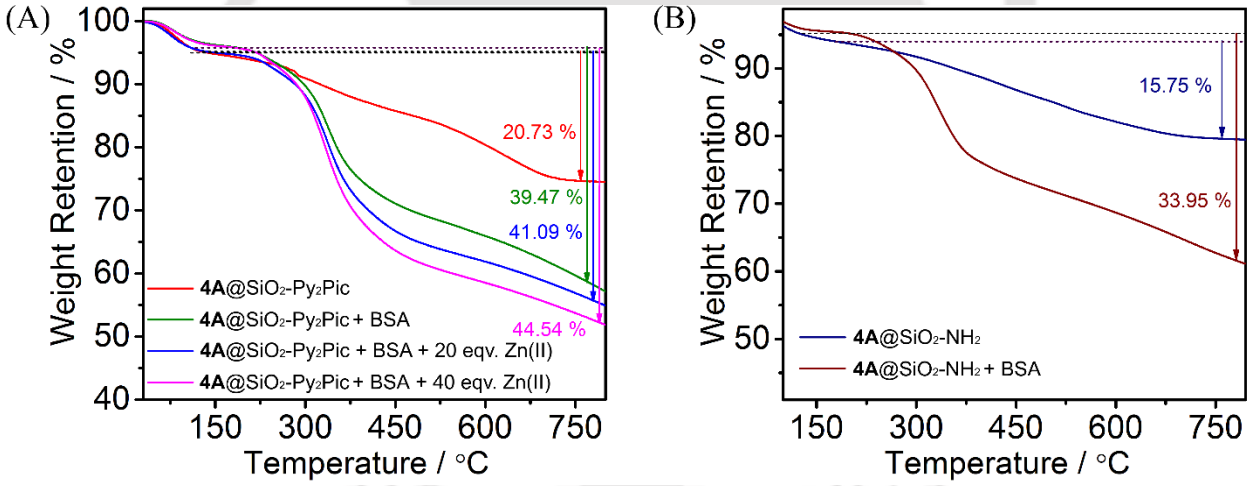

Figure 4.22. TGA analysis spectra for (A) **4A**@SiO_2–Py_2PicNP lyophilized solid obtained after isolating **4A**@SiO_2–Py_2PicNP from (i) water (red line), (ii) 0.6 mM BSA solution (green line), (iii) 0.6 mM BSA and 20 equiv. Zn(II) solution (blue line), and (iv) 0.6 mM BSA and 40 equiv. Zn(II) solution (pink line); (B) **4A**@SiO_2–NH_2NP lyophilized solid obtained after isolating **4A**@SiO_2–NH_2NP from (i) water (navy line) and (ii) 0.6 mM BSA (brown line).

Unlike **4A**@SiO_2–NH_2NP, a discernible and gradual augmentation in r_1 relaxivity was noticed in **4A**@SiO_2–Py_2PicNP with the successive elevation in the concentration of Zn(II) ions in HEPES buffer at pH 7.4 and reached to a constant value r_1 = 39.01 $mM^{-1}s^{-1}$ in the presence of 40 equivalent amounts of the ion (**Figure 4.19** and **4.20; Table 4.5**). Hence, the presence of the surface-bound Py_2Pic unit reinforced the interaction of the nanoparticle with BSA in the presence of Zn(II) ions. To further investigate the interaction phenomenon, the nanoparticle [0.1 mM Mn(II) concentration] was added to a solution premixed with 0.6 mM BSA protein and 4 mM Zn(II) ions (40 equiv. excess, *w.r.t* [Mn(II)]) at pH 7.4. In this case, the relaxivity value was found to be 46.3 $mM^{-1}s^{-1}$. Thus, a better interaction between the nanoparticle and Zn(II)-interacted BSA compared to BSA-interacted nanoparticle with Zn(II) ions was warranted.

Table 4.5. Relaxivity values for **4A**@SiO_2-NH_2NP and **4A**@SiO_2–Py_2PicNP in the absence and presence of Zn(II) ions/serum albumin.

Nanomaterial type	**r_1 ($mM^{-1}s^{-1}$), at pH ~ 7.4, 1.41 T, and 37 °C**			
	(-) Zn(II)	**(+) Zn(II)**	**(+) 0.6 mM BSA**	**(+) 0.6 mM BSA, (+) Zn(II)**
4A@SiO_2-NH_2	12.19	12.25	17.02	19.85
4A@SiO_2–Py_2Pic	13.19	12.92	20.38	39.01

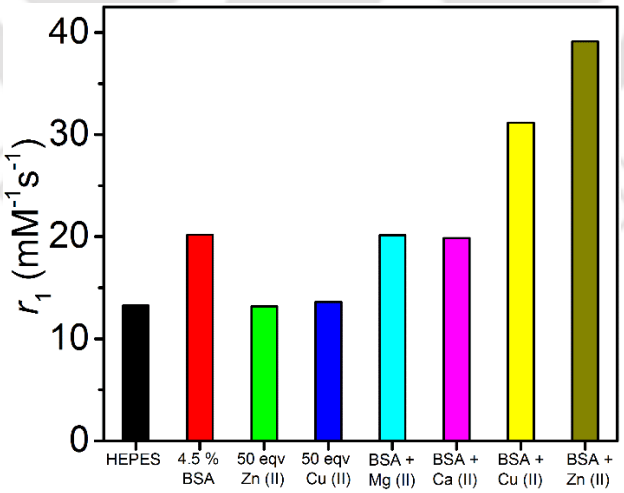

Figure 4.23. r_1 value for **4A**@SiO_2–Py_2PicNPs, [Mn(II)] = 0.1 mM, suspended in an aqueous medium containing 50 equivalent excess of Zn(II), Cu(II), Mg(II), and Ca(II) ions, in the absence and presence of 0.6 mM BSA at pH ~ 7.4, 1.41 T, and 37 °C.

To determine the ion selectivity in the presence of BSA conjugated **4A**@SiO_2–Py_2Pic nanomaterial, it was allowed to interact with 0.6 mM BSA and a 50-fold excess of the biologically relevant metal ions, Zn(II), Ca(II), Mg(II), and Cu(II). The longitudinal relaxivity of the subsequent nanoparticle suspensions was recorded at 1.41 T, 37 °C and pH ~ 7.4 (**Figure 4.23**). While no alteration in the relaxivity was noticed in the presence of Ca(II) and Mg(II) ions, amplification in the relaxivity value to r_1 = 31.17 $mM^{-1}s^{-1}$ was realized in the presence of 40 equivalent amounts of Cu(II) ions (w.r.t. [Mn(II)]). Firstly, the concentration of free Cu(II) ions is lower than Zn(II) in the extracellular space.[23] Secondly, the relaxivity enhancement was lower than Zn(II) ions. Hence, the prepared **4A**@SiO_2–Py_2PicNP can be utilized as a promising Zn(II) ion-selective biomarker.

***Fluorescence quenching experiment*:** The fluorescence quenching experiments were also conducted to evaluate the nature of interactions between the serum albumin protein and **4A**@SiO_2–Py_2PicNP (**Figures 4.24**).[24] Samples (aqueous suspensions) were recorded on FluoroMax-4 spectrofluorimeter (Horiba), at 25 °C, in a rectangular quartz cell with a path of 10 mm. Each set of suspensions was excited at 275 nm, using 5 per 5 nm (excitation/emission) slit widths. Emission spectra were recorded in the 280 to 530 nm range.

Stern-Volmer equation:

$$F_0/F = 1 + K_{sv}[Q] = 1 + k_q \tau_0[Q] \quad \textbf{(1)}$$

F_0 and F are the maximum fluorescence intensities in the absence and presence of quencher, respectively. k_q is the bimolecular quenching constant, which is a measurement of the efficiency of quenching. τ_0 is the average lifetime of the Trp 214 unit and it is equal to 5.8×10^{-9} s.[24b] [Q] is the quencher concentration.

$$\log[(F_0 - F)/F] = \log K_a + n\log[Q] \quad \textbf{(2)}$$

n is the number of binding sites and K_a represents the binding constant.

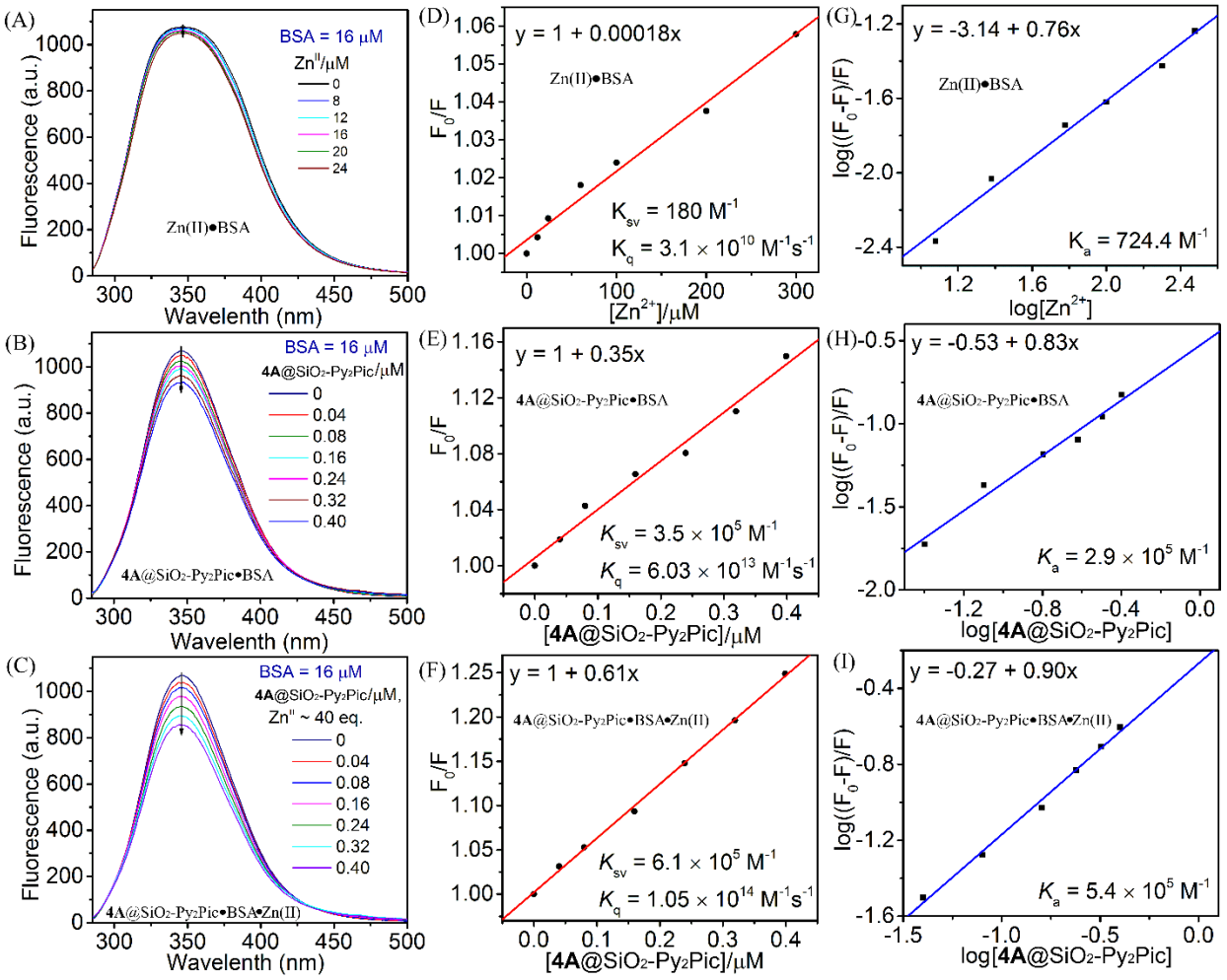

Figure 4.24. Estimation of Zn(II)•BSA, **4A**@SiO_2–Py_2Pic•BSA and **4A**@SiO_2–Py_2Pic:BSA•Zn(II) interactions by fluorescence spectroscopy. Fluorescence spectra of 16 μM BSA in the presence of an increasing concentration of (A) Zn(II) ions, (B) **4A**@SiO_2–Py_2PicNPs, and (C) Zn(II) ions and **4A**@SiO_2–Py_2PicNPs together. Respective Stern-Volmer constant plots (D)-(F); and log (F_0-F)/F plots (G)-(I) to find out corresponding quenching and affinity constants.

To an aqueous 16 μM solution of BSA, an increasing concentration of the nanoparticle (0 to 0.4 μM) was added. It was noticed that the quenching was expedited with the escalation of the concentration (K_{SV} = 3.5 × 10^5 M^{-1}; K_q = 6.03 × 10^{13} $M^{-1}s^{-1}$; K_a = 2.9 × 10^5 M^{-1}; **Figure 4.24, Table 4.6**). Interestingly, the quenching process was further boosted in the presence of 40 equivalent amounts of Zn(II) ions (K_{SV} = 6.1 × 10^5 M^{-1}; K_q = 10.5 × 10^{13} $M^{-1}s^{-1}$; K_a = 5.4 × 10^5 M^{-1}), asserting the ion promoted higher interaction between the nanoparticle and the protein. The

K_q value provides information on the nature and strength of the interactions. For the dynamic interaction, the value lies below 2×10^{12} $M^{-1}s^{-1}$, while, K_q greater than 2×10^{12} $M^{-1}s^{-1}$ refers to a static interaction. Herein, the high $K_q = 6.03 \times 10^{13}$ $M^{-1}s^{-1}$ emphasized a static interaction between **4A**@SiO_2–Py_2PicNP and BSA. The interaction further escalated in the presence of Zn(II) ions ($K_q = 10.5 \times 10^{13}$), consolidating a higher static interaction. The quenching experiments justified thus the upliftment of r_1 relaxivity *via* the formation of a much slowly rotating ternary system in the presence of Zn(II) ions.

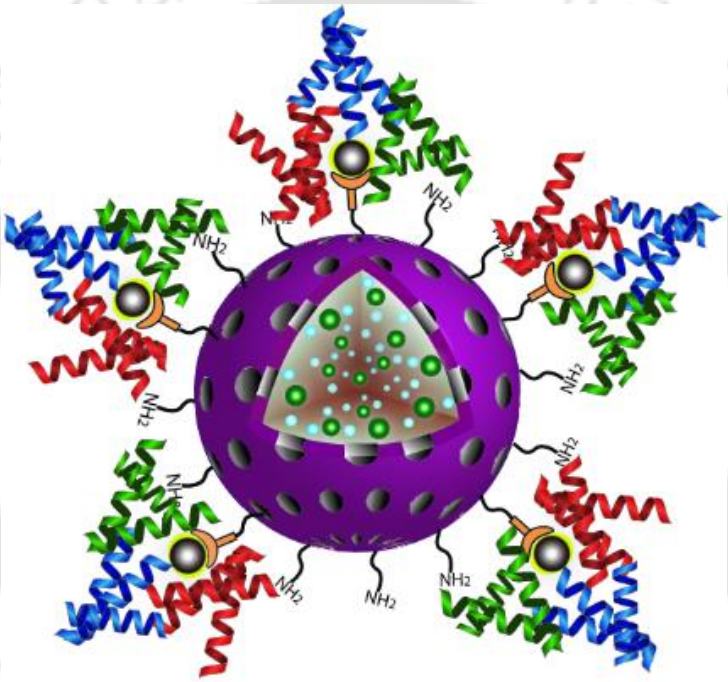

Figure 4.25. Schematic representation of **4A**@SiO_2–Py_2Pic•BSA•Zn(II) ternary system.

Table 4.6. Evaluation of interaction between **4A**@SiO_2–Py_2Pic and BSA, in the absence and presence of 40 equiv. excess Zn(II) ions by relaxometry, zeta potential, TGA, and fluorescence quenching studies.

Suspension medium	[a]r_1 ($mM^{-1}s^{-1}$)	ζ (mV)	TGA weight loss (%)	[b]r_1^{sat} ($mM^{-1}s^{-1}$)	[c]K_{sv} ($10^5\ M^{-1}$)	[c]K_q ($10^{13}\ M^{-1}s^{-1}$)	[c]K_a ($10^5\ M^{-1}$)
Water	13.19	16.6	20.73	—	—	—	—
BSA, 0.6 mM	20.18	-11.5	39.47	37.08	3.5	6.0	2.9
BSA, 0.6 mM and 40 equiv. Zn(II) ions	39.01	-11.6	44.54	46.55	6.1	10.5	5.4

Relaxometric studies were done at pH 7.4, 1.41 T, and 37 °C. [a] Each relaxivity value was obtained from $1/T_1$ versus [Mn(II)] ([Mn(II)] = 0.02, 0.04, 0.08, 0.10 mM) plots with samples suspended in different mediums, as mentioned. [Zn(II)] maintained at 40 equivalent excess amount, *w.r.t.* Mn(II) concentration. [b]Saturated relaxivity values obtained after fitting the titration curves of **4A**@SiO_2–Py_2PicNP (0.06 mM Mn(II) concentration) with increasing concentration of BSA, in the absence and presence of 40 equiv. excess of Zn(II) ions. [c]Binding sites (n) were found to be equal to 1 in each case.

4.8 Stability of 4A confined porous silica nanomaterials

Water protons, bicarbonates, biphosphates, citrates, and Zn(II) ions are abundantly present inside the living body and can potentially disintegrate the paramagnetic centre, thereby influencing the relaxivity of the system. The stability of the synthesized contrasting moiety must be estimated in the presence of these physiologically relevant scavenger ions prior to *in vivo* applications. In this context, pH stability as well as the rigidity of complex **4A** and **4A**@SiO_2–Py_2PicNP against the mentioned ions was tested by determining the corresponding r_1 values.

The complex **4A** showed appreciable stability as a subtle change in the longitudinal relaxivity value was evidenced in the pH range of 4-10, or when challenges with 200-fold excess of HCO_3^{1-}, HPO_4^{2-} and $C_6H_5O_7^{3-}$ ions at physiological pH (~ 7% increase, presumably due to the formation of or aggregation of complex molecules by the quaternary interactions with the anions); measured at 1.41 T and 37 °C (**Figure 4.26**). However, the complex showed minimal kinetic

inertness akin to similar acyclic, mono-aquated Mn(II)-systems (MnEDTA, MnTMDTA, MnEGTA, *etc*.). The relaxivity value, therefore, increases instantaneously to 6.62 $mM^{-1}s^{-1}$ on the additions of zinc ions, reflecting the formation of free Mn(II) ions. This prevented the applicability of the bare complex for *in vivo* studies.

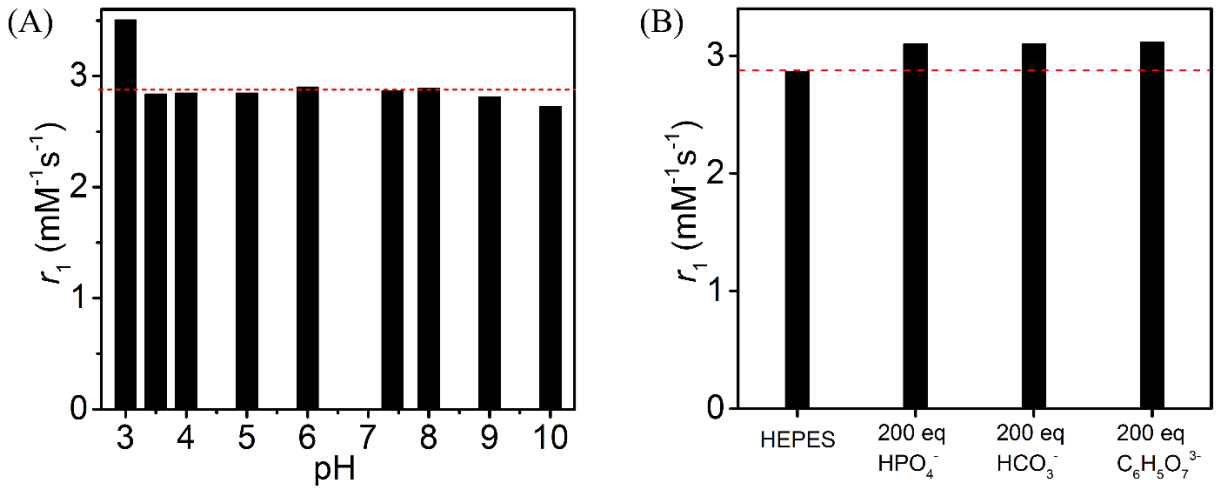

Figure 4.26. r_1 values for **4A** solutions, (A) in the pH range 4.0-8.0, and (B) in the presence of 200 equivalents excess of different physiologically relevant anions, at pH 7.4; [Mn(II)] = 0.1 mM.

In **4A**@SiO_2–Py_2PicNP, no alteration in the relaxivity (13.19 $mM^{-1}s^{-1}$) was realized in the pH range 4-8 and the presence of 200-fold excess of biologically relevant anions; citrate, biphosphate, and bicarbonate (**Figure 4.27**). Furthermore, the kinetic inertness of the synthesized nanomaterial (**4A**@SiO_2–Py_2Pic) was evaluated against 40-fold excess Zn(II) ions, following time-dependent r_1 values for **4A**@SiO_2–Py_2PicNPs suspension, 0.1 mM w.r.t. [Mn(II)], at pH ~ 6.0 (MES buffer, 0.01M), 1.41 T, and 37 °C. The synthesized nanomaterial having a positively charged surface (ζ = +16.6 mV) showed efficient inertness towards Zn(II) ions as only ~ 3% decrease in r_1 value was observed after 24 hours (**Figure 4.27C**). This minute change could be ascribed to spontaneous coagulation of nanoparticles with time leading to lowered accessibility of water molecules towards the core, as previously reported for a similar nanomaterial in the previous chapter. Thus, it is expected that the contrast efficiency of the nanoparticle *in vivo* would not be hampered due to the presence of the physiologically prevalent cations and anions, consolidating its potential for *in vivo* applicability.

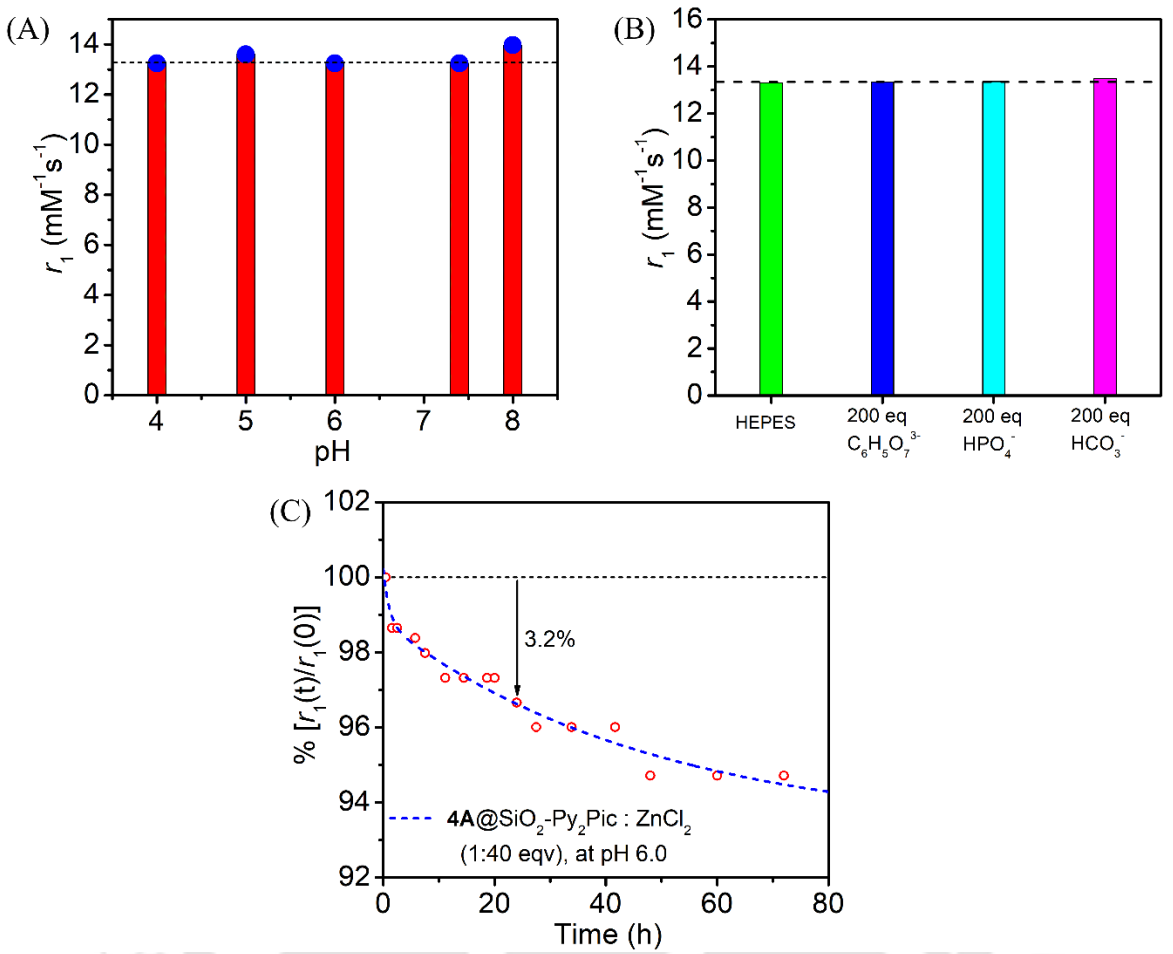

Figure 4.27. r_1 values for **4A**@SiO$_2$–Py$_2$PicNP suspension, (A) in the pH range 4.0-8.0, and (B) in the presence of 200 equivalents excess of different physiologically relevant anions, at pH 7.4; [Mn(II)] = 0.1 mM.

4.9 Phantom Imaging of 4A@SiO$_2$–Py$_2$PicNP in water and serum albumin, at 1.5 T

To shed light on the contrast ability of **4A**@SiO$_2$–Py$_2$PicNP in the presence of BSA and Zn(II) ions *in vitro*, phantom images were recorded using a MAGNETOM Avanto 1.5 T clinical MRI scanner at 25 °C. For T_1-weighted images, respective parameters were adopted: TR (repetition time) = 550 ms, TE (echo time) = 8.4 ms, slice thickness = 2.5 mm, and field of view (FOV) = 175×200 mm^2.

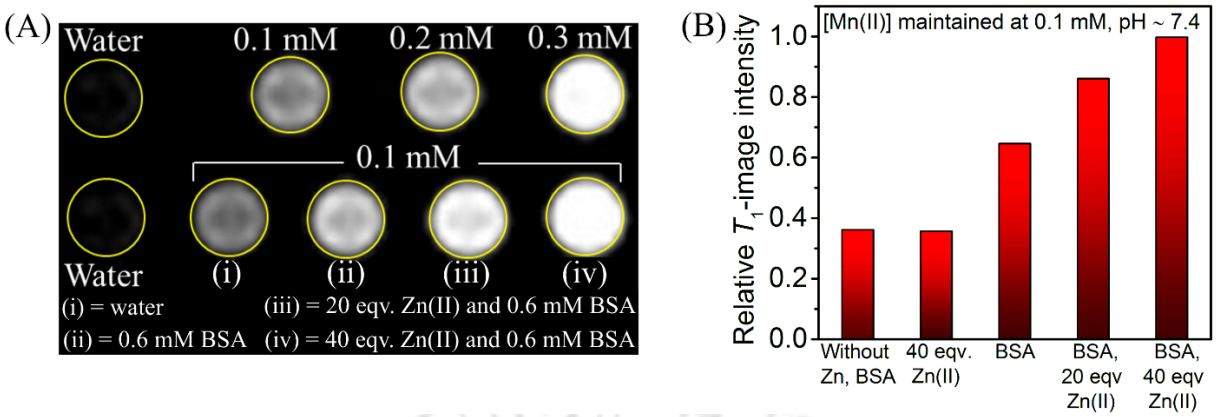

Figure 4.28. *In-vitro* studies of **4A**@SiO_2–Py_2PicNPs at 1.5 T and 25 °C. (A) T_1-weighted phantom MR images of micro-centrifuge tubes containing different concentrations of the nanomaterial (top). In the bottom, **4A**@SiO_2–Py_2PicNPs, 0.1 mM [Mn(II)], were suspended in a different medium, as mentioned; (B) Respective MR-image intensity plots using *ImageJ* software.

Herein, phantoms are micro-centrifuge tubes filled with: (1) **4A**@SiO_2–Py_2PicNP suspension; (2) **4A**@SiO_2–Py_2PicNP suspension in 0.6 mM BSA; and (3) **4A**@SiO_2–Py_2PicNP suspension, 0.6 mM BSA and Zn(II) ions with various concentration in HEPES buffer at pH 7.4. The observed contrast changes are depicted in **Figure 4.28**. The gradual increase in the concentration of **4A**@SiO_2–Py_2PicNP from 0.1 to 0.3 mM resulted in simultaneous brighter T_1-weighted images. Hence, the nanoparticle can be recognized as a brightening (positive) contrast agent. After adding BSA, about 75% brightness enhancement of 0.1 mM **4A**@SiO_2–Py_2PicNP suspension was realized. Accordingly, the successive increase in Zn(II) ions concentration in the BSA-containing solution gradually amplified the image brightness. Thus, the relaxivity boosting in the presence of BSA and Zn(II) ions has also been recognized *in vitro* phantom MR images.

4.10 Cytotoxicity Assay of 4A@SiO_2–Py_2PicNP

Before in vivo administration, the biocompatibility of **4A**@SiO_2–Py_2PicNPs was examined on PC3 and HeLa cells by performing the MTT assay. In the studies, cells were incubated for 48 hours with an increasing concentration of the nanoparticle up to 150 μM level, and

respective absorbance was measured at 570 nm. After that, cell viability was calculated, considering 100% viability for untreated cells (**Figure 4.29**). About 80% cell viability was realized at 150 μM concentration for both types of cells, emphasizing the biocompatibility of the nanoparticle.

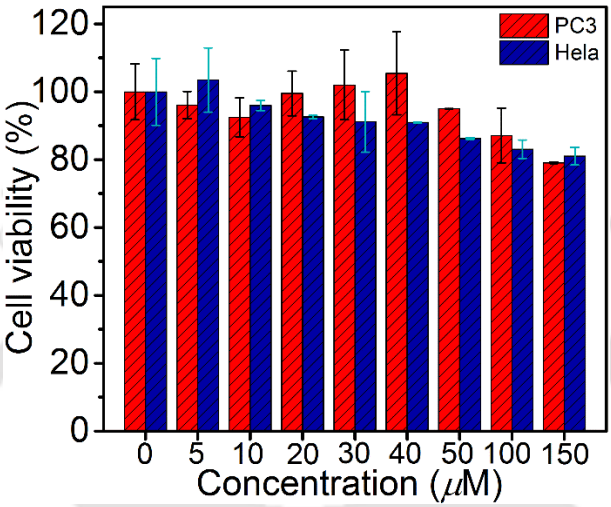

Figure 4.29. % Cell viability of HeLa and PC3 cell line after 48 hours of treatment of each with increasing concentration of **4A**@SiO_2–Py_2PicNPs. The concentrations are represented in terms of Mn(II) ions.

4.11 In vivo MRI of 4A@SiO_2–Py_2PicNP, at 7 T

Depending on the aforementioned *in vitro* experimental results, we attempted to emulate the Zn(II) ion-driven contrast enhancement in the pancreas in the presence of glucose bolus in the biological system.[14a] In this regard, *in vivo* MR imaging was recorded on a batch of healthy C57BL/6 male mice (total number = 30), at 7 T. 12 hours fasted mice were anaesthetized with 1-3% isoflurane/oxygen mixture maintaining normal respiration and the body temperature to 37 °C. It was subsequently imaged at 7 T using a small-bore animal scanner (Biospec 70/20, M/s Bruker Biospin GmBH, Germany). The imaging protocol at baseline comprised multislice two-dimensional rapid acquisition with refocused echo (RARE) imaging to delineate anatomy. Imaging parameters were: Coronal orientation, TR/TE = 3647.4 ms/8 ms, the field of view (FOV) = 50×50 mm, matrix = 256×256, slice thickness = 1 mm, 256 slices; Axial orientation: TR/TE = 3647.4 ms/8 ms, matrix = 256×256, slice thickness = 1 mm, 84 slices.

In separate experiments, a bolus of **4A**@SiO_2–Py_2PicNP (10 μmol/kg w.r.t. [Mn(II)]) was injected into the intraperitoneal (i.p.) space with and without the presence of glucose (2.2 mmol/kg) in 12 hours of fasted mice. Elaborately, five groups of mice (n = 3/group) were each intraperitoneally (i.p.) administered with **(I)** 10 μmol/kg w.r.t. [Mn(II)] of **4A**@SiO_2–Py_2PicNPs plus 2.2 mmol/kg D-glucose (45 min post administration of contrast agent), **(II)** 10 μmol/kg w.r.t. [Mn(II)] of **4A**@SiO_2–Py_2PicNPs plus saline (0.9%), **(III)** 10 μmol/kg w.r.t. [Mn(II)] of **4A**@SiO_2–NH_2NPs plus 2.2 mmol/kg D-glucose (45-minute post administration of contrast agent), **(IV)** 10 μmol/kg w.r.t. [Mn(II)] of **4A**@SiO_2–NH_2NPs plus saline (0.9%), and **(V)** 10 μmol/kg w.r.t. [Gd(III)] of Dotarem® solution in PBS; followed with sequential T_1-weighted scans. Animals were scanned at different times, from 50 min post-contrast injection (5 min after glucose bolus) to 24 h. *ImageJ* software was used to analyse image intensity in the region of interest (ROI) of different organs, and the intensity values were normalized with the ROIs estimated on the back muscle of that animal of the same slice and time point (considered as contrast-to-noise ratio, CNR). The change in respective image intensity has been reported in percentage values compared to pre-contrast injection scans (% ΔCNR). Signal intensities of ROIs of different organs were monitored for 24 h post contrast administration, and the area under analysis and statistical significance was calculated using unpaired two-tailed *t*-tests to correlate between each material; p-values < 0.05 were considered significant.

T_1-weighted MR images in coronal and axial view (post 1 h **4A**@SiO_2–Py_2PicNPs injection or 15 min post glucose injection) are presented in **Figure 4.30**. The contrast enhancement became almost twice (ΔCNR ~ 100%) in the pancreas compared to the pre-injected MR image in the presence of **4A**@SiO_2–Py_2PicNP after 1 hour of the bolus injection. However, in the presence of glucose, a substantial contrast enhancement (ΔCNR ~ 138%) was realized buttressing the interaction of the contrast agent with the secreted Zn(II) ions (**Figure 4.30C**) forming **4A**@SiO_2–Py_2PicNPs•HSA•Zn(II) ternary complex. Further elucidation of Zn(II) ions secretion and the contrast enhancement due to entrapment of the ion within **4A**@SiO_2–Py_2PicNP•HSA binary system appeared when **4A**@SiO_2–NH_2NP, which has already been recognized to promote a little r_1 relaxivity enhancement *in vitro* in the presence of Zn(II) ions (*vide supra*), was investigated under the same experimental condition (as control). A subtle contrast enhancement (~ 8%) was

realized in this case, and the finding consolidated the effectiveness of **4A**@SiO_2–Py_2PicNP to bind with HSA and Zn(II) ions *in vivo*.

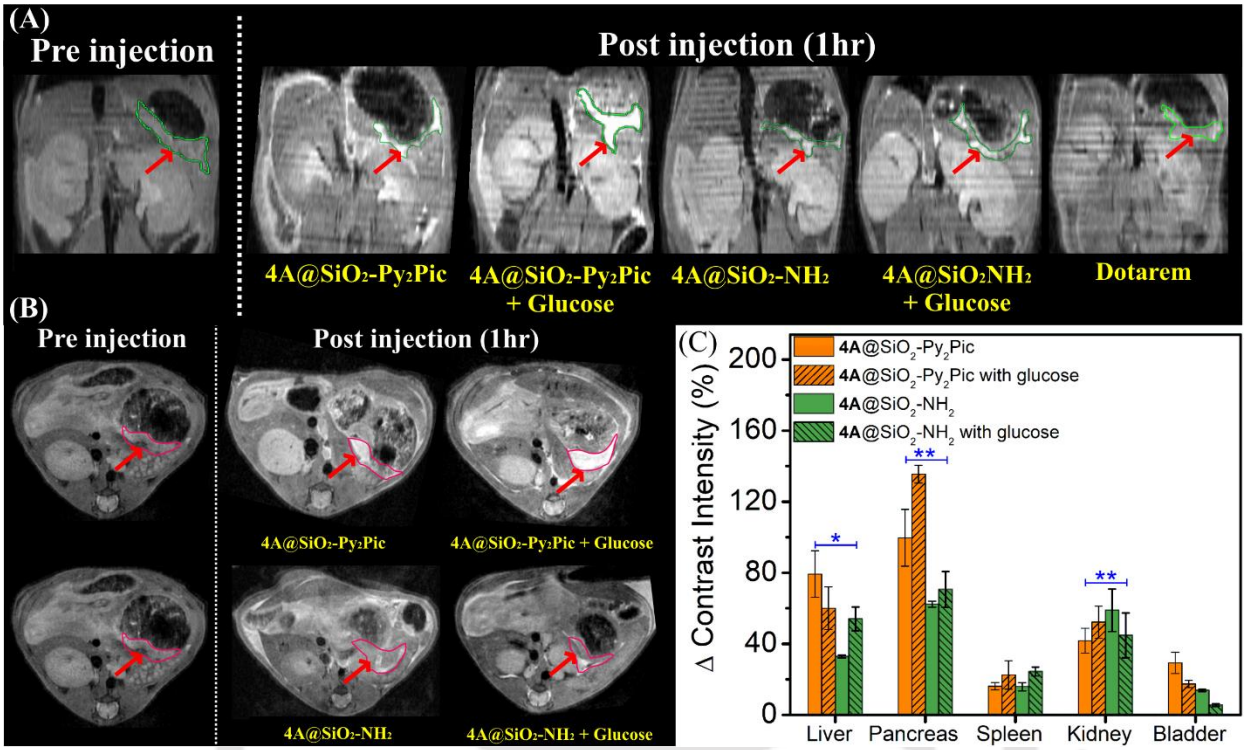

Figure 4.30. (A) Coronal view, and (B) Axial view of T1-weighted MR images of 12-hour fasted C57BL/6 mice, before and 1 hour after i.p. administration of **4A**@SiO_2–NH_2 or **4A**@SiO_2–Py_2Pic (10 μmol/kg w.r.t [MnII]), without or with single bolus (i.p.) of 2.2 mmol/kg D-glucose (given after 45 min contrast injection), at 7 T animal MR scanner. The red arrow marks the Pancreas region. Dotarem was injected at the same dosage, along with a glucose bolus. (C) Quantitative image analysis by measuring signal intensity changes in each organ post-injection, normalized to the muscle (n = 3 animal per group). Bars represent the standard error of the mean. ∗P < 0.05, ∗∗P < 0.001.

Thus, the porous silica nanoparticle entrapped complex **4A** with the Py_2Pic silica-surface-binding unit was successful in engendering Zn(II) ion-responsive T_1-weighted MRI contrast agent as previously reported by Sherry and coworkers employing $[Mn^{II}PyC3A-BPEN(OH_2)]^-$ complex molecule.[14a] In the case of the small Mn(II) complex molecule, a maximum of ~ 55%

contrast enhancement was realized. On the other hand, **4A**@SiO_2–Py_2PicNP could provide ~ 138% contrast enhancement in an hour due to the formation of a slow-moving system.

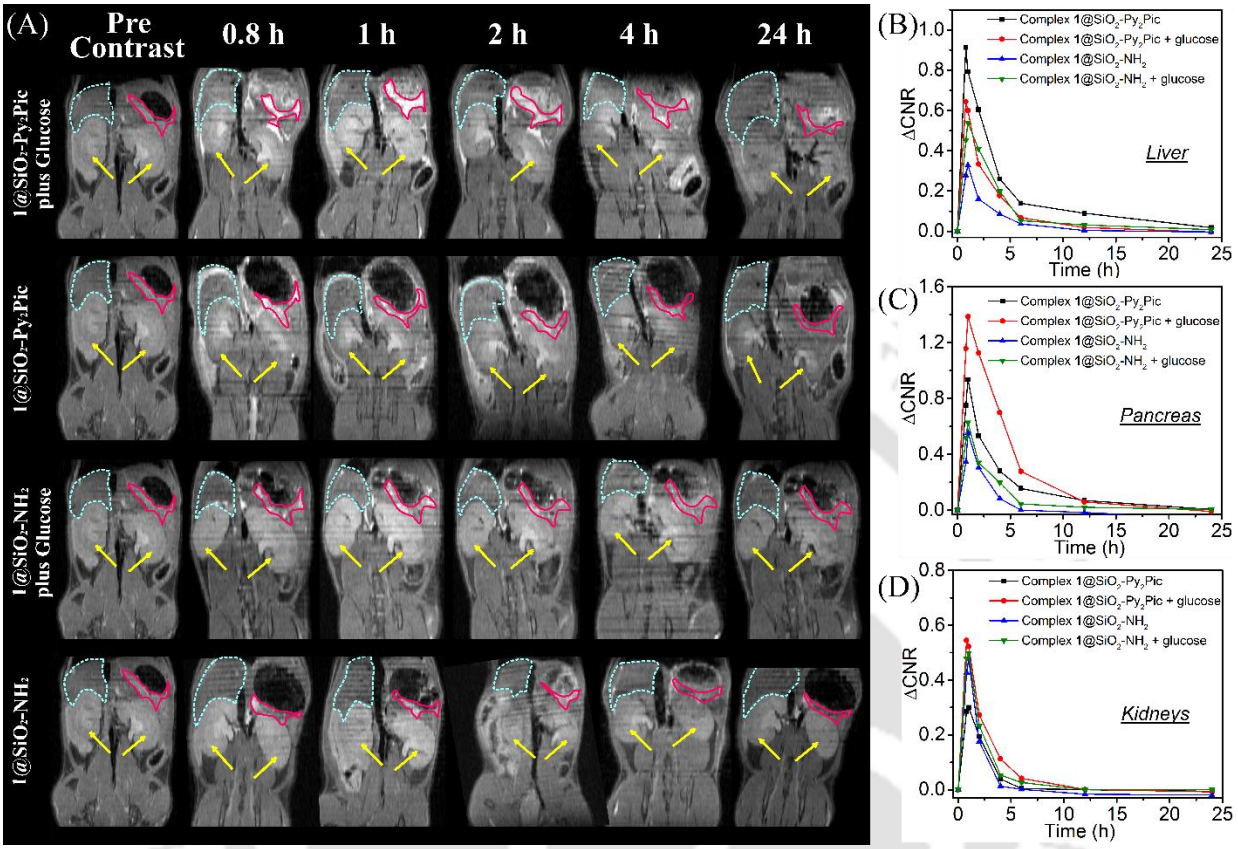

Figure 4.31. (A) T_1-weighted coronal images of mice showing contrast changes in the liver (blue dotted line), pancreas (red line), and kidneys (yellow arrow) at different time points, post administration of **4A**@SiO_2–NH_2 or **4A**@SiO_2–Py_2Pic, without or with D-glucose, at 7 T animal MR scanner. Images at 0.8 h are the images immediately collected after the glucose bolus injection. Average contrast-to-noise ratio (CNR) changes in the different regions of interest (ROIs): (B) Liver, (C) Pancreas, and (D) Kidneys; plotted with time after contrast administration (pre-contrast image intensity considered as baseline).

The biodistribution of **4A**@SiO_2–Py_2PicNPs and **4A**@SiO_2–NH_2NPs without and with the presence of glucose was examined at 1 hour of post-injection of the nanoparticles (**Figure 4.32**). In this context, the liver, pancreas, spleen, muscle, kidney, and bladder were resected, and the Mn content was determined by the ICP-MS technique after digestion of the tissues in aqua-regia. The time-dependent contrast enhancement studies in respective organs together with the biodistribution

studies consolidated the presence of the manganese ions in the liver and the kidney. This reinforced that the nanoparticles excreted from the body *via* both hepatobiliary (40%) and renal (60%) pathways.[25] However, the renal path was more favourable. Further investigations are essential to illuminate the interactions of the nanoparticles with various organs. Herein, it is noted that the mice engaged in the experiments were monitored further for 15 days after the completion of *in vivo* experiments. No death or abnormal behaviours were noticed.

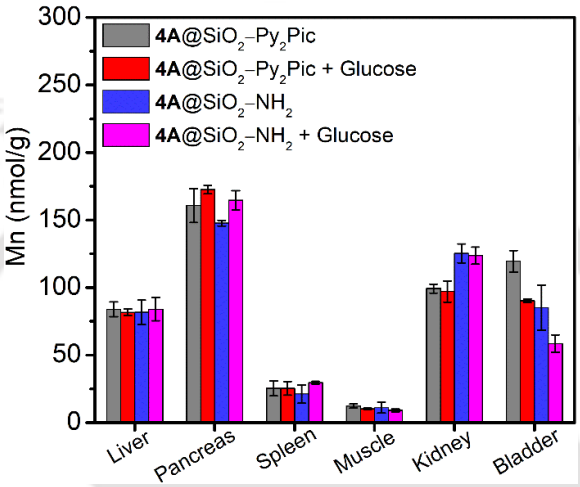

Figure 4.32. Manganese content in mice organ tissues, obtained by ICP-MS studies, 1 hour after intraperitoneal administration of respective contrast agents (10 μmol/kg w.r.t. [Mn(II)]) along without or with glucose (2.2 mmol/kg).

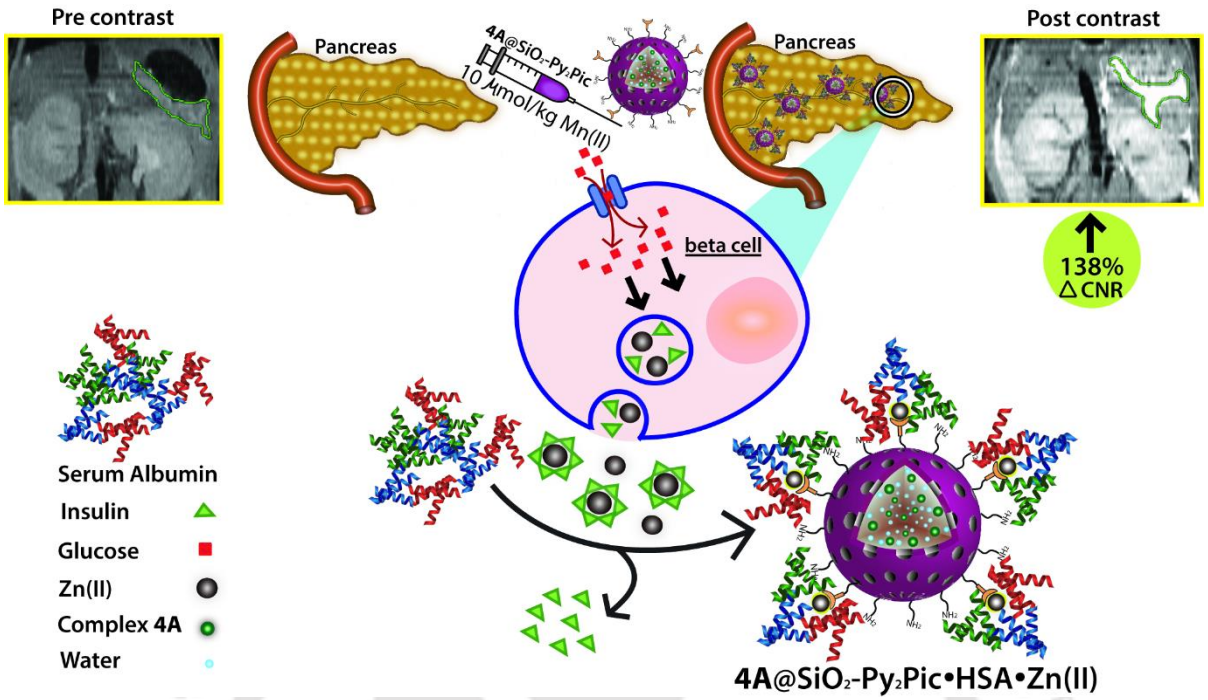

Figure 4.33. Schematic illustration of the glucose-stimulated insulin and Zn(II) secretion (GSIZS) and interaction with **4A**@SiO_2–Py_2PicNPs

4.12 Conclusion

- In this chapter, we have synthesized and characterized a novel ligand H_2AlcDPA along with the corresponding neutral and mono-aquated Mn(II)-complex, **4A**.

- The synthesized complex was found to be thermodynamically stable with a high logK_{MnL} value of 15.06. It was impervious in the vast pH range of 3-10, and in the presence of 200-fold excess of physiological anions. However, it was kinetically labile.

- Complex was successfully incorporated within porous silica nanomaterial, with the surface functionalized with NH_2 or Zn(II) selective Py_2Pic groups. Correspondingly, the nanomaterials were characterized thoroughly to establish stability in the physiological condition.

- The relaxometric studies of complex **4A**, as well as the complex confined nanomaterials (**4A**@SiO_2–NH_2 and **4A**@SiO_2–Py_2Pic) in water and in the presence of 0.67 mM serum

albumin protein, consolidated the formation of Mn(II)-based paramagnetic units with promising MRI contrasting properties.

- The presence of Py_2Pic units over the nanosphere favoured the interaction of the nanoparticle with serum albumin protein and Zn(II) ions selectively, constituting a bulky ternary association [**4A**@SiO_2–Py_2Pic•BSA•Zn(II)] with slow rotational correlation time, and thus exhibiting superior relaxivity reaching up to 46.3 $mM^{-1}s^{-1}$, at 1.41 T and 37 °C.

- *In vivo* intraperitoneal administration of **4A**@SiO_2–Py_2PicNP suspension with a glucose trigger evidenced a signal intensity boost of 138% in the pancreas, thus tracking the secretion of Zn(II) ions (GSIZS). Simultaneous ~ 52% contrast enhancement was noticed in the kidney and ~ 60% in the liver.

- Nanomaterials were biocompatible and the biodistribution analysis on Mn(II) ions after the tissue digestion suggested its excretion from the body in both hepatobiliary and renal pathways.

4.13 Reference

1. (a) S. Lange, W. Mędrzycka-Dąbrowska, K. Zorena, S. Dąbrowski, D. Ślęzak, A. Malecka-Dubiela and P. Rutkowski, *Int. J. Environ. Res. Public Health*, 2021, **18**, 3000; (b) M. Botta, F. Carniato, D. E.-Gómez, C. Platas-Iglesias and L. Tei, *Future Med. Chem.*, 2019, **11**, 1461-1483; (c) N. N. Nystrom, H. Liu, F. M. Martinez, X.-an Zhang, T. J. Scholl and J. A. Ronald, *J. Med. Chem.*, 2022, **65**, 9846−9857; (d) G. J. Soufi, A. Hekmatnia, S. Iravani and R. S. Varma, *ACS Appl. Nano Mater.*, 2022, **5**, 10151−10166.

2. (a) K. Chen, P. Li, C. Zhu, Z. Xia, Q. Xia, L. Zhong, B. Xiao, T. Cheng, C. Wu, C. Shen, X. Zhang and J. Zhu, *J. Med. Chem*., 2021, **64**, 9182−9192; (b) S. Aime and P. Caravan, *J. Magn. Reson. Imaging*, 2009, **30**, 1259−1267; (c) W. Cheng, I. E. Haedicke, J. Nofiele, F. Martinez, K. Beera, T. J. Scholl, H. Margaret Cheng and X.-an Zhang, *J. Med. Chem*., 2014, **57**, 516−520.

3. (a) R. Antwi-Baah, Y. Wang, X. Chen and K. Yu, *Adv. Mater. Interfaces*, 2022, **9**, 2101710; (b) R. Zheng, J. Guo, X. Cai, L. Bin, C. Lu, A. Singh, M. Trivedi, A. Kumar and J. Liu, *Colloids Surf. B.* 2022, **213**, 112432; (c) R. R. Zairov, B.S. Akhmadeev, S.V. Fedorenko and A.R. Mustafina, *Chem. Eng. J*, 2023, **459**, 141640; (d) J. Ruan and H. Qian, *Adv. Ther.*, 2021, **4**, 2100018.

4. M. Veit, R. van Asten, A. Olie and P. Prinz, *Eur. J. Clin. Nutr.*, 2022, **76**, 1497 – 1501.

5. B. Thapa, E. H. Suh, D. Parrott, P. Khalighinejad, G. Sharma, S. Chirayil and A. Dean Sherry, *Front. Endocrinol*., 2022, **12**, 809867.

6. (a) A. Ojha, U. Ojha, R. Mohammed, A. Chandrashekar and H. Ojha, *Clin. Pharmacol*., 2019, **11**, 57-65; (b) E. Haythorne, M. Rohm, M. van de Bunt, M. F. Brereton, A. I. Tarasov, T. S. Blacker, G. Sachse, M. S. dos Santos, R. T. Exposito, S. Davis, O. Baba, R. Fischer, M. R. Duchen, P. Rorsman, J. I. MacRae and F. M. Ashcroft, *Nat. Commun*., 2019, **10**, 247; (c) P. E. MacDonald, J. W. Joseph and P. Rorsman, *Philos Trans R Soc Lond B Biol Sci*, 2005, **360**, 2211–25.

7. (a) G. D. S. Xavier, *J Clin Med*, 2018, **7**, 1–17; (b) J. A. G. Pertusa, T. L. n-Quinto1, G. BernaÂ, J. R. Tejedo, A. Hmadcha, F. J. Bedoya, F. MartõÂn and B. Soria, *PLOS ONE*, 2017, **12** (11), e0187547; (c) A. Fukunaka and Y. Fujitani, *Int. J. Mol. Sci.*, 2018, **19**, 476.

8. C. S. Bonnet and É. Tóth, *Curr Opin Chem Biol*, 2021, **61**, 154–169.

9. (a) Y. Stefan, P. Meda, M. Neufeld and L. Orci, *J. Clin. Invest.*, 1987, **80**, 175−183; (b) S. Zhu, D. Larkin, S. Lu, C. Inouye, L. Haataja, A. Anjum, R. Kennedy, D. Castle and P. Arvan, *Diabetes*, 2016, **65**, 699 − 709; (c) J. Yu, A. F. Martins, C. Preihs, V. C. Jordan, S. Chirayil, P. Zhao, Y. Wu, K. Nasr, G. E. Kiefer and A. D. Sherry, *J. Am. Chem. Soc.*, 2015, **137**, 14173–14179 (d) A. F. Martins, V. C. Jordan, F. Bochner, S. Chirayil, N. Paranawithana, S. Zhang, S. T. Lo, X. Wen, P. Zhao, M. Neeman and A. D. Sherry, *J. Am. Chem. Soc.*, 2018, **140**, 17456−17464.

10. J. Wasko, M. Wolszczak, Z.J. Kaminski, M. Steblecka and B. Kolesinska, *Biomolecules*, 2020, **10**, 1366.

11. (a) L. M. De León-Rodríguez, A. J. M. Lubag, J. A. López, G. Andreu-de-Riquer, J. C. Alvarado-Monzón and A. D. Sherry, *Med. Chem. Commun*., 2012, **3**, 480–483; (b) G.-L. Davies, I. Kramberger and J. J. Davis, *Chem. Commun.*, 2013, **49**, 9704-9721; (c) V. C. Pierre, S. M. Harris and S. L. Pailloux, *Acc. Chem. Res.*, 2018, **51**, 342 − 351; (d) P. Khalighinejad, D. Parrott and A.D. Sherry, *Pharmaceuticals*, 2020, **13**, 268.

12. (a) G. J. Stasiuk, F. Minuzzi, M. Sae-Heng, C. Rivas, H. P. Juretschke, L. Piemonti, P. R. Allegrini, D. Laurent, A. R. Duckworth, A. Beeby, G. A. Rutter and N. J. Long, *Chem. Eur. J.*, 2015, **21** (13), 5023−5033; (b) A. J. M. Lubag, L. M. De Leon-Rodriguez, S. C. Burgess and A. D. Sherry, *Proc. Natl. Acad. Sci. U.S.A.*, 2011, **108**, 18400−18405; (c) J. Lux and A D. Sherry, *Curr Opin Chem Biol.*, 2018, **45**, 121-130; (d) G. Wang, H. Martin, S. Amézqueta, C. Ràfols, C. S. Bonnet and G. Angelovski, *Inorg. Chem.*, 2022, **61** (41), 16256–16265; (e) A. C. Esqueda, J. A. López, G. Andreu-de-Riquer, J. C. Alvarado-Monzón, J. Ratnakar, A. J. M. Lubag, A. D. Sherry and L. M. De León-Rodríguez, *J. Am. Chem. Soc*., 2009, **131**, 11387–11391; (f) G. Wang and G. Angelovski, *Angew. Chem. Int. Ed.*, 2021, **60**, 5734–5738.

13. (a) R. Agarwal, S. M. Brunelli, K. Williams, M. D. Mitchell, H. I. Feldman and C. A. Umscheid, *Nephrol. Dial.*

14. *0Transplant.*, 2009, **24** (3), 856–863; (b) PRAC Confirms Restrictions on the Use of Linear Gadolinium Agents; EMA/424715/2017; *European Medicines Agency*, July 7, 2017; (c) FDA Drug Safety Communication: FDA Warns That Gadolinium-based Contrast Agents (GBCAs) are Retained in the Body; Requires New Class Warnings; U.S. Food and Drug Administration, December 19, 2017.

15. (a) S. Chirayil, V. C. Jordan, A. F. Martins, N. Paranawithana, S. J. Ratnakar and A. D. Sherry, *Inorg. Chem.*, 2021, **60**, 2168–2177; (b) R. Botár, E. Molnár, Z. Garda, E. Madarasi, G. Trencsényi, J. Kiss, F. K. Kálmán and G. Tircsó, *Inorg. Chem. Front*., 2022, **9**, 577-583.

16. (a) E. M. Gale, I. P. Atanasova, F. Blasi, I. Ay and P. Caravan, *J. Am. Chem. Soc.*, 2015, **137**, 15548−15557; (b) D. Ndiaye, M. Sy, A. Pallier, S. Même, I. de Silva, S. Lacerda, A. M. Nonat, L. J. Charbonnière and É. Tóth, *Angew. Chem. Int. Ed*., 2020, **59**, 11958–11963; (c) Z. Garda, A. Forgács, Q. N. Do, F. K. Kálmán, S. Timári, Z. Baranyai, L. Tei, I. Tóth, Z. Kovács and G.Tircsó, *J. Inorg. Biochem*., 2016, **163**, 206 –213; (d) S. Anbu, S. H. L. Hoffmann, F. Carniato, L. Kenning, T. W. Price, T. J. Prior, M. Botta, A. F. Martins and G. J. Stasiuk, *Angew. Chem. Int. Ed.*, 2021, **60**, 10736 − 10744.

17. L. Leone, A. Anemone, A. Carella, E. Botto, D. Livio Longo and L. Tei, *ChemMedChem*, 2022, **17**, e202200508.

18. T. Kojima, Y. Hirai, T. Ishizuka, Y. Shiota, K. Yoshizawa, K. Ikemura, T. Ogura and S. Fukuzumi, *Angew. Chem. Int. Ed.*, 2010, **49**, 8449 –8453.

19. (a) A. Forgács, R. Pujales-Paradela, M. Regueiro-Figueroa, L. Valencia, D. Esteban-Gómez, M. Botta and C. Platas-Iglesias, *Dalton Trans*., 2017, **46**, 1546–1558; (b) M. Khannam, T. Weyhermüller, U. Goswami and C. Mukherjee, *Dalton Trans.*, 2017, **46**, 10426-10432.

20. (a) B. Drahoš, J. Kotek, P. Hermann, I. Lukeš and É. Tóth, *Inorg. Chem.*, 2010, **49**, 3224–3238; (b) R. Uzal-Varela, D. Lalli, I. Brandariz, A. Rodríguez-Rodríguez, C. Platas-Iglesias, M. Botta and D. Esteban-Gómez, *Dalton Trans*., 2021, **50**, 16290 –16303; (c) R. Uzal-Varela, F. Pérez-Fernández, L. Valencia, A. Rodríguez-Rodríguez, C. Platas-Iglesias, P. Caravan and D. Esteban-Gómez, *Inorg. Chem.*, 2022, **61**, 14173–14186.

21. Y.-H. Chiu and J. W. Canary, *Inorg. Chem.*, 2003, **42**, 5107–5116.

22. N. T. Vo, A. K. Patra and D. Kim, *Phys. Chem. Chem. Phys*., 2017, **19**, 1937−1944.

23. M. Yu, L. Zhou, J. Zhang, P. Yuan, P. Thorn, W. Gu and C. Yu, *J. Colloid Interface Sci.*, 2012, **376**, 67 − 75.

24. (a) H. Tapiero, D. M. Townsend and K. D. Tew, *Biomed Pharmacother*., 2003, **57** (9), 386–398; (b) N. N. Paranawithana, A. F. Martins, V. Clavijo Jordan, P. Zhao, S. Chirayil, G. Meloni and A. Dean Sherry, *J. Am. Chem. Soc.*, 2019, **141**, 11009−11018.

25. (a) J. R. Lakowicz, *Principles of Fluorescence Spectroscopy*, 3rd ed, Plenum Press, New York, 2006, **277**; (b) C. Moya, R. Escudero, D. C. Malaspina, M. de la Mata, J. Hernández-Saz, J. Faraudo, A. Roig, *ACS Appl. Bio Mater*. **2019**, *2*, 3084-3094.

26. (a) G. Ghibellini, E. M. Leslie and K. L. R. Brouwer, *Mol. Pharm.*, 2006, **3**, 198-211; (b) K. Chen, P. Li, C. Zhu, Z. Xia, Q. Xia, L. Zhong, B. Xiao, T. Cheng, C. Wu, C. Shen, X. Zhang and J. Zhu, *J. Med. Chem*., 2021, **64**, 9182−9192.

भारतीय प्रौद्योगिकी संस्थान गुवाहाटी
Indian Institute of Technology Guwahati

Chapter V

Folate Decorated Mn(II)-Complex Confined Porous Silica Nanoparticles as MRI Contrast Agent to Detect Cancer Cells

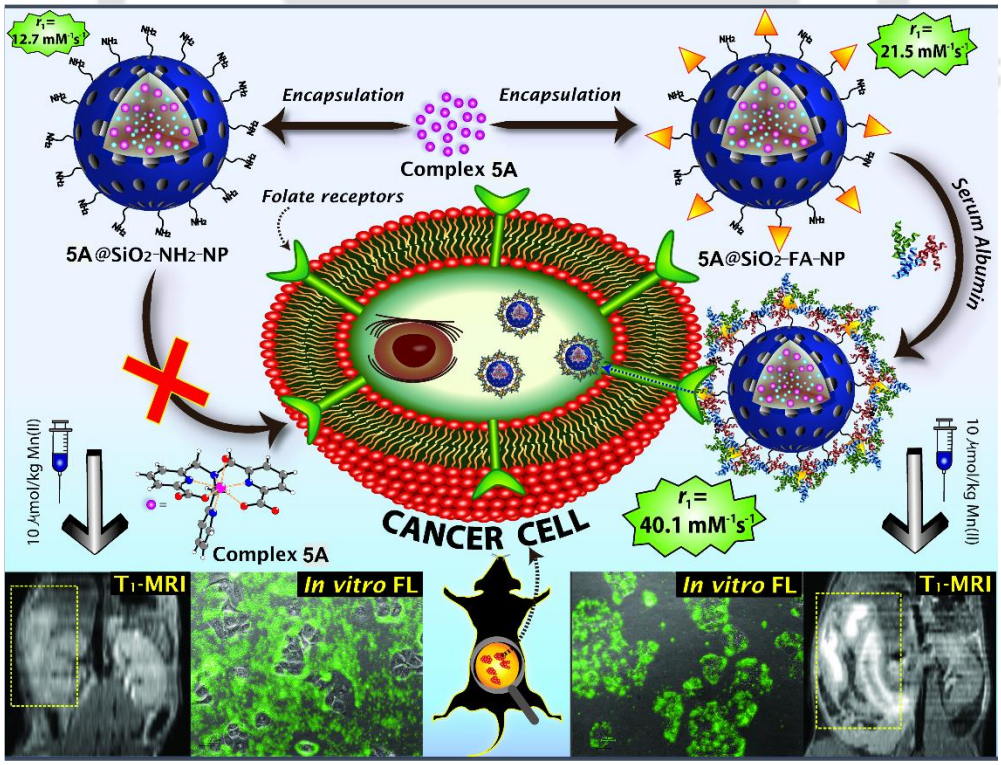

∗ Results have been accepted in *Small*.

5.1 Introduction

Carcinoma is a lethal disease that has caused an enormous threat to human health over the last few decades.[1] It induces various abnormalities at the cellular level thereby, promoting the proliferation, metastasis, and retarded immunity of the affected tumour tissues. Due to multiple recurrences, high mortality rates, and various limitations toward recovery procedures, cancer has become one of the most challenging and life-threatening diseases. Early diagnosis is a key factor for cancer treatment and minimising its adverse effects. In fact, detecting tumour cells at the preliminary stage decreased the mortality rate by 35%.[2] Molecular imaging (MI) has emerged as a pivotal diagnostic technique for early identification of tumour cells *in vivo*.[3] In this context, Magnetic resonance imaging (MRI) has evolved to be a prime molecular imaging modality over other techniques (X-ray, PET, fluorescence imaging, *etc*.).[4] Being non-invasive, it is advantageous and provides three-dimensional high-resolution images with no depth limit. Hence, it is routinely used to estimate the location and size of the tumour site at the primary stages.

Commercially available Gd(III)-based contrast agents are often administered prior to the imaging to compensate for the low sensitivity issue and obtain accurate imaging.[5] The recent concern raised by the FDA and EMA regarding gadolinium usage due to its link to renal toxicity has become a critical drawback for the application of these contrast agents.[6] Meanwhile, there has been a profound urge to develop alternative non-gadolinium-based contrast agents for targeted tumour diagnosis.[7]

This group of contrast agents is responsive to the pathological changes induced by the tumour environment imparting signal enhancement or contrast, preferably the brightening T_1-weighted images, that is beneficial for the detection of lesions.[8] Some Gd(III)- and Mn(II)-based small molecules have been reported in the literature that behaved as a biomarker and exhibited enhanced relaxivity near the tumour environment.[9] However, oncological imaging (visualization and monitoring of cancer development) involves a longer scan time to achieve useful contrast. Thus, conventionally investigated Mn(II)-based complexes with low molecular weight and faster clearance in the human body, are often not suitable for these applications.[1c,10] In this context, nanoparticulate contrast agents are favourable as they demonstrate prolonged retention time *in vivo*. A number of manganese oxide-based nanoparticles as well as Mn(II)-complex conjugated to

biomacromolecules have been extensively studied in the last few years (**Table 5.1**).[11] Although they exhibit promising advancements, the relaxivity values remained lower than the Gd(III)-based agents. Moreover, they suffer from poor bioavailability and internal toxicity which affects their overall performance as potential *in vivo* contrast agents.[11j] Therefore, there has been a drive to design an appropriate Mn(II)-based nanoprobe with high relaxivity for efficient tracking of tumour cells at the early stage.

Table 5.1. Longitudinal relaxivity values for some Mn(II)-based nanoprobes employed in tumour-targeted MR imaging.[11]

Mn(II)-based Nanosystem	r_1 ($mM^{-1}s^{-1}$)	Applied Field	Time taken for maximum signal enhancement
MnO-TETT	4.84	7 T	2 h
MnO-TETT-FA	4.83		
Gd/$MnCO_3$−PEG-Cy5.5-FA	6.58	7 T	2 h
FA-PAA-coated MnO	9.3	3 T	4 h
Mn_3O_4@SiO_2–PEG	0.49	0.5 T	4 h
Mn_3O_4@SiO_2(PEG)–FA	0.52		
MnO_2 -PEG-FA/DOX with 2 mM GSH	0.0, at pH 7.4 2.0, at pH 5.0	0.5 T	4 h
FA-Mn_3O_4@PDA@PEG	14.47	3 T	36 h
GO-PDA-BSA/FOA-DTPA-Mn(II)	14.7	1.5 T	3 h
GNs@PAA-[DFO-Mn(II)]/FOA	13.0	1.5 T	—
Me&Flu@MSN@MnO_2-FA	10.38, pH 6.0	4.7 T	3 h
MnO_2-BSA	2.77	7 T	2 h

In the previous chapters, we have established the reverse microemulsion procedure to confine Mn(II)-complexes inside the porous silica nanoparticles. Synthesized nanomaterials demonstrated enhanced longitudinal relaxivity value in water and physiological conditions (in the presence of serum albumin) when compared to manganese oxide-based nanocontrast (**Table 3.2**).

Being impervious to biologically relevant scavenger ions, these are suitable for further modifications and thereafter *in vivo* applications. The metabolism and the surrounding environment for tumour cells distinctively differ from the healthy cells. Consequently, there is a change in nutrient concentration, albumin content, pH, rate of folate receptor expression, *etc*. in the vicinity of the tumour region.[11,12] These cells are believed to show enhanced permeability and retention (EPR) effect and hence can be easily penetrated.[13] Judicious fabrication of target groups onto the surface of the Mn(II)-complex confined porous silica nanomaterials could achieve tumour-responsive change in r_1 relaxivity value, rendering useful tumour-recognising contrast in the corresponding T_1-weighted MR imaging.

The mesoporous silica nanoparticles offer an appreciable surface area that could be efficiently modified to covalently link tumour-targeting ligands like antibodies, aptamers, biomolecules, peptides, organic fragments, etc.[14] This technique has been adapted to augment cell-membrane penetration. Antibody and peptide conjugation over the nanoparticle surface and further application, even though gave promising initial results, eventually suffered from immunogenicity and retarded tissue penetration ability. Alternatively, among these appendants, folic acid (FA) moiety showed a high affinity towards the folate receptors.[15] To note, cancer cells are characterized to have 500-fold overexpressed folate receptors compared to normal cells which facilitate the movement of folate molecules across the lipid bilayer of the cell membrane (**Figure 5.1** and **5.2**).[16] Contrast nanoprobes tethered with folic acid utilize this distinguishing feature to be preferentially uptaken and accumulated within the cancer cells, thus furnishing the role of tumour-targeted cell permeable biomarkers. Furthermore, folate receptors are overexpressed as a consequence of chronic inflammation, as evidenced in the cases of autoimmune diseases like rheumatoid arthritis.[17] The folate-conjugated nanoprobes can facilitate the diagnosis of this fatal illness altogether.

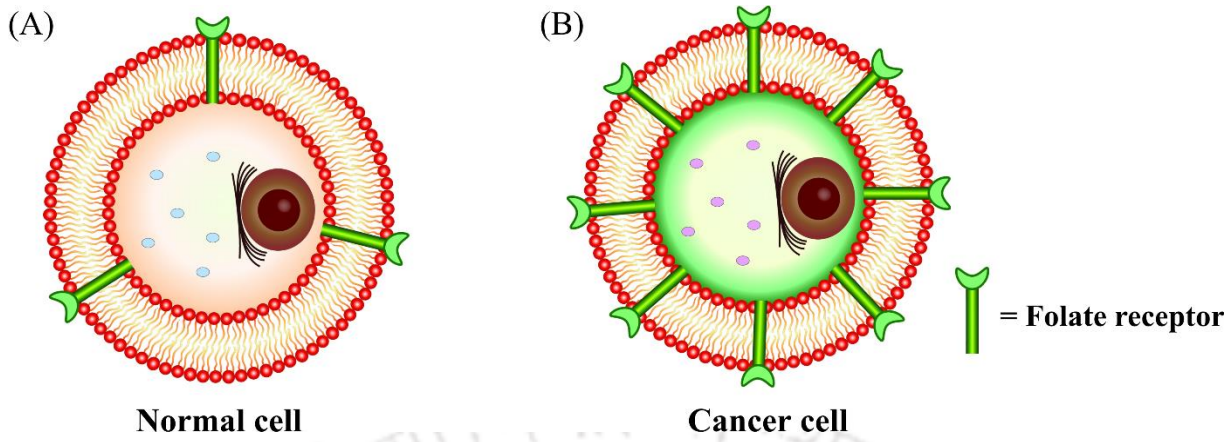

Figure 5.1. Schematic diagram of a (A) normal and (B) cancer cell representing overexpressed folate receptors (FR) in the latter one.

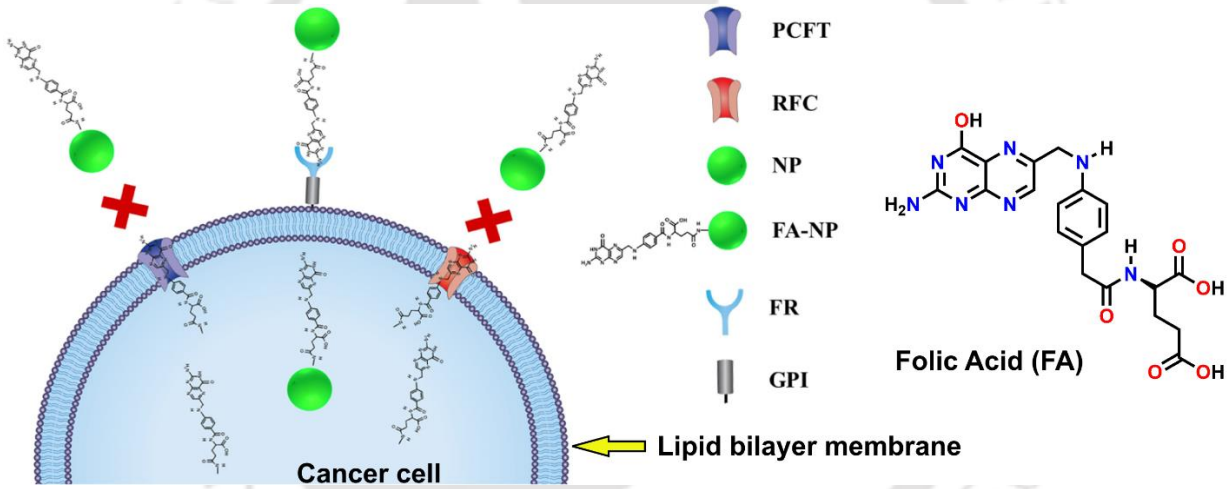

Figure 5.2. Illustration demonstrating the three functionally distinct folate transport systems: the folate receptor (FR), reduced folate carrier (RFC), and the proton-coupled folate transporter (PCFT). PCFT and RFC exhibit no affinity for folate-targeted NPs and hence are not able to get internalized, while high-affinity FRs are efficient in the internalization of folate-targeted NPs.[1a]

In recent times, few MnO-, MnO_2- or Mn_3O_4-based nanoparticles with folic acid appendant, as well as, Mn(II)-complexes immobilized over graphene oxide systems had been investigated exhibiting fair progress in tumour localisation (**Table 5.1**). However, they still suffered from limited sensitivity as diffused contrast was achieved. This phenomenon could be ascribed to the lower relaxivity values obtained for these systems than similar Gd(III)-

counterparts.[4] Moreover, efficient signal amplification was obtained after the administration of a large dosage of nanoparticles, which imparted some toxicity afterwards.[10a,b] For a majority of these nanoprobes, optimum contrast was visualized after a prolonged time (a minimum of 2 h) which elongated the time scan of MR imaging. Notwithstanding, there is a challenge along with the opportunity for betterment in developing novel Mn(II)-based nanocontrast agents to provide a conspicuous tumour-responsive diagnosis within a shorter time span.

In this context, we have successfully synthesized a thermodynamically stable complex **5A** and subsequently incorporated the complex molecules within the porous silica nanoparticles. The outer surface of the silica nanoparticle has been modified by folic acid as a tether group producing the nanomaterial **5A**@SiO_2–FA which exhibited a promising r_1 value of 21.45 $mM^{-1}s^{-1}$, at pH ~ 7.4, 1.4 T and 37 °C. The nanosystem positively interacted with the serum albumin protein eventually lowering the overall tumbling rate. A distinctive boost in the relaxivity value was achieved due to this association. Moreover, the grafting of the folic acid over the nanosphere selectively accelerated the rate of cancer cell uptake. Cancer tissues with higher albumin concentration at the extracellular space, as well as, overexpressed folate receptors could be effectively double-targeted **5A**@SiO_2–FA, furnishing significant signal enhancement in the localized affected region when subsequently scanned for T_1-weighted MR images. The tumour-responsive cell penetration properties of **5A**@SiO_2–FA were examined by *in vitro* fluorescence imaging experiments along with developing an *in vivo* tumour model in C57BL/6 mice. Corresponding time-dependent T_1-weighted contrast enhancement studies were performed to understand the aforementioned tumour-selective behaviour of the synthesized nanosystem.

5.2 Synthesis and Characterization of Ligand H_2tpada

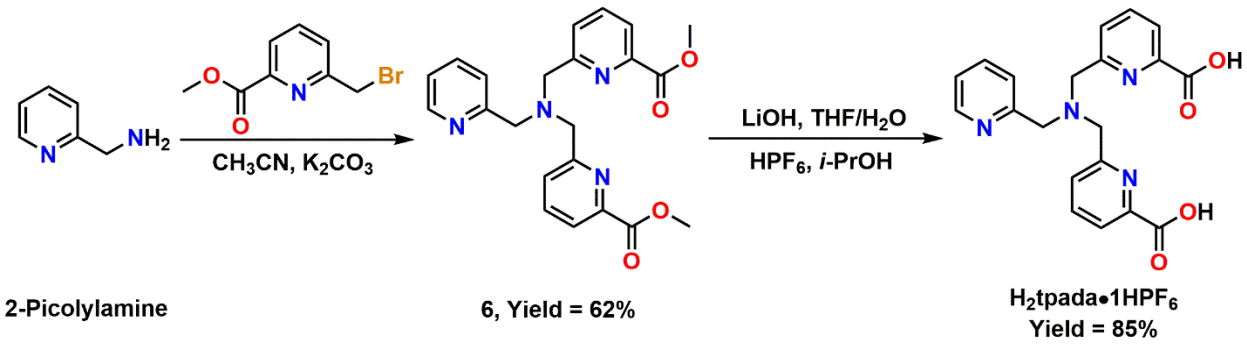

Scheme 5.1. Schematic presentation for the synthesis of ligand **H_2tpada•1HPF_6**.

Ligand H_2tpada was synthesized in two steps with an overall 52% yield, adopting the synthetic procedure reported in the literature.[18] In the first step, 2-Picolylamine was reacted with 2 equivalents of 6-(bromomethyl)picolinate in CH_3CN in the presence of K_2CO_3 to obtain compound **6** which was subsequently hydrolysed by an excess amount of aqueous LiOH solution. The crude obtained was acidified with HPF_6 in an *i*-PrOH medium to obtain the ligand as colourless needle-shaped crystals (H_2tpada•1HPF_6). The formation and purity of the ligand were examined through FTIR, ESI-MS, ^{1}H-NMR and ^{13}C-NMR spectral analyses.

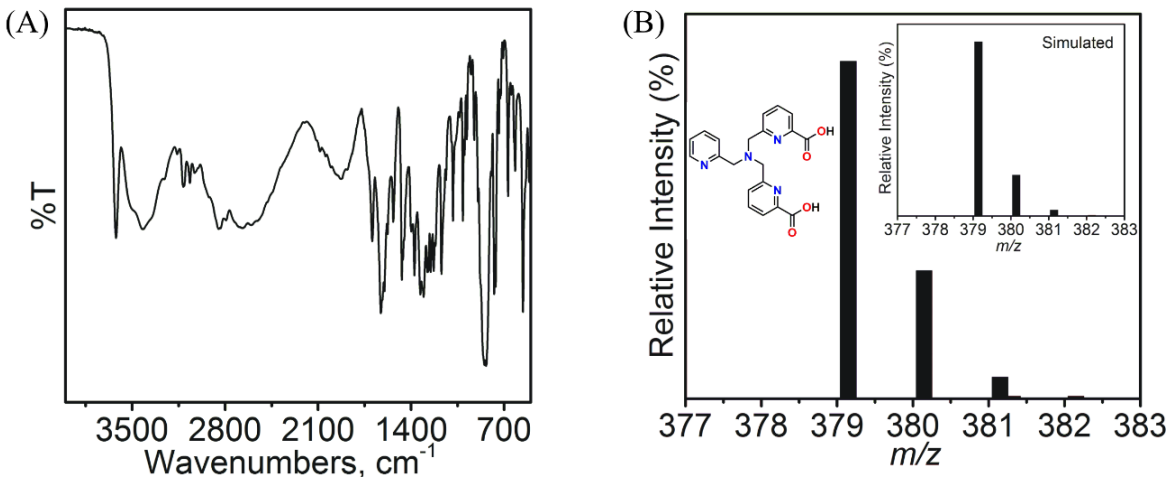

Figure 5.3. (A) FTIR and (B) ESI-MS (+ve) spectra of ligand H_2tpada. The simulated spectrum is given as an inset.

The infrared spectrum of the ligand H_2tpada (**Figure 5.3A**) evidenced the presence of 3614 cm^{-1} and 3423 cm^{-1} due to ν_{O-H} asymmetric stretching of water and the carboxylic acid group, respectively. The broad band at 2853 cm^{-1} appeared due to the ν_{N-H} stretching of the protonated tert-amine group. The $\nu_{C=O}$ asymmetric stretching strong peak was observed at 1690 cm^{-1} (carboxylic acid groups) and 1626 cm^{-1} (μ-bridged carboxylic group). The band at 1584 cm^{-1} corresponded to the characteristic aromatic $\nu_{C=N}$ stretching (pyridine group). The sharp peak at 845 cm^{-1} ascribed to the ν_{P-F} stretching proved the existence of the ligand as a monohexafluorophosphoric acid salt. The ESI-MS (+)ve mode spectrum of the aqueous solution of the ligand demonstrated a 100% molecular ion peak at *m/z* = 379.1470, which corresponded to the molecular composition $[C_{20}H_{18}N_4O_4+H]^+$ (*m/z* = 379.1400) along with the isotropic pattern. concerned Mn-complex (**5A**).

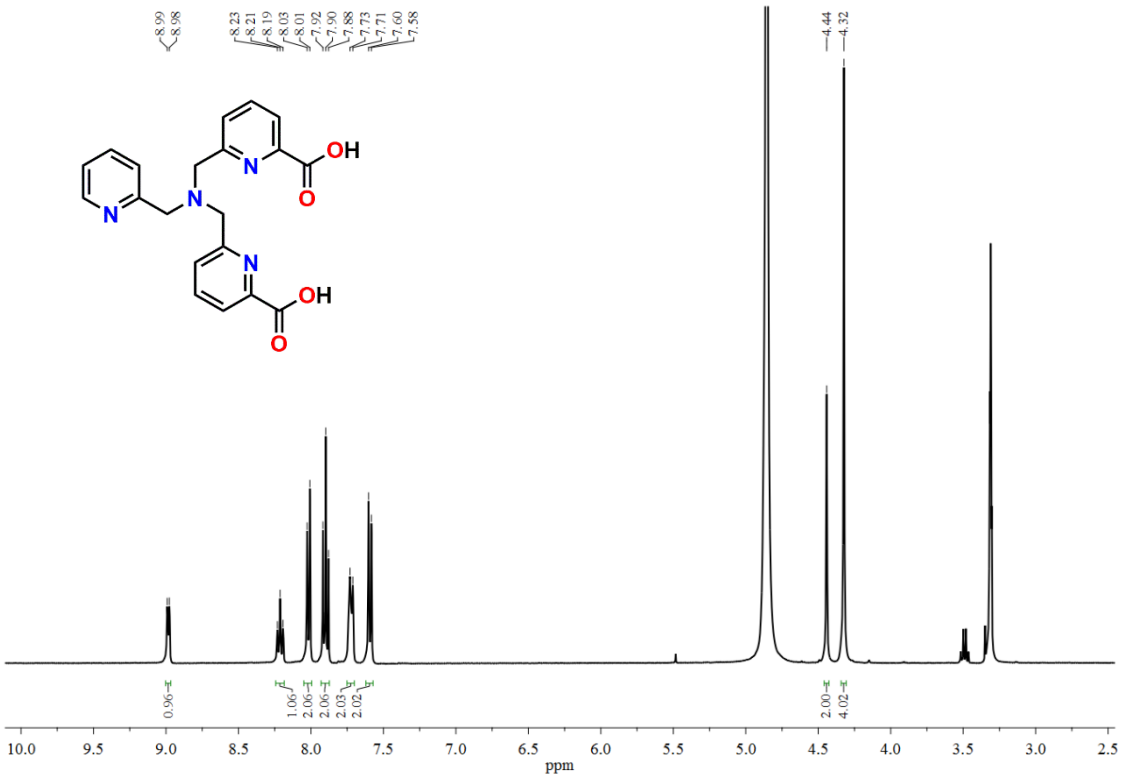

Figure 5.4. ^{1}H NMR spectrum of ligand H_2tpada in CD_3OD solvent.

The ^{1}H-NMR spectrum of the ligand H_2tpada, recorded in CD_3OD solvent, showed the presence of 10 aromatic protons in the range 8.99-7.58 ppm corresponding to three pyridine rings in the ligand backbone (**Figure 5.4**). Six non-aromatic protons of the methylene groups appeared as two singlets at 4.44 and 4.32 ppm. The ^{13}C-NMR spectrum of the ligand in the D_2O medium is

presented in **Figure 5.5**. It indicated the presence of 11 types of aromatic and 2 types of non-aromatic carbon atoms in the ligand framework.

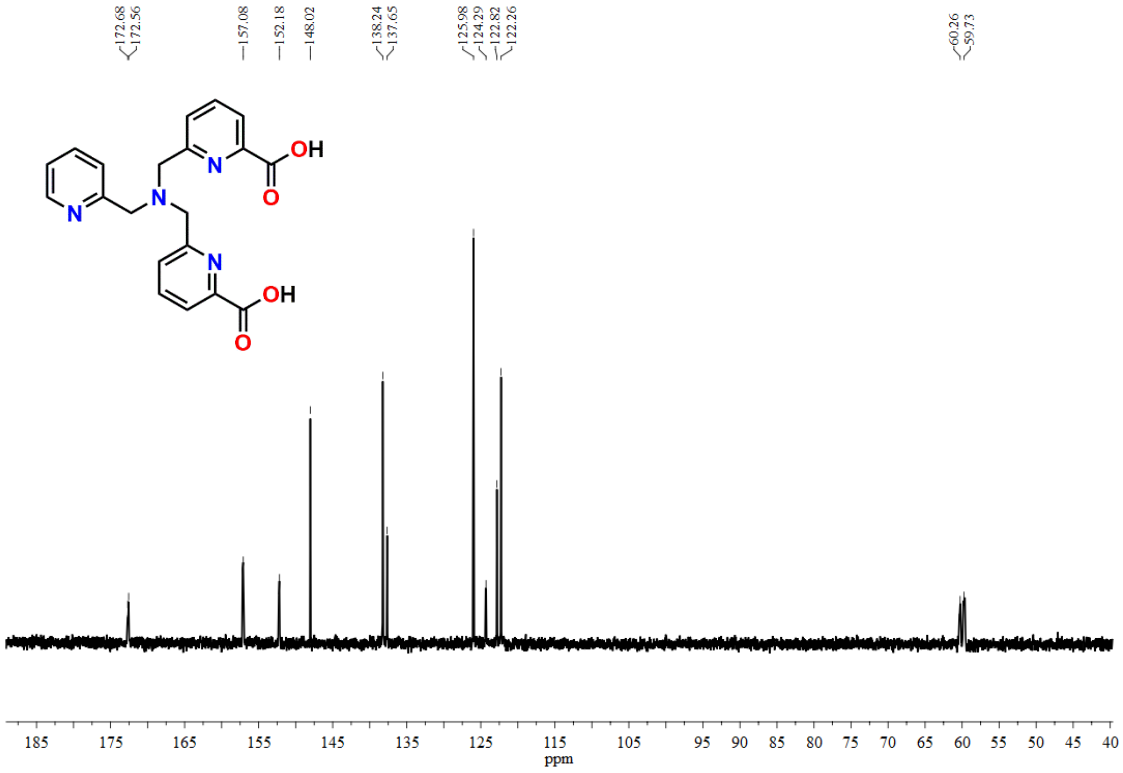

Figure 5.5. ^{13}C NMR spectrum of ligand H_2tpada in D_2O solvent.

5.3 Synthesis and Characterization of Mono-aquated Mn(II)-Complex of Ligand H_2tpada, 5A

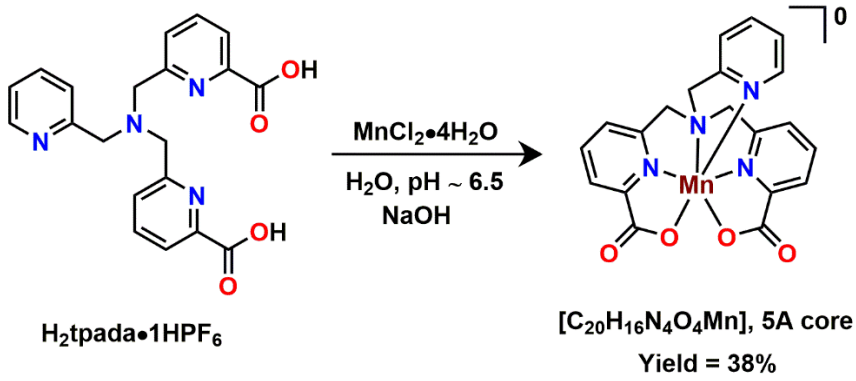

Scheme 5.2. Schematic representation for the synthesis of complex **5A,** $[C_{20}H_{16}N_4O_4Mn]$.

The synthesized ligand H_2tpada was reacted with an equivalent amount of $MnCl_2 \bullet 4H_2O$ in an aqueous medium at pH 6.5, attained by the addition of to dilute NaOH solution, to obtain a colourless solid as precipitate (**Scheme 5.2**). This crude was dissolved in methanol and kept in a diethyl ether environment for 3 weeks to obtain needle-shaped pale-yellow X-ray suitable single crystals of complex **5A** in 38% yield. It was further characterized by FTIR and ESI-MS spectroscopy.

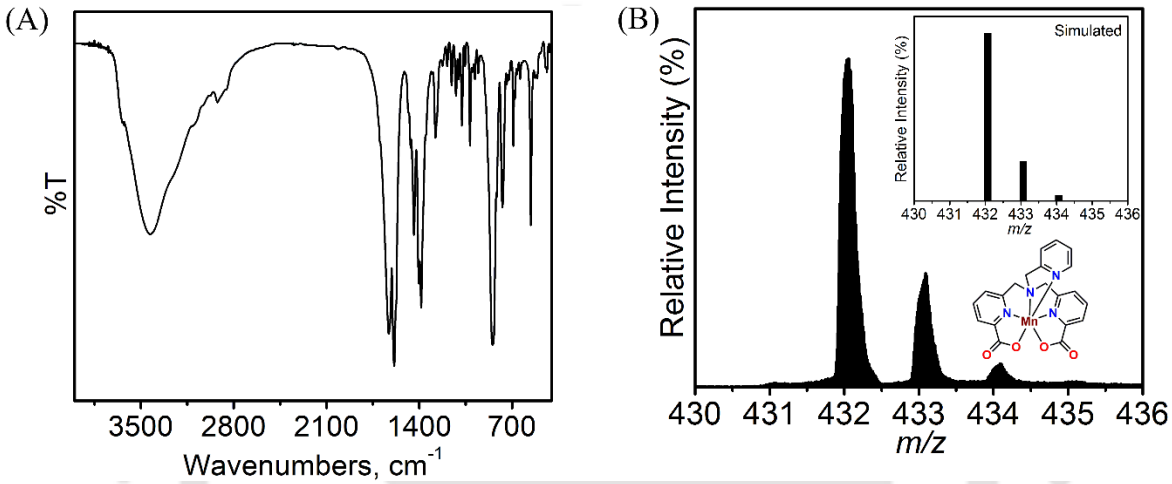

Figure 5.6. (A) FTIR spectrum, and (B) ESI-MS (+ve) mass spectrum of complex **5A**. The simulated spectrum was given as inset.

The infrared and (+ve) mode ESI-MS spectra of complex **5A** are illustrated in **Figure 5.6**. The shift in the $\nu_{C=O}$ asymmetric stretching band to 1622 cm^{-1} in the complex spectra from 1696 cm^{-1} in the case of ligand was observed corroborating the formation of Mn(II)-coordinated complex. The ESI-MS spectrum of complex **5A** exhibited a 100% molecular ion peak at *m/z* = 432.0568 which corresponded to the molecular composition of the mononuclear complex **5A** core $[C_{20}H_{16}N_4O_4Mn + H]^+$ (*m/z* = 432.0624) with reciprocating isotropic distribution pattern confirming the complexation. Contrary to the molecular structure obtained from X-ray analysis (*vide infra*), this indicated the dissociation of the carboxylate bridging at the axial position in the aqueous medium. Water molecules presumably coordinate to the central Mn(II) along this vacant site forming the seven-coordinated mono-aquated complex.

Single crystal X-ray analysis of the complex **5A** crystals was performed at 296(2) K and was found to be crystallized in the 'monoclinic' 'C12/c1' space group. The molecular structural

view of the synthesized complex is shown in **Figure 5.7**. Moreover, selected bond distances and angles are listed in **Table 5.2**. The ORTEP representation of complex **5A** demonstrated three interconnected molecular units through carboxylate carbonyl oxygen bridging. Each Mn(II) complex unit adopted a pentagonal bipyramidal geometry with two picolinate units and the tert-amine nitrogen (N2) constituted the basal plane. The N3 atom of the picolyl ring occupied one of the axial positions. Another apical position was occupied by the bridging oxygen atom (O12) of the carboxylate arm of another complex unit, completing the coordination geometry. Individual complex units are neutral in charge. A sodium atom at the centre held the complex units and the presence of the PF_6 counter-anion maintained the charge neutrality. The $Mn–N1_{Py}$ = 2.208(10), $Mn–N4_{Py}$ = 2.278(9), $Mn–N2_{amine}$ = 2.435(13), $Mn–N3_{apical}$ = 2.298(12), $Mn–O2_{acid}$ = 2.248(7), $Mn–O3_{acid}$ = 2.207(6), and $Mn–O12_{bridg}$ = 2.209(6) Å bond distances commensurate well with the previously reported Mn(II) complexes of this ligands.[18]

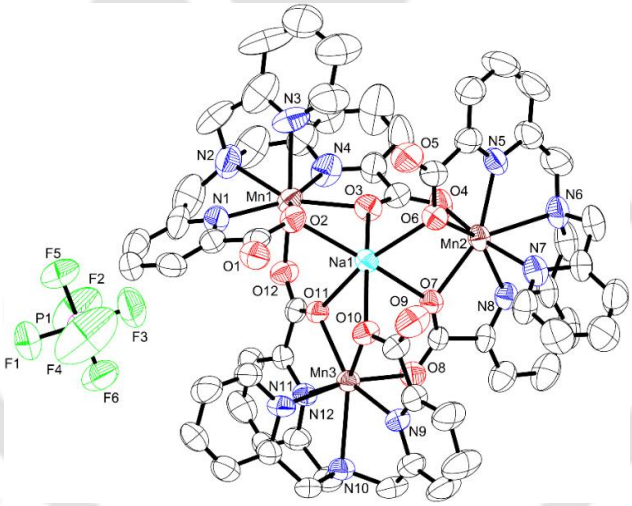

Figure 5.7. ORTEP representation of complex **5A**, drawn at 40% probability level.

Table 5.2. Selected bond distances (Å) and bond angles (°) for complex **5A**.

Mn1–O2	2.248(7)	O2–Mn1–O3	81.02(23)
Mn1–O3	2.207(6)	O2–Mn1–N1	72.48(31)
Mn1–O12	2.209(6)	O3–Mn1–N4	70.73(29)
Mn1–N1	2.208(10)	O5–Mn1–N3	168.97(33)
Mn1–N2	2.435(13)	N1–Mn1–N2	67.71(35)
Mn1–N3	2.298(12)	N4–Mn1–N2	72.19(33)
Mn1–N12	2.209(6)		

Table 5.3. Crystallographic and Structural refinement parameters for complex **5A**.

Empirical formula	$C_{61}H_{51}Mn_3N_{12}NaO_{13}PF_6$
CCDC Number	2334262
Formula weight	1492.91
Crystal habit, color	Needle-shaped/ yellow
Crystal size, mm^3	0.34×0.32×0.30
Temperature, T	296(2)
Wavelength, λ(Å)	0.71073
Crystal system	monoclinic
Space group	'C12/c1'
Unit cell dimension	a = 24.8688(18) Å, b = 32.669(2) Å, c = 19.1382(14) Å, α = 90.00°, β = 94.674°, γ = 90.00°
Volume, V ($Å^3$)	15496.7(19)
Z	8
Calculated density, mg•mm^{-3}	1.280
Absorption coefficient, μ (mm^{-1})	0.583
F(000)	6080
θ range for data collection	2.274° to 25.000°
Limiting indices	$-27 \le h \le 29$, $-38 \le k \le 38$, $-22 \le l \le 22$
Reflection collected / unique	13609/ 9138 [$R_{(int)}$ = 0.1158]
Completeness to θ	99.7% (θ = 25°)
Max. and min. transmission	1.0000/ 0.4575
Refinement method	'SHELXL 2018/3 (Sheldrick, 2015)'
Data / restrains / parameters	13609/216/ 931
Goodness-of-fit on F^2	1.081
Final R indices [I>2sigma(I)]	R_1 = 0.1158, wR_2 = 0.3246
R indices (all data)	R_1 = 0.1444, wR_2 = 0.3393
Largest diff. peak and hole	0.807/-0.709

5.4 Thermodynamic Stability of Complex 5A

The thermodynamic aspects of the **5A** were estimated by determining the step-wise protonation constant of the ligand H_2tpada and the stability constant of the corresponding Mn(II)-complex direct pH-potentiometric titrations. Experiments were performed in the pH range from 2.3 to 12.0, with 0.1 M NaOH as titrant and the ionic strength was maintained using 0.15 M NaCl.

The protonation constant of the ligand could be defined by the equation:

$$K_i^{\mathrm{H}} = \frac{[\mathrm{H}_i\mathrm{L}]}{[\mathrm{H}_{i-1}\mathrm{L}][\mathrm{H}^+]} \quad \textbf{(1)}$$

where, i = number of replaceable protons, and L = deprotonated ligand.

The protonation and stability constants were calculated by simulations of respective curves using *Hyperquad2008* software. Ligand H_2tpada exhibited $\log K_1^H$ = 9.41(13), $\log K_2^H$ = 6.36(11), and $\log K_3^H$ = 4.53(9) (**Figure 5.8A**, **Table 5.4**). The data obtained agreed with the values reported for the ligand H_2PyDPA (**Chapter IIIB**) with a similar framework. Correspondingly, the highest pK_a could be attributed to the protonation of the highly basic *tert*-amine nitrogen and the second one was assigned to the $N_{pyridine.}$ The lowest could be related to the protonation of the carboxylate unit.

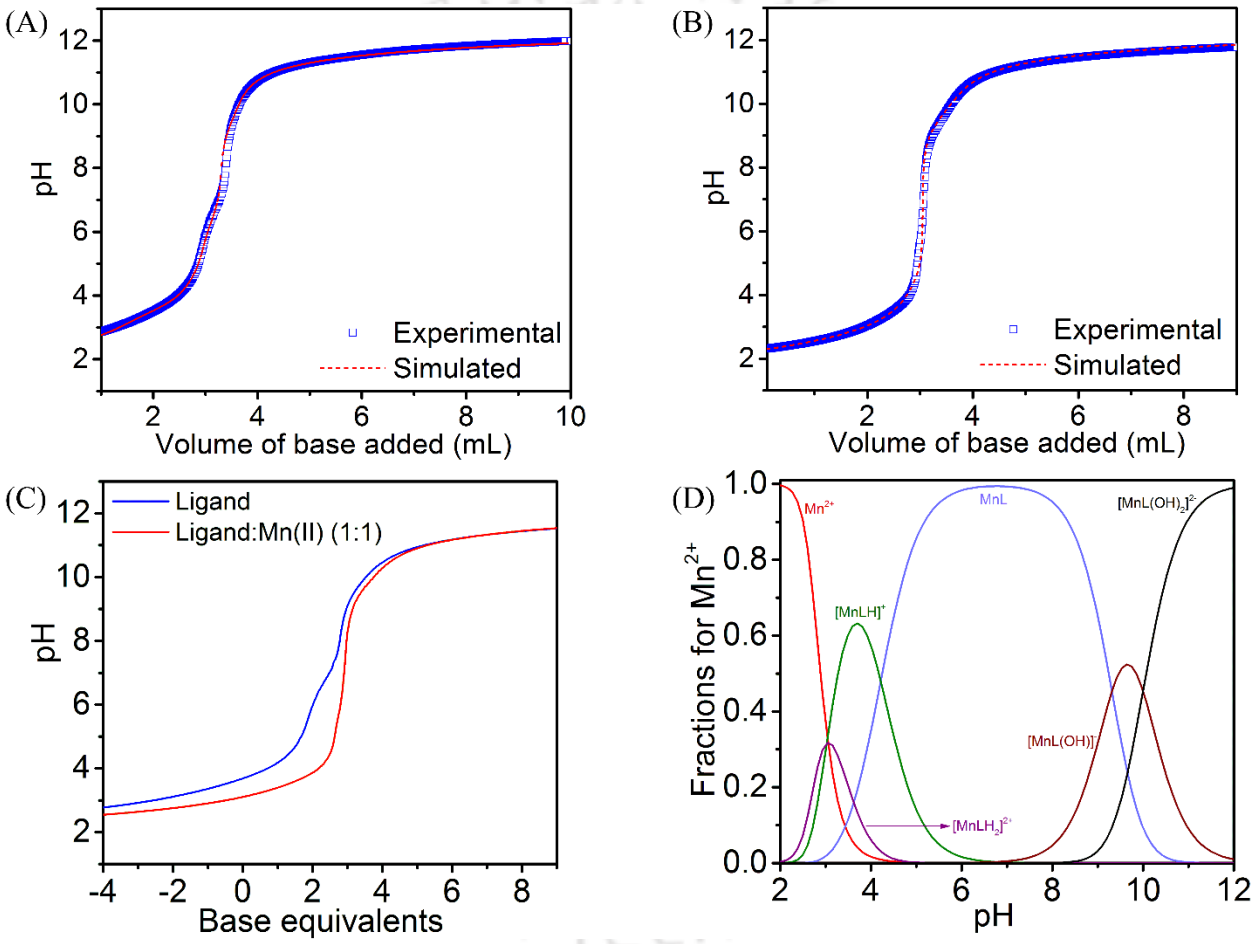

Figure 5.8. Experimental and simulated curves representing pH-potentiometric titration of (A) ligand H_2tpada solution against standard NaOH solution, (B) ligand H_2tpada:Mn(II) (1:1) solution against standard NaOH solution, and (C) Base equivalent plot in 0.15 M NaCl, 298 K; (D) Species distribution diagram for Mn/H_2tpada: $[Mn^{2+}]$ = [L] = 1 mM.

The stability constant for the corresponding Mn(II) complex was determined by direct pH-potentiometric titration using 1:1 ligand-to-metal [Mn(II)/Cu(II)/Zn(II)] molar ratio and collected data sets were fitted to equation **(2)**, (**Figure 5.8B**).

$$K_{\mathrm{MnL}} = \frac{[\mathrm{MnL}]}{[\mathrm{Mn}][\mathrm{L}]} \qquad \textbf{(2)}$$

The thermodynamic stability constant ($\log K_{\mathrm{MnL}}$) for complex **5A** was found to be 14.67(9). The value obtained is commensurate with other reported mono-aquated Mn(II)-chelates with similar coordination motifs [PyDPA (14.80), *trans*-CDTA (14.32), PyC3A (14.14), *etc.*],[19] reciprocating commendable stability for the synthesized Mn(II)-system. The pMn (pMn = $-\log[Mn^{2+}]_{free}$, where $[Mn^{2+}] = [L] = 10\ \mu M$) value for this system was calculated at pH = 7.4, to be 8.80. The base equivalent plot (**Figure 5.8C**) indicated the presence of three replaceable protons in the ligand structure, thus implying the existence of H_2tpada as the protonated salt (H_2tpada•HPF_6). Considering the thermodynamic stability data, the species distribution diagram is obtained (**Figure 5.8D**). It reflected the abundance of the mono-aquated Mn(II)-complex of the ligand H_2tpada as the dominant species beyond pH 4.5 until 9.0.

Table 5.4. Ligand protonation constants and corresponding stability constants for Mn(II) complexes.[19]

		PyC3A[19a]	*t*CDTA[19b]	EDTA[19b]	CyBET-OMe[19c]	PyDPA*	Tpada**
H^+	$\log K_1^H$	10.16	9.36	9.17	12.58	9.21	9.41(13)
	$\log K_2^H$	6.39	5.95	5.99	9.87	6.45	6.36(11)
	$\log K_3^H$	3.13	3.62	2.73	3.99	3.50	4.53(9)
	$\log K_4^H$	—	2.57	2.01	2.97	—	—
	$\log K_5^H$	—	1.49	1.38	—	—	—
	$\sum \log K_i^H$	19.68	22.99	21.28	29.41	19.16	20.30
Mn^{2+}	$\log K_{\mathrm{MnL}}$	14.14	14.32	12.46	14.61	14.80	14.67(9)
	$\log K_{\mathrm{MnHL}}$	2.43	2.90	2.95	7.73	3.82	4.21(8)
	$\log K_{\mathrm{MnH2L}}$	—	1.89	—	—	2.55	3.02(11)
	$\log K_{\mathrm{MnL(OH)}}$	—	—	—	—	5.41(6)	5.36(4)
	$\log K_{\mathrm{MnL(OH)2}}$	—	—	—	—	–8.06(2)	–4.64(9)
	pMn	8.17	8.68	7.83	6.24	8.97	8.80

[*] Chapter IIIB (I= 0.15 M NaCl, 25 °C), [**] This work (I= 0.15 M NaCl, 25 °C).

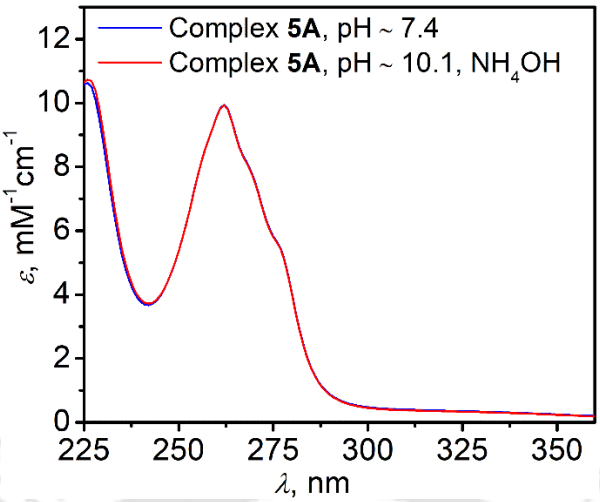

Figure 5.9. UV-Vis spectroscopy of complex **5A** at pH ~ 7.4 and pH ~ 10.1 (attained by addition of NH_4OH).

The stability of complex 5A at the pH ~ 10.1, in the presence of ammonium hydroxide was elucidated by recording the UV-Vis spectra of the aqueous solution of the complex at varied pH. No alteration in the spectral envelope verified the rigidity of the Mn(II)- coordination at the experimental conditions necessary for further encapsulation technique.

5.5 Synthesis and Characterization of Complex 5A Confined PSNs and Surface Modification with Folic Acid

The synthesized thermodynamically stable complex **5A** was enclosed within porous silica nanoparticles (PSNs) adopting the reverse microemulsion method. Methodically, an aqueous solution of complex **5A** (160 µL of 8 mM complex **5A** stock solution mixed with 320 µL of HEPES, 0.1 M, pH ~ 7.4) was doped into a solution of Igepal-CO-520 in cyclohexane, resulting in the formation of a stabilized reverse microemulsion system. Ammonia hydrolysis of tetraethyl orthosilicate (TEOS) added thereupon developed a silica nano-shell. The silanol groups were further functionalized with the addition of (3-Aminopropyl)triethoxysilane (APTES). Careful removal of the surfactants produced the NH_2-functionalized porous silica nanospheres, incorporated with the complex molecules (**5A**@SiO_2–NH_2). Folic acid groups were covalently tethered to the amine groups present in the silica surface, triggered by a combination of 1-(3-

Dimethylaminopropyl)-3-Ethyl Carbodiimide (EDC) and N-Hydroxysuccinimide (NHS), providing **5A**@SiO_2–FA (**Scheme 5.3**).

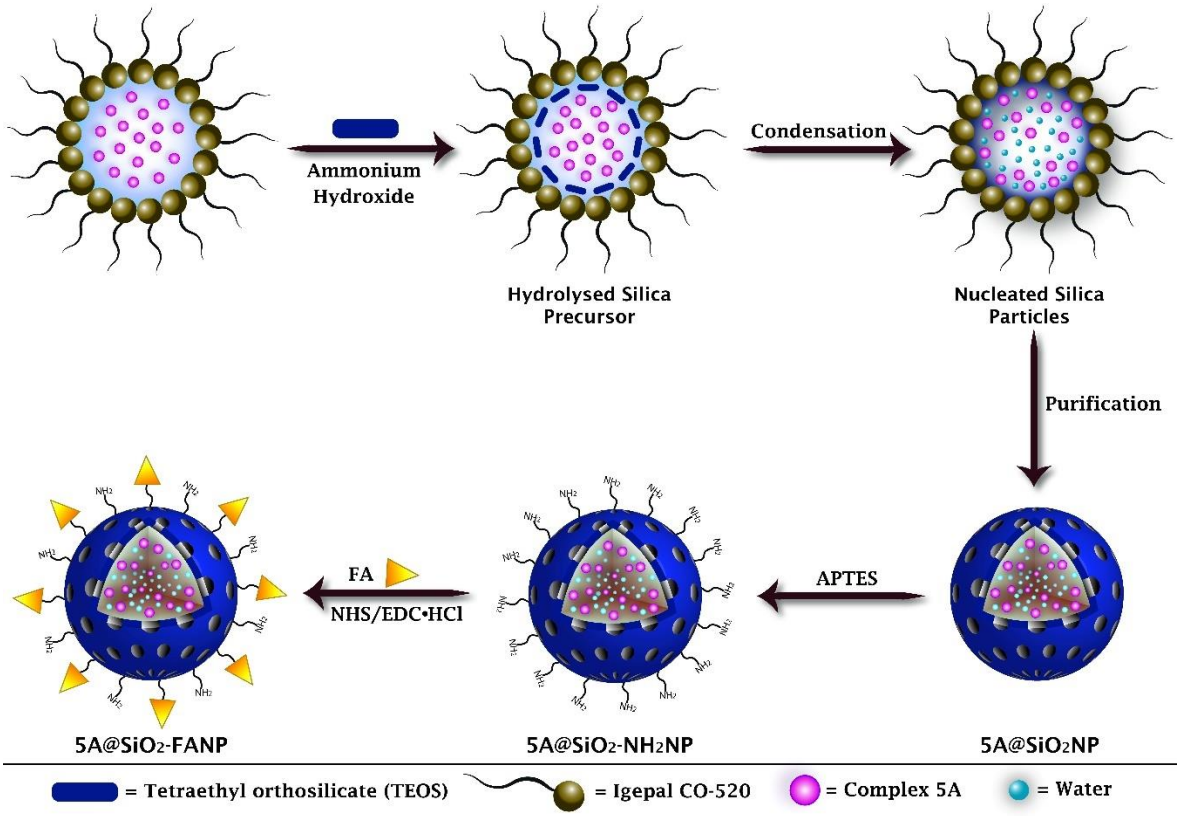

Scheme 5.3. Representative illustration for the preparation of **5A**@SiO_2–NH_2NP and **5A**@SiO_2–FA.

The finalized nanoparticles were recovered and eventually dispersed in 1 mL HEPES buffer (pH ~ 7.4) to form **5A**@SiO_2–FA stock solution. For the non-functionalized nanoparticle system **5A**@SiO_2, prepared omitting the subsequent addition of APTES and FA, an average of 40 complex **5A** molecules were found to be incorporated within each nanosphere (calculated according to the method presented in **Chapter III**).

The formation and morphology of the synthesized nanomaterials were examined by recording the FETEM images and performing corresponding EDX, FTIR, EPR, TGA and N_2 adsorption-desorption isotherm analyses.

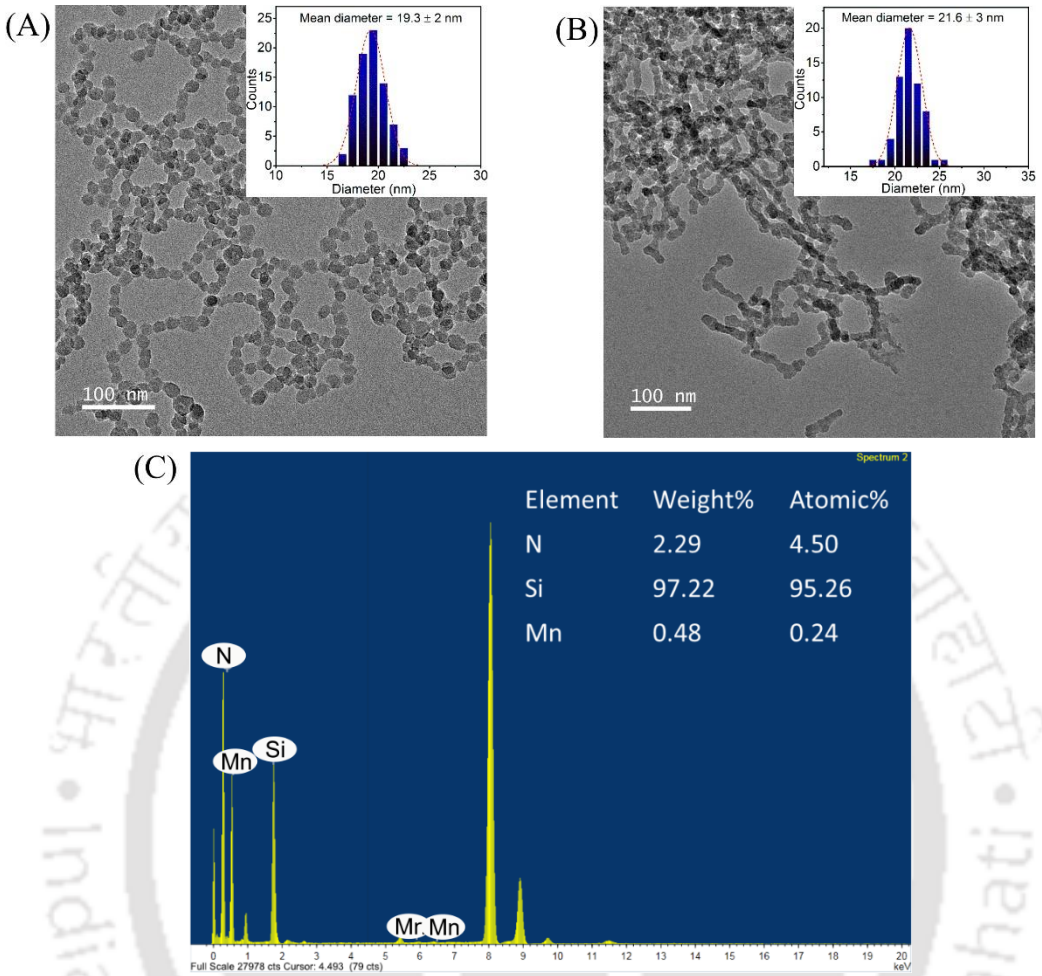

Figure 5.10. (A) FETEM images of (A) **5A**@SiO_2-NH_2 and (B) **5A**@SiO_2–FA nanoparticles; inset- corresponding particle size distribution. (C) corresponding energy dispersive X-ray (EDS) analysis of **5A**@SiO_2–FA.

The representative FETEM images of **5A**@SiO_2–NH_2 revealed the formation of well-defined, monodispersed and spherical-shaped nanoparticles with an average size of 19.3±2 nm. Organic modification on the surface of NPs by covalent amide linkage of folate units led to a slight increase in average particle size to 21.6±3 nm for **5A**@SiO_2–FA, along with a decrease in uniformity (**Figure 5.10B**). The inclusion of complex **5A** molecules inside the silica nanoparticles was indicated by the coexistence of Mn, Si, and N elements in the corresponding energy-dispersive X-ray spectroscopy (EDS) analysis of finalized nanomaterial **5A**@SiO_2–FA (**Figure 5.10C**).

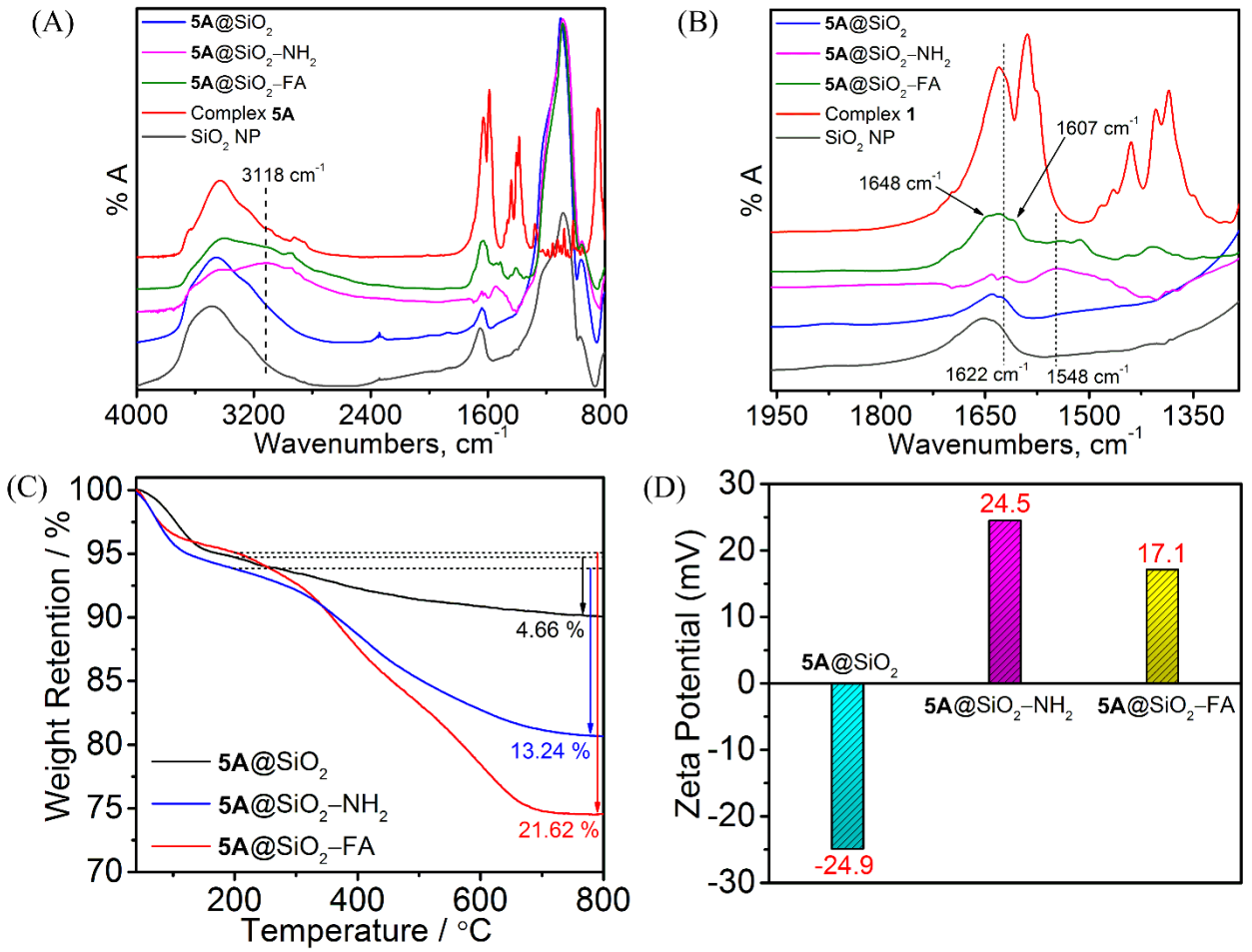

Figure 5.11. (A), (B) FTIR spectra and (C) TGA curves for **5A**@SiO_2, **5A**@SiO_2–NH_2, and **5A**@SiO_2–FA. (D) The zeta potential values of **5A**@SiO_2, **5A**@SiO_2–NH_2, and **5A**@SiO_2–FA aqueous suspensions at pH 7.4.

Moreover, the existence of complex molecules confined within the nanospheres was further examined by recording the infrared spectra of lyophilized nanoparticles as presented in **Figure 5.11A**. The FTIR spectra of **5A**@SiO_2, **5A**@SiO_2–NH_2, and **5A**@SiO_2–FA evidenced the presence of a low-intensity band at 1622 cm^{-1} which corresponded to the $\nu_{C=O}$ asymmetric stretching sharp peak of the bare complex **5A** spectrum and it was absent in the pristine SiO_2NP spectrum. Considering the spectral line for **5A**@SiO_2–NH_2 (**Figure 5.11A**, pink line), the appearance of an additional broad band, centered at 3118 cm^{-1} (ν_{N-H} stretching) along with the moderate hump at 1548 (ν_{N-H} bending) confirmed the grafting of the amino groups onto the surface of the complex confined nanoparticles. The additional peak at 1648 cm^{-1} (ν_{N-H} bending, amide

group) in the spectra for **5A**@SiO_2–FA (**Figure 5.11B**, green line) indicated the afterwards organo-modification by covalent conjugation of folic acid moiety through amide bond formation and the other peak at 1607 cm^{-1} could be attributed to the non-bonded carboxylate unit of folic acid ligand. Additionally, the thermogravimetric analyses (TGA) on all three types of nanomaterials were done in the range of 30-800 °C (**Figure 5.11C**). **5A**@SiO_2–NH_2 (blue line) evidenced an ~8.6 % increased organic weight loss compared to the naked **5A**@SiO_2 above 200 °C, designating the inclusion of amine groups. For **5A**@SiO_2–FA, another steep decrease in weight percentage (red line, ~8.3 % weight loss) directly reciprocated the tethering of folate units onto the nanoparticle surface. The surface charge of the nanomaterials was assessed by recording the zeta potential (ζ) of their respective aqueous suspension, at pH ~ 7.4 (**Figure 5.11D**). **5A**@SiO_2, having a negatively charged surface with a large number of hydroxyl groups exhibited a ζ value of -24.9 mV. The inclusion of surface-conjugated basic amine groups in **5A**@SiO_2–NH_2 caused a sharp inversion of the ζ value to +24.5 mV. Thereafter introduction of negatively charged folate units (with a free carboxylate arm at pH ~ 7.4) further reduced the ζ value for **5A**@SiO_2–FA to +17.1 mV. Thus, the characterization suggested the successful formation of complex **5A** incorporated porous silica nanoparticles with amine and folic acid units grafted on the outer surface.

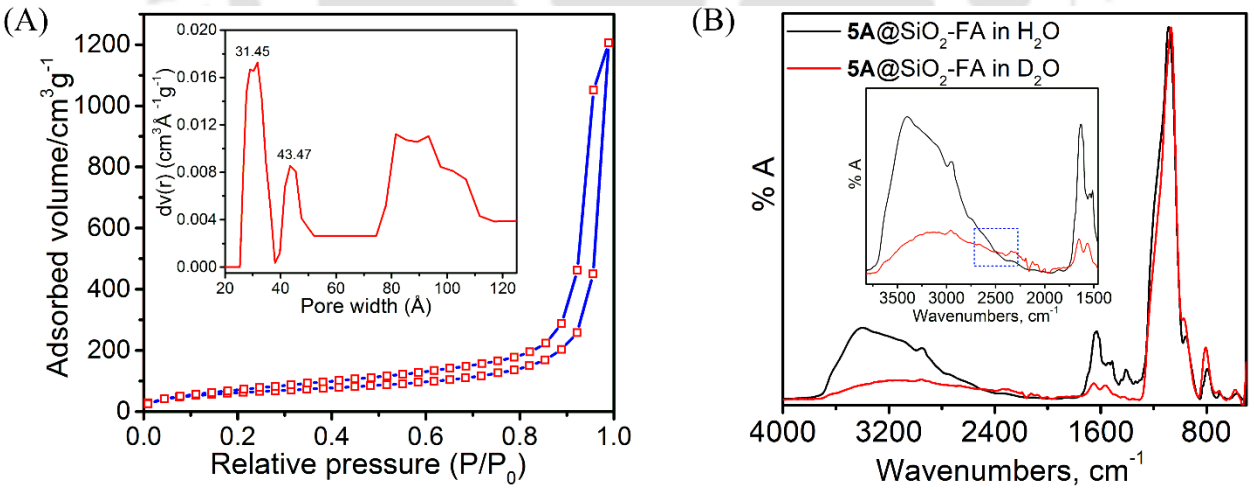

Figure 5.12. (A) N_2 adsorption isotherm of degassed **5A**@SiO_2–FA NPs. Inset: Pore size distribution. (B) FTIR spectra of lyophilized **5A**@SiO_2–FA NPs, isolated from H_2O or D_2O medium.

The surface area along with the porous nature of the surface-modified **5A**@SiO_2–FA NPs was elucidated from the N_2 adsorption-desorption isotherm, recorded at 77 K (**Figure 5.12A**). The dried nanoparticles were degassed for 12 h before the experiment. **5A**@SiO_2–FA NPs exhibited a type-IV isotherm with a hysteresis loop, indicating a well-defined porous nature of the silica shell.[20] Based on the Brunauer–Emmett–Teller (BET) method, the overall surface area of the nanomaterial was determined to be 216.0 m^2/g. The pore-size distribution was obtained from Barrett-Joyner-Helenda (BJH) calculations revealing two types of pore diameter, 3.1 nm and 4.3 nm. Other pores with larger diameters could be because of the inter-particle voids.[21] The unperturbed movement of water molecules across the pores of the organo-modified silica shell was proved by comparing the FTIR spectra of **5A**@SiO_2–FA NPs, lyophilized after suspending for 24 h in D_2O medium (**5A**@SiO_2–FA_D_2O, red line), with that for H_2O suspended nanoparticles (**Figure 5.12B**). In the case of **5A**@SiO_2–FA_D_2O, the emergence of a broad band centred at 2390 cm^{-1} could be assigned to the ν_{O-D} asymmetric stretching, indicating the accessibility of the D_2O molecules into the core of nanoparticle through the available pores. This result warranted the water exchange towards the core of the nanoparticle across the silica layer, even after the attachment of bulky and hydrophobic folate appendants.

Table 5.5. Characterization of **5A**@SiO_2, **5A**@SiO_2–NH_2, **5A**@SiO_2–FA nanomaterials: corresponding FETEM particle size, zeta potential values (at pH 7.4) and percentage organic weight loss, measured at 37 °C, pH ~ 7.4, 1.41 T.

Material	Particle Size (nm)	ζ potential (mV)	TGA, weight loss %
5A@SiO_2	18.6	-24.9	4.66
5A@SiO_2–NH_2	19.3	24.5	13.24
5A@SiO_2–FA	21.6	17.1	21.62

5.6 Relaxometric Studies of 5A and 5A-Confined Silica Nanomaterials

The relaxometric studies of complex **5A** along with the complex incorporated nanomaterials were done using a buffered solution (HEPES, pH ~ 7.4) of four different concentrations, estimated by ICP-MS analysis. Respective T_1 values were recorded according to the inversion recovery method using BRUKER minispec mq60 NMR, at pH ~ 7.4, 1.41 T and 37 °C. Corresponding plots for the relaxation rates ($1/T_1$) *versus* [Mn(II)] were obtained. The slope represented the respective relaxivity values (r_1) which defined the contrast efficiency of 1 mM concentration of each paramagnetic substance.

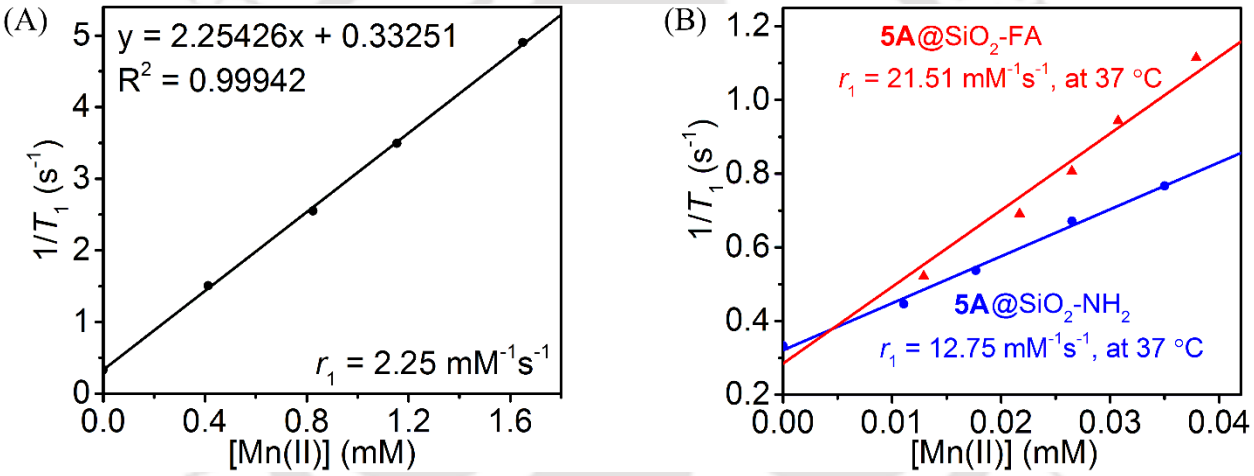

Figure 5.13. $1/T_1$ versus [Mn(II)] plot for (A) complex **5A**, (B) **5A**@SiO_2–NH_2 and **5A**@SiO_2–FA at pH ~ 7.4, 1.41 T, and 37 °C.

For complex **5A**, the r_1 value was estimated to be 2.25 $mM^{-1}s^{-1}$ at pH ~ 7.4, 1.41 T, and 37 °C. The value was in accordance with the data reported for similar mono-aquated Mn(II) complexes. On impregnating the complex **5A** molecules inside the porous silica nanoparticles functionalized with the amine chains (**5A**@SiO_2–NH_2), an obvious 4.5-fold elevation in relaxivity value was achieved as r_1 reached up to 12.75 $mM^{-1}s^{-1}$. This increment could be attributed to the longer rotation correlation time (τ_R) and faster water exchange of the paramagnetic centre upon non-covalent confinement of **5A** molecules along with sufficient water molecules inside the porous silica nanosphere. About ~ 40 complex molecules are contained inside each nanosphere, leading

to a closely spaced big cluster-type entity which was less prone to come out, rendering a stable nanocomposite. Results were similar to other nanomaterials, previously reported in the earlier chapters. Upon conjugation of the bulky folate units to the amine-functionalized **5A**@SiO_2–NH_2 NPs *via* an amide linkage, the particle weight is increased by about 21% (TGA analysis, **Table 5.5**). Henceforth, the longitudinal relaxivity of the **5A**@SiO_2–FA nanosystem correspondingly increased to 21.51 $mM^{-1}s^{-1}$. Multiple bulky folic acid units attached to the silica surface were expected to create a corona over each nanoparticle trapping water molecules within the network through hydrogen bonding with the non-coordinated carboxylate arm (of folic acid). This would eventually increase the accessibility of water molecules and the overall weight of the nanosystem altogether, thus positively affecting the relaxivity value of the folate-modified nanoparticle, **5A**@SiO_2–FA.

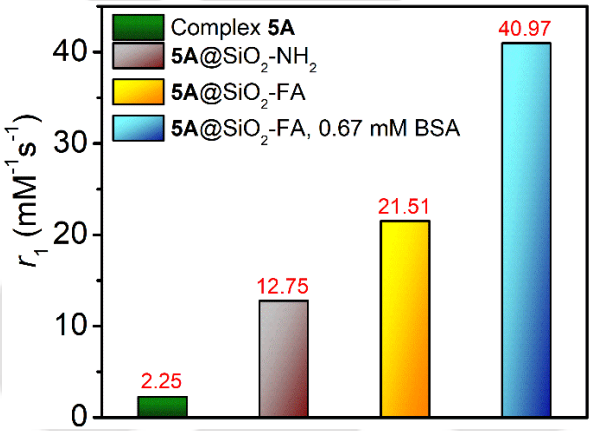

Figure 5.14. Longitudinal relaxivity values for Complex **5A**, **5A**@SiO_2–NH_2 and **5A**@SiO_2–FA in HEPES buffer (pH 7.4) and in the presence of 4.5% (w/v) BSA, measured at 1.41 T and 37 °C.

The interaction of the surface-modified nanomaterial **5A**@SiO_2–FA with the serum albumin protein was studied at the physiological condition (maintained at 0.67 mM BSA and 37 °C; **Figure 5.14**). A prominent improvement in the relaxivity was observed as the r_1 value elevated to 40.97 $mM^{-1}s^{-1}$ in the presence of albumin protein. This interaction is further investigated by following the respective surface potential of the nanoparticle suspension, before and after the addition of BSA. The nanomaterial exhibited a spontaneous decrease in the zeta potential to -10 mV (~27 units change from 17.1 mV) after the addition of 0.67 BSA solution, indicating an extensive association with the albumin protein moiety. The results reflected a profound

electrostatic and non-covalent interaction between the negatively charged albumin protein moiety and the positively charged surface of **5A**@SiO_2–FA NPs, at pH ~ 7.4. The hydrophobic rings of the folate ligands attached to the nanoparticle surface were anticipated to bind the albumin protein, forming a bulky corona (**5A**@SiO_2–FA•BSA). The overall tumbling rate is further reduced thereby increasing the longitudinal relaxivity value.

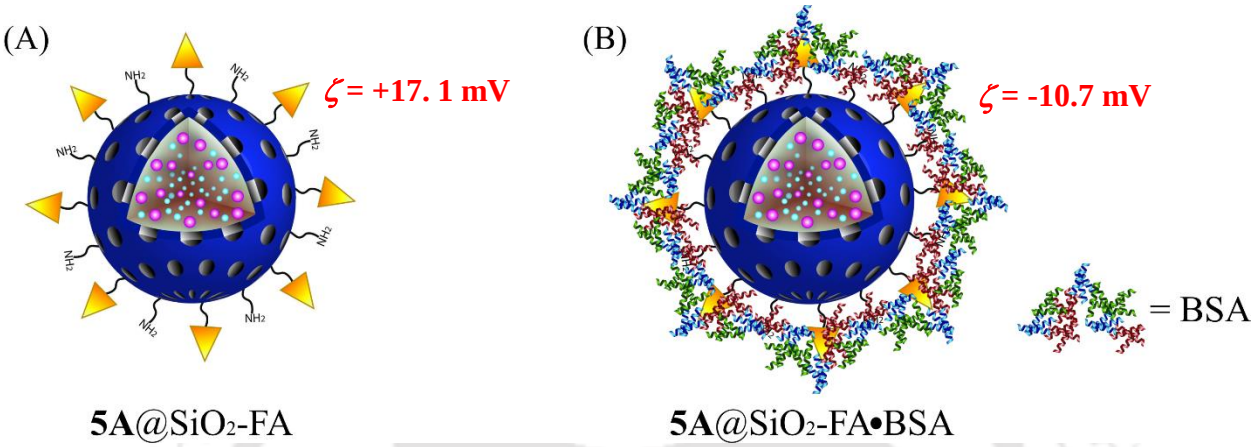

Figure 5.15. Schematic illustration of (A) **5A**@SiO_2–FA and (B) BSA associated **5A**@SiO_2–FA along with the zeta potential values.

Consequently, **5A**@SiO_2–FA NPs could potentially utilize the pathological condition of cancer tissues of having higher albumin content, hence rendering brighter MR signals in the localized region, creating a vivid contrast.

5.7 Stability of 5A Confined FA-Modified Silica Nanomaterial

The microenvironment of tumour tissues is slightly acidic (5.5-6.5) than healthy ones.[13] Moreover, the stomach, spleen, kidneys and other major organs that are involved in the clearance of administered contrast agents are reported to have a pH varying from 7.4 (the pH of blood). Physiologically important bicarbonates, biphosphates and citrates that are present inside the body at non-negligible concentration could potentially hamper the stability along with the relaxometric properties of the paramagnetic nanomaterial.[22] Thus, the stability of the complex **5A** confined FA-modified nanomaterials has to be tested in a broad pH range and challenging conditions with the mentioned ions, before administration for *in vivo* studies.

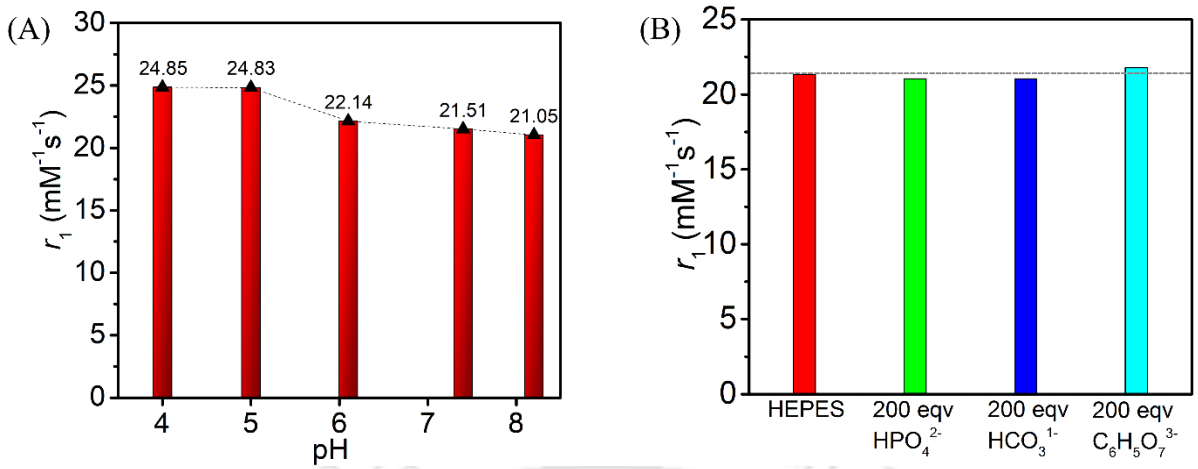

Figure 5.16. r_1 values for **5A**@SiO_2–FA in different mediums: (A) Variable pH solutions and (B) in the presence of 200 equivalents of physiological anions, at pH ~ 7.4. Experiments were done at 37 °C and 1.41 T.

In this context, the longitudinal relaxivity of **5A**@SiO_2–FA NPs was monitored in the pH range of ~ 4-8. The value was almost unaltered between pH 6-8, but a 12% increase in relaxivity value was evidenced approaching lower pH onwards 5 (**Figure 5.16A**). To introspect this effect, the zeta potential of **5A**@SiO_2–FA suspensions was recorded at varied pH. An increasing ζ trend was observed on decreasing the pH with a major ~ 4 unit change at pH 5.05 [ζ, mV: 17.1 (pH 7.4), 17.6 (pH 6.1), 21.4 (5.05), 22.01 (4.06)]. To note, one of the pK_a values of folic acid is 4.98.[23] Consequently, protonation of the corresponding groups occurred at this pH region, increasing the overall zeta charge of **5A**@SiO_2–FA NPs. Henceforth, the higher surface zeta potential of the nanoparticles would have increased the interparticle repulsion factor by lowering the pH to 5, reducing the agglomeration rate. The pores on the nanoparticle surface were believed to be more accessible for water exchange at this pH to reach the complex molecules confined within the core. This could be a plausible explanation for the increase in relaxivity by decreasing the pH to 5.

The synthesized **5A**@SiO_2–FA NPs were found to be stable when challenged by 200 equivalents of different physiological anions as relaxivity values remained unchanged when NPs were incubated with the respective anions (**Figure 5.16B**).

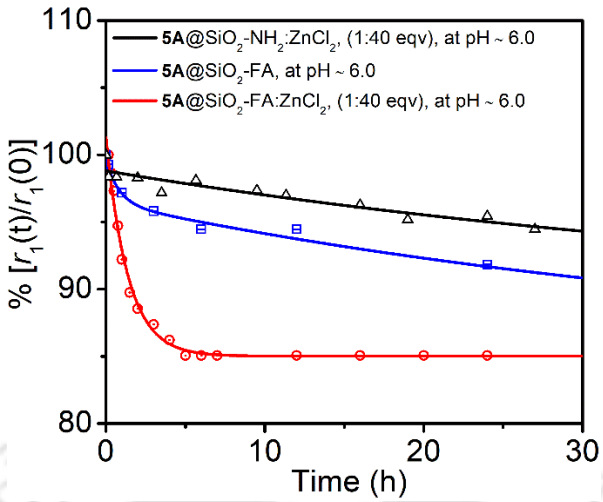

Figure 5.17. Time profile of **5A**@SiO_2–NH_2 and **5A**@SiO_2–FA suspensions in MES buffer, pH ~ 6.0, when challenged with 40 equivalents of Zn(II) ions (concentration represented in terms of Mn^{II}). Measurements were done at 37 °C and 1.41 T.

Kinetic inertness is a key factor in determining the applicability of contrast agents *in vivo*.[24] It is defined as the time required for 20% decrease in the initial relaxivity value for pristine material in the presence of scavenger ions. Zn(II) ions are present in significant concentration inside the body and are capable of dechelation of the paramagnetic Mn(II)-chelate. In this context, the stability of **5A**@SiO_2–NH_2 and **5A**@SiO_2–FA nanomaterials were tested by recording the r_1 value of aqueous suspensions of respective nanomaterial against time, in the absence and presence of 40 equivalents excess of Zn(II) ions, at 37 °C. For **5A**@SiO_2–NH_2, irrespective of Zn(II) ions concentration, a shuttle change in relaxivity value (~5%) was observed upto 24 hours. However, in the same time scale, 8% and 15% decrease in r_1 values were visualized for **5A**@SiO_2–FA, in the absence and presence of Zn(II) ions, respectively. Conjugation of bulky folic acid units would have caused an increased rate of agglomeration of nanoparticles, reducing the water accessibility towards the core and diminishing the r_1 value. In the presence of Zn(II) ions, the agglomeration of nanoparticles is further enhanced. The negatively charged carboxylate parts of the different folate moieties were expected to associate with the Zn(II) ions, hindering the suspendability of **5A**@SiO_2–FA. Notwithstanding, the overall diminishing effect is minimal in the time scale required for *in vivo* MRI scans certifying the suitability of the synthesized nanomaterial (**5A**@SiO_2–FA) for further biological applications.

5.8 Phantom Imaging of 5A@SiO$_2$–FA NPs in water, at 1.5 T

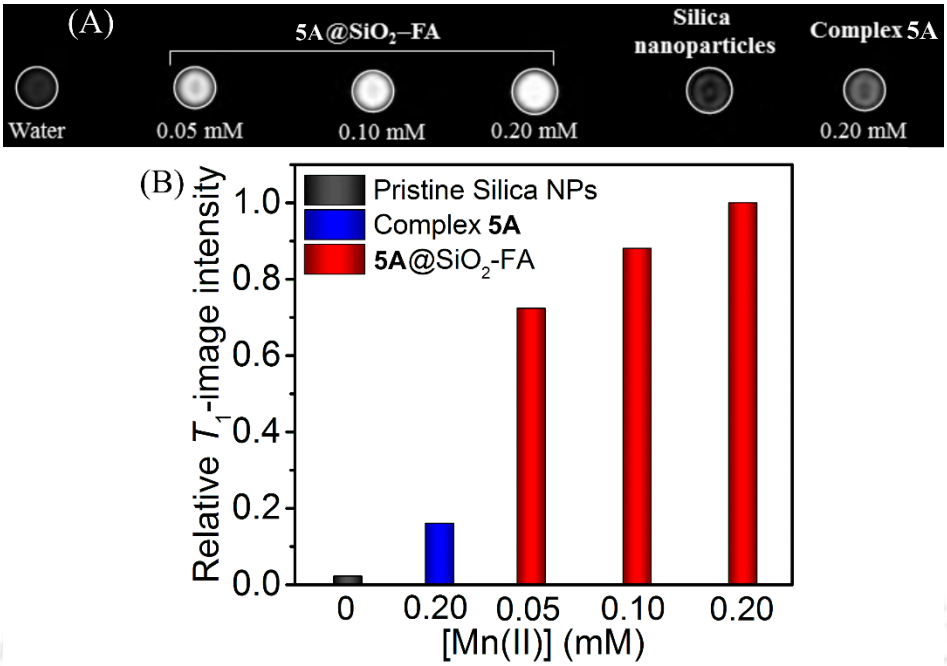

Figure 5.18. (A) T_1-weighted phantom images of micro-centrifuge tubes containing pristine SiO_2 NPs, Complex **5A** and **5A**@SiO_2–FA, at 1.5 T and 25 °C. (B) Respective image intensity plots *versus* paramagnetic metal concentration.

The applicability of the synthesized folic acid-modified nanomaterial as an efficient T_1-weighted contrast agent for MR imaging was investigated *in vitro* by recording clinical MR images of **5A**@SiO_2–FA suspension in HEPES buffer. Micro-centrifuges containing **5A**@SiO_2–FA at different [Mn(II)] concentrations were considered as phantoms and imaged under MAGNETOM Avanto 1.5 T clinical MRI scanner, at 25 °C (**Figure 5.18A**). For T_1-weighted images, respective parameters were adopted: TR (repetition time) = 550 ms, TE (echo time) = 8.4 ms, slice thickness = 2.5 mm, and field of view (FOV) = 175×200 mm^2.

Successive increase in paramagnetic concentration revealed brighter T_1-weighted images. The intensity of each image was quantified using *ImageJ* software and plotted respectively (**Figure 5.18B**). The **5A**@SiO_2–FA NP suspensions (0.2 mM w.r.t [Mn^{II}]) imparted a ~7-fold brighter image when compared to bare complex **5A** solution at the same concentration. Thus, a vivid boost

in relaxivity, as well as, image brightness had been accomplished upon confinement of complex **5A** inside the folate functionalized silica nanomaterial.

5.9 In Vitro Studies of 5A Incorporated Silica Nanomaterials

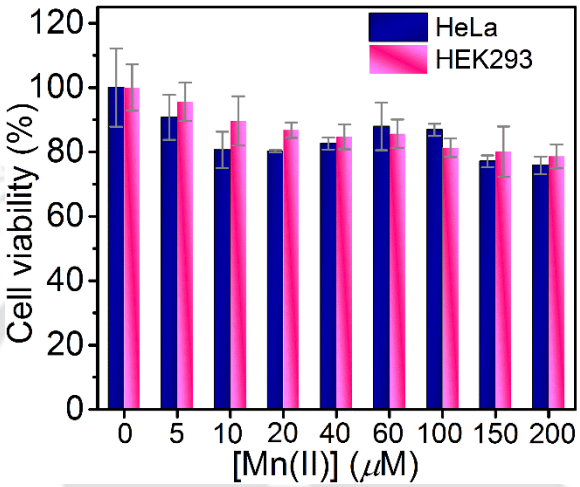

Figure 5.19. Percentage cell-viability plot for HeLa and HEK293 cells 48 hours post-treatment with **5A**@SiO_2–FA.

Cytotoxicity of **5A**@SiO_2–FA was assessed by performing MTT [3-(4,5-dimethyl-thiazol-2-yl) 2,5 diphenyltetrazolium bromide] assay on HeLa and HEK293 cell lines. During the experiment, cells were incubated for 48 hours with an increasing concentration of the nanoparticle up to 200 μM Mn(II) concentration, and the absorbance of each vial was measured at 570 nm. Subsequently, viable cells were quantified considering 100% viability for untreated cells (**Figure 5.19**). **5A**@SiO_2–FA nanomaterial was found to be efficiently inert for bio-applications as more than 80% cells were tolerant towards the synthesized nanoprobe after the course of the experiment.

Folate-Mediated Cell Uptake

The selective internalization process of the synthesized complex **5A** incorporated nanomaterials inside the cancer cells was visualized by recording the fluorescent images of the treated cells. Prior to the experiments, respective nanomaterials were tagged with the fluorescence-active FITC (Fluorescein isothiocyanate) group by covalent conjugation (**5A**@SiO_2–NH_2/FITC and

5A@SiO_2–FA/FITC). Both types of nanomaterials (25 µM, w.r.t. Mn concentration) were treated on the HeLa and HeK293 cell line for 1 h and repeatedly washed with PBS buffer to remove the unattached particles. Cells were resuspended in a buffer medium and trypan blue (200 µg/mL) was added to quench the fluorescence of exocellular nanoparticle residue. After another washing with the buffer solution, suspended cells were viewed under Zoe fluorescence microscope.

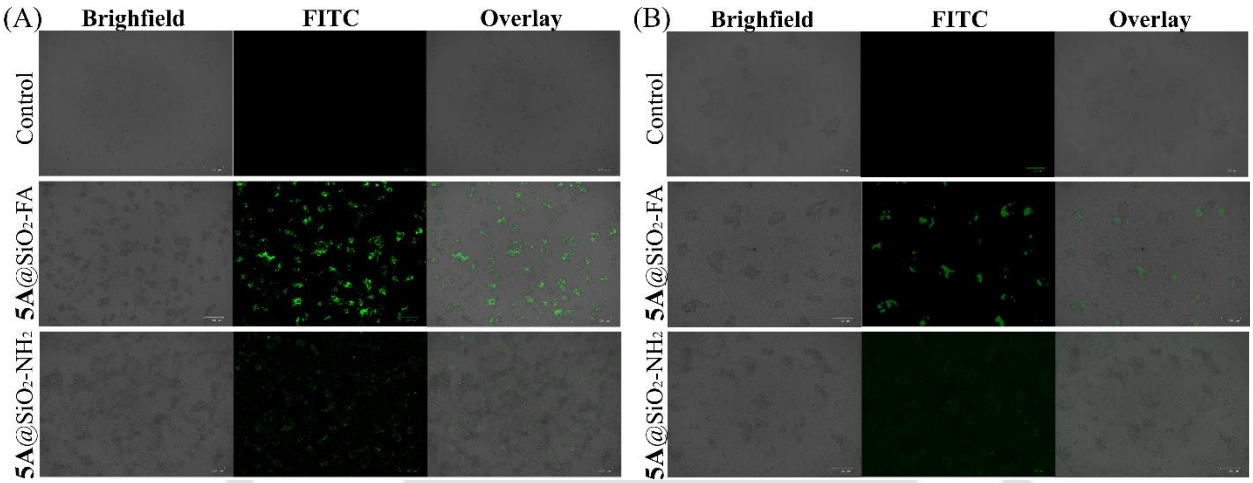

Figure 5.20. Fluorescence imaging of HeLa cells or HEK293 cells before and 1 h after treatment with **5A**@SiO_2–FA/FITC and **5A**@SiO_2–NH_2/FITC. Trypan blue was added to each sample after incubation to minimize the exocellular fluorescence.

For the folate-modified nanomaterial, a rapid uptake of the nanoparticle inside the HeLa cell membrane was observed (**Figure 5.20A**, second line). Most of the **5A**@SiO_2–FA/FITC particles added to the cancer cells had entered the intracellular space as bright green fluorescence was shown in the region corresponding to the cell positions. However, in the case of **5A**@SiO_2–NH_2/FITC system, particles mostly resided in the extracellular space and the fluorescence was subsequently quenched by the addition of trypan blue. To compare the rate of internalization of the **5A**@SiO_2–FA/FITC NPs in cancer cells to the healthy cells, similar fluorescence images of HEK293 cells were considered (**Figure 5.20B**). Lower fluorescence intensity inside the cells corresponded to increased cell uptake in the cancerous HeLa cell line. Thus, the folate-mediated improved cell-uptake property of **5A**@SiO_2–FA was established from the study.

Flow cytometric analysis was done to quantify the relative number of HEK293 and HeLa cells targeted with **5A**@SiO_2–NH_2–NP/FITC or **5A**@SiO_2–FA–NP/FITC (**Figure 5.21**). The shift of the chromatogram towards the high-intensity fluorescence region indicated increased cellular uptake of the respective NPs. The mean fluorescence intensity value for cells with or without NP uptake (after the addition of trypan blue) was recorded and a comparative plot is presented in **Figure 5.21E**. Within an hour of treatment, almost 3 times higher **5A**@SiO_2–FA–NP/FITC uptake for HeLa cells contrary to non-cancerous HEK293 cells has been observed, similar to the previous results from fluorescence imaging. Thus, the contemplated MRI contrast agent for folate-mediated cell uptake selectively for the cancerous cells has been materialized. Additionally, the aforementioned studies unequivocally established the applicability of **5A**@SiO_2–FA–NP as dual-mode fluorescent (in the presence of FITC) and MR imaging agents.

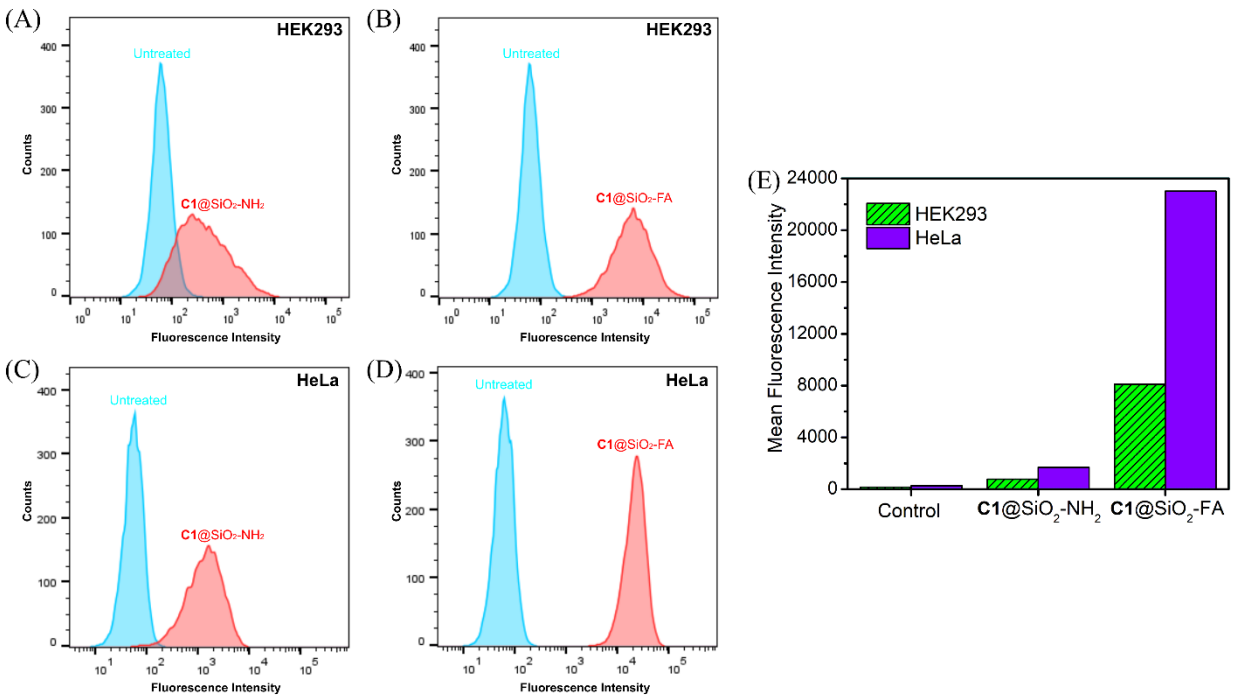

Figure 5.21. Cellular uptake studies by flow cytometry on HEK293 and HeLa cells. HEK293 cells were treated with (A) **5A**@SiO_2–NH_2–NP/FITC and (B) **5A**@SiO_2–FA–NP/FITC for 1 h. HeLa cells were treated with (C) **5A**@SiO_2–NH_2–NP/FITC and (D) **5A**@SiO_2–FA–NP/FITC for 1 h. Trypan blue was added to each sample after incubation to minimize the exocellular fluorescence. (D) Mean fluorescence intensity plot for each sample.

5.10 MRI of 5A Incorporated Silica Nanomaterials to Detect Cancer Cells In Vivo, at 7 T

Preceding *in vitro* studies concreted the capabilities of **5A**@SiO_2–FA NPs to selectively accumulate and penetrate inside the cancer cells, increasing the relaxivity value alongside. Herein, to validate the applicability of the nanomaterial inside the living system, a batch of C57BL/6 male mice (total number = 12) were procured and half of them were infected with HeLa cells (1.2×10^6) by intraperitoneal injection (i.p.). After 3 days, mice were anaesthetized with 1-3% isoflurane/oxygen mixture maintaining normal respiration and subsequently imaged at 7 T post-administration (i.p.) of the synthesized nanoparticles (**5A**@SiO_2–NH_2 and **5A**@SiO_2–FA). A small-bore animal scanner (Biospec 70/20, M/s Bruker Biospin GmBH, Germany) was used for imaging. The protocol adopted at baseline comprised multislice two-dimensional rapid acquisition with refocused echo (RARE) imaging to delineate anatomy. Imaging parameters were: Coronal orientation, TR/TE = 3647.4 ms/8 ms, the field of view (FOV) = 50×50 mm, matrix = 256×256, slice thickness = 1 mm, 256 slices; Axial orientation: TR/TE = 3647.4 ms/8 ms, matrix = 256×256, slice thickness = 1 mm, 84 slices.

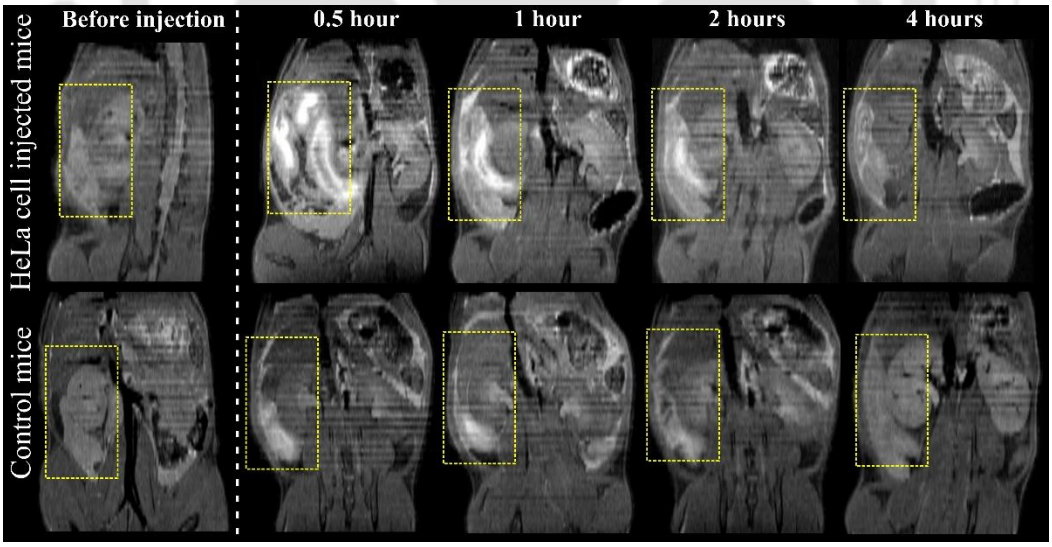

Figure 5.22. Coronal view of T_1-weighted MR images of cancer cell affected and healthy C57BL/6 mice, pre- and post-i.p. administration of **5A**@SiO_2–FA (10 μmol/kg w.r.t [MnII]) at different time points, measured at 7 T animal MR scanner. The yellow box indicated the region of interest.

The cancer cell-infected mice were separated into 2 groups (n = 3) and the healthy cells were also similarly divided. In separate experiments, each group received a dosage of **5A**@SiO_2–FA NPs or **5A**@SiO_2–NH_2, 10 μmol/kg w.r.t. [Mn(II)] into the intraperitoneal (i.p.) space of (A)/(B) cancer affected mice; (C)/(D) healthy mice. T_1-weighted imaging sequences were performed at different time points (**Figure 5.22** and **5.23**). Images were analyzed by quantizing the signal intensity (SI) in the region of interest (ROI) of respective organs using *ImageJ* software, after subtracting over the noise intensity. Normalized signal-to-noise ratio (nSNR) was calculated by dividing the SI at each time point to the pre-contrast image SI. Contrast to noise ratio (CNR) was estimated by normalizing the signal intensity of ROIs with that of the back muscles in the same slide. Pre-injection SNRs and CNRs were considered as baseline and percentage change in the respective CNR (% ΔCNR) upon contrast injection was plotted. The ROIs analyzed were considered and statistical significances were examined using unpaired two-tailed t-tests to validate the significance of the experiment; results with *P*-values < 0.05 were considered useful.

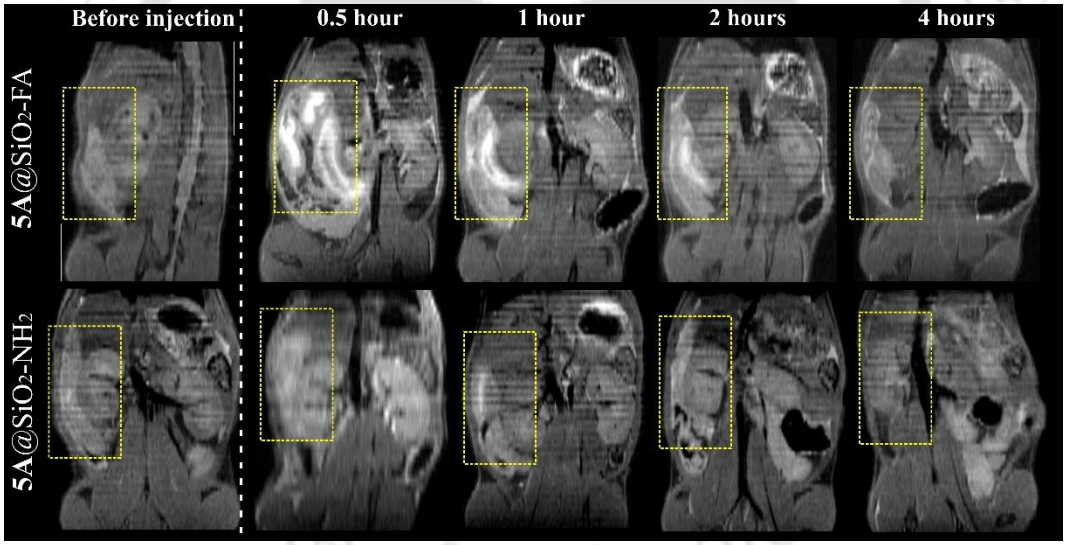

Figure 5.23. Coronal view of T_1-weighted MR images of cancer cells affected C57BL/6 mice, pre- and post-i.p. administration of **5A**@SiO_2–FA and **5A**@SiO_2–NH_2 (10 μmol/kg w.r.t [MnII]) at different time points, imaged at 7 T MR scanner. The yellow box indicated the region of interest.

Post 30 minutes administration of the **5A**@SiO_2–FA NP suspension into the cancer-cell infected mice provided a ~100% contrast enhancement in the region where the cancer cells were accumulated, compared to that of the control mice (healthy mice, injected with the same dosage

of **5A**@SiO_2–FA NPs) (**Figure 5.24A**). A slight drop in signal intensity was observed by 1 h and the significant contrast was evident till 4 h of contrast administration. The ΔSNR gradually dropped with time, indicating the clearance of the nanoparticles (**Figure 5.25B**).

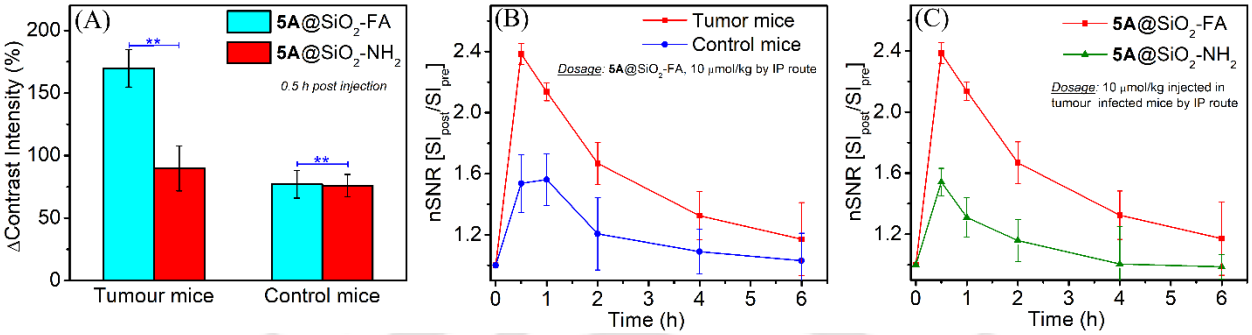

Figure 5.24. Quantitative image analysis of the respective MR images of mice after receiving **5A**@SiO_2–FA or **5A**@SiO_2–NH_2 (10 μmol/kg w.r.t [MnII]) by measuring signal intensity changes in the region of interest, normalized to the muscle (n = 3 animal per group). (A) Contrast enhancement after 0.5 h of contrast administration. (B) and (C) Time-dependent changes in signal intensity in each image. Bars represent the standard error of the mean. ∗P < 0.05, ∗∗P < 0.001.

The effect of the folate group in directing the cancer cell selectivity was rationalized by comparing the signal enhancement induced by **5A**@SiO_2–FA NPs to the similar images obtained after injecting **5A**@SiO_2–NH_2 NP suspensions (**Figure 5.23**). A modest increase in signal intensity was imparted by the **5A**@SiO_2–NH_2 NPs at the mentioned time scale proving the superior cancer-selective accumulation and contrast enhancement properties of **5A**@SiO_2–FA NPs. Thus, the FA-attached porous silica nanoparticle confined complex **5A** was successful in targeting and selectively enhancing the MR contrast of the cancer cell microenvironment inside the body.

5.11 Conclusion

- Herein, we reported the synthesis and characterization of ligand H_2tpada based mono-aquated Mn(II)-complex, **5A**. The complex was thermodynamically stable exhibiting logK_{MnL} value of 14.67 and pMn (at pH ~ 7.4) = 8.80. The chelate remained unchanged at pH 10.1, attained by the addition of ammonium hydroxide.

- Complex **5A** molecules were incorporated within the porous silica nanoparticles (PSNs) with the surface functionalized with amine groups, **5A**@SiO_2–NH_2 (sized 19.3 nm). The folic acid ligand was successfully grafted over the surface of the synthesized nanoparticles yielding **5A**@SiO_2–FA NPs.

- All of the synthesized nanoparticles were carefully characterized and a number average of 40 **5A** molecules were derived to be confined within each unfunctionalized nanomaterial.

- Relaxometric studies on **5A**@SiO_2–FA NPs revealed a longitudinal relaxivity value of 21.51 $mM^{-1}s^{-1}$ in water and 40.97 $mM^{-1}s^{-1}$ in 0.67 mM BSA solution, when measured at pH ~ 7.4, 1.41 T and 37 °C.

- The synthesized nanomaterial exerted high stability against external protons, Zn(II) ions and other physiologically important anions.

- The contrast enhancement ability of **5A**@SiO_2–FA NPs was studied by analyzing the concentration-dependent phantom images, obtained at a 1.5 T clinical MRI scanner.

- The comparative cytotoxicity and cell uptake studies on cancerous HeLa and healthy HEK293 cell lines authenticated the folate-mediated rapid and selective accumulation of **5A**@SiO_2–FA NPs inside the cancer cells.

- The cancer cell-targeting and serum albumin binding contrast enhancement properties of **5A**@SiO_2–FA NPs were evidenced *in vivo* by performing MRI scans on cancer-affected C57BL/6 mice.

5.12 References

1. (a) A. S.-Zadeh, A. Rezaeyan, A. Sarikhani, H. Ghaffari, H. Samadian, S. Khademi, H. Ghaznavi and J. W. M. Bulte, *Nano Today*, 2021, **39**, 101173; (b) S. Siddique and J. C. L. Chow, *Nanomater*., 2022, **12**, 2826; (c) Y. Gao, K. Wang, J. Zhang, X. Duan, Q. Sun and K. Men, *MedComm.*, 2023, **4**, e187.

2. (a) H. Hu, F. Arena, E. Gianolio, C. Boffa, E. D. Gregorio, R. Stefania, L. Orio, S. Baroni and S. Aime, *Nanoscale*, 2016, **8**, 7094–7104; (b) Q. Wen, Y. Zhang, C. Li, S. Ling, X. Yang, G. Chen, Y. Yang and Q. Wang, *Angew. Chem. Int. Ed*., 2019, **58**, 11001–11006; (c) J. Yan, Z. Lu, M. Xu, J. Liu, Y. Zhang, J. Yin, Y. Cao and R. Pei, *J. Mater. Chem. B*, 2023, **11**, 3176.

3. (a) F.A. Gallagher, *Clinical Radiology*, 2010, **65**, 557e566; (b) J. C. Gore, H. Charles Manning, C. C. Quarles, K. W. Waddell and T. E. Yankeelov, *Magn. Reson. Imaging*, 2011, **29**. 587–600; (c) T. Hussain and Q. T. Nguyen, *Adv. Drug Deliv. Rev.*, 2014, **66**, 90–100; (d) C. Peng, J. Qin, B. Zhou, Q. ian Chen, M. Shen, M. Zhu, X. Lu and X. Shi, *Polym. Chem*., 2013, **4**, 4412–4424; (e) S.L. Ho, H. Yue, S. Lee, T. Tegafaw, M.Y. Ahmad, S. Liu, A. K. A. A. Saidi, D. Zhao, Y. Liu, S.-W. Nam, K. S. Chae, Y. Chang and G. H. Lee, *Pharmaceutics*, 2022, **14**, 1458.

4. (a) G.-L. Davies, I. Kramberger and J. J. Davis, *Chem. Commun.*, 2013, **49**, 9704-9721; (b) Z. Zhou, M. Qutaish, Z. Han, R. M. Schur, Y. Liu, D. L. Wilson and Z.-R. Lu, *Nat. Commun.*, 2015, **6**, 7984; (c) J. Lux and A. D. Sherry, *Curr Opin Chem Biol*., 2018, **45**, 121–130; (d) M.M. Otero-García, A. Mesa-Álvarez, O. Nikolic, P. Blanco-Lobato, M. Basta-Nikolic, R. M. de Llano-Ortega, L. Paredes-Velázquez, N. Nikolic and M. Szewczyk-Bieda, *Insights Imaging*, 2019, **10**, 19.

5. (a) V. Bhargava, K. Singh, P. Meena, R. Sanyal, Nephrogenic systemic fibrosis: A frivolous entity. *World J Nephrol*, 2021, **10**, 29-36; (b) S. Gallo-Bernal, N. Patino-Jaramillo, C. A. Calixto, S. A. Higuera, J. F. Forero, J. Lara Fernandes, C. Góngora, M. S.

Gee, B. Ghoshhajra and H. M. Medina, *Diagnostics*, 2022, **12**, 1816; (c) S. Anbu, S. H. L. Hoffmann, F. Carniato, L. Kenning, T. W. Price, T. J. Prior, M. Botta, A. F. Martins and G. J. Stasiuk, *Angew. Chem. Int. Ed.* 2021, **60**, 10736–10744.

6. (a) PRAC Confirms Restrictions on the Use of Linear Gadolinium Agents; EMA/424715/2017; *European Medicines Agency*, July 7, 2017; (b) FDA Drug Safety Communication: FDA Warns That Gadolinium-based Contrast Agents (GBCAs) are Retained in the Body; Requires New Class Warnings; U.S. Food and Drug Administration, December 19, 2017.

7. (a) D. Pan, A. H. Schmieder, S. A. Wickline and G. M. Lanza, *Tetrahedron*, 2011, **67** 8431e8444; (b) W. Lin, T. Hyeon, G. M. Lanza, M. Zhang and T. J. Meade, *MRS Bulletin*, 2009, **34**, 441–448; (c) C. Henoumont, M. Devreux and S. Laurent, *Molecules*, 2023, **28**, 7275.

8. (a) J. R. Morrow and É. Tóth, *Inorg. Chem.* 2017, **56**, 6029–6034; (b) H. Li and T. J. Meade, *J. Am. Chem. Soc.*, 2019, **141**, 17025–17041; (c) J. Peng, P. Gong, S. Li, F. Kong, X. Ge, B. Wang, L. Guo, Z. Liua and J. You, *Chem. Eng. J.*, 2020, **391**, 123619; (d) H. Hu, *Front. Chem.*, 2020. **8**, 203; (e) Y. Yang, W. Zeng, P. Huang, X. Zeng and L. Mei, *VIEW*, 2021, **2**, 20200042.

9. (a) J. L. Major and T. J. Meade, *Acc. Chem. Res.*, 2009, **42**, 893-903; (b) L. K. Moore, M. A. Caldwell, T. R. Townsend, K. W. MacRenaris, G. Moyle-Heyrman, N. Rammohan, E. K. Schonher, J. E. Burdette, D. Ho and T. J. Meade, *Bioconjugate Chem.*, 2019, **30**, 2947–2957; (c) X. Wang, X. Zhong, H. Lei, N. Yang, X. Gao, L. Cheng, *J. Bio-X Res*, 2020, **3**, 144-156; (d) H. Li, G. Parigi, C. Luchinat and T. J. Meade, *J. Am. Chem. Soc.*, 2019, **141**, 6224–6233; (e) S. M. Pinto, V. Tomé, M. J. F. Calvete, M. M. C.A. Castro, É. Tóth and C. F. G. C. Geraldes, *Coord. Chem. Rev.*, 2019, **390**, 1–31.

10. (a) M. Kueny-Stotz, A. Garofalo and D. Felder-Flesch, *Eur. J. Inorg. Chem.*, 2012, 1987–2005; (b) R. Wei, X. Gong, H. Lin, K. Zhang, A. Li, K. Liu, H. Shan, X. Chen and J. Gao, *Nano Lett.*, 2019, **19**, 5394–5402; (c) Z. Zhou, R. Bai, Z. Wang, H. Bryant, L. Lang, H.

Merkle, J. Munasinghe, L. Tang, W. Tang, R. Tian, G. Yu, Y. Ma, G. Niu, J. Gao and X. Chen, *Bioconjugate Chem*., 2019, **30**, 1821−1829; (d) P. Wang, X. Xu, Y. Wang, B. Zhou, J. Qu, J. Li, M. Shen, J. Xia and X. Shi, *Langmuir*, 2019, **35**, 4336−4341.

11. (a) N. Chen, C. Shao, Y. Qu, S. Li, W. Gu, T. Zheng, L. Ye and C. Yu, *ACS Appl. Mater. Interfaces*, 2014, **6**, 22, 19850–19857; (b) C. Shao, S. Li, W. Gu, N. Gong, J. Zhang, N. Chen, X. Shi and Ling Ye, *Anal. Chem.*, 2015, **87,** 12, 6251–6257; (c) X. Yang, Z. Zhou, L. Wang, C. Tang, H. Yang and S. Yang, *Mater. Res. Bull.*, 2014, **57**, 97–102; (d) Y. Hao, L. Wang, B. Zhang, H. Zhao, M. Niu, Y. Hu, C. Zheng, H. Zhang, J. Chang, Z. Zhang and Y. Zhang, *Nanotechnology*, 2016, **27**, 025101; (e) X. Ding, J. Liu, J. Li, F. Wang, Y. Wang, S. Song and H. Zhang, *Chem. Sci*., 2016, **7**, 6695–6700; (f) M. S. Foroushani, R. K. Shervedani, A. Kefayat, M. Torabi, F. Ghahremani and F. Yaghoobi, *J Drug Deliv Sci Technol*, 2019, **54**, 101223; (g) M. Torabi, F. Yaghoobi, R. K. Shervedani, A. Kefayat, F. Ghahremani and P. R. Harsini, *Colloids Surf. A: Physicochem. Eng.*, 2022, **652**, 129797; (h) Z.-X. Chen, M.-D. Liu, D.-K. Guo, M.-Z. Zou, S.-B. Wang, H. Cheng, Z. Zhong and X.-Z. Zhang, *Nanoscale*, 2020, **12**, 2966–2972; (i) H. Zhang, T. Wang, Y. Zheng, C. Yan, W. Gu and L. Ye, *BBRC*, 2018, **499** 488e492; (j) B. Y. W. Hsu, G. Kirby, A. Tan, A. M. Seifalian, X. Li and J. Wang, *RSC Adv.*, 2016, **6**, 45462-45474.

12. (a) J. Huang, J. Xie, K. Chen, L. Bu, S. Lee, Zhen. Cheng, X. Li and X. Chen, *Chem. Commun.*, 2010, **46**, 6684–6686; (b) K. D. Addisu, B. Z. Hailemeskel, S. L. Mekuria, A. T. Andrgie, Y.-C. Lin and H.-C. Tsai, *ACS Appl. Mater. Interfaces*, 2018, **10**, 5147−5160; (c) J. M. Rosenholm, A. Meinander, E. Peuhu, R. Niemi, J. E. Eriksson, C. Sahlgren and M. Lindén, *ACS Nano*, 2009, **3**, 1, 197–206.

13. A. M. Demin, A. G. Pershina, A. S. Minin, O. Ya. B., A. M. Murzakaev, N. A. Perekucha, A. V. Romashchenko, O. B. Shevelev, M. A. Uimin, I. V. Byzov, D. Malkeyeva, E. Kiseleva, L. V. Efimova, S. V. Vtorushin, L. M. Ogorodova and V. P. Krasnov, *ACS Appl. Mater. Interfaces*, 2021, **13**, 36800−36815.

14. (a) K. He, J. Li, Y. Shen and Y. Yu, *J. Mater. Chem. B*, 2019, **7**, 6840-6854; (b) H. Yan, Y. You, X. Li, L. Liu, F. Guo, Q. Zhang, D. Liu, Y. Tong, S. Ding and J. Wang, *Front. pharmacol*., 2020, **11**, 898; (c) D. Lalli, G. Ferrauto, E. Terreno, F. Carniato and M. Botta, *J. Mater. Chem. B*, 2021, **9**, 8994–9004; (d) C. Yu, Z. Ding, H. Liu, Y. Ren, M. Zhang, Q. Liao, T. Luo, L. Gao, S. Lyu, H. Tan, L. Hu, Z. Chen, P. Xu and E. Xiao, *Front. Chem.*, 2023, **11**, 1253379.

15. (a) P. S. Low, W. A. Henne and D. D. Doorneweerd, *Acc. Chem. Res.*, 2008, **41**, 120-129; (b) E.I. Sega and P.S. Low, *Cancer Metastasis Rev*, 2008, **27**, 655–664; (c) S. Marasini, H. Yue, S.-L. Ho, J.-A. Park, S. Kim, J.-U. Yang, H. Cha, S. Liu, T. Tegafaw, M. Y. Ahmad, A. K. A. A. Saidi, D. Zhao, Y. Liu, K.-S. Chae, Y. Chang and G.-H. Lee, *Appl. Sci*., 2021, **11**, 2596.

16. (a) R. Vivek, C. Rejeeth and R. Thangam, Multifunctional Systems for Combined Delivery, *Biosensing and Diagnostics*, Elsevier, 2017, 229-244; (b) M. Fernández, F. Javaid and V. Chudasama, *Chem. Sci.*, 2018, **9**, 790-810.

17. (a) Y. Feng, J. Shen, E.D. Streaker, M. Lockwood, Z. Zhu, P.S. Low, D.S. Dimitrov, *Arthritis Res. Ther.*, 2011, **13**, 1–12; (b) F. Dai, M. Du, Y. Liu, G. Liu, Q. Liu and X. Zhang, *J. Mater. Chem. B*, 2014, **2**, 2240–2247.

18. B. Gerey, M. Gennari, E. Gouré, J. Pécaut, A. Blackman, D. A. Pantazis, F. Neese, F. Molton, J. Fortage, C. Duboca and M.-N. Collomb, *Dalton Trans*., 2015, **44**, 12757–12770.

19. (a) E. M. Gale, I. P. Atanasova, F. Blasi, I. Ay and P. Caravan, *J. Am. Chem. Soc.*, 2015, **137**, 15548–15557; (b) K. Pota, Z. Garda, F. K. Kálmán, J. L. Barriada, D. Esteban-Gómez, C. Platas-Iglesias, I. Tóth, E. Brücher and G. Tircsó, *New J. Chem.*, 2018, **42**, 8001-8011; (c) E. M. Gale, S. Mukherjee, C. Liu, G. S. Loving and P. Caravan, *Inorg. Chem.*, 2014, **53**, 10748.

20. N. T. Vo, A. K. Patra and D. Kim, *Phys. Chem. Chem. Phys.*, 2017, **19**, 1937-1944.

21. M. Yu, L. Zhou, J. Zhang, P. Yuan, P. Thorn, W. Gu and C. Yu, *J. Colloid Intef. Sci.*, 2012, **376**, 67-75.

22. (a) E. M. Gale, N. Kenton and P. Caravan, *Chem. Commun*., 2013, **49**, 8060-8062; (b) O. Porcar-Tost, J. A. Olivares, A. Pallier, D. Esteban-Gómez, O. Illa, C. Platas-Iglesias, É. Tóth, and R. M. Ortuño, *Inorg. Chem.*, 2019, **58**, 13170-13183.

23. Z. Szakács and B. Noszál Dr., *Electrophoresis*, 2006, **27**, 3399-409.

24. (a) M. Port, J.M. Idée, C. Medina, C. Robic, M. Sabatou and C. Corot, *Biometals*., 2008, **21**, 469-490; (b) S. Laurent, L. Elst. Vander, C. Henoumont and R. N. Muller, *Contrast Media Mol. Imaging*, 2010, **5**, 305-308.

भारतीय प्रौद्योगिकी संस्थान गुवाहाटी
Indian Institute of Technology Guwahati

Thesis Conclusion and Perspectives

Thesis Conclusion and Perspectives

This work focused on the designing, syntheses, and detailed investigation of novel Gd(III)- and Mn(II)-based paramagnetic complexes and nanomaterials with improved relaxivity and stability compared to the clinically used chelates as potential contrast agents. The *in vitro* and *in vivo* toxicity, contrast enhancement ability, and other biophysical aspects of the synthesized agents were analyzed to estimate their aptness for further pre-clinical uses in the field of MRI.

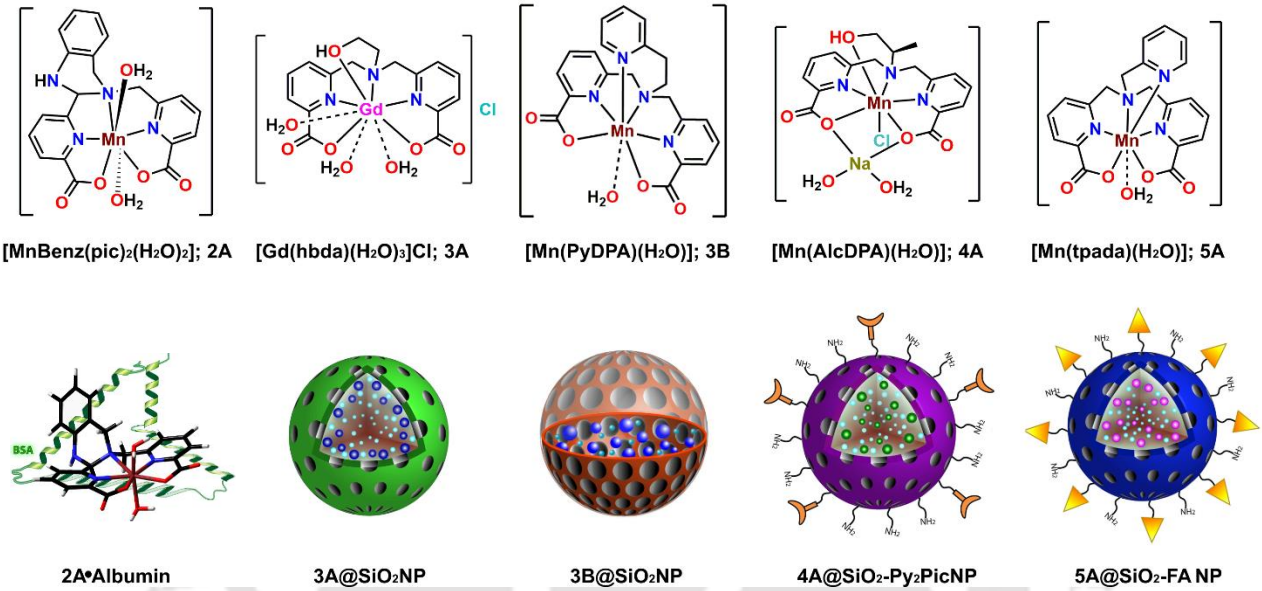

A bis-aquated Mn(II)-complex, **2A**, including a hydroquinazoline unit in the ligand backbone, provided higher thermodynamic and kinetic stability than mono-aquated MnEDTA and clinically used GdDTPA complexes. At physiological conditions, the complex is efficiently associated with the hydrophobic albumin protein (**2A•**BSA, $K_A = 1.66\times10^3\ M^{-1}$), rendering a high longitudinal relaxivity value of 19.09 $mM^{-1}s^{-1}$ (~ 6-fold higher than GdDTPA), at pH ~ 7.4, 1.41 T, and 37 °C. *In vivo* administration of the complex solution offered excellent vascularisation of blood vessels in the liver region along with brightening of the gallbladder and the kidney.

In the search for kinetically stable acyclic contrast agents with high relaxivity values, thermodynamically stable Gd(III) or Mn(II) complex molecules (**3A**/**3B**) with directly coordinated water molecules were non-covalently confined within the porous silica nanoparticles (**3A**@SiO_2/**3B**@SiO_2). Varying the charge of the complex, the location of encapsulation of the paramagnetic unit inside the silica nanosphere was controlled, thereby affecting the relaxivity of

the composite nanosystem. Upon complex encapsulation, the nanoparticles exhibited remarkable relaxivity values in water as well as serum albumin solution (r_1 obtained to be 6- to 12-fold higher than commercially available Mn(II)- and Gd(III)-based contrast agents). T_1-weighted phantom imaging and cytotoxicity studies confirmed the development of nanomaterials with promising potential for application in MR imaging.

The stable nanomaterial **4A**@SiO_2–NH_2 was obtained by confining complex **4A** into a porous silica nanoparticle having amine groups grafted over the nano-surface. A Zn(II) ion-selective group, Py_2Pic, was subsequently conjugated through amide linkage generating **4A**@SiO_2–Py_2Pic. In the presence of serum albumin protein, the finalized nano-suspension demonstrated Zn(II)-dependent enhancement in longitudinal relaxivity value indicating the formation of a slowly rotating ternary system, **4A**@SiO_2–Py_2Pic•BSA•Zn(II); the relaxivity value reached upto 46.3 $mM^{-1}s^{-1}$, at pH ~ 7.4, 1.41 T, and 37 °C. *In vivo* experiments proved this Zn(II)-dependent contrast enhancement, establishing the potential use of **4A**@SiO_2–Py_2Pic to track glucose-stimulated insulin and Zn(II) secretion in the pancreas.

The surface of **5A**@SiO_2–NH_2 (another complex-incorporated nanomaterial) was utilized to conjugate cancer-targeting folic acid units synthesizing **5A**@SiO_2–FA. It exhibited a significant boost to the longitudinal relaxivity value in the presence of serum albumin (r_1 increasing from 21.51 $mM^{-1}s^{-1}$ in water to 40.97 $mM^{-1}s^{-1}$ in 0.67 mM BSA solutions, at ~ 7.4, 1.41 T, and 37 °C). Corresponding *in vitro* and *in vivo* studies suggested cancer cell-selective rapid accumulation and cell permeability of **5A**@SiO_2–FA, indicating its utility to visualize the selective detection of cancer xenografts.

The results discussed in the thesis suggest these new ligands for Mn(II)-complexation, generating water soluble, aquated, and amphiphilic complexes with efficient stability. The inclusion of a pH-sensitive arm (–NHTs) to the ligand framework (**L1**) is expected to render a pH-dependent change in relaxivity value, a crucial factor in marking tumour development inside the body. **L2** being a six-coordinate ligand, will increase the stability of the corresponding Mn(II)-complex. Moreover, the distant carboxylate functional group can be alternatively utilized to react with the alcohol group (forming ester; liver targeting agent) or bind with amine-functionalized silica nanoparticles or hydrogels to elevate the longitudinal relaxivity value. Additionally, the bis-

aquated complex **2A**, synthesized in Chapter II, can be internalized within porous silica nanoparticles to attain very high relaxivity values.

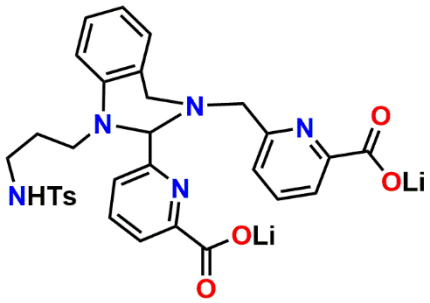

L1

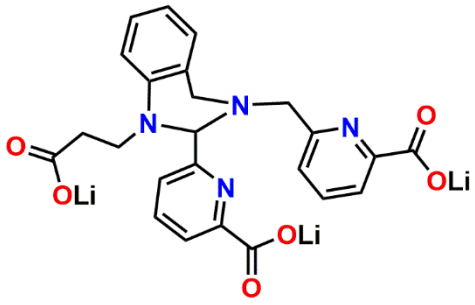

L2

Scheme: Proposed ligands for the syntheses of new Mn(II)-based MRI contrast agents.The

The technique of incorporating paramagnetic complexes within porous silica nanoparticles can be efficiently tuned by changing the concentration of the doping solution (complex solution) or the size of each nanoparticle. Herein, an optimal condition can be achieved for the highest boost toward relaxivity and kinetic inertness. The wide surface area of the silica surface can be effectively utilized for conjugation with a vast scope of linker groups for specific applications. Vividly, the conjugation of organic fragments like para-methoxybenzoic acid or para-hydroxybenzoic acid over the amine-functionalized silica surface is expected to selectively increase the uptake of CA in the hepatobiliary organs. Alongside, the attachment of suitable peptides/antigens through PEG linkers can enable target-specific delivery toward various metastatic cancers.

भारतीय प्रौद्योगिकी संस्थान गुवाहाटी
Indian Institute of Technology Guwahati

भारतीय प्रौद्योगिकी संस्थान गुवाहाटी
Indian Institute of Technology Guwahati

Chapter VI

Equipment and Experimental Section

6.1 Methods and Equipments

All the analyses were performed at the 'Instrumental Lab, Department of Chemistry' and 'Central Instrumental Facility' IITG, unless otherwise mentioned.

Chemicals and Solvents

All the chemicals and solvents were obtained from commercial sources and were used as supplied, unless noted otherwise.

Infrared Spectroscopy

Solid state FTIR spectra were recorded (4000–400 cm^{-1}) on the 'Perkin Elmer Instrument' at room temperature. Samples were either placed as ATR or pallets made by grinding the sample with IR-grade KBr powder.

NMR Spectroscopy

^{1}H, ^{13}C NMR spectra were recorded on 'Bruker AVANCE 400 MHz' and on 'Bruker AVANCE NEO 500 MHz' nuclear magnetic resonance (NMR) spectrometer at 298 K. Chemical shifts, δ (in ppm), are reported relative to TMS [δ (^{1}H) 0.0 ppm, δ (^{13}C) 0.0 ppm] which was used as the inner reference. Otherwise, the solvents ($CHCl_3$) residual proton resonance and carbon resonance were taken as reference [[For $CDCl_3$, δ (^{1}H) 7.26 ppm, and δ (^{13}C) 77.2 ppm; for CD_3OD δ (1H) 3.31, 4.87 ppm, and δ (13C) 49.0 ppm; for D_2O δ (1H) 4.79 ppm]. The resultant spectrums were drawn by using the 'MestReNova' NMR data processing software.

Mass Spectroscopy

Mass spectra were recorded on QTOF–MS Spectrometer ('Waters, Model: Q–Tof Premier') or 'Agilent Accurate–Mass Q–TOF LC/MS 6520' spectrometer, and peaks were given in *m/z* (% of basis peak). Mass spectra were taken in HPLC grade CH_3CN solvent, CH_3OH, and Milli Q water.

UV-Vis Spectroscopy

The electronic absorption spectrum (UV–Vis) of the sample(s) was recorded on the 'Perkin Elmer, Lambda 750, UV/Vis/NIR spectrometer' in Milli Q water at room temperature, using a cuvette of 1 cm width.

Elemental Analysis

The determination of the C, H, N was performed on the 'FLASH EA 1112 series' CHN Analyzer at SAIF, Mumbai.

Single Crystal X-ray Crystallography

Suitable crystals for X-ray diffraction study were obtained from solvent evaporation or solvent diffusion method. X−ray crystallographic data were collected by using either a 'Bruker SMART APEX−II CCD diffractometer', equipped with a fine focus 1.75 kW sealed tube Mo−Kα radiation (λ = 0.71073 Å) at 296(2) or 293(2) K, with increasing w (width of 0.3° per frame) at a scan speed of 3 s/frame or a 'Super Nova, Single source at the offset, Eos diffractometer'. The data refinement and cell reductions were carried out by CrysAlisPro. Structure was solved with the Superflip, structure solution program using Charge Flipping and refined by direct methods using 'SHELXS–97' or 'SHELXS–2013' or 'SHELXS–2018' and with full–matrix least squares on F2 using 'SHELXL–97', or 'SHELXS–2013' or 'SHELXS–2018' or with the Superflip structure solution program using Charge Flipping and refined with the olex2.refine refinement package using Gauss–Newton minimization. All the non−hydrogen atoms were refined anisotropically. SQUEEZE operations were performed using the WinGX program to remove disordered solvent molecules.

X-band EPR Spectroscopy

First derivative X–Band EPR spectra of powdered or frozen solution samples were measured with a 'JEOL JES–FA200 Spectrometer'. The resulting data was simulated by using the W95EPR–program written by Frank Neese (MPI for Bioinorganic Chemistry, Mülheim, and University of Bonn).

Potentiometric Titration

Potentiometric measurements were carried out in the 'Metrhom 888 Titrando' workstation combined with 'Metrhom 6.0259.100 glass electrode'. The number of the protonation constants of the ligands and the stability constant of the metal complexes were determined by potentiometric titrations at a constant ionic strength by using 0.15 M NaCl at 25 °C, against standardized 0.1 M NaOH as the titrant. The protonation and stability constants were evaluated using base mL-pH data pairs obtained in the pH range 2-12, using Hyperquad2008.

Relaxivity Measurement

The longitudinal relaxation times at 1.41 T, were measured using 'BRUKER minispec mq60NMR Analyzer' at 25 °C, and 37 °C. Milli Q water was used as the solvent. Exact metal concentrations in different samples were estimated by ICP-MS (Model-Element XR, Thermo Fisher Scientific) and ICP-AES (Model- ARCOS, Simultaneous ICP Spectrometer, SPECTRO Analytical Instruments GmbH, Germany) techniques after treatment of each with dilute HNO_3 solution.

Inversion Recovery Method

In this method, the spin at the equilibrium position is first exposed to a 180° pulse which inverts the magnetization M_0 to its opposite direction and becomes antiparallel to the direction of the applied magnetic field. After a delay time, known as inversion recovery time (TI), the system is exposed to another 90° pulse. During this delay time, the magnetization starts to recover to its original position, which becomes observable in xy-plane upon application of another 90° pulse. A schematic representation of the method is shown in **Figure 6.1**.

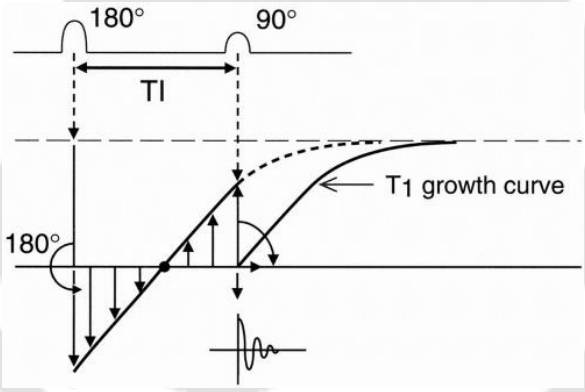

Figure 6.1. Pulse sequence and recovery curves in inversion recovery method.

Saturation Recovery Method

In this method, the spin system in the equilibrium position is first exposed to a 90° pulse which tips down the magnetization in xy-plane. After a delay time known as repetition time (TR), the system is exposed to another 90° pulse which again pushes the magnetization to xy-plane where FID is monitored. During this delay time (TR), the magnetization starts to recover to its original position, which is detected in the xy-plane upon application of another 90° pulse. A schematic representation of the method is shown in **Figure 6.2**.

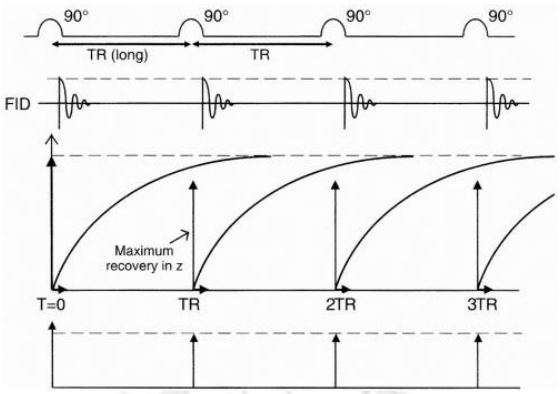

Figure 6.2. Pulse sequence and recovery curves in saturation recovery method.

Competition Batch Titration Method

Spectrophotometric competitive batch titrations were done against Na_2H_2EDTA, to estimate the affinity of the ligand for Mn(II) ions. Various aliquots of a standardized Na_2H_2EDTA stock solution ranging from 0.5 to 200 equivalents relative to the ligand concentration were added to a constant [Mn(II)-L] solution (with a typical concentration ratio of 1:1) and equilibrated for 48 hours to attain thermodynamic equilibrium. The ionic strength of the reacting mixture was maintained with 0.15 M NaCl, at pH ~ 7.4 (0.01 M HEPES buffer). The overall UV-Vis absorbance spectra were observed and a particular range of wavelengths was selected where gradual spectral changes were considered. The absorbance value of each set was recorded with respect to the value of ligand $Li_2Benz(pic)_2$ (represented as L) at that particular wavelength. Na_2H_2EDTA solution of exact concentration and pH was used as background for each scan. Utilizing the respective absorbance values, further calculations gave the concentrations of $MnBenz(pic)_2$ complex, MnEDTA complex, free ligand $Li_2Benz(pic)_2$, and free Na_2H_2EDTA for each set were calculated from the variation in absorbance in each set of samples. The logarithmic value of the concentration ratio of [MnEDTA] to [MnL] was plotted against the similar logarithmic value of the respective ratio of free [Na_2H_2EDTA] to free [L] of each sample. The X-intercept of the linear plot obtained was employed to calculate the logK_{cond} value for the synthesized ligand $Li_2Benz(pic)_2$, using the formula mentioned below.

$[MnL] + [Na_2H_2EDTA] \rightleftharpoons [MnEDTA] + [L]$;

$$K_{cond} = \frac{[MnEDTA][L]}{[MnL][Na_2H_2EDTA]};$$

$\log([MnEDTA]/[MnL]) = \log K_{cond} + \log([Na_2H_2EDTA]/[L]$

Transmetallation Kinetic Studies

Gradual changes in the relaxation rate (R_1 or R_2) of samples containing paramagnetic complex solution, challenged with 10-40 equivalents of $ZnCl_2$ were monitored over the course of time. Measurements were done in either an aqueous medium or in the BSA medium (0.67 mM), at pH ~ 6.0-6.5 (MES buffer) or ~7.0 (phosphate buffer), I = 0.15 M NaCl, 1.41 T, and 25 °C, using BRUKER minispec mq60 NMR analyser.

Octanol-water Partition Coefficient

The aqueous solution of the complex was added to a mixture of octanol and water (2 mL, 1:1 v/v) and gently shaken for 48 h to equilibrate the mixture. Further on, it was kept untouched for 24 h to settle down. Layers were carefully separated and Mn(II) content in each layer was estimated by the ICP-AES technique. The partition coefficient, log *P* = log (C_o/C_w). Here, P = partition coefficient; C_o and C_w = complex concentration in the octanol and water layers, respectively.

Transmission Electron Microscopy

The size and morphology of the synthesized nanoparticles were analyzed from Transmission electron microscopy (TEM) images captured on a JEOL, Model:2100F electron microscope operated at 200 kV, together with Energy-dispersive X-ray spectroscopy (EDS). 10 μL of prepared mother suspension was diluted to 10 mL with ethanol, and 10 μL of the final solution was dropped on a carbon-coated copper grid (CARBON FILM 300 MESH, COPPER) and kept overnight for drying and then used for imaging. *ImageJ* software was used to calculate particle size distributions from a sample containing at least 100 particles.

Surface Area and Pore Analysis

Nitrogen sorption Brunauer–Emmett–Teller (BET) isotherms were acquired on a Quantachrome, Model: Autosorb-IQ MP surface area and pore size analyzer at 77 K. Ahead of the experiment, dry samples (obtained by lyophilizing the suspension for 24 h) were degassed at 373 K for 10 h. Pore diameters were calculated by the Barrett-Joyner-Helenda (BJH) method,

Thermogravimetric Analysis

Thermogravimetric analyses (TGA) of lyophilized solid nanomaterials were done using PerkinElmer TGA 4000.

Dynamic Light Scattering Analysis

Zeta potential and particle size distribution of suspended synthesized nanoparticles were measured at 25 °C by Dynamic Light Scattering (DLS) using Malvern ZETASIZER Nano-ZS90 (equilibrium time set to 2 min; 5 measurements taken on each sample set, only quality criteria values were accepted). Ambient pH was maintained using appropriate buffers.

Fluorescence Spectroscopy

Samples (aqueous suspensions) were recorded on FluoroMax-4 spectrofluorimeter (Horiba), at 25 °C, in a rectangular quartz cell with a path of 10 mm. Each set of suspensions was excited at 275 nm, using 5 per 5 nm (excitation/emission) slit widths. Emission spectra were recorded in the 280 to 530 nm range.

Cytotoxicity and Cell-Uptake Studies

Cervical cancer cells (HeLa), Human Embryonic Kidney (HEK293), Human prostate cancer cells (PC3), and macrophage cell lines RAW 264.7 were purchased from the National Centre for Cell Science, Pune. All the cell lines were sustained in Dulbecco's modified Eagle's medium (DMEM) supplemented with 10% (v/v) fetal bovine serum (FBS) and 1% penicillin and streptomycin at 37 °C in humidified air containing 5% CO_2. Respective cells were seeded in a 96-well plate at a density of 5×103 cells/well and grown overnight, replicating the abovementioned conditions. After treatment with increasing concentration of synthesized complexes and nanoparticles (time scale mentioned in each experiment), *w.r.t.* [Mn(II)], 0.5 mg/ml of MTT in DMEM was added to each well and incubated for 1.5 h. Thereafter, 150 µl DMSO was added to each well. Absorbance was measured at 570 nm, and after that, cell viability was calculated, considering 100% viability for untreated cells. For cell labeling studies, the treated cells were subsequently washed with PBS (phosphate-buffered saline) to remove any unbound NPs. Cells were then trypsinized and fixed using 4 % formaldehyde for 15 min and washed twice with PBS. Subsequently, for FETEM imaging, the resuspended cells were added to the carbon-coated copper grid and allowed to air dry. Images were collected in a FETEM microscope (JEOL, 2100F). Trypsinized were digested in conc. HNO_3 for 12 h and concentration of metal attached/up taken by cell was quantified by ICP-MS analysis. For fluorescence imaging to visualize cell uptake, the cells were thoroughly washed after treatment with synthesized NPs with PBS to remove any unbound particles. Trypan blue (200

μg/mL) was added and incubated. Cells were subsequently fixed with 4% formaldehyde solution for 15 mins, subsequently washed thrice with PBS, and then observed under a Fluorescence inverted microscope *Nikon* ECLIPSE T*i*-U. For flow cytometry, the cells were resuspended in PBS and the amount of endocytosed nanomaterials was analyzed by FACSMelody (BD Biosciences, NJ, USA). Fluorescence intensity was quantified in the FITC-A channel, thereafter analyzed with FlowJo (BD) software and histograms were plotted accordingly.

Phantom MRI

MR images were obtained using clinical 7 T Biospec 70/20, M/s Bruker Biospin GmBH, Germany, or MAGNETOM Avanto 1.5 T MRI scanner, or BRIVO MR355 1.5 T MRI scanner.

In vivo MRI

8 weeks old male C57BL/6 mice (total number = 10) were acquired from the National Institute of Biologicals (NIB), Noida, Uttar Pradesh (UP), India. They were housed in micro isolator cages at biosafety level 2 in the animal house of Maharshi Dayanand University, Rohtak, India, and their feeding pattern was regularly monitored. Animal experimental protocol was approved by the Institutional Animal Ethical Committee (IAEC), with approval number CAH 114-120 dated 23-05-2022. During studies, mice were anesthetized with 1-3% isoflurane/oxygen mixture. Normal respiration and body temperature (37 °C) were maintained during experiments. Subsequently, animals were scanned at 7 T using a small-bore animal scanner (Biospec 70/20, M/s Bruker Biospin GmBH, Germany) at AIIMS Delhi, prior to and post-contrast administration implying T_1-weighted 3D fast low-angle low-shot (FLASH) and two-dimensional rapid acquisition with refocused echo (RARE) imaging protocols.

Biodistribution Studies

Mice (n =3/group) were sacrificed at different time points post-administration of synthesized paramagnetic complexes and nanomaterials along with the control group receiving saline (0.9%) only. Selected organs were dissected and digested upon treatment with 2 mL of freshly prepared aqua regia (1:3 mixture of HNO_3 and HCl) and lysed for 24 h. The tissue samples were dried by heating at 120 °C, sonicated thoroughly after the addition of 0.5 N HCl, and centrifuged (4000g, 5 min) to collect a clear supernatant solution. This crude was diluted with 4% HNO_3 acid solution and subsequent Mn content in each sample as estimated by the ICP-MS technique.

6.2 Experimental Section

6.2.1. Synthesis of ligand $Li_2[Benz(pic)_2]$

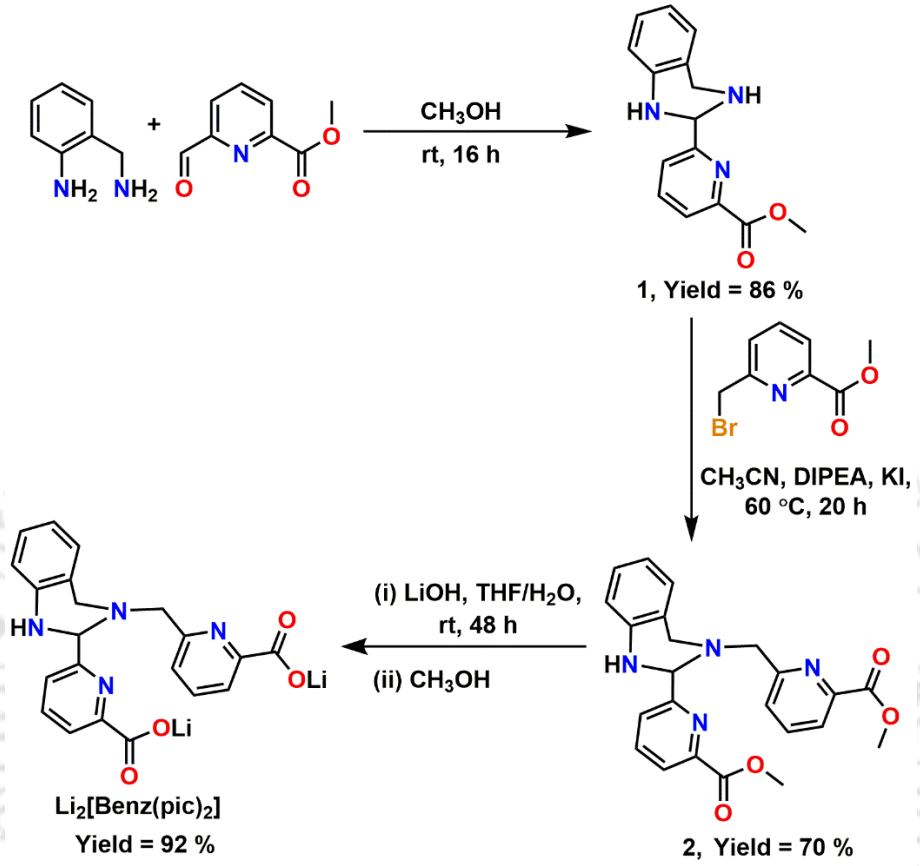

Scheme 6.1. Synthetic scheme for the preparation of ligand **$Li_2[Benz(pic)_2]$**.

Synthesis of $[C_{15}H_{15}N_3O_2]$, (1): An equivalent amount of Methyl 6-formyl-2-pyridinecarboxylate (0.66 g, 4.0 mmol) was dissolved in methanol (5 mL) and slowly added to a methanolic solution of 2-aminobenzyl amine (0.49 g, 4.0 mmol) and stirred for 16 h. Removal of solvent gave a brownish crude oil, which on trituration with hexane gave compound **1** as a white solid.

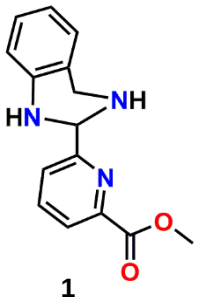

1

Yield = 0.92 g (86%).

FTIR (KBr pellet cm^{-1}): 3383, 3294, 3052, 3005, 2925, 2882, 2840, 1719, 1603, 1587, 1492, 1471, 1436, 1415, 1301, 1251, 1197, 1151, 1073, 1001, 962, 867, 836, 745, 622.

^{1}H NMR ($CDCl_3$, 500 MHz): δ 8.08 (d, *J* = 5 Hz, 1H), 7.88 (m, 2H), 7.06 (t, *J* = 5 Hz, 1H), 6.95 (d, *J* = 10 Hz, 1H), 6.72 (m, 2H), 5.35 (s, 1H), 5.20 (s br, 1H), 4.32 (d, *J* = 20 Hz, 1H), 4.05 (d, *J* = 15 Hz, 1H), 4.00 (s, 3H) ppm.

^{13}C NMR ($CDCl_3$, 125 MHz): δ 165.69, 159.71, 147.44, 143.21, 138.02, 127.47, 126.25, 124.76, 124.68, 121.61, 118.46, 116.10, 69.15, 52.95, 46.84 ppm.

ESI-MS (+) m/z for $[C_{15}N_{15}N_3O_2 + H]^+$ calcd., 270.1237; found, 270.1245.

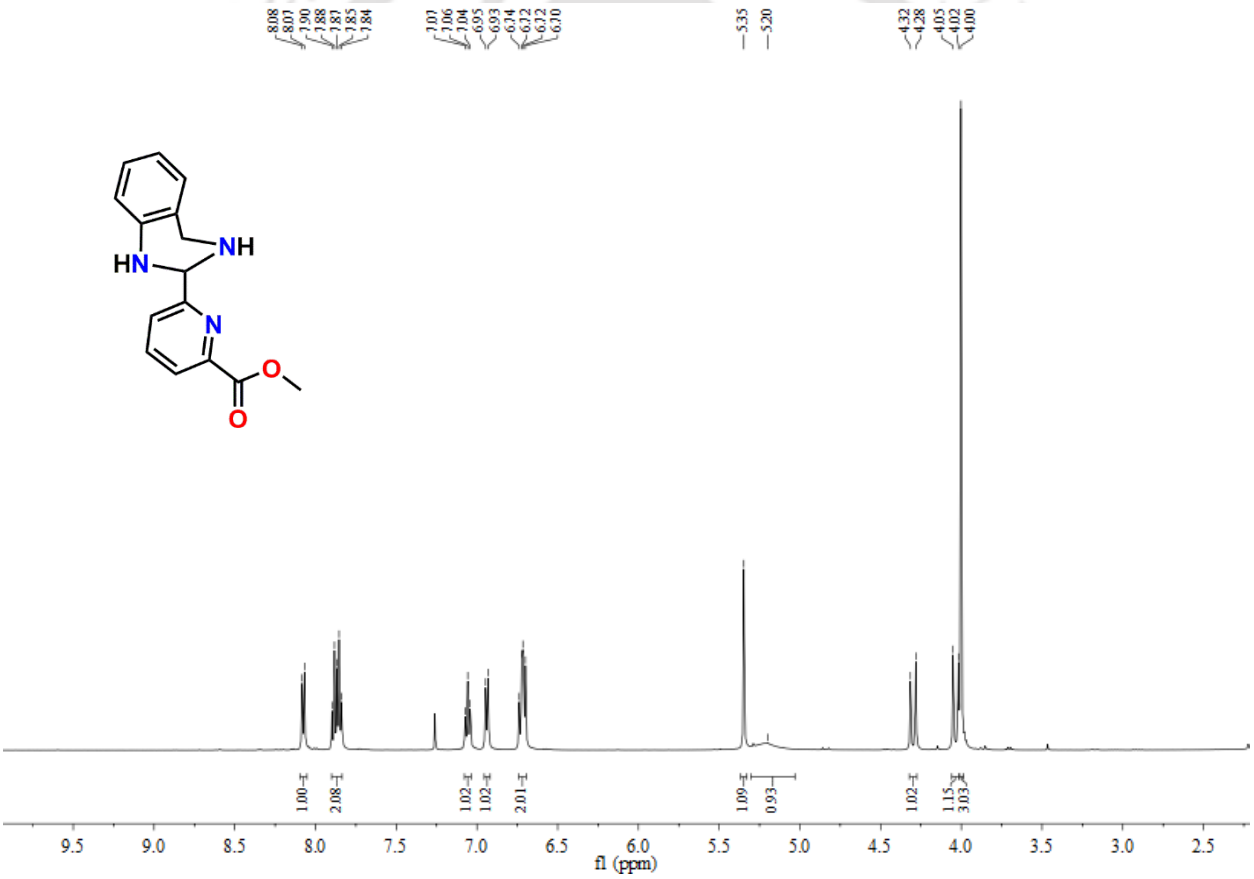

Figure 6.3. ^{1}H NMR spectra for $[C_{15}N_{15}N_3O_2]$, (**1**).

Synthesis of [$C_{23}H_{22}N_4O_4$], (2): A solution of compound **1** (0.79 g, 2.9 mmol) was prepared in dry acetonitrile (15 mL), KI (0.58 g, 3.5 mmol) and DIPEA (0.95 g, 7.3 mmol) were added afterward under N_2 atmosphere and stirred for 15 minutes. Methyl 6-(bromomethyl)picolinate (0.80 g, 3.5 mmol) was finally added, at a time, and the mixture was heated to 60 °C. After 20 h, the reaction ceased and the solvent was evaporated to dryness. The residue was extracted with CH_2Cl_2 (3×30 mL) after thoroughly washing with water and brine. The organic part was partitioned and collected. After drying over Na_2SO_4, the solvent was evaporated to obtain a yellow solid, which was purified by column chromatography on silica gel using hexane/ethyl acetate (1:2) as eluent to get compound **2** as a sticky yellow solid.

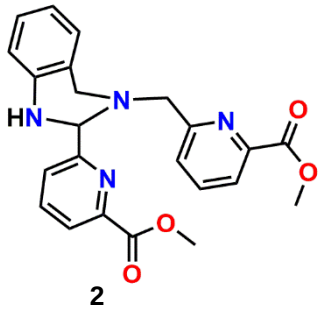

2

Yield = 0.84 g (70%).

FTIR (KBr pellet cm^{-1}): 3595, 3395, 3060, 3009, 2951, 2907, 2853, 1722, 1608, 1588, 1494, 1457, 1437, 1314, 1293, 1257, 1226, 1194, 1137, 1083, 994, 912, 759, 731, 647.

^{1}H NMR ($CDCl_3$, 400 MHz): δ 8.04 (d, *J* = 8 Hz, 1H), 7.98 (d, *J* = 8 Hz, 1H), 7.93 (d, *J* = 8 Hz, 1H), 7.87 (d, *J* = 8 Hz, 1H), 7.82 (t, *J* = 8 Hz, 2H), 7.09 (t, *J* = 8 Hz, 1H), 6.88 (d, *J* = 8 Hz, 1H), 6.79 (d, *J* = 8 Hz, 1H), 6.70 (t, *J* = 8 Hz, 1H), 5.54 (s, 1H), 4.29 (d, *J* = 16 Hz, 1H), 4.02 (s, 3H), 3.94 (s, 3H), 3.82 (m, 4H) ppm.

^{13}C NMR ($CDCl_3$, 100 MHz): 171.23, 161.56, 159.78, 151.67, 149.84, 140.61, 132.39, 130.80, 123.28, 121.92, 117.39, 112.79, 92.78, 60.69, 59.24, 49.62.

ESI-MS (+) m/z for $[C_{23}H_{22}N_4O_4 + H]^+$ calcd., 419.1713; found, 419.1776.

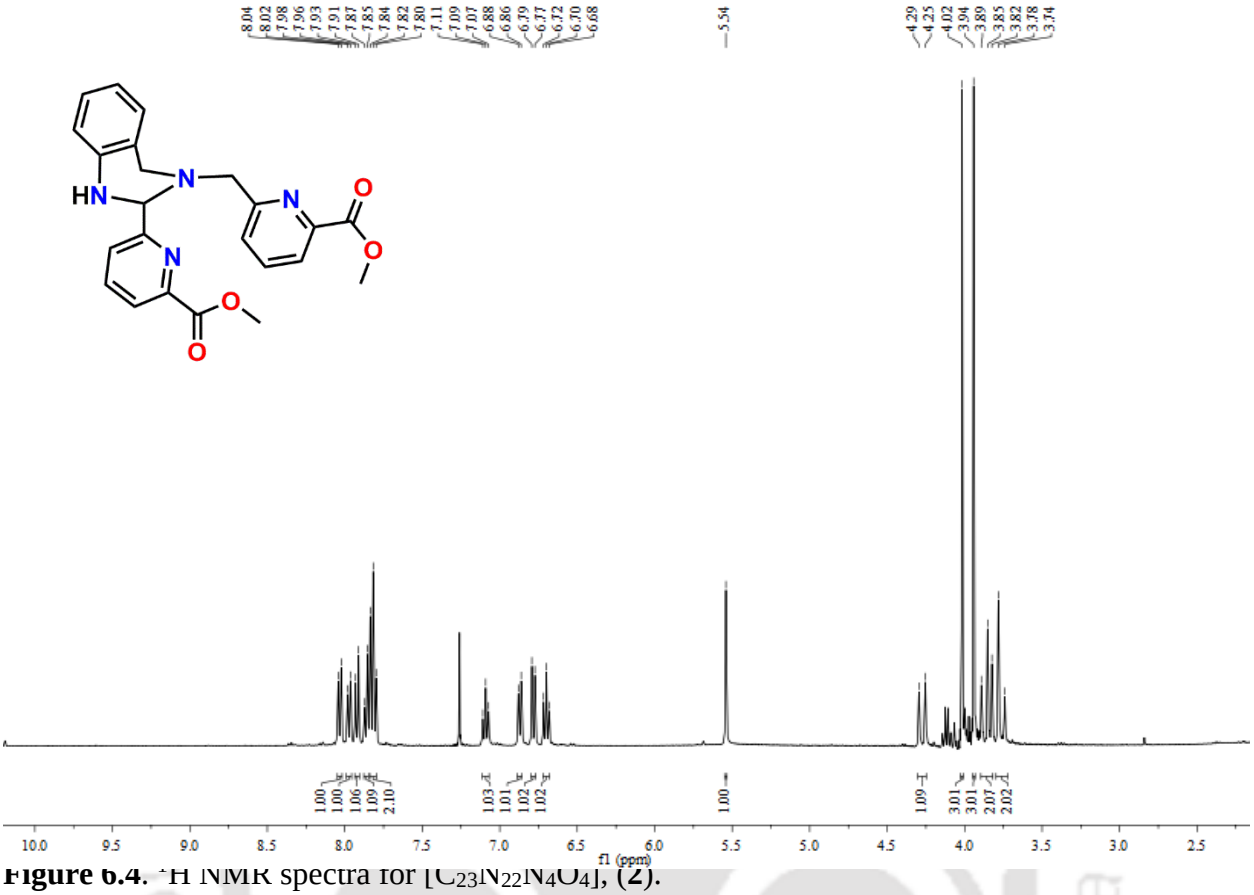

Figure 6.4. ^{1}H NMR spectra for $[C_{23}N_{22}N_4O_4]$, (**2**).

Synthesis of $[C_{21}H_{16}N_4O_4Li_2]$, $Li_2[Benz(pic)_2]$: To a solution of compound **2** (0.33 g, 0.8 mmol) in THF (6 mL), aqueous solution of lithium hydroxide (0.04 g, 1.7 mmol) was slowly added and stirred for 2 days under dark condition. Afterward, the solvent was evaporated to dryness to afford a pale-yellow solid. Rapid wash with a minimum amount of methanol (~4 mL) gave ligand **$Li_2Benz(pic)_2$** as a white solid.

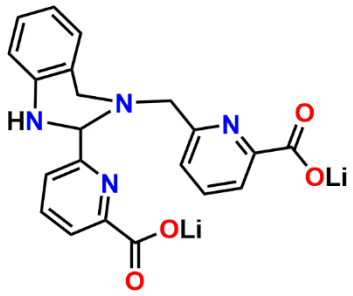

$Li_2[Benz(pic)_2]$

Yield = 0.29 g (92%).

FTIR (KBr pellet cm^{-1}): 3482, 3359, 3100, 2906, 2859, 1633, 1615, 1586, 1574, 1494, 1427, 1395, 1264, 1187, 1117, 1080, 1007, 858, 786, 748, 687, 491.

^{1}H NMR (D_2O, 400 MHz): δ 7.82 (m, 1H), 7.76 (m, 3H), 7.56 (d, *J* = 8 Hz, 1H), 7.21 (m, 2H), 7.03 (d, *J* = 4 Hz, 1H), 6.91 (d, *J* = 8 Hz, 1H), 6.84 (t, *J* = 8 Hz, 1H), 5.31 (s, 1H), 4.02 (d, *J* = 12 Hz, 1H), 3.80 (m, 3H) ppm.

^{13}C NMR (D_2O, 400 MHz): δ 173.12, 172.95, 157.20, 157.08, 152.79, 152.65, 141.84, 138.31, 138.19, 128.00, 127.80, 125.77, 124.74, 123.50, 122.20, 119.34, 119.05, 115.84, 73.33, 55.52, 51.43 ppm.

ESI-MS (–) *m/z* for $[C_{21}H_{16}N_4O_4 - 2Li + H]^-$ calc., 389.1249, found 389.1246.

6.2.2. Synthesis of ligand H_2PyDPA

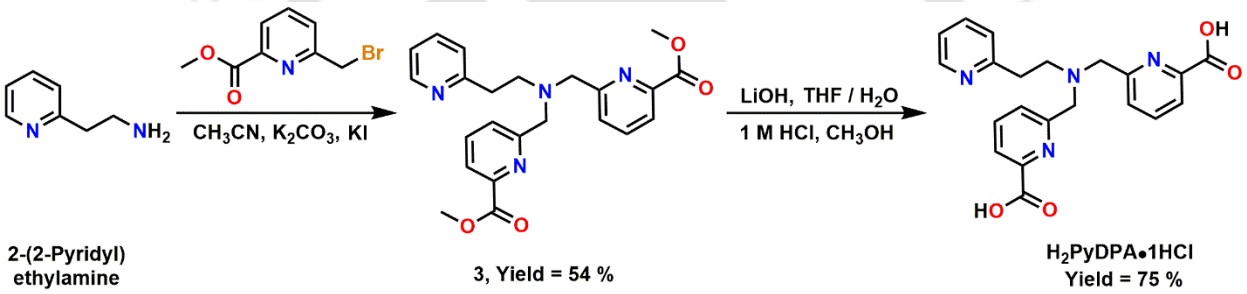

Scheme 6.2. Synthetic scheme for the preparation of ligand **H_2PyDPA**.

Synthesis of $[C_{23}H_{24}N_4O_4]$, (3): To a stirred solution of 2-(2-Pyridyl)ethylamine (0.244 g, 2 mmol) in dry acetonitrile, Methyl 6-(bromomethyl)picolinate (1.012 g, 4.4 mmol), K_2CO_3 (1.104 g, 8 mmol) and KI (0.730 g, 4.4 mmol) were added under a nitrogen atmosphere and the resulting solution was refluxed for 5 days. After this, the reaction mixture was cooled down to room temperature and filtered. The filtrate was evaporated to dryness. A small amount of water (~ 5 mL) was added to the residue and extracted with $CHCl_3$ (3×30 mL). The organic part was collected and dried over Na_2SO_4, and the solvent was evaporated to obtain a brownish liquid, which was purified by column chromatography on silica gel using ethyl acetate/methanol (50:1) as eluent to obtain a light-yellow solid, **3**.

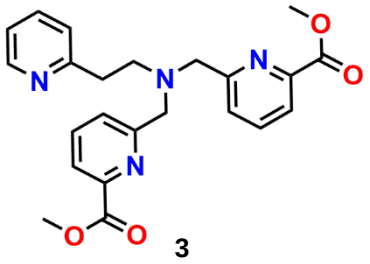

Yield = 0.454 g (54%).

FTIR (KBr pellet cm^{-1}): 3412, 3064, 3012, 2958, 2934, 2840, 1731, 1645, 1589, 1568, 1474, 1454, 1438, 1364, 1205, 1247, 1194, 1169, 1145, 1132, 1083, 995, 766.

^{1}H NMR ($CDCl_3$, 400 MHz): δ 8.48 (d, J = 4 Hz, 1H), 7.98 (d, J = 8 Hz, 2H), 7.71 (t, J = 8 Hz, 2H), 7.58-7.53 (m, 3H), 7.13-7.09 (m, 2H), 4.00 (s, 4H), 3.99 (s, 6H), 3.05-2.99 (m, 4H) ppm.

^{13}C NMR ($CDCl_3$, 100 MHz): δ165.95, 160.53, 160.38, 149.22, 147.36, 137.50, 136.35, 126.07, 123.70, 123.64, 121.33, 60.17, 54.66, 53.01, 36.14 ppm.

ESI-MS (+) m/z for $[C_{23}H_{24}N_4O_4 + H]^+$ calcd., 421. 1870; found, 421.1888.

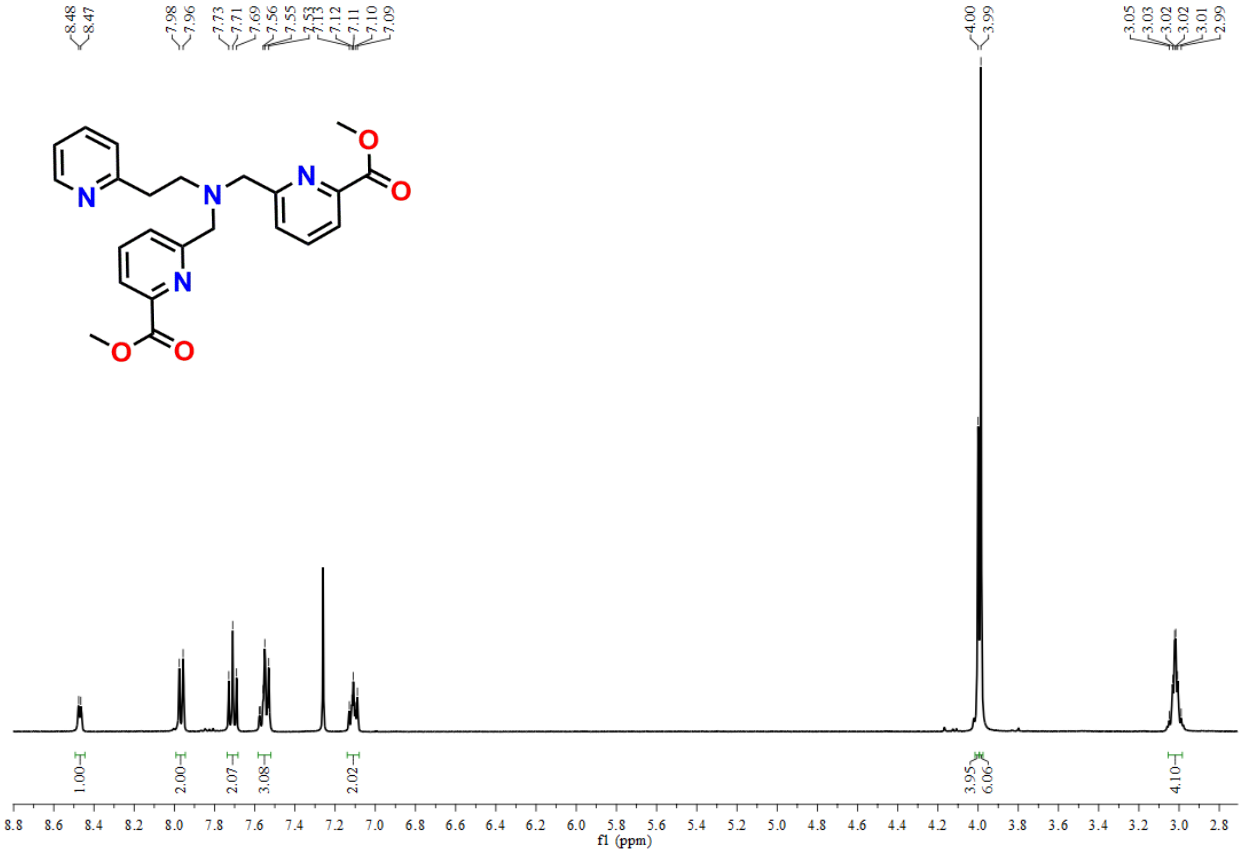

Figure 6.5. ^{1}H NMR spectra for $[C_{23}H_{24}N_4O_4]$, (**3**).

Synthesis of [$C_{21}H_{20}N_4O_4$], H_2PyDPA: To a solution of **3** (0.204 g, 0.49 mmol) in THF (6 mL), aqueous solution of LiOH (0.047 g, 1.94 mmol in 2 mL H_2O) was added dropwise and allowed to stir at room temperature for 48 h. After this, THF was evaporated and the pH of the solution was adjusted to ~ 1 by adding 1 M HCl solution. A white amorphous compound was obtained that was washed thoroughly with diethyl ether. This residue was then dissolved in methanol to obtain the colorless crystals of the ligand as its HCl salt with a crystallographic composition of H_2PyDPA•HCl•5.5H_2O.

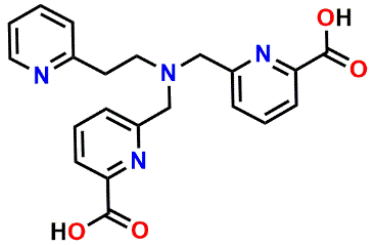

H_2PyDPA

Yield = 0.184 g (75%; crystals).

FTIR (KBr pellet cm^{-1}): 3529, 3371, 3119, 3070, 3047, 2804, 2739, 2542, 2000, 1722, 1710, 1632, 1621, 1590, 1545, 1462, 1443, 1310, 1292, 1231, 1142, 1092, 995, 768, 661.

^{1}H -NMR ($CDCl_3$, 400 MHz): δ 8.71 (d, J = 4 Hz, 1H), 8.52 (t, J = 8 Hz, 1H), 8.06-8.04 (m, 4H), 7.98-7.95 (m, 2H), 7.67-7.65 (m, 2H), 4.75 (s, 2H), 4.72 (s, 2H), 3.92-3.85 (m, 2H), 3.75-3.70 (m, 2H) ppm.

^{13}C NMR ($CDCl_3$, 100 MHz): δ 166.83, 151.13, 150.27, 147.36, 146.78, 141.66, 140.61, 128.13, 127.65, 125.93, 125.34, 58.40, 53.97, 28.59 ppm.

ESI-MS (+) m/z for $[C_{21}H_{20}N_4O_4 + H]^+$ calcd., 393. 1557; found, 393.1565.

Anal. Calcd. for $C_{21}H_{20}N_4O_4$•HCl•5.5H_2O: C, 47.80; H, 6.12; N, 10.62. Found: C, 48.09; H, 5.87; N, 10.54.

6.2.3. Synthesis of ligand H_2AlcDPA

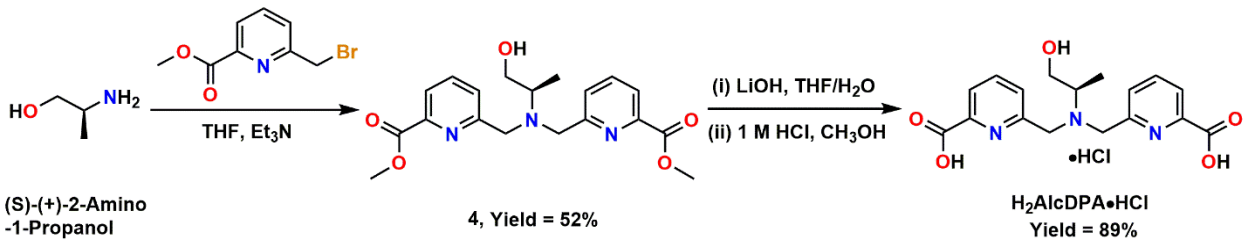

Scheme 6.3. Synthetic scheme for the preparation of ligand **H_2AlcDPA**.

Synthesis of $[C_{19}H_{23}N_3O_5]$, (4): To a solution of (S)-(+)-2-Amino-1-propanol (0.150 g, 2 mmol) in dry THF under N_2 atmosphere, triethyl amine (0.61 mL, 4.4 mmol) was added at a time. Methyl 6-(bromomethyl)picolinate (0.92 g, 4.0 mmol) was subsequently added and the resulting mixture was allowed to stir for 24 h, at room temperature. After this, the reaction mixture was dried to remove THF, and the residue was extracted with CH_2Cl_2 (3×30 mL) after thoroughly washing with water and brine. The organic part was collected and dried over Na_2SO_4, and the solvent was evaporated to obtain a pale-yellow oil, which was purified by column chromatography on silica gel using hexane/ethyl acetate (1:4) as eluent to get **4** as a white solid.

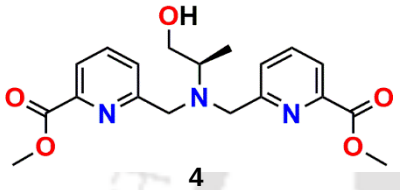

Yield = 0.388 g (52%).

FTIR (KBr pellet cm^{-1}): 3413, 2957, 1728, 1590, 1441, 1316, 1248, 1140, 1085, 833, 764.

^{1}H NMR ($CDCl_3$, 400 MHz): δ 7.98 (d, *J* = 8 Hz, 2H), 7.59 (t, *J* = 8 Hz, 2H), 7.48 (d, *J* = 8 Hz, 2H), 5.46 (s br, 1H), 4.70 (s, 1H), 4.05 (m, 2H), 3.99 (s, 6H), 3.93 (d, J= 12, 2H), 3.55 (m, 2H), 3.15 (m, 1H), 1.04 (d, J = 8 Hz, 3H) ppm.

^{13}C NMR ($CDCl_3$, 100 MHz): δ 161.14, 138.65, 132.75, 129.54, 125.19, 121.01, 60.93, 57.34, 54.35, 49.78, 8.83 ppm.

ESI-MS (+) m/z for $[C_{19}H_{23}N_3O_5 + H]^+$ calcd., 374.1710; found, 374.1743.

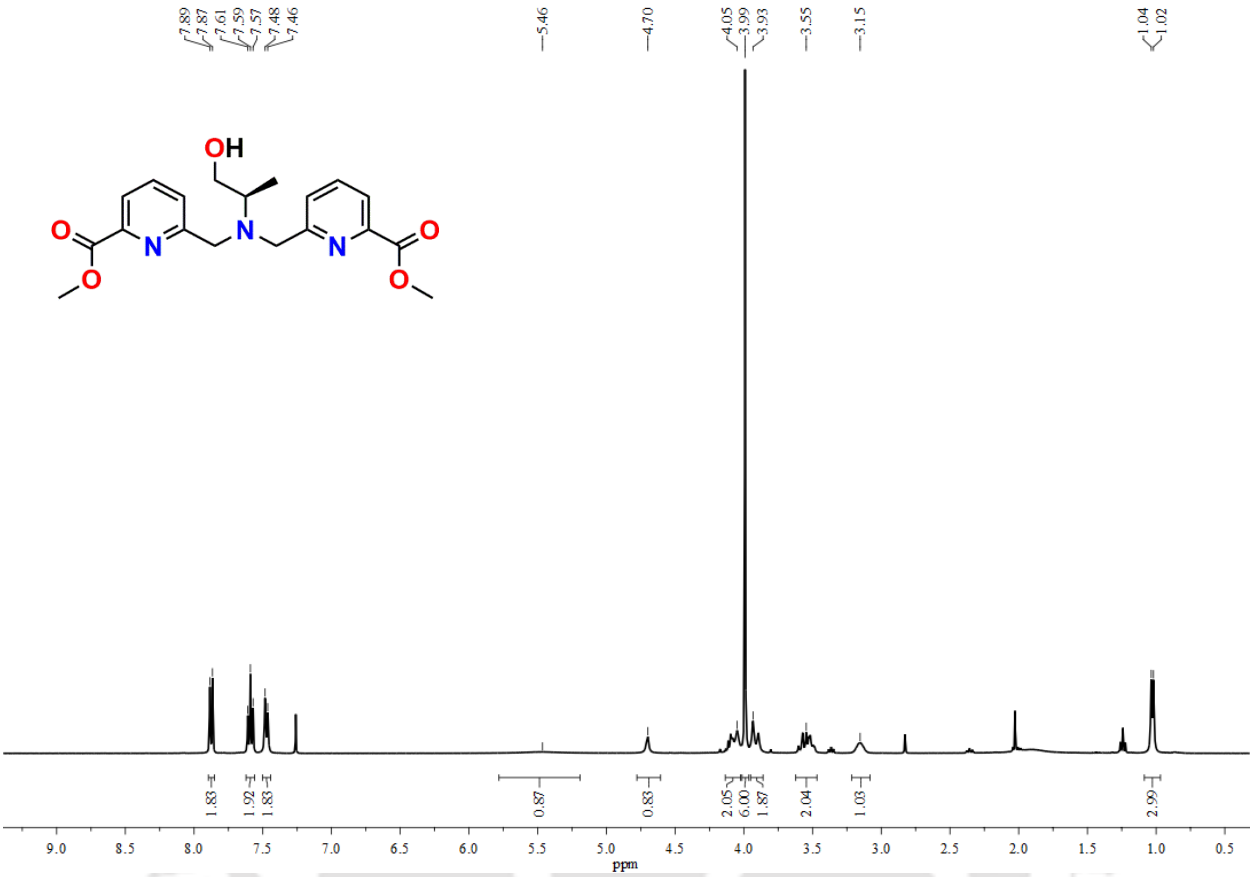

Figure 6.6. ^{1}H NMR spectra for [$C_{19}H_{23}N_3O_5$], (**4**).

Synthesis of [$C_{17}H_{19}N_3O_5$], H_2AlcDPA: Aqueous solution of LiOH (0.033 g, 1.36 mmol in 2 mL H_2O) was dropwise added to a prepared solution of **4** (0.230 g, 0.62 mmol) in THF (6 mL), and the mixture was allowed to stir at room temperature for 24 h. Afterward, the THF part was evaporated, and the pH of the resultant aqueous solution was adjusted to ~ 1 by adding 1 N HCl. A sticky compound was obtained after evaporation of the solvent and washed thoroughly with diethyl ether. This residue was then dissolved in methanol to obtain the colorless solid precipitate of the ligand H_2AlcDPA as its HCl salt.

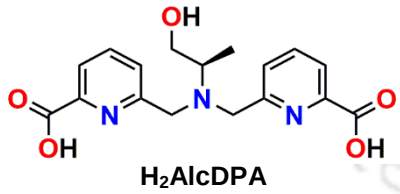

H_2AlcDPA

Yield = 0.211 g (89%).

FTIR (KBr pellet cm^{-1}): 3331, 3200, 3008, 2981, 2963, 2877, 2808, 1746, 1735, 1594, 1573, 1464, 1384, 1351, 1262, 1156, 995, 834, 750, 692.

^{1}H -NMR (D_2O, 400 MHz): δ 7.87 (m, 4H), 7.51 (m, 2H), 4.77 (m, 2H), 4.73 (d, *J* = 8 Hz), 4.03 (d, *J* = 8 Hz, 1H), 3.95 (m, 2H), 1.52 (m, 3H) ppm.

^{13}C NMR (D_2O, 100 MHz): δ 167.03, 149.96, 146.55, 139.78, 127.75, 125.01, 63.93, 60.34, 55.35, 9.73 ppm.

ESI-MS (+) m/z for $[C_{17}H_{19}N_3O_5 + H]^+$ calcd., 346.1691; found, 346.1601.

6.2.4. Synthesis of ligand HPy_2Pic

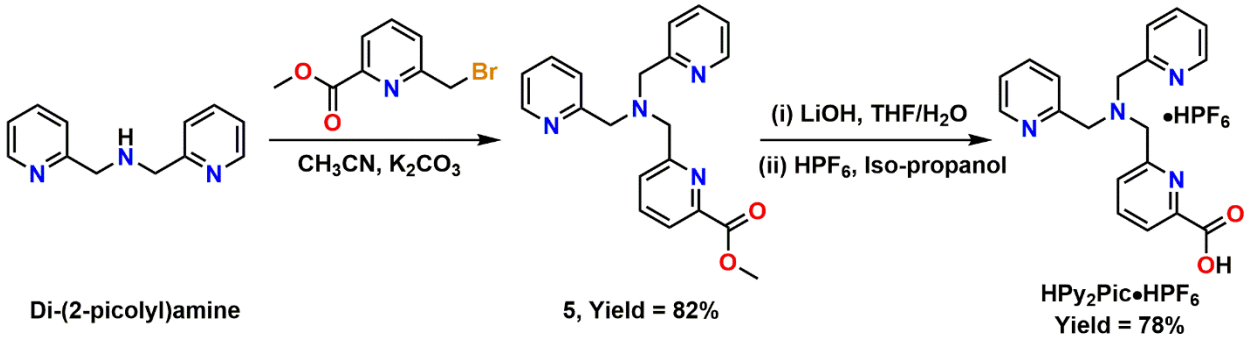

Scheme 6.4. Synthetic scheme for the preparation of ligand **HPy_2Pic**.

Synthesis of $[C_{20}H_{20}N_4O_2]$, (5): To a solution of Di-(2-picolyl)amine (0.612 g, 3 mmol) in dry acetonitrile, K_2CO_3 (0.828 g, 6 mmol) and Methyl 6-(bromomethyl)picolinate (0.690 g, 3 mmol) were added in succeeding order, under a nitrogen atmosphere and the resulting solution was heated at 60 °C for 3 h. The reaction mixture was thereafter cooled down to room temperature and filtered. The filtrate was evaporated to dryness. Water was added to the residue and extracted with ethyl acetate (3 × 30 mL). The organic part was collected, dried over Na_2SO_4, concentrated to 5 mL, refrigerated overnight to obtain compound **5** as a white precipitate, and collected by filtration.

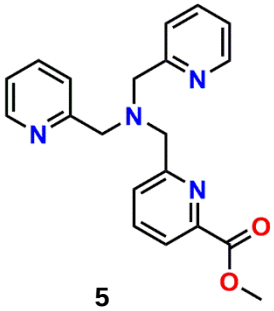

5

Yield = 0.857 g (82%).

FTIR (KBr pellet cm^{-1}): 3406, 3008, 2950, 2841, 1721, 1588, 1569, 1434, 1316, 1291, 1138, 1082, 994, 977, 763.

^1H NMR ($CDCl_3$, 400 MHz): δ 8.55 (d, J = 4 Hz, 2H), 7.99 (d, J = 8 Hz, 1H), 7.88 (d, J = 8Hz, 1H), 7.80 (t, J = 8 Hz, 1H), 7.66 (t, J = 8 Hz, 2H), 7.58 (d, J = 8Hz, 2H), 7.17 (t, J = 4Hz, 2H), 4.04 (s, 2H), 3.98 (s, 3H), 3.95 (s, 4H) ppm.

^{13}C NMR ($CDCl_3$, 100 MHz): δ 159.47, 154.76, 151.64, 147.45, 144.37, 141.89, 138.23, 124.47, 122.19, 120.45, 64.65, 56.21, 55.76, 52.78 ppm.

ESI-MS (+) m/z for $[C_{20}H_{20}N_4O_2 + H]^+$ calcd., 349.1659; found, 349.1647.

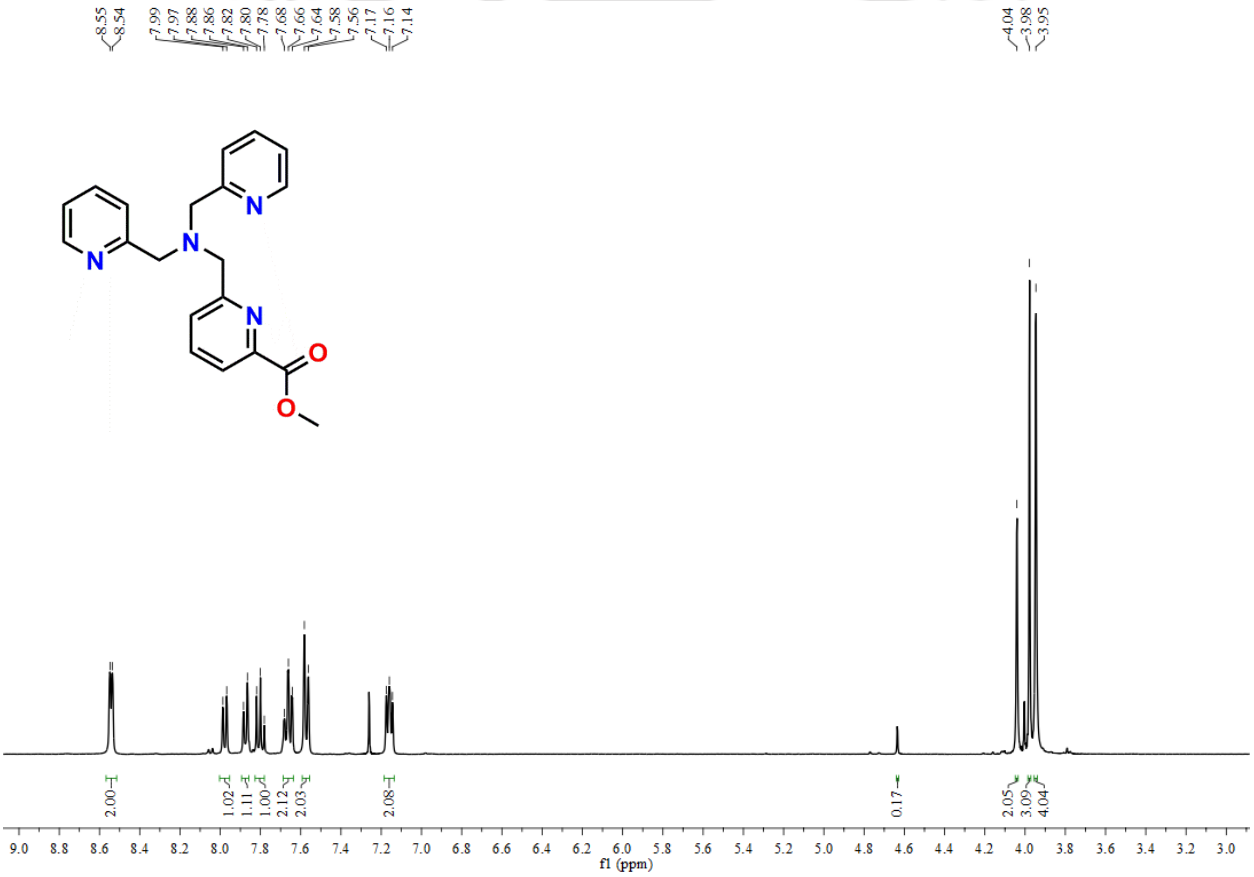

Figure 6.7. ^1H NMR spectra for $[C_{20}H_{20}N_4O_2]$, (**5**).

Synthesis of [$C_{19}H_{18}N_4O_2$], HPy_2Pic: To a solution of **5** (0.348 g, 1.0 mmol) in THF (6 mL), an aqueous solution of LiOH (0.048 g, 2.0 mmol in 2 mL H_2O) was slowly added and stirred at room temperature for 24 h. After this, THF was evaporated, and the residue was diluted with water (1 mL) and isopropanol (5 mL). The resulting mixture was acidified by the addition of HPF_6 (88 μL, 1 mmol), leading to the precipitation of a white solid; filtered, washed with isopropanol, and dried under air to obtain the ligand HPy_2Pic as HPF_6 salt.

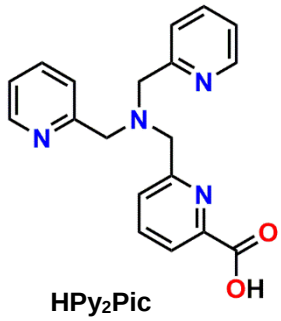

HPy_2Pic

Yield = 0.374 g (78%).

FTIR (KBr pellet cm^{-1}): 3430, 3245, 3132, 3070, 2998, 2927, 2853, 1718, 1632, 1614, 1603, 1594, 1536, 1440, 1308, 1268, 1156, 1055, 877, 839, 767, 557.

^1H -NMR (CD_3OD), 400 MHz): δ 8.89 (d, *J* = 4 Hz, 2H), 8.45 (t, *J* = 8 Hz, 2H), 8.14 (d, *J* = 4 Hz, 1 H), 8.00 (m, 3H), 7.91 (t, *J* = 8 Hz, 2H), 7.57 (d, *J* = 4 Hz, 1H), 4.43 (s, 4H), 4.26 (s, 2H) ppm.

^{13}C NMR (CD_3OD, 100 MHz): δ 167.80, 158.56, 157.16, 149.43, 147.74, 141.69, 140.29, 127.94, 126.19, 125.21, 66.89, 59.81, 59.68 ppm.

ESI-MS (+) m/z for $[C_{19}H_{18}N_4O_2 + H]^+$calcd., 335.1502; found, 335.1509.

6.2.5. Synthesis of ligand H_2tpada

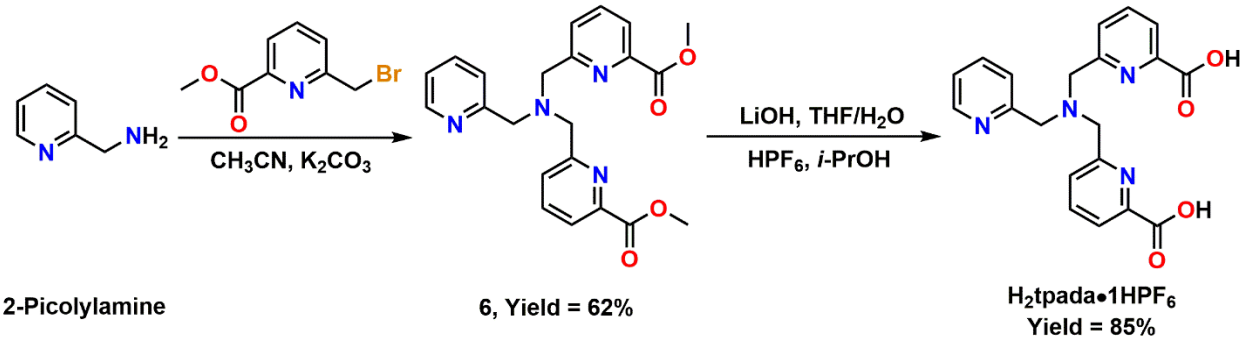

Scheme 6.5. Synthetic scheme for the preparation of ligand **H_2tpada**.

Synthesis of [$C_{22}H_{22}N_4O_4$], (6): To a solution of 2-polyamine (0.216 g, 2 mmol) in dry acetonitrile, 4 equivalents of K_2CO_3 (1.104 g, 8 mmol) and 2 equivalents of Methyl 6-(bromomethyl)picolinate (0.920 g, 4 mmol) was added in succeeding order, under a nitrogen atmosphere and the resulting solution was heated at 60 °C for 3 h. The reaction mixture was thereafter cooled down to room temperature and filtered. The filtrate was evaporated to dryness. Water was added to the residue and extracted with ethyl acetate (3 × 30 mL). The organic part was collected, dried over Na_2SO_4, concentrated to 5 mL, and refrigerated overnight to obtain compound **6** as a white precipitate. It is collected by filtration and subsequently washed with a small amount of ethyl acetate/cyclohexane mixture (1:1).

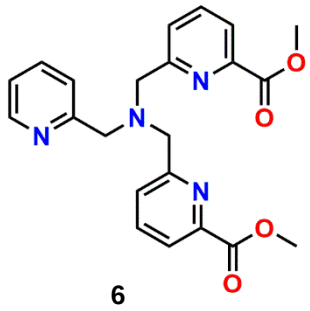

6

Yield = 0.567 g (70%).

FTIR (KBr pellet cm^{-1}): 3428, 3067, 2954, 2846, 1728, 1591, 1439, 1315, 1246, 1140, 1086, 766.

^{1}H NMR ($CDCl_3$, 400 MHz): δ 8.54 (d, J = 4 Hz, 1H), 7.99 (d, J = 8 Hz, 2H), 7.87 (d, J = 4Hz, 2H), 7.80 (t, J = 8 Hz, 2H), 7.64 (t, J = 8 Hz, 1H), 7.54 (d, J = 8Hz, 1H), 7.15 (t, J = 4Hz, 1H), 4.01 (s, 4H), 3.98 (s, 6H), 3.89 (s, 2H) ppm.

^{13}C NMR ($CDCl_3$, 100 MHz): δ 157.41, 154.64, 147.45, 144.37, 141.89, 138.23, 136.56, 124.47, 121.5, 122.19, 120.45, 64.65, 56.21, 55.76, 52.78 ppm.

ESI-MS (+) m/z for $[C_{22}H_{22}N_4O_4 + H]^+$ calcd., 407.1713; found, 307.1687.

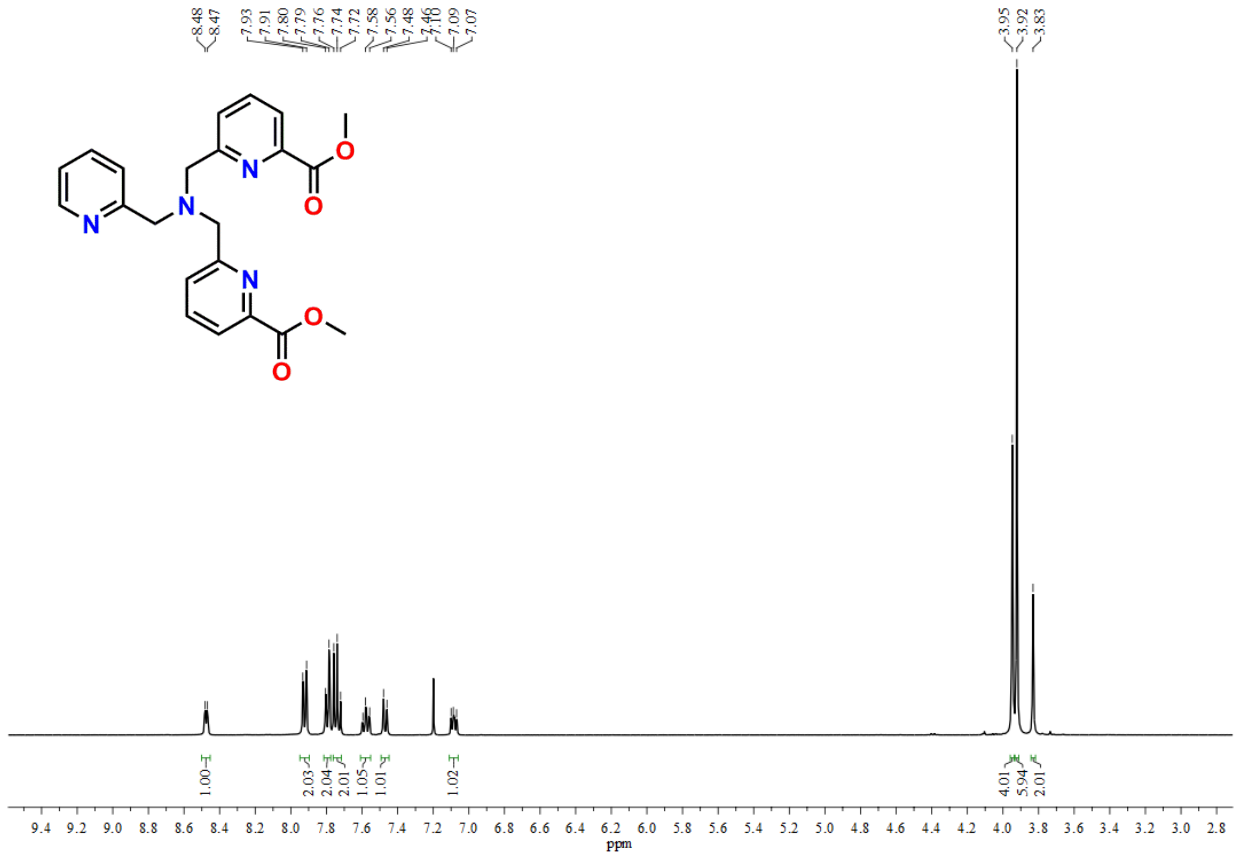

Figure 6.8. ^{1}H NMR spectra for $[C_{20}H_{20}N_4O_2]$, (**6**).

Synthesis of $[C_{20}H_{18}N_4O_4]$, H_2tpada: To a solution of **6** (0.406 g, 1.0 mmol) in THF (6 mL), an aqueous solution of LiOH (0.096 g, 4.0 mmol in 2 mL H_2O) was slowly added and stirred at room temperature for 24 h. After this, the solvent was evaporated, and the residue was diluted with water (1 mL) and isopropanol (5 mL). The resulting mixture was acidified by the addition of HPF_6 (352 µL, 4 mmol), leading to the precipitation of a white solid; filtered, washed with isopropanol, and dried under air to obtain the ligand HPy_2Pic as HPF_6 salt.

H_2tpada

Yield = 0.425 g (79%).

FTIR (KBr pellet cm^{-1}): 3614, 3423, 3064, 2853, 2668, 1690, 1626, 1584, 1469, 1374, 1305, 1271, 1171, 845, 763.

^{1}H -NMR (CD_3OD), 400 MHz): δ 8.99 (d, *J* = 4 Hz, 1H), 8.21 (t, *J* = 8 Hz, 1H), 8.03 (d, *J* = 8 Hz, 2 H), 7.90 (t, *J* = 8 Hz, 2H), 7.73 (d, *J* = 8 Hz, 2H), 7.60 (d, *J* = 8 Hz, 2H), 4.44 (s, 2H), 4.32 (s, 4H) ppm.

^{13}C NMR (D_2O, 100 MHz): δ 172.68, 172.56, 157.08, 152.18, 148.02, 138.24, 137.65, 125.98, 124.29, 122.82, 122.26, 60.26, 59.73 ppm.

ESI-MS (+) m/z for $[C_{19}H_{18}N_4O_2 + H]^+$calcd., 379.1400; found, 379.1470.

6.2.6. Synthesis of complexes and complex incorporated nanoparticles

Synthesis of complex 2A: Aqueous solution of **Li_2Benz(pic)$_2$** (0.12 g, 0.3 mmol), at pH ~ 6.5 (maintained using dilute HCl solution), was reacted with $MnCl_2$•$4H_2O$ (0.05 g, 0.28 mmol) by stirring for 15 minutes at room temperature. pH of the resultant solution was checked another time and allowed to stir for another 24 h to obtain a dirty yellow solution. Slow evaporation of the solution gave a brown solid, which was dissolved in a minimum amount of methanol (~ 5 mL) and diffused under a diethyl ether atmosphere to obtain complex **2A** as a white shiny solid in 42 % yield (0.06 g). High-Performance Liquid Chromatography (HPLC) was performed to ensure >95% purity of the synthesized compound.

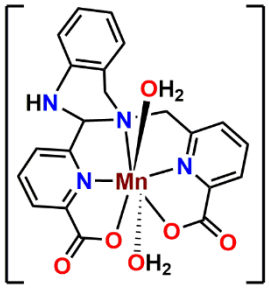

[MnBenz(pic)$_2$(H_2O)$_2$]; 2A

Yield = 0.060 g (42%).

FTIR (KBr pellet cm^{-1}): 3473, 3388, 3270, 3086, 3020, 2911, 2854, 1622, 1585, 1571, 1493, 1427, 1389, 1265, 1185, 1150, 1119, 1072, 1019, 981, 859, 770, 753, 701, 675, 651, 524.

ESI-MS (+) m/z for $[C_{21}H_{16}MnN_4O_4 + H]^+$ calc., 444.0624, found 444.0519.

Synthesis of complex 3A: Complex was reproduced according to the procedure reported by M. Khannam in 'Synthesis, characterization and investigation on water-soluble, aquated Gd(III) and Mn(II) complexes as MRI contrast agents' (TH-2022_136122016), [Doctoral thesis, IIT Guwahati]. Elaborately, $GdCl_3 \bullet xH_2O$ (0.090 g, 0.34 mmol) was added to an aqueous solution of ligand **H_2hbda** (0.140 g, 0.38 mmol), and kept on stirring until the solution became transparent. The pH of the reaction mixture was adjusted to ~ 6.5 by adding an aqueous NaOH solution dropwise; followed by continuous stirring at room temperature for 24 h. The resultant solution was filtered, and a white solid product was obtained after complete evaporation of the filtrate. The obtained white solid was washed thoroughly with MeOH and the absence of free Gd(III) was confirmed by the xylenol orange test. The molar conductivity of 5 mM aqueous solution of complex **3A** was evaluated to be 81 Scm^2mol at 25 °C, which is close to the typical molar conductivity range for (1:1) strong electrolytes. Metal:ligand stoichiometry was established by Job's plot.

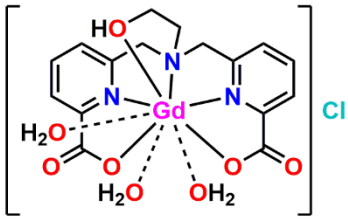

[Gd(hbda)(H_2O)$_3$]Cl; 3A

Yield = 0.070 g (38%).

FTIR (KBr pellet cm^{-1}): 3436, 2851, 2829, 1626, 1591, 1468, 1444, 1406, 1378, 1279, 1226, 1188, 1156, 1116, 1093, 1046, 1012, 974, 955, 942, 812, 775, 690.

ESI-MS (+) *m/z* for $[C_{16}H_{15}N_3O_5Gd]^+$: calcd, 487.0209; found, 487.0291.

Synthesis of 3A@SiO_2NP: **3A**@SiO_2NP was synthesized following the reverse microemulsion procedure. A homogenous solution of Igepal-CO-520 (1.3 mL) in cyclohexane (10 mL) was prepared by stirring for 10 min. A doping solution comprising complex **3A** solution (160 μL, 4.2 mM) in water (320 μL) at pH ~ 7.4 was cautiously added to the surfactant mixture. It was followed by NH_4OH (120 µL, 25% by w/v) and stirred for another 30 minutes. Finally, TEOS (100 μL) was added, and the resultant mixture was kept at room temperature for 24 h with gentle stirring. **3A**@SiO_2NP was obtained by adding acetone (30 mL) to the mixture, which was repeatedly washed with ethanol and water by centrifugation at 10,000 rpm for 15 minutes. The residue obtained was dispersed in 400 μL water (pH maintained at 7.4)

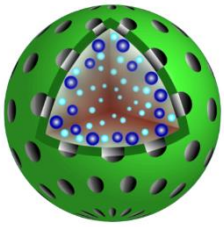

3A@SiO_2NP

to obtain 500 μL of 0.088 mM suspension, concentration given in terms of Gd(III), (8% complex molecules incorporated inside nanoparticles). This mother suspension was further used for relaxometry and other studies.

FTIR (KBr pellet cm^{-1}): 3466, 1639, 1626, 1470, 1099, 962, 799, 467.

Synthesis of complex 3B: $MnCl_2 \bullet 4H_2O$ (0.051 g, 0.26 mmol) was added to a solution of ligand **H_2PyDPA** (0.140 g, 0.28 mmol) in water (5 mL), and it was stirred for 15 minutes. pH of the resultant solution was adjusted to ~ 6.5 with dropwise addition of NaOH solution. The mixture was stirred for another 24 h at room temperature (25 °C). After this, it was filtered, and slow evaporation of the filtrate gave needle-shaped pale-yellow crystals of complex **3B**, which were washed with methanol. The crystals obtained were suitable for a single-crystal X-ray diffraction study.

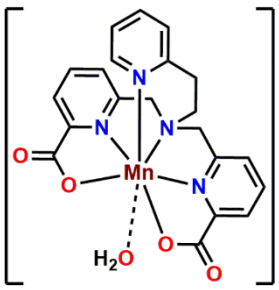

[Mn(PyDPA)(H_2O)]; 3B

Yield = 0.070 g, (45%).

FTIR (KBr pellet cm^{-1}): 3392, 1635, 1625, 1586, 1487, 1438, 1404, 1387, 1304, 1273, 1156, 1124, 1081, 1016, 1002, 780, 755, 690.

ESI-MS (+) m/z for $[\{(C_{21}H_{20}MnN_4O_5)–(H_2O)\}+H]^+$ calcd, 446.07; found: 446.09. Anal. Calcd. for $C_{21}H_{20}MnN_4O_5 \bullet 5H_2O$: C, 45.56; H, 5.47; N, 10.13. Found: C, 45.58; H, 5.23; N, 10.15.

Synthesis of 3B@SiO_2NP: **3B**@SiO_2NP was synthesized following the reverse microemulsion procedure. Igepal-CO-520 (1.3 mL) was added to cyclohexane (10 mL) and stirred for 10 minutes to obtain a homogenous mixture. A doping solution was prepared by adding complex **3B** solution (160 µL, 13.40 mM) in water (320 µL) at pH ~ 7.4. This doping solution was added carefully to the surfactant mixture followed by NH_4OH (120 µL, 25% by w/v), and stirred for another 30 minutes. Then, TEOS (100 µL) was added, and the final mixture was kept at room temperature for 24 h with gentle stirring. **3B**@SiO_2NP was obtained by adding acetone (30 mL) to the mixture, which was repeatedly

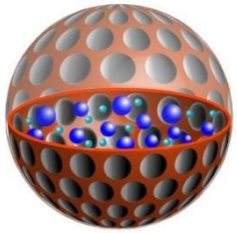

3B@SiO_2NP

washed with ethanol and water by centrifugation at 10,000 rpm for 15 minutes. The residue obtained was dispersed in 400 μL water (pH maintained at 7.4), and this mother suspension was further used for relaxometry and other studies.

FTIR (KBr pellet cm^{-1}): 3629, 3469, 1640, 1518, 1213, 1104, 959, 798.

Synthesis of complex 4A: $MnCl_2 \bullet 4H_2O$ (0.057 g, 0.29 mmol) was combined with a solution of **H_2AlcDPA** (0.119 g, 0.31 mmol) in water (5 mL), and the solution was stirred for 15 minutes. pH of this reaction mixture was adjusted to ~ 6.5 with the dropwise addition of aqueous NaOH. The resultant was stirred for another 24 h at room temperature (25 °C). After this, a clear solution was obtained and left for slow evaporation to obtain a white solid residue. Methanolic solution of the residue (with a few drops of water) was diffused in a diethyl ether environment for one week to obtain needle-shaped colorless crystals of complex **4A**, which were washed with Et_2O. Crystals obtained were analyzed by single-crystal X-ray diffraction.

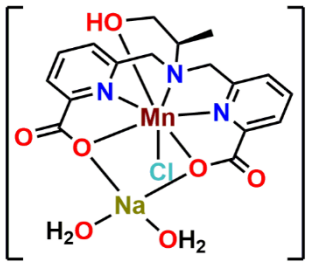

[Mn(AlcDPA)(H_2O)]; 4A

Yield = 0.090 g, (64%).

FTIR (KBr pellet cm^{-1}): 3471, 3317, 3172, 2966, 2937, 2890, 2317, 1692, 1649, 1613, 1587, 1443, 1398, 1268, 1159, 1026, 826, 789, 692.

ESI-MS (+) m/z for $[\{(C_{17}H_{17}ClMnN_3O_5)–(Cl)\}+H]^+$ calcd: 399.0621; found: 398.9919.

Synthesis of 4A@SiO$_2$NP: Reverse microemulsion process was employed for the preparation of **4A**@SiO$_2$NP. A pH ~ 7.4 buffered doping solution of complex **4A** (480 µL, 2.50 mM) was carefully added to a homogenous mixture of Igepal-CO-520 (1. 3 mL) in cyclohexane (10 mL) and stirred for 15 minutes. It was followed by the addition of NH_4OH (120 µL, 25% by w/v) and TEOS (100 µL) afterward, the final mixture was kept at room temperature for 24 h with gentle stirring. **4A**@SiO$_2$NP was obtained by the addition of methanol (10 mL) to the mixture, which was repeatedly washed with methanol and water. Nanoparticles were collected by centrifugation at 10,000 rpm for 15 minutes. The residue obtained was dispersed in 400 µL water (pH maintained at 7.4), and this mother suspension was further used for relaxometry and other studies.

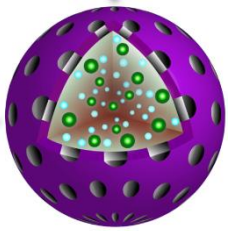

4A@SiO$_2$NP

FTIR (KBr pellet cm^{-1}): 3450, 1694, 1634, 1578, 1444, 1400, 1102, 955, 800.

Synthesis of 4A@SiO$_2$–NH$_2$NP: Aforementioned procedure (for preparation of **4A**@SiO$_2$NP) was repeated along with the addition of 3-Aminopropyl)triethoxysilane (APTES, 50 µL) after 24 h of addition of TEOS. The reaction mixture was left for another 24 h, thereby disrupting the microemulsion with the addition of methanol (10 mL). **4A**@SiO$_2$–NH$_2$NPs was obtained after subsequent washes with copious amounts of methanol, ethanol, and water (centrifugation at 10,000 rpm, 15 minutes in each washing). The residue obtained was dispersed in 400 µL water (pH maintained at 7.4) to obtain the stock suspension was further used for further syntheses, relaxometry, and other studies.

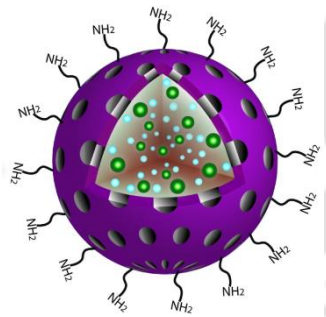

4A@SiO$_2$-NH$_2$NP

FTIR (KBr pellet cm^{-1}): 3444, 3321, 3080, 2941, 2898, 1694, 1643, 1634, 1628, 1588, 1550, 1472, 1450, 1338, 1087, 953, 792.

Synthesis of 4A@SiO$_2$–Py$_2$PicNP: A solution of HPy$_2$Pic ligand (0.049 g, 0.1 mmol) was prepared in PBS buffer (7 mL, 0.01 M, at pH ~ 7.0), activated by successive addition of EDC•HCl (0.192 g, 1.0 mmol) and NHS (0.115 g, 1.0 mmol). After 1 h, monodispersed suspension of **4A**@SiO$_2$–NH$_2$NPs (prepared by dispersing 1.6 mL, 0.80 mM [Mn(II)] **4A**@SiO$_2$–NH$_2$NPs stock solution in 5 mL PBS buffer by 30 minutes sonication) was added to the mixture and gently stirred for 12 h, at room temperature. A pale-yellow turbid solution was obtained and centrifuged (g = 10,000, 20 min) to get the **4A**@SiO$_2$–Py$_2$Pic nanoparticles after several washings with methanol and water. Nanoparticles were re-suspended in 1 mL HEPES buffer (pH ~ 7.4) to form **4A**@SiO$_2$–Py$_2$PicNP stock solution, further used for characterization and relaxometry studies.

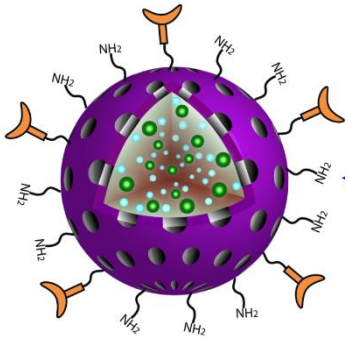

4A@SiO$_2$-Py$_2$PicNP

FTIR (KBr pellet cm^{-1}): 3453, 3246, 2946, 1765, 1665, 1657, 1651, 1643, 1632, 1619, 1546, 1470, 1394, 1094, 955, 796.

Synthesis of complex 5A: MnCl$_2$•4H$_2$O (0.036 g, 0.18 mmol) was combined with a solution of **H$_2$tpada** (0.120 g, 0.18 mmol) in water (5 mL), and the solution was stirred for 15 minutes. pH of this reaction mixture was adjusted to ~ 6.5 with dropwise addition of aqueous NaOH. The resultant was stirred for another 24 h at room temperature (25 °C). After this, a clear solution was obtained and left for slow evaporation to obtain a white solid residue. Methanolic solution of the residue (with a few drops of water) was diffused in a diethyl ether environment for three weeks to obtain needle-shaped pale-yellow crystals of complex **5A**, which were washed with Et$_2$O. Crystals obtained were analyzed by single-crystal X-ray diffraction.

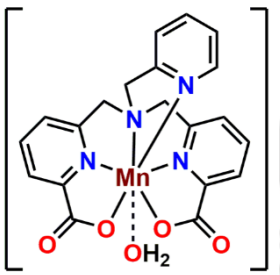

[Mn(tpada)(H$_2$O)]; 5A

Yield = 0.061 g, (55%).

FTIR (KBr pellet cm^{-1}): 3435, 2921, 2851, 1622, 1591, 1438, 1406, 1388, 1272, 1124, 1078, 1013, 847, 763.

ESI-MS (+) m/z for $[C_{20}H_{16}N_4O_4Mn + H]^+$ calcd: 432.0624; found: 432.0568.

Synthesis of 5A@SiO₂NP: The reverse microemulsion process was utilized to synthesize **5A**@SiO_2NP. A pH ~ 7.4 buffered solution of complex **5A** (480 μL, 2.50 mM) constituted the doping solution, which was gradually added to a homogenous mixture of Igepal-CO-520 (1.0 mL) in cyclohexane (15 mL) and stirred for 15 minutes. It was followed by the addition of NH_4OH (150 μL, 25% by w/v) and TEOS (100 μL) afterward, the final mixture was kept at room temperature for 24 h with gentle stirring. **5A**@SiO_2NP separated with the addition of methanol (10 mL) to the mixture, which was repeatedly washed with methanol and water. Nanoparticles were collected by centrifugation at 10,000 rpm for 15 minutes. The residue obtained was dispersed in 400 μL water (pH maintained at 7.4), and this mother suspension was further used for relaxometry and other studies.

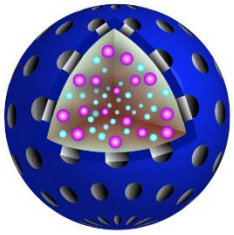

5A@SiO₂NP

FTIR (KBr pellet cm^{-1}): 3640, 3452, 3238, 1637, 1622, 1477, 1102, 964, 806.

Synthesis of 5A@SiO₂–NH₂NP: The preceding method (for preparation of **5A**@SiO_2NP) was repeated along with the addition of 3-Aminopropyl)triethoxysilane (APTES, 50 μL) post 24 h of addition of TEOS. The reaction mixture was slowly stirred for another 24 h, thereby disrupting the microemulsion with the addition of methanol (10 mL). **5A**@SiO_2–NH_2NPs was obtained after subsequent washes with copious amounts of methanol, ethanol, and water (centrifugation at 10,000 rpm, 15 minutes in each washing). The residue obtained was dispersed in 400 μL water (pH maintained at 7.4) to obtain the stock suspension was further used for further syntheses, relaxometry, and other studies.

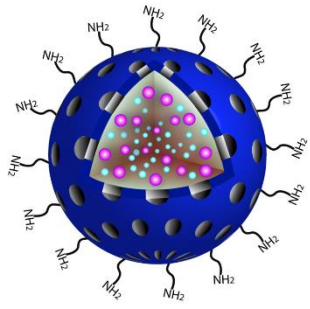

5A@SiO₂-NH₂NP

FTIR (KBr pellet cm^{-1}): 3646, 3433, 3118, 2938, 2880, 1638, 1622, 1548, 1472, 1415, 1388, 1099, 959, 794.

Synthesis of 5A@SiO_2–FA NP: A solution of folic acid (FA) ligand (0.009 g, 0.02 mmol) was prepared in DMSO (5 mL), activated by subsequent addition of EDC•HCl (0.039 g, 0.2 mmol) and NHS (0.023 g, 0.2 mmol). After 1.5 h, a monodispersed suspension of **5A**@SiO_2–NH_2NPs (prepared by dispersing 0.8 mL, 0.2 mM [Mn(II)] **5A**@SiO_2–NH_2NPs stock solution in 5 mL DMSO by 15 minutes sonication) was added to the mixture and stirred for 3 days, at room temperature. A yellow turbid solution was obtained and centrifuged (g = 10,000, 20 min) to get the deep yellow **5A**@SiO_2–FA nanoparticles after several washings with DMSO, methanol, and water. Nanoparticles were re-suspended in 1 mL HEPES buffer (pH ~ 7.4) to form **5A**@SiO_2–FA NP stock solution, further used for characterization and relaxometry studies.

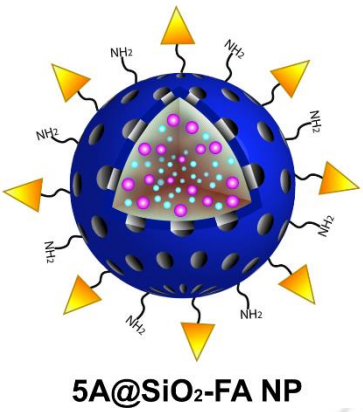

FTIR (KBr pellet cm^{-1}): 3646, 3432, 3118, 3090, 2938, 2847, 1648, 1635, 1622, 1607, 1545, 1511, 1446, 1410, 1372, 1335, 1092, 959, 794.

ACS APPLIED BIO MATERIALS

www.acsabm.org Article

Porous Silica Nanospheres with a Confined Mono(aquated) Mn(II)-Complex: A Potential T_1-T_2 Dual Contrast Agent for Magnetic Resonance Imaging

Riya Mallik, Muktashree Saha, and Chandan Mukherjee*

Cite This: *ACS Appl. Bio Mater.* 2021, 4, 8356–8367 Read Online

ACCESS | Metrics & More | Article Recommendations | Supporting Information

ABSTRACT: Magnetic resonance imaging has emerged as an indispensable imaging modality for the early-stage diagnosis of many diseases. The imaging in the presence of a contrast agent is always advantageous, as it mitigates the low-sensitivity issue of the measurements and provides excellent contrast in the acquired images even in a short acquisition time. However, the stability and high relaxivity of the contrast agents remained a challenge. Here, molecules of a mononuclear, mono(aquated), thermodynamically stable [log K_{MnL} = 14.80(7) and pMn = 8.97] Mn(II)-complex (**1**), based on a hexadentate pyridine-picolinate unit-containing ligand (H_2PyDPA), were confined within a porous silica nanosphere in a noncovalent fashion to render a stable nanosystem, complex **1**@SiO_2NP. The entrapped complex **1** (complex **1**@SiO_2) exhibited r_1 = 8.46 mM^{-1} s^{-1} and r_2 = 33.15 mM^{-1} s^{-1} at pH = 7.4, 25 °C, and 1.41 T in *N*-(2-hydroxyethyl)piperazine-*N*′-ethanesulfonic acid buffer. The values were about 2.9 times higher compared to the free (unentrapped)-complex **1** molecules. The synthesized complex **1**@SiO_2NP interacted significantly with albumin protein and consequently boosted both the relaxivity values to r_1 = 24.76 mM^{-1} s^{-1} and r_2 = 63.96 mM^{-1} s^{-1} at pH = 7.4, 37 °C, and 1.41 T. The kinetic inertness of the entrapped molecules was established by recognizing no appreciable change in the r_1 value upon challenging complex **1**@SiO_2NP with 30 and 40 times excess of Zn(II) ions at pH 6 and 25 °C. The water molecule coordinated to the Mn(II) ion in complex **1**@SiO_2 was also impervious to the physiologically relevant anions (bicarbonate, biphosphate, and citrate) and pH of the medium. Thus, it ensured the availability of the inner-coordination site of complex **1** for the coordination of water molecules in the biological media. The concentration-dependent changes in image intensities in T_1- and T_2-weighted phantom images and uptake of the nanoparticles by the HeLa cell put forward the biocompatible complex **1**@SiO_2NP as a potential dual-mode MRI contrast agent, an alternative to Gd(III)-containing contrast agents.

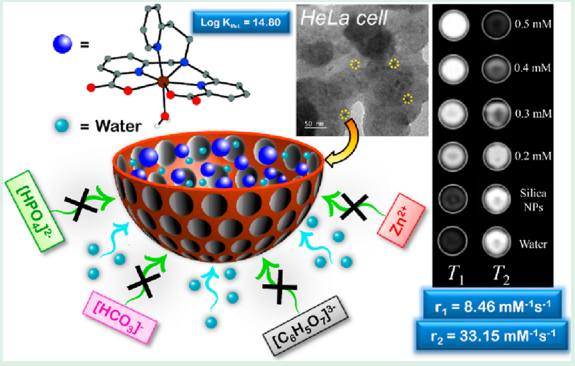

KEYWORDS: *magnetic resonance imaging, relaxivity, T_1-T_2 contrast agents, Mn(II)-complex, porous silica nanoparticles*

INTRODUCTION

Magnetic resonance imaging is a noninvasive technique that provided *in vivo* anatomical soft tissue images with high spatial resolution and has found its immense use as a diagnostic tool in the last few decades.[1−8] In this imaging modality, images are produced by recording the relaxivity (r; $r = 1/T$; T = relaxation time) of water protons using NMR techniques. Hence, no harmful ionizing radiation is required for MRI as necessary in X-ray, computed tomography, and positron emission tomography. However, the modality is limited by low sensitivity; hence, imaging remains a prolonged process and often does not provide conspicuous contrast in the images. To overcome the issue, paramagnetic materials, called contrast agents, have been administered prior to imaging as additional supplements.[8] The contrast agents reduce longitudinal (spin−lattice) relaxation time (T_1) and transverse (spin−spin) relaxation time (T_2) of the nearby protons in many folds and consequently provide better contrast in the images. The efficiency of a contrast agent is represented by the enhancement of relaxivity of water protons in the presence of 1 mM paramagnetic metal ion-containing species.[8]

Contrast agents are classified into two groups depending on the overall signal enhancement property in the region of interest.[1−2] The positive contrast agents (T_1-contrast agents), which are mainly low-molecular-weight Gd(III),[9−18] Mn(II),[19−35,69] and Fe(III)[36,37] complexes, render brighter images by enhancing the signal intensity, while a loss in the signal intensity results in darker images in the presence of negative

Received: August 27, 2021
Accepted: November 17, 2021
Published: December 3, 2021

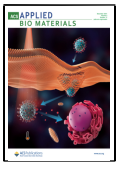

https://doi.org/10.1021/acsabm.1c00937
ACS Appl. Bio Mater. 2021, 4, 8356–8367

contrast agents (T_2-contrast agents), which are usually superparamagnetic nanoparticles.[38−41] The clinical applications of T_2-contrast agents have some drawbacks. Because of the image darkening property, the use of T_2-contrast agents misleads with the signals that appeared due to endogenous conditions,[40,41] such as metal ion depositions, calcification, blood clots, hemorrhage, and magnetic susceptibility artifacts. In these concerns, the administration of only T_1- or T_1-T_2 dual contrast agents is advantageous.[14,42−44]

The clinically approved T_1-contrast agents are small molecule Gd(III)-based complexes that exhibit r_1 relaxivity values in the range of 3.3−5.2 mM^{-1} s^{-1} at 1.5 T, 37 °C in water.[45] The small relaxivity values require administering a hefty dose of the T_1-contrast agents to realize good image contrast. However, the use of Gd(III)-based contrast agents in a large concentration is not safe as the leached bare Gd(III) ions are poisonous and known to develop nephrogenic systemic fibrosis in patients with renal failure.[17,46] Thus, attention has been revived for alternative metal ions.

In this context, complexes of more biofriendly, five-unpaired electrons-containing paramagnetic Mn(II) ions [$3d^5$] have drawn interest.[8,19] In fact, $MnCl_2{\cdot}4H_2O$ (LumenHance) and Mn(II)-DPDP complexes (DPDP = di-pyridoxal diphosphate; Teslascan) have already been administered *in vivo* for neurological applications, cell-labeling, and liver-specific contrast images.[47−50] Nevertheless, the administration of free Mn(II) ions in high doses is also not safe.[51] Although the complexation of Mn(II) ions with organic chelates mitigates the toxicity, the relaxivity values decrease as the number of inner-sphere water molecules diminishes. Thus, a new strategy is required to develop thermodynamically stable and kinetically inert Mn(II)-based T_1 or T_1-T_2 dual contrast agents with high relaxivity values.

The SBM theory interpretation reveals that r_1 relaxivity enhancement in a molecular system is possible by reducing the tumbling rate within an applied magnetic field range of 0.5 to 1.5 T.[14,16,52−55] Thus, grafting of stable small Mn(II) complexes onto a nanosystem or confining the complexes within a nanosphere should serve the purposes. Furthermore, the circulation time of contrast agent-loaded nanosystems would be higher compared to small chelate molecules. Therefore, the administration of such contrasting systems would be advantageous for MR imaging that continues for a long time (e.g., oncological imaging).[56] In these regards, investigation on Mn(II)-containing nanomaterials is under continuous progress by the following: (1) immobilizing Mn(II)-complexes onto solid silica nanosphere and solid nanodiamond; and (2) entrapping Mn(II)-complexes within lipidic nanovesicles or nanobeads.[57−65] Nevertheless, the attainment of kinetic inertness of the surface-bound, aquated, small-molecule Mn(II) complexes always remained an intriguing task and required genuine kinetically inert Mn(II) complexes, which are very rare indeed.[1,19,29,66]

Herein, to develop an Mn(II)-based contrast agent with high r_1 and r_2 relaxivity values, we envisaged confining molecules of a thermodynamically stable, aquated Mn(II)-complex within a porous, biocompatible silica nanosphere. The porous nature should permit the free movement of water molecules across the pores and interact with the paramagnetic Mn(II)-complex molecules. The silica nanosphere would help to retain kinetic inertness by shielding the complex from exposure to the external metal ions and anions. Furthermore, the rotation dynamics of the entrapped molecules within the confinement zone are expected to be slower compared to the free molecules; consequently, a high r_1 relaxivity value could be achieved. The presence of many paramagnetic molecules within a nanosphere might also increase r_2 relaxivity by experiencing a greater extent of spin−spin interactions. Hence, a T_1 or a T_1-T_2 dual contrast agent could emerge.

To pursue the objective, a mononuclear, mono(aquated) Mn(II)-complex (**1**; $[Mn^{II}(PyDPA)(OH_2)]^0$), based on a hexadentate ligand (H_2PyDPA) containing one pyridine, one amine, and two picolinate coordinating units, has been synthesized. The complex was found thermodynamically stable with log K_{MnL} = 14.80(7) and pMn = 8.97. The r_1 = 2.88 mM^{-1} s^{-1} and r_2 = 11.10 mM^{-1} s^{-1} exhibited by the complex at 1.41 T, pH = 7.4, and 25 °C and the relaxivity values remained almost unaltered in the presence of 200 equivalent amounts of physiological anions (biphosphate, bicarbonate, and citrate). However, the complex was kinetically labile (Figure S11). Perceptibly, the entrapment of the complex molecules within a porous nanosphere subdues the kinetic lability. In addition, approximately a 2.9-fold enhancement in the relaxivity values (r_1 = 8.46 mM^{-1} s^{-1} and r_2 = 33.15 mM^{-1} s^{-1}) compared to the free-complex molecule was realized. About 6% decrease in the r_1 relaxivity value in 48 h was noticed in the presence of 30- and 40-fold excess Zn(II) ions. However, the decrease was not due to kinetic lability and leaching of Mn(II) ions. Instead, it was being ascribed to a subtle hindrance of water accessibility inside the nanoparticles because of the coagulation. HeLa cell internalization of the biocompatible complex **1**@SiO_2NP and phantom T_1- and T_2-weighted in vitro images unambiguously established a dual contrast ability of the newly developed nanosystem.

RESULTS AND DISCUSSION

The synthetic route for the preparation of ligand $H_2PyDPA{\cdot}HCl$ and the corresponding Mn(II) complex (**1**) is shown in Scheme 1. Compound **B** was isolated in 54% yield by reacting 1:2.2 equivalent amounts of 2-(pyridin-2-yl)ethanamine (**A**) and 6-(bromomethyl)picolinate in CH_3CN in the presence of K_2CO_3 and KI. Ligand H_2PyDPA was obtained as a monohydrochloride salt ($H_2PyDPA{\cdot}1HCl$) in 75% yield by the hydrolysis of compound B with an aqueous LiOH solution in the THF/H_2O solvent mixture, followed by acidification of the solution with 1 M HCl. The reaction of equivalent amounts of the isolated ligand and $MnCl_2{\cdot}4H_2O$ in water at pH ∼ 6.5 followed by slow evaporation of the reaction mixture provided complex **1** in the crystalline form in 45% yield. X-ray single-crystal diffraction measurement revealed that in complex **1**, the central Mn atom was seven-coordinate with trigonal bipyramidal geometry (Scheme 1B). The coordination of two picolinate units and aliphatic N2 atom constructed the basal N_3O plane. Pyridine N3 occupied one of the apical positions, and the other position was empty and eventually occupied by a solvent water molecule. The presence of a water molecule in the primary coordination sphere of Mn(II) ion indicated that the complex could be a potential T_1-weighted contrast agent.

pH-potentiometric titrations were carried out on the ligand and a 1:1 ligand/Mn(II) ion mixture in 0.15 M NaCl solutions at 25 °C to determine the thermodynamic stability constant of complex **1**. The stability constant was found to be log K_{MnL} = 14.80(7) by the simulation of the experimental curve. The value was comparatively higher than the previously reported mono(aquated), seven-coordinate Mn(II) complexes of PyC3A, DPAAA, *trans*-CDTA, and ethylenediaminetetraacetic

https://doi.org/10.1021/acsabm.1c00937
ACS Appl. Bio Mater. 2021, 4, 8356−8367

Scheme 1. (A): Synthetic Route for the Preparation of H_2PyDPA·1HCl and Complex 1; (B,C): Representation of Molecular Structures of Complex 1 and the Protonated Ligand; C = Gray, N = Blue, O = Red, Cl = Green, and Mn = Brown; (i) Methyl 6-(bromomethyl)picolinate, CH_3CN, K_2CO_3, and KI, (ii) LiOH in THF/H_2O, (iii) 1 M HCl, and (iv) $MnCl_2·4H_2O$, H_2O, pH ∼ 6.5

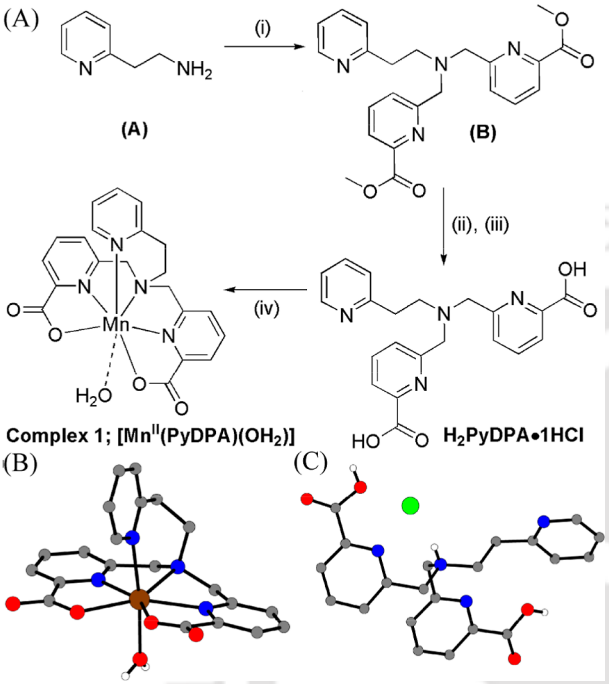

acid ligands (Scheme S1 and Table S2).[66−68] The presence of three pyridine moieties in the ligand H_2PyDPA thus imparted high thermodynamic stability in complex **1** due to Mn(II)(t_{2g})-to-pyridine π^*-interactions. Under physiological conditions, the thermodynamic stability of any metal complex is represented by its pM value.[21,66] The pM value is defined as $-\log[M]_{free}$, considering [M] = [L] = 10^{-5} M at pH ∼ 7.4.[26] The complex $[Mn^{II}(PyDPA)(OH_2)]^0$ exhibited a pMn value of 8.97 that further consolidated the high thermodynamic stability.

A reverse microemulsion method was used to confine the molecules of complex **1** within a porous silica nanosphere (Scheme 2). In this process, Igepal CO-520 was dissolved in cyclohexane, and an aqueous solution of complex **1** was added to it to generate nanosized aqueous droplets. The hydrolysis of added TEOS created the silica nanospheres around the water droplets in the presence of ammonia solution. After that, acetone was added to disrupt the microemulsion. Finally, complex **1**-entrapped porous silica nanospheres (complex **1**@SiO_2NPs) were collected by centrifugation.

The formation of monodispersed and spherical nanoparticles of complex **1**@SiO_2 with a uniform size of 14.3 ± 2 nm was recognized by transmission electron microscopy (TEM) images (Figure 1). The elemental analysis using the energy-dispersive X-ray spectroscopy (EDS) technique consolidated the existence of manganese and nitrogen elements (Figure 1B) and indicated the presence of complex **1** within the nanosphere. Furthermore, no appreciable change in the UV−vis spectrum features of the complex measured at pH ∼ 7.4 and ∼9.5 (Figure S23) refuted the possibility of decomposition of the complex during the encapsulation. The presence of an infrared band at 1625 cm^{-1} [ν(C═O)] (Figure S24) and a six-line X-band EPR spectrum (Figure S26), which is typical for Mn(II) ions-based systems, also indicated the incorporation.

The hollow and porous nature of the silica nanosphere was verified by nitrogen gas (N_2) adsorption−desorption isotherm recorded on dried complex **1**@SiO_2. Type-IV isotherm was observed with hysteresis loop (Figure 1D) as expected for silica nanospheres with mesopores.[69] Nanospheres were of 211.03 m^2/g surface area. By the Barrett−Joyner−Halenda

Scheme 2. Schematic Representation to the Formation of Complex 1@SiO_2NPs

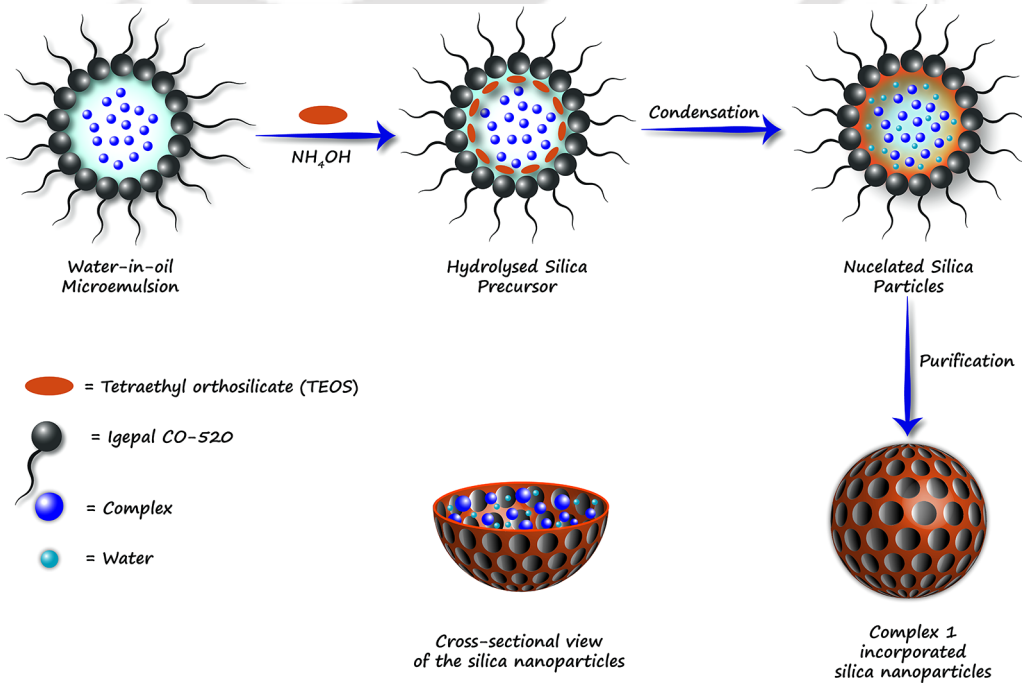

https://doi.org/10.1021/acsabm.1c00937
ACS Appl. Bio Mater. 2021, 4, 8356−8367

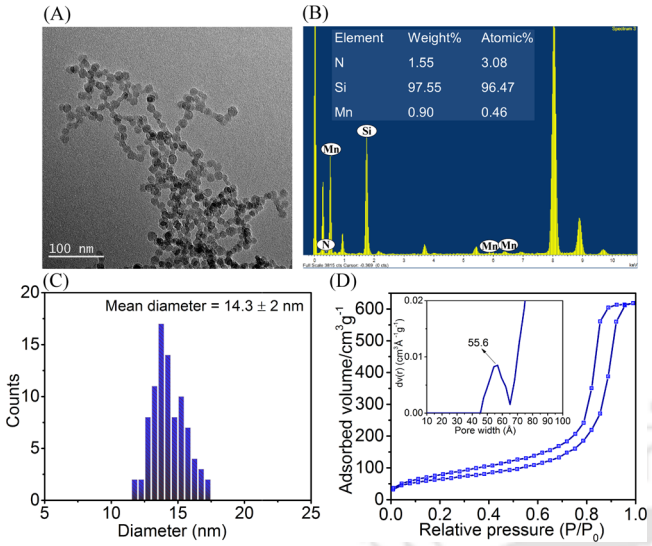

Figure 1. (A) TEM image of freshly prepared complex **1**@SiO_2NP. (B) Presence of Mn, Si, and N in the isolated NPs by TEM-EDS. (C) Particle-size distribution plot. (D) 77 K N_2 adsorption/desorption isotherms and pore size distributions (inset) of complex **1**@SiO_2NPs.

method, the pore diameter was calculated. The pore size distribution plot (Figure 1D; inset) indicated the presence of two peaks, one at 5.56 nm, which attributed to the internal pores of complex **1**@SiO_2, and the other at 9.04 nm was anticipated due to interparticle voids.[70] The presence of such large pores on the nanospheres is expected to allow free movement of small water molecules across the silica layer and interact with complex **1**. Crystal structure analysis of complex **1** indicated the presence of π-to-π interactions within the complex molecules through pyridine units (Figure 2). Thus,

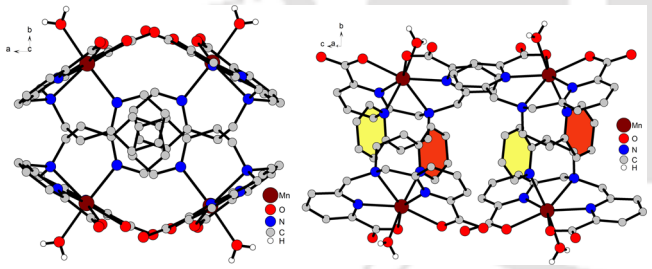

Figure 2. Stacking $\pi-\pi$ interactions among pyridine units of four different molecules. Red- and yellow-color rings represent two adjacent, interacting pyridine units of two closely located molecules.

a big cluster of molecules might result within the sphere, which would be less prone to come out from the sphere rendering a stable complex **1**@SiO_2 system. To investigate water exchangeability by complex **1**@SiO_2NPs through the pores, complex **1**@SiO_2NP was suspended in D_2O for 48 h and then lyophilized for 24 h to isolate dry complex **1**@SiO_2NP with feasibly incorporated D_2O (complex **1**@SiO_2NP_D_2O). Fourier transform infrared (FTIR) spectra of complex **1**@SiO_2NPs and complex **1**@SiO_2NPs_D_2O were being recorded. The decrease in the band intensity in the region 3100−3450 cm^{-1} and the appearance of a broad band, due to ν(O−D) and ν(H−O−D) asymmetric stretches, centered around 2606 cm^{-1} indicated the presence of D_2O inside the nanoparticles via the exchange of H_2O (Figure S25). Hence, the water-exchange capability of the synthesized complex **1**@SiO_2NPs was consolidated.

Concentration-dependent T_1 and T_2 relaxation times were recorded on complex **1** in *N*-(2-hydroxyethyl)piperazine-*N*′-ethanesulfonic acid (HEPES) buffer at 1.41 T, pH ∼ 7.4, 25 °C using the inversion recovery and Curr−Purcell−Meiboom−Gill methods. A linear increase in $1/T_i$ as a function of increasing Mn(II) ion concentration, determined by inductively coupled plasma−mass spectrometry (ICP−MS) analyses of each solution, was noticed (Figure 3A,B). By linear fitting of

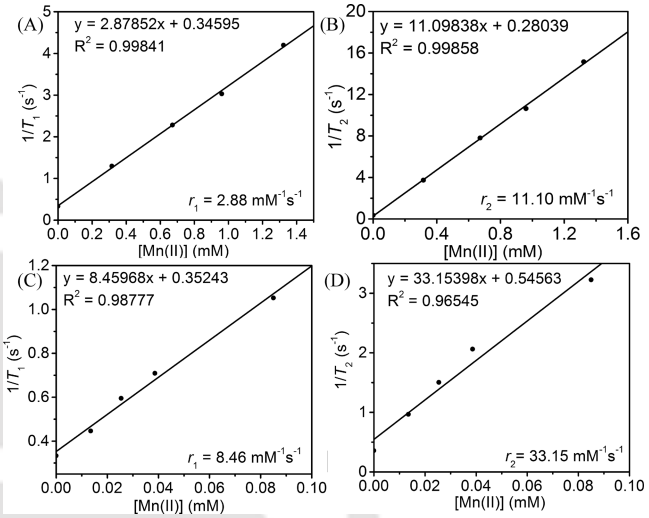

Figure 3. (A) $(1/T_1)$ and (B) $(1/T_2)$ vs [Mn(II)] plot for complex **1**. Likewise, (C) $(1/T_1)$, and (D) $(1/T_2)$ versus [Mn(II)] plot for complex **1**@SiO_2NPs. Measurements were done at pH ∼ 7.4, 1.41 T, and 25 °C.

the plots, r_1 = 2.88 mM^{-1} s^{-1} and r_2 = 11.10 mM^{-1} s^{-1} were obtained.[71] The r_1 relaxivity value of complex **1** was higher than Mn(II)-based contrast agent Teslascan (1.6 mM^{-1} s^{-1})[45] and lower, albeit close to Gd(III)-based contrast agents Prohance (2.9 mM^{-1} s^{-1}), Dotarem (2.9 mM^{-1} s^{-1}), Omniscan (3.3 mM^{-1} s^{-1}), Magnevist (3.3 mM^{-1} s^{-1}), and Gadovist (3.3 mM^{-1} s^{-1}).[45] Upon the entrapment of the complex within a nanosphere, that is, of complex **1**@SiO_2NP, the respective r_1 and r_2 values increased to 8.46 and 33.15 mM^{-1} s^{-1} (Figures 3C,D and S3) with r_2/r_1 = 3.92. To note, the ratio was found to be r_2/r_1 = 5.62 mM^{-1} s^{-1}/2.12 mM^{-1} s^{-1} = 2.65 using $MnCl_2$ instead of complex **1** to the formation of the NPs. Nonetheless, an approximately threefold increase in the respective relaxivity values of complex **1** was attained by confining the complex molecules within a porous nanosphere. The relaxivity values of complex **1**@SiO_2NPs were greater than those of reported manganese oxide impregnated silica nanoparticles and were better or almost equal to the silica-surface-attached mono(aquated) Mn(II) complexes (Table S3). Noteworthy, the relaxivity values increased slightly (8.61 and 34.59 mM^{-1} s^{-1}; Figure S4) with the increase in the temperature of medium from room temperature (25 °C) to physiological temperature (37 °C). The observation demonstrated stronger interactions between the molecules, and because of these, the effect of temperature to rotation correlation time was insignificant.[72] Upon decreasing the particle size of complex **1**@SiO_2NPs from 14.30 to 10.04 nm (Figure S2), higher relaxivity values, r_1 = 12.45 mM^{-1} s^{-1} and r_2 = 45.76 mM^{-1} s^{-1} (Figure S6), could be achieved. It is

https://doi.org/10.1021/acsabm.1c00937
ACS Appl. Bio Mater. 2021, 4, 8356−8367

noteworthy that the r_1 relaxivity value of complex **1**@SiO_2 was much greater than that found in clinically approved superparamagnetic iron oxide (SPIO)-based contrast agent Feridex (4.7 mM^{-1} s^{-1}) and very much similar to another SPIO-based contrast agent Resovist (8.7 mM^{-1} s^{-1}).[45] However, the advantage of present nanovesicles, that is, complex **1**-entrapped nanosphere system, is the r_2/r_1 = 4.02, which is much higher in the case of Feridex (r_2/r_1 = 8.72) and Resovist (r_2/r_1 = 7.01).[45] Thus, unlike the clinically approved superparamagnetic contrast agents, which are mainly T_2 contrast agents, complex **1**@SiO_2NPs can be utilized as either a T_1- or T_1−T_2 dual-mode contrast agent.

Serum albumin is the most abundant protein that exists in the human blood plasma. The protein interacts with the administered contrast agents and governs the uptake, transportation, biodistribution, and finally, the excretion of the contrast agents.[29,64,73−75] Therefore, to realize the possible interactions of complex **1**@SiO_2NP with serum albumin, r_1 and r_2 relaxivity values of the suspensions in 4.5% (w/v) bovine serum albumin (BSA) were being recorded at pH ∼ 7.4, 37 °C, and 1.41 T. A significant increase in r_1 (24.76 mM^{-1} s^{-1}) and r_2 (63.96 mM^{-1} s^{-1}) (Figure 4) values inferred

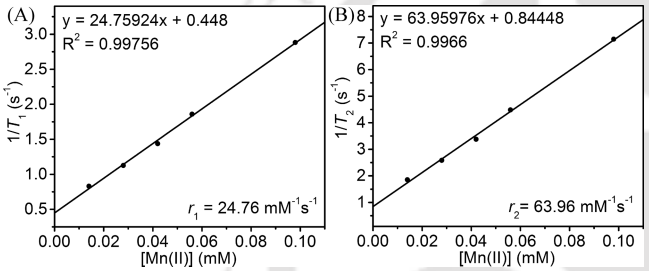

Figure 4. (A) $(1/T_1)$ and (B) $(1/T_2)$ versus [Mn(II)] plot for complex **1**@SiO_2NPs in the presence of 4.5% (w/v) BSA at pH ∼ 7.4, 1.41 T, and 37 °C.

interactions between the protein and the Mn(II)-complex-encapsulated nanoparticles which reduced the mobility and rendered a higher relaxivity. The protein under the experimental conditions remains in its anionic form. The zeta (ζ) potential −18.3 mV of complex **1**@SiO_2NP at pH ∼ 7.4 evinced the negatively charged surface of the nanosphere. Therefore, Coulombic interactions between the protein and complex **1**@SiO_2NPs would not be feasible. It has previously been established that negatively surface-charged protein corona, generated by functionalizing mesoporous silica nanoparticles with hyaluronic acid, interacts with BSA at pH 7.4 via van der Waal interaction.[76] Akin to the report, herein, noncovalent supramolecular interactions and van der Waal interactions between complex **1**@SiO_2NP and BSA were being suggested. Indeed, ζ potential of complex **1**@SiO_2NP suspended in BSA was −27.5 mV at pH 7.4. Thus, the decrease in ζ potential in the presence of BSA consolidated the proposed interactions. Furthermore, the measurement of dynamic light scattering (DLS) inferred that the increase in the hydrodynamic diameter from 307.4 to 796.1 nm (Figure S9) supported the association of complex **1**@SiO_2NP with BSA.

To examine the effect of physiologically relevant anions, both complex **1** [0.67 mM] and complex **1**@SiO_2NPs [0.10 mM] were treated with about 200 equivalent amounts of biphosphate ($[HPO_4]^{2-}$), bicarbonate ($[HCO_3]^{1-}$), and citrate ($[C_6H_5O_7]^{3-}$) anions in HEPES buffer at pH = 7.4, 25 °C for 12 h. The anions could interact with the central metal, Mn(II) ion, and could coordinate to the ion by replacing the Mn(II)-coordinated (inner-sphere) water molecule. In that case, the r_1 relaxivity value will decrease as the T_1 relaxation time of water protons will be affected only by the secondary interactions and not by both primary and secondary interactions. However, the substantial increase in the value refers either to the decomposition of the complex and release of Mn(II) ions [r_1 = 6.62 mM^{-1} s^{-1}; Figure S7] or aggregation of complex molecules by the quaternary interactions with the anions. This aggregation renders a slowly rotating molecular system and consequently increases r_1 relaxivity. Complex **1** exhibited only a slight change in the r_1 value: Δr_1 = 0.17; ∼6% increase for biphosphate and Δr_1 = 0.24; ∼8% decrease for citrate (Figure 5A). This feature indicated no pronounced

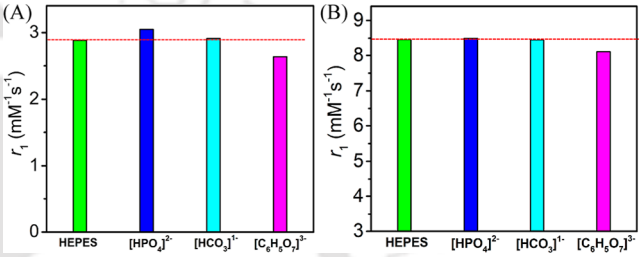

Figure 5. Longitudinal relaxivity (r_1) of (A) complex **1** and (B) complex **1**@SiO_2 estimated in the presence of 200 equivalents of different physiological anions at pH ∼ 7.4, 1.41 T, and 25 °C. During experiments, Mn(II) concentrations were maintained at 0.67 and 0.10 mM for complex **1** and complex **1**@SiO_2NPs, respectively.

interactions between the complex coordination sphere and the anions. For complex **1**@SiO_2NP, r_1 value remained almost unaltered (Δr_1 = 0.33; ∼4% decrease only for citrate) in the presence of the anions (Figure 5B). Thus, the synthesized nanospheres were impervious to the anions.

To investigate the effect of pH on complex **1** and complex **1**@SiO_2NP, the change in r_1 relaxivity of the entities as a function of pH was determined. A sharp increase in the relaxivity value of complex **1** was noticed with the decrease in the pH of the medium below 4, while, the relaxivity diminished at a pH higher than 8 (Figure 6A). To rationalize the phenomena, the species distribution of complex **1** across the pH range 2−12 was examined. The formation of monoprotonated $[Mn^{II}(HPyDPA)(OH_2)_n]^+$ species followed by the decomposition of complex **1** finally resulted in free Mn(II) ions in the solution (Figure 6). The formed $[Mn(OH_2)_6]^{2+}$

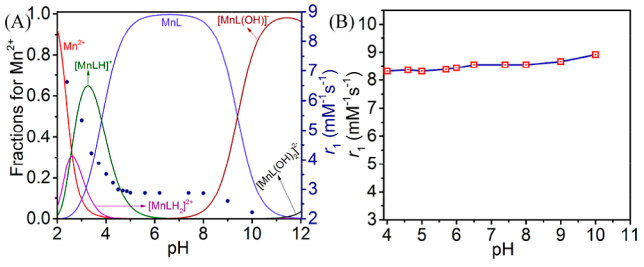

Figure 6. (A) Species distribution diagram for Mn/H_2PyDPA: [Mn(II)] = [L] = 1 mM, and pH-dependent relaxometry of complex **1**, and (B) r_1 values for complex **1**@SiO_2NPs in the pH range from 4.0−10.0 at 1.41 T and 25 °C.

https://doi.org/10.1021/acsabm.1c00937
ACS Appl. Bio Mater. 2021, 4, 8356−8367

exhibits r_1 = 6.62 mM^{-1} s^{-1}. Hence, r_1 increased with the decrease in pH of the medium (pH ≤ 3). In $[Mn^{II}(HPyDPA)(OH_2)_n]^+$ species, the *tert*-amine N atom could undergo protonation as suggested by the X-ray structure (Scheme 1) of the isolated ligand, and hence, the N atom no longer participated in the metal coordination. The originated vacant site thus facilitated the inner-sphere coordination of another water molecule. Therefore, due to the formation of species with the inner-sphere coordination number, q = 2, an elevation in the relaxivity resulted in the pH range 3−4. At a pH greater than 8, the r_1 value diminished due to the appearance of $[Mn^{II}(PyDPA)(OH)]^-$ species by either deprotonation of a proton of the coordinated water molecule or substitution of the water molecule by a hydroxyl anion (HO^-). Contrarily, r_1 = 8.45 mM^{-1} s^{-1} diminished by ∼2% at pH 4 and elevated by ∼5% at pH 10 in **1**@SiO_2NP. Hence, the influence of protons to complex **1** was successfully eliminated by confining complex **1** within the nanosphere.

The kinetic inertness is the essential parameter that determines the suitability of the contrast agent for its possible *in vivo* application. The index for the kinetic inertness is the time required for the 20% decrease of the initial r_1 relaxivity of the pristine material in the presence of scavenger metal ions, for example, Zn(II) ions.[66] Herein, to evaluate the kinetic inertness of **1**@SiO_2NP, the suspension of the NPs was challenged with 30 and 40 equivalent amounts of $ZnCl_2$ at pH 6.0. The change in the relaxivity ratio was then monitored as a function of time. Initially, a sharp change (∼3% in 1.5 h) was noticed, irrespective of the concentration of Zn(II) ions, and the rate of the change was almost equal in both cases (Figure 7). This result discarded the possibility of substitution of

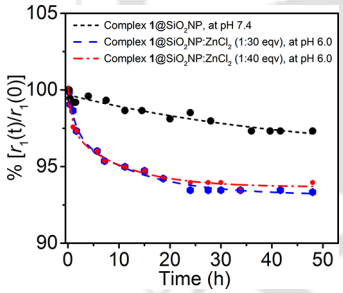

Figure 7. Percentage changes in $r_1(t)/r_1(0)$ for complex **1**@SiO_2NPs with time when challenged with 30 and 40 equivalent excess of Zn(II) ions at pH ∼ 6.0 (MES buffer), 1.41 T, and 25 °C. The sample contained suspensions of complex **1**@SiO_2NPs at [Mn(II)] = 0.056 mM.

Mn(II) ions from the complex molecules by Zn(II) ions as no Zn(II) ion-dependent decrease in the relaxivity was realized. Gratifyingly, the change in the relaxivity ratio was limited to only ∼6% in 24 h and remained unaltered up to 48 h. The slight change could be because of the lowering of water accessibility inside the nanoparticles due to the coagulation (*vide infra*).

To elucidate the effect of Zn(II) ions on the NPs, TEM images were recorded on the isolated NPs after 48 h exposure to 40 equivalent amounts of Zn(II) ions at pH 6.0. No disintegration in the nanosphere was noticed (Figure 8). Additionally, the diameter of the isolated particles remained almost unaltered as 14.6 ± 3.0 nm (Figure 8). Thus, no adverse effect was exerted by Zn(II) ions to the nanoparticle morphology. To examine the possible adsorption of Zn(II)

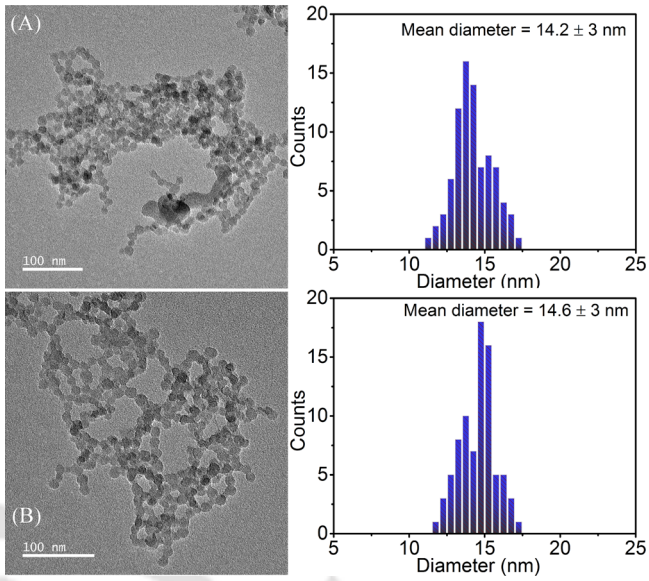

Figure 8. Representative TEM images of complex **1**@SiO_2NPs obtained after 48 h suspension at pH 6.0 (A) without and (B) with 40 equivalent Zn(II) ions along with corresponding size distribution plots.

ions on the surface of the nanoparticles, ζ potentials of the pristine complex **1**@SiO_2NP and the Zn(II)-added systems were recorded at pH 6.0. The linear decrease of ζ potential of complex **1**@SiO_2NP upon the progressive addition of Zn(II) ions; −18.1 mV [0.0], −15.2 mV [10], −13.3 mV [20], −11.1 mV [30], and −9.07 mV [40] (parenthesis refers the equivalence of added Zn(II) ions) inferred the adsorption. Furthermore, DLS studies were carried out on complex **1**@SiO_2NP and in the presence of 10, 20, 30, and 40 equivalent amounts of Zn(II) ions at pH 6.0, 25 °C in MES buffer. A squarely increase in the hydrodynamic diameter with the increase in concentration of Zn(II) ions (Table 1 and Figure

Table 1. Hydrodynamic Diameters and Zeta Potentials of Suspensions of Complex 1@SiO_2NPs When Challenged with Increasing Equivalence Excess of Zn(II) Ions at pH ∼ 6.0

Equivalence of Zn^{2+} added	Zeta potential (mV)	Hydrodynamic diameter (nm)	PdI
0.0	−18.1	319.7	0.456
10.0	−15.2	543.1	0.400
20.0	−13.3	716.4	0.364
30.0	−11.1	817.7	0.358
40.0	−9.07	833.2	0.350

S10) suggested the coagulation of the nanoparticles facilitated by the decrease in the ζ-potential of the resulted particles. Nonetheless, Zn(II) ion-based competition results demonstrated that complex **1**@SiO_2NP was kinetically inert and competent for *in vivo* application.

MTT[3-(4,5-dimethyl-thiazol-2-yl)-2,5 diphenyltetrazolium bromide] assays on HeLa (human cervical carcinoma) cell line were performed to determine the cytotoxicity of complex **1**@SiO_2NP. In the processes, cells were incubated at 37 °C with different suspensions containing variable amounts of complex **1**@SiO_2 [0−100 μM concentrations in Mn(II) ion]. Figure 9 illustrates the percentage of cell viability with the increased

https://doi.org/10.1021/acsabm.1c00937
ACS Appl. Bio Mater. 2021, 4, 8356−8367

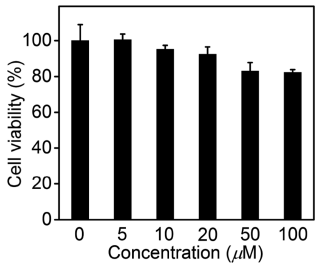

Figure 9. % Cell viability for complex **1**@SiO_2NP performed on HeLa cell-line.

dosage of complex **1**@SiO_2 relative to untreated cells. While no damage in cells was noticed up to 20 μM in 48 h, a subtle change in the viability was noticed at the elevated concentrations. At 100 μM dosage of complex **1**@SiO_2NP, 82% HeLa cells were viable. This result interprets that synthesized nanoparticles were biocompatible and could suitably be employed for biological investigation.

Internalization of complex **1**@SiO_2NPs inside the HeLa cell was visualized by performing TEM investigation of the cell line after treatment with the nanoparticles (Figure 10). Elaborately,

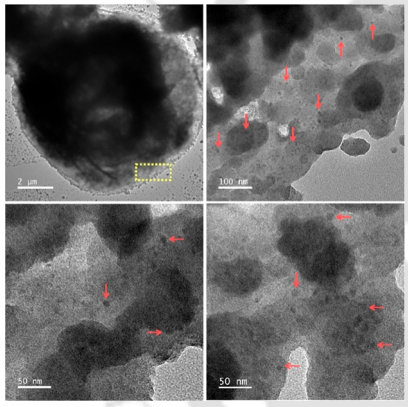

Figure 10. TEM images of HeLa cells after internalization of complex **1**@SiO_2NPs. Yellow rectangle showing the presence of the NPs inside a cell and magnified to visualize internalization of complex **1**@SiO_2NPs. Red arrows indicate the NPs' position inside the cells.

cells were seeded in a 30 mm^2 Petri plate and thereby treated with 25 μM complex **1**@SiO_2NPs and incubated for 48 h at 37 °C in humidified air containing 5% CO_2. Representative TEM images of the cell confirmed the existence of complex **1**@SiO_2NPs (size = 11.7 ± 3 nm; Figure S12) inside the cell. Due to the presence of electron-rich manganese, nanoparticles appeared to be darker than the surrounding inside the cell. Complex **1**@SiO_2NPs were not observed outside the cell and it was obvious as cells were washed with phosphate-buffered saline (PBS) to remove any unbound nanoparticles. EDS analysis illustrated the existence of manganese, nitrogen, and silicon elements inside the cell (Figure S12), further corroborating the presence of complex **1**@SiO_2NPs.

To investigate the contrast ability of complex **1** and complex **1**@SiO_2NP, phantom images were recorded using MAGNETOM Avanto 1.5 T clinical MRI scanner on different concentrations of the paramagnetic species in HEPES buffer at pH ∼ 7.4, 25 °C. Herein, phantoms are micro-centrifuge tubes filled with the solutions or suspensions. The gradual increase in the concentration of complex **1** resulted in simultaneous brighter T_1-weighted images and darker T_2-weighted images (Figure 11). The same effects were also

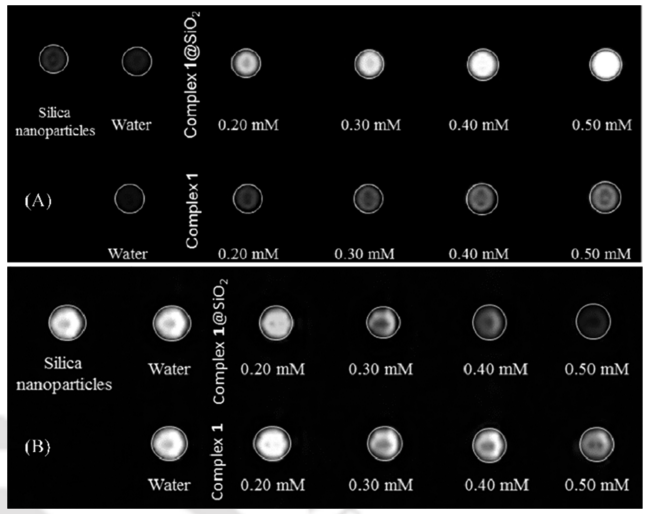

Figure 11. (A) T_1-weighted, and (B) T_2-weighted phantom MR images of micro-centrifuge tubes containing different concentrations of complex **1** and complex **1**@SiO_2NP [concentration in terms of Mn(II) ion] at 1.5 T, and 25 °C.

noticed for complex **1**@SiO_2NP in both the imaging modalities (Figure 11). However, the contrast enhancement (Figure S13), compared to water/silica NPs, in complex **1**@SiO_2NP was significantly higher than that in complex **1**. This result consolidated the formation of a better contrast agent upon the confinement of complex **1** in silica nanoparticles.

CONCLUSIONS

To conclude, the aforementioned results demonstrated the successful synthesis of a thermodynamically stable mono-(aquated), seven-coordinate Mn(II) complex of the hexadentate ligand H_2PyDPA. With the help of the reverse microemulsion method, molecules of the complex were impregnated within porous (pore size = 5.56 nm) silica nanospheres of size 14 ± 2 nm. The confinement achieved a commendable increase in the kinetic inertness to the external anions, protons, and Zn(II) metal ions. Thus, the present study paves the way to develop a stable Mn(II)-based nanosystem-contrast agent employing a kinetically labile complex. The relaxivity values of complex **1**@SiO_2 also increased about 3 folds to r_1 = 8.46 mM^{-1} s^{-1} and r_2 = 33.15 mM^{-1} s^{-1} compared to the free complex **1**. The high r_1 value with the r_2/r_1 = 3.92 indicated that complex **1**@SiO_2NP could be utilized as a T_1 or a T_1-T_2 dual contrast agent. The association of the nanoparticles with serum albumin protein elevated the relaxivity values further with the improvement of r_2/r_1 from 4.02 to 2.58 (37 °C, 1.41 T). The biocompatibility, HeLa cell internalization study, and the significant contrast ability of the nanoparticles thus conferred a genuine Mn(II)-based alternate to Gd(III)-containing contrast agents.

EXPERIMENTAL SECTION

Materials. All materials and solvents were obtained from commercial sources and were used as supplied, unless noted otherwise. 2-(2-Pyridyl)ethylamine (A), 2,6-pyridinedicarboxylic acid, LiOH, and Igepal-CO-520 were purchased from Aldrich. $MnCl_2·4H_2O$, K_2CO_3, KI, NH_4OH, HCl, NaOH, and solvents were

https://doi.org/10.1021/acsabm.1c00937
ACS Appl. Bio Mater. 2021, 4, 8356−8367

obtained from Merck (India). TEOS was purchased from Alfa Aeser. HEPES and MES buffers were purchased from SRL. *N*-methylpiperazine was obtained from Spectrochem. Water used for experiments was purified by millipore-water-purifier, MilliQ, Merck.

Physical Methods. X-ray crystallographic data were collected using Super Nova, a single source at offset, Eos diffractometer. The data refinement and cell reductions were carried out by CrysAlisPro.[77] Structures were solved by direct methods using SHELXS-2013.[78] All the nonhydrogen atoms were refined anisotropically. FT-IR spectra were recorded on a PerkinElmer Instrument at room temperature by making the KBr pellet grind the sample with KBr (IR grade). Mass spectra were recorded from either high-resolution mass spectrometry or a Q-TOF/MS spectrometer. UV/vis spectra were recorded on a PerkinElmer, Lambda 35, UV/vis spectrometer. ^{1}H- and ^{13}C NMR analyses were done using Bruker 400 MHz NMR machines. Nitrogen sorption isotherms were acquired on a Quantachrome, Model: Autosorb-IQ MP surface area and pore size analyzer at 77 K. Ahead of the experiment, dry samples (obtained by lyophilizing the suspension for 24 h) were degassed at 373 K for 10 h. Zeta potential and particle size distribution of suspended complex **1**@SiO_2 nanoparticles were measured at 25 °C by DLS using Malvern ZETASIZER Nano-ZS90 (equilibrium time set to 2 min; five measurements taken on each sample set, only quality criteria values were accepted). Ambient pH was maintained using buffers. Longitudinal and transverse relaxivity values at 1.41 T were recorded using a BRUKER minispec mq60 NMR analyzer.

Potentiometric Measurements. Protonation constants of the H_2PyDPA ligand and stability constant of the corresponding complex **1** were determined by direct pH-potentiometric titrations. Experiments were performed at a constant ionic strength using 0.15 M NaCl and 25 °C. For ligand protonation constants, pH-potentiometric titration was done with 0.001 M ligand solution against standardized 0.1 M NaOH solution as titrant. Stability of complex **1** was obtained by direct pH-potentiometric titration using 1:1 ligand to metal molar ratio. Metrohm 888 Titrando titration workstation equipped with a Metrohm-6.0259.100 glass electrode was used for titrations in the pH range of 2.3−12.0. Extra 0.1 M HCl was added to the starting solution to attain the pH range. Standard pH solutions (pH 4.0, 7.0, and 9.0) were used to calibrate the pH electrode. Titration was done with constant magnetic stirring, and an inert atmosphere was maintained by bubbling Ar gas throughout the experiment. Equilibrium constants were calculated from the data obtained from the titration curve using *Hyperquad2008*.

Relaxometric Analyses. Longitudinal and transverse relaxation times (T_1 and T_2) for aqueous solutions of complex **1** and aqueous suspensions of complex **1**@SiO_2 were measured using a BRUKER minispec mq60 NMR analyzer, at pH ∼ 7.4, 1.41 T, 25 and 37 °C. Samples were treated with diluted HNO_3, and the exact concentration of Mn(II) was determined by the ICP−MS technique. Relaxation rates ($1/T_1$ and $1/T_2$) versus Mn concentration values were plotted and slope for linear regression gave relaxivity values (r_1 and r_2, respectively).

Relaxivity values for complex **1**@SiO_2NPs were estimated in the presence of bovine serum albumin (BSA) at physiological conditions (pH ∼ 7.4, 310 K, BSA concentration maintained at 4.5% w/v; measured at 1.41 T). Samples were incubated at 37 °C for 3 h before the experiment.

Kinetic Measurements. Kinetic inertness of complex **1** and complex **1**@SiO_2 was investigated at 25 °C by relaxometry at 1.41 T using a BRUKER minispec mq60 NMR analyzer. Zn(II) was used as an exchanging ion, which was present in high excess (30−40 times) to attain pseudo-first-order conditions, and $c_{Mn(II)}$ = 0.056 mM was maintained in the complex **1**@SiO_2 suspension. Kinetic studies were done at pH ∼ 6.0 and noncoordinating buffer 2-(4-morpholino)-ethanesulfonicacid (MES, pH range 4.7−6.0) was used at 0.01 M concentration to maintain constant pH in the sample. Change in relaxivity with time was followed for 3 days, and percentage change versus time was plotted.

Transmission Electron Microscopy. The size and morphology of the complex **1**@SiO_2 nanoparticles were analyzed from TEM images captured on a JEOL, Model:2100F electron microscope operated at 200 kV, together with EDS. 10 μL of the prepared mother suspension was diluted to 10 mL with ethanol, and 10 μL of the final solution was dropped on a carbon-coated copper grid (CARBON FILM 300 MESH, COPPER) and kept overnight for drying and then used for imaging. ImageJ software was used to calculate particle size distributions from a sample containing at least 100 particles.

MTT Assay of Complex 1@SiO_2NPs. Cervical cancer cells (HeLa) were purchased from National Centre for Cell Science, Pune. All the cell lines were maintained in Dulbecco's modified Eagle's medium (DMEM) supplemented with 10% (v/v) fetal bovine serum (FBS) and 1% penicillin and streptomycin at 37 °C in humidified air containing 5% CO_2. Cells were seeded in a 96-well plate at a density of 5 × 103 cells/well and grown overnight, maintaining the same conditions mentioned above. After 48 h of treatment with an increasing concentration of complex **1**@SiO_2NPs [concentration in terms of Mn(II)], 0.5 mg/ml MTT in DMEM was added to each well and incubated for 1.5 h. Thereafter, 150 μl of DMSO was added to each well. The absorbance was measured at 570 nm, and after that, cell viability was calculated, considering 100% viability for untreated cells.

Cell Labeling Studies of Complex 1@SiO2NPs. Cervical cancer cells (HeLa) were purchased from National Centre for Cell Science, Pune. All the cell lines were maintained in DMEM supplemented with 10% (v/v) FBS and 1% penicillin and streptomycin at 37 °C in humidified air containing 5% CO_2. Cells were seeded in a 30 mm^2 Petri plate at a density of 1.5 × 105 cells and allowed to attach. Thereafter, they were treated with 25 μM suspension of complex **1**@SiO_2NPs and incubated for 48 h at 37 °C in humidified air containing 5% CO_2. The cells were subsequently washed with PBS to remove any unbound complex **1**@SiO_2. Cells were then trypsinized and fixed using 4% formaldehyde for 15 min and washed twice with PBS. Subsequently, for FETEM imaging, the re-suspended cells were added to the carbon-coated copper grid and allowed to air dry. Images were collected in a FETEM microscope (JEOL, 2100F).

MR Imaging. MR images were obtained using clinical MAGNETOM Avanto 1.5 T MRI scanner. For T_1-weighted images, following parameters were adopted: TR (repetition time) = 758 ms, TE (echo time) = 10 ms, slice thickness = 2.5 mm, and field of view (FOV) = 260 × 260 mm^2. For T_2-weighted images, following parameters were adopted: TR (repetition time) = 2690 ms, TE (echo time) = 78 ms, slice thickness = 3.0 mm, and FOV = 320 × 320 mm^2.

Syntheses of [$C_{23}H_{24}N_4O_4$] (B). To a stirred solution of compound **A** (0.244 g, 2 mmol) in dry acetonitrile, Methyl 6-(bromomethyl)-picolinate[79] (1.012 g, 4.4 mmol), K_2CO_3 (1.104 g, 8 mmol), and KI (0.730 g, 4.4 mmol) were added under a nitrogen atmosphere and the resulting solution was refluxed for 5 days. After this, the reaction mixture was cooled down to room temperature and filtered. The filtrate was evaporated to dryness. A small amount of water (∼5 mL) was added to the residue and extracted with $CHCl_3$ (3 × 30 mL). The organic part was collected and dried over Na_2SO_4, and the solvent was evaporated to obtain a brownish liquid, which was purified by column chromatography on silica gel using ethyl acetate/methanol (50:1) as eluent to obtain a light yellow solid. Yield = 0.454 g (54%). FTIR (KBr pellet cm^{-1}): 3412, 3064, 3012, 2958, 2934, 2840, 1731, 1645, 1589, 1568, 1474, 1454, 1438, 1364, 1205, 1247, 1194, 1169, 1145, 1132, 1083, 995, 766. ^{1}H NMR ($CDCl_3$, 400 MHz): δ 8.48 (d, J = 4 Hz, 1H), 7.98 (d, J = 8 Hz, 2H), 7.71 (t, J = 8 Hz, 2H), 7.58−7.53 (m, 3H), 7.13−7.09 (m, 2H), 4.00 (s, 4H), 3.99 (s, 6H), 3.05−2.99 (m, 4H) ppm. ^{13}C NMR ($CDCl_3$, 100 MHz): δ165.95, 160.53, 160.38, 149.22, 147.36, 137.50, 136.35, 126.07, 123.70, 123.64, 121.33, 60.17, 54.66, 53.01, 36.14 ppm. ESI-MS (+) *m*/*z*: for $[C_{23}H_{24}N_4O_4+H]^+$ calcd., 421. 1870; found, 421.1888.

Syntheses of [$C_{21}H_{20}N_4O_4$] (H_2PyDPA). To a solution of **B** (0.204 g, 0.49 mmol) in tetrahydrofuran (THF) (6 mL), aqueous solution of LiOH (0.047 g, 1.94 mmol in 2 mL H_2O) was added dropwise and allowed to stir at room temperature for 48 h. After this, THF was evaporated and pH of the solution was adjusted to ∼1 by adding 1 N HCl solution. A white powder-like compound was obtained that was

https://doi.org/10.1021/acsabm.1c00937
ACS Appl. Bio Mater. 2021, 4, 8356−8367

washed thoroughly with diethyl ether. This residue was then dissolved in methanol to obtain the colorless crystals of the ligand as its HCl salt with a crystallographic composition of $H_2PyDPA{\cdot}HCl{\cdot}5.5H_2O$. Yield = 0.184 g (75%; crystals). FTIR (KBr pellet cm^{-1}): 3529, 3371, 3119, 3070, 3047, 2804, 2739, 2542, 2000, 1722, 1710, 1632, 1621, 1590, 1545, 1462, 1443, 1310, 1292, 1231, 1142, 1092, 995, 768, 661. ^1H -NMR ($CDCl_3$, 400 MHz): δ 8.71 (d, J = 4 Hz, 1H), 8.52 (t, J = 8 Hz, 1H), 8.06−8.04 (m, 4H), 7.98−7.95 (m, 2H), 7.67−7.65 (m, 2H), 4.75 (s, 2H), 4.72 (s, 2H), 3.92−3.85 (m, 2H), 3.75−3.70 (m, 2H) ppm. ^{13}C NMR ($CDCl_3$, 100 MHz): δ 166.83, 151.13, 150.27, 147.36, 146.78, 141.66, 140.61, 128.13, 127.65, 125.93, 125.34, 58.40, 53.97, 28.59 ppm. ESI-MS (+) m/z for $[C_{21}H_{20}N_4O_4+H]^+$calcd., 393.1557; found, 393.1565. Anal. Calcd. for $C_{21}H_{20}N_4O_4{\cdot}HCl{\cdot}5.5H_2O$: C, 47.80; H, 6.12; N, 10.62. Found: C, 48.09; H, 5.87; N, 10.54.

Syntheses of Complex **1** *[$C_{21}H_{20}MnN_4O_5$].* $MnCl_2{\cdot}4H_2O$ (0.051 g, 0.26 mmol) was added to a solution of H_2PyDPA (0.140 g, 0.28 mmol) in water (5 mL), and it was stirred for 15 min. pH of the resultant solution was adjusted to ∼6.5 with the dropwise addition of NaOH solution. The mixture was stirred for another 24 h at room temperature (25 °C). After this, it was filtered, and slow evaporation of the filtrate gave needle-shaped pale-yellow crystals, which were washed with methanol. Crystals obtained were suitable for single-crystal X-ray diffraction study. Yield = 0.070 g, (45%). FTIR (KBr pellet cm^{-1}): 3392, 1635, 1625, 1586, 1487, 1438, 1404, 1387, 1304, 1273, 1156, 1124, 1081, 1016, 1002, 780, 755, 690. ESI-MS (+) m/z for $[\{(C_{21}H_{20}MnN_4O_5)\text{-}(H_2O)\}+H]^+$ calcd, 446.07; found: 446.09. Anal. Calcd for $C_{21}H_{20}MnN_4O_5{\cdot}5H_2O$: C, 45.56; H, 5.47; N, 10.13. Found: C, 45.58; H, 5.23; N, 10.15.

Syntheses of Complex **1***@SiO$_2$NPs.* Complex **1**@SiO_2NP was synthesized following the reverse microemulsion procedure. Igepal-CO-520 (1.3 mL) was added to cyclohexane (10 mL) and stirred for 10 min to obtain a homogeneous mixture. A doping solution was prepared by adding complex **1** solution (160 μL, 13.40 mM) in water (320 μL) at pH ∼ 7.4. This doping solution was added carefully to the surfactant mixture, followed by NH_4OH (120 μL, 25% by w/v) and stirred for another 30 min. Then, TEOS (100 μL) was added, and the final mixture was kept at room temperature for 24 h with gentle stirring. Complex **1**@SiO_2NP was obtained by adding acetone (30 mL) to the mixture, which was repeatedly washed with ethanol and water by centrifugation at 10,000 rpm for 15 min. The residue obtained was dispersed in 400 μL of water (pH maintained at 7.4), and this mother suspension was further used for relaxometry and other studies. FTIR (KBr pellet cm^{-1}): 3629, 3469, 1640, 1518, 1213, 1104, 959, 798.

■ ASSOCIATED CONTENT

Supporting Information

The Supporting Information is available free of charge at https://pubs.acs.org/doi/10.1021/acsabm.1c00937.

Characterization of complex **1**@SiO_2NPs; reproducibility of the relaxivity values; IR, NMR, mass, and UV−vis spectra of the ligand and **1**; and potentiometric titration curves (PDF)

Crystallographic bond distances and bond angles and refinement data (CIF)

Crystallographic bond distances and bond angles and refinement data (CIF)

■ AUTHOR INFORMATION

Corresponding Author

Chandan Mukherjee − *Department of Chemistry, Indian Institute of Technology Guwahati, Guwahati 781039 Assam, India;* orcid.org/0000-0002-2771-2468; Email: cmukherjee@iitg.ernet.in

Authors

Riya Mallik − *Department of Chemistry, Indian Institute of Technology Guwahati, Guwahati 781039 Assam, India*

Muktashree Saha − *Department of Biosciences and Bioengineering, Indian Institute of Technology Guwahati, Guwahati 781039 Assam, India*

Complete contact information is available at: https://pubs.acs.org/10.1021/acsabm.1c00937

Notes

The authors declare the following competing financial interest(s): Patent filing on the system is under process. Indian Institute of Technology Guwahati has already submitted a patent application (application no. 202131039091) on the research findings.

■ ACKNOWLEDGMENTS

The Department of Biotechnology funds this project (BT/PR23622/NNT/281294/2017), Govt. of India. R.M. thanks IIT Guwahati for her doctoral fellowship. The Department of Chemistry, Central Instruments Facility, IIT Guwahati, and FIST programme supported by DST (SR/FST/CS-II/2017/23C) are thankfully acknowledged for instrumental facilities. We thank Primus, Guwahati, Assam, India for providing T_1- and T_2-weighted imaging facility. C.M. is indebted to Prof. Siddhartha Sankar Ghosh for his help in general.

■ REFERENCES

(1) Gupta, A.; Caravan, P.; Price, W. S.; Platas-Iglesias, C.; Gale, E. M. Applications for Transition-Metal Chemistry in Contrast-Enhanced Magnetic Resonance Imaging. *Inorg. Chem.* **2020**, *59*, 6648−6678.

(2) Wahsner, J.; Gale, E. M.; Rodríguez-Rodríguez, A.; Caravan, P. Chemistry of MRI Contrast Agents: Current Challenges and New Frontiers. *Chem. Rev.* **2019**, *119*, 957−1057.

(3) Werner, E. J.; Datta, A.; Jocher, C. J.; Raymond, K. N. High-Relaxivity MRI Contrast Agents: Where Coordination Chemistry Meets Medical Imaging. *Angew. Chem., Int. Ed.* **2008**, *47*, 8568−8580.

(4) Hermann, P.; Kotek, J.; Kubíček, V.; Lukeš, I. Gadolinium(III) complexes as MRI contrast agents: ligand design and properties of the complexes. *Dalton Trans.* **2008**, 3027−3047.

(5) Li, H.; Meade, T. J. Molecular Magnetic Resonance Imaging with Gd(III)-Based Contrast Agents: Challenges and Key Advances. *J. Am. Chem. Soc.* **2019**, *141*, 17025−17041.

(6) Terreno, E.; Castelli, D. D.; Viale, A.; Aime, S. Challenges for Molecular Magnetic Resonance Imaging. *Chem. Rev.* **2010**, *110*, 3019−3042.

(7) Que, E. L.; Chang, C. J. Responsive magnetic resonance imaging contrast agents as chemical sensors for metals in biology and medicine. *Chem. Soc. Rev.* **2010**, *39*, 51−60.

(8) Merbach, A. E.; Helm, L.; Tóth, E. *The Chemistry of Contrast Agent in Medical Magnetic Resonance Imaging*, 2nd ed.; Wiley, 2013; pp 1−23.

(9) Lee, M. H.; Kim, E.-J.; Lee, H.; Kim, H. M.; Chang, M. J.; Park, S. Y.; Hong, K. S.; Kim, J. S.; Sessler, J. L. Liposomal Texaphyrin Theranostics for Metastatic Liver Cancer. *J. Am. Chem. Soc.* **2016**, *138*, 16380−16387.

(10) Bianchi, A.; Calabi, L.; Corana, F.; Fontana, S.; Losi, P.; Maiocchi, A.; Paleari, L.; Valtancoli, B. Thermodynamic and structural properties of Gd(III) complexes with polyamino-polycarboxylic ligands: basic compounds for the development of MRI contrast agents. *Coord. Chem. Rev.* **2000**, *204*, 309−393.

(11) Boros, E.; Karimi, S.; Kenton, N.; Helm, L.; Caravan, P. Gd(DOTAlaP): Exploring the Boundaries of Fast Water Exchange in Gadolinium-Based Magnetic Resonance Imaging Contrast Agents. *Inorg. Chem.* **2014**, *53*, 6985−6994.

(12) Verwilst, P.; Park, S.; Yoon, B.; Kim, J. S. Recent advances in Gd-chelate based bimodal optical/MRI contrast agents. *Chem. Soc. Rev.* **2015**, *44*, 1791−1806.
(13) Aime, S.; Baroni, S.; Delli Castelli, D.; Brücher, E.; Fábián, I.; Serra, S. C.; Fringuello Mingo, A.; Napolitano, R.; Lattuada, L.; Tedoldi, F.; Baranyai, Z. Exploiting the Proton Exchange as an Additional Route to Enhance the Relaxivity of Paramagnetic MRI Contrast Agents. *Inorg. Chem.* **2018**, *57*, 5567−5574.
(14) Wang, L.; Lin, H.; Ma, L.; Jin, J.; Shen, T.; Wei, R.; Wang, X.; Ai, H.; Chen, Z.; Gao, J. Albumin-based nanoparticles loaded with hydrophobic gadolinium chelates as T_1-T_2 dual-mode contrast agents for accurate liver tumor imaging. *Nanoscale* **2017**, *9*, 4516−4523.
(15) Yang, Z.; Lin, H.; Huang, J.; Li, A.; Sun, C.; Richmond, J.; Gao, J. A gadolinium-complex-based theranostic prodrug for in vivo tumour-targeted magnetic resonance imaging and therapy. *Chem. Commun.* **2019**, *55*, 4546−4549.
(16) Taylor, K. M. L.; Kim, J. S.; Rieter, W. J.; An, H.; Lin, W.; Lin, W. Mesoporous Silica Nanospheres as Highly Efficient MRI Contrast Agents. *J. Am. Chem. Soc.* **2008**, *130*, 2154−2155.
(17) Clough, T. J.; Jiang, L.; Wong, K.-L.; Long, N. J. Ligand design strategies to increase stability of gadolinium-based magnetic resonance imaging contrast agents. *Nat. Commun.* **2019**, *10*, 1420.
(18) Lattuada, L.; Horváth, D.; Colombo Serra, S.; Fringuello Mingo, A.; Minazzi, P.; Bényei, A.; Forgács, A.; Fedeli, F.; Gianolio, E.; Aime, S.; Giovenzana, G. B.; Baranyai, Z. Enhanced relaxivity of Gd^{III}-complexes with HP-DO3A-like ligands upon the activation of the intramolecular catalysis of the prototropic exchange. *Inorg. Chem. Front.* **2021**, *8*, 1500−1510.
(19) Lacerda, S.; Ndiaye, D.; Tóth, É. Manganese Complexes as Contrast Agents for Magnetic Resonance Imaging. In *Metal Ions in Bio-Imaging Techniques*; Sigel, A., Freisinger, E., Sigel, R. K. O., Eds.; De Gruyter: Berlin, Boston, 2021; pp 71−100.
(20) Wang, J.; Wang, H.; Ramsay, I. A.; Erstad, D. J.; Fuchs, B. C.; Tanabe, K. K.; Caravan, P.; Gale, E. M. Manganese-Based Contrast Agents for Magnetic Resonance Imaging of Liver Tumors: Structure-Activity Relationships and Lead Candidate Evaluation. *J. Med. Chem.* **2018**, *61*, 8811−8824.
(21) Phukan, B.; Patel, A. B.; Mukherjee, C. A water-soluble and water-coordinated Mn(II) complex: synthesis, characterization and phantom MRI image study. *Dalton Trans.* **2015**, *44*, 12990−12994.
(22) Kálmán, F. K.; Nagy, V.; Váradi, B.; Garda, Z.; Molnár, E.; Trencsényi, G.; Kiss, J.; Même, S.; Même, W.; Tóth, É.; Tircsó, G. Mn(II)-Based MRI Contrast Agent Candidate for Vascular Imaging. *J. Med. Chem.* **2020**, *63*, 6057−6065.
(23) Botár, R.; Molnár, E.; Trencsényi, G.; Kiss, J.; Kálmán, F. K.; Tircsó, G. Stable and Inert Mn(II)-Based and pH-Responsive Contrast Agents. *J. Am. Chem. Soc.* **2020**, *142*, 1662−1666.
(24) Porcar-Tost, O.; Pallier, A.; Esteban-Gómez, D.; Illa, O.; Platas-Iglesias, C.; Tóth, É.; Ortuño, R. M. Stability, relaxometric and computational studies on Mn^{2+} complexes with ligands containing a cyclobutane scaffold. *Dalton Trans.* **2021**, *50*, 1076−1085.
(25) Khannam, M.; Weyhermüller, T.; Goswami, U.; Mukherjee, C. A highly stable L-alanine-based mono(aquated) Mn(II) complex as a T_1-weighted MRI contrast agent. *Dalton Trans.* **2017**, *46*, 10426−10432.
(26) Vanasschen, C.; Molnár, E.; Tircsó, G.; Kálmán, F. K.; Tóth, É.; Brandt, M.; Coenen, H. H.; Neumaier, B. Novel CDTA-based, Bifunctional Chelators for Stable and Inert Mn^{2+} Complexation: Synthesis and Physicochemical Characterization. *Inorg. Chem.* **2017**, *56*, 7746−7760.
(27) Garda, Z.; Molnár, E.; Hamon, N.; Barriada, J. L.; Esteban-Gómez, D.; Váradi, B.; Nagy, V.; Pota, K.; Kálmán, F. K.; Tóth, I.; Lihi, N.; Platas-Iglesias, C.; Tóth, É.; Tripier, R.; Tircsó, G. Complexation of Mn(II) by Rigid Pyclen Diacetates: Equilibrium, Kinetic, Relaxometric, Density Functional Theory, and Superoxide Dismutase Activity Studies. *Inorg. Chem.* **2021**, *60*, 1133−1148.
(28) Phukan, B.; Mukherjee, C.; Goswami, U.; Sarmah, A.; Mukherjee, S.; Sahoo, S. K.; Moi, S. C. A New Bis(aquated) High Relaxivity Mn(II) Complex as an Alternative to Gd(III)-Based MRI Contrast Agent. *Inorg. Chem.* **2018**, *57*, 2631−2638.
(29) Anbu, S.; Hoffmann, S. H. L.; Carniato, F.; Kenning, L.; Price, T. W.; Prior, T. J.; Botta, M.; Martins, A. F.; Stasiuk, G. J. A Single-Pot Template Reaction Towards a Manganese-Based T_1 Contrast Agent. *Angew. Chem., Int. Ed.* **2021**, *60*, 10736−10744.
(30) Chirayil, S.; Jordan, V. C.; Martins, A. F.; Paranawithana, N.; Ratnakar, S. J.; Sherry, A. D. Manganese(II)-Based Responsive Contrast Agent Detects Glucose-Stimulated Zinc Secretion from the Mouse Pancreas and Prostate by MRI. *Inorg. Chem.* **2021**, *60*, 2168−2177.
(31) Haedicke, I. E.; Li, T.; Zhu, Y. L. K.; Martinez, F.; Hamilton, A. M.; Murrell, D. H.; Nofiele, J. T.; Cheng, H.-L. M.; Scholl, T. J.; Foster, P. J.; Zhang, X.-a. An enzyme-activable and cell-permeable Mn^{II}- porphyrin as a highly efficient T_1 MRI contrast agent for cell labeling. *Chem. Sci.* **2016**, *7*, 4308−4317.
(32) Paul, G.; Prado, Y.; Dia, N.; Rivière, E.; Laurent, S.; Roch, M.; Elst, L. V.; Muller, R. N.; Sancey, L.; Perriat, P.; Tillement, O.; Mallah, T.; Catala, L. Mn^{II}-containing coordination nanoparticles as highly efficient T_1 contrast agents for magnetic resonance imaging. *Chem. Commun.* **2014**, *50*, 6740−6743.
(33) Forgács, A.; Tei, L.; Baranyai, Z.; Tóth, I.; Zékány, L.; Botta, M. A Bisamide Derivative of [Mn(1,4-DO2A)] − Solution Thermodynamic, Kinetic, and NMR Relaxometric Studies. *Eur. J. Inorg. Chem.* **2016**, *2016*, 1165−1174.
(34) Devreux, M.; Henoumont, C.; Dioury, F.; Boutry, S.; Vacher, O.; Elst, L. V.; Port, M.; Muller, R. N.; Sandre, O.; Laurent, S. Mn^{2+}Complexes with Pyclen-Based Derivatives as Contrast Agents for Magnetic Resonance Imaging: Synthesis and Relaxometry Characterization. *Inorg. Chem.* **2021**, *60*, 3604−3619.
(35) Ndiaye, D.; Sy, M.; Pallier, A.; Même, S.; Silva, I.; Lacerda, S.; Nonat, A. M.; Charbonnière, L. J.; Tóth, É. Unprecedented Kinetic Inertness for a Mn^{2+}-Bispidine Chelate: A Novel Structural Entry for Mn^{2+}-Based Imaging Agents. *Angew. Chem., Int. Ed.* **2020**, *59*, 11958−11963.
(36) Synder, E. M.; Asik, D.; Abozeid, S. M.; Burgio, A.; Bateman, G.; Turowski, S. G.; Spernyak, J. A.; Morrow, J. R. A Class of Fe^{III} Macrocyclic Complexes with Alcohol Donor Group as Effective T_1 MRI Contrast Agents. *Angew. Chem., Int. Ed.* **2020**, *59*, 2414−2419.
(37) Asik, D.; Abozeid, S. M.; Turowski, S. G.; Spernyak, J. A.; Morrow, J. R. Dinuclear Fe(III) Hydroxypropyl-Appended Macrocyclic Complexes as MRI Probes. *Inorg. Chem.* **2021**, *60*, 8651−8664.
(38) Dadfar, S. M.; Camozzi, D.; Darguzyte, M.; Roemhild, K.; Varvarà, P.; Metselaar, J.; Banala, S.; Straub, M.; Güvener, N.; Engelmann, U.; Slabu, I.; Buhl, M.; Leusen, J. V.; Kögerler, P.; Hermanns-Sachweh, B.; Schulz, V.; Kiessling, F.; Lammers, T. Size-isolation of superparamagnetic iron oxide nanoparticles improves MRI, MPI and hyperthermia performance. *J. Nanobiotechnol.* **2020**, *18*, 22.
(39) He, Y.; Mao, Z.; Zhang, Y.; Lv, H.; Yan, J.; Cao, Y.; Pei, R. Tumor Acid Microenvironment-Triggered Self-Assembly of ESPIONs for T_1/T_2 Switchable Magnetic Resonance Imaging. *ACS Appl. Bio Mater.* **2020**, *3*, 7752−7761.
(40) Ma, M.; Zhu, H.; Ling, J.; Gong, S.; Zhang, Y.; Xia, Y.; Tang, Z. Quasi-amorphous and Hierarchical Fe_2O_3Supraparticles: Active T_1-Weighted Magnetic Resonance Imaging in Vivo and Renal Clearance. *ACS Nano* **2020**, *14*, 4036−4044.
(41) Lu, C.; Dong, P.; Pi, L.; Wang, Z.; Yuan, H.; Liang, H.; Ma, D.; Chai, K. Y. Hydroxyl-PEG-Phosphonic Acid-Stabilized Superparamagnetic Manganese Oxide-Doped Iron Oxide Nanoparticles with Synergistic Effects for Dual-Mode MR Imaging. *Langmuir* **2019**, *35*, 9474−9482.
(42) Shin, T.-H.; Choi, J.-S.; Yun, S.; Kim, I.-S.; Song, H.-T.; Kim, Y.; Park, K. I.; Cheon, J. T_1 and T_2 Dual −Mode MRI Contrast Agent for Enhancing Accuracy by Engineered Nanomaterials. *ACS Nano* **2014**, *8*, 3393−3401.
(43) Wang, J.; Jia, Y.; Wang, Q.; Liang, Z.; Han, G.; Wang, Z.; Lee, J.; Zhao, M.; Li, F.; Bai, R.; Ling, D. An Ultrahigh-Field-Tailored T_1-

T_2 Dual-Mode MRI Contrast Agent for High-Performance Vascular Imaging. *Adv. Mater.* **2021**, *33*, 2004917.
(44) Courant, T.; Roullin, V. G.; Cadiou, C.; Callewaert, M.; Andry, M. C.; Portefaix, C.; Hoeffel, C.; de Goltstein, M. C.; Port, M.; Laurent, S.; Elst, L. V.; Muller, R.; Molinari, M.; Chuburu, F. *Angew. Chem., Int. Ed.* **2012**, *51*, 9119−9122.
(45) Rohrer, M.; Bauer, H.; Mintorovitch, J.; Requardt, M.; Weinmann, H.-J. Comparison of Magnetic Properties of MRI Contrast Media Solutions at Different Magnetic Field Strengths. *Invest. Radiol.* **2005**, *40*, 715−724.
(46) Dekkers, I. A.; Roos, R.; van der Molen, A. J. Gadolinium retention after administration of contrast agents based on linear chelators and the recommendations of the European Medicines Agency. *Eur. Radiol.* **2018**, *28*, 1579−1584.
(47) Pautler, R. G. In vivo, trans-synaptic tract-tracing utilizing manganese-enhanced magnetic resonance imaging (MEMRI). *NMR Biomed.* **2004**, *17*, 595−601.
(48) Cloyd, R. A.; Koren, S. A.; Abisambra, J. F. Manganese-Enhanced Magnetic Resonance Imaging: Overview and Central Nervous System Applications With a Focus on Neurodegeneration. *Front. Aging Neurosci.* **2018**, *10*, 403.
(49) García-Hevia, L.; Bañobre-López, M.; Gallo, J. Recent Progress on Manganese-Based Nanostructures as Responsive MRI Contrast Agents. *Chem.—Eur. J.* **2019**, *25*, 431−441.
(50) Silva, A. C.; Lee, J. H.; Aoki, I.; Koretsky, A. P. Manganese-enhanced magnetic resonance imaging (MEMRI): methodological and practical considerations. *NMR Biomed.* **2004**, *17*, 532−543.
(51) Dobson, A. W.; Erikson, K. M.; Aschner, M. Manganese neurotoxicity. *Ann. N.Y. Acad. Sci.* **2004**, *1012*, 115−128.
(52) Ananta, J. S.; Godin, B.; Sethi, R.; Moriggi, L.; Liu, X.; Serda, R. E.; Krishnamurthy, R.; Muthupillai, R.; Bolskar, R. D.; Helm, L.; Ferrari, M.; Wilson, L. J.; Decuzzi, P. Geometrical confinement of gadolinium-based contrast agents in nanoporous particles enhances T_1 contrast. *Nat. Nanotechnol.* **2010**, *5*, 815−821.
(53) Ni, K.; Zhao, Z.; Zhang, Z.; Zhou, Z.; Yang, L.; Wang, L.; Ai, H.; Gao, J. Geometrically confined ultrasmall gadolinium oxide nanoparticles boost the T_1 contrast ability. *Nanoscale* **2016**, *8*, 3768−3774.
(54) Carniato, F.; Tei, L.; Botta, M. Gd-Based Mesoporous Silica Nanoparticles as MRI Probes. *Eur. J. Inorg. Chem.* **2018**, *2018*, 4936−4954.
(55) Wartenberg, N.; Fries, P.; Raccurt, O.; Guillermo, A.; Imbert, D.; Mazzanti, M. A Gadolinium Complex Confined in Silica Nanoparticles as a Highly Efficient T_1/T_2 MRI Contrast Agent. *Chem.—Eur. J.* **2013**, *19*, 6980−6983.
(56) Liu, Y.; Solomon, M.; Achilefu, S. Perspectives and Potential Applications of Nanomedicine in Breast and Prostate Cancer. *Med. Res. Rev.* **2013**, *33*, 3−32.
(57) Niu, D.; Luo, X.; Li, Y.; Liu, X.; Wang, X.; Shi, J. Manganese-Loaded Dual-Mesoporous Silica Sphere for Efficient T1- and T2-Weighted Dual Mode Magnetic Resonance Imaging. *ACS Appl. Mater. Interfaces* **2013**, *5*, 9942−9948.
(58) Dahanayake, V.; Pornrungroj, C.; Pablico-Lansigan, M.; Hickling, W. J.; Lyons, T.; Lah, D.; Lee, Y.; Parasido, E.; Bertke, J. A.; Albanese, C.; Rodriguez, O.; Van Keuren, E.; Stoll, S. L. Paramagnetic Clusters of $Mn_3(O_2CCH_3)_6(Bpy)_2$ in Polyacrylamide Nanobeads as a New Design Approach to a T_1-T_2 Multimodal Magnetic Resonance Imaging Contrast Agent. *ACS Appl. Mater. Interfaces* **2019**, *11*, 18153−18164.
(59) Mulas, G.; Rolla, G. A.; Geraldes, C. F. G. C.; Starmans, L. W. E.; Botta, M.; Terreno, E.; Tei, L. Mn(II)-Based Lipidic Nanovesicles as High-Efficiency MRI Probes. *ACS Appl. Bio Mater.* **2020**, *3*, 2401−2409.
(60) Hou, W.; Toh, T. B.; Abdullah, L. N.; Yvonne, T. W. Z.; Lee, K. J.; Guenther, I.; Chow, E. K.-H. Nanodiamond-Manganese dual mode MRI contrast agents for enhanced liver tumor detection. *Nanomed. Nanotechnol.* **2017**, *13*, 783−793.
(61) Qian, X.; Han, X.; Yu, L.; Xu, T.; Chen, Y. Manganese-Based Functional Nanoplatforms: Nanosynthetic Construction, Physiochemical Property, and Theranostic Applicability. *Adv. Funct. Mater.* **2020**, *30*, 1907066.
(62) Pálmai, M.; Pethő, A.; Nagy, L. N.; Klébert, S.; May, Z.; Mihály, J.; Wacha, A.; Jemnitz, K.; Veres, Z.; Horváth, I.; Szigeti, K.; Máthé, D.; Varga, Z. Direct immobilization of manganese chelates on silica nanospheres for MRI applications. *J. Colloid Interface Sci.* **2017**, *498*, 298−305.
(63) Pan, D.; Schmieder, A. H.; Wickline, S. A.; Lanza, G. M. Manganese-based MRI contrast agents: past, present, and future. *Tetrahedron* **2011**, *67*, 8431−8444.
(64) Pablico-Lansigan, M. H.; Hickling, W. J.; Japp, E. A.; Rodriguez, O. C.; Ghosh, A.; Albanese, C.; Nishida, M.; Van Keuren, E.; Fricke, S.; Dollahon, N.; Stoll, S. L. Magnetic Nanobeads as Potential Contrast Agents for Magnetic Resonance Imaging. *ACS Nano* **2013**, *7*, 9040−9048.
(65) Wu, C.; Li, D.; Yang, L.; Lin, B.; Zhang, H.; Xu, Y.; Cheng, Z.; Xia, C.; Gong, Q.; Song, B.; Ai, H. Multivalent manganese complex decorated amphiphilic dextran micelles as sensitive MRI probes. *J. Mater. Chem. B* **2015**, *3*, 1470−1473.
(66) Gale, E. M.; Atanasova, I. P.; Blasi, F.; Ay, I.; Caravan, P. A Manganese Alternative to Gadolinium for MRI Contrast. *J. Am. Chem. Soc.* **2015**, *137*, 15548−15557.
(67) Pota, K.; Garda, Z.; Kálmán, F. K.; Barriada, J. L.; Esteban-Gómez, D.; Platas-Iglesias, C.; Tóth, I.; Brücher, E.; Tircsó, G. Taking the next step towards inert Mn^{2+} complexes of open-chain ligands: the case of the rigid PhDTA ligand. *New J. Chem.* **2018**, *42*, 8001−8011.
(68) Forgács, A.; Pujales-Paradela, R.; Regueiro-Figueroa, M.; Valencia, L.; Esteban-Gómez, D.; Botta, M.; Platas-Iglesias, C. Developing the family of picolinate ligands for Mn^{2+}complexation. *Dalton Trans.* **2017**, *46*, 1546.
(69) Vo, N. T.; Patra, A. K.; Kim, D. Pore size and concentration effect of mesoporous silica nanoparticles on the coefficient of thermal expansion and optical transparency of poly(ether sulfone) films. *Phys. Chem. Chem. Phys.* **2017**, *19*, 1937−1944.
(70) Yu, M.; Zhou, L.; Zhang, J.; Yuan, P.; Thorn, P.; Gu, W.; Yu, C. A simple approach to prepare monodisperse mesoporous silica nanospheres with adjustable sizes. *J. Colloid Interface Sci.* **2012**, *376*, 67−75.
(71) r_1 = 2.31 mM^{-1} s^{-1} and r_2 = 9.51 mM^{-1} s^{-1} for complex 1, measured at 1.41 T, 37 °C, and pH ∼ 7.4.
(72) Marangoni, V. S.; Neumann, O.; Henderson, L.; Kaffes, C. C.; Zhang, H.; Zhang, R.; Bishnoi, S.; Ayala-Orozco, C.; Zucolotto, V.; Bankson, J. A.; Nordlander, P.; Halas, N. J. Enhancing T_1 magnetic resonance imaging contrast with internalized gadolinium(III) in a multilayer nanoparticle. *Proc. Natl. Acad. Sci. U.S.A.* **2017**, *114*, 6960−6965.
(73) Zhou, Z.; Bai, R.; Wang, Z.; Bryant, H.; Lang, L.; Merkle, H.; Munasinghe, J.; Tang, L.; Tang, W.; Tian, R.; Yu, G.; Ma, Y.; Niu, G.; Gao, J.; Chen, X. An Albumin-Binding T_1-T_2 Dual-Modal MRI Contrast Agents for Improved Sensitivity and Accuracy in Tumor Imaging. *Bioconjugate Chem.* **2019**, *30*, 1821−1829.
(74) Park, J. C.; Lee, G. T.; Kim, H.-K.; Sung, B.; Lee, Y.; Kim, M.; Chang, Y.; Seo, J. H. Surface Design of Eu-Doped Iron Oxide Nanoparticles for Tuning the Magnetic Relaxivity. *ACS Appl. Mater. Interfaces* **2018**, *10*, 25080−25089.
(75) Li, Z.; Li, W.; Li, X.; Pei, F.; Wang, X.; Lei, H. Mn(II)-monosubstituted polyoxometalates as candidates for contrast agents in magnetic resonance imaging. *J. Inorg. Biochem.* **2007**, *101*, 1036−1042.
(76) Nairi, V.; Medda, S.; Piludu, M.; Casula, M. F.; Vallet-Regì, M.; Monduzzi, M.; Salis, A. Interactions between bovine serum albumin and mesoporous silica nanoparticles functionalized with biopolymers. *Chem. Eng. J.* **2018**, *340*, 42−50.
(77) Sheldrick, G. M. A short history of SHELX. *Acta Crystallogr., Sect. A: Found. Crystallogr.* **2008**, *64*, 112.
(78) Farrugia, L. J. WinGX and ORTEP for Windows: an update. *J. Appl. Crystallogr.* **2012**, *45*, 849.

(79) Price, E. W.; Cawthray, J. F.; Bailey, G. A.; Ferreira, C. L.; Boros, E.; Adam, M. J.; Orvig, C. H_4octapa: An Acyclic Chelator for ^{111}In Radiopharmaceuticals. *J. Am. Chem. Soc.* **2012**, *134*, 8670−8683.

https://doi.org/10.1021/acsabm.1c00937
ACS Appl. Bio Mater. 2021, 4, 8356−8367

Dalton Transactions

ROYAL SOCIETY OF CHEMISTRY

PAPER

View Article Online
View Journal | View Issue

Check for updates

Cite this: *Dalton Trans.*, 2022, **51**, 14138

The electrostatic confinement of aquated monocationic Gd(III) complex-molecules within the inner core of porous silica nanoparticles creates a highly efficient T_1 contrast agent for magnetic resonance imaging†

Riya Mallik,‡[a] Mahmuda Khannam,‡[a] Muktashree Saha,[b] Shivani Marandi,[c] Sachin Kumar[b] and Chandan Mukherjee *[a]

Received 13th July 2022,
Accepted 22nd August 2022

DOI: 10.1039/d2dt02272a

rsc.li/dalton

Contrast-agent enhanced magnetic resonance imaging (MRI) has been under continuous investigation for the conspicuous imaging of lesions and the early-stage detection of tumors. To achieve the development of a T_1-weighted contrast agent with a high relaxivity value, herein, porous silica nanoparticles that had internalized about 20 aquated cationic Gd(III) complexes (**1**) of the hexadentate hydroxyethyl-appended picolinate-based ligand H_2hbda were demonstrated. Complex **1** exhibited a longitudinal relaxivity value per mM Gd(III) ions, r_1, of 9.05 mM^{-1} s^{-1} (pH 7.4, 37 °C, 1.41 T), which increased to 86.41 mM^{-1} s^{-1} because of the grafting of complex **1** in the inner core of porous silica nanospheres through electrostatic interactions between the anionic silica surface and the cationic complex **1** molecules. A further augmentation in the relaxivity value to 118.32 mM^{-1} s^{-1} was realized because of the interaction of the complex **1**@SiO_2NPs with serum albumin protein. The synthesized nanosystem was impervious to physiologically available anions (HPO_4^{2-} and HCO_3^{1-}) and also kinetically inert, as evidenced *via* a transmetallation experiment in the presence of Zn(II) ions. The developed complex-incorporated nanomaterial was bio- and hemo-compatible. Cellular uptake measurements employing HeLa cells and the concentration-dependent enhancement in the brightness of *in vitro* phantom images, recorded under a clinical scanner at 1.5 T, demonstrated that the developed biocompatible **1**@SiO_2NP complex has promising diagnostic applications as a T_1-weighted MRI contrast agent.

Introduction

Magnetic resonance imaging (MRI) is an NMR-based noninvasive bioimaging modality that provides anatomical tissue images with high spatial resolution without using any ionizing radiation.[1] However, the low intrinsic sensitivity of the technique is the main disadvantage. To mitigate this issue, nowadays, about 40% of imaging is carried out in the presence of contrast agents, which are paramagnetic species.[2] The clinically approved T_1-weighted (positive/brightening) contrast agents are mainly low-molecular-weight Gd(III) complexes that shorten the longitudinal relaxation time (T_1) of the nearby water molecule-protons by dipolar interaction and have relaxivity values ranging from 3.3 to 4.2 mM^{-1} s^{-1} at 1.5 T.[3] Because of the small relaxivity values, a hefty dose (about 0.1 mmol kg^{-1}) of the paramagnetic complexes needs to be administered prior to imaging. Thus, the probability of the accumulation of free Gd(III) ions inside the human body increases. Free Gd(III) ions are not biocompatible and are known to cause several detrimental effects, *e.g.*, nephrogenic systemic fibrosis (NSF), Gd(III) retention and accumulation in tissues, Fe(III) deficiency, *etc.*[4] In addition, the small-size complexes extravagate from the vascular system very rapidly.[5] Therefore, imaging that takes a long time is not advantageous in the presence of such complexes. Hence, the development of T_1-weighted contrast agents with high relaxivity values and higher vascular retention time remains of primary interest.

The interpretation of SBM theory indicates that a high relaxivity value can be achieved within a 10–100 MHz external magnetic field (B) by increasing the rotational correlation time,[6,7]

[a]*Department of Chemistry, Indian Institute of Technology Guwahati, Guwahati 781039, Assam, India. E-mail: cmukherjee@iitg.ac.in*
[b]*Department of Biosciences and Bioengineering, Indian Institute of Technology Guwahati, Guwahati 781039, Assam, India*
[c]*Centre for the Environment, Indian Institute of Technology Guwahati, Assam-781039, India*

†Electronic supplementary information (ESI) available: Characterization data for the ligand, complex **1**, and complex **1**@SiO_2NPs are supplied. See DOI: https://doi.org/10.1039/d2dt02272a

‡These authors contributed equally.

i.e., boosting the tumbling time (τ_R) of the system. The overall longitudinal relaxivity value can be further amplified by elevating the number of inner-sphere water molecules (q) as the longitudinal relaxivity (per mM of paramagnetic ions $r_1 = 1/T_1$ mM^{-1} s^{-1}) is directly proportional to q. Hence, in an attempt to develop contrast agents with a high r_1 relaxivity value and a sufficient vascular retention time, covalent and non-covalent confinement/immobilization of aquated Gd(III)-complexes within/onto nanosized units has been under continuous investigation for the last decade.[7a,8–10] For instance, Lin and coworkers have reported mesoporous hybrid silica nanoparticles with covalent grafting of bis(aquated) Gd(III)–Si-diethylenetriaminetetraacetate (DTTA) complexes within the inner core of the nanoparticles. The developed hybrid nanosystem exhibits r_1 of 28.8 mM^{-1} s^{-1} at 3 T, and 10.2 mM^{-1} s^{-1} at 9.4 T.[9c] A similar effect, *i.e.*, a boost in the relaxivity value (60 mM^{-1} s^{-1} at 0.70 T), is also noticed upon covalent immobilization of bis(aquated) Gd(III) complexes of a thiol derivative of DTTA onto Au nanoparticles.[10] Richard *et al.* showed that non-covalent immobilization of a mono(aquated) Gd(III) complex of an amphiphilic ligand, made of a lipid chain and diethylenetriamine pentaacetate (DTPA) chelate, onto multiwalled carbon nanotubes increases the r_1 relaxivity values to 50.3 mM^{-1} s^{-1} compared to 4.7 mM^{-1} s^{-1} of $[Gd(OH_2)(DTPA)]^{2-}$ at 0.47 T.[8b] The confinement of a trianionictris (aquated) Gd(III) complex of 2,2′-(2-hydroxy-5-sulfonatobenzylazanediyl)bis(methylene)bis(8-hydroxy-quinoline-5-sulfonic acid (H_3dhqN-SO_3H) ligand, $[Gd(OH_2)_3(dhqN\text{-}SO_3)]^{3-}$, into mesoporous silica nanoparticles is reported to give a high r_1 relaxivity of 78 mM^{-1} s^{-1} at 1.2 T.[8a] Although a significant improvement in the quest for Gd(III)-based contrast agents with a high r_1 relaxivity value has been attained, an expected high relaxivity value on the order of 100 mM^{-1} s^{-1} has rarely been achieved.[11]

In this endeavor, we study biocompatible, porous silica nanoparticles impregnated with monopositive, tris(aquated) Gd(III) complexes $\{[Gd(OH_2)_3(hbda)]^{1+}\}$ of hexadentate ligand, 6,6′-(2-hydroxyethylazanediyl)bis(methylene)dipicolinic acid (H_2hbda). We envisaged that the confined-monopositive complex core would be in close contact with the inner surface of the negatively charged porous silica nanospheres, experiencing coulombic attraction. Thus, the stable non-covalent confinement of the complex near the inner surface and inside the porous nanospheres could be achieved. The interaction is expected to increase the effective mass and overall rotation correlation time of the paramagnetic Gd(III) complex, resulting in r_1 relaxivity value augmentation. Furthermore, the implantation of the complex-molecules near the inner surface would facilitate the exposure of paramagnetic Gd(III) ions to the outer nanosphere-water molecules. This arrangement would engender better relaxivity in the nanosystem (complex **1**@SiO_2NPs; NPs = nanoparticles). Additionally, by increasing the payload of the complex within the porous nanospheres, a high r_1 relaxivity per nanosphere is envisaged to materialize.

In this report, we present the synthesis, biocompatibility, and T_1-weighted contrast ability of porous silica nanoparticles each confining about 20 molecules of $\{[Gd(OH_2)_3(hbda)]\}Cl$ complex (**1**). The free (untrapped) complex molecule exhibited r_1 = 9.05 mM^{-1} s^{-1} at 1.41 T, pH 7.4, and 37 °C. Upon confinement (complex **1**@SiO_2), the relaxivity value increased to 86.41 mM^{-1} s^{-1}/Gd(III) at 1.41 T, pH 7.4, and 37 °C. Thus, the expected amplification in the relaxivity value has been successfully achieved in Gd(III)-complex-impregnated porous silica nanoparticles, and described herein.

Results and discussion

A diagram illustrating the synthetic route of the ligand H_2hbda, and complexes **1** and **2** is presented in Scheme 1. The reaction of 1 : 2.2 molar equivalent amounts of 2-aminoethanol and methyl 6-(bromomethyl)picolinate in the presence of Et_3N in THF yielded a solid white compound **A**. Upon reacting with an aqueous LiOH solution in THF and subsequent acidification with 1 M HCl, the compound provided the expected ligand H_2hbda·HCl in 89% yield. Complex **1** was isolated in 38% yield by reacting an equivalent amount of $GdCl_3$ salt with the ligand in water at pH ~ 6.5. Several attempts could not provide single crystals of complex **1** that were suitable for X-ray diffraction analysis. Therefore, a photoluminescence study needs to be performed to indirectly determine the number of water molecules coordinated to the Gd(III) ion. Gd(III) ions do not show photoluminescence in the visible region, while Tb(III) ions do. It is also known that Gd(III) and Tb(III) ions form a similar coordination complex. Therefore, the number of coordinated-water molecules (q) in complex **1** can be determined by measuring the luminescence-lifetime of the Tb(III)-congener. In this context, the corresponding Tb(III) congener was synthesized by reacting ligand H_2hbda with an equimolar amount of $TbCl_3·6H_2O$ at pH ~ 6.5 in water.

The H_2O and D_2O solutions of complex **2** at pH ~ 7.4 and 25 °C were excited at 272 nm, and the emission decay times

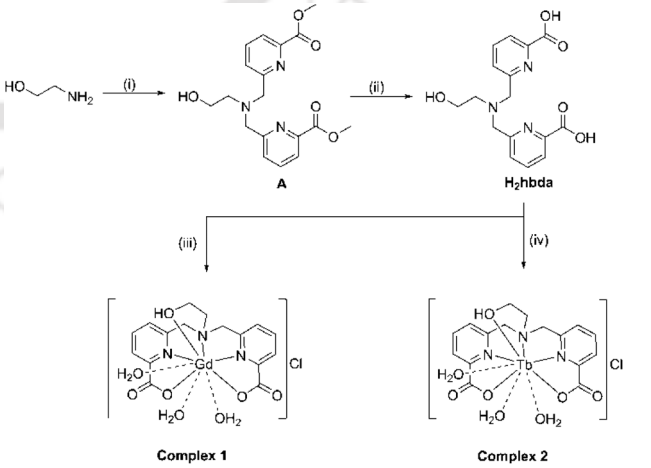

Scheme 1 A schematic diagram of the pathway for the preparation of H_2hbda, complex **1**, and complex **2**. (i) Methyl 6-(bromomethyl)picolinate, THF, and Et_3N; (ii) LiOH, THF/H_2O, H^+; (iii) $GdCl_3·xH_2O$, water, pH ~ 6.5; and (iv) $TbCl_3·6H_2O$, water, pH ~ 6.5.

TH-3359_186122030

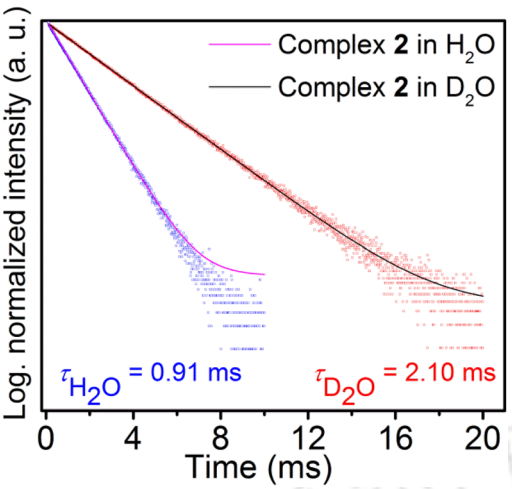

Fig. 1 Luminescence lifetime decay curves of complex **2** in H_2O and D_2O solvents. Mono-exponential convolution was used for the fitting of both curves (R^2 = 0.9997).

were recorded at 548 nm (Fig. S1†). The exponential-decay fitting of the experimentally obtained curves provided the respective lifetimes (τ) of the Tb ($^5D_4$) level in H_2O (τ_{H_2O} = 0.91 ms) and D_2O (τ_{D_2O} = 2.10 ms) (Fig. 1). Using the modified Horrocks' equation,[12] $q = A\,(1/\tau_{H_2O} - 1/\tau_{D_2O} - \alpha)$, where A_{Tb} = 5 ms, and α_{Tb} = 0.06 ms^{-1}, respectively, the number of inner-sphere water molecules in complex **1** was calculated as q = 2.8 ± 0.1.

The pH-dependent UV-Vis spectra of [Gd(III)] = [H_2hbda] = 0.1 mM in 0.15 M NaCl solutions indicated the formation of complex **1** at pH ≤ 2.0 (Fig. 2A). Thus, the potentiometric titration method (pH = 2.0 to 12.0) would not be suitable for determining the thermodynamic stability constant of complex **1** as the concentration of free Gd(III) ions would be negligible at pH ≥ 2. In this regard, the spectrophotometric competition titration method has been implemented. Herein, the conditional stability constant pM value is used to express the thermodynamic stability of the ligand with Gd(III) ions. Under physiological conditions, the most precise way to describe the stability of any complex is the pM value, which is defined by −log $[M]_{free}$ at pH ~ 7.4, and 25 °C, where [M] = 1 μM and $[L]_{total}$ = 10 μM.[13] The titrations were carried out by adding varying volumes of a standard solution of H_5DTPA to a constant concentration of the ligand and Gd(III) ions in HEPES buffer, maintaining pH ~ 7.4 (Fig. S2†). H_5DTPA was chosen as the competing ligand as the thermodynamic stability of the [Gd(DTPA)]$^{2-}$ complex (Magnevist®) has already been reported.[3a] The concentrations of free and chelated ligand present in those solutions were calculated by measuring the absorbance spectra of the respective solutions. The difference of pGd value between H_5DTPA and the ligand was obtained from the *x*-axis intercept of a linear plot of log[(GdDTPA)/(Gdhbda)] *vs.* log [(H_5DTPA)/(H_2hbda)] (Fig. 2B). This difference is the value of log([H_5DTPA]/[H_2hbda]), when log([GdDTPA]/[Gdhbda]) = 0 or when the concentration of H_5DTPA generates an equal partition of Gd(III) ions between H_2hbda and H_5DTPA. The calculated ΔpM = pGd(H_5DTPA) − pGd(H_2hbda) was 0.58. The pGd value of [Gd(DTPA)]$^{2-}$ is 19.1.[3a] Therefore, the calculated pGd value for complex **1** was 18.5. This value was indeed impressive for a tris(aquated) Gd(III) complex and found to be better than those of some of the already reported tris(aquated) Gd(III)-based complexes, *e.g.*, [Gd(dpaa)] (pGd = 12.3)[14] and [Gd(tpaa)] (pGd = 11.2),[15] and close to that of [Gd$(OH_2)_3$(dhqN-SO_3)]$^{3-}$ (pGd = 18.9).[8a] The high thermodynamic stability indicated that the alcoholic group contributes significantly to the improvement of the thermodynamic stability.

The synthesized stable {[Gd$(OH_2)_3$(hbda)]}Cl complex (complex **1**) molecules were incorporated within porous silica nanospheres by the reverse micelle mechanism (Fig. 3). In this process, droplets of an aqueous solution of complex **1** were generated within a cyclohexane medium (microemulsion). In the presence of Igepal-CO-520 surfactant, reverse micelles were constructed. After the addition of tetraethyl orthosilicate (TEOS), followed by NH_4OH, silica nanoparticles were created by the sol–gel technique. The removal of the surfactant rendered the expected porous nanoparticles with impregnated complex **1**, *i.e.*, complex **1**@SiO_2NP. The morphology, presence of the complex, and porous nature of the isolated nanoparticles were investigated by field-emission transmission electron microscope (FE-TEM) imaging (Fig. 4), elemental

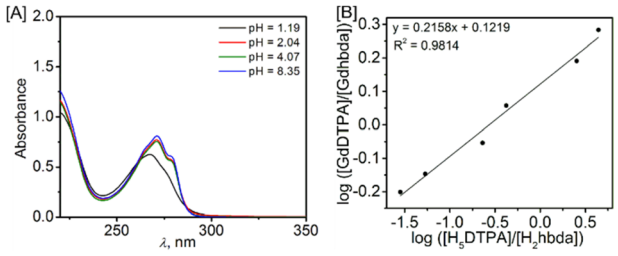

Fig. 2 (A) Variable pH UV-vis spectra of [Gd(III)] = [ligand] = 0.1 mM in 0.15 M NaCl solution. (B) The competition batch titration of the ligand H_2hbda against H_5DTPA.

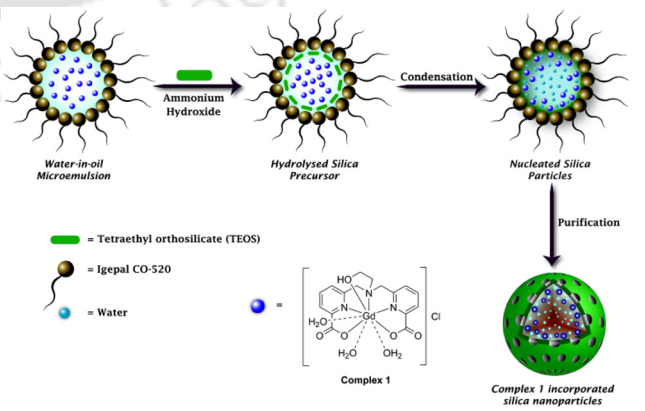

Fig. 3 A schematic illustration depicting the formation of complex **1**@SiO_2NPs.

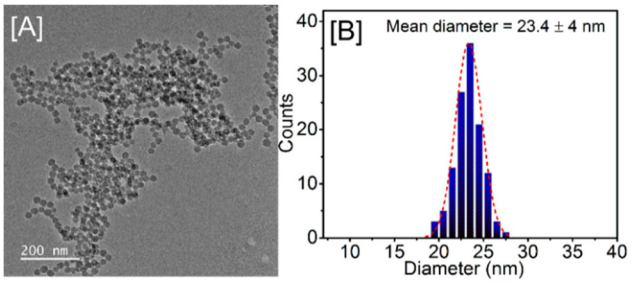

Fig. 4 (A) A representative TEM image of complex **1**@SiO_2NPs and (B) the corresponding particle size distribution diagram considering a minimum of 100 particles.

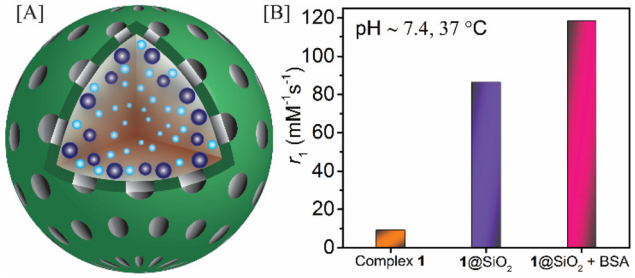

Fig. 5 (A) A schematic representation of the complex **1**@SiO_2NPs, showing the presence of complex **1** (blue) inside the silica layer and water (cyan) molecules. (B) Longitudinal relaxivity values for complex **1**, the complex **1**@SiO_2NPs, and the complex **1**@SiO_2NPs in the presence of 4.5% (w/v) BSA solution. Measurements were done at 37 °C, pH ~ 7.4, and 1.41 T.

mapping, energy dispersive X-ray spectroscopy (EDS), fourier transform infrared (FTIR), and N_2 adsorption–desorption isotherm analyses.

The FE-TEM images of the synthesized nanoparticles (complex **1**@SiO_2NPs) confirmed the formation of monodispersed and spherical nanoparticles of size 23.4 ± 4 nm (Fig. 4). EDS analyses (Fig. S3†) confirmed the presence of Gd, N and Cl atoms in the synthesized complex **1**@SiO_2NPs, and therefore the presence of the complex within the nanoparticles. Furthermore, the FTIR spectrum of the complex **1**@SiO_2NPs exhibited a stretching band at 1626 cm^{-1} that could be attributed to the coordinated carboxylate ν(C═O) stretching found in complex **1** and confirmed the incorporation of the complex within the porous nanoparticles (Fig. S4 and S5†). To investigate the hollow and porous nature of the isolated complex-incorporated NPs, N_2 adsorption–desorption isotherm measurements were carried out at 77 K. A type-IV isotherm was observed with a hysteresis loop (Fig. S6 and Table S1†), which confirmed the formation of mesoporous nanoparticles. The Barrett–Joyner–Halenda (BJH) pore diameter was 6.05 nm, which was slightly smaller than that of the bare porous silica nanoparticles (7.79 nm). A change in the hysteresis pattern from H2-type to H1-type upon confinement of complex **1** within the nanospheres (Fig. S6†) implied the adsorption of the complex in the inner core of the pores, rendering a cylindrical pore shape from an ink-bottle form.

The efficiency of a contrast agent is determined by its relaxivity value, which is defined as the change in the relaxation time with respect to its medium in the presence of 1 mM paramagnetic ions. The higher the value, the better the efficiency of the contrast agent. To examine the efficiency, the r_1 relaxivity values of complex **1**, the complex **1**@SiO_2NPs and the complex **1**@SiO_2NPs in the presence of serum albumin protein (BSA) were examined at 1.4 T, pH 7.4, and 37 °C. Complex **1** gave r_1 = 9.05 mM^{-1} s^{-1} (Fig. 5B and Table S3†). The relaxivity value was almost three times those of the clinically approved contrast agents; Magnevist® (3.3 mM^{-1} s^{-1}, 1.5 T, 37 °C), Gadovist® (3.3 mM^{-1} s^{-1}, 1.5 T, 37 °C), Omniscan (3.3 mM^{-1} s^{-1}, 1.5 T, 37 °C), Dotarem (2.9 mM^{-1} s^{-1}, 1.5 T, 37 °C), and Prohance® (3.3 mM^{-1} s^{-1}, 1.5 T, 37 °C).[3d] The higher relaxivity value was commensurate with the presence of three exchangeable inner-sphere water molecules in the complex.

The relaxivity value of complex **1** increased by about 9.5-fold in the complex **1**@SiO_2NPs (r_1 = 86.41 mM^{-1} s^{-1}) [Fig. 5B, S7, Tables S2 and S3†]. The porous nanoparticles of size 22.0 ± 2 nm (Fig. S8†) in the absence of complex **1** exhibited a zeta (ζ) potential of −23.9 mV at pH 7.4 (Fig. S9†). This value for the complex **1**@SiO_2NPs at the same pH was −19.0 mV (Table S3†). Thus, the shift in the zeta potential to a more positive value is a clear indication that monopositively charged complex **1** interacted with the layer of the silica nanoparticles (Fig. 5A). This static entrapment and the geometrical confinement within the nanosphere decreased the motion of complex **1** and resulted in the enhancement.

A further amplification in r_1 relaxivity value to 118.32 mM^{-1} s^{-1} (Fig. 5B) in the presence of serum albumin protein was observed. This implied the formation of a slow tumbling system due to interaction between the nanoparticles and the protein. To investigate the possible interactions, the ζ potential values of the complex **1**@SiO_2NPs in the absence and the presence of serum albumin protein (4.5%, w/v) in the pH range of 3.0 to 8.6 were recorded. The hydrodynamic diameter of the nanoparticles employing the dynamic light scattering (DLS) technique has also been determined simultaneously in the presence of the protein in the pH range of 3.4 to 8.6. The findings are presented in Fig. S10 and S11.† Significant changes in the ζ potential values of the nanoparticles in the presence of serum albumin protein were observed in the pH ranges of 3.0 to 4.0 and 5.0 to 8.6. Meanwhile, the ζ potential values increased towards more positive values in the lower pH range (below pH 5.5), and an increase in the potential towards more negative values was noticed at pH values higher than 5.5. The isoelectric point for BSA lies at pH 4.7. Below that pH, the overall charge of the protein is positive, and at a higher pH it is negatively charged. Therefore, the pH-dependent changes in the ζ potential values (positive-negative interaction at lower pH, and negative-negative interaction at higher pH) indicated interactions of the serum albumin protein with the nanoparticles, whose ζ potential values range from −13.6 to −20.2

at pH 3.0–8.6. These interactions could be a combination of supramolecular, van der Waals, and electrostatic interactions.

The hydrodynamic diameter of the nanoparticles in the presence of the protein increased with increased pH and reached the maxima at pH 5.2. Above this pH, the diameter of the nanoparticles diminished; however, it remained higher than that found in the pH range of 3.4 to 4.0. These findings suggested that the maximum interaction between the protein and the nanoparticles occurred when it was neutral in charge, followed by the negatively charged protein. These results also discerned the presence of a substantial amount of supramolecular and van der Waals interactions between the nanoparticles and the protein.

To confirm the existence of these interactions, thermogravimetric analysis (TGA) of the complex **1**@SiO_2NPs in the absence and the presence of the protein was performed at pH 3.0, 5.0, and 7.4 (Fig. S12†). The percentage of weight loss for each protein-added sample was compared with that of the complex **1**@SiO_2NPs. The weight loss sequence, pH 5 (26.0%) > pH 7.4 (23.0%) > pH 3.0 (21.4%), suggested a higher protein loading at pH 7.4 compared to pH 3.0. This protein adsorption trend was in accordance with similar reports in the literature[16] and herein, it established that supramolecular and van der Waals interactions predominated over the electrostatic interactions. Hence, at pH 7.4, the association of the protein, which was due to van der Waals and supramolecular interactions, produced a slow-tumbling system and presumably also lowered the mobility of the outer-sphere water molecules as suggested previously.[7a] These cumulative effects consequently elevated the r_1 relaxivity value to 118.32 mM^{-1} s^{-1} compared to r_1 = 86.41 mM^{-1} s^{-1} found for the complex **1**@SiO_2NPs. With an increase in the concentration of BSA, the relaxivity value further increased and it attained the maximum value of 128 mM^{-1} s^{-1} at a 1.6 mM concentration of BSA (Fig. S13†).

Complex **1** exhibited r_1 = 9.82 mM^{-1} s^{-1} at 1.41 T, pH 7.4 and 25 °C, which increased to 13.08 mM^{-1} s^{-1} upon lowering the pH to 2.13 (Fig. 6A). In contrast, the relaxivity value diminished to 6.70 mM^{-1} s^{-1} at pH 10.0. Thus, a pH dependence in the relaxivity of the complex was noticed (Fig. 6A). Firstly, to rationalize the decrement, the q value was determined at pH 10.0 and it was found to be q = 1.78 ± 0.10 (Fig. S14†). Thus, at high pH, the depletion in the relaxivity value was in accordance with the reduction of the inner-sphere water molecules, which might occur due to the replacement of the water molecules by a hydroxyl anion or by the deprotonation of the coordinated-water molecules. It should be noted that the observed r_1-value corroborated well with those reported for the bis(aquated)Gd(III) complexes; $[Gd(CyPic3A)(H_2O)_2]^-$ (5.70 mM^{-1} s^{-1}, 1.41 T, 37 °C),[17] $[Gd(peada)(H_2O)_2]^-$ (6.08 mM^{-1} s^{-1}, 1.41 T, 25 °C).[18] At low pH, pH 4.0 (r_1 = 12.51 mM^{-1} s^{-1}), the q value was found to be 2.99 ± 0.10 (Fig. S15†). Thus, the elevation of the relaxivity value despite no appreciable change in the number of inner-sphere water molecules of complex **1** at that pH compared to pH 7.4 reflected the proton (H^+)-influenced aggregation[19] of the complex molecules, which possibly occurred through the hydroxyethyl group (Fig. 6B). If the complexes aggregate, then dipole–dipole intramolecular interactions amongst the proximal Gd(III) ions would persist, resulting in a higher electronic relaxation rate.[20] To ensure the pH-dependent aggregation, X-band EPR spectra of complex **1** were measured at pH 7.4 and 2.13. The peak-to-peak linewidth, ΔH_{pp}, increased at pH 2.13 (ΔH_{pp} = 53.08 mT) compared to pH 7.4 (ΔH_{pp} = 24.64 mT) [Fig. S17†], reinforcing a faster electronic relaxation rate at low pH. Furthermore, the aggregation of complex **1** was expected to lead to a slowly rotating system, which increases the overall correlation time and thus the longitudinal relaxivity.

The r_1 relaxivity of the complex **1**@SiO_2NPs [0.05 mM] was recorded at 1.41 T and 25 °C within the pH range 2–10 to elucidate the effect of pH on the complex **1**-molecules after their impregnation within the nanoparticles. While a constant value of 95.3 ± 0.5 mM^{-1} s^{-1} was observed between pH 4.0 to 9.0, a subtle elevation in the relaxivity value (100.53 mM^{-1} s^{-1}) was noticed at pH 10.0. In contrast, a discernible pH effect was observed at pH = 2.13 and an approximately 37% drop in the relaxivity value to 59.54 mM^{-1} s^{-1} was realized. To rationalize this observation, the ζ potentials of the hollow porous pristine silica nanospheres were considered in the pH range of 2.13 to 10.0 (Fig. S9†). With a decrease in the pH from 7.4 to 2.13, the ζ potential increased to +2.65 mV from −23.9 mV. Because of the change in ζ potential to a positive value at pH 2.13, repulsive interactions between the cationic complex **1** and the nanoparticle-layers prevailed. As a result, some of the layer-confined-complex-molecules, having a calculated volume of 631 $Å^3$ per molecule (Fig. S18†), transuded from the porous nanospheres to the solution. The Gd ion concentration in the supernatant solution at pH 2.13 was measured as 38.3 μM after 20 hours, which was about 39% of the total concentration of the confined molecules (experiment started with a suspension of 100 μM of complex **1**@SiO_2NPs at pH 2.13). Complex **1** was stable at pH 2.04 (Fig. 2A) and exhibited r_1 = 13.08 mM^{-1} s^{-1} at 1.41 T and 25 °C (Fig. 6A and 7A), which was lower than that of the confined-form at the same pH. Therefore, the percolation of complex **1** at pH 2.13 led to the coexistence of both unconfined and confined complex **1** in the solution and conse-

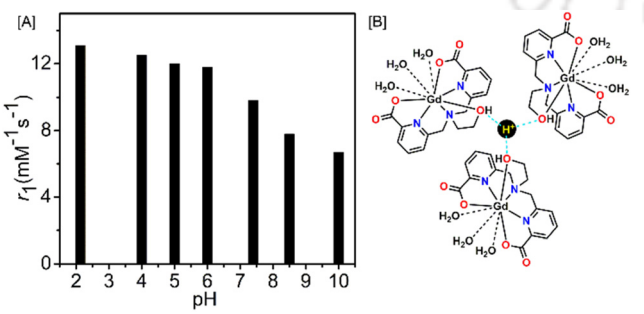

Fig. 6 (A) r_1 values for complex **1** recorded in the pH range of 2.1–10.0, at 25 °C, and 1.41 T. (B) A diagrammatic representation of the H^+-influenced aggregation of the complex molecules at lower pH.

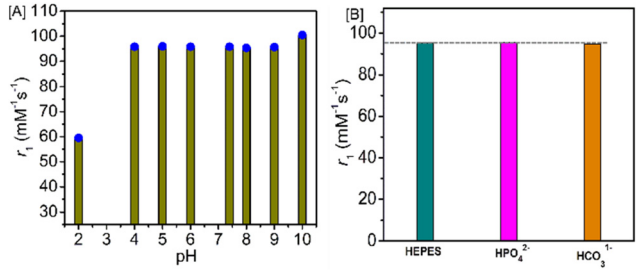

Fig. 7 r_1 values for complex **1**@SiO_2NPs recorded (A) in the pH range of 2.1–10.0, and (B) in the presence of 200 equivalents excess of different physiological anions, at pH ~ 7.4. Experiments were performed at 25 °C and 1.41 T.

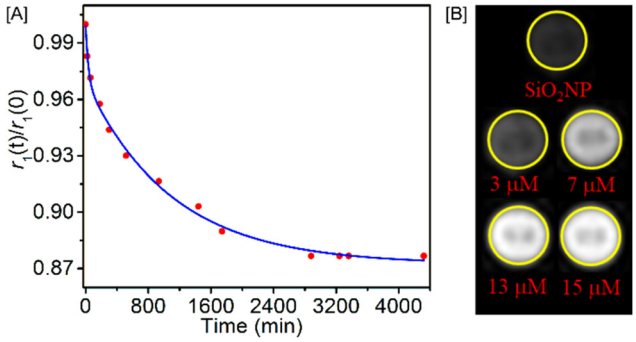

Fig. 8 (A) A time profile of the percentage changes in relative relaxivity, $r_1(t)/r_1(0)$, of the complex **1**@SiO_2NPs [0.01 mM] when challenged with an equivalent amount of Zn(II) ions. The pH was maintained at ~7.0 using phosphate buffer and the experiment was done at 37 °C. (B) T_1-weighted phantom MR images of micro-centrifuge tubes containing suspensions of different concentrations of complex **1**@SiO_2NPs, recorded at 25 °C, and 1.5 T.

quently diminished the overall relaxivity value. At pH 10.0, the reduction in ζ potential to −25.7 mV strengthened the interactions between the silica nanospheres and the cationic complex **1**. The interactions possibly reduced the molecular motion further to engender a subtle increase in the relaxivity value from 95.24 mM^{-1} s^{-1} to 100.53 mM^{-1} s^{-1}.

The physiologically available anions, which are present in a non-negligible concentration in blood plasma, may remove the inner-sphere water molecules by interacting with the metal ion and consequently reduce the efficiency of the contrast agent.[17] Thus, to examine the effect of anions, 200 equivalent amounts of HPO_4^{2-} and HCO_3^{1-} were added to the complex **1**@SiO_2NPs [0.05 mM] at pH 7.4 and 25 °C. The change in r_1 relaxivity value of the complex **1**@SiO_2NPs was then monitored at 1.41 T. Gratifyingly, no change in r_1 = 95.24 mM^{-1} s^{-1} was realized (Fig. 7B). This feature implied that the negatively charged nanoparticles protected the positively charged complex **1** from any deleterious interactions with external anions.

The kinetic inertness of complex **1** and the complex **1**@SiO_2NPs was evaluated by the transmetallation method using Zn(II) ions as the scavenger cation in phosphate buffer at pH 7.0 and 37 °C.[21] In this process, the changes in the initial r_1 relaxivity values of complex **1** and the complex **1**@SiO_2NPs were monitored with respect to time in the presence of one equivalent amount of Zn(II) ions. The index of kinetic inertness is given as the time required for an 80% decrease in the initial r_1 relaxivity value. The reduction would be because of dechelation or transmetallation of Gd(III) and insoluble $Gd(PO_4)$ precipitate formation. For complex **1**, an 80% decrease in the value was reached at 43 min (Fig. S19†). The values are 70 min, 250 min, and >5000 min for clinically approved mono (aquated) GdDTPA(BMA) [Omniscan®], GdDTPA [Magnevist®] and GdDOTA [Dotarem®], respectively.[22] Herein, the lower value complied with the low denticity of the H_2hbda ligand. Nonetheless, upon encapsulation within the porous nanoparticles, there was only a 3% decrease in the initial relaxivity value at 50 min. The total reduction in the initial value was restricted to only 12% in ≥4320 min (Fig. 8A). Thus, the encapsulation achieved kinetic inertness for complex **1**. A similar effect in terms of increase in kinetic inertness has also been observed by Mazzanti and colleagues, where 80% of the initial relaxivity value was reached in 1000 min by entrapping the trianionic $[Gd(OH_2)_3(dhqN\text{-}SO_3)]^{3-}$ complex.[8a] Thus, a significant improvement in the depletion-time of the initial relaxivity value has been achieved by implanting monocationic complex **1** closer to the inner surface of the nanoparticles. The attenuation in the initial r_1 value of the complex **1**@SiO_2NPs was originated merely because of agglomeration. In phosphate buffer, the hydrodynamic diameter of the complex **1**@SiO_2NPs was 644 nm (PDI = 0.395), which increased to 1352 nm (PDI = 0.196) in the presence of Zn(II) ions (Fig. S20†). The agglomeration reduced the exposure of the entrapped-complex **1**-molecules to outer-nanosphere water molecules and consequently diminished the value. Nonetheless, the agglomeration did not result in a substantial change in the relaxivity value.

To judge the capability of the synthesized complex **1**@SiO_2NPs as a T_1-weighted contrast agent, *in vitro* phantom images of varying concentrations were recorded at pH 7.4 on a BRIVO MR355 1.5 T MRI scanner at TR = 560 ms, and TE = 15 ms. By considering the same area for all the images, the relative image intensity was plotted as a bar diagram. The images (Fig. 8B) and the diagram (Fig. S21†) showed an enhancement in brightness with increasing concentration of the complex **1**@SiO_2NPs [Gd(III) ions], and thus, this consolidated the complex **1**@SiO_2NPs as a T_1-weighted contrast agent.

Cellular uptake, followed by cell tracking, therapy, drug delivery, *etc.*, leading to theranostic applications have become important in modern medical sciences.[23] In this context, the biocompatibility of the complex **1**@SiO_2NPs was initially evaluated in HeLa cells[24] and macrophages[24c] by performing an MTT assay. In these studies, the cells were incubated with an increasing concentration of complex **1**@SiO_2NPs. For the HeLa cells, after 48 h of incubation, 88% cell viability (Fig. 9A) was realized in the presence of 100 μM amount of the complex **1**@SiO_2NPs (*i.e.*, [silica nanoparticles] = 32 mg mL^{-1}). In the case of macrophages, 82% viability (Fig. 9B) was noticed after

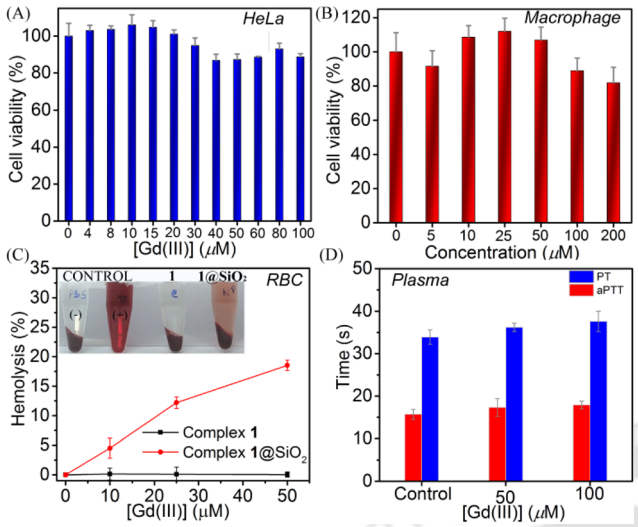

Fig. 9 *In vitro* cytotoxicity analysis of complex **1**@SiO_2NPs done *via* MTT assays on (A) the HeLa cell line and (B) macrophages. (C) Hemolysis percentages after the treatment of RBC with complex **1** and complex **1**@SiO_2NPs. Inset: photographs of RBC pellets after treatment with negative control, positive control, complex **1** (50 μM) [denoted as C], and complex **1**@SiO_2NPs (50 μM) [denoted as NP]. (D) The coagulation properties of complex **1**@SiO_2NPs, tested *via* PT and aPTT measurements. All data are within limits.

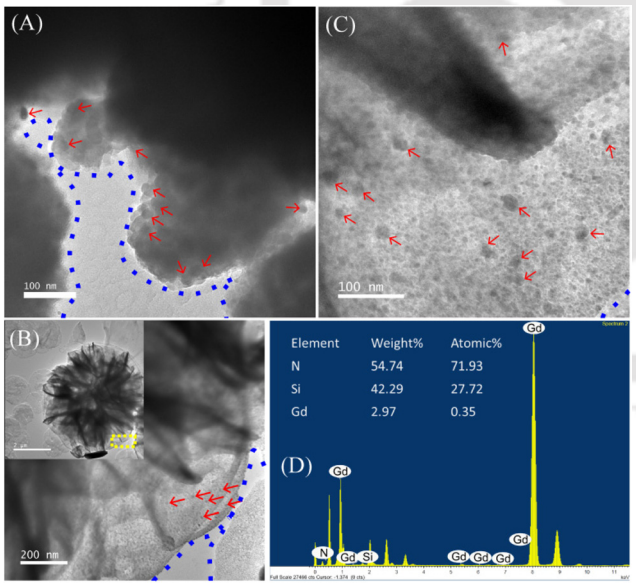

Fig. 10 TEM images of HeLa cells (A) after 12 hours of incubation, and (B and C) after 48 hours of incubation with the complex **1**@SiO_2NPs, showing the uptake of the nanoparticles. (B) Inset: a full view of the cell that has been zoomed in on. Red arrows are used to locate the presence of complex **1**@SiO_2NPs inside the cell. The yellow marked area in the inset in (B) is magnified to visualize the internalization of the nanoparticles. (D) EDS analysis inside the cell indicating the presence of Gd, Si, and N. The cell membrane is indicated by a blue-dotted line in the zoomed-in images.

4 h of incubation with 200 μM of the nanoparticles. Thus, the biocompatibility of the synthesized nanoparticles was confirmed.

Hemocompatibility was assessed by incubating freshly isolated red blood cells (RBC) and plasma with various concentrations of the complex **1**@SiO_2NPs.[24d] The results are presented in Fig. 9C and D. The complex **1**@SiO_2NPs exhibited mild toxicity toward human RBCs and caused about 18% hemolysis on treatment with 50 μM complex-incorporated nanoparticles. Furthermore, no toxicity of the nanoparticles was recorded towards the plasma.

The cell permeability of the complex **1**@SiO_2NPs was tested in HeLa cells. To visualize the cell uptake, a TEM image was recorded of HeLa cells after 12 h and 48 h incubation with 25 μM of the complex **1**@SiO_2NPs. The images and EDS elemental analyses, presented in Fig. 10 and Fig. S22,† suggested the incorporation of complex **1**@SiO_2NPs within the cells in the measurement time frame. The cellular uptake was quantified by ICP-MS of the solution prepared by digesting the treated cells (48 h) in conc. HNO_3. The Gd content was estimated to be about 55% of the initially treated amount. In order to further support the cell uptake phenomenon, cells were treated with the nanoparticles incubated with a fluorescence-active Tb(III) congener of complex **1**, *i.e.*, complex **2**@SiO_2NPs. The fluorescence images of the cells showed green fluorescence due to the intracellular incorporation of the complex **2**-based nanoparticles (Fig. S23†). Therefore, the above-stated studies concurred with incorporating and possibly using the synthesized nanosystem for cell labelling.

Conclusions

To conclude, tris(aquated) Gd(III) complexes with an overall monocationic charge/molecule have been successfully synthesized employing the hexadentate $[hbda]^{2-}$ ligating unit. The encapsulation of about 20 molecules of complex **1** non-covalently through electrostatic interactions at the negatively charged inner surface of porous silica nanospheres resulted in complex **1**@SiO_2NPs. The entrapment of the complex within the nanospheres imparted kinetic and coordination stability. Additionally, the association of cationic complex **1** molecules close to the porous surface rendered a very high relaxivity r_1 value of 86.41 mM^{-1} s^{-1} at pH 7.4, 37 °C and 1.41 T, which was further enhanced to 118.32 mM^{-1} s^{-1} in the presence of serum albumin protein. Thus, the envisaged high r_1 relaxivity has been achieved. The amplification of the relaxivity value in the presence of the protein was possibly due to the reduction of (1) the mobility of the nanospheres and (2) outer-sphere water molecules trapped within the protein surface and the outer nanoparticle surface.[7a] The concentration-dependent enhancement in the brightness of the *in vitro* phantom images established the T_1-weighted contrast capabilities of the complex **1**@SiO_2NPs. The synthesized biocompatible nanoparticles with negative surface charge were taken up by HeLa cells. Thus, we have successfully demonstrated that a charged

Gd(III) complex can be entrapped within the inner surface of porous nanoparticles to develop a highly efficient Gd(III)-based T_1-weighted contrast agent that could also be utilized for cell-labelling purposes. Studies related to the functionalization of the presented system for selective cell internalization and, thereafter, its therapeutic application are in progress in our laboratory.

Experimental section

Materials

All materials and solvents were acquired from commercial sources and were used as supplied, unless mentioned otherwise. 2,6-Pyridinedicarboxylic acid, LiOH, $GdCl_3{\cdot}xH_2O$, $TbCl_3{\cdot}6H_2O$, H_5DTPA, xylenol orange, and Igepal® CO-520 were purchased from Sigma-Aldrich. 2-Aminomethan-1-ol, triethylamine, $NaHCO_3$, Na_2HPO_4, NaF, HNO_3 (69%), ammonium hydroxide (25%), acetone, HCl and NaOH solutions were purchased from Merck (India). Tetraethoxysilane (TEOS, 99 + %) was purchased from Alfa Aesar. THF and cyclohexane were purchased from Spectrochem. HEPES buffer was purchased from SRL. Ethyl alcohol was purchased from TEDIA. Water used for the experiments was purified by using a Millipore-water purifier, Milli-Q, Merck.

Physical methods

FTIR spectra were recorded on a PerkinElmer Instrument at room temperature by making KBr pellets by grinding the sample with KBr (IR Grade). Mass spectral data were obtained using an HRMS spectrometer. Conductance was measured with an aqueous solution of complex **1** on an ELICO CM180 CONDUCTIVITY METER. UV-Vis spectra were obtained using a PerkinElmer, Lamda 25, UV/Vis spectrometer. Lifetime fluorescence measurements were accomplished on a FluoroMax-4 spectrofluorometer (Horiba). Nitrogen sorption isotherms were acquired on a Quantachrome, model: Autosorb-IQ MP surface area and pore size analyzer at 77 K. Before the experiments, dry samples (obtained by lyophilizing the suspension for 24 h) were degassed at 100 °C for 4 h. The zeta potential and particle size distribution of the suspended complex **1**@SiO_2 nanoparticles were measured at 25 °C by Dynamic Light Scattering (DLS) using a Malvern ZETASIZER Nano-ZS90 (equilibrium time set to 2 min; 5 measurements taken on each sample set, only quality criteria values were accepted). The desired pH was maintained using appropriate buffers. The longitudinal relaxivity, r_1, at 1.41 T was measured using a BRUKER minispec mq60NMR Analyzer.

The exact concentration of Gd in the samples was determined by the ICP-MS technique (Model-Element XR, Thermo Fisher Scientific) after treatment of the nanoparticle suspension with dilute HNO_3 solution (45%) at 90 °C for 12 hours, and the supernatant solution was tested by ICP-MS for quantification of the Gd(III) content. Complex **1**@SiO_2 was synthesized and the metal content was determined thrice in independent sets to secure the reproducibility and minimize the error in the relaxivity data. Complete digestion of Gd metal was ensured by measuring the T_1 values of the left-over residue.

Set	T_1 of the residue	T_1 of blank SiO_2
I.	2980 ms	2970 ms
II.	3019 ms	
III.	2960 ms	

Additionally, the concentration of the complex **1**@SiO_2 suspension was determined by measuring the bulk magnetic susceptibility (BMS) of the suspension.[25] A paramagnetic suspension of complex **1**@SiO_2 in D_2O (containing 1% *tert*-butanol) was placed in the inner compartment of a coaxial tube and a diamagnetic solution (1% *tert*-butanol in D_2O) was placed in the outer compartment. The frequency shift in the *tert*-butanol signals in the NMR spectra represented the BMS shift. The Gd(III) concentration of the suspension was subsequently calculated.

Luminescence lifetime measurements

Lanthanide luminescence lifetime measurements were accomplished on a FluoroMax-4 spectrofluorometer (Horiba). A 50 μM solution of complex **2** was prepared in 10 mM HEPES buffer maintaining the pH at ~7.4, at 25 °C. The solution was excited at 272 nm with a pulsed Xenon lamp having a pulse width of ~3 μs and time per pulse of 61 ms. Emission at 548 nm was recorded and the luminescence decay curves were generated by the 'decay by delay' method with an initial delay of 0.1 ms and maximum delay up to 10 ms. It was then evaporated completely under reduced pressure. Addition of an equal volume of D_2O to the completely dry residue resulted in a solution of the same concentration of the complex in D_2O-buffer. All transfers of D_2O-containing samples were performed inside a glove bag under an argon atmosphere to avoid contamination of moisture (H_2O) and lifetime measurements were done in a cuvette, sealed under argon, maintaining all instrumental parameters at the same values as previously used in H_2O (only the maximum delay was changed to 20 ms in the case of the D_2O sample).

Competition titration

The competition titration method was used to determine the affinity of the ligand for Gd(III) ions. Various volumes of a standardized H_5DTPA stock solution were added to solutions containing a constant concentration of ligand (H_2hbda), Gd(III) ions, electrolyte (NaCl) and HEPES buffer. All solutions were brought to pH ~ 7.4 by adding NaOH solution. The samples were kept for 48 h to attain thermodynamic equilibrium. The concentration of free and complexed ligand in each sample was determined from the absorbance spectra considering a particular range of wavelengths where spectral changes occurred. With respect to the absorbance of ligand H_2hbda at that particular concentration, the variation in absorbance for each solution set was determined. The concentrations of

Gdhbda complex, GdDTPA complex, free H_2hbda and free H_5DTPA for each set were calculated from the variation in absorbance in each set of samples.

Relaxometric analyses

Aqueous solutions of complex **1** and aqueous suspensions of complex **1**@SiO_2 with increasing Gd(III) concentration were prepared and longitudinal relaxation times (T_1) were measured using a BRUKER minispec mq60 NMR analyzer, at pH ~ 7.4, 1.41 T, 25 °C and 37 °C. Relaxation rates ($1/T_1$) *versus* Gd concentration values were plotted and the slope for linear regression gave the relaxivity values (r_1).

The relaxivity values for complex **1**@SiO_2NPs were recorded in the presence of bovine serum albumin (BSA) under physiological conditions (pH ~ 7.4, 310 K, BSA concentration maintained at 4.5% w/v; measured at 1.41 T). The samples were incubated at 37 °C for 3 hours before the experiment.

Kinetic measurements

Kinetic inertness was studied at 1.41 T and 37 °C using a BRUKER minispec mq60NMR Analyzer. Equimolar aqueous solution of $ZnCl_2$ was added to a suspension of complex **1**@SiNPs ($c_{Gd^{3+}}$ = 0.010 mM) in PBS buffer, at pH ~ 7, and T_1 values were recorded at regular time intervals for 4 days. The gradual decrease in longitudinal relaxivity was noted against time and percentage change *versus* time was plotted.

Transmission electronic microscopy (TEM)

The size and morphology of the $[Gd(hbda)(H_2O)_3]^+$-doped silica nanoparticles [complex **1**@SiO_2NPs] were examined from transmission electron microscopy (TEM) images obtained from a JEOL, model: 2100F electron microscope operated at 200 kV, together with energy-dispersive X-ray spectroscopy (EDS). 10 μL of the prepared mother suspension was diluted to 10 mL with ethanol and 10 μL of the final solution was dropped onto a carbon-coated copper grid (CARBON FILM 300 MESH, COPPER) and kept overnight for drying and then used for imaging. ImageJ software was used to calculate the particle size distributions from a sample containing at least 100 particles.

MTT assay of complex 1@SiO_2NPs

Cervical cancer cells (HeLa) and macrophage cell lines RAW 264.7 were purchased from the National Centre for Cell Science, Pune. All the cell lines were maintained in Dulbecco's modified Eagle's medium (DMEM) supplemented with 10% (v/v) fetal bovine serum (FBS) and 1% penicillin & streptomycin at 37 °C in humidified air containing 5% CO_2. The cells were seeded in a 96-well plate at a density of 5×10^3 cells per well and allowed to attach for 24 h, maintaining the same conditions as mentioned above. The HeLa cell line was treated for 48 h with increasing concentrations of complex **1**@SiO_2NPs (concentration in terms of Gd^{3+}). For the macrophage cell line, after 24 h, the cells were treated for 4 h with increasing concentrations of complex **1**@SiO_2NPs (concentration in terms of Gd^{3+}). 0.5 mg ml^{-1} of MTT in DMEM was added to each well and incubated for 1.5 h (for HeLa) or 4 h (for macrophages). Subsequently, 150 μl DMSO was added to each well. The absorbance was measured at 570 nm using a Cary 60 UV-Vis spectrophotometer, and after that, cell viability was calculated, considering 100% viability for untreated cells.

Cell labelling studies of complex 1@SiO_2NPs

Cervical cancer cells (HeLa) were purchased from the National Centre for Cell Science, Pune. All the cell lines were maintained in Dulbecco's modified Eagle's medium (DMEM) supplemented with 10% (v/v) fetal bovine serum (FBS) and 1% penicillin & streptomycin at 37 °C in humidified air containing 5% CO_2. The cells were seeded in a 30 mm^2 Petri plate at a density of 1.5×10^5 cells and allowed to attach. Subsequently, they were treated with 25 μM of a suspension of complex **1**@SiO_2NPs and incubated for 12 h and 48 h, in two sets, at 37 °C in humidified air containing 5% CO_2. The cells were subsequently washed with PBS (phosphate-buffered saline) to remove any unbound complex **1**@SiO_2. The cells were then trypsinized and fixed using 4% formaldehyde for 15 min and washed twice with PBS. Subsequently, for FETEM imaging, the resuspended cells were added to the carbon-coated copper grid and allowed to air dry. Images were collected in an FETEM microscope (JEOL, 2100F).

The trypsinized cell suspension in PBS was digested in conc. HNO_3 for 12 h and the concentration of Gd attached/taken up by the cells was quantified by ICP-MS analysis.

Fluorescence microscopy

HeLa cells were seeded in a 96-well plate at a density of 1.5×10^5 cells and allowed to attach. Subsequently, they were treated with 100 μM of a suspension of complex **2**@SiO_2NPs and incubated for 24 h, at 37 °C in humidified air containing 5% CO_2. The cells were thoroughly washed with PBS to remove any unbound nanoparticles and subsequently fixed with 4% formaldehyde solution for 15 min, then washed thrice with PBS and then observed under a Nikon ECLIPSE T*i*-U fluorescence inverted microscope.

Hemolysis assay

RBC pellets were collected by centrifugation of 4 mL of EDTA-stabilized human blood at 1600 rpm for 5 minutes. Blood plasma was removed and the remaining RBCs were washed with PBS 2 times. Finally, the RBC pellet collected was re-suspended in PBS (10 mL). Increasing concentrations of complex **1**/complex **1**@SiO_2NP suspension were mixed with the RBC solution and incubated on ice for 2 hours. Positive and negative controls were prepared in a similar way with PBS and 0.1 mM Triton-x solution, respectively. Afterward, all samples were centrifuged at 1600 rpm for 5 minutes and the supernatant solution of each was taken in a 96-well plate and the absorbance was recorded at 550 nm.

Coagulation assay

Citrated human blood (4 mL) was centrifuged at 1600 rpm for 5 minutes. RBCs were discarded and the supernatant plasma

collected and thawed at 37 °C. Increasing concentrations of nanoparticle suspension were added to the plasma and incubated at 37 °C for 5 minutes. A control was prepared by adding PBS to plasma. Then, the samples were centrifuged and the upper clear solution was collected for PT and APTT measurements on a fully automatic Tulip haemostar XF 1.0 blood coagulation analyzer.

MR imaging

MR images were obtained using a clinical BRIVO MR355 1.5 T MRI scanner. Parameters adopted while recording the images were: TR (repetition time) = 560 ms, TE (echo time) = 15 ms, slice thickness = 5.0 mm and field of view (FOV) = 512 × 512 mm^2.

Synthesis of $[C_{18}H_{21}N_3O_5]$, A

2-Aminoethanol (0.275 g, 4.5 mmol) and Et_3N (1.37 mL, 9.9 mmol) were added to a solution of methyl 6-(bromomethyl)picolinate (2.27 g, 9.9 mmol) in THF (20 mL). The mixture was allowed to stir for a period of 24 h at room temperature (25 °C). The resultant solution was concentrated to dryness; the oily residue was extracted with a H_2O/CH_2Cl_2 (1 : 3) mixture. The organic phase was evaporated to dryness to give a yellowish liquid, which was purified by column chromatography on silica with a methanol/ethyl acetate (gradient = 1%) mixture as the eluent to render 0.725 g of compound **A** as a white solid. Yield = 45%. FTIR (KBr pellet per cm): 3358, 3088, 2988, 2948, 2869, 2809, 1738, 1722, 1591, 1440, 1370, 1346, 1324, 1305, 1287, 1269, 1226, 1202, 1191, 1163, 1140, 1082, 1066, 1039, 978, 962, 909, 888, 829, 791, 767, 719, 679, 627, 534. ^{1}H-NMR ($CDCl_3$, 600.17 MHz): δ 7.98 (d, J = 6 Hz, 2H), 7.73 (t, J = 6 Hz, 2H), 7.58 (d, J = 6 Hz, 2H), 4.04 (s, 4H), 4.01 (s, 6H), 3.70 (t, J = 6 Hz, 2H), 2.90 (t, J = 6 Hz, 2H) ppm. ^{13}C-NMR ($CDCl_3$, 101 MHz): δ 165.11, 159.73, 146.75, 137.03, 125.85, 123.15, 59.74, 59.30, 56.92, 52.44 ppm. ESI-MS (+) m/z for $[C_{18}H_{21}N_3O_5 + H]^+$: calcd, 360.1554; found, 360.1558.

Synthesis of $[C_{16}H_{17}N_3O_5]$, H_2hbda

To a solution of compound **A** (0.359 g, 1 mmol) in THF (6 mL), LiOH (0.051 g, 2.1 mmol in 2 mL H_2O) was added and stirred at room temperature for 24 h in the dark. The reaction mixture was then acidified by adding 1 N HCl solution. The ligand was obtained as the pyridinium chloride salt. After complete evaporation of the solvents followed by washing with diethyl ether and methanol, the ligand was isolated. Yield = 328 mg, 89%. FTIR (KBr pellet per cm): 3405, 3351, 3076, 3037, 2938, 2774, 2612, 1745, 1732, 1595, 1488, 1465, 1444, 1407, 1339, 1254, 1179, 1175, 1135, 1081, 997, 836, 755, 523.^{1}H-NMR (D_2O, 600.17 MHz): δ 7.76 (t, J = 6 Hz, 2H), 7.71 (d, J = 6 Hz, 2H), 7.46 (d, J = 6 Hz, 2H), 3.92 (s, 4 H), 3.74 (t, J = 6 Hz, 2H), 2.86 (d, J = 6 Hz, 2H) ppm. ^{13}C-NMR (D_2O, 150.93 MHz): δ 173.03, 157.36, 152.36, 138.20, 126.16, 122.12, 59.10, 58.68, 56.29 ppm. ESI-MS (+) m/z for $[C_{16}H_{17}N_3O_5 + H]^+$: calcd, 332.1241; found, 332.1245 (Fig. S24–S27†).

Synthesis of $[C_{16}H_{21}N_3O_8Gd]$, complex 1

$GdCl_3{\cdot}xH_2O$ (0.090 g, 0.34 mmol) was added to an aqueous solution of ligand H_2hbda (0.140 g, 0.38 mmol), and kept under stirring until the solution became transparent. The pH of the reaction mixture was adjusted to ~6.5 by adding an aqueous NaOH solution dropwise, followed by continuous stirring at room temperature for 24 h. The resultant solution was filtered, and a white solid product was obtained after complete evaporation of the filtrate. The obtained white solid was washed thoroughly with MeOH and the absence of free Gd(III) was confirmed by a xylenol orange test. Yield = 0.070 g, 38%. The molar conductivity of a 5 mM aqueous solution of complex **1** was evaluated to be 81 Scm^2 mol at 25 °C, which is close to the typical molar conductivity range for (1 : 1) strong electrolytes. Metal : ligand stoichiometry was established by Job's plot. FTIR (KBr pellet per cm): 3436, 2851, 2829, 1626, 1591, 1468, 1444, 1406, 1378, 1279, 1226, 1188, 1156, 1116, 1093, 1046, 1012, 974, 955, 942, 812, 775, 690. ESI-MS (+) m/z for $[C_{16}H_{15}N_3O_5Gd]^+$: calcd, 487.0209; found, 487.0291 (Fig. S28–S32†).

Synthesis of $[C_{16}H_{21}N_3O_8Tb]$, complex 2

An aqueous solution of ligand H_2hbda (0.132 g, 0.36 mmol) and $TbCl_3{\cdot}6H_2O$ (0.125 g, 0.35 mmol) was stirred until it became transparent. The pH of the solution was adjusted to ~6.5 by adding aqueous NaOH solution dropwise, followed by stirring at room temperature for 24 h. The reaction mixture was filtered, and a white solid compound was collected on complete evaporation of the solvent. The obtained complex was washed thoroughly with MeOH to remove excess ligand and Tb(III) salt. Yield = 0.085 g, 45%. FTIR (KBr pellet per cm): 3413, 1623, 1591, 1472, 1447, 1409, 1280, 1224, 1191, 1158, 1116, 1085, 1017, 812, 774, 689. ESI-MS (+) m/z for $[C_{16}H_{15}N_3O_5Tb]^+$: calcd, 488.0265; found, 488.0313 (Fig. S33 and S34†).

Synthesis of complex 1@SiO_2NPs

Complex **1**@SiO_2NPs were synthesized following the reverse microemulsion procedure. A homogenous solution of Igepal-CO-520 (1.3 mL) in cyclohexane (10 mL) was prepared by stirring for 10 min. Doping solution comprising complex **1** solution (160 μL, 4.2 mM) in water (320 μL) at pH ~ 7.4 was cautiously added to the surfactant mixture. This was followed by the addition of NH_4OH (120 μL, 25% by w/v) and the mixture was stirred for another 30 minutes. Finally, TEOS (100 μL) was added, and the resultant mixture was kept at room temperature for 24 h with gentle stirring. Complex **1**@SiO_2NPs were obtained by adding acetone (30 mL) to the mixture, which was repeatedly washed with ethanol and water by centrifugation at 10 000 rpm for 15 minutes. The residue obtained was dispersed in 400 μL water (pH maintained at 7.4) to obtain 500 μL of 0.088 mM suspension, with the concentration given in terms of Gd(III) (8% complex molecules incorporated inside nanoparticles). The residue obtained was dispersed in 400 μL water (pH maintained at 7.4), and this mother suspension was further used for relaxometry and other studies. FTIR (KBr pellet per cm): 3466, 1639, 1626, 1470, 1099, 962, 799, 467.

Author contributions

RM and MK synthesized and characterized the ligand and complex **1**; RM regenerated complex **1** and performed all the experiments on complex **1**@SiO_2NPs. MS carried out cell viability and cell internalization experiments on supplied samples. SM and SK performed the viability studies on macrophages. The overall idea was developed by CM. The manuscript was written through contributions from RM and CM. All authors have given approval to the final version of the manuscript.

Notes

A patent application has been (Application No. 201831020332) filed by the Indian Institute of Technology Guwahati on the ligand.

Conflicts of interest

There are no conflicts to declare.

Acknowledgements

This project is funded by Department of Biotechnology (BT/PR23622/NNT/281294/2017), Govt. of India. CM thanks Dr Amrit Sarmah for assistance with the DFT-based structural optimization of complex 1. RM, MK, and MS thank IIT Guwahati for doctoral fellowships. CM is indebted to Dr Baijayanta Saharia, Director, Department of Radiology and Imaging, GNRC Hospital, Guwahati, India, for assistance with MRI image measurements at 1.5 T. The Department of Chemistry, and Central Instruments Facility, IIT Guwahati are gratefully acknowledged for instrumental facilities.

References

1 (*a*) J. Wahsner, E. M. Gale, A. Rodríguez-Rodríguez and P. Caravan, *Chem. Rev.*, 2019, **119**, 957–1057; (*b*) E. J. Werner, A. Datta, C. J. Jocher and K. N. Raymond, *Angew. Chem., Int. Ed.*, 2008, **47**, 8568–8580.

2 (*a*) L. M. de Leõn-Rodríguez, A. F. Martins, M. C. Pinho, N. M. Rofsky and A. D. Sherry, *Magn. Reson. Imaging*, 2015, **42**, 545–565; (*b*) S. Aime, M. Botta, S. G. Crich, G. B. Giovenzana, G. Jommi, R. Pagliarin and M. Sisti, *Inorg. Chem.*, 1997, **36**, 2992–3000; (*c*) E. Brücher, G. Tircsó, Z. Baranyai, Z. Kovács and A. D. Sherry, in *The Chemistry of Contrast Agents in Medical Magnetic Resonance Imaging*, ed. A. Merbach, L. Helm and É. Tóth, John Wiley & Sons, Ltd., 2013.

3 (*a*) P. Caravan, J. J. Ellison, T. J. McMurry and R. B. Lauffer, *Chem. Rev.*, 1999, **99**, 2293–2352; (*b*) G. Tircsó, M. Regueiro-Figueroa, V. Nagy, Z. Garda, T. Garai, F. K. Kálmán, D. Esteban-Gómez, É. Tóth and C. Platas-Iglesias, *Chem. – Eur. J.*, 2016, **22**, 896–901; (*c*) M. Ndiaye, V. Malytskyi, T. Vangijzegem, F. Sauvage, M. Wels, C. Cadiou, J. Moreau, C. Henoumont, S. Boutry, R. N. Muller, D. Harakat, S. D. Smedt, S. Laurent and F. Chuburu, *Inorg. Chem.*, 2019, **58**, 12798–12808; (*d*) M. Rohrer, H. Bauer, J. Mintorovitch, M. Requardt and H. J. Weinmann, *Invest. Radiol.*, 2005, **40**, 715–724.

4 (*a*) M. A. Sieber, H. Pietsch, J. Walter, W. Haider, T. Frenzel and H.-J. Weinmann, *Invest. Radiol.*, 2008, **43**, 65–75; (*b*) M. Taupitz, N. Stolzenburg, M. Ebert, J. Schnorr, R. Hauptmann, H. Kratz, B. Hamm and S. Wagner, *Contrast Media Mol. Imaging*, 2013, **8**, 108–116; (*c*) S. Swaminathan, *Magn. Reson. Imaging*, 2016, **34**, 1373–1376.

5 T. H. Shin, P. K. Kim, S. Kang, J. Cheong, S. Kim, Y. Lim, W. Shin, J. Y. Jung, J. D. Lah, B. W. Choi and J. Cheon, *Nat. Biomed. Eng.*, 2021, **5**, 252–263.

6 (*a*) T. Courant, V. G. Roullin, C. Cadiou, M. Callewaert, M. C. Andry, C. Portefaix, C. Hoeffel, M. C. de Goltstein, M. Port, S. Laurent, L. V. Elst, R. Muller, M. Molinari and F. Chuburu, *Angew. Chem., Int. Ed.*, 2012, **51**, 9119–9122; (*b*) V. S. Marangonia, O. Neumannc, L. Hendersona, C. C. Kaffese, H. Zhangd, R. Zhangd, S. Bishnoia, C. Ayala-Orozcoa, V. Zucolottob, J. A. Banksone, P. Nordlanderd and N. J. Halasa, *Proc. Natl. Acad. Sci. U. S. A.*, 2017, **114**, 6960–6965; (*c*) B. Phukan, K. P. Malikidogo, C. S. Bonnet, É. Tóth, S. Mondal and C. Mukherjee, *ChemistrySelect*, 2018, **3**, 7668–7673.

7 (*a*) J. S. Ananta, B. Godin, R. Sethi, L. Moriggi, X. Liu, R. E. Serda, R. Krishnamurthy, R. Muthupillai, R. D. Bolskar, L. Helm, M. Ferrari, L. J. Wilson and P. Decuzzi, *Nat. Nanotechnol.*, 2010, **5**, 815–821; (*b*) P. Caravan, C. T. Farrar, L. Frullano and R. Uppal, *Contrast Media Mol. Imaging*, 2009, **4**, 89–100.

8 (*a*) M. M. Karimdjy, G. Tallec, P. H. Fries, D. Imbert and M. Mazzanti, *Chem. Commun.*, 2015, **51**, 6836–6838; (*b*) C. Richard, B. T. Doan, J. C. Beloeil, M. Bessodes, É. Tóth and D. Scherman, *Nano Lett.*, 2008, **8**, 232–236.

9 (*a*) S. V. Fedorenko, S. L. Grechkina, A. R. Mustafina, K. V. Kholin, A. S. Stepanov, I. R. Nizameev, I. E. Ismaev, M. K. Kadirov, R. R. Zairov, A. N. Fattakhova, R. R. Amirov and S. E. Soloveva, *Colloids Surf., B*, 2017, **149**, 243–249; (*b*) S. Fedorenko, A. Stepanov, R. Zairov, O. Kaman, R. Amirov, I. Nizameev, K. Kholin, I. Ismaev, A. Voloshina, A. Sapunova, M. Kadirov and A. Mustafina, *Colloids Surf., A*, 2018, **559**, 60–67; (*c*) M. L. T. Kathryn, J. S. Kim, W. J. Rieter, H. An, W. Lin and W. Lin, *J. Am. Chem. Soc.*, 2008, **130**, 2154–2155.

10 (*a*) L. Moriggi, C. Cannizzo, E. Dumas, C. R. Mayer, A. Ulyanov and L. Helm, *J. Am. Chem. Soc.*, 2009, **131**, 10828–10829; (*b*) R. Zairov, G. Khakimullina, S. Podyachev, I. Nizameev, G. Safiullin, R. Amirov, A. Vomiero and A. Mustafina, *Sci. Rep.*, 2017, **7**, 14010.

11 K. B. Hartman, S. Laus, R. D. Bolskar, R. Muthupillai, L. Helm, E. Toth, A. E. Merbach and L. J. Wilson, *Nano Lett.*, 2008, **8**, 415–419.

12 (*a*) A. Beeby, I. M. Clarkson, R. S. Dickins, S. Faulkner, D. Parker, L. Royle, A. S. de Sousa, J. A. Gareth Williams and M. Woods, *J. Chem. Soc. Perkin Trans. 2*, 1999, **3**, 493–504; (*b*) W. D. Horrocks Jr. and D. R. Sudnick, *J. Am. Chem. Soc.*, 1979, **101**(2), 334–340; (*c*) M. Tropiano, O. A. Blackburn, J. A. Tilney, L. R. Hill, T. J. Sørensen and S. Faulkner, *J. Lumin.*, 2015, **167**, 296–304.

13 (*a*) V. C. Pierre, M. Botta, S. Aime and K. N. Raymond, *Inorg. Chem.*, 2006, **45**, 8355–8364; (*b*) C. J. Jocher, M. Botta, S. Avedano, E. G. Moore, J. Xu, S. Aime and K. N. Raymond, *Inorg. Chem.*, 2007, **46**, 4796–4798.

14 A. Nonat, P. Fries, J. Pécaut and M. Mazzanti, *Chem. – Eur. J.*, 2007, **13**, 8489–8506.

15 Y. Bretonnière, M. Mazzanti, J. Pécaut, F. A. Dunand and A. E. Merbach, *Inorg. Chem.*, 2001, **40**, 6737–6745.

16 B. E. Givens, Z. Xu, J. Fiegel and V. H. Grassian, *J. Colloid Interface Sci.*, 2017, **493**, 334–341.

17 E. M. Gale, N. Kenton and P. Caravan, *Chem. Commun.*, 2013, **49**, 8060–8062.

18 B. Phukan, C. Mukherjee and R. Varshney, *Dalton Trans.*, 2018, **47**, 135–142.

19 (*a*) S. Laus, A. Sour, R. Ruloff, É. Tóth and A. E. Merbach, *Chem. – Eur. J.*, 2005, **11**, 3064–3076; (*b*) S. Aime, S. Baroni, D. D. Castelli, E. Brücher, I. Fábián, S. C. Serra, A. F. Mingo, R. Napolitano, L. Lattuada, F. Tedoldi and Z. Baranyai, *Inorg. Chem.*, 2018, **57**, 5567–5574; (*c*) E. Boros, R. Srinivas, H. Kim, A. M. Raitsimring, A. V. Astashkin, O. G. Poluektov, J. Niklas, A. D. Horning, B. Tidor and P. Caravan, *Angew. Chem., Int. Ed.*, 2017, **56**, 5603–5606; (*d*) M. Boccalon, L. Leone, G. Marino, N. Demitri, Z. Baranyai and L. Tei, *Inorg. Chem.*, 2021, **60**, 13626–13636.

20 É. Tóth, L. Helm, K. E. Kellar and A. E. Merbach, *Chem. – Eur. J.*, 1999, **5**, 1202–1211.

21 (*a*) M. Port, J. M. Idée, C. Medina, C. Robic, M. Sabatou and C. Corot, *BioMetals*, 2008, **21**, 469–490; (*b*) S. Laurent, L. Vander Elst, C. Henoumont and R. N. Muller, *Contrast Media Mol. Imaging*, 2010, **5**, 305–308.

22 A. Bianchi, L. Calabi, F. Corona, S. Fontana, P. A. Losi, A. Maiocchi, L. Paleari and B. Valtancoli, *Coord. Chem. Rev.*, 2000, **204**, 309–393.

23 (*a*) J. L. Vivero-Escoto, R. C. Huxford-Phillips and W. Lin, *Chem. Soc. Rev.*, 2012, **41**, 2673–2685; (*b*) E. Ruoslahti, *Adv. Drug Delivery Rev.*, 2017, **110**, 3–12; (*c*) N. Rammohan, R. J. Holbrook, M. W. Rotz, K. W. MacRenaris, A. T. Preslar, C. E. Carney, V. Reichova and T. J. Meade, *Bioconjugate Chem.*, 2017, **28**, 153–160; (*d*) S. Behzadi, V. Serpooshan, W. Tao, M. A. Hamaly, M. Y. Alkawareek, E. C. Dreaden, D. Brown, A. M. Alkilany, O. C. Farokhzad and M. Mahmoudi, *Chem. Soc. Rev.*, 2017, **46**, 4218–4244; (*e*) A. Verma and F. Stellacci, *Small*, 2010, **6**, 12–21; (*f*) H. Y. Chiu, W. Deng, H. Engelke, J. Helma, H. Leonhardt and T. Bein, *Sci. Rep.*, 2015, **6**, 25019.

24 (*a*) S. L. C. Pinho, J. Sereno, A. J. Abrunhosa, M. H. Delville, J. Rocha, L. D. Carlos and C. F. G. C. Geraldes, *Inorg. Chem.*, 2019, **58**, 16618–16628; (*b*) H. Yan, Y. You, X. Li, L. Liu, F. Guo, Q. Zhang, D. Liu, Y. Tong, S. Ding and J. Wang, *Front. Pharmacol.*, 2020, **11**, 898; (*c*) D. Lalli, G. Ferrauto, E. Terreno, F. Carniato and M. Botta, *J. Mater. Chem. B*, 2021, **9**, 8994–9004; (*d*) A. Yildirim, E. Ozgur and M. Bayindir, *J. Mater. Chem. B*, 2013, **1**, 1909–1920.

25 D. M. Corsi, C. Platas-Iglesias, H. Bekkum and J. A. Peters, *Magn. Reson. Chem.*, 2001, **39**, 723–726.

Journal of Materials Chemistry B

ROYAL SOCIETY OF CHEMISTRY

PAPER

View Article Online
View Journal | View Issue

Cite this: J. Mater. Chem. B, 2023, 11, 8251

Mn(II) complex impregnated porous silica nanoparticles as Zn(II)-responsive "Smart" MRI contrast agent for pancreas imaging†

Riya Mallik,[a] Muktashree Saha,[b] Vandna Singh,[c] Hari Mohan,[c] S. Senthil Kumaran[d] and Chandan Mukherjee*[a]

Received 5th June 2023,
Accepted 31st July 2023

DOI: 10.1039/d3tb01289a

rsc.li/materials-b

Type-1 and type-2 diabetes mellitus are metabolic disorders governed by the functional efficiency of pancreatic β-cells. The activities of the cells toward insulin production, storage, and secretion are accompanied by Zn(II) ions. Thus, for non-invasive pathology of the cell, developing Zn(II) ion-responsive MRI-contrast agents has earned considerable interest. In this report, we have synthesized a seven-coordinate, mono(aquated) Mn(II) complex (**1**), which is impregnated within a porous silica nanosphere of size 13.2 nm to engender the Mn(II)-based MRI contrast agent, complex **1**@SiO_2NP. The surface functionalization of the nanosphere by the Py_2Pic organic moiety for the selective binding of Zn(II)-ions yields complex **1**@SiO_2-Py_2PicNP, which exhibits r_1 = 13.19 mM^{-1} s^{-1}. The relaxivity value elevates to 20.38 mM^{-1} s^{-1} in the presence of 0.6 mM BSA protein at pH 7.4. Gratifyingly, r_1 increases linearly with the increase of Zn(II) ion concentration and reaches 39.01 mM^{-1} s^{-1} in the presence of a 40 fold excess of the ions. Thus, Zn(II)-responsive contrast enhancement *in vivo* is envisaged by employing the nanoparticle. Indeed, a contrast enhancement in the pancreas is observed when complex **1**@SiO_2-Py_2PicNP and a glucose stimulus are administered in fasted healthy C57BL/6 mice at 7 T.

Introduction

Magnetic resonance imaging (MRI) has already been established as an indispensable diagnostic modality for the early-stage detection of many diseases.[1–6] However, the imaging process is limited by its low sensitivity due to its NMR-based operational technique. The administration of a paramagnetic species (approximately 0.1 mmol kg^{-1}), which is known as a contrast agent, has been recognized to mitigate the low-sensitivity issue by producing conspicuous images in a relatively shorter measurement period.[7–11] In fact, nowadays, about 40% of MR imaging is accompanied by a contrast agent. Although several Gd(III)-based small molecules have been clinically approved as MRI contrast agents, the prolonged retention of the Gd(III) ions in the central nervous system and ion-aggravated nephrogenic systemic fibrosis (NSF) in patients with renal impairment have switched attention to Mn(II) complexes.[12–17] Furthermore, the Gd(III)-based contrast agents are primarily nonspecific and the observed signal is solely due to the distribution of the contrast agent across the body.[18–20] Hence, developing non-gadolinium-based, organ-specific and bio-responsive contrast agents through pH, enzyme action, temperature, and ion reflux has drawn paramount attention for better diagnosis of lesions and for non-invasive pathology.[21–24]

Blood glucose level is one of the factors that control the normal functionality of the human body.[25] The pancreas, a vital gland nestled behind the stomach, secrets glucagon and insulin hormones into the blood to maintain glucose levels.[26–28] In pancreatic β-cells, present in the islets of Langerhans along with four other types of cells (α-cells, δ-cells, γ-cells, and ε-cells), Zn(II) ions participate in the synthesis and storage of insulin as Zn(II)-insulin (2 : 6) hexamer crystals in the secretory granules.[29–31] Hence, normal β-cells have relatively high Zn(II) content. At a higher glucose level in the blood, insulin, along with Zn(II) ions, is secreted from the cells. Consequently, the concentration of Zn(II) ions across the extracellular space increases from 40 μM to 500 μM.[32] Hence, Zn(II) ion concentration-dependent contrast enhancement as a whole or as "hot spots" would reveal the pathological condition of the pancreas and/or the β-cells.[33–35]

[a] Department of Chemistry, Indian Institute of Technology Guwahati, Guwahati, 781039 Assam, India. E-mail: cmukherjee@iitg.ac.in
[b] Department of Biosciences and Bioengineering, Indian Institute of Technology Guwahati, Guwahati 781039, Assam, India
[c] Department of Medical Biotechnology, Maharshi Dayanand University, Rohtak, 124001, Haryana, India
[d] Department of NMR, All India Institute of Medical Sciences, Ansari Nagar, 110029, New Delhi, India

† Electronic supplementary information (ESI) available. CCDC 2260190. For ESI and crystallographic data in CIF or other electronic format see DOI: https://doi.org/10.1039/d3tb01289a

The association of the co-released free Zn(II) ions within a contrast agent in the presence of human serum albumin (HSA) protein has thus been considered when developing Zn(II)-responsive contrast agents for the pancreas by engendering a slowly rotating ternary system.[36–39] Although some Gd(III)-based Zn(II)-responsive contrast agents have been reported in the literature,[40–47] Mn(II)-based contrast agents are scarce.[48,49] In the recent past, Sherry and colleagues have reported a Zn(II) ion-responsive contrast agent by implanting a BPEN [BPEN = *N*,*N*-bis(2-pyridinylmethyl)-1,2-ethanediamine] tether unit with an acyclic PyC3A (PyC3A = *N*-picolyl-*N*,*N*′,*N*′-*trans*-l,2-cyclohexylenediaminetriacetate) ligand in the $[Mn^{II}PyC3A(OH_2)]^-$ complex that provides glucose-stimulated contrast enhancement in the pancreas and prostate.[48] However, Mn(II)-based contrast agents with high thermodynamic stability and kinetic inertness along with high relaxivity values are scarce. As attaining high kinetic inertness in acyclic ligand-based Mn(II) complexes remains a significant challenge, Mn(II) complexes with macrocyclic ligands imparting high thermodynamic stability and large relaxivity values are rare.[50–53] Furthermore, the core structural modification scope for the macrocyclic ligands is limited.

In this context, we envisaged encapsulating thermodynamically stable Mn(II)-complex molecules in a porous silica nanoparticle. Silica nanoparticles (NPs) are biogenic and their porous nature permits free access to water molecules within the nanoparticles. Furthermore, the silica core will protect the incorporated Mn(II)-complex molecules from exposure to other external metal ions, *e.g.*, Zn(II), Cu(II), *etc.* Hence, the kinetic inertness can be retained. Incorporating Mn(II)-complex molecules within the core of nanoparticles also restricts their molecular free rotation. Thus, the rotational correlation time (τ_R) is expected to increase, leading to a higher relaxivity value.

Herein, we synthesized the hexadentate ligand H_2AlcDPA. The ligand, upon complexation with Mn(II) ions, engendered the corresponding neutral, mono(aquated) Mn(II) complex $[Mn^{II}(AlcDPA)(OH_2)]^0$ (complex **1**) with a thermodynamic stability constant of $\log K_{MnL}$ = 15.06 (p_{Mn} = 9.56). Impregnation of the complex molecules within a porous silica nanoparticle of size 13.2 nm rendered complex **1**@SiO_2. Gratifyingly, a 4.6-fold enhancement in the longitudinal relaxivity (r_1) value, from 2.86 mM^{-1} s^{-1} (complex **1**) to 13.27 mM^{-1} s^{-1} (complex **1**@SiO_2), was realized at 1.41 T, 37 °C, and pH ∼ 7.4. To promote the synthesized contrast agent as a Zn(II)-responsive "smart" contrast agent, the outer surface of the nanoparticle was functionalized with Py_2Pic [Py_2Pic = 6-((bis(pyridin-2-ylmethyl)amino)methyl)picolinamide] units. The generated complex **1**@SiO_2-Py_2Pic nanoparticle [complex **1**@SiO_2-Py_2PicNP] exhibited r_1 = 13.19 mM^{-1} s^{-1} which increased to 20.38 mM^{-1} s^{-1} in the presence of 0.6 mM bovine serum albumin (BSA) protein at pH 7.4. A further amplification in the value to 39.01 mM^{-1} s^{-1} was noticed in the presence of 40 equivalent amounts of Zn(II) ions (w.r.t. [MnII]). Thus, Zn(II)-responsive contrast enhancement is expected to be realized in the presence of serum albumin protein in humans. Indeed, a brightness enhancement in the pancreas was noticed when the contrast agent and glucose solutions were administered intraperitoneally in fasted healthy C57BL/6 mice at 7 T, as discussed herein.

Results and discussion

Ligand H_2AlcDPA·HCl was synthesized in an overall 46% yield by substituting both the amine-H atoms of (*S*)-(+)-2-amino-1-propanol with 6-(methylene)picolinic acid units (Scheme 1 and Fig. S1–S4, ESI†). The ligand, upon reacting with an equivalent amount of $MnCl_2·4H_2O$ in water at pH ∼ 6.5 provided complex **1** (yield = 64%, Fig. S5 and S6, ESI†). The anchoring ligand 6-((bis(pyridin-2-ylmethyl)amino)methyl)picolinic acid [HPy_2Pic] was synthesized as described in Scheme 2 (Fig. S7–S10, ESI†).[54] Di-(2-picolyl)amine in acetonitrile was heated with one equivalent of 6-(bromomethyl)picolinate in the presence of K_2CO_3 to provide compound **A**. The hydrolysis of compound **A** in LiOH solution followed by acidification with HPF_6 gave HPy_2Pic·HPF_6 salt in 78% yield. Detailed synthetic procedures are provided in the experimental section.

Single crystal X-ray diffraction was carried out for the complex at 298 K to evaluate the geometry and the metal ion–ligand coordination motif. The complex crystallized in the monoclinic space group *P*21. The ORTEP diagram is presented in Scheme 1. Selected bond distances and bond angles are provided in the ESI,† Table S1. In the complex, the central Mn atom was seven-coordinate, where the pentagonal basal plane was comprised of the amide N atom and two N atoms and two O atoms from the two picolinate units. A chloride atom and the alcoholic O atom of the propanol unit occupied the axial positions. The

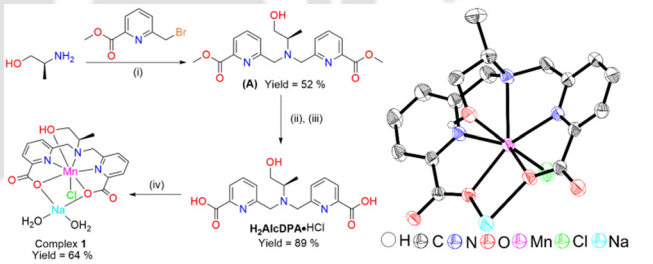

Scheme 1 (A) Synthetic pathway for the preparation of ligand H_2AlcDPA·HCl and its corresponding Mn(II) complex, complex **1**. [(i) THF, Et_3N; (ii) LiOH in THF/H_2O (3 : 1); (iii) 1 M HCl, MeOH; (iv) $MnCl_2·4H_2O$, H_2O, pH ∼ 6.5]. (B) ORTEP representation of complex **1** drawn at 40% probability.

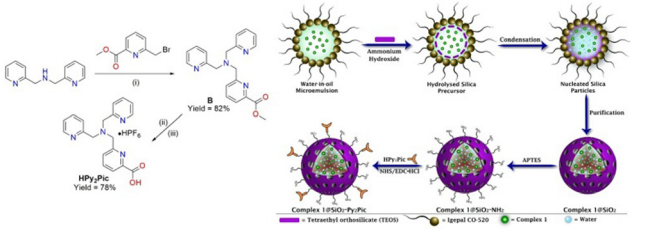

Scheme 2 (A) Synthetic route for the preparation of ligand HPy_2Pic·HPF_6, [(i) CH_3CN, K_2CO_3; (ii) LiOH in THF/H_2O (3 : 1); (iii) HPF_6, ^{i}PrOH]. (B) Representative illustration for the preparation of complex **1**@SiO_2-NH_2NP and complex **1**@SiO_2-Py_2PicNP.

$Mn–N1_{Py}$ = 2.276(2), $Mn–N3_{Py}$ = 2.251(2), $Mn–N2_{Amide}$ = 2.540(2), $Mn–O2_{acid}$ = 2.256(2) and $Mn–O4_{acid}$ = 2.261(2) Å bond distances were commensurate with previously reported Mn(II) complexes with similar ligands.[55,56] Thus, in complex **1**, the Mn atom was in the +2 oxidation state. The complex core was mononegative in charge due to the presence of the coordinated chloride ion. A sodium ion was present as the counter cation.

The electrospray ionization mass spectrum (ESI-MS) of complex **1** was recorded in the positive mode in water, providing a 100% molecular ion peak at m/z = 398.99 (Fig. S6, ESI†). The peak corresponded to $[(M–Cl) + H]^+$, where M–Cl = $C_{17}H_{17}N_3O_5Mn$, which is the molecular composition of the complex core. The appearance of the mass peak in the positive mode indicated the chloride ion disintegration from the complex core in water. Therefore, water molecules are expected to interact with the Mn(II) ion at the same position as that occupied by the chloride ion in the molecular structure of the complex.

The stability constant of complex **1** was determined by the potentiometric titration method. In this regard, the potentiometric titrations were carried out with bare ligand H_2AlcDPA and 1 : 1 ligand:$MnCl_2$ solutions at 25 °C in 0.15 M NaCl. The stepwise protonation constant values[57] for the ligand were found to be $\log K_1^H$ = 7.69(3) and $\log K_2^H$ = 3.75(2). The highest pKa value was ascribed to the tertiary nitrogen unit and the pK_a = 3.75 was due to the carboxylic group of a picolinate moiety. The thermodynamic stability constant[58] ($\log K_{MnL}$) of the complex was determined to be 15.06 (Table S2 and Fig. S11, ESI†). Noteworthily, the stability constant of complex **1** was in line with those of $[Mn^{II}PyC3A(OH_2)]^-$ = 14.14 and [Mn(PC2A-DPA)] = 15.87.[49,50] Hence, a thermodynamically stable complex was created by the coordination of the $[AlcDPA]^{2-}$ ligand.

Prior to the incubation of complex **1** within the porous silica nanoparticle (NP), the stability of the complex was evaluated under the condition of nanoparticle synthesis. In this context, the UV-Vis spectra of complex **1** were recorded at pH ~7.4 and ~10.1 (Fig. S13, ESI†). No appreciable change in the spectral features was noticed. Thus, no impairment of the complex during nanoparticle formation was anticipated. A reverse microemulsion method was then followed to create complex **1**@SiO_2NP (Scheme 2). In the presence of Igepal-CO-520 surfactant solution in cyclohexane, aqueous complex **1** was added dropwise, forming a stable water-in-oil reverse microemulsion. Tetraethyl orthosilicate (TEOS) was added afterward and was hydrolysed by ammonium hydroxide to form the silica outer nanosphere. (3-Aminopropyl)triethoxysilane (APTES) was added at this point for further amine-functionalization of the silica-surfaced hydroxide units. Surfactant removal finally produced the complex **1** confined amine surface-functionalized porous silica nanoparticle, complex **1**@SiO_2-NH_2NP. Afterward, the HPy_2Pic ligand was combined with the amine unit by amide bond formation, promoted by the 1-(3-dimethylaminopropyl)-3-ethyl carbodiimide (EDC) and *N*-hydroxysuccinimide (NHS) activators, to engender the surface modified complex **1**@SiO_2-Py_2PicNP (Scheme 2).

Spherical and monodispersed nanoparticles of complex **1**@SiO_2-NH_2 and complex **1**@SiO_2-Py_2Pic with respective sizes of 14.05 nm and 14.95 nm were examined using field emission transmission electron microscopy (FETEM) images (Table 1 and Fig. 1(A), (B)). Energy-dispersive X-ray spectroscopy (EDS) analysis on the synthesized nanomaterials demonstrated the presence of Mn, N, Cl, and Si atoms (Fig. S14 and S15, ESI†). Hence, the study confirmed the confinement of complex **1**-molecules within the nanospheres. To buttress the confinement, X-band EPR spectra of the dried complex **1**@SiO_2-NH_2 and complex **1**@SiO_2-Py_2Pic nanomaterials were compared with that of complex **1**. All the spectra exhibited a similar broad

Table 1 Characterization of complex **1**@SiO_2, complex **1**@SiO_2-NH_2, and complex **1**@SiO_2-Py_2Pic nanomaterials: corresponding FE-TEM particle size, zeta potential values (at pH 7.4), percentage organic weight loss and longitudinal relaxivity values measured at 37 °C, pH ~ 7.4, 1.41 T

Material	Particle size (nm)	ζ potential (mV)	TGA, weight loss %	r_1 (mM^{-1} s^{-1})
Complex **1** @SiO_2	13.22	−21.3	6.39	13.27
Complex **1** @SiO_2-NH_2	14.05	22.5	15.75	12.19
Complex **1** @SiO_2-Py_2Pic	14.95	16.6	20.73	13.19

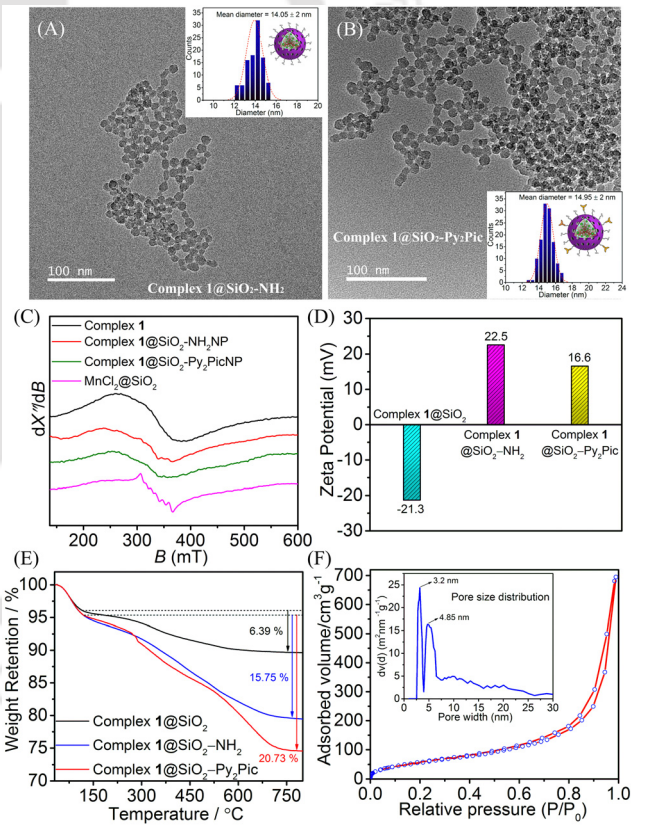

Fig. 1 Representative FETEM images of (A) complex **1**@SiO_2-NH_2NP and (B) complex **1**@SiO_2-Py_2PicNP; inset: corresponding particle size distributions. (C) X-band EPR spectra of complex **1**, complex **1**@SiO_2-NH_2, complex **1**@SiO_2-Py_2Pic and $MnCl_2$@SiO_2 measured in solid state at room temperature, power = 0.995 mW, modulation frequency = 100 kHz, and modulation amplitude = 100 G. (D) Zeta potentials [measured at pH ~ 7.4] and (E) TGA analysis spectra of complex **1**@SiO_2NP, complex **1**@SiO_2-NH_2NP, and complex **1**@SiO_2-Py_2PicNP. (F) Nitrogen adsorption–desorption isotherm and pore size distribution (inset) of complex **1**@SiO_2-Py_2PicNP.

signal, verifying the existence of incorporated complex **1**-molecules within the nanomaterials (Fig. 1(C)). Note that the X-band EPR spectral envelope differed significantly compared to that of bare $MnCl_2$ solution-doped SiO_2 nanoparticles prepared by the identical method (Fig. 1(C), pink line).

To further support the incorporation, infrared (IR) spectra of complex **1**@SiO_2 (prepared by omitting the addition of APTES), complex **1**, and pristine silica NPs were compared. In the complex **1**@SiO_2 IR spectrum, low-intensity bands at 1694, 1578, 1444, and 1400 cm^{-1} appeared which were also present in the IR spectrum of complex **1** (Fig. S16A and B, ESI†). Thus, we inferred the inclusion of complex **1**-molecules within the nanoparticle. The presence of the additional broad band at 3321 cm^{-1} due to ν_{N-H} stretching and the moderate peak at 1559 cm^{-1} because of ν_{N-H} bending confirmed the formation of complex **1**@SiO_2-NH_2NP (Fig. S16C, ESI†). The appearance of additional peaks in the 1665–1619 cm^{-1} region ascertained the conjugation of the Py_2Pic moiety with the amine group, resulting in the amide linkage (Fig. S16D, ESI†).

The surface modification was further examined by determining the change in the zeta (ζ) potential profile of each nanomaterial in a buffered solution at pH ~7.4 (Table 1 and Fig. 1(D)). Complex **1**@SiO_2 exhibited a strongly negative ζ potential value (−21.3 mV) due to the presence of –OH functional groups at the surface of the NP. Upon functionalization with the highly basic amino group, an inversion of ζ potential value to 22.5 mV was noticed. The value diminished moderately to 16.6 mV upon Py_2Pic conjugation with some of the amino groups.

Thermogravimetric analyses (TGA) of the three different nanomaterials were performed to discover the organic loading percentage (Fig. 1(E)) on the outer surface. A steep increase in weight loss from 6.39% in complex **1**@SiO_2 to 15.75% in complex **1**@SiO_2-NH_2 was observed above 120 °C. This feature implied the inclusion of APTES units on the silica surface. The percent of weight loss further increased by 5 units in the case of complex **1**@SiO_2-Py_2PicNP, suggesting the successful inclusion of Py_2Pic units.

The N_2 adsorption–desorption isotherm was recorded at 77 K to evaluate the porous nature of the silica nanosphere in complex **1**@SiO_2-Py_2PicNP. A type-IV isotherm was seen, typical for porous silica nanoparticles (Fig. 1(F)).[59] The overall surface area of the nanoparticle was 219.48 m^2 g^{-1}. The pore size distribution, derived by the Barrett–Joyner–Halenda (BJH) method, showed the presence of two different sizes of pores: 3.2 nm and 4.85 nm. The larger pores might be because of inter-particle voids.[60] To evaluate the free access of water molecules across the pores, complex **1**@SiO_2-Py_2PicNP was suspended in H_2O for 48 hours in the presence of 0.6 mM BSA and 40 equivalent amounts of Zn(II) ions and then lyophilized for 24 hours to isolate the dry complex **1**@SiO_2@Py_2-PicNP·BSA·Zn ternary system (*vide infra*). A portion of the isolated system was again immersed in D_2O for 48 hours. After lyophilization for 24 hours, the dried nanoparticles were isolated. The IR spectral comparison of the isolated particles from H_2O and D_2O media revealed the appearance of additional $\nu_{(O-D)}$ asymmetric stretching in 2400–2500 cm^{-1} region in the presence of D_2O, indicating the existence of the molecules inside the nanoparticle (Fig. S17, ESI†). Therefore, IR spectral analyses confirmed the accessibility of outside water molecules across the nanopores.

The longitudinal relaxivity (r_1) value of complex **1** was determined to be 2.86 mM^{-1} s^{-1} at 1.41 T, 37 °C, and pH ~7.4. The value increased to 13.27 mM^{-1} s^{-1} in complex **1**@SiO_2NP (Table 1). This result implied that the rotational correlation time (τ_R) of the impregnated complex **1** molecules (about 34 molecules per nanosphere; calculation provided in ESI,† eqn (S1)) increased upon confinement. Note that a similar observation has already been made previously.[55] Notwithstanding, the surface functionalization of complex **1**@SiO_2NP either with APTES or APTES-Py_2Pic imparted no appreciable changes in the relaxivity value (Table 1 and Fig. S18, ESI†), indicating that the increase in the weight of the nanoparticles by means of the outer sphere surface functionalization did not exert any profound effect on the τ_R of the incubated complex **1** molecules.

Gratifyingly, a 53% increase in the relaxivity value to r_1 = 20.38 mM^{-1} s^{-1} occurred in the presence of 0.6 mM BSA at 1.41 *T*, 37 °C, and pH ~ 7.4, suggesting a considerable interaction between the nanoparticle and the negatively charged serum albumin protein to engender a slowly rotating binary system (Fig. 2(B), (C) and Fig. S21, ESI†). The change in the ζ potential value from 16.6 mV to −11.4 mV proved the substantial electrostatic and non-covalent interactions of the negatively charged serum albumin protein with the nanoparticle, forming a corona (Fig. S22 and Table S3, ESI†). The thermogravimetric weight loss analyses of complex **1**@SiO_2-Py_2PicNP (Fig. S23A, ESI†) in the absence and presence of BSA

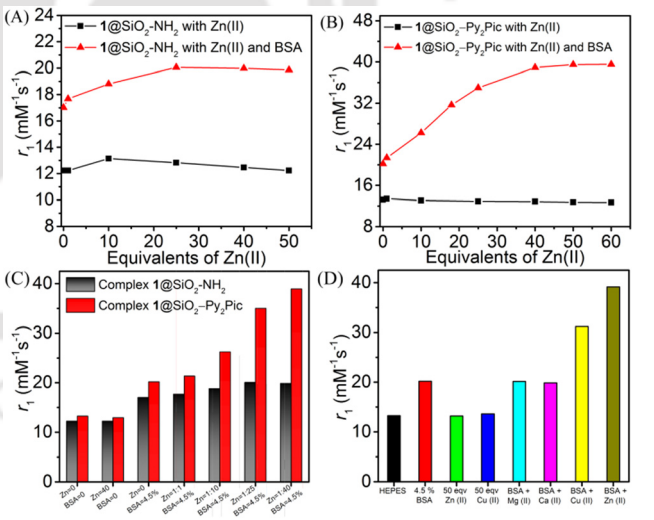

Fig. 2 Relaxometric titrations for (A) complex **1**@SiO_2-NH_2 and (B) complex **1**@SiO_2-Py_2Pic suspensions, [Mn(II)] = 0.1 mM, as a function of increasing Zn(II) ions, w.r.t. [Mn(II)] with or without bovine serum albumin (constant concentration of 0.6 mM). (C) Comparative representation of the r_1 values for complex **1**@SiO_2-NH_2NPs and complex **1**@SiO_2-Py_2PicNPs in different mediums. (D) r_1 value for complex **1**@SiO_2-Py_2PicNPs suspended in an aqueous medium containing 50 equivalent excesses of Zn(II), Cu(II), Mg(II), and Ca(II) ions, in the absence and presence of 0.6 mM BSA. Experiments were done with nanoparticle suspensions containing [Mn(II)] = 0.1 mM at pH ~7.4, 1.41 T, and 37 °C.

Table 2 Relaxivity values for complex **1**@SiO_2-NH_2NP and complex **1**@SiO_2-Py_2PicNP in the absence and presence of Zn(II) ions/serum albumin

	r_1 (mM^{-1} s^{-1}), at pH ~7.4, 1.41 T, and 37 °C			
Nanomaterial type	(−) Zn(II)	(+) Zn(II)	(+) 0.6 mM BSA	(+) 0.6 mM BSA (+) Zn(II)
Complex **1**@SiO_2-NH_2	12.19	12.25	17.02	19.85
Complex **1**@SiO_2-Py_2Pic	13.19	12.92	20.38	39.01

Each relaxivity value was obtained from $1/T_1$ *versus* [Mn(II)] ([Mn(II)] = 0.02, 0.04, 0.08, 0.10 mM) plots with samples suspended in different mediums, as mentioned. [Zn(II)] was maintained at a 40 equivalent excess amount with respect to Mn(II) concentration.

exhibited about 19% more weight loss for the nanoparticle isolated after the interactions with BSA and proved the corona formation. Akin to complex **1**@SiO_2-Py_2PicNP, an increase of r_1 relaxivity to 17.02 mM^{-1} s^{-1} from 12.19 mM^{-1} s^{-1}, *i.e.*, about 40%, in complex **1**@SiO_2-NH_2NP (Fig. 2(A), (C) and Table 2) was also found in the presence of 0.6 mM BSA at 1.41 T, 37 °C, and pH ~7.4. The TGA showed about 18% more weight loss for the BSA-interacting complex **1**@SiO_2-NH_2NP than for the pristine nanoparticle (Fig. S23B, ESI†). Therefore, almost the same loading of BSA onto both nanoparticles was accounted for. The higher relaxivity value for complex **1**@SiO_2-Py_2PicNP in the presence of BSA thus suggested superior interaction between the BSA and the nanoparticle which materialized due to the existence of the Py_2Pic units.

Unlike in complex **1**@SiO_2-NH_2NP, a discernible and gradual augmentation in r_1 relaxivity was noticed in complex **1**@SiO_2-Py_2PicNP with successive elevation of the concentration of Zn(II) ions in HEPES buffer at pH 7.4; it reached a constant value of r_1 = 39.01 mM^{-1} s^{-1} in the presence of 40 equivalent amounts of the ion (Fig. 2(B) and Table 2). Hence, the presence of the surface-bound Py_2Pic unit reinforced the interaction of the nanoparticle with BSA in the presence of Zn(II) ions. To further investigate the interaction phenomenon, the nanoparticle [0.1 mM Mn(II) concentration] was added to a solution premixed with 0.6 mM BSA protein and 4 mM Zn(II) ions (40 equiv. excess w.r.t [Mn(II)]) at pH 7.4. In this case, the relaxivity value was found to be 46.3 mM^{-1} s^{-1}. Thus, better interaction between the nanoparticle and Zn(II)-interacting BSA compared to the BSA-interacting nanoparticle with Zn(II) ions was shown.

Fluorescence quenching experiments were also conducted to evaluate the nature of the interactions between serum albumin protein and complex **1**@SiO_2-Py_2PicNP (Fig. S24, ESI†).[61] To an aqueous 16 μM solution of BSA, an increasing concentration of the nanoparticle (0 to 0.4 μM) was added. It was noticed that the quenching was expedited with the increase of concentration (K_{SV} = 3.5 × 10^5 M^{-1}, K_q = 6.03 × 10^{13} M^{-1} s^{-1}, K_a = 2.9 × 10^5 M^{-1}; Fig. S24, and Table S3, ESI†). Interestingly, the quenching process was further boosted in the presence of 40 equivalent amounts of Zn(II) ions (K_{SV} = 6.1 × 10^5 M^{-1}, K_q = 10.5 × 10^{13} M^{-1} s^{-1}, K_a = 5.4 × 10^5 M^{-1}; Table S3, ESI†), suggesting that the ion promoted higher interaction between the nanoparticle and the protein. The K_q value provides information on the nature and strength of the interactions. For a dynamic interaction, the value is below 2 × 10^{12} M^{-1} s^{-1}, while a K_q greater than 2 × 10^{12} M^{-1} s^{-1} refers to a static interaction. Herein, the high K_q = 6.03 × 10^{13} M^{-1} s^{-1} emphasized a static interaction between complex **1**@SiO_2-Py_2PicNP and BSA. The interaction further escalated in the presence of Zn(II) ions (K_q = 10.5 × 10^{13}), proving a higher static interaction. The quenching experiments justified the uplift of r_1 relaxivity *via* the formation of a slowly rotating system in the presence of Zn(II) ions.

In complex **1**@SiO_2-Py_2PicNP, no alteration in the relaxivity (13.19 mM^{-1} s^{-1}) was realized in the pH range 4–8 in the presence of 50 equivalent amounts of Zn(II) and Cu(II) ions or 200 fold excess of the biologically relevant anions citrate, biphosphate, and bicarbonate (Fig. 2(D) and Fig. S18–S20, ESI†). Furthermore, the kinetic inertness of the synthesized nanomaterial complex **1**@SiO_2-Py_2Pic was evaluated against 40 fold excess Zn(II) ions at pH ~ 6.0, 1.41 T, and 37 °C. The synthesized nanomaterial with a positively charged surface (ζ = +16.6 mV) showed efficient inertness towards Zn(II) ions, as only a ~3% decrease in r_1 value was observed after 24 hours (Fig. S20, ESI†). This minute change could be ascribed to spontaneous coagulation of the nanoparticles with time, leading to a lowered accessibility of water molecules towards the core, as previously reported for a similar nanomaterial.[55] Thus, it is expected that the contrast efficiency of the nanoparticle *in vivo* would not be hampered due to the presence of the cations and anions prevalent in the human body.

In order to find out the ion selectivity in the presence of BSA, complex **1**@SiO_2-Py_2PicNP and 0.6 mM BSA were allowed to interact with a 50-fold excess of the biologically relevant metal ions Ca(II), Mg(II), and Cu(II) at 1.41 T, 37 °C, and pH ~7.4 (Fig. 2(D)). While no alteration in the relaxivity was noticed in the presence of Ca(II) and Mg(II) ions, amplification in the relaxivity value to r_1 = 31.17 mM^{-1} s^{-1} was realized in the presence of 40 equivalent amounts of Cu(II) ions (w.r.t [Mn(II)]). Firstly, the concentration of free Cu(II) ions is lower than that of Zn(II) in the extracellular space.[62,63] Secondly, the relaxivity enhancement was lower than that for Zn(II) ions. Hence, the prepared complex **1**@SiO_2-Py_2PicNP can be utilized as a promising Zn(II) ion-selective biomarker.

To shed light on the contrast ability of complex **1**@SiO_2-Py_2PicNP in the presence of BSA and Zn(II) ions *in vitro*, phantom images were recorded using a MAGNETOM Avanto 1.5 T clinical MRI scanner at 25 °C. Herein, the phantoms are micro-centrifuge tubes filled with (1) only complex **1**@SiO_2-Py_2PicNP suspension, (2) complex **1**@SiO_2-Py_2PicNP suspension and 0.6 mM BSA, and (3) complex **1**@SiO_2-Py_2PicNP suspension, 0.6 mM BSA and Zn(II) ions of various concentrations in HEPES buffer at pH 7.4. The observed contrast changes are depicted in Fig. 3(A). The gradual increase in the concentration of complex **1**@SiO_2-Py_2PicNP from 0.1 to 0.3 mM resulted in simultaneously brighter T_1-weighted images. Hence, the nanoparticle can be recognized as a brightening (positive) contrast agent. After adding BSA, about 75% brightness enhancement of 0.1 mM complex **1**@SiO_2-Py_2PicNP suspension was realized (Fig. 3(B)). Gratifyingly, the successive increase in Zn(II) ion concentration

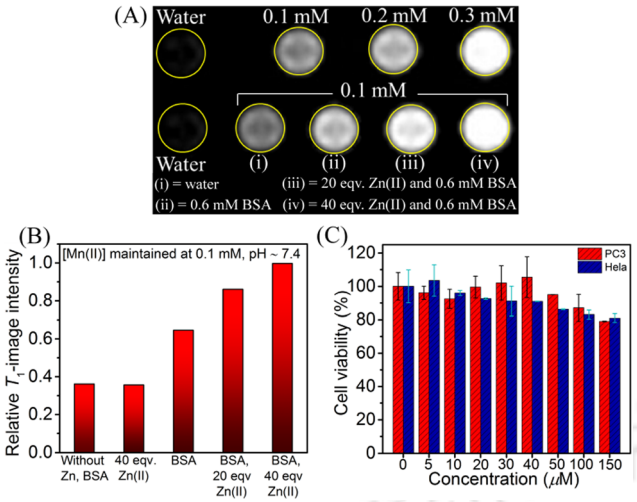

Fig. 3 *In vitro* studies of complex **1**@SiO_2-Py_2PicNPs. (A) T_1-weighted phantom MR images of micro-centrifuge tubes containing different concentrations of complex **1**@SiO_2-Py_2PicNPs (top). At the bottom, complex **1**@SiO_2-Py_2PicNPs, 0.1 mM [Mn(II)], was suspended in different mediums. (B) Respective MR-image intensity plots using ImageJ software. (C) % cell viability of HeLa and PC3 cell-lines after 48 hours of treatment with increasing concentrations of complex **1**@SiO_2-Py_2PicNPs. All the concentrations are represented in terms of Mn(II) ions. MR images were recorded at 1.5 T, 25 °C.

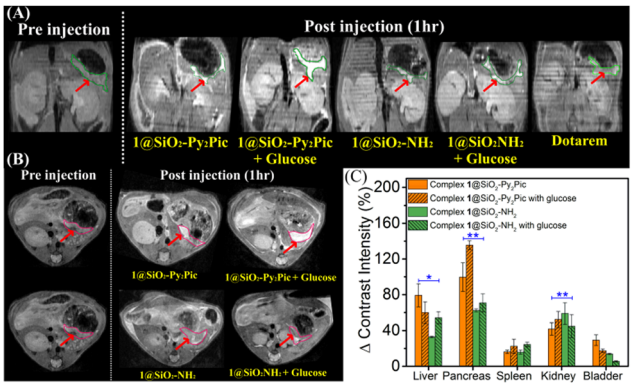

Fig. 4 (A) Coronal view and (B) axial view of T_1-weighted MR images of 12-hour fasted C57BL/6 mice, before and 1 hour after i.p. administration of complex **1**@SiO_2-NH_2 or complex **1**@SiO_2-Py_2Pic (10 μmol kg^{-1} w.r.t [MnII]), without or with single bolus (i.p.) of 2.2 mmol kg^{-1} D-glucose (given 45 min after contrast injection) in 7 T animal MR scanner. The red arrow marks the pancreatic region. Dotarem was injected at the same dosage, along with a glucose bolus. (C) Quantitative image analysis measuring signal intensity changes in each organ post-injection, normalized to the muscle (n = 3 animal per group). Bars represent the standard error of the mean. *$P < 0.05$, **$P < 0.001$.

in the BSA-containing solution gradually amplified the image brightness. Thus, the relaxivity boosting in the presence of BSA and Zn(II) ions was also recognized in the *in vitro* phantom MR images.

Prior to *in vivo* administration, the biocompatibility of complex 1@SiO_2-Py_2PicNPs was examined in PC3 and HeLa cells by performing a MTT assay. In the studies, cells were incubated for 48 hours with increasing concentrations of the nanoparticle up to 150 μM (Fig. 3(C)). About 80% cell viability was realized at the 150 μM concentration for both types of cells, emphasizing the biocompatibility of the nanoparticle.

Based on the aforementioned *in vitro* experimental results (Fig. 3), we attempted to emulate the Zn(II) ion-driven contrast enhancement in the pancreas in the presence of a glucose bolus in the biological system.[48] The *in vivo* MR imaging was recorded on a batch of C57BL/6 mice at 7 T. In separate experiments, a bolus of complex **1**@SiO_2-Py_2PicNP (10 μmol kg^{-1} w.r.t. [Mn(II)]) was injected into the intraperitoneal (i.p.) space with and without the presence of glucose (2.2 mmol kg^{-1}) in mice fasted for 12 hours. In the experiment with glucose, the glucose bolus was injected 45 minutes after the initial complex **1**@SiO_2-Py_2PicNPs injection. T_1-weighted MR images in coronal and axial views (1 hour post complex **1**@SiO_2-Py_2PicNPs injection or 15 min post glucose injection) are presented in Fig. 4.

The contrast enhancement in the pancreas almost doubled (ΔCNR ~ 100%) compared to the pre-injection MR image in the presence of complex **1**@SiO_2-Py_2PicNP 1 hour after the bolus injection. However, in the presence of glucose, a substantial contrast enhancement (ΔCNR ~ 138%) was realized, supporting the interaction of the contrast agent with the secreted Zn(II) ions (Fig. 4(C)) in the presence of HSA, forming the complex **1**@SiO_2-Py_2PicNPs·HSA·Zn(II) ternary complex. Further elucidation of Zn(II) ion secretion and the contrast enhancement due to entrapment of the ion within the complex **1**@SiO_2-Py_2PicNP·HSA binary system appeared when complex **1**@SiO_2-NH_2NP, which has already been recognized to promote a little r_1 relaxivity enhancement *in vitro* in the presence of Zn(II) ions (*vide supra*), was investigated under the same experimental conditions. A subtle contrast enhancement (~8%) was realized in this case (Fig. 4(C)) and the finding solidified the effectiveness of complex **1**@SiO_2-Py_2PicNP binding with HSA and Zn(II) ions *in vivo*. Thus, the porous silica nanoparticle entrapped complex **1** with the Py_2Pic silica-surface-binding unit was successful in engendering a Zn(II) ion-responsive T_1-weighted MRI contrast agent as previously reported by Sherry and coworkers employing the $[Mn^{II}PyC3A\text{-}BPEN(OH_2)]^-$ complex molecule.[48] In the case of the small Mn(II) complex molecule, a maximum of ~55% contrast enhancement was realized. Here, complex **1**@SiO_2-Py_2PicNP could provide ~138% contrast enhancement in an hour due to the formation of a slow-moving system.

The biodistribution of complex **1**@SiO_2-Py_2PicNPs and complex **1**@SiO_2-NH_2NPs without and with the presence of glucose was examined at 1 hour post-injection of the nanoparticles (Fig. S26, ESI†). For this, the liver, pancreas, spleen, muscle, kidney, and bladder were resected and the Mn content was determined by ICP-MS after digestion of the tissues. The presence of the ion in the liver and the kidney reinforced that the nanoparticles are excreted from the body *via* both hepatobiliary (40%) and renal (60%) pathways.[64,65] However, the renal path was more favourable. Further investigations are essential to illuminate the interactions of the nanoparticles with various organs. Note that the mice used in the experiments were monitored further for 15 days after the completion of the *in vivo* experiments. No death or abnormal behaviour was noticed.

Conclusions

To summarize, we successfully synthesized complex **1** and the complex-entrapped surface unfunctionalized and functionalized porous nanoparticles complex **1**@SiO_2, complex **1**@SiO_2-NH_2NP, and complex **1**@SiO_2-Py_2PicNP. It was demonstrated that the presence of Py_2Pic over the nanosphere favoured the interaction of the nanoparticle with serum albumin protein and, selectively, Zn(II) ions. Utilizing the ion-selective property of complex **1**@SiO_2-Py_2PicNP, the T_1-weighted contrast enhancement of the pancreas of healthy C57BL/6 mice was studied employing a clinical MRI scanner at 7 T. Indeed, a 138% contrast enhancement of the organ was recorded in the presence of glucose which stimulated Zn(II) ion secretion. Apart from that, ~52% contrast enhancement was noticed in the kidney and ~60% in the liver (Fig. 4). The biodistribution analysis on Mn(II) ions after tissue digestion suggested that the nanoparticle is excreted from the body through both hepatobiliary and renal pathways. The time-dependent contrast analyses indicated that the nanoparticles are ejected from the body almost entirely in 24 hours (Fig. 4). In short, we report a non-gadolinium-based Mn(II)-complex entrapped silica nanoparticle as an MRI contrast agent that can behave as a ''smart'' contrast agent in the presence of Zn(II) ions.

Experimental section

Materials and methods

All materials and solvents were acquired from commercial sources and were used as supplied, unless noted otherwise. 2,6-Pyridinedicarboxylic acid, 2-picolylamine, 2-pyridinecarboxaldehyde, SeO_2, LiOH, and Igepal-CO-520 were purchased from Aldrich. (*S*)-(+)-2-Amino-1-propanol, $MnCl_2{\cdot}4H_2O$, triethylamine, sodium citrate, $NaHCO_3$, Na_2HPO_4, HNO_3 (69%), NH_4OH, HCl, NaOH, and solvents were obtained from Merck (India). TEOS and APTES were purchased from Alfa Aesar. HEPES and MES buffer were purchased from SRL. *N*-(3-Dimethylaminopropyl)-*N*′-ethylcarbodiimidehydrochloride (EDC·HCl), *N*-hydroxysuccinimide (NHS), albumin bovine fraction V, THF, and cyclohexane were obtained from Spectrochem. Water used for experiments was purified by a Millipore water purifier (MilliQ, Merck).

X-Ray crystallographic data were collected using an Oxford SuperNova diffractometer. The data refinement and cell reductions were carried out in CrysAlisPro.[66] Structures were solved by direct methods using SHELXS-2018.[67] All the non-hydrogen atoms were refined anisotropically. FT-IR spectra were recorded on a PerkinElmer instrument at room temperature in a KBr pellet made by grinding the sample with KBr (IR grade). Mass spectra were obtained from either HRMS or a Q-TOF/MS spectrometer. UV/Vis spectra were obtained on a PerkinElmer Lambda 25 UV/Vis spectrometer. ^{1}H- and ^{13}C-NMR analyses were done using Bruker 400 MHz and 500 MHz NMR machines. Nitrogen sorption isotherms were acquired on a Quantachrome (Model: Autosorb-IQ MP) surface area and pore size analyzer at 77 K. Before the experiment, lyophilized dry samples were degassed at 373 K for 10 h. X-band EPR measurements were performed using a JEOL (Model: JES-FA200) spectrometer. Thermogravimetric analyses (TGA) of lyophilized solid nanomaterials were done using a PerkinElmer TGA 4000. Zeta potential and particle size distribution of all suspended nanomaterials were measured at 25 °C by dynamic light scattering (DLS) using a Malvern ZETASIZER Nano-ZS90 (equilibrium time set to 2 min, 5 measurements taken on each sample set, only quality criteria values accepted). Optimum pH was maintained using buffers. Longitudinal and transverse relaxivity values at 1.41 T were measured using a BRUKER minispec mq60 NMR analyzer. Exact Mn concentrations in different samples were estimated by ICP-MS (Model: Element XR, Thermo Fisher Scientific) and ICP-AES (Model: ARCOS, Simultaneous ICP Spectrometer, SPECTRO Analytical Instruments GmbH, Germany) after treatment of the nanoparticle suspensions with dilute HNO_3 solution.

Potentiometric measurements

Direct pH-potentiometric titrations were employed to determine the protonation constants of the H_2AlcDPA and HPy_2Pic ligands along with the stability constant of the corresponding metal complexes. Each set of experiments was performed at room temperature and a fixed ionic strength of 0.15 M NaCl. For ligand protonation constants, titration was done with 0.001 M ligand solution against standardized 0.1 M NaOH solution as titrant. The stability of complex **1** was obtained by direct pH-potentiometric titration using a 1 : 1 ligand to metal molar ratio. A Metrohm 888 Titrando titration workstation equipped with a Metrohm-6.0259.100 glass electrode was used for titrations in the pH ranges of 2.3–12.0 for H_2AlcDPA and 2.0–12.0 for HPy_2Pic. Extra 0.1 M HCl was added to the starting solution to attain the pH range. Standard pH solutions (pH 4.0, 7.0, and 9.0) were used to calibrate the pH electrode. Titration was done with constant magnetic stirring and argon gas was bubbled to maintain an inert atmosphere throughout the experiment. Equilibrium constants were evaluated from the data obtained by simulating the titration curve using Hyperquad2008 software.

Field emission transmission electronic microscopy (FETEM)

The size and morphology of the complex **1** incorporated nanomaterials (complex **1**@SiO_2-NH_2 and complex **1**@SiO_2-Py_2Pic) were analyzed from transmission electron microscopy (FETEM) images taken on a JEOL Model:2100F electron microscope operated at 200 kV, together with energy-dispersive X-ray spectroscopy (EDS). An ethanolic dilution of 10 μL of each prepared mother suspension was dropped on a carbon-coated copper grid (CARBON FILM 300 MESH, COPPER), kept overnight for drying, and imaged. ImageJ software was employed to calculate particle size distributions from a sample containing at least 100 particles.

Relaxometric analyses

Relaxometric properties (T_1 and T_2) of complex **1** solutions and **1**@SiO_2, **1**@SiO_2-NH_2, and **1**@SiO_2-Py_2Pic suspensions were determined using a BRUKER minispec mq60 NMR analyzer at pH ~7.4, 1.41 T, and 37 °C. Samples of each stock solution

were prepared by digesting solutions/suspensions in nitric acid solution. Clear aliquots were used to measure exact Mn concentrations using ICP-MS and ICP-AES techniques. Plots of relaxation rates ($1/T_1$ and $1/T_2$) *versus* [Mn(II)] gave straight lines, with the slopes representing the respective relaxivity values (r_1).

r_1 values for complex **1**@SiO_2-NH_2 and complex **1**@SiO_2-Py_2Pic suspensions were measured in the presence of bovine serum albumin (BSA) at physiological conditions (pH ~7.4, 310 K, BSA concentration maintained at 4.5% w/v; measured at 1.41 T) or, as mentioned, in the absence and presence of external ions (Zn^{II}, Cu^{II}, Mg^{II}, and Ca^{II}). Samples were incubated at 37 °C for 3 hours before the experiments.

Relaxometric titrations of complex **1**@SiO_2-Py_2PicNP suspension (0.06 mM w.r.t. Mn(II) concentration) in HEPES buffer at pH 7.4 were done with increasing concentrations of BSA, in the absence and presence of 40 equivalents excess of Zn(II) ions (2.4 mM, equal to the highest concentration of BSA). Exponential fits of the corresponding curve gave the r_1^{sat} value.

Kinetic measurements

Kinetic inertness was examined by following the time-dependent r_1 values for 0.1 mM [Mn(II)] complex **1**@SiO_2-Py_2PicNPs suspension at 37 °C and 1.41 T using a BRUKER minispec mq60 NMR analyzer. Zn^{2+} was used as the exchanging ion and was present in 40 equivalents excess to attain a pseudo-first-order condition. Kinetic studies were done at pH ~6.0 and non-coordinating buffer 2-((4-morpholino)ethanesulfonic acid) (MES, pH range 4.7–6.0) was used at 0.01 M concentration to maintain constant pH in the sample. Change in relaxivity was recorded for three days and the percentage change *versus* time was plotted.

Fluorescence measurements

Samples (aqueous suspensions) were recorded on a FluoroMax-4 spectrofluorometer (Horiba) at 25 °C in a rectangular quartz cell with a path of 10 mm. Each set of suspensions was excited at 275 nm, using 5 per 5 nm (excitation/emission) slit widths. Emission spectra were recorded in the 280 to 530 nm range.

MTT assay

Human prostate cancer cells (PC3) and cervical cancer cells (HeLa) were purchased from the National Centre for Cell Science, Pune. All the cell lines were sustained in Dulbecco's modified Eagle's medium (DMEM) supplemented with 10% (v/v) fetal bovine serum (FBS) and 1% penicillin and streptomycin at 37 °C in humidified air containing 5% CO_2. The respective cells were seeded in a 96-well plate at a density of 5 × 103 cells per well and grown overnight in the abovementioned conditions. After 48 h of treatment with increasing concentrations of complex **1**@SiO_2-Py_2PicNPs w.r.t. [Mn(II)], 0.5 mg ml^{-1} of MTT in DMEM was added to each well and incubated for 1.5 h. Thereafter, 150 μl DMSO was added to each well. Absorbance was measured at 570 nm and, after that, cell viability was calculated, assuming 100% viability for untreated cells.

In vitro MR imaging

Phantom MR images were obtained using a clinical MAGNETOM Avanto 1.5 T MRI scanner. For T_1-weighted images, these parameters were adopted: TR (repetition time) = 550 ms, TE (echo time) = 8.4 ms, slice thickness = 2.5 mm, and field of view (FOV) = 175 × 200 mm^2. Increasing concentrations of complex **1**@SiO_2-Py_2PicNP in microcentrifuge tubes were treated as phantoms and scanned for images.

In vivo MR imaging

Healthy C57BL/6 male mice (total number = 30) were purchased from the National Institute of Biologicals (NIB), Noida, Uttar Pradesh (UP), India. They were kept in micro isolator cages at biosafety level 2 in the animal house of Maharshi Dayanand University, Rohtak, India. The experimental protocol was approved by the Institutional Animal Ethical Committee (IAEC), with approval number CAH 201-209 dated 23/10/2017. 12 hour fasted mice were anesthetized with a 1–3% isoflurane/oxygen mixture, maintaining normal respiration and a body temperature of 37 °C. They were subsequently imaged at 7 T using a small bore animal scanner (Biospec 70/20, M/s Bruker Biospin GmBH, Germany). The imaging protocol at baseline was comprised of multislice two-dimensional rapid acquisition with refocused echo (RARE) imaging to delineate anatomy. The imaging parameters were as follows. Coronal orientation: TR/TE = 3647.4 ms/8 ms, field of view (FOV) = 50 × 50 mm, matrix = 256 × 256, slice thickness = 1 mm, 256 slices. Axial orientation: TR/TE = 3647.4 ms/8 ms, matrix = 256 × 256, slice thickness = 1 mm, 84 slices.

Five groups of mice (n = 3/group) were each intraperitoneally administered with (I) 10 μmol kg^{-1} w.r.t. [Mn(II)] of complex **1**@SiO_2-Py_2PicNPs plus 2.2 mmol kg^{-1} D-glucose (45 minutes post administration of contrast agent), (ii) 10 μmol kg^{-1} w.r.t. [Mn(II)] of complex **1**@SiO_2-Py_2PicNPs plus saline (0.9%), (III) 10 μmol kg^{-1} w.r.t. [Mn(II)] of complex **1**@SiO_2-NH_2NPs plus 2.2 mmol kg^{-1} D-glucose (45 minutes post administration of contrast agent), (IV) 10 μmol kg^{-1} w.r.t. [Mn(II)] of complex **1**@SiO_2-NH_2NPs plus saline (0.9%), and (V) 10 μmol kg^{-1} w.r.t. [Gd(III)] of Dotarem solution in PBS, followed by sequential T_1-weighted scans. Animals were scanned at different times, from 50 min post contrast injection (5 min after glucose bolus) to 24 hours after. ImageJ software was used to analyze the image intensity in the region of interest (ROI) of different organs and the intensity values were normalized with the ROIs estimated on the back muscle of that animal at the same slice and time point (considered as contrast to noise ratio, CNR). The change in respective image intensity was reported in percentage values compared to pre-contrast injection scans (% ΔCNR). Signal intensities of ROIs of different organs were monitored for 24 hours post contrast administration and the area under analysis and statistical significance were calculated using unpaired two-tailed t tests to correlate between each material; p values <0.05 were considered significant.

Biodistribution

Another four groups (n = 3/group) were similarly administered as mentioned above and sacrificed at 1 hour post contrast

administration. The fifth group of mice was administered with saline (0.9%) only and sacrificed. The kidney, liver, spleen, muscle, pancreas, and bladder of each animal were incised to monitor Mn accumulation/excretion in different tissues. Whole organ tissue was digested by treatment in 2 mL of freshly prepared aqua regia (1 : 3 mixture of HNO_3 and HCl) and lysing for 24 h. The lysed tissue samples were heated at 120 °C to dry the aqua regia. Leftover digested tissue was further dissolved in 0.5 N HCl by sonicating for 15 min. For each sample, a clear supernatant solution, obtained after centrifugation (4000 *g*, 5 min) of the tissue mixture, was diluted to 5 mL with 4% HNO_3 and subsequent Mn content was estimated by ICP-MS measurements.

Syntheses

Syntheses of $[C_{19}H_{23}N_3O_5]$, (A). To a solution of (*S*)-(+)-2-amino-1-propanol (0.150 g, 2 mmol) in dry THF under N_2 atmosphere, triethyl amine (0.61 mL, 4.4 mmol) was added. Methyl 6-(bromomethyl)picolinate (0.92 g, 4.0 mmol) was subsequently added and the resulting mixture was stirred for 24 h at room temperature. After this, the reaction mixture was dried to remove THF and the residue was extracted with CH_2Cl_2 (3 × 30 mL) after thoroughly washing with water and brine. The organic part was collected and dried over Na_2SO_4 and the solvent was evaporated to obtain a pale yellow oil, which was purified by column chromatography on silica gel using hexane/ethyl acetate (1 : 4) as eluent to get colourless solid. Yield = 0.388 g (52%). FTIR (KBr pellet cm^{-1}): 3413, 2957, 1728, 1590, 1441, 1316, 1248, 1140, 1085, 833, 764. ^{1}H NMR ($CDCl_3$, 400 MHz): δ 7.98 (d, J = 8 Hz, 2H), 7.59 (t, J = 8 Hz, 2H), 7.48 (d, J = 8 Hz, 2H), 5.46 (s br, 1H), 4.70 (s, 1H), 4.05 (m, 2H), 3.99 (s, 6H), 3.93 (d, J= 12, 2H), 3.55 (m, 2H), 3.15 (m, 1H), 1.04 (d, J = 8 Hz, 3H) ppm. ^{13}C NMR ($CDCl_3$, 100 MHz): δ 161.14, 138.65, 132.75, 129.54, 125.19, 121.01, 60.93, 57.34, 54.35, 49.78, 8.83 ppm.

ESI-MS (+) m/z for $[C_{19}H_{23}N_3O_5 + H]^+$ calcd., 374.1710; found, 374.1743.

Syntheses of $[C_{17}H_{19}N_3O_5]$, (H_2AlcDPA). Aqueous solution of LiOH (0.033 g, 1.36 mmol in 2 mL H_2O) was added dropwise to an as prepared solution of **A** (0.230 g, 0.62 mmol) in THF (6 mL) and the mixture was stirred at room temperature for 24 h. Afterward, the THF part was evaporated and the pH of the resultant aqueous solution was adjusted to ∼1 by adding 1 N HCl. A sticky compound was obtained after evaporation of the solvent and was washed thoroughly with diethyl ether. This residue was then dissolved in methanol to obtain the colorless solid precipitate of the ligand as its HCl salt. Yield = 0.211 g (89%). FTIR (KBr pellet cm^{-1}): 3331, 3200, 3008, 2981, 2963, 2877, 2808, 1746, 1735, 1594, 1573, 1464, 1384, 1351, 1262, 1156, 995, 834, 750, 692. ^{1}H NMR (D_2O, 400 MHz): δ 7.87 (m, 4H), 7.51 (m, 2H), 4.77 (m, 2H), 4.73 (d, J = 8 Hz), 4.03 (d, J = 8 Hz, 1H), 3.95 (m, 2H), 1.52 (m, 3H) ppm. ^{13}C NMR (D_2O, 100 MHz): δ 167.03, 149.96, 146.55, 139.78, 127.75, 125.01, 63.93, 60.34, 55.35, 9.73 ppm. ESI-MS (+) m/z for $[C_{17}H_{19}N_3O_5 + H]^+$ calcd., 346.1691; found, 346.1601.

Syntheses of complex 1, $[C_{17}H_{17}MnN_3O_5Cl]$. $MnCl_2{\cdot}4H_2O$ (0.057 g, 0.29 mmol) was combined with a solution of H_2AlcDPA (0.119 g, 0.31 mmol) in water (5 mL) and the solution was stirred for 15 minutes. The pH of this reaction mixture was adjusted to ∼6.5 with dropwise addition of aqueous NaOH. The resultant was stirred for another 24 h at room temperature (25 °C). After this, a clear solution was obtained and left for slow evaporation to obtain a white solid residue. A methanolic solution of the residue (with a few drops of water) was diffused in a diethyl ether environment for one week to obtain needle-shaped colorless crystals which were washed with Et_2O. The obtained crystals were analyzed by single-crystal X-ray diffraction. Yield = 0.090 g (64%). FTIR (KBr pellet cm^{-1}): 3471, 3417, 3172, 2966, 2937, 2890, 2317, 1692, 1649, 1613, 1587, 1443, 1398, 1268, 1159, 1026, 826, 789, 692. ESI-MS (+) m/z for $[\{(C_{17}H_{17}ClMnN_3O_5)-(Cl)\} + H]^+$ calcd: 399.0621; found: 398.9919.

Syntheses of $[C_{20}H_{20}N_4O_2]$, (B). To a solution of di-(2-picolyl)amine (0.612 g, 3 mmol) in dry acetonitrile, K_2CO_3 (0.828 g, 6 mmol) and methyl 6-(bromomethyl)picolinate (0.690 g, 3 mmol) were added successively under a nitrogen atmosphere and the resulting solution was heated at 60 °C for 3 h. The reaction mixture was then cooled to room temperature and filtered. The filtrate was evaporated to dryness. Water was added to the residue and extracted with ethyl acetate (3 × 30 mL). The organic part was collected, dried over Na_2SO_4, concentrated to 5 mL, and refrigerated overnight to obtain a colourless precipitate which was collected by filtration. Yield = 0.857 g (82%). FTIR (KBr pellet cm^{-1}): 3406, 3008, 2950, 2841, 1721, 1588, 1569, 1434, 1316, 1291, 1138, 1082, 994, 977, 763. ^{1}H NMR ($CDCl_3$, 400 MHz): δ 8.55 (d, J = 4 Hz, 2H), 7.99 (d, J = 8 Hz, 1H), 7.88 (d, J = 8Hz, 1H), 7.80 (t, J = 8 Hz, 1H), 7.66 (t, J = 8 Hz, 2H), 7.58 (d, J = 8Hz, 2H), 7.17 (t, J = 4Hz, 2H), 4.04 (s, 2H), 3.98 (s, 3H), 3.95 (s, 4H) ppm. ^{13}C NMR ($CDCl_3$, 100 MHz): δ 159.47, 154.76, 151.64, 147.45, 144.37, 141.89, 138.23, 124.47, 122.19, 120.45, 64.65, 56.21, 55.76, 52.78 ppm.

ESI-MS (+) m/z for $[C_{23}H_{24}N_4O_4 + H]^+$ calcd., 349.1659; found, 349.1647.

Syntheses of $[C_{19}H_{18}N_4O_2]$, (HPy_2Pic). To a solution of **B** (0.348 g, 1.0 mmol) in THF (6 mL), an aqueous solution of LiOH (0.048 g, 2.0 mmol in 2 mL H_2O) was slowly added and stirred at room temperature for 24 h. After this, the THF was evaporated and the residue was diluted with water (1 mL) and isopropanol (5 mL). The resulting mixture was acidified by addition of HPF_6 (88 μL, 1 mmol), leading to the precipitation of a white solid, which was filtered, washed with isopropanol and dried under air to obtain the ligand HPy_2Pic as its HPF_6 salt. Yield = 0.374 g (78%). FTIR (KBr pellet cm^{-1}): 3430, 3245, 3132, 3070, 2998, 2927, 2853, 1718, 1632, 1614, 1603, 1594, 1536, 1440, 1308, 1268, 1156, 1055, 877, 839, 767, 557. ^{1}H NMR (CD_3OD, 400 MHz): δ 8.89 (d, J = 4 Hz, 2H), 8.45 (t, J = 8 Hz, 2H), 8.14 (d, J = 4 Hz, 1 H), 8.00 (m, 3H), 7.91 (t, J = 8 Hz, 2H), 7.57 (d, J = 4 Hz, 1H), 4.43 (s, 4H), 4.26 (s, 2H) ppm. ^{13}C NMR (CD_3OD, 100 MHz): δ 167.80, 158.56, 157.16, 149.43, 147.74, 141.69, 140.29, 127.94, 126.19, 125.21, 66.89, 59.81, 59.68 ppm.

ESI-MS (+) m/z for $[C_{21}H_{20}N_4O_4 + H]^+$ calcd., 335.1502; found, 335.1509.

Syntheses of complex 1@SiO_2NPs. A reverse microemulsion process was employed for the preparation of complex **1**@SiO_2NP. A pH ∼ 7.4 buffered doping solution of complex

1 (480 μL, 2.50 mM) was carefully added to a homogenous mixture of Igepal-CO-520 (1.3 mL) in cyclohexane (10 mL) and stirred for 15 minutes. This was followed by the addition of NH_4OH (120 μL, 25% by w/v) and TEOS (100 μL). The final mixture was kept at room temperature for 24 h with gentle stirring. complex **1**@SiO_2NP was obtained upon the addition of methanol (10 mL) to the mixture and was repeatedly washed with methanol and water. The nanoparticles were collected by centrifugation at 10 000 rpm for 15 minutes. The residue obtained was dispersed in 400 μL water (pH maintained at 7.4) and this mother suspension was further used for relaxometry and other studies. FTIR (KBr pellet cm^{-1}): 3450, 1694, 1634, 1578, 1444, 1400, 1102, 955, 800.

Syntheses of complex 1@SiO_2-NH_2NPs. The aforementioned procedure (for the preparation of complex **1**@SiO_2NP) was repeated along with the addition of (3-aminopropyl)triethoxysilane (APTES, 50 μL) 24 h after the addition of TEOS. The reaction mixture was left for another 24 h, then the microemulsion was disrupted with the addition of methanol (10 mL). Complex **1**@SiO_2-NH_2NPs were obtained after subsequent washes with copious amounts of methanol, ethanol, and water (centrifugation at 10 000 rpm, 15 minutes in each washing). The residue obtained was dispersed in 400 μL water (pH maintained at 7.4) to obtain a stock suspension which was used for further syntheses, relaxometry, and other studies. FTIR (KBr pellet cm^{-1}): 3444, 3321, 3080, 2941, 2898, 1694, 1643, 1634, 1628, 1588, 1550, 1472, 1450, 1338, 1087, 953, 792.

Syntheses of complex 1@SiO_2-Py_2PicNPs. A solution of HPy_2Pic ligand (0.049 g, 0.1 mmol) was prepared in PBS buffer (7 mL, 0.01 M, pH ~ 7.0) and activated by the successive additions of EDC·HCl (0.192 g, 1.0 mmol) and NHS (0.115 g, 1.0 mmol). After 1 h, a monodispersed suspension of complex **1**@SiO_2-NH_2NPs (prepared by dispersing 1.6 mL of 0.80 mM [Mn(II)] complex **1**@SiO_2-NH_2NPs stock solution in 5 mL PBS buffer by 30 minutes sonication) was added to the mixture and gently stirred for 12 h at room temperature. A pale-yellow turbid solution was obtained and centrifuged (g = 10 000, 20 min) to get colourless complex **1**@SiO_2-Py_2Pic nanoparticles after several washings with methanol and water. Nanoparticles were re-suspended in 1 mL HEPES buffer (pH ~ 7.4) to form complex **1**@SiO_2-Py_2PicNP stock solution which was further used for characterization and relaxometry studies. FTIR (KBr pellet cm^{-1}): 3453, 3246, 2946, 1765, 1665, 1657, 1651, 1643, 1632, 1619, 1546, 1470, 1394, 1094, 955, 796.

Author contributions

CM designs the whole concept and wrote the manuscript with the help of other authors. RM performs all the experiments and biostudies. MS contributes to cell viability measurements. VS, HM and SK supervise biostudies (*in vivo* and MR imaging).

Conflicts of interest

There are no conflicts to declare.

Acknowledgements

This project is funded by Department of Biotechnology (BT/PR23622/NNT/281294/2017), Govt. of India. RM and MS thank IIT Guwahati for doctoral fellowship. The Department of Chemistry, Central Instruments Facility, IIT Guwahati, FIST programme supported by DST (SR/FST/CS-II/2017/23C), are thankfully acknowledged for instrumental facilities. We thank Primus, Guwahati, Assam, India for providing T_1-weighted imaging facility. CM is indebted to Prof. Siddhartha Sankar Ghosh for his help in general.

Notes and references

1 J. Wahsner, E. M. Gale, A. Rodríguez-Rodríguez and P. Caravan, *Chem. Rev.*, 2019, **119**, 957–1057.
2 E. J. Werner, A. Datta, C. J. Jocher and K. N. Raymond, *Angew. Chem., Int. Ed.*, 2008, **47**, 8568–8580.
3 B. P. Bonner, S. R. Yurista, J. Coll-Font, S. Chen, R. A. Eder, A. N. Foster, K. D. Nguyen, P. Caravan, E. M. Gale and C. Nguyen, *J. Am. Heart Assoc.*, 2023, **12**, e026923.
4 S. Aime, D. L. Longo, F. Reineri and S. G. Crich, *J. Magn. Reson.*, 2022, **338**, 107198.
5 E. Terreno, D. D. Castelli, A. Viale and S. Aime, *Chem. Rev.*, 2010, **110**, 3019–3042.
6 H. Li and T. J. Meade., *J. Am. Chem. Soc.*, 2019, **141**, 17025–17041.
7 A. E. Merbach and E. Tóth, *The Chemistry of Contrast Agent in Medical Magnetic Resonance Imaging*, Wiley, 2nd edn, 2013.
8 A. Gupta, P. Caravan, W. S. Price, C. Platas-Iglesias and E. M. Gale, *Inorg. Chem.*, 2020, **59**, 6648–6678.
9 S. Aime, M. Botta, D. E.-Gómez and C. Platas-Iglesias, *Mol. Phys.*, 2019, **117**, 898–909.
10 D. Ni, E. B. Ehlerding and W. Cai, *Angew. Chem., Int. Ed.*, 2019, **58**, 2570–2579.
11 E. P. Lancelot, J.-S. Raynaud and P. Desché, *Invest. Radiol.*, 2020, **55**, 589–591.
12 S. Lange, W. Mędrzycka-Dąbrowska, K. Zorena, S. Dąbrowski, D. Ślęzak, A. Malecka-Dubiela and P. Rutkowski, *Int. J. Environ. Res. Public Health*, 2021, **18**, 3000.
13 B. A. Dekkers, R. Roos and A. J. V. D. Molen, *Eur. Radiol.*, 2018, **28**, 1579–1584.
14 E. Di Gregorio, G. Ferrauto, C. Furlan, S. Lanzardo, R. Nuzzi, E. Gianolio and S. Aime, *Invest. Radiol.*, 2018, **53**, 167–172.
15 M. Botta, F. Carniato, D. E.-Gómez, C. Platas-Iglesias and L. Tei, *Future Med. Chem.*, 2019, **11**, 1461–1483.
16 N. N. Nystrom, H. Liu, F. M. Martinez, X.-A. Zhang, T. J. Scholl and J. A. Ronald, *J. Med. Chem.*, 2022, **65**, 9846–9857.
17 G. J. Soufi, A. Hekmatnia, S. Iravani and R. S. Varma, *ACS Appl. Nano Mater.*, 2022, **5**, 10151–10166.
18 K. Chen, P. Li, C. Zhu, Z. Xia, Q. Xia, L. Zhong, B. Xiao, T. Cheng, C. Wu, C. Shen, X. Zhang and J. Zhu, *J. Med. Chem.*, 2021, **64**, 9182–9192.
19 S. Aime and P. Caravan, *J. Magn. Reson. Imaging*, 2009, **30**, 1259–1267.
20 W. Cheng, I. E. Haedicke, J. Nofiele, F. Martinez, K. Beera, T. J. Scholl, H. Margaret Cheng and X.-A. Zhang, *J. Med. Chem.*, 2014, **57**, 516–520.

21 R. Antwi-Baah, Y. Wang, X. Chen and K. Yu, *Adv. Mater. Interfaces*, 2022, **9**, 2101710.
22 R. Zheng, J. Guo, X. Cai, L. Bin, C. Lu, A. Singh, M. Trivedi, A. Kumar and J. Liu, *Colloids Surf., B*, 2022, **213**, 112432.
23 R. R. Zairov, B. S. Akhmadeev, S. V. Fedorenko and A. R. Mustafina, *Chem. Eng. J.*, 2023, **459**, 141640.
24 J. Ruan and H. Qian, *Adv. Theory*, 2021, **4**, 2100018.
25 M. Veit, R. van Asten, A. Olie and P. Prinz, *Eur. J. Clin. Nutr.*, 2022, **76**, 1497–1501.
26 A. Ojha, U. Ojha, R. Mohammed, A. Chandrashekar and H. Ojha, *Clin. Pharmacol.*, 2019, **11**, 57–65.
27 E. Haythorne, M. Rohm, M. van de Bunt, M. F. Brereton, A. I. Tarasov, T. S. Blacker, G. Sachse, M. S. dos Santos, R. T. Exposito, S. Davis, O. Baba, R. Fischer, M. R. Duchen, P. Rorsman, J. I. MacRae and F. M. Ashcroft, *Nat. Commun.*, 2019, **10**, 2474.
28 P. E. MacDonald, J. W. Joseph and P. Rorsman, *Philos. Trans. R. Soc., B*, 2005, **360**, 2211–2225.
29 G. D. S. Xavier, *J. Clin. Med.*, 2018, **7**, 1–17.
30 J. A. G. Pertusa, T. L. n-Quinto1, G. BernaÂ, J. R. Tejedo, A. Hmadcha, F. J. Bedoya, F. MartõÂn and B. Soria, *PLoS One*, 2017, **12**(11), e0187547.
31 A. Fukunaka and Y. Fujitani, *Int. J. Mol. Sci.*, 2018, **19**, 476.
32 B. Thapa, E. H. Suh, D. Parrott, P. Khalighinejad, G. Sharma, S. Chirayil and A. D. Sherry, *Front. Endocrinol.*, 2022, **12**, 809867.
33 Y. Stefan, P. Meda, M. Neufeld and L. Orci, *J. Clin. Invest.*, 1987, **80**, 175–183.
34 S. Zhu, D. Larkin, S. Lu, C. Inouye, L. Haataja, A. Anjum, R. Kennedy, D. Castle and P. Arvan, *Diabetes*, 2016, **65**, 699–709.
35 A. F. Martins, V. C. Jordan, F. Bochner, S. Chirayil, N. Paranawithana, S. Zhang, S. T. Lo, X. Wen, P. Zhao, M. Neeman and A. D. Sherry, *J. Am. Chem. Soc.*, 2018, **140**, 17456–17464.
36 G.-L. Davies, I. Kramberger and J. J. Davis, *Chem. Commun.*, 2013, **49**, 9704.
37 V. C. Pierre, S. M. Harris and S. L. Pailloux, *Acc. Chem. Res.*, 2018, **51**, 342–351.
38 J. Lux and A. D. Sherry, *Curr. Opin. Chem. Biol.*, 2018, **45**, 121–130.
39 P. Khalighinejad, D. Parrott and A. D. Sherry, *Pharmaceuticals*, 2020, **13**, 268.
40 G. J. Stasiuk, F. Minuzzi, M. Sae-Heng, C. Rivas, H. P. Juretschke, L. Piemonti, P. R. Allegrini, D. Laurent, A. R. Duckworth, A. Beeby, G. A. Rutter and N. J. Long, *Chem. – Eur. J.*, 2015, **21**(13), 5023–5033.
41 A. J. M. Lubag, L. M. De Leon-Rodriguez, S. C. Burgess and A. D. Sherry, *Proc. Natl. Acad. Sci. U. S. A.*, 2011, **108**(45), 18400–18405.
42 C. S. Bonnet and É. Tóth, *Curr. Opin. Chem. Biol.*, 2021, **61**, 154–169.
43 G. Wang, H. Martin, S. Amézqueta, C. Ràfols, C. S. Bonnet and G. Angelovski, *Inorg. Chem.*, 2022, **61**(41), 16256–16265.
44 J. Yu, A. F. Martins, C. Preihs, V. Clavijo Jordan, S. Chirayil, P. Y. Zhao, Y. K. Wu, K. Nasr, G. E. Kiefer and A. D. Sherry, *J. Am. Chem. Soc.*, 2015, **137**, 14173–14179.
45 L. M. De Leon-Rodrıguez, A. J. M. Lubag, J. A. Lopez, G. Andreu-de-Riquer, J. C. Alvarado-Monzona and A. D. Sherry, *Med. Chem. Commun.*, 2012, **3**, 480–483.
46 A. C. Esqueda, J. A. López, G. Andreu-de-Riquer, J. C. Alvarado-Monzón, J. Ratnakar, A. J. M. Lubag, A. D. Sherry and L. M. De León-Rodríguez, *J. Am. Chem. Soc.*, 2009, **131**, 11387–11391.
47 G. Wang and G. Angelovski, *Angew. Chem., Int. Ed.*, 2021, **60**, 5734–5738.
48 S. Chirayil, V. C. Jordan, A. F. Martins, N. Paranawithana, S. J. Ratnakar and A. D. Sherry, *Inorg. Chem.*, 2021, **60**(4), 2168–2177.
49 R. Botár, E. Molnár, Z. Garda, E. Madarasi, G. Trencsényi, J. Kiss, F. K. Kálmán and G. Tircsó, *Inorg. Chem. Front.*, 2022, **9**, 577–583.
50 E. M. Gale, I. P. Atanasova, F. Blasi, I. Ay and P. Caravan, *J. Am. Chem. Soc.*, 2015, **137**, 15548–15557.
51 D. Ndiaye, M. Sy, A. Pallier, S. Même, I. de Silva, S. Lacerda, A. M. Nonat, L. J. Charbonnière and É. Tóth, *Angew. Chem., Int. Ed.*, 2020, **59**, 11958–11963.
52 Z. Garda, A. Forgács, Q. N. Do, F. K. Kálmán, S. Timári, Z. Baranyai, L. Tei, I. Tóth, Z. Kovács and G. Tircsó, *J. Inorg. Biochem.*, 2016, **163**, 206–213.
53 S. Anbu, S. H. L. Hoffmann, F. Carniato, L. Kenning, T. W. Price, T. J. Prior, M. Botta, A. F. Martins and G. J. Stasiuk, *Angew. Chem., Int. Ed.*, 2021, **60**, 10736–10744.
54 T. Kojima, Y. Hirai, T. Ishizuka, Y. Shiota, K. Yoshizawa, K. Ikemura, T. Ogura and S. Fukuzumi, *Angew. Chem., Int. Ed.*, 2010, **49**, 8449–8453.
55 R. Mallik, M. Saha and C. Mukherjee, *ACS Appl. Bio Mater.*, 2021, **4**(12), 8356–8367.
56 A. Forgács, R. Pujales-Paradela, M. Regueiro-Figueroa, L. Valencia, D. Esteban-Gómez, M. Botta and C. Platas-Iglesias, *Dalton Trans.*, 2017, **46**, 1546–1558.
57 The protonation constants were calculated by fitting the ligand titrations data pairs to the equation $K_i^H = [H_iL]/[H_{i-1}L][H^+]$, $i = 1$–3.
58 The Mn–L stability constant was calculated by fitting the metal:ligand titrations data pairs to the equation $K_{Mn-L} = [MnL]/[Mn][L]$.
59 N. T. Vo, A. K. Patra and D. Kim, *Phys. Chem. Chem. Phys.*, 2017, **19**, 1937–1944.
60 M. Yu, L. Zhou, J. Zhang, P. Yuan, P. Thorn, W. Gu and C. Yu, *J. Colloid Interface Sci.*, 2012, **376**, 67–75.
61 J. R. Lakowicz, *Principles of Fluorescence Spectroscopy*, Plenum Press, New York, 3rd edn, 2006, vol. 277.
62 H. Tapiero, D. M. Townsend and K. D. Tew, *Biomed. Pharmacother.*, 2003, **57**(9), 386–398.
63 N. N. Paranawithana, A. F. Martins, V. Clavijo Jordan, P. Zhao, S. Chirayil, G. Meloni and A. Dean Sherry, *J. Am. Chem. Soc.*, 2019, **141**, 11009–11018.
64 G. Ghibellini, E. M. Leslie and K. L. R. Brouwer, *Mol. Pharmaceutics*, 2006, **3**, 198–211.
65 K. Chen, P. Li, C. Zhu, Z. Xia, Q. Xia, L. Zhong, B. Xiao, T. Cheng, C. Wu, C. Shen, X. Zhang and J. Zhu, *J. Med. Chem.*, 2021, **64**, 9182–9192.
66 I. Usón and G. M. Sheldrick, *Acta Crystallogr.*, 2018, **D74**, 106–116.
67 L. J. Farrugia, WinGX and ORTEP for Windows: an update, *J. Appl. Crystallogr.*, 2012, **45**, 849.

ACS APPLIED BIO MATERIALS

www.acsabm.org Article

A Bis(Aquated) Mn(II)-Based MRI Contrast Agent with a Rigid Hydroquinazoline Unit: Synthesis, Characterization, and *in Vivo* MR Imaging Study

Riya Mallik, Muktashree Saha, Amrit Sarmah, Vandna Singh, Hari Mohan, Priyanka Bhat, S. Senthil Kumaran, and Chandan Mukherjee*

Cite This: *ACS Appl. Bio Mater.* 2024, 7, 1831−1841 Read Online

ACCESS | Metrics & More | Article Recommendations | Supporting Information

ABSTRACT: Since the finding of nephrogenic systemic fibrosis (NFS) in patients with renal impairment and the long-term accumulation of Gd(III) ions in the central nervous system, the search for nongadolinium ion-based MRI contrast agents made of nutrient metal ions has drawn paramount attention. In this context, the development of Mn(II)-based MRI contrast agents has been a subject of interest for the last few decades. Herein, we report a pentadentate ligand (Li_2[$BenzPic_2$]) composed of two picolinate moieties and a rigid 1,2,3,4-tetrahydroquinazoline unit and the corresponding bis(aquated) Mn(II) complex (Complex **1**). The complex exhibited high thermodynamic stability (log K_{cond} = 11.62) and kinetic inertness similar to that of the clinically approved Gd(III)-based contrast agent Magnevist. Complex **1** exerted longitudinal relaxivity (r_1) of 5.32 mM^{-1} s^{-1} at 1.41 T, 37 °C, pH 7.4, and it increased by 3.6-fold in the presence of serum albumin protein, confirming a substantial rigidifying interaction (albumin association constant K_A = 1.66 × 10^3 M^{-1}) between the protein and the amphiphilic (log *P* = −0.45) contrast agent. An intravenous dose of 0.08 mmol/kg in a healthy mouse, excellent MRI signal intensity enhancement in the vasculature of the mouse liver, and brightened images of the gallbladder, kidney, and liver were realized.

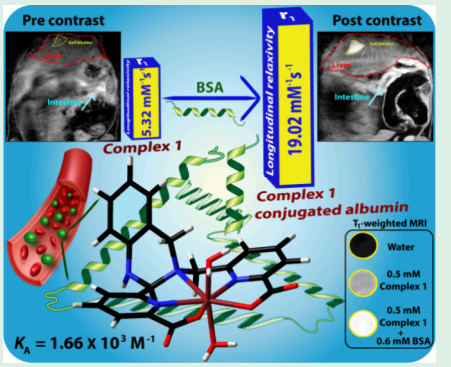

KEYWORDS: *magnetic resonance imaging, MRI contrast agents, manganese(II) complex, rigid complex, blood pool contrast agent, bis(aquated), lipophilicity, serum albumin affinity*

INTRODUCTION

Nuclear magnetic resonance (NMR)-based imaging, *i.e.*, magnetic resonance imaging (MRI), provides anatomical tissue images with a high spatial resolution (1−2 mm).[1−6] Nonetheless, the methodology suffers from low sensitivity.[7−9] In this context, the administration of a contrast agent (CA) prior to the imaging has been popularized. Nowadays, about 40% of clinical MR imaging is carried out in the presence of a contrast agent to engender conspicuous images in a relatively shorter period.[10−13] Contrast agents (CAs) are paramagnetic substances that shorten the longitudinal (T_1) and transverse (T_2) relaxation times of the nearby water protons. The change in the relaxation times per mM concentration of the paramagnetic species is designated as relaxivity ($r_{1,2}$ = 1/$T_{1,2}$[M]; [M] in mM). The high efficiency of a CA is thus determined by its high relaxivity value. A brightened image can result from diminishing the T_1 relaxation time, while the shortening of the T_2 relaxation time engenders a darkened image.[2,3] A dark image inside a human body can also appear from metal ion depositions, blood clots, tissue burning, and internal hemorrhage, which mislead the diagnosis.[14,15] Hence, the administration of T_1-weighted or T_1-T_2-weighted dual mode CAs has retained the priority to avoid such ambiguity.[16−19]

To develop low molecular weight paramagnetic complexes as T_1-weighted MRI CAs; thermodynamically and kinetically stable, slowly rotating metal complexes with a high total spin-value (*S*) and a large number of inner sphere water molecules (*q*) have been the primary interest.[20−22] Consequently, Gd(III) complexes with an *S* = 7/2 electronic spin state were the center of attention until the reports on Gd(III) aggravated nephrogenic systemic fibrosis (NSF) in patients with renal failure and long-term accumulation of Gd(III) ions in the central nervous system.[23−25] In fact, the U.S. Food and Drug Administration (FDA) and the European Medicines Agency (EMA) have already raised their concern regarding the safety of using clinically approved, kinetically less stable Gd(III)-based MRI CAs made of acyclic ligands.[26−29]

Received: December 14, 2023
Revised: February 2, 2024
Accepted: February 21, 2024
Published: March 1, 2024

https://doi.org/10.1021/acsabm.3c01236
ACS Appl. Bio Mater. 2024, 7, 1831−1841

Notwithstanding, $[Gd(EOB\text{-}DTPA)(OH_2)]^{2-}$ (Eovist) and $[Gd(BOPTA)(OH_2)]^{2-}$ (Multihance) are the two available hepatocyte-specific MRI CAs allowed only for the diagnosis of severe liver diseases.[30−32] Hence, developing Gd-free contrast agents is of paramount interest.

An Mn(II) ion in its high-spin state contained five unpaired electrons, and the Mn(II)-H (water proton) distance was found to be in the 2.5−2.8 Å range.[33−35] Hence, the ion has been considered as a possible substitute for the Gd(III) ion. Nonetheless, the metal ion belongs to the 3*d* transition series and does not possess additional stability through *d*-orbital splitting (CFSE = crystal field stabilization energy = 0). Thus, in the Mn(II)-based complexes, the stability materializes only in the form of the metal ion-ligand interactions. Pyridine is a σ-donor and π-acceptor unit and has been recognized as the crucial ligating unit to engender stability in Mn(II) complexes of acyclic coordinating ligands.[35,36] In addition, the recent report by Comba, Tóth, and colleagues indicates that in the acyclic ligands, the ligand rigidity bestows high thermodynamic stability and kinetic inertness to the corresponding Mn(II) complex.[13,37] Considering the aforementioned points, we envisaged synthesizing a rigid acyclic ligand containing picolinate moieties as the metal coordinating units. In Mn(II) complexes, the +II ionic charge and the small ionic radius of the Mn(II) ion restrict the coordination number mostly within seven. It is known that r_1 relaxivity is directly proportional to the number of inner-sphere water molecules (q).[21] Hence, to enhance the contrast efficiency by increasing the q value to 2 in the corresponding Mn(II) complex, we restricted the potential coordination number of the ligand to five.

Herein, we report the new pentadentate ligand $Li_2[BenzPic_2]$ (Scheme 1) comprising two picolinate moieties

Scheme 1. Synthetic Representation for the Formation of Ligand $Li_2Benz(pic)_2$ and Complex 1[a]

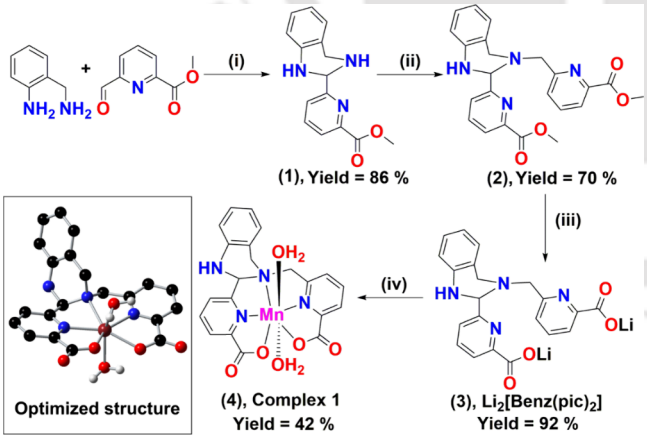

[a](i) CH_3OH, (ii) methyl 6-(bromomethyl)picolinate, CH_3CN, DIPEA, and KI, (iii) LiOH in THF/H_2O, and (iv) $MnCl_2{\cdot}4H_2O$, H_2O, pH ∼ 6.5. **Inset:** The optimized structure of bis(aquated) Complex **1** at the ωB97XD/cc-pVDZ level.

and a rigid 1,2,3,4-tetrahydroquinazoline unit. The idea of using hydroquinazoline is threefold: 1) the rigidity exerted by the unit can impose high thermodynamic and kinetic stability in the corresponding bis(aquated) Mn(II) complex, 2) the phenyl ring present in the hydroquinazoline unit can strengthen the interaction of the complex with serum albumin protein; consequently, the circulatory lifetime of the CA will increase, and 3) the lipophilic nature of the unit along with the picolinate moieties can engender an amphiphilic CA that can excrete via both hepatobiliary and renal paths facilitating the imaging options of both systems.[32,38−41] Indeed, the ligand upon reacting with $MnCl_2{\cdot}4H_2O$ endowed a mononuclear, bis(aquated) [q = 2], water-soluble complex (**1**). The complex exhibited the longitudinal relaxivity (r_1) value of 5.32 mM^{-1} s^{-1} at 1.41 T, 37 °C, and pH 7.4, which increased by 3.6-fold in the presence of 0.67 mM bovine serum albumin (BSA) protein, indicating an appreciable interaction and consequent rigidification of the complex as contemplated. It was also noticed that the complex imparts high thermodynamic stability and kinetic inertness similar to that of the clinically approved Gd(III)-based contrast agent Magnevist.[42,43] A subtle change in the relaxivity value within 24 h in human serum consolidated the substantial stability of the complex in the blood. A contrast enhancement in the liver, gallbladder, intestine, and kidney was realized when the complex was intravenously injected into a healthy mouse. The biodistribution and time-dependent contrast-decrement/depletion of the organs were also studied to discern the clearing pathways and the organ-residual time and are included in this article.

RESULTS AND DISCUSSION

The pentadentate ligand $Li_2[Benz(pic)_2]$ and the corresponding water-soluble Mn(II) complex (Complex **1**) were prepared as presented in Scheme 1. Compound **1** was synthesized in 86% yield by reacting equivalent amounts of 2-aminobenzylamine and methyl 6-formyl-2-pyridinecarboxylate in a methanolic medium. The isolated compound was then reacted with an equal quantity of methyl 6-(bromomethyl)picolinate in CH_3CN, in the presence of *N*,*N*-diisopropylethylamine (DIPEA), and KI, to yield compound **2** in 70% yield. Base hydrolysis of this compound by LiOH in a THF/H_2O solvent mixture provided the expected ligand $Li_2[Benz(pic)_2]$ as a white solid with 92% yield in almost racemic form ($[\alpha]_D^{20}$ = 0.313, c = 3.2 g in 100 mL of water) [Figures S1−S6]. The corresponding Mn(II)-complex was prepared by reacting a stoichiometric amount of the isolated ligand $Li_2[Benz(pic)_2]$ and $MnCl_2{\cdot}4H_2O$ in an aqueous medium at pH ∼ 6.5. Followed by diethyl ether diffusion in the methanolic solution of the isolated solid, Complex **1** precipitated as a white powder in 42% yield (Figures S7−S11). The electrospray ionization mass spectrum (ESI-MS) in an aqueous medium in the negative mode for the ligand $Li_2[Benz(pic)_2]$ and the positive mode for the isolated complex exhibited a 100% molecular ion peak at m/z = 389.12 and 444.06, respectively. The isotope distribution patterns (Figures S6 and S8) of the observed masses corresponded to the compositions $[C_{21}H_{17}N_4O_4]^-$ for the ligand and $[C_{21}H_{16}MnN_4O_4 + H]^+$ for the Mn-complex. The compositions corroborated well with the compositions of the ligand ($C_{21}H_{16}N_4O_4Li_2$) and Complex **1** ($C_{21}H_{16}MnN_4O_4$). Thus, mass spectral analyses confirmed the successful formations of the ligand and the corresponding Mn-complex (Figures S6 and S8). Repeated trials for obtaining single crystals suitable for X-ray diffraction analyses were unsuccessful. Thus, the Mn(II) ion-concentration-dependent ^{1}H-chemical shift (*vide infra*) and DFT-based theoretical calculations have been carried out to determine the q and the most favorable structure of Complex **1** (Scheme 1, Inset).

The hydration number (q) of the synthesized Mn(II)-complex (**1**) was estimated by the concentration-dependent paramagnetic chemical shift studies, as proposed by Gale et

https://doi.org/10.1021/acsabm.3c01236
ACS Appl. Bio Mater. 2024, 7, 1831−1841

al.[44] According to Equation S1, the paramagnetic shift ($\Delta\omega_p$) of the ^{1}H NMR or ^{17}O NMR resonance peak generated due to the presence of Mn(II) ions is proportional to the hydration number. Thus, q could be determined from the slope of the linear plot of $\Delta\omega_p$ versus the concentration of the paramagnetic Mn(II) ion at a constant temperature. Consequently, ^{1}H NMR analyses of samples containing increasing concentrations of Complex **1** in H_2O/D_2O medium (1:2) were executed. An increase in the paramagnetic chemical shift with increasing [Mn(II)] concentration was realized at 55 °C and 9.4 T (Figure 1). A similar experiment was done for the well-

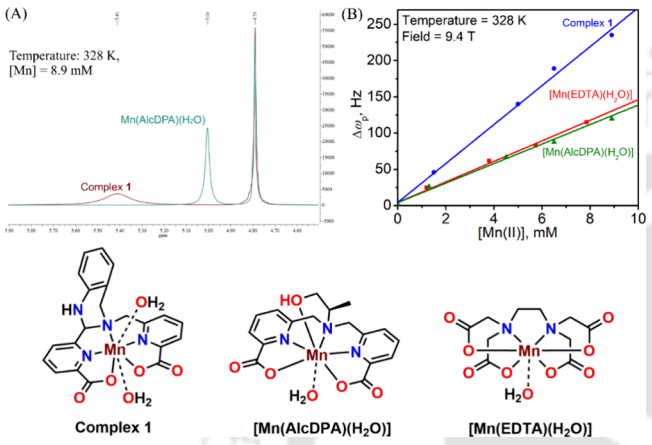

Figure 1. (A) ^{1}H NMR resonance peak broadening for the Complex **1** solution (wine line) and Mn(AlcDPA) (cyan line), [Mn] = 8.9 mM in D_2O, at pH ∼ 7.4, 9.4 T, and 55 °C. (B) Comparison of the paramagnetic concentration dependence on the ^{1}H NMR chemical shift for Complex **1** to monoaquated Mn(EDTA) and Mn(AlcDPA) complexes.

established mono(aquated) Mn(EDTA) and Mn(AlcDPA) complexes.[45,46] The slope for Complex **1** was found to be ∼2-fold higher than that for the previously reported mono-(aquated) complexes, suggesting the presence of two metal-coordinated water molecules in Complex **1**.[47] Moreover, at the identical experimental conditions, the paramagnetic resonance signal for the synthesized complex solution was vividly broader than that of the monoaquated Mn(AlcDPA) complex indicating the presence of more than one water molecule in the inner coordination sphere.

The DFT-level structural optimizations on the complex in the mono(aquated) and bis(aquated) forms have also been carried out. The addition of water molecules to the Mn(II)-ligand framework had a significant impact on the complex's geometry and thermodynamic stability. The calculated results, including relevant energy parameters, are reported in Table S1. When one water molecule was present in the inner coordination sphere, the complex exhibited a distorted octahedral geometry, where a picolinate N atom and the O atom of the water molecule were situated at the apical positions (Figure S9A, Table S3). The N_2O_2 basal plane was constituted by picolinate-belonging N and O atoms, one ring N atom, and one ring O atom of the second picolinate moiety. The addition of the second water molecule to the Mn center resulted in a pentagonal bipyramidal geometry with a higher complex stability. In the complex, the ligand coordinated to the Mn(II) ion at the basal position by employing N_2O_2 atoms, two picolinate units, and a ring N atom (Figure S9B, Table S4). The two water molecules were situated at the two apical positions (Scheme 1, Inset).

The spectrophotometric batch titrations against the competing hexadentate H_2Na_2EDTA ligand were performed in determining the conditional stability constant (log K_{cond}) of the corresponding Mn(II) complex of the $Li_2Benz(pic)_2$ ligand (eq 1).[48] The equilibrium constant for the competition reaction was determined at specific experimental conditions: [M] = 10 μM, [L] = 10 μM, I = 0.15 M NaCl, at pH ∼ 7.4 (HEPES buffer), and 25 °C. An increasing volume of the standardized H_4EDTA stock solution ranging from 0.5 to 200 equiv relative to the ligand [$Li_2Benz(pic)_2$ = L] concentration was added to a [Mn(II)-L] solution. The resulting solutions were allowed to equilibrate for 48 h at 25 °C. The free and the complexed ligand concentration in each solution mixture was then estimated from the subsequent UV−vis absorption spectrum (Figures S11 and S12). The X-intercept of the [Mn-EDTA]/[Mn-L] versus [EDTA]/[L] plot represented the relative affinity of the $Li_2Benz(pic)_2$ ligand for Mn(II), which was found to be 0.6 log K units higher than that for EDTA.[45] Noteworthy, the hexadentate $[EDTA]^{4-}$ ligand results in a seven-coordinate mono(aquated) Mn(II)-EDTA complex, while the bis(aquated) Complex **1** with the pentadentate $Li_2Benz(pic)_2$ ligand provided a seven-coordinate complex with superior stability (Table S2). Thus, the ligand rigidity imparted by the 1,2,3,4-tetrahydroquinazoline backbone was found to impose significantly higher thermodynamic stability in the complex with the pentadentate ligand.

Mn(II)-complexes of acyclic ligands often succumb to *in vivo* transmetalation in the presence of Zn(II) ions[36,43,49−51] and release free Mn(II) ions. The Mn(II) ion is a nutritional element and can be either physiologically absorbed or excreted from the body.[52] Thus, it discards the possibility of long-term accumulation and subsequent toxicity, which is the neurological disorder called manganism.[43,53,54] However, an accumulation of free Mn(II) ions over 3.38 mmol/kg would engender such toxicity.[55,56] Complex **1** exhibited a high r_1 relaxivity (*vide infra*); hence, a lower dose of 0.1 mmol/kg could be administered for MR imaging. Nonetheless, the kinetic inertness of Complex **1** has been investigated in the presence of a 10-fold excess of Zn(II) ions in 0.15 M NaCl, pH 6.5, and 25 °C. To compare the kinetic stability of Complex **1**, the same experiment was repeated employing the standard $[Mn(EDTA)(OH_2)]^{2-}$ and the clinically approved commercially available $[Gd(DTPA)(OH_2)]^{2-}$ (Magnevist) contrast agents.[42,43] The change in the R_2 relaxation rate of water protons with time has been plotted and is presented in Figure S13A. It was observed that the kinetic inertness of Complex **1** (pseudo-first-order, $k = 1.04 \times 10^{-2}$ s^{-1}) was about 8.5 times higher than that of $[Mn(EDTA)(OH_2)]^{2-}$ ($k = 8.86 \times 10^{-2}$ s^{-1}) and almost the same as that of $[Gd(DTPA)(OH_2)]^{2-}$ ($k = 1.16 \times 10^{-2}$ s^{-1}). Furthermore, a 5-fold enhancement in the kinetic stability ($k = 2.13 \times 10^{-3}$ s^{-1}) was realized when the kinetic inertness studies were performed by following the time profile of the R_2 value of the Complex **1** solution challenged with a 10-fold excess of Zn(II) ions in serum albumin (0.67 mM), in 0.15 M NaCl, pH 6.5, and 25 °C (Figure S13B). Thus, despite having two inner-sphere water molecules and the pentadentate coordinating ligand, a higher kinetic inertness in the Mn(II) ion-based Complex **1** can be harnessed by imposing the ligand-based rigidity.

Complex **1** showed impressive relaxometry properties with r_1 = 6.77 mM^{-1} s^{-1} at 25 °C and 5.32 mM^{-1} s^{-1} at 37 °C; r_2 =

https://doi.org/10.1021/acsabm.3c01236
ACS Appl. Bio Mater. 2024, 7, 1831−1841

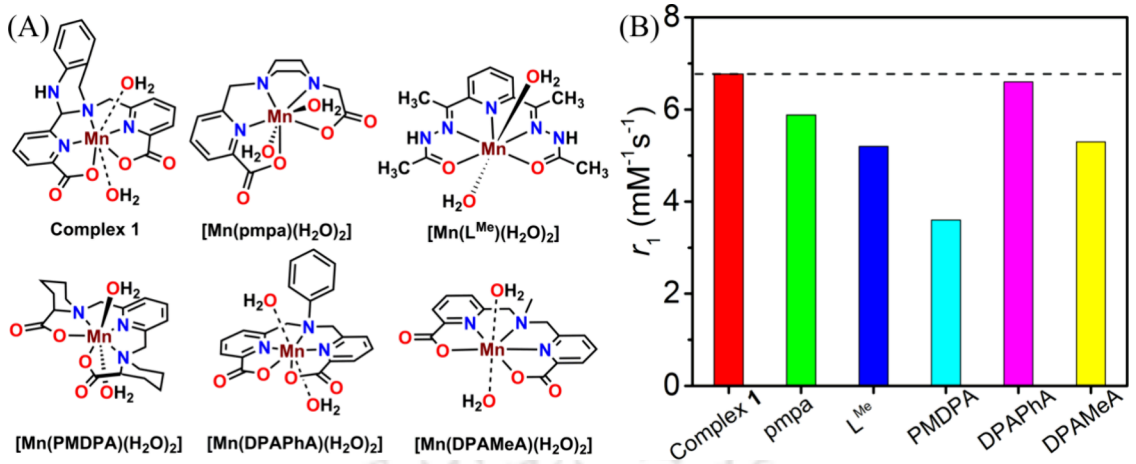

Figure 2. (A) Schematic representation of Complex **1** along with different bis(aquated) Mn(II)-chelates; (B) Corresponding r_1 values, measurements were done at pH 7.4, 1.41 T, and 25 °C.

Table 1. Comparison of Relaxivity, Serum Affinity Constants, and Octanol–Water Partition Coefficients of Complex 1 and Other Reported Mn(II)-Based Systems

		r_1 ($mM^{-1}s^{-1}$)		r_2 ($mM^{-1}s^{-1}$)			
	log*P*	Water	Serum albumin	Water	Serum albumin	r_1[b] ($mM^{-1}s^{-1}$)	K_A (M^{-1})
Complex **1**[a]	−0.45	5.32	19.09	19.20	45.80	27.62	1.66×10^3
Mn-PC2A-BP[b]	—	3.8	23.5	—	—	35.7[c]	2.51×10^3[c]
Mn-1,4-DO2AMBz[d]	—	3.5	17.50	—	—	27.4	1.90×10^3
Mn-EOB-PC2A[e]	—	2.83	5.85	5.27	14.31	—	—
Mn[EDTA-BTA][f]	−1.84	3.5	15.1	4.9	34.5	—	95
Mn-BnO-TyrEDTA[g]	0.18	4.34	15.81	6.21	20.70	—	—
Mn[EDTA][g]	−2.27	2.83	3.46	3.90	4.57	—	—

[a]Measurements done without and with 0.67 mM BSA, at pH ∼ 7.4 (HEPES), 1.41 T, and 37 °C. [b]Data obtained from ref 40. Experimental conditions: 0.67 mM HSA, at pH ∼ 7.4, 0.49 T, and 37 °C. [c]Data obtained at 25 °C. [d]Data obtained from ref 58. Experimental conditions: 0.67 mM HSA, at pH ∼ 7.4, 0.49 T, and 25 °C. [e]Data obtained from ref 59. Experimental conditions: 0.67 mM HSA, at pH ∼ 7.4 and 1.5 T. [f]Data obtained from ref 43. Experimental conditions: 0.67 mM HSA, at pH ∼ 7.4, 1.5 T, and 24 °C. [g]Data obtained from ref 41. Experimental conditions: 0.67 mM BSA, at pH ∼ 7.4, 0.47 T, and 32 °C.

23.94 mM^{-1} s^{-1} at 25 °C and 19.20 mM^{-1} s^{-1} at 37 °C, 1.41 T, and pH ∼ 7.4 (Figures S15A and S15B). The observed relaxation values were a little higher than the previously reported acyclic bis(aquated) Mn(II) complexes, as presented in Figure 2.[34,36,38,49] The effect of anions, which are prevalent in the biological system, on the relaxivity of Complex **1** has been investigated by recording the change in the relaxivity in the presence of a 200-fold excess of biphosphate (HPO_4^{2-}), bicarbonate (HCO_3^-), and citrate ($C_6H_5O_7^{3-}$) anions (Figure S15D). No appreciable difference in the relaxivity value confirmed that the coordination sphere of the complex was not affected by the anions. Furthermore, no appreciable change in the UV–vis spectra of Complex **1** in the presence of the anions also supported the stability of the complex (Figure S14B). A slight increase in the relaxation value in the presence of HPO_4^{2-} and $C_6H_5O_7^{3-}$ alluded to a supramolecular aggregation in the presence of the anions, which increased the rotational correlation time.[57]

Mn-complexes can undergo dechelation at low pH via ligand protonation. Furthermore, the substitution of inner-sphere water molecules or deprotonation of water molecules to the hydroxide anion at a higher pH can significantly affect the contrast ability and the stability of the Mn(II)-based contrast agents. Thus, UV–vis spectra of the complex were recorded at various pH values to examine the stability of Complex **1** (Figure S14A). The spectra obtained at pH 2.1 and pH 7.4 were the same, confirming the complex's stability at pH 2.1. The longitudinal relaxivity value of water protons was also measured in the pH range of 2.1 to 10.0 at 1.41 T and 37 °C (Figure S15C). Gratifyingly, no alteration in the value was noticed that buttressed the stability of the bis(aquated) form of the complex in the pH range.

Serum albumin, the most prominent protein in blood plasma, is known to bind with various lipophilic ligand systems.[40,60] Interaction between small molecules of paramagnetic contrast agents with the bulky protein moiety significantly increases the rotational correlation time (τ_R) and, consequently, enhances the relaxivity value.[58,61] Complex **1** showed ∼360% amplification of the longitudinal relaxivity value (r_1 = 19.09 mM^{-1} s^{-1}) in the presence of 0.67 mM BSA at pH ∼ 7.4, 1.41 T, and 37 °C (Table 1, Figures S16 and S17A). This feature demonstrates a substantial interaction between the protein and Complex **1**. Notably, the relaxivity values obtained are considerably higher than previously reported $[EDTA]^{4-}$ or various macrocyclic-based Mn(II) systems, mentioned in Table 1.[40,41,43,58,62] A deeper insight into the noncovalent interaction between Complex **1** and the albumin protein was done by following the observed relaxation rate (R_1^{obs}) values of the complex aqueous solutions with a constant Mn(II) ion concentration in the presence of an increasing amount of protein at 37 °C. R_1^{obs} gradually amplified with the increment in the albumin concentration.

https://doi.org/10.1021/acsabm.3c01236
ACS Appl. Bio Mater. 2024, 7, 1831–1841

This finding was due to the increment in the albumin-bound complex **1** fragment fraction, as determined by the ultrafiltration method (Figure S17B). Experimental data were fitted to a 1:1 binding isotherm following the Proton Relaxation Enhancement (PRE) equations (Supporting Information). Assuming one independent binding site of the protein moiety for the complex, *i.e.*, $n = 1$, the relaxivity of the bound complex (r_1^b) was found to be 27.62 mM^{-1} s^{-1}, and the albumin association constant $K_A = 1.66 \times 10^3$ M^{-1}. The obtained values were comparable to reported Mn(II)-based ligand systems containing the hydrophobic benzyl unit.[40] Noteworthy, the complex solution used for the study contained both enantiomers in almost an equal concentration as evidenced by $[\alpha]_D^{20} = 0.0$, c = 0.65 g in 100 mL of water. Thus, the realized interactions with the protein are the combined effect of each of the isomers. A pure stereoisomer might experience different interactions compared to the other.

The protein affinity of Complex **1** could be directly related to the octanol−water partition coefficient (log *P*) value of −0.45, reflecting the considerable lipophilicity of the ligand system. This property improved the relaxivity of Complex **1** and reciprocated to 65% binding of complex molecules to the albumin protein at physiological conditions (Figure S17B). Parallelly, ∼252% augmentation in the r_2 value (45.80 mM^{-1} s^{-1} in 0.67 mM BSA versus 19.17 mM^{-1} s^{-1} in water, at pH ∼ 7.4, 1.41 T, and 37 °C) has also been noticed (Figure S16B), which reflected the possibility of the T_1-T_2 dual-mode imaging character of Complex **1** *in vivo*.

The serum stability for Complex **1** was evaluated by monitoring the change in the longitudinal relaxation rate (R_1 value) of an aqueous Complex **1** solution (0.28 mM) with time, in the presence of 0.67 mM BSA, at pH ∼ 7.4, 37 °C, and 1.41 T (Figure S18A). The relaxivity value (r_1) increased to 18.6 mM^{-1} s^{-1} within 90 s due to binding of the complex with the albumin protein (*vide supra*). To note, under the same measurement conditions, the relaxivity value of 70.74 mM^{-1} s^{-1} was observed by employing an aqueous $MnCl_2$ solution as the complex substitute. A minor change in the relaxivity value from 18.6 mM^{-1} s^{-1} to 19.93 mM^{-1} s^{-1} was noticed within 24 h in the presence of Complex **1**, thus eliminating the possibility of serum albumin protein-induced complete dechelation of the complex (Figure S18).

The stability of the complex was also been investigated in human plasma by replicating the *in vivo* analysis condition, *i.e.*, maintaining the complex concentration at 0.8 mM as administered in mice blood (*vide infra*). The r_1 relaxivity value in this case escalated to 13.95 mM^{-1} s^{-1} in 60 s, and the maximum value attained was ∼15.6 mM^{-1} s^{-1} in 24 h (Figure S18B). A complete dechelation would provide r_1 = 30.11 mM^{-1} s^{-1} as determined using free Mn(II) ions of the same concentration, thus, reflecting the existence of Complex **1** in the chelated form during the course of *in vivo* studies.

To evaluate the protein-dependent boost in the relaxivity in terms of magnetic resonance image brightness, T_1-weighted phantom images of the aqueous 0.5 mM Complex **1** solution in the absence and presence of 0.67 mM BSA at 7 T, pH ∼ 7.4, and 25 °C were recorded *in vitro* (Figures 3A, S19). The signal intensity was enhanced by 43% in the presence of the complex, confirming the signal brightening property (T_1-contrast agent). Perceptibly, a substantial boost in the image contrast (57%) on adding 0.67 mM BSA to the Complex **1** solution complied with the protein-binding-dependent r_1 amplification.

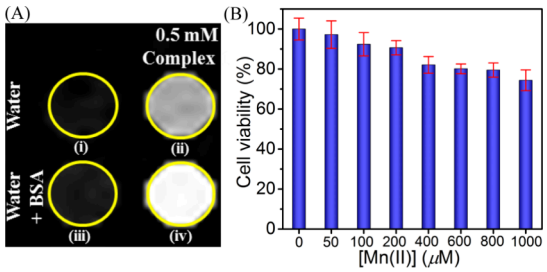

Figure 3. (A) T_1-weighted phantom MR images of (i) water, (ii) 0.5 mM Complex **1**, (iii) 0.67 mM BSA, and (iv) 0.5 mM Complex **1** in the presence of 0.67 mM BSA, at 7 T, pH ∼ 7.4, and 25 °C. (B) Percentage of cell viability analysis for the treatment of Complex **1** on HeLa cells.

Prior to the *in vivo* examination of Complex **1** as an MR-contrast agent, the biocompatibility of the complex was investigated by performing an MTT [3-(4,5-dimethylthiazol-2-yl)-2,5-diphenyltetrazolium bromide] assay on a HeLa cell line. After 48 h of incubation of the cells with an increasing concentration of Complex **1**, the percentage of viable cells was quantified and presented in Figure 3B. A modest decline in the viability was noticed up to a 200 μM concentration of the complex. Upon increasing the concentration, the cell viability decreased gradually and reached 74% at the concentration of 1 mM. Thus, the cell viability experiments conferred the low cytotoxicity of the complex.

The contrast ability of Complex **1**, *in vivo*, was tested by imaging healthy C57BL/6 mice (n = 3) on a small-bore animal MRI scanner (Biospec 70/20, M/s Bruker Biospin GmBH, Germany) at 7 T, before and after 0.08 mmol/kg intravenous administration. The mice were anesthetized with a 1−3% isoflurane/oxygen mixture maintaining the body temperature at 37 °C and sequentially imaged prior to- and postcontrast injection up to 90 min using T_1-weighted 3D fast low-angle low-shot (FLASH) and two-dimensional rapid acquisition with refocused echo (RARE) imaging protocols. Coronal and axial T_1-weighted MR images at different time points are presented in Figures 4A and 5.

An intense contrast enhancement in the gallbladder (160%; Figure 4C) and kidneys (110%; Figure 4C) was noticed after 10 min of the contrast agent application. Moreover, as reflected by serum protein association experiments for Complex **1**, the highly vascularized liver region corresponding to the long retention of the contrast material in the blood vessels was realized (Figure 5, Liver part). Thus, Complex **1** could also be examined as a blood pool contrast agent. Neutral Complex **1** molecules with amphiphilic nature (log *P* = −0.45) are believed to be partially assimilated by hepatocytes with low retention time and excreted via the biliary system.[41] Consequently, the high signal intensity in the gall bladder and intestine was apprehended within 10 min of the contrast agent administration.

The time-dependent signal intensity changes under the region of interest (ROI) of different organs, as depicted in Figure 4, were analyzed by *ImageJ* software. Precontrast signal values were considered as the baseline, and the normalized signal-to-noise ratio (nSNR) for different organs was calculated and plotted as a function of time in Figure 4B. While the brightness engendered by the contrast agent in the gallbladder region gradually fades out within an hour, a considerable residual contrast was noticed in the kidneys compared to the

https://doi.org/10.1021/acsabm.3c01236
ACS Appl. Bio Mater. 2024, 7, 1831−1841

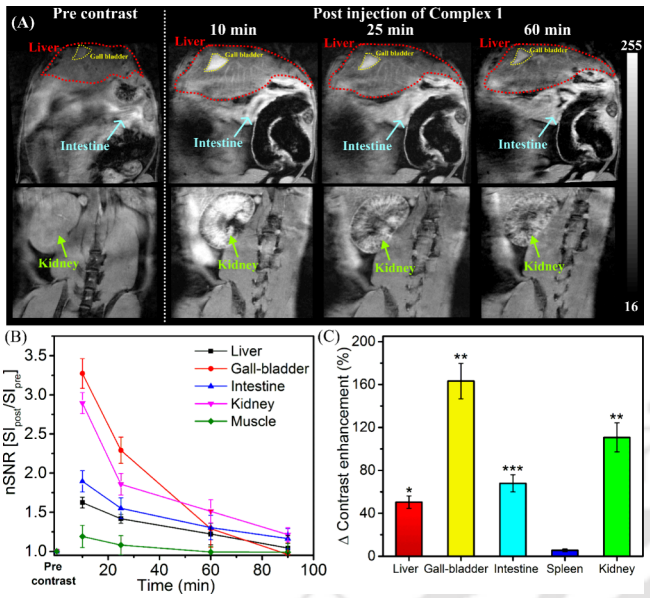

Figure 4. (A) T_1-weighted coronal (FLASH sequence) images of C57BL/6 mice showing contrast changes in liver (red dotted line), gallbladder (yellow dotted line), intestine (cyan dotted line), and kidneys (green dotted line) at different time points, pre- and postadministration of Complex **1** (0.08 mmol/kg w.r.t. [Mn^{II}]), at 7 T from an animal MRI scanner. (B) Normalized signal-to-noise ratio (nSNR) (relative to preinjection) plot for different ROIs as a function of time subsequent to Complex **1** administration. (C) Quantitative image analysis by measuring signal intensity changes in each organ post 10 min of contrast injection, normalized to muscle. Bars represent the standard error of the mean (n = 3 animals per group; $^*P < 0.05$, $^{**}P < 0.02$, $^{***}P < 0.001$).

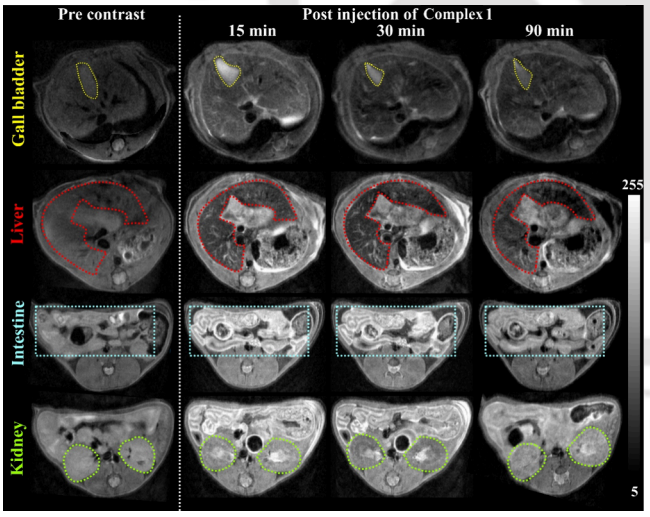

Figure 5. T_1-weighted axial (RARE sequence) images of C57BL/6 mice showing contrast changes in gallbladder (yellow dotted line), liver (red dotted line), intestine (cyan dotted line), and kidneys (green dotted line) at different time points, pre- and postadministration of Complex **1** (0.08 mmol/kg w.r.t. [Mn^{II}]), at 7 T from an animal MRI scanner.

precontrast images (Figures 4B and 5). This indicated a longer retention of Complex **1** in the tubules of the cortex. It is to be noted that no acute toxicity in the mice was observed postinjection while monitored for 15 days.

Nonetheless, *in vivo* biodistribution of Complex **1** after 10 min of its administration was determined by estimating the Mn content in the various organ tissues (liver, gall bladder, pancreas, spleen, kidneys, and bladder). In this context, the organs were resected and digested in aqua regia, followed by ICP-MS analysis. The highest manganese content was obtained in the kidneys (Figure 6) followed by gallbladder

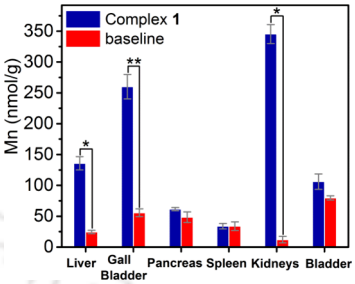

Figure 6. Manganese content in mice organ tissues, obtained by ICP-MS studies, 10 min after intravenous administration of Complex **1**. n = 3/group; $^*P < 0.05$, $^{**}P < 0.01$.

and liver. These findings corroborate well with the organ-based contrast enhancement and consolidate the hepatic and renal uptake of the contrast agent as realized from the MR contrast images.

CONCLUSIONS

To summarize, we have demonstrated that by imparting the structural rigidity in the pentadentate chelate $[BenzPic_2]^{2-}$, the thermodynamically stable (log K_{cond} = 11.62) and kinetically inert ($k = 1.04 \times 10^{-2}$ s^{-1}) bis(aquated) Mn(II) complex (Complex **1**) can be realized. The presence of a 1,2,3,4-tetrahydroquinazoline unit in the ligand backbone engendered a lipophilic character (log $P = -0.45$) in the complex, which facilitated the interaction of Complex **1** with serum albumin protein with an association constant, $K_A = 1.66 \times 10^3$ M^{-1}. The complex exhibited r_1 = 5.32 mM^{-1} s^{-1} that amplified to 19.09 mM^{-1} s^{-1} at 1.41 T, 37 °C, and pH 7.4 in the presence of 0.67 mM BSA protein due to rigidification of the contrast agent. Thus, with an intravenous dose of 0.08 mM/kg in a healthy mouse, an excellent vascularization of the mouse liver along with brightening of the gallbladder, the kidney, and the liver was realized. A further modification of the coordination motif and the lipophilicity of the ligand is ongoing for the materialization of organ-specific Mn(II)-based contrast agents.

EXPERIMENTAL SECTION

Materials. All materials and solvents were acquired from commercial sources and used as supplied, unless noted otherwise. 2,6-Pyridinedicarboxylic acid, 2-aminobenzylamine, SeO_2, LiOH, Na_2H_2EDTA, and H_5DTPA were purchased from Sigma-Aldrich. $MnCl_2{\cdot}4H_2O$, $GdCl_3{\cdot}xH_2O$, sodium citrate, $NaHCO_3$, Na_2HPO_4, HNO_3 (69%), NH_4OH, HCl, NaOH, and solvents were obtained from Merck (India). HEPES and MES buffers were purchased from SRL. DIPEA was procured from TCI India. Albumin bovine fraction V was obtained from Spectrochem. Water used for experiments was purified by a Millipore water purifier, Milli-Q, Merck. HeLa cells (human cervical carcinoma) were procured from the National Center for Cell Sciences (NCCS), Pune, India.

Physical Methods. FT-IR spectra were recorded on a PerkinElmer Instrument at room temperature by making a KBr pellet and grinding the sample with KBr (IR grade). Mass spectra were obtained from either HRMS or a Q-TOF/MS spectrometer. UV/vis

https://doi.org/10.1021/acsabm.3c01236
ACS Appl. Bio Mater. 2024, 7, 1831−1841

spectra were obtained on a PerkinElmer, Lambda 750, UV/vis/NIR spectrometer. ^{1}H- and ^{13}C NMR analyses were done using Bruker 400 and 500 MHz NMR machines. Optimum pH was maintained using buffers. Longitudinal and transverse relaxivity values at 1.41 T were measured using a BRUKER minispec mq60 NMR analyzer. Exact Mn concentrations in different samples were estimated by ICP-MS (Model-Element XR, Thermo Fisher Scientific) and ICP-AES (Model-ARCOS, Simultaneous ICP Spectrometer, SPECTRO Analytical Instruments GmbH, Germany) techniques after treatment of each with a dilute HNO_3 solution.

Computational Details. The computational simulations are performed using the Gaussian 16[63] program and visualized with the GaussView V.5.09[64] packages. The calculations are done at the ωB97XD(ref 65)/cc-pVDZ(ref 66) level. The advantage of using long-range corrected RS-functionals is the range separation parameter ω, which provides a better description of the charge transfer prospect in the calculations.[67] Moreover, the use of all-electron basis sets (cc-PVDZ), including the transition metal atoms for the system, maintains consistency throughout the calculations.

Competition Titration. Spectrophotometric competitive batch titrations were done against Na_2H_2EDTA to estimate the affinity of the ligand for Mn(II) ions. Various aliquots of a standardized Na_2H_2EDTA stock solution ranging from 0.5 to 200 equiv relative to the ligand concentration were added to a constant [Mn(II)-L] solution (with a typical concentration ratio of 1:1, 0.1 mM) and equilibrated for 48 h to attain thermodynamic equilibrium. The ionic strength of the reacting mixture was maintained with 0.15 M NaCl, at pH ∼ 7.4 (0.01 M HEPES buffer). The overall UV−vis absorbance spectra were inspected, and a particular range of wavelengths was selected where gradual spectral changes were considered. The absorbance value of each set was recorded with respect to the value of ligand $Li_2Benz(pic)_2$ (represented as L) at that particular wavelength. The Na_2H_2EDTA solution of exact concentration and pH was used as the background for each scan. Utilizing the respective absorbance values, further calculations gave the concentrations of the $MnBenz(pic)_2$ complex, MnEDTA complex, free ligand $Li_2Benz(pic)_2$, and free Na_2H_2EDTA for each set which were calculated from the variation in absorbance in each set of samples. The logarithmic value of the concentration ratio of [MnEDTA] to [MnL] was plotted against a similar logarithmic value of the respective ratio of free [Na_2H_2EDTA] to free [L] of each sample. The X-intercept of the linear plot obtained was employed to calculate the log K_{cond} value for the synthesized ligand $Li_2Benz(pic)_2$, using the formula mentioned below.

$$[MnL] + [Na_2H_2EDTA] \rightleftharpoons [MnEDTA] + [L]$$

$$K_{cond} = \frac{[MnEDTA][L]}{[MnL][Na^2H^2EDTA]}$$

$$\log([MnEDTA]/[MnL]) = \log K_{cond} + \log([Na_2H_2EDTA]/[L]) \quad (1)$$

Transmetalation Studies. Gradual changes in the transverse relaxation rate (R_2) of samples containing the Complex **1**/MnEDTA/GdDTPA solution (1 mM) challenged with 10 equiv amounts of $ZnCl_2$ were monitored over time. Measurements were performed either in an aqueous medium or in a BSA medium (0.67 mM), at pH ∼ 6.5 (MES buffer), I = 0.15 M NaCl, 1.41 T, and 25 °C, using a BRUKER minispec mq60 NMR analyzer. The ΔR_2 value versus time was plotted for each sample, and data points were fitted to the pseudo-first-order equation to evaluate the rate constant values.

Relaxometric Analyses. T_1 and T_2 values of Complex **1** solutions were recorded using a BRUKER minispec mq60 NMR analyzer at pH ∼ 7.4, 1.41 T, 25 and 37 °C. Relaxivity values (r_i, i = 1/2) were obtained from the slope of linear plots of relaxation rates ($1/T_i$) versus Mn(II) concentration. The exact metal concentration in the sample stock was determined by the ICP-AES technique after digesting the solution with nitric acid. An anion tolerance study was done by measuring T_1 of the Complex **1** solution, after incubation with 200 equiv of the respective anion, at 37 °C.

BSA Interaction Study. r_1 values for Complex **1** solutions were measured after 30 min of incubation of samples in the presence of 0.67 mM bovine serum albumin (BSA) at physiological conditions (pH ∼ 7.4, 37 °C, BSA concentration maintained at 4.5% w/v; measured at 1.41 T).

Determination of the Affinity Constant for the Complex 1·BSA System. The binding constant of Complex **1** with serum albumin was determined following the established procedure.[68] The proton relaxation enhancement titration experiment was performed. The R_1 value (longitudinal relaxation rates) of incubated samples containing a fixed concentration of Complex **1** (0.35 mM) and increasing concentration of BSA (0−1.8 mM) were recorded at pH ∼ 7.4, 37 °C, and 1.41 T. Free- and serum albumin-bound Complex **1** molecules were separated by ultrafiltration (5000 Da cutoff) and subsequently quantified by ICP-MS. Nonlinear increasing points were obtained by plotting the R_1 values against BSA concentration. Fitting of the data points using Equation S2 gave the binding constant, K_A.

Stability of Complex 1 in Serum Albumin and Human Plasma. The R_1 values for Complex **1** or $MnCl_2$ solutions ([Mn^{II}] = 0.28 mM in 0.67 mM BSA and [Mn^{II}] = 0.80 mM in human plasma) were monitored for 24 h and plotted against time. Experiments were performed at pH ∼ 7.4, 1.41 T, and 37 °C.

Octanol−Water Partition Coefficient. The lipophilicity of Complex **1** was tested following the reported procedure.[40] To elaborate, Complex **1** was added to a mixture of octanol and water (2 mL, 1:1 v/v), and the mixture was gently shaken for 48 h to equilibrate the mixture. Further on, it was kept untouched for 24 h to settle down. Layers were carefully separated, and the Mn(II) content in each layer was estimated by the ICP-AES technique. The partition coefficient was calculated by using the formula log P = log(C_o/C_w). Here, P represented the partition coefficient; C_o and C_w implied the concentration of Complex **1** in the octanol and water layers, respectively. The experiment was performed in triplicate to improve accuracy.

***In Vitro* MR Imaging.** T_1-weighted phantom MR images of microcentrifuge tubes containing the Complex **1** solution (0.5 mM), in the absence and presence of 0.67 mM BSA, were recorded using a 7 T Biospec 70/20, M/s Bruker Biospin GmBH, Germany. Parameters adopted are mentioned: Bruker:RAREVTR sequence, TR (repetition time) = 700.0 ms, TE (echo time) = 8.5 ms, slice thickness = 2.5 mm, field of view (FOV) = 6.00 cm, and matrix = 256 × 192.

MTT Assay. Cell viability of Complex **1** was assessed by performing the MTT [3-(4,5-dimethylthiazolyl-2)-2,5-diphenyltetrazolium bromide] test on the cervical cancer (HeLa) cell line. Cells were maintained in Dulbecco's modified Eagle's medium (DMEM) buffer, supplemented with 10% (v/v) fetal bovine serum (FBS), 1% penicillin, and streptomycin at 37 °C in humidified air containing 5% CO_2. Cells were grown overnight in a 96-well plate at a density of 5 × 103 cells/well. A succeeding cell-line was treated with the increasing concentration of Complex **1** (0−1 mM) for 48 h, and 0.5 mg/mL MTT in DMEM was added to each well and incubated for 1.5 h, afterward. DMSO (150 μL) was added to each well, and absorbance was recorded at 570 nm. Untreated cells were considered as control with 100% viability, and respective cell viability was calculated, accordingly.

***In Vivo* MR Imaging.** 8-week-old male C57BL/6 mice (total number = 10) were acquired from the National Institute of Biologicals (NIB), Noida, Uttar Pradesh (UP), India. They were housed in micro isolator cages at biosafety level-2 in the animal house of Maharshi Dayanand University, Rohtak, India, and their feeding pattern was regularly monitored. Animal experimental protocol was approved by the Institutional Animal Ethical Committee (IAEC), with approval number CAH 114-120 dated 23-05-2022. During the studies, mice were anesthetized with a 1−3% isoflurane/oxygen mixture. Normal respiration and body temperature (37 °C) were maintained. Subsequently, animals were scanned at 7 T using a small-bore animal scanner (Biospec 70/20, M/s Bruker Biospin GmBH, Germany) prior to and postcontrast administration implying T_1-weighted 3D fast low-angle low-shot (FLASH) and two-dimensional rapid acquisition with refocused echo (RARE) imaging protocols. Imaging protocols

https://doi.org/10.1021/acsabm.3c01236
ACS Appl. Bio Mater. 2024, 7, 1831−1841

adopted were as follows: T_1-FLASH, TR/TE = 316.0 ms/4.5 ms, Flip angle = 30°, matrix = 256 × 256, slice thickness = 0.7 mm, 22 slices; T_1-RARE, TR/TE = 3647.4 ms/8.0 ms, Flip angle = 90°, the field of view (FOV) = 50 × 50 mm, matrix = 256 × 256, slice thickness = 0.5 mm, 86 slices.

At first, a batch of healthy mice (n = 4) was selected, anesthetized, and imaged by the MRI scanner. Afterward, each mouse received intravenous administration of the Complex **1** solution in PBS, at a dosage concentration of 0.08 mmol/kg w.r.t. [Mn^{II}], in the tail vein. The sequential T_1-weighted scans were performed on the mice at different time points, up to 90 min. Images were analyzed by quantizing the signal intensity (SI) in the region-of-interest (ROI) of the respective organs using *ImageJ* software after subtracting over the noise intensity. The normalized signal-to-noise ratio (nSNR) was calculated by dividing the SI at each time point by the prior contrast image SI. The contrast-to-noise ratio (CNR) was estimated by normalizing the signal intensity of ROIs with that of the back muscles in the same slide. Preinjection SNRs and CNRs were considered as the baseline, and the percentage change in the respective CNR (% ΔCNR) upon the contrast agent injection was plotted. Considering the analyzed-ROIs, the statistical significance was examined by using unpaired two-tailed *t* tests to validate the significance of the experiment. The results with *P*-values < 0.05 were considered useful.

Biodistribution. Mice (n = 3/group) were sacrificed after 10 min post a similar dosage of Complex **1** along with another group receiving only saline (0.9%). Selected organs were dissected and digested upon treatment with 2 mL of freshly prepared aqua regia (1:3 mixture of HNO_3 and HCl) and lysed for 24 h. The tissue samples were dried by heating at 120 °C, sonicated thoroughly after the addition of 0.5 N HCl, and then centrifuged (4000g, 5 min) to collect a clear supernatant solution. This crude was diluted with a 4% HNO_3 acid solution, and subsequently, the Mn content in each sample was estimated by the ICP-MS technique.

Syntheses. *Synthesis of $C_{15}H_{15}N_3O_2$ (**1**).* Methyl 6-formyl-2-pyridinecarboxylate was prepared following the reported procedure.[69] An equivalent amount of it (0.66 g, 4.0 mmol) was slowly added to a methanolic solution of 2-aminobenzyl amine (0.49 g, 4.0 mmol), and the mixture was stirred for 16 h. Removal of the solvent gave a brownish crude oil, which on trituration with hexane gave compound **1** as a white solid. Yield = 0.92 g (86%). FTIR (KBr pellet cm^{-1}): 3383(br), 3294(m), 3052(w), 3005(w), 2925(w), 2882(w), 2840(w), 1719(s), 1603(s), 1587(s), 1492(m), 1471(s), 1436(m), 1415(s), 1301(m), 1251(s), 1197(m), 1151(s), 1073(m), 1001(w), 962(m), 867(m), 836(m), 745(m), 622(w). ^{1}H NMR ($CDCl_3$, 500 MHz): δ 8.08 (d, *J* = 5 Hz, 1H), 7.88 (m, 2H), 7.06 (t, *J* = 5 Hz, 1H), 6.95 (d, *J* = 10 Hz, 1H), 6.72 (m, 2H), 5.35 (s, 1H), 5.20 (s br, 1H), 4.32 (d, *J* = 16 Hz, 1H), 4.05 (d, *J* = 16 Hz, 1H), 4.00 (s, 3H) ppm. ^{13}C NMR ($CDCl_3$, 125 MHz): δ 165.69, 159.71, 147.44, 143.21, 138.02, 127.47, 126.25, 124.76, 124.68, 121.61, 118.46, 116.10, 69.15, 52.95, 46.84 ppm. ESI-MS (+) *m*/*z* for $[C_{15}N_{15}N_3O_2 + H]^+$ calcd, 270.1237; found, 270.1245.

*Synthesis of $C_{23}H_{22}N_4O_4$ (**2**).* Methyl 6-(bromomethyl)picolinate was reproduced according to the literature reported earlier.[70] KI (0.58 g, 3.5 mmol) and DIPEA (0.95 g, 7.3 mmol) were subsequently added to a solution of compound **1** (0.79 g, 2.9 mmol) in dry acetonitrile (15 mL), under N_2 atmosphere, and stirred for 15 min. Methyl 6-(bromomethyl)picolinate (0.80 g, 3.5 mmol) was finally added, over time, and the mixture was heated to 60 °C. After 20 h, the reaction ceased, and the solvent was evaporated to dryness. The residue was thoroughly washed with water and brine and then extracted with CH_2Cl_2 (3 × 30 mL). The organic part, after drying over Na_2SO_4, was evaporated to obtain a yellow solid, which was further purified by column chromatography on silica gel using hexane/ethyl acetate (1:2) as an eluent to get compound **2** as a sticky yellow solid (R_f = 0.4). Yield = 0.84 g (70%). FTIR (KBr pellet cm^{-1}): 3595(w), 3395(br), 3060(w), 3009(w), 2951(w), 2907(w), 2853(w), 1722(s), 1608(s), 1588(s), 1494(m), 1457(s), 1437(m), 1314(s), 1293(s), 1257(m), 1226(m), 1194(m), 1137(s), 1083(s), 994(m), 912(m), 759(w), 731(w), 647(w). ^{1}H NMR ($CDCl_3$, 400 MHz): δ 8.04 (d, *J* = 8 Hz, 1H), 7.98 (d, *J* = 8 Hz, 1H), 7.93 (d, *J* = 8 Hz, 1H), 7.84 (m, 3H), 7.09 (t, *J* = 8 Hz, 1H), 6.88 (d, *J* = 8 Hz, 1H), 6.79 (d, *J* = 8 Hz, 1H), 6.70 (t, *J* = 8 Hz, 1H), 5.54 (s, 1H), 4.29 (d, *J* = 16 Hz, 1H), 4.02 (s, 3H), 3.94 (s, 3H), 3.89 (m, 1H) 3.78 (m, 2H) ppm. ^{13}C NMR ($CDCl_3$, 100 MHz): 171.23, 161.56, 159.78, 151.67, 149.84, 140.61, 132.39, 130.80, 123.28, 121.92, 117.39, 112.79, 92.78, 60.69, 59.24, 49.62. ESI-MS (+) *m*/*z* for $[C_{23}H_{22}N_4O_4 + H]^+$ calcd, 419.1713; found, 419.1776.

*Synthesis of $C_{21}H_{16}Li_2N_4O_4$ (**3**, Li_2Benz(pic)$_2$).* To a solution of compound **2** (0.33 g, 0.8 mmol) in THF (6 mL) was slowly added an aqueous solution of lithium hydroxide (0.04 g, 1.7 mmol), and the mixture was stirred for 2 days under dark conditions. Afterward, the solvent was evaporated to dryness to afford a light-yellow solid. Rapid washing with a minimum amount of methanol (~4 mL) gave ligand **Li_2Benz(pic)$_2$** as a white solid. Yield = 0.29 g (92%). FTIR (KBr pellets cm^{-1}): 3482(w), 3359(br), 3100(w), 2906(w), 2859(w), 1633(w), 1615(s), 1586(s), 1574(s), 1494(m), 1427(s), 1395(s), 1264(s), 1187(m), 1117(m), 1080(m), 1007(m), 858(m), 786(s), 748(m), 687(m). ^{1}H NMR (D_2O, 400 MHz): δ 7.82 (m, 1H), 7.76 (m, 3H), 7.56 (d, *J* = 8 Hz, 1H), 7.21 (m, 2H), 7.03 (d, *J* = 4 Hz, 1H), 6.91 (d, *J* = 8 Hz, 1H), 6.84 (t, *J* = 8 Hz, 1H), 5.31 (s, 1H), 4.02 (d, *J* = 12 Hz, 1H), 3.80 (m, 3H) ppm. ^{13}C NMR (D_2O, 400 MHz): δ 173.12, 172.95, 157.20, 157.08, 152.79, 152.65, 141.84, 138.31, 138.19, 128.00, 127.80, 125.77, 124.74, 123.50, 122.20, 119.34, 119.05, 115.84, 73.33, 55.52, 51.43 ppm. ESI-MS (+) *m*/*z* for $[C_{21}H_{17}N_4O_4Li + H]^+$ calcd 397.1473, found 397.1459.

*Synthesis of $C_{21}H_{20}MnN_4O_6$ (Complex **1**).* An aqueous solution of **Li_2Benz(pic)$_2$** (0.12 g, 0.3 mmol), at pH ~ 6.5 (maintained using a dilute HCl solution), was reacted with $MnCl_2{\cdot}4H_2O$ (0.05 g, 0.28 mmol) by stirring for 15 min at room temperature. The pH of the resultant solution was checked another time and allowed to stir for another 24 h to obtain a dirty yellow solution. Slow evaporation of the solution gave a brown solid, which was dissolved in a minimum amount of methanol (~5 mL) and diffused under a diethyl ether atmosphere to obtain Complex **1** as a white shiny solid with 42% yield (0.06 g). High-Performance Liquid Chromatography (HPLC) was performed to ensure >95% purity of the synthesized compound (Figure S10). FTIR (KBr pellets cm^{-1}): 3473(m), 3388(br), 3270(br), 3086(w), 3020(w), 2911(w), 2854(w), 1622(s), 1585(s), 1571 (s), 1493(s), 1427 (m), 1389(s), 1265(s), 1185(m), 1150(m), 1119(m), 1072(s), 1019(s), 981(m), 859(m), 770(m), 753(m), 701(m), 675(m), 651(m). ESI-MS (+) *m*/*z* for $[C_{21}H_{16}MnN_4O_4 + H]^+$ calcd, 444.0624, found 444.0519.

■ ASSOCIATED CONTENT

Supporting Information

The Supporting Information is available free of charge at https://pubs.acs.org/doi/10.1021/acsabm.3c01236.

Characterization of the ligand and Complex **1**; IR, NMR, mass, and EPR spectra of the ligand and **1**; reproducibility of the relaxivity values; spectrophotometric competition batch titration plot; kinetic inertness analysis data and optimized coordinates (PDF)

■ AUTHOR INFORMATION

Corresponding Author

Chandan Mukherjee − *Department of Chemistry, Indian Institute of Technology Guwahati, Guwahati 781039 Assam, India;* orcid.org/0000-0002-2771-2468; Email: cmukherjee@iitg.ac.in

Authors

Riya Mallik − *Department of Chemistry, Indian Institute of Technology Guwahati, Guwahati 781039 Assam, India*

Muktashree Saha − *Department of Biosciences and Bioengineering, Indian Institute of Technology Guwahati, Guwahati 781039 Assam, India*

https://doi.org/10.1021/acsabm.3c01236
ACS Appl. Bio Mater. 2024, 7, 1831−1841

Amrit Sarmah − *Institute of Organic Chemistry and Biochemistry of the Czech Academy of Sciences, CZ-16610 Prague, Czech Republic;* orcid.org/0000-0001-6429-6654
Vandna Singh − *Department of Medical Biotechnology, Maharshi Dayanand University, Rohtak 124001 Haryana, India*
Hari Mohan − *Department of Medical Biotechnology, Maharshi Dayanand University, Rohtak 124001 Haryana, India*
Priyanka Bhat − *Department of NMR, All India Institute of Medical Sciences, 110029 New Delhi, India*
S. Senthil Kumaran − *Department of NMR, All India Institute of Medical Sciences, 110029 New Delhi, India*

Complete contact information is available at: https://pubs.acs.org/10.1021/acsabm.3c01236

Author Contributions

CM designed the whole concept and wrote the manuscript with the help of the other authors. RM performed all the experiments and biostudies. MS contributed to cell viability measurements. PB recorded MR images. VS, HM, and SK supervised biostudies (*in vivo* and MR imaging).

Notes

The authors declare no competing financial interest.

■ ACKNOWLEDGMENTS

This project (BT/PR23622/NNT/281294/2017) is funded by the Department of Biotechnology, Govt. of India. RM and MS thank IIT Guwahati for the doctoral fellowship. FIST (DST) for the single crystal X-ray facility, the Department of Chemistry, and Central Instruments Facility, IIT Guwahati are thankfully acknowledged for instrumental facilities.

■ ABBREVIATIONS

DIPEA, *N*,*N*-diisopropylethylamine; THF, tetrahydrofuran; DFT, density functional theory; H_2Na_2EDTA, ethylenediaminetetraacetic acid disodium salt dihydrate; HEPES, 4-(2-hydroxyethyl)-1-piperazineethanesulfonic acid; DTPA, diethylenetriamine-*N*,*N*,*N*′,*N*″,*N*″-pentaacetate; r_1, longitudinal relaxivity; R_1, longitudinal relaxation rate; r_2, transverse relaxivity; R_2, transverse relaxation rate; r_1^b, longitudinal relaxivity of the serum-bound Complex **1**; PRE, Proton Relaxation Enhancement; BSA, bovine serum albumin; MTT, 3-(4,5-dimethylthiazol-2-yl)-2,5-diphenyltetrazolium bromide; FLASH sequence, fast low-angle low-shot sequence; RARE, rapid acquisition with refocused echo; ICP-MS, inductively coupled plasma mass spectrometry; ICP-AES, inductively coupled plasma atomic emission spectroscopy

■ REFERENCES

(1) Bonner, B. P.; Yurista, S. R.; Coll-Font, J.; Chen, S.; Eder, R. A.; Foster, A. N.; Nguyen, K. D.; Caravan, P.; Gale, E. M.; Nguyen, C. Contrast-Enhanced Cardiac Magnetic Resonance Imaging With a Manganese-Based Alternative to Gadolinium for Tissue Characterization of Acute Myocardial Infarction. *J. Am. Heart Assoc.* **2023**, *12*, No. e026923.
(2) Werner, E. J.; Datta, A.; Jocher, C. J.; Raymond, K. N. High-Relaxivity MRI Contrast Agents: Where Coordination Chemistry Meets Medical Imaging. *Angew. Chem., Int. Ed.* **2008**, *47*, 8568−8580.
(3) Wahsner, J.; Gale, E. M.; Rodríguez-Rodríguez, A.; Caravan, P. Chemistry of MRI Contrast Agents: Current Challenges and New Frontiers. *Chem. Rev.* **2019**, *119*, 957−1057.
(4) Gupta, A.; Caravan, P.; Price, W. S.; Platas-Iglesias, C.; Gale, E. M. Applications for Transition-Metal Chemistry in Contrast-Enhanced Magnetic Resonance Imaging. *Inorg. Chem.* **2020**, *59*, 6648−6678.
(5) Fu, S.; Cai, Z.; Ai, H. Stimulus-Responsive Nanoparticle Magnetic Resonance Imaging Contrast Agents: Design Considerations and Applications. *Adv. Healthc. Mater.* **2021**, *10*, No. e2001091.
(6) Wendland, M. F. Applications of manganese-enhanced magnetic resonance imaging (MEMRI) to imaging of the heart. *NMR Biomed.* **2004**, *17*, 581−594.
(7) Caravan, P.; Ellison, J. J.; McMurry, T. J.; Lauffer, R. B. Gadolinium(III) Chelates as MRI Contrast Agents: Structure, Dynamics, and Applications. *Chem. Rev.* **1999**, *99*, 2293−2352.
(8) Hingorani, D. V.; Bernstein, A. S.; Pagel, M. D. A Review of Responsive MRI Contrast Agents: 2005−2014. *Contrast Media Mol. Imaging* **2015**, *10*, 245−265.
(9) Li, H.; Luo, D.; Yuan, C.; Wang, X.; Wang, J.; Basilion, J. P.; Meade, T. J. Magnetic Resonance Imaging of PSMA-Positive Prostate Cancer by a Targeted and Activatable Gd(III) MR Contrast Agent. *J. Am. Chem. Soc.* **2021**, *143*, 17097−17108.
(10) Botta, M.; Carniato, F.; Esteban-Gómez, D.; Platas-Iglesias, C.; Tei, L. Mn(II) compounds as an alternative to Gd-based MRI probes. *Future Med. Chem.* **2019**, *11*, 1461−1483.
(11) Merbach, A. E.; Helm, L.; Tóth, E. *The Chemistry of Contrast Agents in Medical Magnetic Resonance Imaging*, 2nd ed.; John Wiley & Sons Inc.: Hoboken, NJ, 2013.
(12) Gupta, A.; Caravan, P.; Price, W. S.; Platas-Iglesias, C.; Gale, E. M. Applications for Transition-Metal Chemistry in Contrast-Enhanced Magnetic Resonance Imaging. *Inorg. Chem.* **2020**, *59*, 6648−6678.
(13) Ndiaye, D.; Cieslik, P.; Wadepohl, H.; Pallier, A.; Même, S.; Comba, P.; Tóth, É. Mn^{2+} Bispidine Complex Combining Exceptional Stability, Inertness, and MRI Efficiency. *J. Am. Chem. Soc.* **2022**, *144*, 22212−22220.
(14) Ma, M.; Zhu, H.; Ling, J.; Gong, S.; Zhang, Y.; Xia, Y.; Tang, Z. Quasi-amorphous and Hierarchical Fe_2O_3 Supraparticles: Active T_1-Weighted Magnetic Resonance Imaging *in Vivo* and Renal Clearance. *ACS Nano* **2020**, *14*, 4036−4044.
(15) Bulte, J. W. M.; Kraitchman, D. L. Iron oxide MR contrast agents for molecular and cellular imaging. *NMR Biomed.* **2004**, *17*, 484−499.
(16) Paranawithana, N. N.; Martins, A. F.; Jordan, V. C.; Zhao, P.; Chirayil, S.; Meloni, G.; Sherry, A. D. A Responsive Magnetic Resonance Imaging Contrast Agent for Detection of Excess Copper(II) in the Liver In Vivo. *J. Am. Chem. Soc.* **2019**, *141*, 11009−11018.
(17) Wang, L.; Lin, H.; Ma, L.; Jin, J.; Shen, T.; Wei, R.; Wang, X.; Ai, H.; Chen, Z.; Gao, J. Albumin-based nanoparticles loaded with hydrophobic gadolinium chelates as T_1-T_2 dual-mode contrast agents for accurate liver tumor imaging. *Nanoscale* **2017**, *9*, 4516−4523.
(18) Li, Z.; Yi, P. W.; Sun, Q.; Lei, H.; Zhao, H. L.; Zhu, Z. H.; Smith, S. C.; Lan, M. B.; Lu, G. Q. Ultrasmall Water-Soluble and Biocompatible Magnetic Iron Oxide Nanoparticles as Positive and Negative Dual Contrast Agents. *Adv. Funct. Mater.* **2012**, *22*, 2387−2393.
(19) Pražáková, M.; Ndiaye, D.; Tóth, É.; Drahoš, B. A seven-coordinate Mn(II) complex with a pyridine-based 15-membered macrocyclic ligand containing one acetate pendant arm: structure, stability and relaxation properties. *Dalton Trans.* **2023**, *52*, 7936−7947.
(20) Clough, T. J.; Jiang, L.; Wong, K.-L.; Long, N. J. Ligand design strategies to increase stability of gadolinium-based magnetic resonance imaging contrast agents. *Nat. Commun.* **2019**, *10*, 1420.
(21) Caravan, P.; Farrar, C. T.; Frullano, L.; Uppal, R. Influence of molecular parameters and increasing magnetic field strength on relaxivity of gadolinium- and manganese-based T_1 contrast agents. *Contrast Media Mol. Imaging.* **2009**, *4*, 89−100.
(22) Garda, Z.; Molnár, E.; Kálmán, F. K.; Botár, R.; Nagy, V.; Baranyai, Z.; Brücher, E.; Kovács, Z.; Tóth, I.; Tircsó, G. Effect of the

Nature of Donor Atoms on the Thermodynamic, Kinetic and Relaxation Properties of Mn(II) Complexes Formed With Some Trisubstituted 12-Membered Macrocyclic Ligands. *Front. Chem.* **2018**, *6*, 232.
(23) Agarwal, R.; Brunelli, S. M.; Williams, K.; Mitchell, M. D.; Feldman, H. I.; Umscheid, C. A. Gadolinium-based contrast agents and nephrogenic systemic fibrosis: a systematic review and meta-analysis. *Nephrol. Dial. Transplant.* **2008**, *24*, 856−863.
(24) McRae, S. W.; Cleary, M.; DeRoche, D.; Martinez, F. M.; Xia, Y.; Caravan, P.; Gale, E. M.; Ronald, J. A.; Scholl, T. J. Development of a Suite of Gadolinium-Free OATP1-Targeted Paramagnetic Probes for Liver MRI. *J. Med. Chem.* **2023**, *66*, 6567−6576.
(25) Di Gregorio, E.; Ferruato, G.; Furlan, C.; Lanzardo, S.; Nuzzi, R.; Gianolio, E.; Aime, S. The Issue of Gadolinium Retained in Tissues: Insights on the Role of Metal Complex Stability by Comparing Metal Uptake in Murine Tissues Upon the Concomitant Administration of Lanthanum- and Gadolinium-Diethylentriammino-pentaacetate. *Invest. Radiol.* **2018**, *53*, 167−172.
(26) Yang, L.; Krefting, I.; Gorovets, A.; Marzella, L.; Kaiser, J.; Boucher, R.; Rieves, D. Nephrogenic systemic fibrosis and class labeling of gadolinium-based contrast agents by the Food and Drug Administration. *Radiology* **2012**, *265*, 248−253.
(27) Dekkers, I. A.; Roos, R.; Van Der Molen, A. J. Gadolinium retention after administration of contrast agents based on linear chelators and the recommendations of the European Medicines Agency. *Eur. Radiol.* **2018**, *28*, 1579−1584.
(28) *PRAC Confirms Restrictions on the Use of Linear Gadolinium Agents*; EMA/424715/2017; European Medicines Agency: July 7, 2017.
(29) *FDA Drug Safety Communication: FDA Warns That Gadolinium based Contrast Agents (GBCAs) are Retained in the Body; Requires New Class Warnings*; U.S. Food and Drug Administration: December 19, 2017.
(30) Löwenthal, D.; Zeile, M.; Lim, W. Y.; Wybranski, C.; Fischbach, F.; Wieners, G.; Pech, M.; Kropf, S.; Ricke, J.; Dudeck, O. Detection and characterization of focal liver lesions in colorectal carcinoma patients: comparison of diffusion weighted and Gd-EOB-DTPA enhanced MR imaging. *Eur. Radiol.* **2011**, *21*, 832−840.
(31) Van Montfoort, J. E.; Stieger, B.; Meijer, D. K. F.; Weinmann, H. J.; Meier, P. J.; Fattinger, K. E. Hepatic Uptake of the Magnetic Resonance Imaging Contrast Agent Gadoxetate by the Organic Anion Transporting Polypeptide OATP1. *J. Pharmacol. Exp. Ther.* **1999**, *290*, 153−157.
(32) Wang, J.; Wang, H.; Ramsay, I. A.; Erstad, D. J.; Fuchs, B. C.; Tanabe, K. K.; Caravan, P.; Gale, E. M. Manganese-Based Contrast Agents for Magnetic Resonance Imaging of Liver Tumors: Structure−Activity Relationships and Lead Candidate Evaluation. *J. Med. Chem.* **2018**, *61*, 8811−8824.
(33) Phukan, B.; Patel, A. B.; Mukherjee, C. A water-soluble and water-coordinated Mn(II) complex: synthesis, characterization and phantom MRI image study. *Dalton Trans.* **2015**, *44*, 12990−12994.
(34) Phukan, B.; Mukherjee, C.; Goswami, U.; Sarmah, A.; Mukherjee, S.; Sahoo, S. K.; Moi, S. C. A New Bis(aquated) High Relaxivity Mn(II) Complex as an Alternative to Gd(III)-Based MRI Contrast Agent. *Inorg. Chem.* **2018**, *57*, 2631−2638.
(35) Molnár, E.; Camus, N.; Patinec, V.; Rolla, G. A.; Botta, M.; Tircsó, G.; Kálmán, F. K.; Fodor, T.; Tripier, R.; Platas-Iglesias, C. Picolinate-Containing Macrocyclic Mn^{2+} Complexes as Potential MRI Contrast Agents. *Inorg. Chem.* **2014**, *53*, 5136−5149.
(36) Anbu, S.; Hoffmann, S. H. L.; Carniato, F.; Kenning, L.; Price, T. W.; Prior, T. J.; Botta, M.; Martins, A. F.; Stasiuk, G. J. A Single-Pot Template Reaction Towards a Manganese-Based T_1 Contrast Agent. *Angew. Chem., Int. Ed.* **2021**, *60*, 10736−10744.
(37) Cieslik, P.; Comba, P.; Dittmar, B.; Ndiaye, D.; Tóth, É.; Velmurugan, G.; Wadepohl, H. Exceptional Manganese(II) Stability and Manganese(II)/Zinc(II) Selectivity with Rigid Polydentate Ligands. *Angew. Chem., Int. Ed.* **2022**, *61*, No. e202115580.
(38) Su, H.; Wu, C.; Zhu, J.; Miao, T.; Wang, D.; Xia, C.; Zhao, X.; Gong, Q.; Song, B.; Ai, H. Rigid Mn(II) chelate as efficient MRI contrast agent for vascular imaging. *Dalton Trans.* **2012**, *41*, 14480−14483.
(39) Ndiaye, D.; Sy, M.; Pallier, A.; Même, S.; de Silva, I.; Lacerda, S.; Nonat, A. M.; Charbonnière, L. J.; Tóth, É. Unprecedented Kinetic Inertness for a Mn^{2+}-Bispidine Chelate: A Novel Structural Entry for Mn^{2+}-Based Imaging Agents. *Angew. Chem., Int. Ed.* **2020**, *59*, 11958−11963.
(40) Kálmán, F. K.; Nagy, V.; Váradi, B.; Garda, Z.; Molnár, E.; Trencsényi, G.; Kiss, J.; Même, S.; Même, W.; Tóth, É.; Tircsó, G. Mn(II)-Based MRI Contrast Agent Candidate for Vascular Imaging. *J. Med. Chem.* **2020**, *63*, 6057−6065.
(41) Chen, K.; Li, P.; Zhu, C.; Xia, Z.; Xia, Q.; Zhong, L.; Xiao, B.; Cheng, T.; Wu, C.; Shen, C.; Zhang, X.; Zhu, J. Mn(II) Complex of Lipophilic Group-Modified Ethylenediaminetetraacetic Acid (EDTA) as a New Hepatobiliary MRI Contrast Agent. *J. Med. Chem.* **2021**, *64*, 9182−9192.
(42) Islam, M. K.; Baek, A.-R.; Yang, B.-W.; Kim, S.; Hwang, D. W.; Nam, S.-W.; Lee, G.-H.; Chang, Y. Manganese (II) Complex of 1,4,7-Triazacyclononane-1,4,7-Triacetic Acid (NOTA) as a Hepatobiliary MRI Contrast Agent. *Pharmaceuticals* **2023**, *16*, 602.
(43) Islam, M. K.; Kim, S.; Kim, H.-K.; Park, S.; Lee, G.-H.; Kang, H. J.; Jung, J.-C.; Park, J.-S.; Kim, T.-J.; Chang, Y. Manganese Complex of Ethylenediaminetetraacetic Acid (EDTA)−Benzothiazole Aniline (BTA) Conjugate as a Potential Liver-Targeting MRI Contrast Agent. *J. Med. Chem.* **2017**, *60*, 2993−3001.
(44) Gale, E. M.; Zhu, J.; Caravan, P. Direct Measurement of the Mn(II) Hydration State in Metal Complexes and Metalloproteins through ^{17}O NMR Line Widths. *J. Am. Chem. Soc.* **2013**, *135*, 18600−18608.
(45) Gale, E. M.; Atanasova, I. P.; Blasi, F.; Ay, I.; Caravan, P. A. Manganese Alternative to Gadolinium for MRI Contrast. *J. Am. Chem. Soc.* **2015**, *137* (49), 15548−15557.
(46) Mallik, R.; Saha, M.; Singh, V.; Mohan, H.; Kumaran, S. S.; Mukherjee, C. Mn(II) complex impregnated porous silica nanoparticles as Zn(II)-responsive "Smart" MRI contrast agent for pancreas imaging. *J. Mater. Chem. B* **2023**, *11*, 8251−8261.
(47) Snyder, E. M.; Asik, D.; Abozeid, S. M.; Burgio, A.; Bateman, G.; Turowski, S. G.; Spernyak, J. A.; Morrow, J. R. A Class of Fe^{III} Macrocyclic Complexes with Alcohol Donor Groups as Effective T_1 MRI Contrast Agents. *Angew. Chem., Int. Ed.* **2020**, *59*, 2414−2419.
(48) Caravan, P.; Comuzzi, C.; Crooks, W.; McMurry, T. J.; Choppin, G. R.; Woulfe, S. R. Thermodynamic Stability and Kinetic Inertness of MS-325, a New Blood Pool Agent for Magnetic Resonance Imaging. *Inorg. Chem.* **2001**, *40*, 2170−2176.
(49) Forgács, A.; Pujales-Paradela, R.; Regueiro-Figueroa, M.; Valencia, L.; Esteban-Gómez, D.; Botta, M.; Platas-Iglesias, C. Developing the family of picolinate ligands for Mn^{2+} complexation. *Dalton Trans.* **2017**, *46*, 1546−1558.
(50) Kálmán, F. K.; Tircsó, G. Kinetic Inertness of the Mn^{2+} Complexes Formed with AAZTA and Some Open-Chain EDTA Derivatives. *Inorg. Chem.* **2012**, *51*, 10065−10067.
(51) Uzal-Varela, R.; Lalli, D.; Brandariz, I.; Rodríguez-Rodríguez, A.; Platas-Iglesias, C.; Botta, M.; Esteban-Gómez, D. Rigid versions of $PDTA^{4-}$ incorporating a 1,3-diaminocyclobutyl spacer for Mn^{2+} complexation: stability, water exchange dynamics and relaxivity. *Dalton Trans.* **2021**, *50*, 16290−16303.
(52) Reddi, A. R.; Jensen, L. T.; Culotta, V. C. Manganese Homeostasis in Saccharomyces cerevisiae. *Chem. Rev.* **2009**, *109*, 4722−4732.
(53) Porcheron, G.; Garenaux, A.; Proulx, J.; Sabri, M.; Dozois, C. M. Iron, copper, zinc, and manganese transport and regulation in pathogenic enterobacteria: correlations between strains, site of infection and the relative importance of the different metal transport systems for virulence. *Front. Cell. Infect. Microbiol.* **2013**, *3*, 90.
(54) Pan, D.; Caruthers, S. D.; Senpan, A.; Schmieder, A. H.; Wickline, S. A.; Lanza, G. M. Revisiting an old friend: manganese-based MRI contrast agents. *Wiley Interdiscip Rev. Nanomed Nanobiotechnol.* **2011**, *3*, 162−173.

https://doi.org/10.1021/acsabm.3c01236
ACS Appl. Bio Mater. 2024, 7, 1831−1841

(55) Poole, D. S.; Doorenweerd, N.; Plomp, J. J.; Mahfouz, A.; Reinders, M. J. T.; van der Weerd, L. Continuous infusion of manganese improves contrast and reduces side effects in manganese-enhanced magnetic resonance imaging studies. *Neuroimage* **2017**, *147*, 1−9.
(56) Nystrom, N. N.; Liu, H.; Martinez, F. M.; Zhang, X.-A.; Scholl, T. J.; Ronald, J. A. Gadolinium-free Magnetic Resonance Imaging of the Liver via an Oatp1-Targeted Manganese(III) Porphyrin. *J. Med. Chem.* **2022**, *65*, 9846−9857.
(57) Develay, S.; Tripier, R.; Baccon, M. L.; Patinec, V.; Serratrice, G.; Handel, H. Cyclen based bis-macrocyclic ligands as phosphates receptors. A potentiometric and NMR study. *Dalton Trans.* **2005**, 3016−3024.
(58) Forgács, A.; Tei, L.; Baranyai, Z.; Esteban-Gómez, D.; Platas-Iglesias, C.; Botta, M. Optimising the relaxivities of Mn^{2+} complexes by targeting human serum albumin (HSA). *Dalton Trans.* **2017**, *46*, 8494−8504.
(59) Hall, R. C.; Qin, J.; Laney, V.; Ayat, N.; Lu, Z.-R. Manganese(II) EOB-Pyclen Diacetate for Liver-Specific MRI. *ACS Appl. Bio Mater.* **2022**, *5*, 451−458.
(60) Boros, E.; Caravan, P. Structure−Relaxivity Relationships of Serum Albumin Targeted MRI Probes Based on a Single Amino Acid Gd Complex. *J. Med. Chem.* **2013**, *56*, 1782−1786.
(61) Rolla, G.; De Biasio, V.; Giovenzana, G. B.; Botta, M.; Tei, L. Supramolecular Assemblies Based on Amphiphilic Mn^{2+} Complexes as High Relaxivity MRI Probes. *Dalton Trans.* **2018**, *47*, 10660−10670.
(62) Leone, L.; Anemone, A.; Carella, A.; Botto, E.; Longo, D. L.; Tei, L. A neutral and stable macrocyclic Mn(II) complex for MRI tumor visualization. *ChemMedChem.* **2022**, *17*, No. e202200508.
(63) Frisch, M. J.; Trucks, G. W.; Schlegel, H. B.; Scuseria, G. E.; Robb, M. A.; Cheeseman, J. R.; Scalmani, G.; Barone, V.; Mennucci, B.; Petersson, G. A.; Nakatsuji, H.; Caricato, M.; Li, X.; Hratchian, H. P.; Izmaylov, A. F.; Bloino, J.; Zheng, G.; Sonnenberg, J. L.; Hada, M.; Ehara, M.; Toyota, K.; Fukuda, R.; Hasegawa, J.; Ishida, M.; Nakajima, T.; Honda, Y.; Kitao, O.; Nakai, H.; Vreven, T.; Montgomery, J. A., Jr.; Peralta, J. E.; Ogliaro, F.; Bearpark, M.; Heyd, J. J.; Brothers, E.; Kudin, K. N.; Staroverov, V. N.; Kobayashi, R.; Normand, J.; Raghavachari, K.; Rendell, A.; Burant, J. C.; Iyengar, S. S.; Tomasi, J.; Cossi, M.; Rega, N.; Millam, J. M.; Klene, M.; Knox, J. E.; Cross, J. B.; Bakken, V.; Adamo, C.; Jaramillo, J.; Gomperts, R.; Stratmann, R. E.; Yazyev, O.; Austin, A. J.; Cammi, R.; Pomelli, C.; Ochterski, J. W.; Martin, R. L.; Morokuma, K.; Zakrzewski, V. G.; Voth, G. A.; Salvador, P.; Dannenberg, J. J.; Dapprich, S.; Daniels, A. D.; Farkas, Ö.; Foresman, J. B.; Ortiz, J. V.; Cioslowski, J.; Fox, D. J. *Gaussian 09*, Revision A.01; Gaussian, Inc.: Wallingford, CT, 2009.
(64) *Gaussview*, Rev. 5.09, Linux version; Gaussian Inc.: Pittsburgh.
(65) Chai, J.-D.; Head-Gordon, M. Long-range corrected hybrid density functionals with damped atom−atom dispersion corrections. *Phys. Chem. Chem. Phys.* **2008**, *10*, 6615−6620.
(66) Dunning, T. H. Gaussian basis sets for use in correlated molecular calculations. I. The atoms boron through neon and hydrogen. *J. Chem. Phys.* **1989**, *90*, 1007−1023.
(67) Halsey-Moore, C. H.; Jena, P.; McLeskey, J. T., Jr Tuning range-separated DFT functionals for modelling the peak absorption of MEH-PPV polymer in various solvents. *Comp. and Theor. Chem.* **2019**, *1162*, 112506.
(68) Martins, A. F.; Morfin, J.-F.; Geraldes, C. F. G. C.; Tóth, É. Gd^{3+} complexes conjugated to Pittsburgh compound B: potential MRI markers of β-amyloid plaques. *J. Biol. Inorg. Chem.* **2014**, *19*, 281−295.
(69) Huang, L.; Quada, J. C., Jr; Lown, J. W. Design, Synthesis, and Sequence Selective DNA Cleavage of Functional Models of Bleomycin. 1. Hybrids Incorporating a Simple Metal-Complexing Moiety of Bleomycin and Lexitropsin Carriers. *Bioconjugate Chem.* **1995**, *6*, 21−33.
(70) Price, E. W.; Cawthray, J. F.; Bailey, G. A.; Ferreira, C. L.; Boros, E.; Adam, M. J.; Orvig, C. H_4octapa: An Acyclic Chelator for ^{111}In Radiopharmaceuticals. *J. Am. Chem. Soc.* **2012**, *134*, 8670−8683.

https://doi.org/10.1021/acsabm.3c01236
ACS Appl. Bio Mater. 2024, 7, 1831−1841